Coplanar Waveguide with Elevated Center Strip Conductor Based on HR-Si Substrate

Xiuzhi Wen[1,2], **Yanling Shi**[1,2], **Jing Liu**[1], **Fuquan Cao**[1], **Yanfang Ding**[1], **Xi Li**[1]
Hao Huang[3], **Hongbo Ye**[3], **and Linyan Xue**[3]

[1]Department of E. E., East China Normal University, China
[2]State Key Laboratories of Transducer Technology, China Academy of Sciences, China
[3]Shanghai IC Research and Development Center, China

Abstract— In this paper, an elevated CPW based on high-resistivity silicon is presented. The center strip conductor is elevated on a silicon dioxide layer which can be easily fabricated by thermal oxidation. This extra silicon dioxide layer under the center strip conductor weakens the magnetic-field, which could be validated by the HFSS simulation. Compared with the conventional CPW with the center strip and ground planes on the same plane, the elevated CPW's insertion loss can be decreased. The simulated and measured results are in good agreement. And the process flow is compatible with the mainstreamed CMOS technology.

1. INTRODUCTION

Coplanar waveguide lines (CPW) is an important component in microwave field and it is widely used in monolithic microwave integrated circuits (MMIC) and modern communication systems [1]. Practical application of integrated circuits requires operation over radio frequency. The investigation on the performances of CPW structures on Si-based substrates as a function of frequency gains interest [2, 3]. The loss of CPW lines on low-resistivity silicon is high in the traditional IC technology. There are several ways to solve this problem at present.

For the CPW lines on low-resistivity silicon produced through MEMS technology, the measured loss at 30 GHz is 6 dB/cm. The backed V-shaped cavity reduces the electromagnetic coupling effect between the substrate and devices, but the difficulty of technology is aroused [4].

Another method is to fabricate CPW on high-resistivity silicon (HR-Si). Gold metalized CPWs with 1.45 μm thickness on 2005 Ω· cm HR-Si substrates have been shown a measured attenuation of 1.03 dB/cm at 30 GHz [5, 6].

This letter proposes an elevated CPW based on high-resistivity silicon. The center strip conductor is elevated on a layer of silicon dioxide which can be easily fabricated by thermal oxidation. The magnetic-field concentrating near the center strip conductor is decreased. As a result, the insertion loss is reduced. Moreover, the technology is compatible with the traditional CMOS technology.

2. ANALYSIS OF THE CPW LOSS

The overall CPW loss can be divided into integration substrate loss and strip metal loss. The loss of CPW lines on low-resistivity silicon is high in the traditional IC technology. The high-resistivity silicon can reduce substrate loss effectively. The magnetic-field which brings loss concentrates near the center strip conductor. Loss is produced due to medium molecule polarization when magnetic field overpasses the medium. Reducing the magnetic distribution on the substrate can decrease the loss.

An extra layer of silicon dioxide under the center strip conductor is fabricated in this elevated structure. The cross section of the elevated structure is shown in Fig. 1. G represents the width of the ground planes, S represents the width of the center strip conductor, W represents the width of the gap between the center strip conductor and the ground plane, H_1 represents the height of SiO_2 under the ground planes, and H_2 represents the height of SiO_2 under the center strip conductor.

The SiO_2 under the center strip conductor is thicker than that under the ground planes ($H_2 > H_1$). This extra silicon dioxide layer under the center strip conductor weakens the magnetic-field, which has been validated by the HFSS simulation. Compared with the conventional CPW with the center strip and ground planes on the same plane, the elevated CPW's insertion loss is decreased. The elevated structure in this paper can improve the performance of CPW lines.

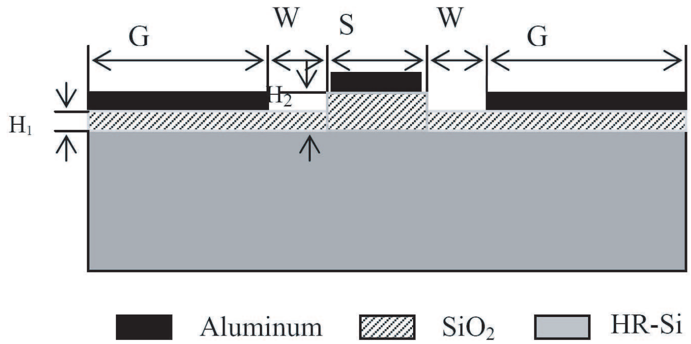

Figure 1: The cross section of the elevated CPW structure.

3. DESIGN AND EXPERIMENT

According to the simulated results by HFSS, 50 Ω Aluminum CPW lines have been fabricated on HR-Si of 1000 Ω · cm. The length of CPW lines is 2000 μm. The width of the center strip conductor S is 39 μm and the gap W is 24 μm. The Aluminum lines are isolated from Si substrate by oxide layer. Three CPW lines with different H_2 heights have been fabricated. Table 1 shows the different heights of oxide layer.

Table 1: CPW with different elevated heights.

Height / CPW Number	H_1	H_2
L_1	0.1 μm	0.1 μm
L_2	0.1 μm	0.2 μm
L_3	0.1 μm	0.3 μm

To fabricate the CPWs in Table 1, the silicon wafers have been cleaned first. Take CPW L_3 for example, 0.3 μm SiO_2 has been grown. Then keep the SiO_2 under the center strip conductor to form a step while SiO_2 elsewhere is removed. Then grow 0.1 μm SiO_2 on the wafers again. Pure aluminum is evaporated and patterned to produce aluminum CPW lines on the silicon dioxide surface. The CPW L_1 and CPW L_2 are fabricated in the same way.

4. RESULTS AND DISCUSSIONS

The simulated S-parameters of CPW L_1 are presented in Fig. 2. There are good transmission coefficient and reflection coefficient.

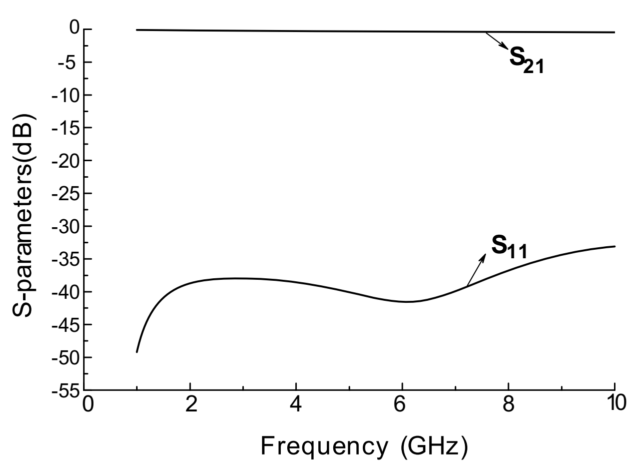

Figure 2: Simulated S-parameters of CPW L_1 based on HR-Si.

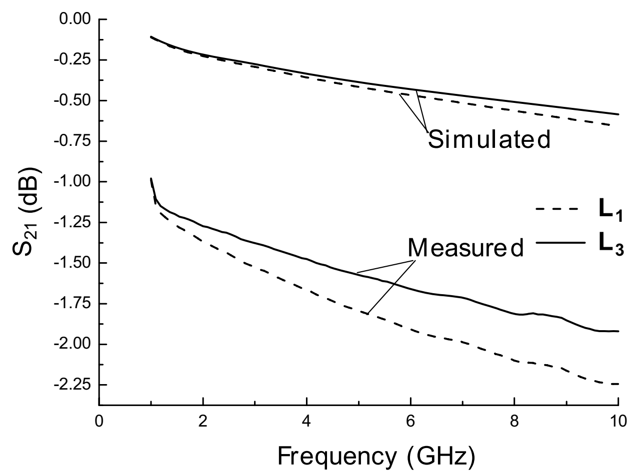

Figure 3: Measured and simulated S_{21}-parameters of L_1, L_3 CPWs.

The simulated and measured results of CPWs L_1, L_3 are in good agreement, as shown in Fig. 3. The loss of elevated CPW L_3 is lower than that of conventional CPW L_1 over the measured frequency range (10 M–10 GHz). At 5 GHz, the measured losses of CPW L_3 and L_1 are -1.6 dB, -1.8 dB seperately. The loss difference of these two structures becomes clear as the frequency rises due to the thicker SiO_2 under the center strip conductor of the elevated CPW L_3. It weakens the magnetic-field between the center strip conductor and substrate. However, the measured insertion loss (-1.91 dB) is -1.33 dB larger than the simulated loss (-0.58 dB) at 10 GHz, which may be due to the loss caused by the probe during test process.

In Fig. 4, the loss of CPW L_3 is 1.91 dB at 10 GHz, and the loss of CPW L_2 is 2.02 dB. That also shows that the magnetic-field is weakened and the performance improves.

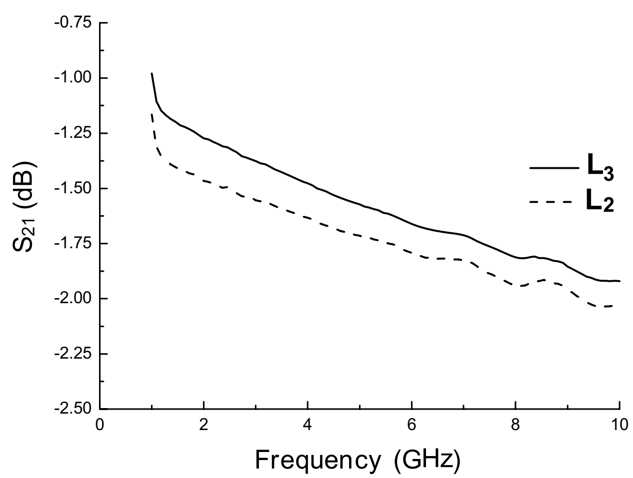

Figure 4: Measured S_{21}-parameters of CPWs L_3, L_2.

5. CONCLUSIONS

In the elevated CPW structure, the SiO_2 under the center strip conductor is higher than that under the ground planes. The elevated SiO_2 not only isolates CPW from the substrate but also weakens magnetic-field apparently. So the performance of CPW is improved. The simulated and measured results of the elevated CPW are in good agreement. Thus this elevated structure is available for low-loss SiMMIC applications up to radio frequency.

ACKNOWLEDGMENT

This work was supported by Natural Science Foundation of China (No. 60676047, 60606010), Foundation of Shanghai Science & Technology Committee (04QMX1419,075007033) and Shanghai-Applied Materials Research and Development Fund (No. 0522).

REFERENCES

1. Liu, H., L. Sun, T. Yoshimasu, et al., "Slot resonator-based electromagnetic bandgap coplanar waveguide and its filter application," *Physics Letters A*, Vol. 359, No. 3, 171–174, 2006.
2. Sohn, J., S. H. Han, M. Yamaguchi, S. H. Lim, et al., "Effects of the magnetic layer length on the high-frequency characteristics of an integrated-type coplanar wave-guide transmission line," *Journal of Magnetism and Magnetic Materials*, Vol. 310, No. 2, Part 3, 2563–2565, 2007.
3. Si, M. M., C. Pavageau, D. Lederer, L. Picheta, et al., "Behaviour of TFMS and CPW line on SOI substrate versus high temperature for RF applications," *Solid-State Electronics*, Vol. 50, No. 11–12, 1822–1827, 2006.
4. Veljko, M., G. Michael, D. B. Edwin, et al., "Micromachined microwave transmission lines in CMOS technology," *IEEE Transactions on Microwave Theory and Techniques*, Vol. 45, 630, 1997.
5. Wu, Y., H. S. Gamble, B. M. Armstrong, et al., "Interface layer effects on microwave loss of high resistivity CPW line," *IEEE Microwave Guided Wave Letters*, Vol. 9, No. 1, 10–12, 1999.
6. Gamble, H. S., B. M. Armstrong, J. N. Mitchell, et al., "Low-loss CPW line on surface stabilized high-resistivity silicon," *IEEE Microwave Guided Wave Letters*, Vol. 9, No. 10, 395–397, 1999.

Miniaturization of Harmonics-suppressed Filter with Folded Loop Structure

Han-Nien Lin[1], **Wen-Lung Huang**[2], **and Jer-Long Chen**[3]

[1]Department of Communications Engineering, Feng-Chia University, Taiwan, R.O.C.
[2]Department of Electrical Engineering, Feng-Chia University, Taiwan, R.O.C.
[3]Department of Electrical Engineering, National Taiwan Ocean University, Taiwan, R.O.C.

Abstract— In this paper we utilize a basic loop resonator to design and realize the bandpass filter, and then use the quarter-wavelength open stub to suppress the second and third harmonics. Electric and magnetic coupling in this filter will be realized by a narrow coupled gap and grounded via to achieve the transmission zeros in either the lower or upper stopband. Since the prototype of the original bandpass filter is a resonator-based one wavelength structure, it is slightly larger compared with the other proposed structures. We therefore utilize the folding loop structure of the circuit to achieve miniaturization. The 30% reduction of the circuit size is achieved. The circuit with folded structure not only can reduce the size but also can maintain the performance as original structure with only slight degradation on the third harmonic. The result of the measurement and simulation is in good agreement to provide an experimental verification on the compact filter design.

1. INTRODUCTION

Microwave/RF filters are the key components in RF front-ends, so the performance of filter is important to the modern wireless communications. In the past, the design rules in many type of filters were quite complete, therefore the future research in filter design will be focused on high selectivity or harmonics suppression capability. Besides the fundamental resonance of unwanted signal, the similar resonance can also be generated on second, third, or even higher order harmonic frequencies, but those higher order resonances might pass the filter and cause the electromagnetic interference. Therefore many literatures have been proposed to suppress the harmonics with quarter-wavelength open stub [1], spurline [2], step impedance resonator [3, 4]; With quarter-wavelength open stub and spurline being used as bandstop filter to filter the unwanted signal, and step impedance resonator being used to shift the harmonic frequency to higher frequencies.

Recently, the higher performance requirement in communication-system was demanded, and the noise control scheme was also become more strictly. If the filter can be designed to improve selectivity, then the noise will be filtered out effectively and provide the better signal to noise ratio. In the past, the most filters were originally designed to provide the selectivity by using the higher order elliptic filter [5], or later by using the cross coupled (electric coupling, magnetic coupling and mixed coupling) to achieved the transmission zeros generated in lower, upper stop or even in both bands [6]. However, the two methodologies above have the disadvantage of their large sizes. The filter in [7] achieved high selectivity by using separate electric and magnetic coupling without any size reduction of filter. In order to reduce physical dimension of the filter, lumped elements [8], capacitive termination [9], aperture coupled [10] or folded structure [11] are frequently used in miniaturizing RF/microwave filters. However the lumped element method is known to have very poor quality factors for the insertion loss and out-of-band rejection. Therefore many miniaturization design techniques are still under investigation.

The filter we proposed in this paper, not only can suppress the second and third harmonics with quarter-wavelength resonators, but also improve the selectivity with narrow coupled gap and grounded vias to generate the transmission zeros in both lower and upper stopbands. Finally, we utilize the folding loop for the filter circuit to achieve the miniaturization.

2. LOOP FILTER

In this paper, a filter configuration (see Fig. 1). The FR-4 dielectric substrate with permittivity of $\varepsilon_r = 4.4$ and thickness of 1.6 mm.

The prototype filter was based on a loop resonator, where the resonant condition occurs when the length of microstrip line equals to one guided wavelength of the resonance frequency. The feeding line in this filter (see Fig. 1) is different from the other filters. This feed type can improve the coupling energy and reduce the insertion loss as used in [8], for the particular structure with l_1 and l_2

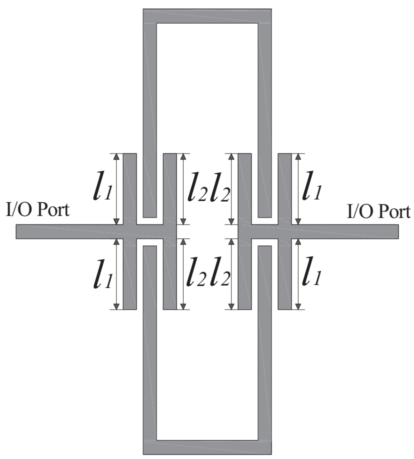

Figure 1: Prototype filter configuration.

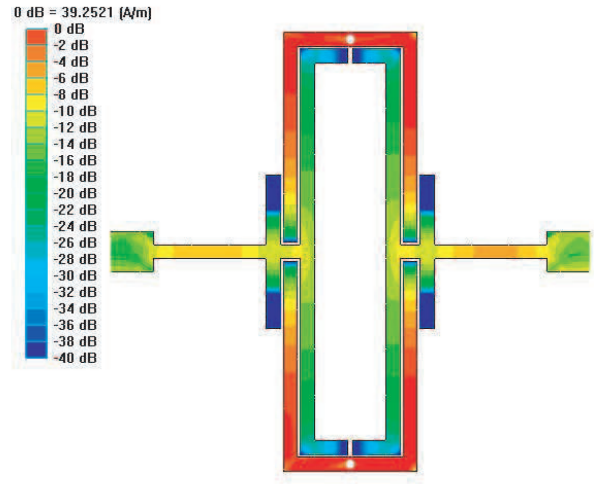

Figure 2: The current distribution at 2.4 GHz.

being used as quarter-wavelength open stubs, where different lengths are used to achieve harmonics suppression. The two quarter-wavelength stubs were close to each other. When we made the length of l_2 longer, the electric coupling can then be realized by utilizing the coupling gap to generate an additional transmission zero at the upper stopband. When the signal is injected to the transmission line, the current distribution can be determined and show the maximal magnitude near the quarter-wavelength of the transmission line (the current distribution can be seen clearly in Fig. 2). Based on this principle, magnetic coupling can also be introduced by a grounded via to generate an additional transmission zero at the lower stopband. After adjusting the filter configuration shown in Fig. 3, the real circuit size (see Fig. 1) can be reduced to about 31.5 mm × 12 mm.

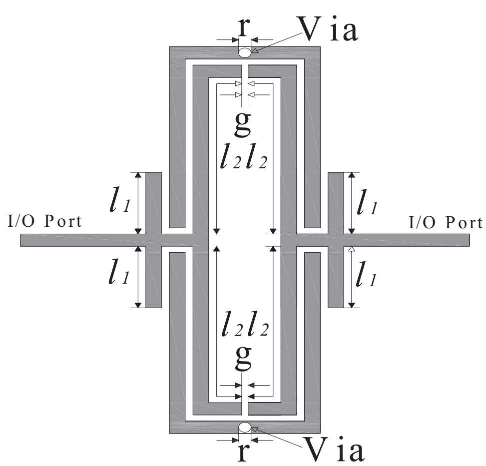

Figure 3: The filter configuration after adjusting. (all the line width is 1 mm; the space of line to line is 0.2 mm).

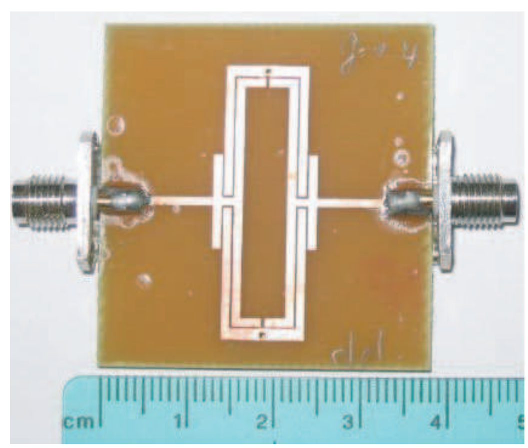

Figure 4: The photograph of the prototype filter.

In this paper, commercial EM software IE3D version 10.0 and PNA network analyzer Agilent E8362B are used in simulation and measurement respectively. To meet the design goal, we first utilize the principle of quarter-wavelength transmission line by adjusting the length of l_1 and l_2 to suppress the second and third harmonics. However, the lengths of l_1 and l_2 are different, because the l_1 and l_2 are both the tightly adjacent paths of the loop resonator with the parasitic effect introduced by the gap between the lines. It thus affects the original quarter-wavelength long open stubs. The resulting effect of different l_1 and l_2 is shown in Fig. 5. We finally obtained the optimum length with $l_1 = 5$ mm and $l_2 = 15.5$ mm with the second and third harmonics being suppressed -30 dB and -15 dB respectively. Although the quarter-wavelength open stubs have good harmonics suppression performance, but the lower frequency response tends to rise up and degrade performance as shown in Fig. 5. Therefore, the grounded via is introduced to achieve magnetic coupling and thus generate an additional transmission zero at the lower stopband. Up to this point, our filter design not only can compensate the effect of different l_1 and l_2, but also can improve the selectivity and therefore enhance the system performance. As to the determination of grounded via location, the maximum magnitude of the current distribution should occur near the quarter-wavelength position of the transmission line (see Fig. 2) from the transmission line effect. Therefore the location of grounded via was chosen at quarter-wavelength distance away from the feed point (see Fig. 3).

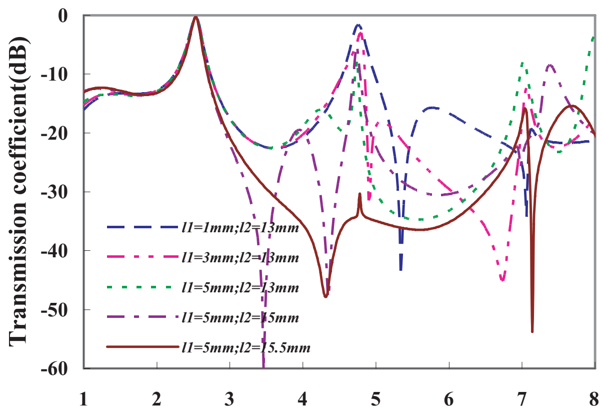

Figure 5: The frequency response of different length with l_1 and l_2.

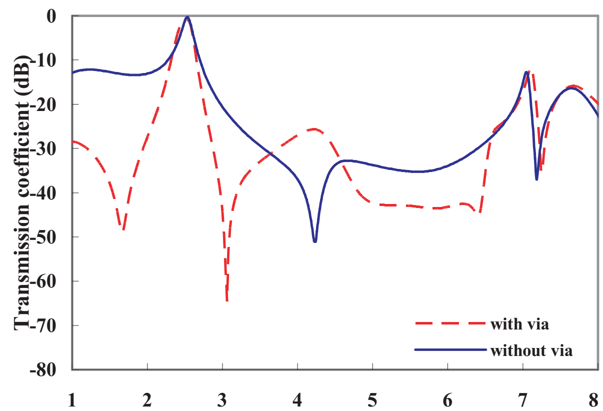

Figure 6: The frequency response with or without via ground.

The frequency response with or without grounded via can be seen clearly from Fig. 6, where an additional transmission zero is generated at about 1.7 GHz with a -46 dB dip. On the other hand, the electric coupling will generate an additional transmission zero at the upper side of the passnband by a narrow gap between two open stubs. Fig. 7 shows the cases with different gap spacing g (0.2 mm $\sim$ 0.7 mm), the smaller the spacing g the closer the transmission zero to the passband and therefore the larger capacitance. For the purpose of suppressing second harmonic, the g = 0.4 mm is considered the optimum value. The Fig. 8 shows the transmission coefficient of the proposed filter with excellent selectivity and good rejection performance in out-of-band.

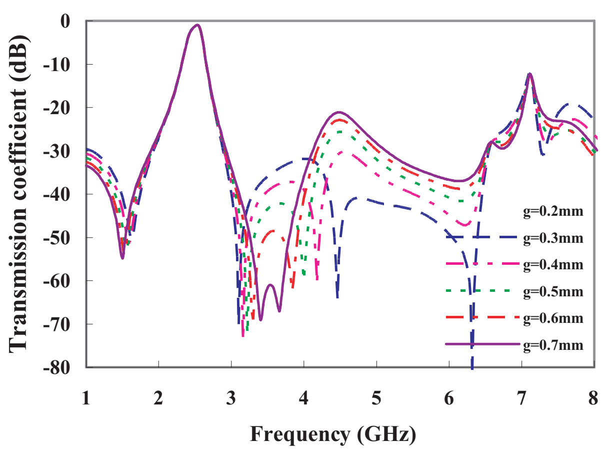

Figure 7: The frequency response of different coupled gap.

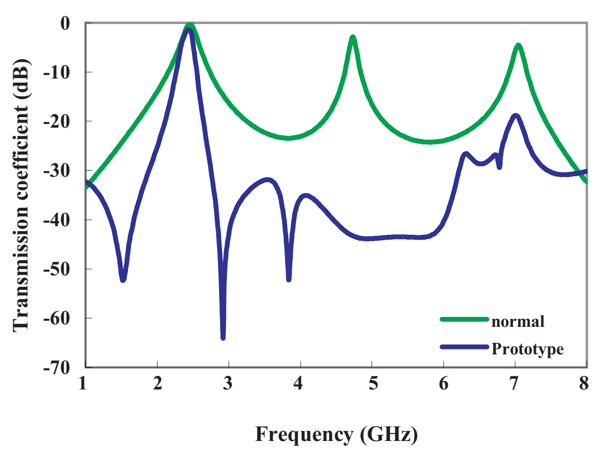

Figure 8: The frequency response of prototype filter.

3. COMPACT SIZE FILTER

In the previous section, we have designed the bandpass filter that not only can suppress the second and third harmonics, but also can improve the selectivity in the same time. However, since the structure of the filter is based on one wavelength resonant condition of a loop, it's dimension is usually larger than others. Therefore, we try to make filter smaller size by folding the prototype structure. The proposed filter structure is shown in the Fig. 9, where the folded structure was used in the resonant loop path and internal quarter-wavelength open stub. The proposed filter is divided into two parts from the symmetrical plane with the spacing n controlling the coupling between two separate parts. The smaller the spacing n, the more coupling will occur between two separate partitions. Therefore, the spacing should be carefully decided. In order to maintain the performance of the selectivity, we double the number of grounded via for more magnetic coupling and to make the transmission zero much closer to the passband. While electric coupling is made by the gap between internal open stubs, it is a little different from the prototype but the same performance is kept.

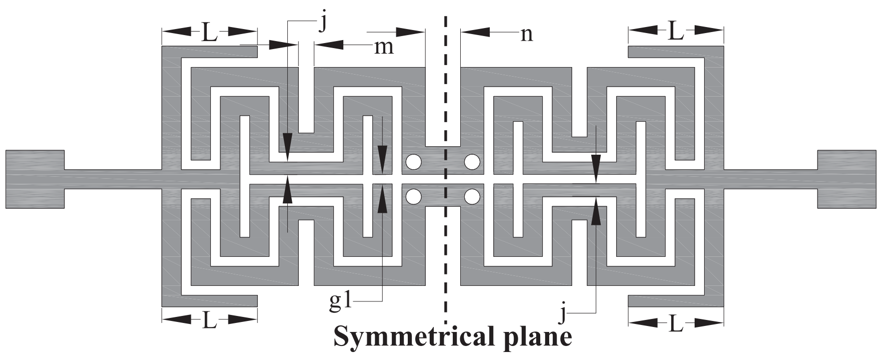

Figure 9: Proposed filter structure. (L = 1.7 mm; m = 0.2 mm; n = 0.9 mm; j = 0.5 mm; g1 = 0.2 mm).

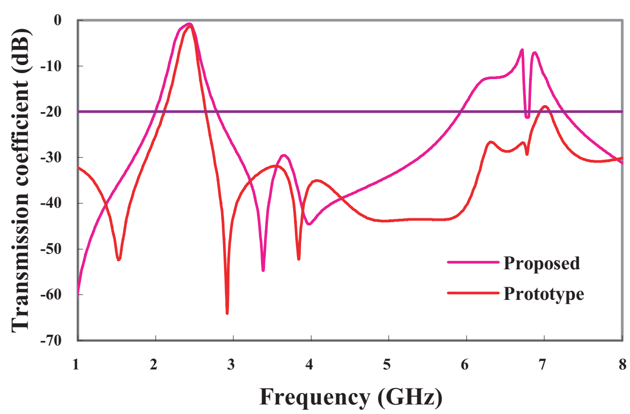

Figure 10: The frequency response compared with proposed and prototype filter.

The transmission coefficients of the proposed filter and original prototype filter were compared in Fig. 10, the transmission zeros of the proposed filter are found located farther away than the prototype because of the effect from folded structure. Meanwhile, the effect of magnetic and electric coupling was also decreased. The second harmonic was found below -30 dB, but the third harmonic was only reduced by -6.5 dB probably because of the open stub bending. The proposed filter was fabricated with a small size 23.5 mm $\times$ 11.5 mm, it is smaller than the original prototype (31.5 mm $\times$ 12 mm) with size reduction up to about 30%.

4. SIMULATION AND MEASUREMENT

The simulated and measured results of S_{11} and S_{21} are illustrated in Figs. 8 and 9 respectively. From the plot of S_{21}, the trend is found to be approximately close to each other. The second and third harmonics suppression is achieved about -25 dB and -17 dB, respectively. The discrepancies in transmission zeros between the measurement and simulation might come from the dimension error of the structure due to inaccurate fabrication of grounded via and narrow coupling gap. While the discrepancies in S_{11} between the measurement and simulation at 7.18 GHz might be due to the material loss. To verify the effect, we use the perfect material characteristics in simulation from

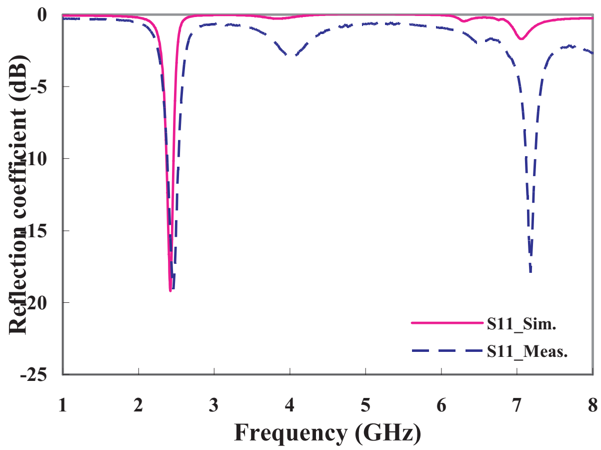

Figure 11: Simulated and measured of reflection coefficient of prototype filter.

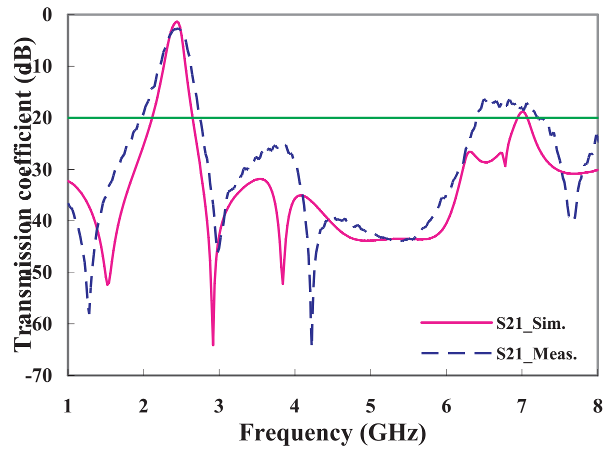

Figure 12: Simulated and measured of transmission coefficient of prototype filter.

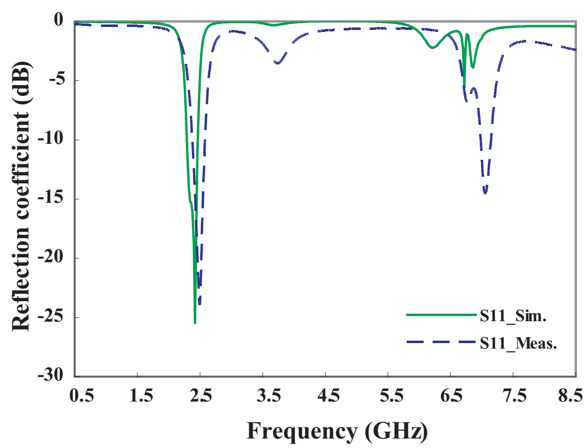

Figure 13: Simulated and measured of reflection coefficient of proposed filter.

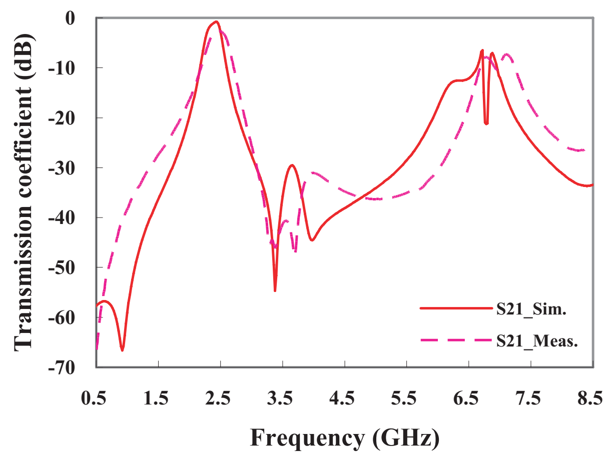

Figure 14: Simulated and measured of transmission coefficient of proposed filter.

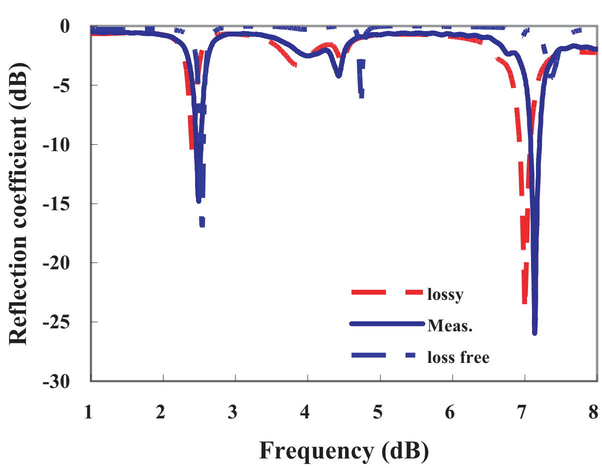

Figure 15: Reflection coefficient of different material.

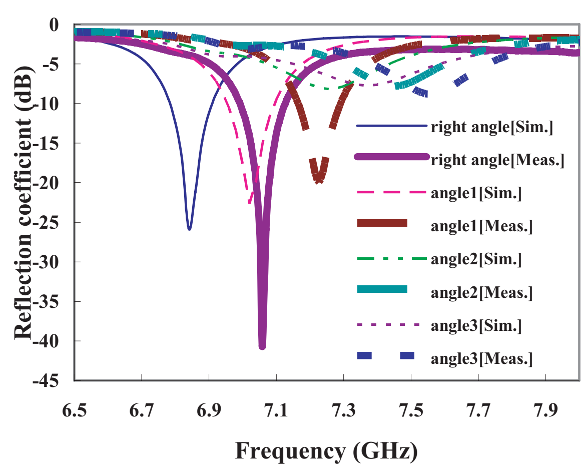

Figure 16: Reflection coefficient of different angle.

the beginning and found the discrepancy around 7.18 GHz is large. However, when we take the material loss into account, the results of simulation and measurement was in good agreement at 7.18 GHz. In order to improve the agreement for high frequency, we modified the bending corner of the structure to different angles for investigation. After modifying the bending corner to the bevel angle, the material loss effect was improved. From the result of Fig. 16, the modified corner technique not only makes the material loss effect reduced from -40 dB to -7 dB, but also proves that the bevel angle corner is necessary for the high frequency implementation.

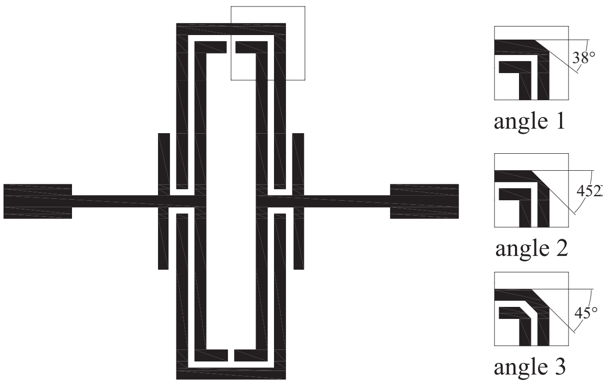

Figure 17: Different angle of the corner.

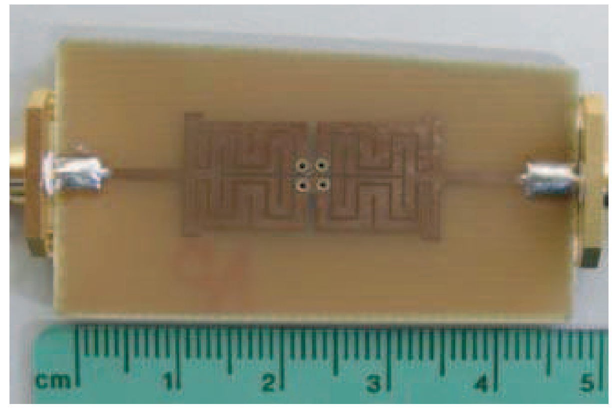

Figure 18: The photograph of the prototype filter.

5. CONCLUSIONS

In this paper, the original prototype filter can obtain the transmission zeros in both the lower and upper stopbands, and also can suppress the second and third harmonics. It is different from the past filter design that must use the higher order to realize the elliptical filter. Furthermore, the proposed folded-loop structure of the circuit not only can achieve miniaturization with size reduction about 30%, but also can maintain the same excellent performance as original structure with only a slight degradation on the third harmonic suppression. Finally, we have modified the angle of the bending corner to reduce the material loss effect and avoid electromagnetic interference problem.

REFERENCES

1. Park, H.-J., J.-Y. Park, J.-C. Lee, J.-H. Kim, B. Lee, N.-Y. Kim, "A new harmonic-suppressed tunable microstrip-ring bandpass filter," *Microwave and Optical Technology Letters*, Vol. 15, No. 1, 26–29, January 2001.
2. Tu, W.-H. and K. Chang, "Compact microstrip bandstop filter using open stub and spurline," *IEEE Microwave and Wireless Components Letters*, Vol. 15, No. 4, 268–270, April 2005.
3. Tang, C.-W. and H.-H. Liang, "Parallel-coupled stacked SIRs bandpass filters with open-loop resonators for suppression of spurious responses," *IEEE Microwave and Wireless Components Letters*, Vol. 15, No. 11, 802–804, Nov. 2005.
4. Choi, W.-W., K.-W. Tam, and R. P. Martins "Spurious suppressed microstrip bandpass filter with two transmission zeros," *Microwave and Optical Technology Letters*, Vol. 48, No. 10, 1979–1981, October 2006.
5. Zhou, J., M. J. Lancaster, and F. Huang, "HTS coplanar meander-line resonator filters with a suppressed slot-line mode," *IEEE Transactions on Applied Superconductivity*, Vol. 14, No. 1, 28–32, March 2004.
6. Ahn, C.-S., J. Lee, and Y.-S. Kim, "Design flexibility of an open-loop resonator filter using similarity transformation of coupling matrix," *IEEE Microwave and Wireless Components Letters*, Vol. 15, No. 4, 262–264, April 2005.
7. Ma, K., J.-G. Ma, S. Y. Kiat, and M. A. Do, "A compact size coupling controllable filter with separate electric and magnetic coupling paths," *IEEE Trans. Microwave Theory Tech.*, Vol. 54, No. 3, 1113–1119, March 2006.
8. Lei, M.-F. and H. Wang, "An analysis of miniaturized dual-mode bandpass filter structure using shunt-capacitance perturbation," *IEEE Trans. Microwave Theory Tech.*, Vol. 53, No. 3, 861–867, March 2005.
9. Cheong, P., S.-W. Fok, and K.-W. Tam, "Miniaturized parallel coupled-line bandpass filter with spurious-response suppression," *IEEE Trans. Microwave Theory Tech.*, Vol. 53, No. 5, 1810–1816, May 2005.

10. Chen, C.-F., T.-Y. Huang, C.-H. Tseng, R.-B. Wu, and T.-W. Chen, "A miniaturized multilayer quasi-elliptic bandpass filter with aperture-coupled microstrip resonators," *IEEE Trans. Microwave Theory Tech.*, Vol. 53, No. 9, 2688–2692, Sept. 2005.
11. Lee, J. and K. Sarabandi, "A miniaturized conductor-backed slot-line resonator filter with two transmission zeros," *IEEE Microwave Wireless Components Lett.*, Vol. 16, No. 12, 660–662, Dec. 2006.

Broadband Amplifier Gain Slope Equalization Filter

Qian Ma[1] **and Mingbo Ma**[2]

[1]Zhejiang University, China
[2]Jilin University, China

Abstract— Since the achievable gain of transistors typically falls off as the frequency increases, an equalization filter with positive gain slope is necessary to compensate for the gain roll-off of broadband amplifiers. This paper proposed an novel equalizer structure and design a equalization filter by applying this novel structure and a modified SIW-PBG (Substrate Intergrated Waveguide-Photon BandGap) filter. The numerical simulated results show that the proposed design of Gain Slope Equalization Filter has a positive gain slope from 8.5 GHz to 18.5 GHz with good impedance matching,low excess loss,and good selectivity.

1. INTRODUCTION

With the new and increasing demand of the internet and multimedia on the commercial side, RF and microwave amplifiers are being used in many broadband applications in the 2 GHz to 20 GHz [6]. However, Modern microwave and millimeter-wave receivers have long struggle with the excessive pass-band negative ripple and gain slopes [4]. Therefore,the equalization filter with a sloped pass-band performance are needed to provide compensation for the gain roll-off of the active devices.

The ideal passive slope equalizer should be no excess slope(that is, the minimum loss should be 0 dB), and the good matching should present to both source and load. Many types of equalizer circuits are provided in G. Vendelin's work [2]. However, according to momentum-simulated results, simple-form equalizer circuits based on lumped capacitors or inductors usually have a large excess loss and a poor input matching characteristics. One of most direct causes is the parasitic effect of lumped elements at the very high frequencies. These problems are well solved in Matt.Morgan and Travis Newton's work [4] by using non-reflective transmission lines.

However, different from their designs, in this paper we proposed another improved equalizer circuit in which the series resonant circuit in traditional models is substituted by series microstrip gap and high-resistance microstrip lines. In addition, we also apply the SIW-PBG technology and design a filter which provide a high-selectivity stop-band for the equalizer. The numerical simulated results of each parts and the entire performance would be presented in the 3rd section. By applying and synthesizing the two parts, we also design an example which could yield a positive gain compensation of 10 dB between 8.5 GHz–18.5 GHz. It has the characteristics of well-matching, low excess loss, low non-linear distortion and high selectivity.

2. THE DESIGN OF GAIN SLOPE EQUALIZATION FILTER

To meet the both requirements of compensating and filtering, we propose an entire network model as shown in Figure 1. The design of equalizer would be discussed in Section 2.1, and the PBG filter in Section 2.2.

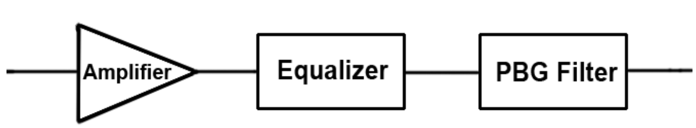

Figure 1: The entire network model.

2.1. Improved Equalizer Structure

Among various equalizer circuits provided by Mellor [3], the circuit shown in Figure 2 presents the best characteristics in good linear slope, good matching and low excess loss. The operating frequency of both the series resonant circuit and the one-quarter-wavelength transmission lines is 5 GHz, which is also the high end frequency of the positive gain slope.

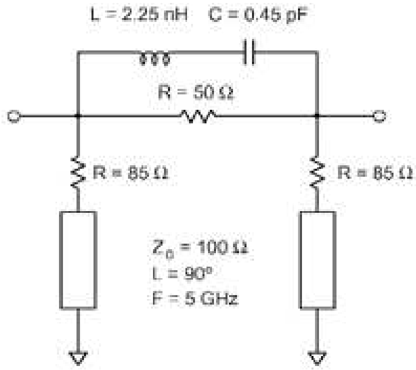

Figure 2: The traditional equalizer circuit.

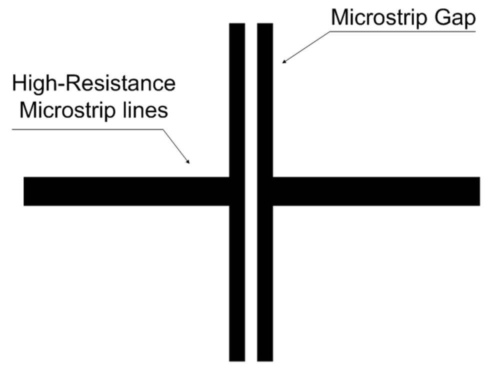

Figure 3: The LC structure after improved.

However, for the parasitic effect, the performance of this circuit get worse a lot when we implement this circuit with chip elements. We find the situation would become much better if we apply boradband adaptive lumped elements, but the cost is also increased at the same time.

To seek less drift effect, the LC series resonant circuit in traditional equalizer model is substituted by microstrip gap and high-resistance microstrip lines as shown in Figure 3. After synthesis and optimization steps, the frequency response of this structure presents approximately the same with the LC series resonant circuit. The entire structure and the parameter definition could be seen in Figure 4.

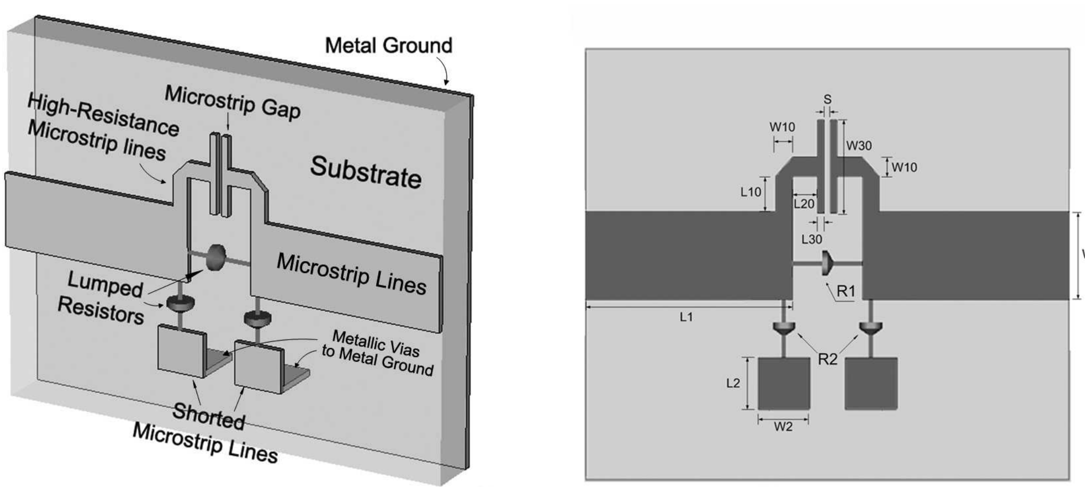

Figure 4: Improved equalizer structure with parameter denition.

2.2. Compact Super-wide Bandpass SIW-PBG Filters

The improved structure described in Section 2.1 could provided a positive gain slope from DC to 18 GHz. To filter out the out-of-band frequencies, we design and apply the SIW-PBG filter for its characteristics of low insertion loss, low band ripples and high selectivity.

On the basis of PBG equivalent circuits and the SIW-DGS (Defect Ground Structure) developed by Zhang-Cheng Hao and Wei Hong [2], we modify the PBG cell structure to meet the requirement of our work as shown in Figure 5. The main purpose of this modification is to reduce the equivalent capacitance and inductance, then increase the cut-off frequency.

The substrate intergrated waveguide provide a excellent high-pass effect, and the photon bandgap yield a periodic stop-band. The entire modified structure and the definition of parameters are presented in Figure 7.

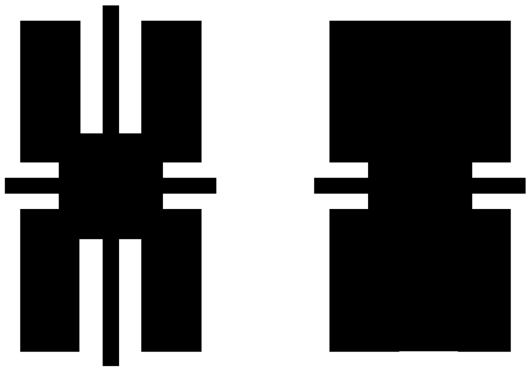

(a) (b)

Figure 5: Modification of PBG cell, (a) The classical cell structure, (b) Modified PBG cell structure.

TABLE I
GEOMETRIC PARAMETERS OF THE EUQALIZER

S (mm)	0.05	W10 (mm)	0.1
W30 (mm)	0.85	L10 (mm)	0.3
L20 (mm)	0.3	L30 (mm)	0.1
W1 (mm)	0.85	W2 (mm)	1
L1 (mm)	4.3	L2 (mm)	0.75
R1 (Ω)	70	R2 (Ω)	35

TABLE II
GEOMETRIC PARAMETERS OF THE SIW-PBG FILTER

Eb (mm)	3.5	Ew (mm)	2
gap (mm)	0.2	Ec (mm)	0.25
Ea (mm)	0.1	sw (mm)	1
Ws (mm)	10.5	Ds (mm)	0.7
Radius (mm)	0.4		

Figure 6: The value of parameters.

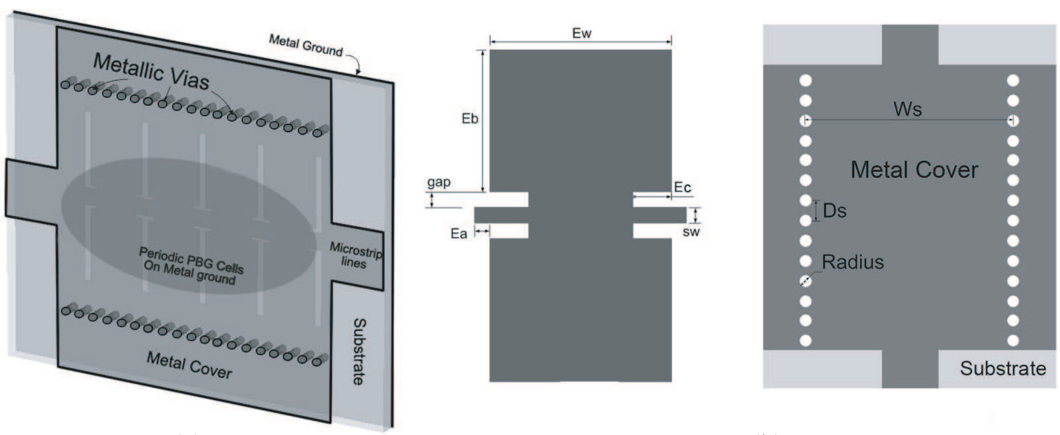

(a) (b)

Figure 7: The proposed PBG structure and the parameter definition, (a) Modified PBG structure, (b) Congurations for PBG cell and the SIW with their geometric parameters.

3. NUMERICAL SIMULATION

To demonstrate performances of positive gain slope equalizer and the wide-band filters, we have investigated these parts with the aid of two software-ADS (Advanced Design System 2003A) and CST (CST Microwave Studio 5.1.3). The dielectric substrate in the simulation model has a thickness of 0.8 mm, a relative permittivity of 4.3, the thickness of metal is 0.03 mm.

3.1. Simulation Results of Gain Slop Equalizer

Simulated by ADS, Figure 8, Figure 9 show the simulation results of schematic models of the improved equalizer structure discussed in Section 2.1. It can be found that the improved equalizer structure proposed provide a linear gain slope between 8.5 GHz–18.5 GHz from −10 dB to 0 dB. The loss at the 18.5 GHz is 0.08 dB. The return loss is better than −15 dB.

With the geometric parameters listed in Table I, the Momentum simulation results of the same structure made by CST could be seen in Figure 10. in the plot of S_{21}, The excess loss is 0.88 dB, and the average value of S_{11} parameter approximates −15 dB.

From the results yielded by CST, we can find that the parasitics of the lumped elements have been greatly reduced. Although worse than schematic results, the performance of this proposed structure show the characteristics of slope, matching and excess loss, which are well enough to meet the requirement of the entire system.

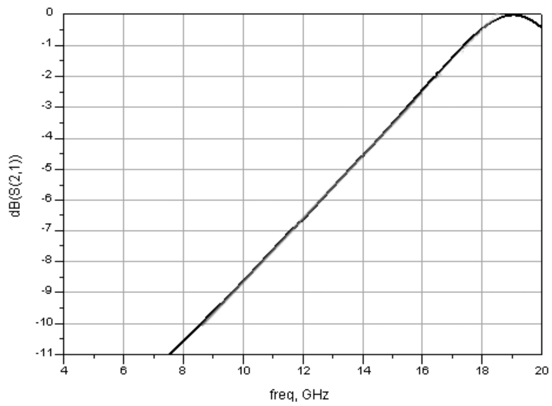

Figure 8: S_{21} plot achieved by ADS.

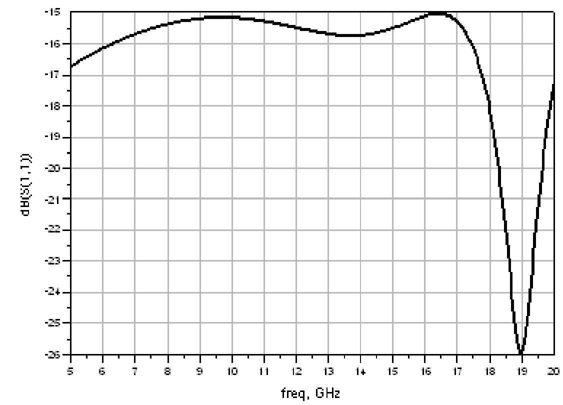

Figure 9: S_{11} plot achieved by ADS.

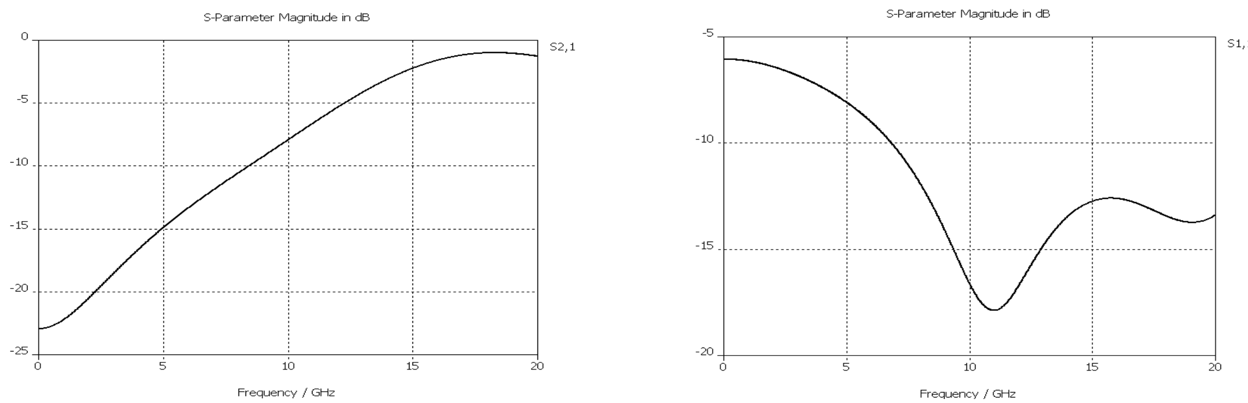

Figure 10: S-parameter plot achieved by CST momentum simulation.

3.2. Simulation Results of SIW-PBG Filter

Obtaining the improved structure equalizer, we design a super-band filter with the passband from 8.5 GHz to 18.5 GHz by applying the new PBG structure discussed in Section 2.2. To enhance the performance, we add the number of PBG cells to 11, and with the parameters listed in Table II, the S-parameters simulated results by CST are shown in Figure 11. According to the results, the average insertion loss of this filter is lower than 0.32 dB, and the return loss is better than -10 dB.

3.3. Simulation of Gain Slope Equalization Filter

To combine the filter and the equalizer proposed in former sections into a series system, we pack and export the data of SIW-PBG filter we designed from CST and import it into ADS. For the two parts have the same input resistance and output resistance (both of their input resistance and output

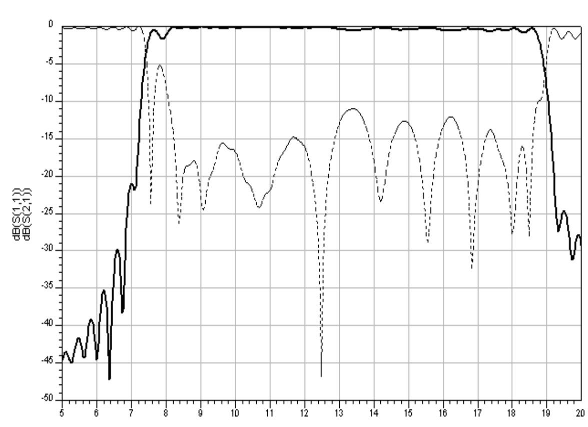

Figure 11: Simulation results of modified SIW-PBG structure achieved by CST.

resistance are 30 Ω), we connect the data package of SIW-PBG filter and the improved equalizer structure in ADS without impedance transformation. The performance of the entire system — Gain Slope Equalization Filter(GSEF) in ADS would be described in Figure 12.

From the Figure 12, we can see that with the excess loss of −0.79 dB, the passband is from 8.5 GHz to 18.5 GHz, and the return loss is better than −10 dB, showing good characteristics of filter selectivity, low insertion loss, linear slope and the impedance matching. In addition, to described the linear performance of this work, we add a ideal reference slope (the lighter line) between 8.5 GHz to 18.5 GHz from −10 dB to 0 dB as shown in Figure 13. The variance and the largest offset between the reference slope and the simulated one are respective 0.164(0.66 dB) and 0.093(0.34 dB).

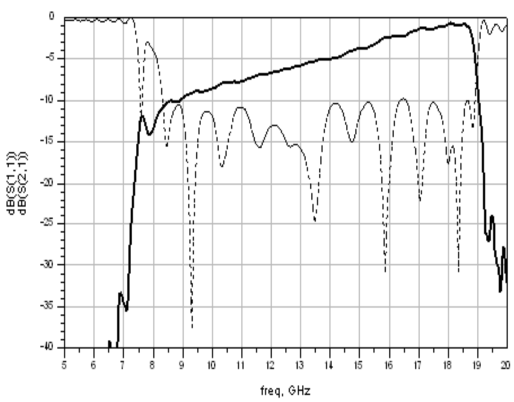

Figure 12: S-parameter plot of the GSEF by ADS.

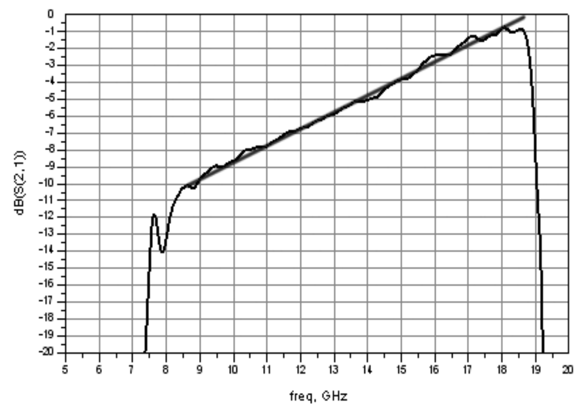

Figure 13: S_{21} plot of the GSEF with reference line.

4. CONCLUSION

Improved equalizer circuit and modified SIW-PBG structure has been proposed. By applying these designs, the GSEF developed in this paper could provide a 10 dB compensation from 8.5 GHz to 18.5 GHz with the excellent characteristics of selectivity, matching, low insertion loss, wide band and low nonlinear distortion.

ACKNOWLEDGMENT

The authors wish to thank Kang-Sheng Chen, Hua-Feng Zhang, Chi Han, and others of ZheJiang University for helpful suggestions and encouragement given throughout the course of this work.

REFERENCES

1. Mellor, D., “On the design of matched equalizers of prescribed gain versus frequency profiles,” *IEEE MTT-S Intl Microwave Symposium*, 308–311, San Diego, CA., June 1977.
2. Hao, Z.-C., W. Hong, J.-X. Chen, X.-P. Chen, and K. Wu, “Compact super-wide bandpass substrate integrated waveguide(SIW) filters,” *IEEE*, 0018–9480, 2005.
3. Vendelin, G., A. Pavio, and U. Rohde, *Microwave Circuit Design Using Linear and Nonlinear Techiques*, J. Wiley and Sons, New York, 1990.
4. Morgan, M., T. Newton, B. Hayward, and T. Boyd, “Non-reflective transmission-line filters for gain slope equalization,” National Radio Astronomy Observatory-NTC, Charlottesville, VA., 22903, 2007.
5. Chen, K.-S., *Electromagnetic Fields and Electromagnetic Waves*, Higher Education Press, 2003.
6. Fejzuli, A., R. Kaarsberg, and N. Roldan, “Broadband amplifier gain slope equalization with a single passive component,” *High Frequency Electronics*, June 2006.

The PBG Filter Design

Cheng-Hung Lin[1], **Guan-Yu Chen**[2], **Jwo-Shiun Sun**[2], **Kwong-Kau Tiong**[1], **and Y. D. Chen**[3]

[1]Department of Electrical Engineering, National Taiwan Ocean University, Taiwan
[2]Department of Electronic Engineering, National Taipei University of Technology, Taiwan
[3]Antenna and EMC Laboratory, High Tech Computer Corp. (HTC), Taiwan

Abstract— The performances of the periodic surface structures of defected shapes on the ground plane for low-pass filter (LPF) co-design are studied. Simulated results with full wave electromagnetic analyses are in good agreement with those experimental data. The optimal structure of double periodic structure bringing about the perturbation electromagnetic waves will be determined. The proposed LPF has defect ground surface with the characteristics of band-gap characteristics.

1. INTRODUCTION

The periodic surface structure is like photonic band-gap (PBG) [1, 2] structures are effective in RF and microwave application that provides an effective control of electromagnetic (EM) waves along specific direction and performance. Controlling the periodic distance of PBG that exist band reject characteristic. Periodic and defected ground structure (DGS) have some excellent performance applied microwave transmission line guide such as the microstrip PBG [3], coplanar waveguide PBG [4], coplanar-stripline PBG [5], uniplanar compact PBG [6] and multiplayer PBG [7]. The perforation patterns of PBG on the ground surface with band-stop and slow wave characteristics are studied. The DGS show great promise in improving the power added efficiency and radiation pattern in high power amplifiers [8], increase the Q value of planar inductor [9] or high efficiency planar antenna [10] application to suppress unwanted sub-harmonic compared to conventional harmonic turning techniques. Some papers also report a new tunable technique on traditional planar filter [11] or DR filter [12] to reject undesired resonator modes.

2. DESIGN & RESULTS

In this paper, a traditional LPF (Figure 1) placed at center the DGS with various PBG structures (Figure 2 and Figure 3) are studied, then proposed high harmonic reject low pass characteristic on PBG microstrip line. By the way of measurement and simulation (Figure 4) to detect this structure exist obvious passband, stopband and leaky wave band region then compare with interrelate research papers [13–17]. Via measurement to calculate EM structures [18, 19] on band-gap region, then find DGS structure can apply high reject band characteristic as a perfect low-pass filter circuit. FR4 substrate (dielectric constant 4.4, loss $\tan\delta = 0.015$ and height 1.6 mm) was used for this design and implement, as shown in Figure 5 and Figure 6.

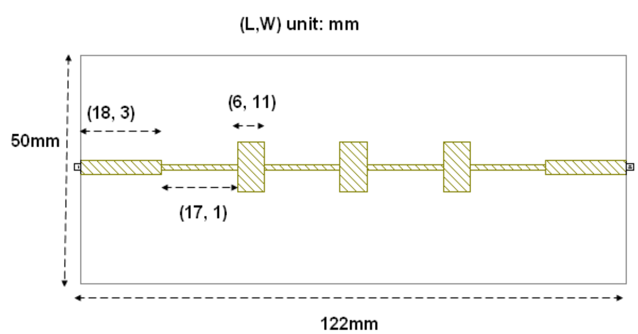

Figure 1: Traditional LPF design with perfect ground plane.

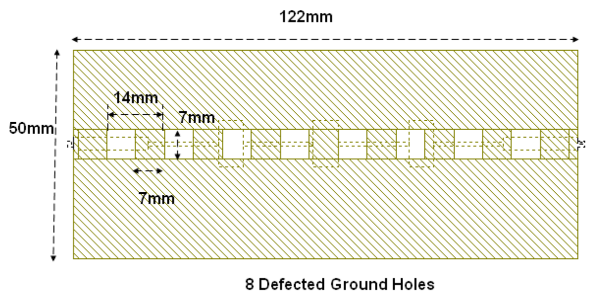

Figure 2: LPF design with periodic and defected ground plane.

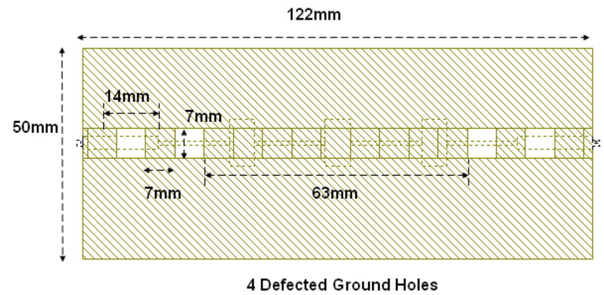

Figure 3: LPF design with non-periodic and defected ground plane.

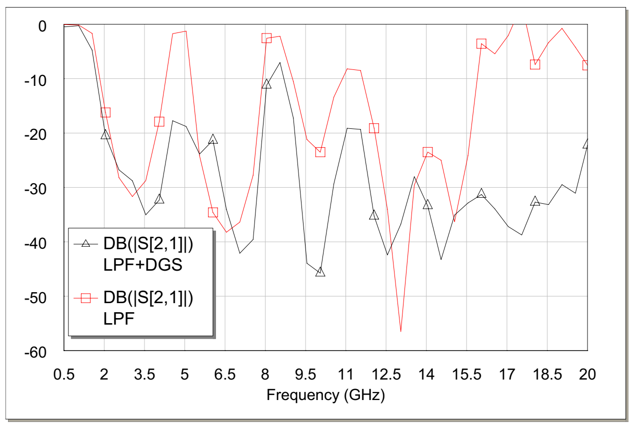

Figure 4: The simulated data of LPF embedded DGS (Fig. 3) and traditional LPF (Fig. 1).

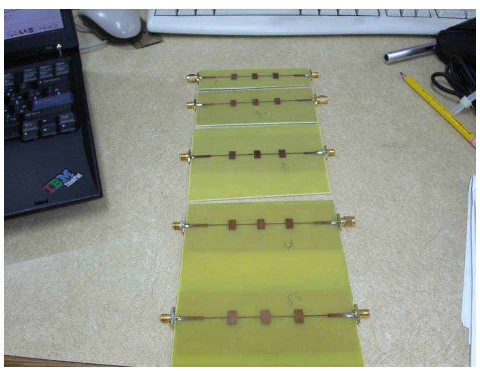

Figure 5: The practical LPF with DGS design (top-plane).

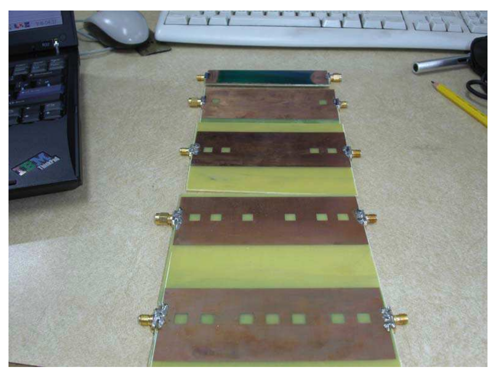

Figure 6: The practical LPF with DGS design (bottom-plane).

3. CONCLUSIONS

This paper describes a harmonic tuning for embedded defected ground plane. EM modeling for a LPF embedded defected ground plane structure co-design is determined. The structure with stop-band characteristic for broadband harmonic rejection tuning has been experimentally verified. Method of moment is applied to simulate the fields and currents distribution of the design. The results of full wave electromagnetic analyses are in good agreement with those experimental data. An optimal structure of the LPF and defected ground plane structure is determined.

ACKNOWLEDGMENT

The authors acknowledge the Antenna and Wireless System Integration Department of High Tech Computer, Corp. (HTC), Taiwan for sport the wireless technique and measurement environment.

REFERENCES

1. Munk, B. A., *Frequency Selective Surfaces: Theory and Design*, John Wiley, New York, 2000.
2. Soukoulis, C. M., *Photonic Band Gaps and Localization*, Plenum Press, New York, 1993.
3. Radisic, V., Y. Qian, R. Coccioli, and T. Itoh, "Novel 2-D photonic bandgap structure for microstrip lines," *IEEE Microwave Guided Wave Letters*, Vol. 8, 69–71, Feb. 1998.
4. Fu, Y. Q., G. H. Zhang, and N. C. Yuan, "A novel PBG coplanar waveguide," *IEEE Microwave and Wireless Components Letters*, Vol. 11, 447–449, Nov. 2001.
5. Yun, T. Y. and K. Chang, "Uniplanar one dimensional photonic bandgap structures and resonators," *IEEE Transactions on Microwave Theory and Techniques*, Vol. 49, 549–2553, Mar. 2001.
6. Caloz, C. and T. Itoh, "A super-compact super broadband tapered uniplanar PBG structure for microwave and millimeter wave applications," *IEEE MTT-S Digest*, 1919–1922, 2002.
7. Caloz, C., C.C. Chang, and T. Itoh, "A novel multiplayer super-compact inharmonic photonic band-gap structure for microstrip applications," *Asia Pacific Microwave Conference (APMC)*, 651–1654, Dec. 2001
8. Radisic, V., Y. Qian, and T. Itoh, "Broadband power amplifier using dielectric photonic bandgap structure [J]," *IEEE Microwave Guided Wave Lett.*, Vol. 8, No. 1, 13–14, 1998.
9. Wu, H. S. and C. K. C. Tzuang, "PBG-enhanced inductor," *IEEE MTT-S Digest*, 1087–1090, 2002.
10. Park, J. Y., C. Caloz, Y. Qian, and T. Itoh, "A compact subdivided square microstrip path antenna for c-band application," *Asia Pacific Microwave Conference (APMC)*, 1143–146, Dec. 2001
11. Yang, F. R., K. P. Ma, Y. Qian, R. Coccioli, and T. Itoh, "A uniplanar compact photonic-bandgap (UC-PBG) structure and its applications for microwave circuits,," *IEEE Transactions on Microwave Theory and Techniques*, Vol. 47, 1509–1514, Aug. 1999.
12. Sun, J. S. and G. Y. Chen, "A new DRF with microstrip PBG structure," *3rd International Conference on Microwave and Millimeter Wave Technology (ICMMT2002)*, 1047–1050, Beijing, Aug. 2002.
13. Shino, N. and Z. Popovic, "Radiation from ground plane photonic bandgap microstrip waveguide," *IEEE MTT-S Digest*, 1079–1082, 2002.
14. Mao, S. G. and M. Y. Chen, "Propagation characteristics of finite width conductor backed coplanar waveguides with periodic electromagnetic bandgap cells," *IEEE Transactions on Microwave Theory and Techniques*, Vol. 50, 2624–2628, Nov. 2002.
15. Wu, C. K., H. S. Wu, and C. K. C. Tzuang, "Electric-magnetic-electric slow wave microstrip line and bandpass filter of compressed size," *IEEE Transactions on Microwave Theory and Techniques*, Vol. 50, 1996–2004, Aug. 2002.
16. Wu, C. K. and C. K. C. Tzuang, "Dual band microstrip leaky mode antenna of similar radiation characteristics," *IEEE AP-S URSI Symposium*, 387–390, 2002.
17. Collin, R. E., *Field Theory of Guided Waves*, IEEE Press, 2nd, New York, 1991.
18. Microwave Office User's Guide, 2000.
19. Sun, J. S. and G. Y. Chen, "Simulation and experiment of the periodic PBG structures at C band," *International Symposium on Communications (ISCOM)*, 97, Nov. 2001.

Optimization of the SAW Transducer Design by Probabilistic Global Search Lausanne

Guiling Huang[1,2], **Qida Zhao**[1], **Luming Zhao**[3], **Shuhong Li**[1]
Junfeng Lv[1], **Fei Wang**, **and Jiping Liao**[1]

[1]Institute of Modern Optics, Nankai University, Tianjin 300071, China
[2]Institute of Photo Electronic Thin Film Devices & Technology
Nankai University, Tianjin 300071, China
[3]Department of Physics, Nankai University, Tianjin 300071, China

Abstract— Complexity is a main shortcoming for designing surface acoustic wave transducer. It is effective to use the optimization program to design SAW transducer IDTs to aim at improvement in the transducer characteristics and shortening of the lead time of the product design. In general, it is difficult to apply the gradient method because there are a lot of semi-optimal solutions in the allowable range of the design parameters. Some researches have done by using global optimization algorithms, in which Genetic algorithms (GAs) are the most widely used. In this paper, a new and promising method based on Probabilistic Global Search Lausanne (PGSL), a new global optimization algorithm which was proposed by Benny Raphael is proposed.

1. INTRODUCTION

Surface acoustic waves (SAWs) are ultrasonic waves propagating along the surface of solids, discovered by Lord Rayleigh [1]. In constrast to plane-wave like bulk-acoustic wave (BAWs), SAWs are localized to the surface of the surface of the substrate with most of their energy confined to within a few wave lengths from the surface. Surface acoustic wave (SAW) devices have been used since the early 1990s as critical components in many radio frequency (RF) transmitters and receivers due to their small size, efficient operation, and excellent performance characteristics. In today's wireless applications, the number of passive SAW components used is on the increase. SAW devices are being used in mobile phones and wireless devices as RF resonator filters, intermediate frequency filters, and local oscillators. In addition, SAW devices have recently been defined and used for sensing various measurands, including gases, liquids, ice, and mechanical vibrations. Various types of SAW devices based on Rayleigh wave, SH-SAW, Love wave, acoustic plate mode (APM), flexural plate wave (FPM) have been explored for sensors and telecommunication applications [2, 3]. A typical SAW device consists of a pattern of electrodes fabricated atop a piezoelectric crystal wafer using lithograghic processes. An interdigital transducer (IDT) [4] performs the function of conversion of electrical energy to mechanical energy and vice versa. IDT is a comb-shaped structure fabricated over the piezoelectric substrate. A voltage applied to the IDT produces dynamic strains in the substrate and initiates elastic waves that travel along the surface. It is effective to use the optimization program to design the IDT structure of the SAW transducer to aim at improvement in the transducer characteristics and shortening of the lead time of the product design. The first optimization algorithm proposed for the linear design of SAW filters was the Remez Exchange algorithm [5, 6]. The least squares method for the design of SAW filters was suggested in [7, 8]. Some researches have done by using global optimization algorithms, in which Genetic algorithms (GAs) are the most widely used [9, 10]. In this paper, a new and promising method based on Probabilistic Global Search Lausanne (PGSL), a new global optimization algorithm which was proposed by Benny Raphael is proposed.

2. THEORY

PGSL is another global optimization algorithm which was proposed by Benny Raphael [11]. It is a direct search algorithm that utilizes global sampling for finding the minimum of a user defined objective function. The power of PGSL is in handling blackbox objective functions (the objective function does not require to be expressed in an explicit mathematical form) and constraints. Gradients are not needed and no special characteristics of the objective functions (such as convexity) are required. PGSL is founded on the assumption that optimal solutions can be identified through focusing search around sets of good solutions. The algorithm includes four nested cycles: Sampling cycle, Probability updating cycle, Focusing cycle and Subdomain cycle, illustrated in Fig. 1 [11].

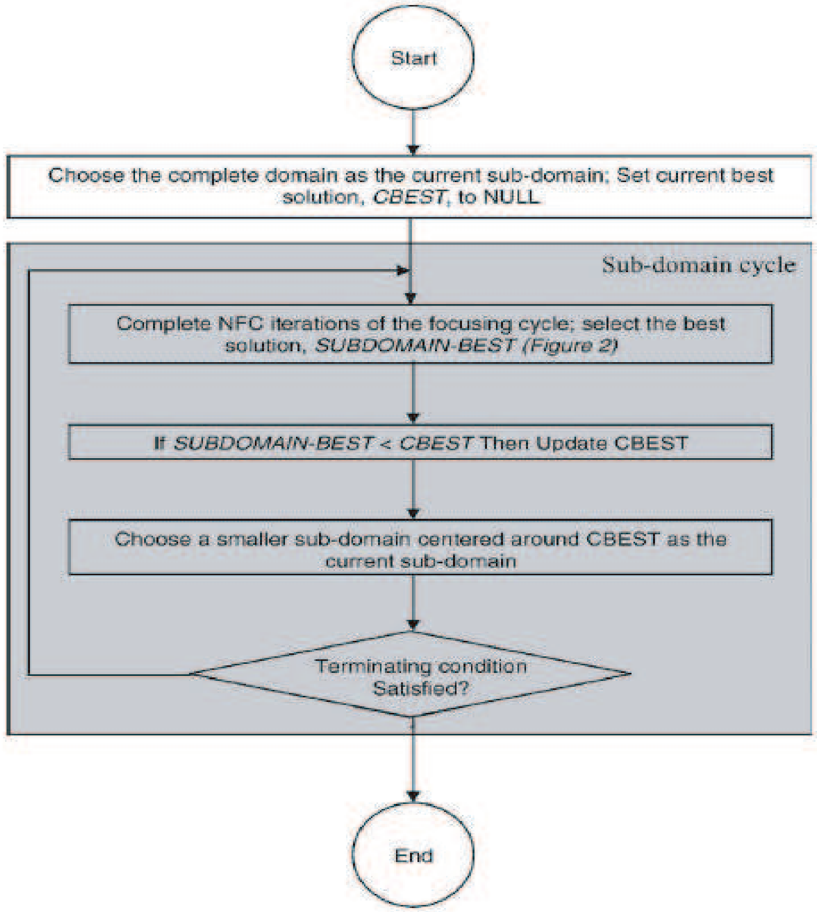

Figure 1: The terminating condition for all cycles, except the sampling cycle, is the completion of the specified number of iterations or the value of the objective function becoming smaller than a user defined threshold.

In the sampling cycle (innermost cycle), a certain number of samples (NS) are generated randomly according to the current probability density function (PDF). Each point is evaluated by the user-defined objective function and the best point is selected. In the next cycle, probabilities of regions containing good solutions are increased and probabilities decreased in regions containing less attractive solutions. In the third cycle, search is focused on the interval containing the best solution after a number of probability updating cycles by further subdivision of the interval. In the subdomain cycle, the search space is progressively narrowed by selecting a subdomain of smaller size centered on the best point after each focusing cycle. Each cycle serves a different purpose in the search for a global optimum. The sampling cycle permits a more uniform and exhaustive search over the entire search space than other cycles. Probability updating and focusing cycles refine search in the neighborhood of good solutions. Convergence is achieved by means of the subdomain cycle. For more details on PGSL the reader is referred to Ref. [11, 12].

3. DISCUSSION AND EXPERIMENT

Here, we take the design of a Withdrawal weighted SAW IDT as an example. To begin with, the objective function E is defined by Eq. (1), which provides a measurement of the deviation between the target frequency responses of withdrawal weighted SAW IDT Htarget (f) and the calculated Hcal (f):

$$E = \sum_{k=1}^{M} \left| \mathrm{Htarg}(f_k) - \sum_{j=1}^{N} a_j \exp\left(-j\frac{2\pi f_k}{V_s}X_j\right) \right| \qquad k = 1, 2, \ldots, \quad j = 1, 2, \ldots, N \tag{1}$$

where V_s is the velocity of the SAW, X_j is the center position of the jth IDT finger, $a_j = 1$ when the volt on the finger is positive and $a_j = -1$ when the volt is negative, M is the number of frequency samples and N is the number of electrode positions in the IDT.

When $N = 50$, $V_s = 3488\,\mathrm{m/s}$, the center frequency $f_0 = 100\,\mathrm{MHz}$ and

$$\begin{aligned}\{a_j\} =&[1,-1,-1,1,-1,-1,-1,1,-1,1,1,1,1,1,-1,1,-1,1,1,1,-1,1,-1,-1,-1,1,\\ &-1,1,-1,-1,-1,1,-1,1,1,1,-1,-1,-1,1,-1,-1,-1,1,1,1,-1,-1,-1,-1];\end{aligned} \tag{2}$$

The target frequency response can be numerically calculated, showed in Fig. 3 (solid curve). Let $\{a_j\}$ be the optimization parameters, we can reconstruct the target frequency response with the PGSL, showed in Fig. 3 (dot curve).

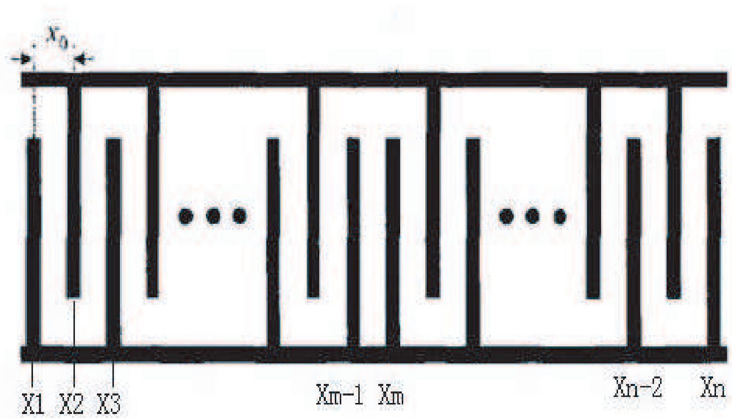

Figure 2: Withdrawal weighted SAW IDT.

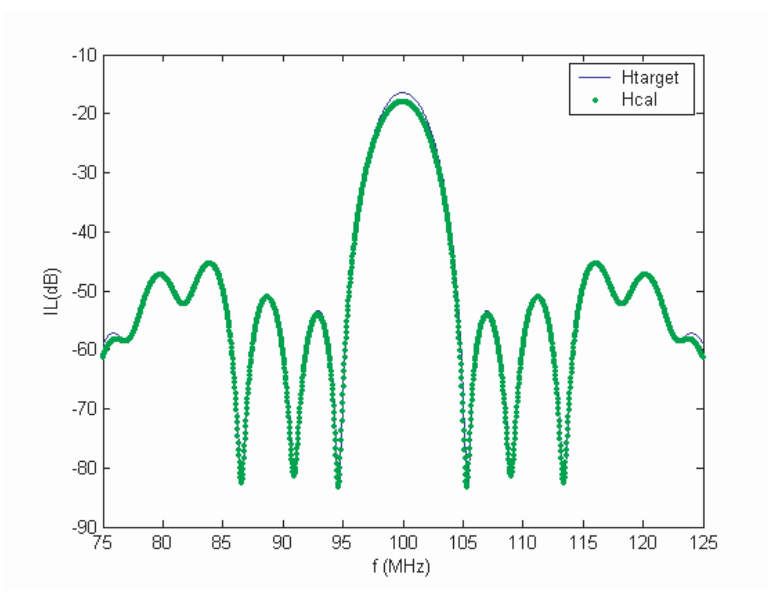

Figure 3: Frequency responses of withdrawal weighted SAW IDT: target (solid curve) and reconstructed with PGSL (dot curve).

4. CONCLUSIONS

In conclusion, the PGSL algorithm has been first used to design the IDT structure of the SAW transducer. We find that such a simple method help to solve complicated problems in a high convergence speed as well as high reliability. Another attractive characteristic of PGSL is that there are not a large number of interrelated parameters in it need to be appropriately fixed. There are only two parameters to be set: one is NFC (the maximum number of focusing cycles), the other is NSDC (the number of subdomain cycles). NFC $= 20 \times n$ (n is the dimension of the problem) and NSDC $= 300/n$ can be used as default values in many tests and the users can tune them for better result if necessary.

ACKNOWLEDGMENT

This work was supported in part by the National Natural Science Foundation under Grant 60572018, by the Tianjin Development Project of Science and Technology under Grant 05YFGPG04900, by the Key Projects in the Tianjin Science & Technology Pillar Program under Grant 07ZCKFGX00200.

REFERENCES

1. Rayleigh, L., "On waves propagated along the plane surface of elastic solid," *Proc. London Math. Society*, Vol. 17, 4–11, 1885.
2. Ballantine, D. S., R. M. White, S. I. Martin, A. I. Ricco, E. T. Zellers, G. C. Frye, and H. Wohltjen, *Acoustic Waves Sensors Theory, Design, and Physico-chemical Applications*, Academic Press, 1997.
3. Gardner, J. W., V. K. Vardhan, and O. O. Awadelkarim, *Microsensors, MEMS, and Smart Devices*, John Wiley & Sons, England, 303–416, 2001.
4. White, R. M. and F. W. Voltmer, "Direct piezoelectric coupling to surface elastic waves," *Appl. Phys. Lett.*, Vol. 7, 314–316, 1965.
5. McClellan, J. H., T. W. Parks, and L. R. Rabiner, "A computer program for designing optimum FIR linear phase digital filters," *IEEE Transactions on Audio and Electroacoustics*, Vol. 21, No. 6, 506–526, December 1973.
6. Parks, T. W. and J. H. McClellan, "Chebyshev approximation for nonrecursive digital filters with linear phase," *IEEE Transactions on Circuit Theory*, Vol. 19, No. 3, 189–194, 1972.
7. Deacon, J. M., "SAW bandpass filter with improved impulse response," *IEE Colloquium on 'Physics and Device Applications of Acoustic Waves'*, London, England, May 22, 1987.
8. Huang, Z., "A least squares approximation design of complex FIR filters," *IEEE International Conference on Acoustics, Speech, and Signal Processing*, Vol. 8, 232–234, 1983.
9. Franz, J., C. C. Ruppel, F. Seifert, and R. Weigel, "Hybrid optimization techniques for the design of SAW-filters," *IEEE Ultrasonics Symposium Proceedings*, 33–36, 1997.
10. Raphael, B. and I. F. C. Smith, "A direct stochastic algorithm for global search," *Appl. Math. Comp.*, Vol. 146, 729–758, 2003.
11. Prabhu, V., B. Panwar, and S. Priyanka, "Linkage learning genetic algorithm for the design of withdrawal weighted SAW filters," *Proceedings of IEEE Ultrasonics Symposium*, Vol. 1, 357–360, 2002.
12. http://imac.epfl.ch/imac/Team/Raphael/PGSL/index.jsp.

Design of Wideband Filter Using Split-ring Resonator DGS

Zheng-Zheng Hou, **Xing-Xing Li**, **and Chao-Kun Hao**

College of Information and Electronic Engineering, Zhejiang Gongshang University
Hangzhou 310018, China

Abstract— The split-ring resonator defected ground structure (SRR DGS) is applied to the wideband filter design in the paper. A micro-strip band-pass filter with a transmission zero at right out-of-band are designed using the equivalent-circuit analysis and curve-fitting method, which is then realized in the actual compact structure, making use of lumped chip capacitors and T-shaped open-circuit stub to achieve series and shunt capacitance, respectively. A band-pass filter with a wide pass-band from 1 GHz to 2.4 GHz is fabricated and measured, and the experimental results have a good agreement with the simulation results.

1. INTRODUCTION

Defected ground structure was firstly proposed by Park et al. based on the idea of photonic band-gap (PBG) structure [1] in 1999, and had found its application in the design of planar circuits and low-pass filters [2, 3]. Defected ground structure is realized by etching a defective pattern in the ground plane of the micro-strip line, which disturbs the shield current distribution in the ground plane, then change the characteristics of a transmission line such as equivalent capacitance and inductance to obtain the slow-wave effect and band-stop property. Compared with the conventional PBG structures, defected ground structure requires only one defected unit to obtain the forbidden-gap property, and the center frequency of the gap is fully determined by the configuration of the defected unit, so it has the advantages of small size, compact structure as well as the facility of equivalent-circuit analysis and filter design [4–6].

Split-ring resonator DGS is becoming one of the most popular DGS types in recent years [7, 8], which introduces a transmission zero at the out-of-band, so it has a much steeper slope for the filter design. In this paper, the split-ring resonator DGS is successfully applied to the design of micro-strip band-pass filter. First, the equivalent-circuit values are extracted by the curve-fitting method; second, a novel wideband filter circuit model is constructed and analyzed; the filter is then realized by using lumped chip capacitances and T-shaped open-circuit stubs and fabricated. Measured pass-band loss is below 1 dB with a wide pass-band from 1 GHz to 2.4 GHz, and from 3 GHz to 8 GHz, the out-band suppression is no less than 25 dB.

2. ANALYSIS OF SPLIT-RING RESONATOR DGS CELL

The SRR DGS is obtained by etching two concentric split-ring defective patterns which have different size and inverse split direction in the ground plane, due to the discontinuity of impedance in defective region, an electromagnetic resonance is obtained and thus a band-gap is formed. As shown in Fig. 1(a), the permittivity of the micro-strip line is $\varepsilon_r = 2.65$, the height of the dielectric board is $h = 1.5$ mm, and width of the conductor line is 4 mm.

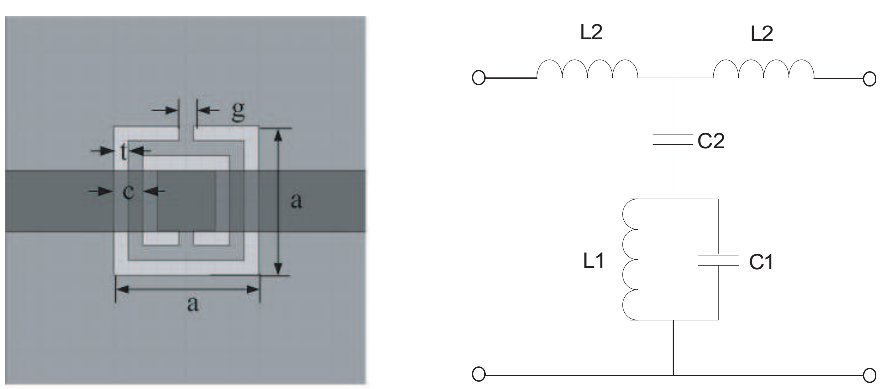

(a) (b)

Figure 1: (a) Structure of the SRR DGS cell, (b) Equivalent-circuit of the SRR DGS cell.

Generally speaking, the split-ring resonator forms a parallel resonator, so etching split-ring defective pattern in the ground plane will add a parallel resonator to the equivalent right-hand transmission line which is composed of two serial inductors and a shunt capacitor. In addition, the parallel tank L_1-C_1 has a capacitive coupling with the conductor line, so the whole equivalent-circuit is achieved as shown in Fig. 1(b). When $a = 10\,\text{mm}$, $g = 1\,\text{mm}$, $t = 1\,\text{mm}$ and $c = 2\,\text{mm}$, by using the curve-fitting and parameter extraction technology, the corresponding equivalent-circuit values of the SRR DGS can be determined as follows: $L_1 = 3.300\,\text{nH}$, $C_1 = 0.430\,\text{pF}$, $L_2 = 2.818\,\text{nH}$, $C_2 = 0.652\,\text{pF}$, Fig. 2 shows the comparison of two different simulation results.

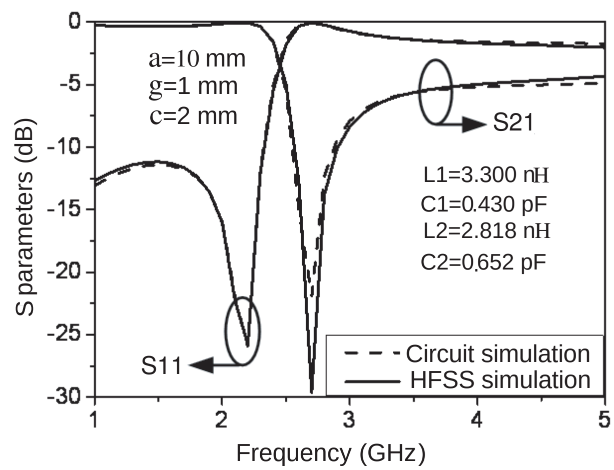

Figure 2: Simulation results of the SRR DGS cell.

3. CIRCUIT MODEL OF SRR DGS BAND-PASS FILTER

In order to apply the SRR DGS to the band-pass filter design, series capacitors are used to realize external coupling and shunt capacitors are introduced to improve the out-of-band suppression. Firstly, we construct a two-stage topology of band-pass filter as shown in Fig. 3, and make an analysis of this circuit model. The transmission zero location of the circuit is determined by the resonant frequency of the shunt circuit, that means it is codetermined by L_1, C_1 and C_2, and the resonant frequency is

$$f_s = \frac{1}{2\pi\sqrt{L_1(C_1 + C_2)}} \tag{1}$$

The frequency response of the circuit model is depicted in Fig. 4, which shows a wide pass-band property. With the optimized circuit values, the filter has a center frequency of 1.7 GHz and a wide relative bandwidth of 0.9. Furthermore, it also has a transmission zero at the right-hand side of the main pass-band, which forms a asymmetry frequency response of wide pass-band filter, so a

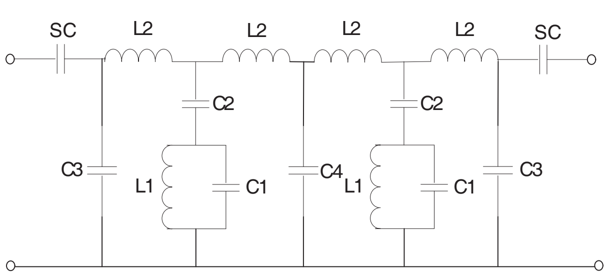

Figure 3: Circuit model of the SRR DGS band-pass filter.

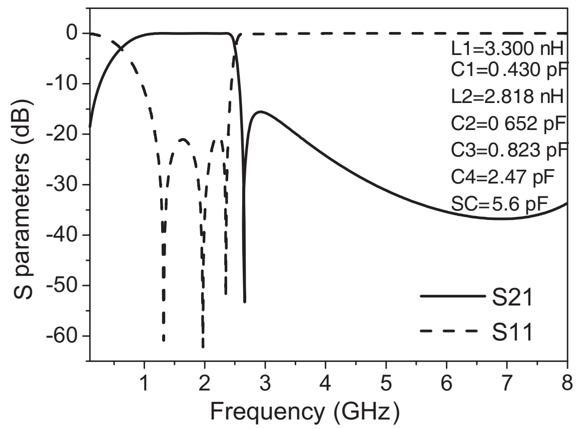

Figure 4: Frequency response of the circuit model for the band-pass filter.

sharp slop and high suppression are obtained at the band-edge. Within a wide frequency range from 3 GHz to 8 GHz, the out-of-band suppression is no less than 25 dB.

4. STRUCTURE AND MEASUREMENT RESULTS

In this paper, we make use of lumped chip capacitor to realize series capacitance of SC=5.6 pF, and T-shaped open-circuit stub to achieve the large shunt capacitance C_3 and C_4, then we can get the corresponding structure model of the pass-band filter as shown in Fig. 5. The size of SRR DGS is the same as the above section, and other parameters are: $w1 = 3$ mm, $w2 = 4$ mm and $L = 7$ mm.

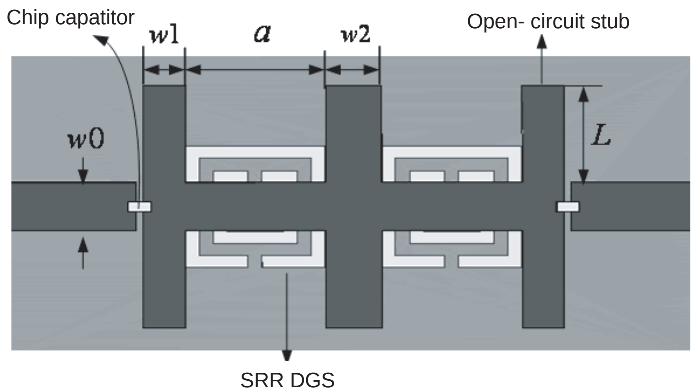

Figure 5: Structure of the proposed SRR DGS band-pass filter.

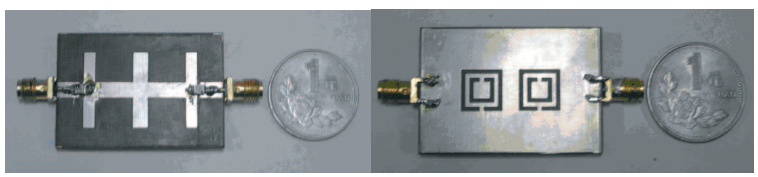

Figure 6: Photographs of the fabricated SRR DGS wideband filter.

To verify the filtering property of this structure, the SRR DGS band-pass filter is fabricated as illustrated in Fig. 6, which is composed of Teflon substrate with thickness $h = 1.5$ mm and dielectric constant $\varepsilon_r = 2.65$, the conductor line has a width of 4 mm. The measured result shows a low pass-band loss of no more than 1 dB within wide pass-band from 1 GHz to 2.4 GHz, and the out-of-band suppression is no less than 25 dB until almost 7.5 GHz, which shows a good agreement with the simulation results by EM simulator Ansoft HFSS software (Fig. 7).

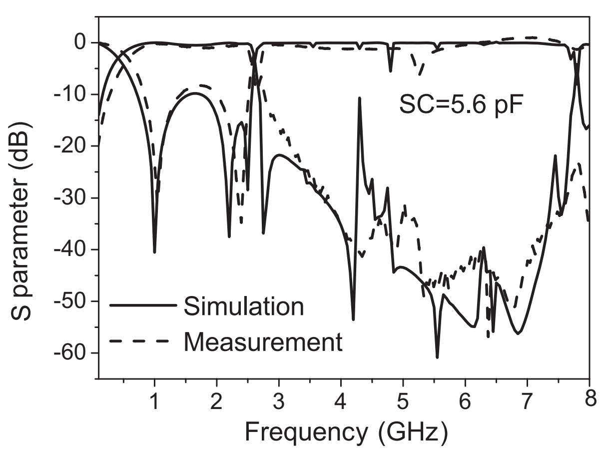

Figure 7: Comparison between EM simulation result and measurement result.

5. CONCLUSIONS

The split-ring resonator DGS founds its application in the design of micro-strip band-pass filter in this paper. A novel circuit model of band-pass filter with a transmission zero is proposed on the basis of the analysis of SRR DGS cell. Then the chip capacitors and T-shaped open-circuit stubs are used to realize series and shunt capacitance, respectively. Finally, a wideband filter with low insertion loss of 1 dB and wide rejection band until 7.5 GHz is fabricated and measured. Other kinds of SRR DGS band-pass filter can be achieved by replacing the lumped capacitor by interdigital capacitor or series gap, and considering the SRR DGS as an independent resonant unit, which can be applied to the miniaturized microwave integrated circuit design.

REFERENCES

1. Park, J. I., C. S. Kim, J. Kim, et al., "Modeling of a photonic bandgap and its application for the low-pass filter design," *Asia Pacific Microwave Conference*, Singapore, 331–334, 1999.
2. Kim, C. S., J. I. Park, A. Dal, et al., "A novel 1-D periodic defected ground structure for planar circuits," *IEEE Microwave Guided Wave Lett*, Vol. 10, No. 4, 131–133, 2000.
3. Park, J. S., J. Kim, J. Lee, and S. Myung, "A novel equivalent circuit and modeling method for defected ground structure and its application to optimization of a DGS lowpass filter," *IEEE Microwave Theory Tech. Symp. Dig.*, Seattle WA, 417–420, 2002.
4. Zhu, L., H. Bu, and K. Wu, "Broadband and compact multi-pole microstrip bandpass filters using ground plane aperture technique," *Proc. Inst. Elect. Eng.*, Vol. l49, 71–77, Feb. 2002.
5. Azadegan, R., and K. Sarabandi, "Miniature high-Q double-spiral slotline resonator filters," *IEEE Trans. Microw. Theory Tech.*, Vol. 52, No. 5, 1548–1557, 2004.
6. A-Rahman, A., A. R. Ali, S. Amari, and A. S. Omar, "Compact bandpass filters using defected ground structure (DGS) coupled resonators," *IEEE MTT-S Int. Dig.*, 1479–1482, 2005.
7. Bonache, J., F. Martin, F. Falcone, et al. "Application of complementary split-ring resonators to the design of compact narrow band-pass structures in microstrip technology," *Microwave and Optical Technology Letters*, Vol. 46, No. 5, 508–512, 2005.
8. Bonache, J., F. Martin, I. Gil, and J. Garcia-Garcia, "Novel microstrip filters based on complementary split rings resonators," *IEEE Trans. Microw. Theory Tech.*, Vol. 54, No. 1, 265–271, 2006.

Novel Trisection Cross-coupled Filter Based on Mixed Split-ring Resonators

Bian Wu[1], **Zheng-Zheng Hou**[2], **and Chang-Hong Liang**[1]

[1]National Laboratory of Antennas and Microwave Technology, Xidian University, Xi'an 710071, China
[2]College of Information and Electronic Engineering, Zhejiang Gongshang University
Hangzhou 310018, China

Abstract— This paper presents a novel trisection cross-coupled filter by using defected split-ring resonator combined with the conventional microstrip split-ring resonators. Defected split-ring can be used as an independent resonator, which has a coupling with two microstrip split-ring resonators, considering the existing coupling between the two microstrip rings, a trisection cross-coupled filter with a pair of transmission zeros is then obtained. Such a practical filter which operates at 1.4 GHz is successfully designed and fabricated, compared with the conventional trisection microstrip split-ring filter, this filter has a more compact structure and a symmetrical frequency response with a pair of transmission zeros.

1. INTRODUCTION

Recent development in wireless communication system has created a need of bandpass filter with low insert loss, high out-of-band suppression and compact size. Cross-coupled filters are widely investigated because they introduce one or more additional coupling between nonadjacent resonators and creates finite transmission zeros out of band [1, 2]. Microstrip open-loop or split-ring is one of the most popular resonant units that be used, it is equivalent to a half-wavelength resonator, the coupling between two split-rings can be electric, magnetic or mixed depending on the orientation of the resonators, and the input/output coupling can be realized by strip-gap or tapped line. This structure can be easily applied to the exact filter design using classical theories of coupled resonator circuits [3–5]. In recent years, there has been an increasing interest in the planar filter design with defected ground structure due to its compact size and band-gap property [6–8].

In this paper, both microstrip split-ring and defected split-ring are applied to the design of a mixed split-ring cross-coupled filter. First, the resonant property of defected split-ring is studied and compared with that of the microstrip split-ring. Then the defected split-ring is loaded at the bottom of the two-section microstrip split-ring filter, which have a mutual coupling with each other, and a bandpass filter with a pair of transmission zeros is obtained. At last, such a kind of trisection mixed split-ring cross-coupled filter which has a center frequency of 1.4 GHz is fabricated, the experimental results agree well with the simulation that validates the presented method.

2. RESONANT PROPERTY OF DEFECTED SPLIT-RING CELL

In the previous work, the defected split-ring has been proposed and used to construct lowpass filter

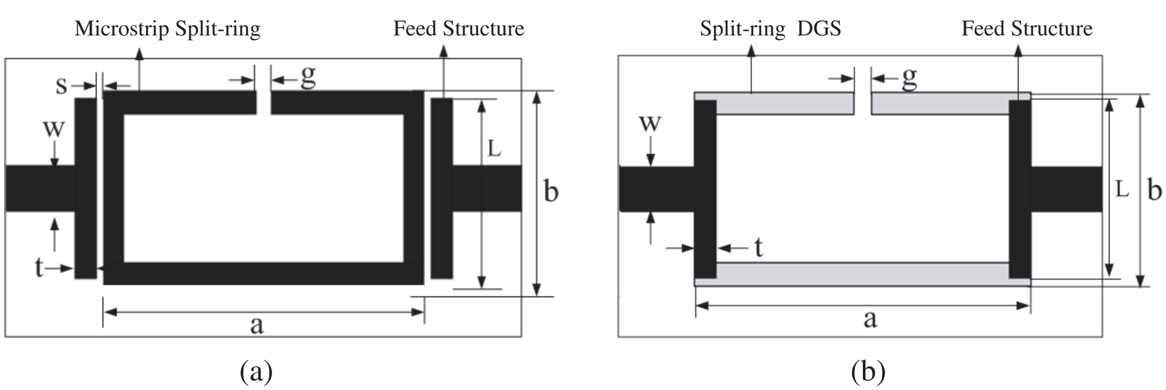

Figure 1: (a) Microstrip split-ring unit, (b) Defected split-ring unit.

and suppress the harmonic effect. Here the defected split-ring is considered as an independent resonant unit, and its resonant property is studied.

As shown in Fig. 1, the defected split-ring is etched at the bottom of the microstrip substrate with a relative dielectric constant of 2.65 and a thickness of 1 mm. The length and width of the ring are $a = 23$ mm and $b = 12$ mm, respectively, and the split-gap is $g = 1.2$ mm, each narrow side of the split-ring is fed by a microstrip T-shaped branch, which has a length of $L = 11$ mm and width of $t = 1.4$ mm, and is connected with the 50 ohm conductor at the end. The difference between (a) and (b) is that, microstrip split-ring has a capacitive gap with the T-shaped branch, but the defected split-ring is overlapped with the T-shaped branch in two different sides of substrate.

The two different split-ring units are then analyzed with the 3D simulation software Ansoft HFSS, we found that they have the similar resonant properties. As illustrated in Fig. 2, the defected split-ring has a resonant peak at about 2 GHz. For the same magnitude of S21, defected split-ring has a much wider passband than that of the microstrip split-ring.

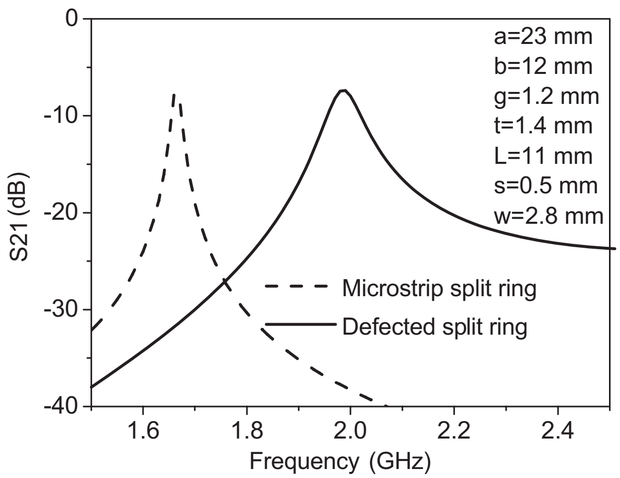

Figure 2: Comparison of resonance between microstrip and defected split-ring.

3. MIXED SPLIT-RING CROSS-COUPLED FILTER

Considering the resonant property of defected split-ring, they can be used to design a novel compact filter combined with the conventional microstrip split-ring. Fig. 3(a) shows a simple two-pole coupled resonator split-ring filter, when a defected split-ring with the same size is etched at the bottom of the microstrip split-ring, a novel trisection filter is formed as depicted in Fig. 3(b). The main transmission passage is from one microstrip split-ring to the bottom defected split-ring, then to the another above split-ring. The cross-coupled filter is obtained due to the additional coulpling between the two microstrip split-rings.

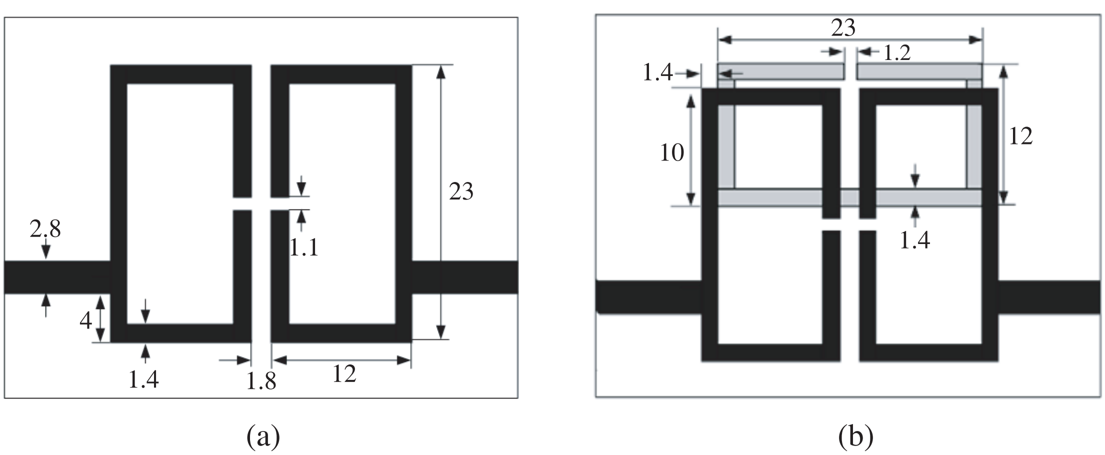

Figure 3: (a) Two-pole microstrip split-ring filter, (b) Trisection mixed split-ring filter.

The simulation frequency responses of the two different split-ring filter are compared in Fig. 4. It can be found that, by adding the defected split-ring at a proper location, a trisection cross-coupled filter with good performance and a pair of transmission zeros is achieved, which has a much wider bandwidth as well as low return loss. By adjusting the distance between two split-ring resonators, the locations of the out-of-band transmission zeros will shift at the same time.

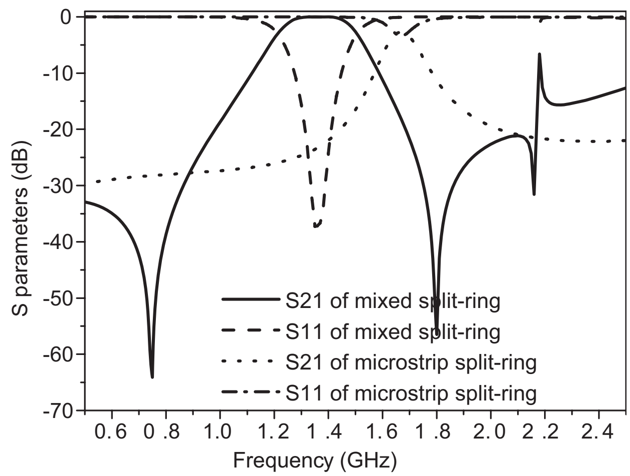

Figure 4: Frequency responses of mixed split-ring filter and microstrip split-ring filter.

4. MEASUREMENT RESULTS

To validate this method, a practical mixed split-ring cross-coupled filter which operates at 1.4 GHz is fabricated on the RF printed circuit board. The substrate has a permittivity of 2.65 and a height of 1 mm. Fig. 5 shows the photographs of the fabricated mixed split-ring cross-coupled

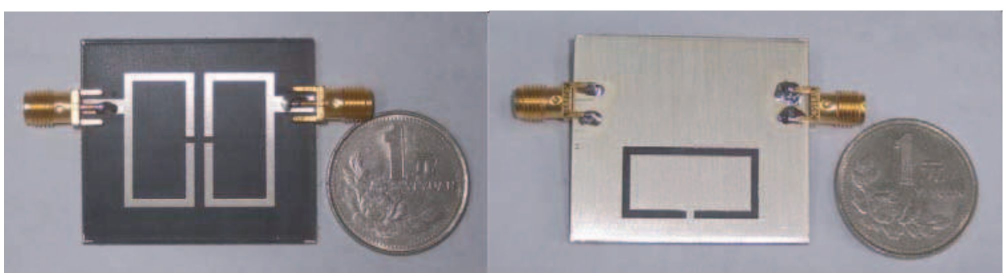

Figure 5: Photographs of the fabricated mixed split-ring cross-coupled filter.

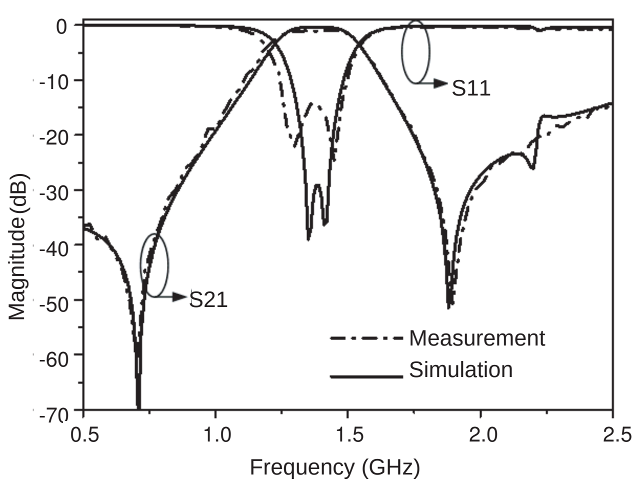

Figure 6: Comparison of frequency responses between EM simulation and measurement.

filter, and the measured results are depicted and compared with the simulation in Fig. 6. It shows this compact filter has a low insertion loss of no more than 1 dB around the center frequency, and a relative bandwidth of 0.14. Moreover, the measured transmission zeros appear at $f1 = 0.7\,\mathrm{GHz}$ and $f2 = 1.9\,\mathrm{GHz}$, the experiment and simulation agree well with each other.

5. CONCLUSIONS

The design method of mixed split-ring cross-coupled filter is proposed in this paper. The defected split-ring is found to have the similar resonant property as the microstrip split-ring, by combining the two kinds of split-rings, a novel trisection mixed split-ring filter is successfully designed. Compared with the conventional trisection microstrip split-ring filter, the new filter has a broad bandwidth, compact size and a pair of out-of-band transmission zeros, which improve the filter performance at various aspects. This kind of filter may find its applications in the miniaturized planar microstrip circuit design.

ACKNOWLEDGMENT

This work is supported by the NSFC under project No. 60501023.

REFERENCES

1. Atia, A. E., A. E. William, and R. W. Newcomb, "Narrow-band multi-coupled cavity synthesis," *IEEE Trans. CAS*, Vol. 21, 649–655, 1974.
2. Cameron, R. J., "General coupling matrix synthesis methods for Chebyshev filtering functions," *IEEE Trans. MTT*, Vol. 47, 433–442, 1999.
3. Hong, J.-S. and M. J. Lancaster, "Couplings of microstrip square open-loop resonators for cross-coupled planar microwave filters," *IEEE Trans. MTT*, Vol. 44, 099–2109, 1996.
4. Levy, R., "Filters with single transmission zeros at real and imaginary frequencies," *IEEE Trans. MTT*, Vol. 24, 172–181, 1976.
5. Hong, J.-S., M. J. Lancaster, "Microstrip cross-coupled trisection bandpass filters with asymmetric frequency characteristics," *IEEE Proc.-Microw. Antennas Propag.*, Vol. 146, No. 1, 84–90, 1999.
6. Kim, C. S., J. I. Park, A. Dal, et al., "A novel 1-D periodic defected ground structure for planar circuits," *IEEE Microwave Guided Wave Lett.*, Vol. 10, No. 4, 131–133, 2000.
7. Gay-Balmaz, P. and O. J. F. Martin, "Electromagnetic resonances in individual and coupled split-ring resonators," *Journal of Applied Physics*, Vol. 92, No. 5, 2929–2936, 2002.
8. Wu, B., B. Li, and C. H. Liang, "Design of lowpass filter using a novel split-ring resonator defected ground structure," *Microwave and Optical Technology Letters*, Vol. 49, No. 2, 288–291, 2007.

Some Differences among HiFi, Tuned Amplifiers and Oscillators

S. L. Vesely[1] **and A. A. Vesely**[2]

[1]I.T.B., C.N.R., Italy
[2]via L. Anelli 13, Milano 20122, Italy

Abstract— In our opinion, employing the same set of solutions to the Maxwell's equations for representing both oscillations and signals, deserves a disambiguation. In radio communications, indeed, the distinction between received signal and carrier wave is paramount. At microwaves, and for resonating cavities in particular, classical electromagnetism concepts can be applied. However, that distinction is not acknowledged when treating the MASER, which is considered an oscillator as well as a tuned amplifier. In accordance with this a MASER emission is required to be as steady as a carrier, while still supplying information about the internal structure of the active material. In order to explain the latter fact, then, it is common practice to resort to quantal principles that are totally extraneous to electromagnetism. In this article we propose to consider the MASER emission in its entirety to be a saturation effect, in an attempt to show how classical theory can in principle explain those observed facts, provided that steady oscillations are distinguished from signals.

1. INTRODUCTION

Today the difference between signal and carrier is central in telecommunications. The two corresponding kinds of waves are obtained and processed in different ways on both transmitting and receiving. Typically, the carrier wave is required to be stable, and the signal is demodulated and filtered from it before amplification. For such reasons, signal distortions brought about by a narrow-band amplifier are considered to be different from shock excitation [1]. Rather than leaning on XIX century theory, the latter distinction is concerned with telecommunication practices. The habit to decompose the solutions to Maxwell's equations into Fourier components, established after mathematical reasons, further hinders any attempt at distinguishing between signals and steady waves. To get more insight, we have to recall that bases of solutions to the wave equation were originally regarded as mere abstractions. After H. Hertz discovery, an electromagnetic emission $s(t)$ was thought of as being generated by an electrically balanced elastic motion [2] and irradiated in unison with it. It is worth recalling also that the low distortion amplification G of a signal, $s(t) = G_{(I,V)}e(t)$, which is meant to linearly magnify as well as to increase resolution, was explained in terms of electromagnetic forces on charged particles. Here $e(t)$ is the input, whilst I and V are the operating current and voltage of a high vacuum tube. After World War II, electronic techniques developed for radio detection and ranging have allowed to extend optical spectroscopy, that had previously been practiced using only "natural" sources, to an intermediate spectral portion where antennas are still required for irradiation. In the latter portion, absorption lines [3] are very narrow and buried in noise. Their linear amplification is hard either. Thus, the signal enhancement basically consists of tuning the receiver to the expected absorption frequencies and narrowing its passband [4] around them at the price of some distortion. The contribution of a tuned amplifier is taken into account using the formula $s(t) = G_{(I,V)}\int_{-\infty}^{\infty} e(\tau)h(t-\tau)d\tau$, where $h(t)$ is the receiver's response. Considerable saturation effects, leading to the disappearance of absorption lines, have been noticed by irradiating the relevant samples at higher intensities. Attempts to better the resolution finally resulted in the MASER, acronym for Microwave Amplification by Stimulated Emission of Radiation, as a further technology fallout [1]. For explanatory purposes, extending concepts from hertzian to light waves, enables to treat masing as an electromagnetic radiation of hertzian kind, not just formally but dealing with its transmission and reception comprehensively. In the opposite direction, the extension of optical concepts to microwaves required the assumption of quantal principles. Therefore, we next consider a linear alternative to the latter approach.

[1]This expression was used for instance by E. H. Armstrong for describing spark interference on regenerative audions.
[2]According to $\mathbf{F}_{electric} = m\mathbf{a}$
[3]Corresponding to dark lines on positive photos.
[4]Doing so one believes to be cutting off the noise due to thermal agitation of molecules.

2. A LINEAR PICTURE ALTERNATIVE TO QUANTUM JUMPS

The problem of interpreting optical spectra came about because classical optics does not distinguish at all between radiating sources and illuminated bodies, but rather assumes that point objects always spread any radiation in an isotropic fashion [5]. In addition the theory is strictly exempt from any consideration about the radiations' strengths. Bohr's atomic model was substituted for Lorentz' electrodynamics in the interpretation of absorption and emission experiments, because during the early 1900s it became apparent that assuming a continuous distribution of the field energy was not compatible with the observation of lines characteristic of each gas compound. In fact quantization came about after the need for an energetic account of optical spectra and has been used in optics to give an energetic account of the Nadelstrahlung [6]. Nowadays, the emissions of advanced electronic devices like a MASER are also considered elementary radiations and are represented as finite amplitude sinusoids. Although quantum physics can justify them, as a probabilistic theory it provides no help for an interpretation of those microwave emissions so as to be useful for telecommunication purposes.

A MASER is a highly sophisticated device provided with a resonator, that can either be pulsed or continuously emit an almost monochromatic collimated beam obtained, in principle, by tuning its cavity to one of the specific frequencies of an active substance contained therein. Today's physicists accept that that beam represents a specimen of the steady electromagnetic field that is present inside the cavity, much like for the black-body radiation, at least until the escaping energy is small enough to avoid perturbing the thermodynamic equilibrium inside (in other words, the matching with the output must be bad). If it is granted to apply energetics to radiations with specific features, a MASER beam thus differs from conventional "black" light since its cavity amplifies only a single frequency, by stimulating emission at the expenses of the internal energy of the atoms placed inside it. As the coefficients that Einstein used to derive Planck's radiation formula apply separately to each frequency, they are deemed to be amenable to computing an energetic balance of the MASER radiation too. The computation is carried out in terms of probabilities of spontaneous or stimulated quanta absorption and emission in steady conditions. From a radio engineer standpoint, assuming that the cavity admits normal modes, the steady oscillation of the system represents the limit case where losses due to outward radiations are compensated exactly. In that case the MASER works as a continuous wave (CW) oscillator. Otherwise, if Einstein's spontaneous emission [7] represented the input signal, the MASER could be considered an amplifier [8].

Whilst MASER technology applied to a scalpel doubtless involves a transfer of power (transduction), a high Q factor of the eye sensors adapted to darkness is enough to explain why stars are visible (signal reception). In the latter case "small signal" circuital schemata exist that are capable of gathering weak signals owing to the Q, which indicates that the corresponding functioning is amenable to electrical explanations. Besides, spectral lines are a phenomenon and as such they are subject to alternative interpretations. Let's take as an example an experiment that A. Kundt interprets as anomalous dispersion [2]. In that article he mentions an observation upon the behavior of sodium vapor illuminated by a sodium lamp. It is described how the cold gas, rather than getting dimly lit by spreading the lamp's light, visibly quenches a doublet, which finally gets black. This behavior, only observable when the monochromatic light emitted by the hot gas is well visible, used to be called "Umkehrung" [9] in ancient times. As it is a relatively common experience today that different LASER beams interfere with each other, it is apparent that the doubled and quenched sodium D line can be explained linearly as a negative interference of the lamp's emission and the excited cold gas. This explanation assumes the superposition principle, but also hypothesizes that both the hot and the cold gases emit anyway. It is also apparent that the phenomenon that Kundt relates with anomalous dispersion, and that we'd be inclined to call shock excitation in virtue of resonance coupling, is called the absorption in Bohr's linear theory.

[5] Geometrically, a collimation is achieved moving the beam's center from finite to infinite.

[6] Needle radiation, i.e. the "natural" narrowband emission.

[7] The distinction between spontaneous and stimulated emissions applies just to Einstein's calculation, unless "spontaneous" is taken to mean, for instance, emissions without antenna. In the latter case all emissions where an antenna is necessary, should be considered stimulated.

[8] The difference between amplifying and oscillating completely vanishes when one takes into account vacuum fluctuations of the electromagnetic field.

[9] Reversion.

3. RESONANT SIGNAL ACQUISITION

Optical absorption spectra are taken at steady conditions, essentially because measuring practices used to adopt such conditions in the past. Hence, the black lines on a positive photogram are those that are quenched at steady conditions, and which quantum mechanics ascribes to transitions of the so-called optical electron from the ground state E_0 to an excited atomic energy level $E_n(n = 1, 2, \ldots)$ due to an energy supply per light-quantum $\hbar\omega$. Absorption lines that saturate easily, between 0.5 and 18 GHz, in general measure the polarizability of substances, and are ascribed to quantized roto-vibrational degrees of freedom. The analogous nuclear rotational transitions at radio frequencies are completely buried in thermal noise, despite the number of good linear amplifiers at those frequencies. However, to measure transients is the business of electronics. Thus, besides those standard methods for measuring "steady state occupation levels", a resonance method has been devised, at first precisely in the VHF band, for measuring free precession of the nuclear induction of liquids polarized by an uniform magnetic field of some kilogauss. The latter method is devised to receive the signal induced orthogonally to the irradiation direction at the resonance condition. Resonance condition usually means that the system interacting with radiation has to fulfill Bohr's rule $\hbar\omega = E_n - E_0$. Therefore the conspicuous part of the device, which is called a marginal oscillator, or "pound box" after the name of its inventor, is the same for induction and spectrometric measurements [3]. Only its rationale is different, as it is understood as a tuned antenna in the first case, and as a lengthening of the optical path in the second. Its pick up essentially consists of a tank circuit with a high quality factor Q_C fed by a frequency modulated generator at the center band frequency $\omega_C/2\pi$ of the LC. The sample of polarized substance is inserted within the coil. If the sample resonates near the LC, and its intrinsic Q_S is high enough, the ensuing variation of the total Q can trigger a dumped oscillation of the circuit around its resonating frequency [10]. This Q changes as the detecting circuit gets transitorily "coupled up" during the frequency sweep. Because of the mathematical treating of the induction response given by F. Bloch, we have to point out that the pound box detection amplifies differently from what is experienced during superheterodyne detection. This time, the sharply tuned stages at intermediate frequencies (IF) must steadily filter a band around $\Omega_F/2\pi$ and Q_F measures this passband. Transients have been broadcast directly in early radiotelegraphy instead of using a CW carrier. Regenerative amplification was by no means distortionless. Hence, there are some differences between resonantly picked up emission and harmonic analysis of an IF-filter response. In modern radio receivers the carrier is used for tuning to a specific channel, and has no significance by itself [11]. Now, it is worthwhile to contemplate whether the MASER beam, which is emitted when its resonant cavity gets coupled up steadily, should still be regarded as a signal originating from the medium inside.

One question related to the previous one is about how the above described triggering can result in an ignition, that is, in a sustained stable emission. At low frequencies multivibrators show oscillating behavior. At radio frequencies there are relatively simple oscillator circuits, e.g., Colpitts' one. Such circuits typically feature a quite narrow passband filter inserted between a transistor's input and its output, so that their self excitation is maintained by coherently feeding part of the output back into the input. During steady oscillation, according to the circuit schema, there is no other input than that fed back from the output. That way, in steady conditions, the feed-back loop governs and modulates the transistor's own oscillation. Replacing the transistor with its signal equivalent, due to Miller capacity, one is assuming in fact that a positive feed-back takes over every time a transistor oscillates. Although from an electrical standpoint the MASER is a much more complex device than a Colpitts' oscillator, in principle an explanation of its functioning might be transposed from radio to microfrequencies, and adapted to the cavity's behavior. That would then imply that spectral theories should consider the MASER emission a saturation phenomenon, that is a depletion of the dominant resonating frequency accompanied by all of the modulation allowed by the feedback loop. If induction is considered a signal, as in NMR spectroscopy, then that signal doesn't exist any more during steady emission.

4. EMISSIONS SUSTAINED BY PUMPING

A parametric amplifier is usually considered a frequency transformer, as it may be employed for up- or down-converting fixed input frequencies. However, transformations taking place between

[10] That's just electrical consonance. In fact "wiggles" have been observed already by R. Pound himself.

[11] Broadband HiFi amplification is possible up to fairly high frequencies. However tuned VHF receiving circuits are liable to oscillate. Hence VHF amplification of audio signals introduces that big difference between signal and carrier, and poses at the same time the question about what exactly the concern of an up to date electromagnetism has to be.

frequencies result from a kind of coupling, known as mixing crosstalk, that settles between oscillating systems out of tune with each other. Since long, their mechanical analogs have been swings. For reporting that, let's recall that energetics evaluates the MASER parametric amplification assuming that operations conform to adiabatic cyclic processes. That way, the gain equals the net amount of energy absorbed each cycle. Before quantum mechanics got its current probabilistic foundation, P. Ehrenfest contributed to the correspondence principle by referring to the adiabatic invariance hypothesis. In order to derive the proportionality relation between energy and frequency $E_n = \hbar(\omega_n - \omega)$ that quantum leaps are based upon, he hypothesized that the length ℓ of an oscillating pendulum string supporting a mass m would slowly shorten by $\delta\ell$ (that is $-\delta\ell$) during the motion. He reckoned the external work required for shortening the string against weight and centrifugal force. From mechanics we get $\delta A = -(mgcos\varphi + m\ell\omega^2)\delta\ell$, where $\omega = d\varphi/dt$, and φ is the angle with respect to the normal. If the string's length is constant, then the centrifugal force is assimilated into a constraining reaction. Hence, by splitting δA into the sum of an external contribution due to the weight $-mg\delta\ell$ and an internal energy increase δE, we get for the latter $\delta E = [mg(1 - cos\varphi) - m\ell\omega^2]\delta\ell$. In that expression, slightly different from the common classical concept, internal energy contributes to the change of a quantity that characterizes the motion. While the formation of an average may lead to a statistical thermodynamic justification of the proportionality assumed for the energetic leap, the same formula has been used to describe parametric amplification, at frequency 2ω. In the latter sense, it is exemplified by a person sitting on a swing seat and swinging at a frequency ω without external intervention. In the example, the oscillatory motion gets "amplified" at the expenses of the constraining energy, given that the string is shortened by $\delta\ell$ twice during a complete cycle, when it is on the vertical, and lengthened also twice, when the bob turns around.

Classical theory establishes that a pendulum's frequency is strictly constant [12], and that possible anharmonic correction terms show up only when oscillations are not small [13]. Instead, the above formula explains how timely tiny impulses imparted to the string can alter the amplitude of the oscillations, eventually "creating" distortions. As far as frequency conversion is concerned, average gain per cycle and pumped parametric amplification are expressed equivalently. The above $2\omega = \omega + \omega$ is a particular case of Ritz's principle, which is formulated as $\omega_{13} = \omega_{12} + \omega_{23}$ in the general case. However, Ritz's combination principle applies to normal modes, while parametric amplification involves crosstalking between pumped and output frequencies. R. H. Dicke made the following experience [4]: "[...] the performance of a standard microwave radar receiver [...] was extremely poor at centimeter wavelengths, and [...] could be vastly improved by rapidly switching the receiver input back and forth between the antenna and a dummy antenna, [...]". Afterwards, he himself applied those ideas to the measurement of thermal noise, and hence could feedback stabilize the gain of his IF amplifier. That allowed him to synchronously drive a lock-in detection at the switching frequency. But if, as it happens during a RADAR signal acquisition, the IF-tuned stage is not neutralized, it behaves like a mixer since its loaded Q varies during the switch. In the latter case, if the receiver is in band K around frequency ω_1, and a front-end relay in the input circuit is switched on and off at a lower frequency ω_2, it picks up: $\ldots, \omega_1 - 2\omega_2, \omega_1 - \omega_2, \omega_1, \omega_1 + \omega_2, \ldots$ Since the intensity of the impulse at frequency ω_2 is stronger than the amplitude of signal ω_1, this mixing betters the sensitiveness. In the case of a MASER, frequency mixing plays another role: the saturation of the line at ω_{13} could boost both an emission at the effective ω_{23} and at the idler's ω_{12}, in accordance with Ritz principle. But if ω_{13} is the pumping or feeding frequency and ω_{23} is steadily irradiated by amplifying one crosstalking frequency, the idler as a rule does not show up. The swing analogy could run as follows: If someone pushes the seat to get a swinging motion, the frequency of the impulses must come in the correct phase relation as required by parametric amplification. However, the small power given with each single push, which is calibrated to increase or maintain the actual amplitude of the oscillations, features a varying spectrum that in acoustic would be called a "formant". That's how we think a MASER device works, as compared to a swing.

In compliance with telecommunications, the stable MASER emission ω_{23} is related to the linear wave equation, and behaves as an electromagnetic radiation to that extent. As an alternative to characterizing it by assigning amplitudes, phases, and frequencies, perhaps we could stress the links with other logical quantities related to the signal, such as maximal channel capacity, or information transfer rate. For example, it is well known that bettering the coupling between cavity and active

[12] In fact it is unique for a given ℓ, unless g varies.

[13] As anharmonic terms give rather an account of the deformation of the steady motion, than of the motion changes that they might cause, they are considered normal modes.

material lowers the Q. According to usual understanding, by doing so the dumping is increased, and one has to compensate for the resulting losses in order to sustain the masing. For the signal transfer rate, the response time is progressively increased by rising the Q.

5. CONCLUSIONS

"Natural" generators produce characteristic emissions, in which one cannot usually discern a carrier and a signal. A telecommunications *carrier* has to be periodic and well known by the receiver, and thus bears no (new) information about its generator. A generator producing a carrier is called an *oscillator*, its carrier-wave may be modulated with a *signal*. Oscillators may be employed inside circuit diagrams, without bothering about the inner working of the corresponding physical devices. Indeed, when an oscillator is present in a radio circuit, it only serves to allow tuning to a channel. Other circuit components, particularly signal amplifiers, are built in order to exhibit a smooth biunivocal relationship between their input and output. Hence, their functioning principles may be captured by providing suitable explanations in terms of classical electromagnetism or circuit theory.

Finally, on explaining a wave provided by an oscillator, it is important to take into account that "amplifying" it quenches the relevant frequency. For that reason, we think that the difference between signal amplifiers and oscillators is a substantial one, and it should be hold.

REFERENCES

1. Gordon, J. P., H. J. Zeiger, and C. H. Townes, "The maser-new type of microwave amplifier, frequency standard, and spectrometer," *Phys. Rev.*, Vol. 99, No. 4, 1264–1274, 1955.
2. Kundt, A., "Über anomale dispersion im glühenden natriumdampf," *Ann. Phys.*, Vol. 246, 321–325, 1880.
3. Pound, R. V. and W. D. Knight, "A radiofrequency spectroghraph and simple magnetic-field meter," *Rev. Sci. Instr.*, Vol. 21, No. 3, 219–225, 1950.
4. Dicke, R. H., "This week's citation classic^{TM}," *CC*, No. 28, July 14, 1980.

X-band Low Phase Noise Quadrature CMOS VCO with Transformer Feedback

Yu-Shun Liao and Christina F. Jou
Institute of Communication Engineering, National Chiao Tung University
Hsinchu 300, Taiwan

Abstract— A fully integrated quadrature VCO with transformer feedback is proposed to achieve low-phase-noise and at a x-band using a TSMC 0.18-μm CMOS technology. The VCO is implemented using a transformer-based LC tank and the transformer feedback configuration from the drain to the back-gate of the switching transistors. The simulation result shows the phase noise is about −114 dBc/Hz at 1MHz offset and the output frequency tuning range of the QVCO is around 800 MHz ranging from 8.9 to 9.7 GHz. The QVCO core circuit draws only 4.1 mA from a 1.5-V supply. Compared with the recent works, the proposed QVCO topology shows phase noise performance 5 dBc/Hz lower than the original and power consumption of 6.15 mW compared to the original VCO core of 6.8 mW.

1. INTRODUCTION

The fully integrated CMOS VCO has been paid great attention due to its low cost and the integrability with other analog and digital circuits although Si substrate has higher loss than GaAs substrate. The disadvantage associated with substrate loss is being conquered by the evolution of the process and the circuit technologies. When the operating frequency of a VCO increases, however, the main bottleneck of a CMOS VCO is the low quality factor of an inductor. Recently it is reported that a transformer-based LC resonator has higher quality factor than that of a single LC tank, lower phase noise VCO can be achieved. Until now, most of transformer based CMOS VCOs are published below 8 GHz.

In [2], the drain terminal is magnetically feedback to source terminal with an impedance transformation of n^2/g_m, where n is the transformer turns-ratio and g_m is the transconductance of the transistor. Since the impedance seen at the source terminal is $1/g_m$, a relatively high turns-ratios is required for the transformer to make an impedance transformation, thereby entailing complexity in transformer design, making it possible to lower the oscillation frequency. If we feedback the drain voltage to the front-gate. Since the impedance seen at the gate of the switching transistor is relatively high, the turns-ratio of the transformer can be optimized with a smaller number of turns. However, the parasitic capacitances of the transformer directly couple to the tank, and lower the oscillation frequency significantly. To obtain both higher frequency and simplify the transformer design (small number of turns ratio), the front-gate feedback path can be modified to have a feedback to the back-gate as shown in Fig. 1(a).

In this paper, a novel transformer-based differential VCO is presented by utilizing the transformer feedback configuration from the drain to the back-gate of the switching transistors to not only maintain high frequency operation, but also the proposed one to have better phase noise performance and save half of power consumption.

2. TRANSFORMER FEEDBACK DIFFERENTIAL VCO

Figure 1(b) shows the proposed VCO, which allows higher oscillation frequency while keeping comparable performances compared to those of the other topologies as in [1–3].

With parallel coupling transistor to generate the I-Q phase. From the Barkhausen criterion, oscillation only occurs when the loop gain is $[A(j\omega)]^4 = 1$, which means $A(j\omega) = 1\angle 90°$. Therefore, this configuration provides quadrature-phase signals from the four outputs of these two proposed VCOs.

The current source in Fig. 1(a) is replaced by resistor providing bias condition and wide-band operation. Besides, two benefits also achieved due to the removal of the current source. First, the current source is the main contributor to the phase noise. Second, when all transistors in the VCO core are put in GHz-switching bias condition, flicker noise will apparently be reduced by about 10 dB.

A 2-μm-thick top AlCu metal is used for the windings to increase the quality factor. The transformer is designed with 1-μm line spacing, 150-μm outer dimension. Besides, the quality

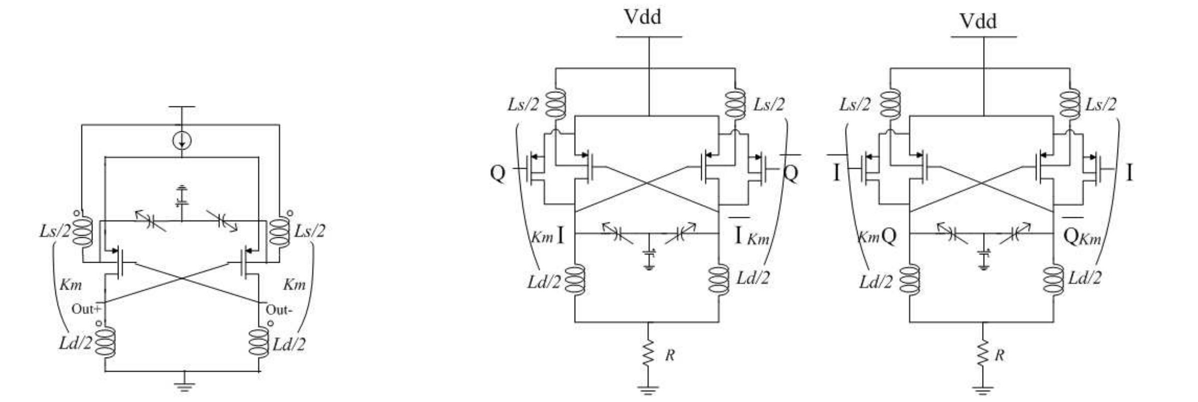

(a) (b)

Figure 1: (a) Transformer feedback to the back-gate, (b) the proposed VCO (with parallel coupling to generate I-Q).

factor of transformer can be optimized by increasing the metal width progressively from the inner to the outer turn [4, 5]. As such, the series loss in the outer turn is reduced while its substrate loss associated with the wider metal width does not degrade the performance due to the virtual ground at the inductor's center tap. Fig. 2 shows the transformer is simulated by ADS Momentum with primary inductance (L_d) 0.46 nH, and the secondary inductance (L_s) 0.13 nH, with quality factors 6.8 and 4.4 respectively. The transformer coupling coefficient k_m is modeled as shown in Fig. 3, which is calculated by (1) as 0.4.

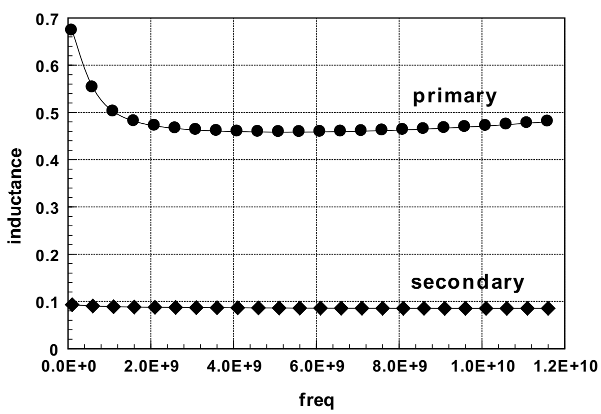

Figure 2: The primary and secondary self-inductances.

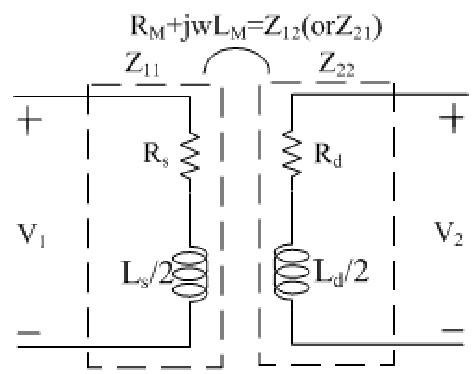

Figure 3: The simplified small signal equivalent circuit model of the transformer [6].

$$K_{im} = \frac{\mathrm{Im}(Z_{12})}{\sqrt{\mathrm{Im}(Z_{11})\mathrm{Im}(Z_{22})}} = \frac{L_M}{\sqrt{L_s/2 \times L_d/2}} \tag{1}$$

MOS varactors are used to provide the frequency tuning capability. AM noise originating from the upconversion of low frequency bias noise cannot be neglected due to AM-PM conversion through the varactors. So the frequency tuning capability will be controlled as varactor's selectivity and traded for lower phase noise. The all-PMOS topology is preferred since PMOS has lower corner frequency of flicker noise, which means less low frequency noise [6, 7].

The most common topology of the buffer is source follower. This architecture has several advantages, such as high isolation between the core circuit and the output pads to reduce the loading effect and oscillation frequency deviation. But it will take $2 \sim 3$ times power dissipation than the core circuit.

3. SIMULATION RESULTS

Figure 4 shows the chip layout size is $0.88 \times 0.49\,\text{mm}^2$ including the pads. The phase noise is about $-114\,\text{dBc/Hz}$ at 1 MHz offset as shown in Fig. 6 and the output frequency tuning range of the QVCO is around 800 kHz ranging from 8.9 to 9.7 GHz as shown in Fig. 5. The QVCO core circuit draws 4.1 mA from a 1.5-V supply (6.15 mW) and the buffer takes 16.2 mW. Fig. 7 shows the quadrature output from the core QVCO and buffer. Moreover, to further compare the performance of the proposed VCO, the power-frequency-normalized figure-of-merit (FOM) is used

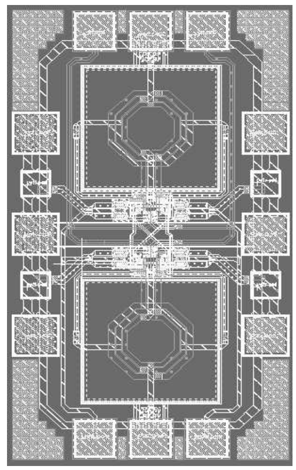

Figure 4: Chip layout.

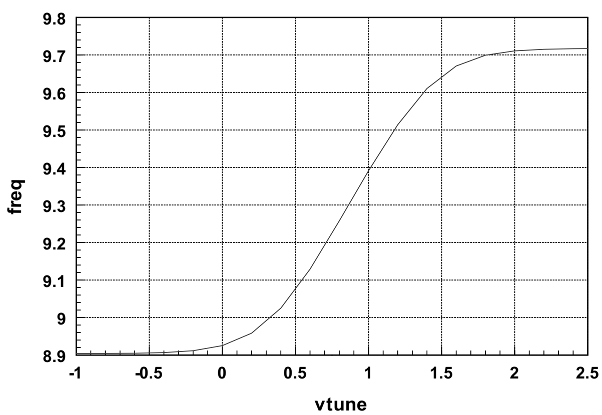

Figure 5: Simulated tuning range of the QVCO.

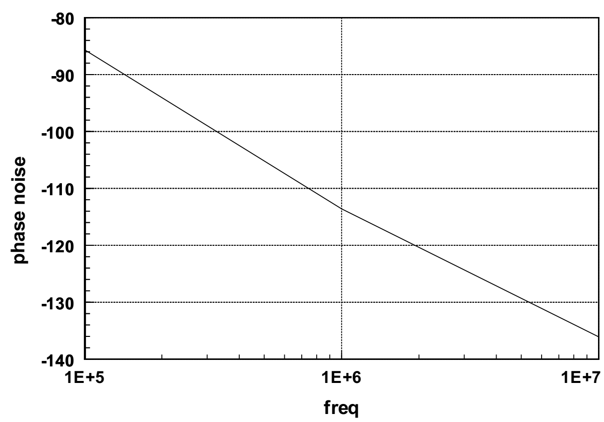

Figure 6: Phase noise of 9391 MHz.

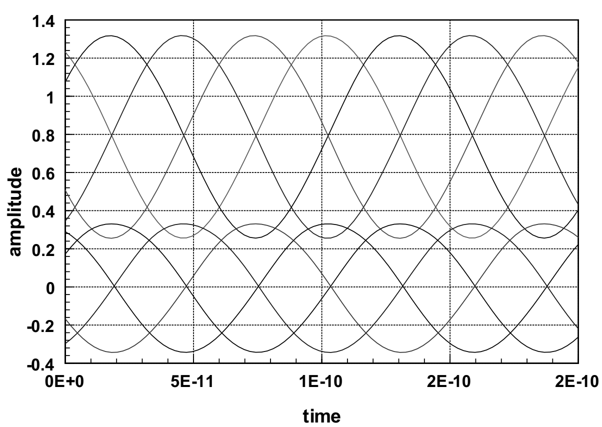

Figure 7: Quadrature output from core QVCO and buffer.

Max. Frequency	9.7 GHz
Core Circuit Power (mW)	6.15
Buffer Power (mW)	16.2
Supply Voltage (V)	1.5
Phase Noise (dBc/Hz)	-114.2@1 MHz
FoM (dBc)	-185.5@1 MHz
Technology	CMOS 0.18 μm
Die Size (mm^2)	0.88×0.49

Table 1: Summary of simulation.

in (2) as $-185.5@1\,\text{MHz}$.

$$FOM = 10\log\left[\left(\frac{\omega_0}{\Delta\omega}\right)^2 \frac{1}{L\{\Delta\omega\} \times V_{DD} \times I_{DD}}\right] \tag{2}$$

where ω_0 is the center frequency, $\Delta\omega$ is the frequency offset, $L\{\Delta\omega\}$ is the phase noise at $\Delta\omega$, V_{DD} is the supply voltage, and I_{DD} is the supply current. Table 1 shows the summary of performance of the proposed QVCO. Table 2 shows the comparison with previously reported works.

Table 2: Comparison with the reference paper.

	This work (Simulation)	MWCL, 2005 [1] (Measurement)	MWCL, 2003 [3] (Measurement)
Technology	**0.18 um CMOS**	0.18 um CMOS	0.18 um CMOS
Voltage	**1.5 V**	1.8V	3 V
Oscillation Frequency	**9.4 GHz**	11.22 GHz	8 GHz
Tuning Range	**8.9 ∼ 9.7 GHz**	300 MHz vtune from 1.6–2 V	8.08 ∼ 7.83 GHz
	9 %		3 %
Phase noise (dBc/Hz)	**−114@1 MHz** **−125@3 MHz**	−109.4@1 MHz	−117@1 MHz
Power Dissipation	**6.2 (qvco core)**	6.84 mW (vco core)	24 mW (vco core)
FOM (dBc)	**−185.5@1 MHz**	−181.8@1 MHz	−181.7@1 MHz

4. CONCLUSIONS

In this paper, a quadrature voltage controlled oscillator with proposed VCOs in a standard TSMC 0.18-μm CMOS 1P6M technology. The proposed VCO circuit employs a the transformer feedback configuration from the drain to the back-gate of the switching transistors to not only maintain high frequency operation, but also to have better phase noise performance and save half of power consumption. The QVCO's phase noise is about −114 dBc/Hz at 1 MHz offset and the output frequency tuning range is around 800 MHz ranging from 8.9 to 9.7 GHz. The QVCO core circuit draws 4.1 mA from a 1.5-V supply (6.15 mW) and the buffer takes 16.2 mW.

ACKNOWLEDGMENT

The authors would like to thank the Chip Implementation Center (CIC) of the National Science Council, Taiwan, R.O.C., for supporting the TSMC CMOS process.

REFERENCES

1. Oh, N.-J. and S.-G. Lee, "11-GHz CMOS differential VCO with back-gate transformer feedback," *IEEE Microwave Wireless Components Letters*, Vol. 15, No. 11, 733–735, Nov. 2005.
2. Kwok, K. and H. C. Luong, "Ultra-low-voltage high-performance CMOS VCOs using transformer feedback," *IEEE Journal of Solid-State Circuits*, Vol. 40, No. 3, 652–660, Mar. 2005.
3. Baek, D., T. Song, E. Yoon, and S. Hong, "8 GHz CMOS quadrature VCO using transformer-based tank," *IEEE Microwave Wireless Components Letters*, Vol. 13, No. 10, 446–448, Oct. 2003.
4. Long, J. R., "Monolithic transformers for silicon RFIC design," *IEEE Journal of Solid-State Circuits*, Vol. 35, No. 9, 1368–1382, Sept. 2000.
5. Ling, Y.-S., "Implemntation of perfect-magnetic-coupling ultralow-loss transformer in RFCMOS technology," *IEEE Electron Device Letters*, Vol. 26, No. 11, 832–835, Nov. 2005.
6. Rael, J. J. and A. A. Abidi, "Physical processes of phase noise in differential *LC*-oscillators," *IEEE Custom Integrated Circuits Conf.*, 569–572, May 2000.
7. Wang, L., P. Upadhyaya, P. Sun, Y. Zhang, D. Heo, Y.-J. E. Chen, and D. Jeong, "A 5.3 GHz low-phase-noise LC VCO with harmonic filtering resistor," *IEEE ISCAS*, 3237–3240, 2006.
8. Hajimiri, A. and T. H. Lee, *The Design of Low Noise Oscillators*, Kluwer Academic Publishers, 1999.

An Image Rejection Low Noise Amplifier for WLAN System

Lien-Sheng Wei and Christina F. Jou

Institute of Communication Engineering, National Chiao Tung University, Hsinchu, Taiwan

Abstract— This paper presents a new structure that combines low noise amplifier with on-chip filter to eliminate external expensive SAW filter, and achieves high performance while consumes low power. The proposed image rejection LNA is optimized for 5.8 GHz application for WLAN with IF frequency of 500 MHz based on TSMC 0.18 μm CMOS technology. The circuit operates at supply voltage of 1 V, and Vbias of 0.7 V. The power consumption is 5.98 mW.

1. INTRODUCTION

At typical ratio frequency front-end receiver, low noise amplifier amplifies very small signal while suppresses the noise of the circuit itself. After the LNA, proper filtering of image signals is mandatory to reject unwanted signal, then enter in mixer that mixes RF and local signals. The image rejection filter usually is an external component, such as surface acoustic wave filters. These kinds of filters are often very expensive and large that is not suitable for SOC. However, image rejection filter is an indispensable component. If not use image rejection filter, image signal will interfere with IF signal. It is highly undesirable. For this purpose, LNA with image rejection filter improves RF integration.

In this paper, LNA with third-order active notch filter will be discussed [1]. However, it consumes more power than general LNA. As a solution to overcome the limitations of previously reported work, this paper proposes a new image rejection LNA topology as shown in Fig. 1. In other words, the proposed image rejection LNA not only has high performance, but also achieves low power consumption. The details of this image rejection LNA will be analyzed in Section 2.

As Fig. 2 shows from [1], the circuit's performance is one of the best. Image rejection LNA is based on current reuse. First stage is a common source (CS) amplifier. In the first stage, an extra capacitor is used to obtain the power constrained simultaneous noise and input matching. Second stage is cascode circuit. An inter-stage inductor is included to resonate with input gate-source capacitor of second stage. The low impedance at output of first stage reduces voltage gain so that the Miller effect is reduced. Image rejection is implemented by third-order active notch filter inserted between the cascode stage as shown in Fig. 3. Observing behavior of this filter, it's input impedance has a deep lowest point at image signal frequency. When image signal passes cascode stage, it will be short to ground. So image signal can be filtered out while wanted signal is amplified.

Image rejection LNA with third-order active notch filter from [1] has high performance. However, using three transistors and an active filter with current source driving costs extra power. To solve this problem, a new image rejection LNA is proposed to improve power.

2. CIRCUIT ANALYSIS

2.1. Image Rejection Filter

The passive image rejection filter is shown in Fig. 4, that includes a shunt connected with LC tank series with a capacitor, then shunts with a inductor. The input impedance is simulated in Fig. 5. The input impedance at RF frequency and image frequency are the highest and lowest respectively. Because of using passive devices to complete, the filter does not consume extra power. It will be inserted in inter-stage of the current reuse circuit to achieve low power dissipation and image rejection.

2.2. Image Rejection LNA Design

The image signal is a serious problem in the ratio frequency front-end receiver. To avoid using off-chip SAW filter, the new on-chip image rejection techniques have been developed. As shown in Fig. 1, the Image rejection LNA has been proposed. Amplification stage is based on current reuse structure. RF signal path is from gate of M1 to drain of M1 and then from gate of M2 to drain of M2. Two NMOS transistors works like two common source amplifiers, but use only one current. Therefore current reuse can achieve high gain and save power efficiently.

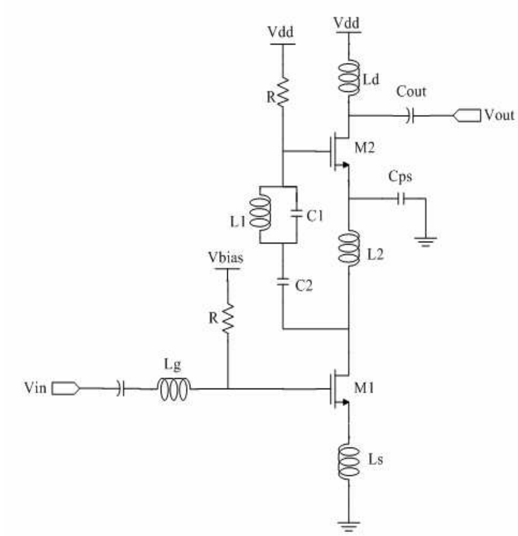

Figure 1: Schematic of proposed image rejection LNA.

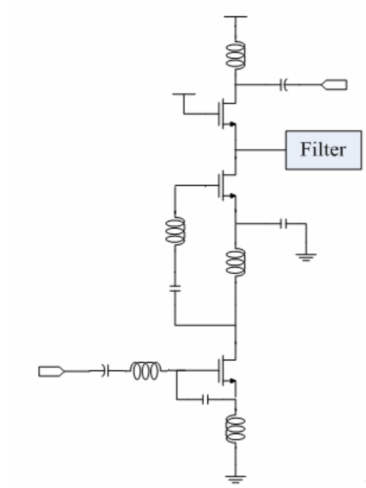

Figure 2: Image rejection LNA from [1].

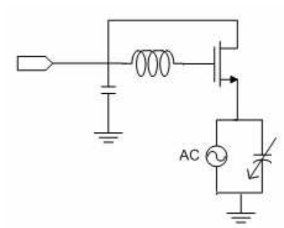

Figure 3: Third-order active notch filter.

The image rejection filter is made up of inductors L1, L2 and capacitors C1, C2, that is located between M1 and M2 transistors. Because looking into gate of M2 is capacitive, effective C2 value will be reduce. We can increase C2 value to cancel reduction of C2. Cps is large capacitor which works like short in AC, so that looking into output of M1 is like image rejection filter as shown in Fig. 4. By suitable adjustment, output impedance of M1 will be like in Fig. 5. Gain of common source is approximately given by (1)

$$\mathrm{Gain} = \mathrm{gm}_1 \times \mathrm{R}_{\mathrm{out1}} \tag{1}$$

The value of $\mathrm{R}_{\mathrm{out1}}$ is very high at RF frequency and low at image frequency respectively. Therefore first stage M1 amplifies wanted signal, and filters out unwanted signal. By adjusting Lg and Ls optimizes input matching and the noise figure. Ld and Cout are for output matching purpose.

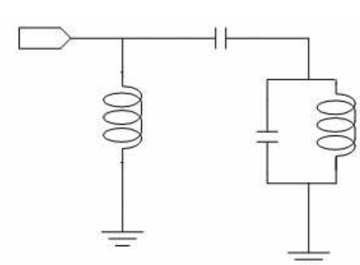

Figure 4: Image rejection filter.

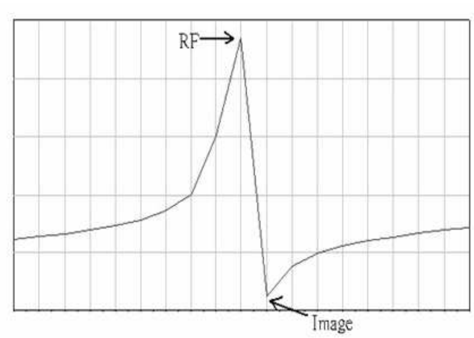

Figure 5: Input impedance from Fig. 4.

3. SIMULATION RESULTS

The image rejection LNA for 5.8 GHz WLAN receiver has been designed based on TSMC 0.18 µm CMOS technology. In this design, the image rejection LNA is operating at 5.8 GHz, and image frequency is at 6.8 GHz. IF is 500 MHz. Power dissipation is 5.9 mW with a 1 V supply. Fig. 6 shows S-parameters. S11 is −15.88 dB. S22 is −26.16 dB. S21 is 15.38 dB and −18.07 dB at RF frequency and image frequency respectively. The Noise figure is 2.85 dB in Fig. 7. The P1db is −19.6 dBm and IIP3 is −6.5 dBm as shown in Fig. 8 and Fig. 9 respectively. This work can achieve high performance and consume lower power. Circuit performance is summarized and listed in Table 1 and compared with those of prior references. Chip layout is shown in Fig. 10.

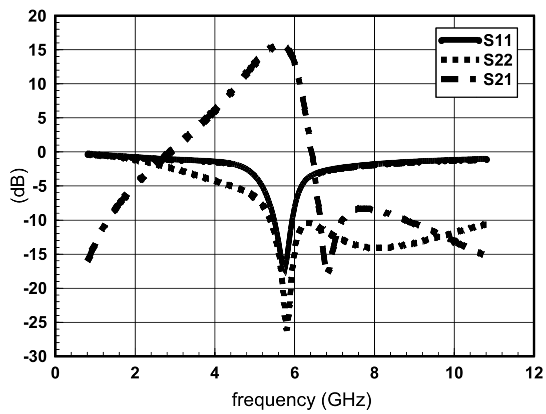

Figure 6: S-parameter.

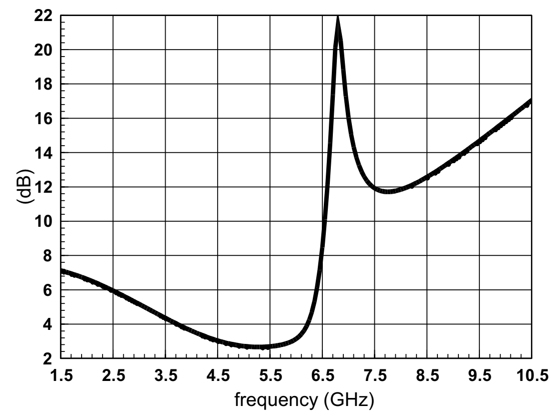

Figure 7: Noise figure.

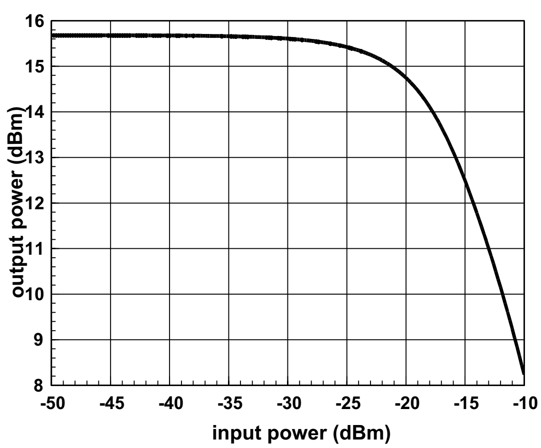

Figure 8: P1 dB.

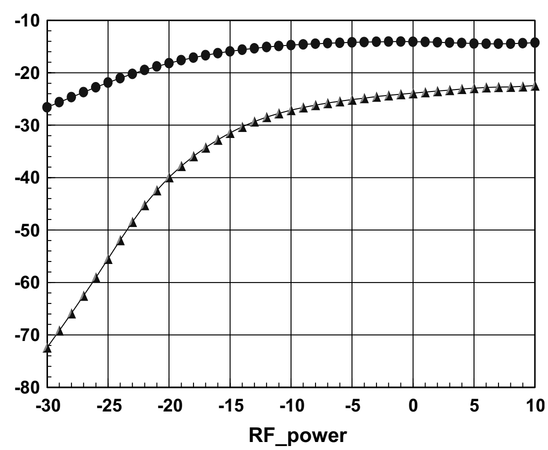

Figure 9: IIP3.

Table 1: Compariation of image rejection LNA.

	Operation frequency (GHz)	Image frequency (GHz)	S11 (dB)	S22 (dB)	S21 (operation) (dB)	S21 (image) (dB)	NF (dB)	Power (mW)
This work	5.8	6.8	-15.9	-26	15.4	-18.1	2.85	5.98
[1]	5.25	4.25	-18	-20	20.5	-15	1.5	12
[2]	2.4	1.8	N/A	N/A	11	-35	3	6.3
[3]	2.4	2	-8	N/A	18	-80 (m ax)	4.6	32

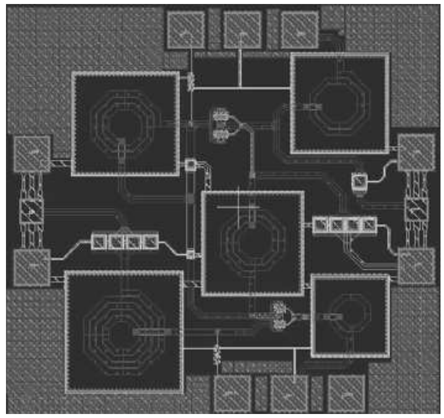

Figure 10: Chip layout.

4. CONCLUSIONS

In order to eliminate external SAW filter, the LNA with new on-chip image rejection techniques have been proposed. This image rejection LNA uses current reuse and reduces the numbers of transistors so that power dissipation can be decrease. By locating image rejection filter in inter-stage of current reuse circuit, high performance LNA with image rejection capability can be achieved.

ACKNOWLEDGMENT

The authors would like to thank the Chip Implementation Center (CIC) of the National Science Council, Taiwan, R.O.C., for supporting the TSMC CMOS process.

REFERENCES

1. Nguyen, T.-K., N.-J. Oh, C.-Y. Cha, Y.-H. Oh, G.-J. Ihm, and S.-G. Lee, "Image-rejection CMOS low-noise amplifier design optimization techniques," *IEEE Transactions on Microwave Theory and Techniques*, Vol. 53, Issue 2, Feb. 2005.
2. Sun, M.-C., S. T., Y.-H. Shu, and W.-S. Feng, "A 2.4 GHz CMOS image-reject low noise amplifier," *ISCAS '03. Proceedings of the 2003 International Symposium on Circuits and Systems*, Vol. 1, 25–28 May, 2003.
3. Chan, A. N. L., C. Guo, and H. C. Ltrong, "A 1-V 2.4-GHz CMOS LNA with source degeneration as image-rejection notch filter," *ISCAS 2001. The 2001 IEEE International Symposium on Circuits and Systems*, Vol. 4, 6–9 May, 2001.
4. Chang, Y., et al., "A Monolithic RF image-reject filter," *Southwest Symposium on Mixed-Signal Design*, 41–44, 2000.
5. Guo, C., et al., "A full integrated 900 MHz CMOS wireless receiver with on-chip RF and IF filters and 79-dB image rejection," *IEEE Journal of Solid-Stage Circuits*, Vol. 37, No. 8, 1084–1089, Aug. 2002.

A 3–8 GHz Broadband Low Power Mixer

Chih-Hau Chen and Christina F. Jou

Institute of Communication Engineering, National Chiao Tung University, Hsinchu, Taiwan

Abstract— A 3–8 GHz broadband mixer is presented in this paper. This broadband mixer is low power and high conversion gain. It provides current reuse and ac-coupled folded switching. This mixer is designed in TSMC 0.18-μm CMOS technology. This broadband mixer achieves simulated conversion gain of 9 ± 1.5 dB, a single sideband noise figure lower than 15.2 dB and IIP3 batter than -7 dBm. From 3–8 GHz, at supply voltage of 1.5 V power consumption without output buffer is 3.27 mW and power consumption with buffer is about 8 mW. The chip area is 1079 μm × 761 μm.

1. INTRODUCTION

In the wireless communication system, low power RF component is a trend recently. However, if we reduce the power and supply voltage, the linearity and conversion gain will be degraded. In order to accomplish low power and low voltage, holding out linearity and conversion gain without degraded is a challenge in the system. A low power mixer for UWB system input broadband matching will be a first challenge getting good return loss. Mixers executed in the receiver afford frequency translation to lower frequency or higher frequency by multiplying two signals in time domain. Mixer can be divided into two regions. One is down-conversion mixer which makes RF frequency down to IF frequency. The other is up-conversion which makes IF frequency up to RF frequency. In this work, we discuss a low power folded switch down conversion mixer.

Because of the development in the CMOS technology, we have a chance to achieve the low currents and low power in CMOS process circuit. However, it may have not enough headroom of supply voltage. Therefore, we require sufficient supply voltage to complete this mixer without cutting off transistor. A 0.3–25 GHz UWB mixer has been proposed [1], and a low voltage 2 mW $6 \sim 10.6$ GHz UWB mixer is reported in [2], a low power up-conversion mixer for 22–29 GHz UWB mixer is reported in [3], wide band and low power mixer is reported in [4].

Gilbert-based mixers can remove the undesired output LO component through the differential pairs providing opposite signal phases to cancel the feed through from the LO to the IF and generates less even-order distortion. The double-balanced mixer also has better port-to-port isolation. In traditional Gilbert cell mixers, the switching stage is stacked on the top of the transconductor stage, and resistor is stacked on the top of the switch stage. In this topology, it would compress voltage headroom. Therefore we adopt folded switching mixer. It can reduce voltage headroom of this circuit and provide broad choice of supply voltage. We can achieve the different headroom voltage from switching stage and transconductor. It will release the limit of the supply voltage. In this work as Fig. 1, we use supply voltage of 1.5 V and get good performance in this folded switching mixer.

2. ARCHITECTURE AND ANALYSIS

In Gilbert cell double-balanced mixer, nmos transistor is used as transconductor. But it may compress the headroom of the supply voltage. Then we test a resistor stacked on the top of the nmos as transconductor stage as shown in Fig. 2, the direction of signal current may be as low as possible through resistor. We would increase R to keep low ac current. However, it may limit the headroom of supply voltage. In this work, we use nmos transistor stacked of pmos transistor as transconductor, just like a CMOS inverter as Fig. 3. Because of this folded switching topology, we can achieve low supply voltage instead of limiting voltage. The components C1, L1, C2, L2, R1 are used as input matching to achieve broadband at $3.1 \sim 8.1$ GHz. $M1 \sim M4$ are transconductor stage used of nmos and pmos stacking. $M5 \sim M8$ are folded as switch stage. $M9 \sim M14$ are used as output buffer just like a common drain with a current source.

In transconductor stage, the advantage of using pmos instead of resistor can be amplified RF signal. The pmos can be used as current reuse. It can not only supply high gain but also provide a low power. The capacitor C affords ac-coupled in RF signal and to be isolated of pmos and nmos

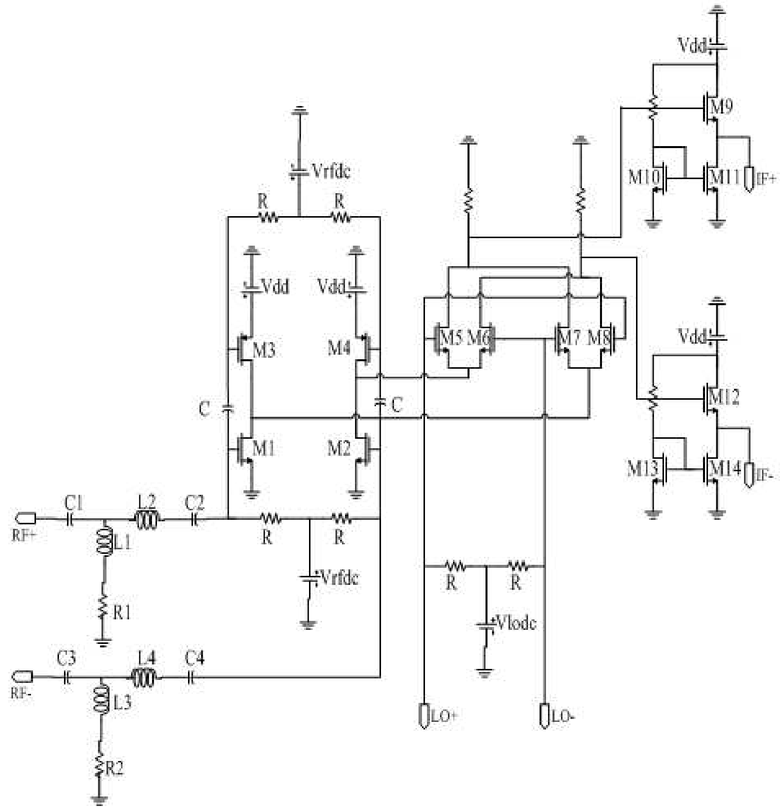

Figure 1: Proposed broadband folded switching mixer.

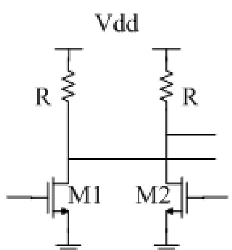

Figure 2: Nmos stacked R as transconductor.

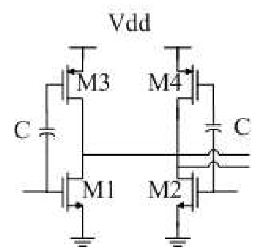

Figure 3: Proposed broadband mixer with current reuse.

in DC. In RF signal, the total g_m is equal to $g_{mn} + g_{mp}$ (g_{mn} is the transconductance of nmos M1, and gmp is the transconductance of pmos). The voltage conversion gain of the mixer shown in [5]

$$CG = 20\log\left(\frac{2}{\pi}\left(g_{mm} + g_{mp}\right)R\right)$$

Therefore, the conversion gain will be increased.

Linearity in the mixers is very important. Nonlinearity in the mixer voltage transfer function is caused by operation of the switching transistors in the linear region. The transistors in switching stage will be cutting off by the large voltage swing at the drain of the M1 and M2. Linearity almost completely decides by the input signal dynamic range. In the folded switching mixer with current reuse, the linearity can be improved by decreasing the DC drain voltages of the M1 and M2 as Fig. 1 [5].

The input matching is important in the broadband mixer. Because this mixer operates for 3–8 GHz, we can use LC ladder to match instead of transmission line. We use C1, C2, L1, L2, R1 to achieve wideband input matching. Therefore, we can achieve good performance of input return loss.

3. SIMULATION AND PERFORMANCE

The down conversion mixer is designed with 0.18 μm TSMC CMOS process. Input RF frequency and LO frequency are 3–8 GHz. Fig. 4 shows input return loss and output return loss. In 3–8 GHz, the input return loss are all lower than −10 dB. This is good performance in broadband input matching. Fig. 5 shows LO power versus conversion gain with RF frequency at 8.1 GHz and LO frequency at 8 GHz. We can see about −4 dBm of LO power, we can get the best conversion gain. With −4 dBm of LO power, we can obtain P1 dB with −22 dBm as shown in Fig. 6. Simulation broadband conversion gain can be shown as Fig. 7. Broadband conversion gain are all around 9 ± 1.5 dB. Based on two tones test with 1 MHz offset frequency, IIP3 is −4.5 dBm at 8 GHz as shown in Fig. 8. For 3–8 GHz, all IIP3 are better than −7 dBm. Compared with other mixers in Table 1, this work provides low power, broad band, good return loss, and good performance for other section. In this mixer, power consumption is 8 mW. Fig. 9 shows the layout of this broadband mixer. And Table 1 shows the comparison with the references.

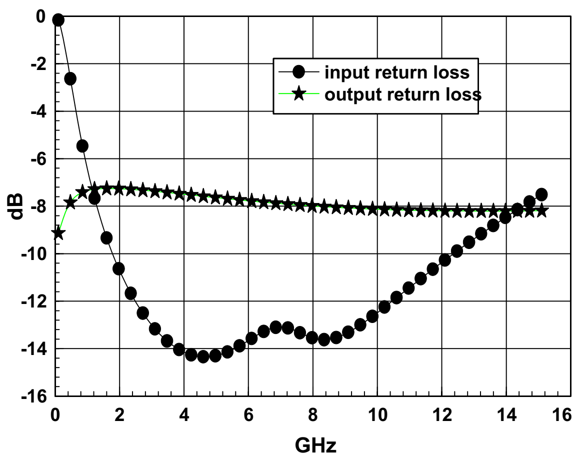

Figure 4: Return loss at 3 ∼ 8 GHz.

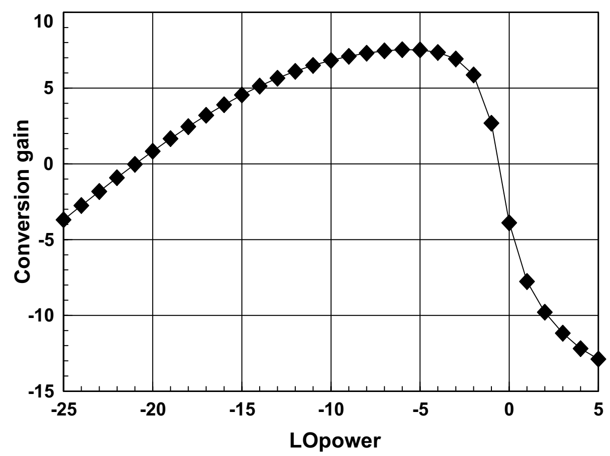

Figure 5: LO power versus conversion gain.

Table 1:

	Tech.	BW (GHz)	S11 (dB)	Conversion Gain (dB)	NF (SSB) (dB)	VDD (V)	Core mixer Power (mW)	IIP3 (dBm)
This work	0.18 μm CMOS	3.1–8.1	< −12	7.5–10.8	12.4–15.2	1.5	8	−3.4–7
[1]	0.18 μm CMOS	0.3–25	< −5	11	N/A	5	71	
[2]	0.18 μm CMOS	6–10.6	N/A	14 ∼ 17	15	1	2	−1 ∼ +1
[3]	0.18 μm CMOS	22–29	< −5	−2 ∼ 0.7	N/A	1.2	8	OIP3 5.8
[4]	0.18 μm CMOS	0.8–2.2	N/A	10.5	N/A	2.7	9.7	+10
[5]	0.18 μm CMOS	2.4	N/A	11.9	13.9	0.7	3.2	−3
[5]	0.18 μm CMOS	2.4	N/A	16	12.9	1.8	8.1	1

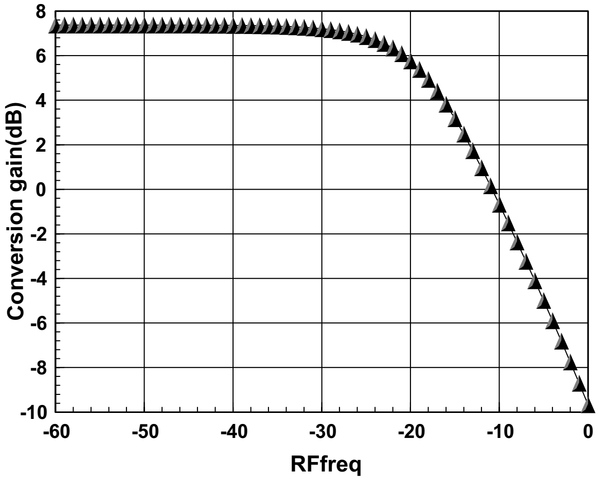

Figure 6: Simulation P1 dB at 8 GHz.

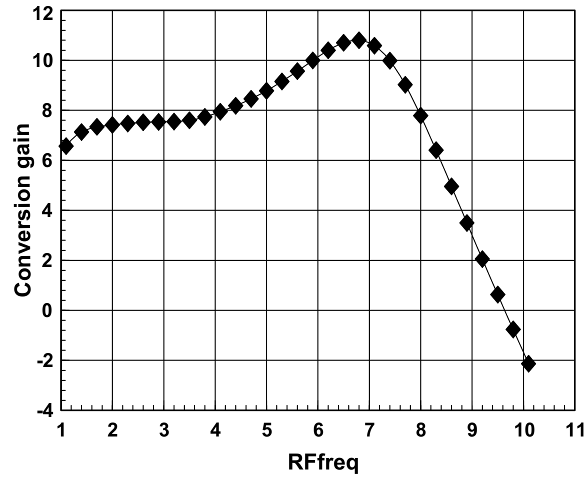

Figure 7: 3–8 GHz conversion gain.

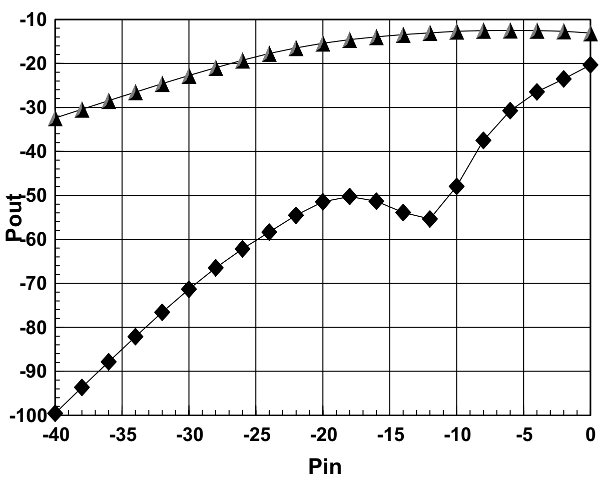

Figure 8: Simulation IIP3 at 8 GHz.

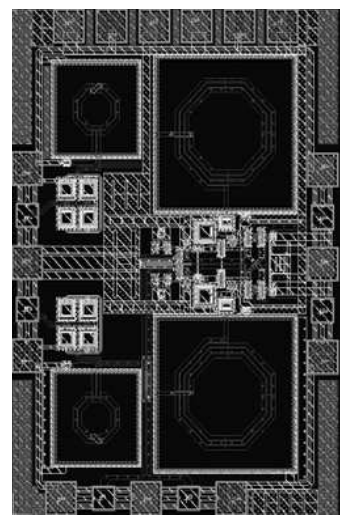

Figure 9: Chip layout.

4. CONCLUSIONS

This proposed mixer for 3 to 8 GHz with UWB system has high conversion, broad band, good return loss, moderate linearity, moderate noise figure, good isolation. This mixer is implemented in 0.18 μm TSMC CMOS technology. The advantages of this mixer are 10.8 dB conversion gain, lower than 11.4 dB noise figure, −3.4 IIP3, and only need 3.27 mW in 3 ∼ 8 GHz. It uses current reuse and folded switching to achieve low power consumption with 1.5 supply voltage. Comparing with other mixers, this mixer has the performance of low power, enough bandwidth, and good performance with current reuse.

ACKNOWLEDGMENT

The authors would like to thank the Chip Implementation Center (CIC) of the National Science Council, Taiwan, R.O.C., for supporting the TSMC CMOS process.

REFERENCES

1. Tsai, M.-D. and H. Wang, "A 0.3–25-GHz ultra-wideband mixer using commercial 0.18-μm CMOS technology," *IEEE Microwave and Wireless Components Letters*, Vol. 14, No. 11, November 2004.
2. Hsu, T.-T. and C.-N. Kuo, "Low voltage 2-mW 6 ∼ 10.6-GHz ultra-wideband CMOS mixer with active balun," *Circuits and Systems, 2006. ISCAS 2006. Proceedings*, 2006.

3. Verma, A., K. K. O, and J. Lin, "A low-power up-conversion CMOS mixer for 22–29-GHz ultra-wideband applications," *IEEE Transactions on Microwave Theory and Techniques*, Vol. 54, No. 8, August 2006.
4. Belkhiri, C., S. Toutain, and T. Razban, "Wide bandwidth and low power CMOS mixer with high linearity for multiband receivers using direct conversion implementation," *2005 European Microwave Conference*, 2005.
5. Vidojkovic, V., J. van der Tang, A. Leeuwenburgh, and A. H. M. van Roermund, "A low-voltage folded-switching mixer in 0.18-/spl mu/m CMOS," *IEEE Journal of Solid-State Circuits*, Vol. 40, No. 6, June 2005.

Frequency Synthesizer Architecture Design for DRM and DAB Receiver

Jianzheng Zhou[1,2] **and Zhigong Wang**[1]

[1]Institute of RF- & OE-ICs, Southeast University, Nanjing, China
[2]School of Computer & Information, Hefei University of Technology, Hefei, China

Abstract— Based on the specifications of DRM/DAB receivers, 4 synthesizer structures were designed for the receiver which supports several radio standards including AM, DRM, FM, and DAB. Comparisons of the characteristics of the four structures were given. Analysis and calculations prove that the synthesizer structure 1 with a single VCO and a single loop filter is the most suitable one to be used in the DRM/DAB receivers with good performance in phase noise, reference spurs and lock time, at expense of little more power consumption.

1. INTRODUCTION

A DRM/DAB receiver will need to support several radio standards including AM, DRM, FM, and DAB, and needs to provide the necessary flexibility for seamless receive. A key challenge in the full integration of such a DRM/DAB receiver is the design and implementation of its beating heart, i.e., the reconfigurable frequency synthesizer which acts as the local oscillator (LO) and covers all the frequency bands of the considered standards. This is due to the difficulty in meeting the performance requirements with on-chip components because of the diverse standards it needs to support. It is also due to the simulation of the synthesizer, a task that requires mixed-signal tools that should provide radio frequency, analog, and digital perspectives.

We have proved that a double-conversion low-IF structure is the most suitable architecture for the DRM/DAB receiver, and the first intermediate frequency (f_{IF1}) is 36.95 MHz and f_{IF2} is 2 MHz for DAB, 175 kHz for other bands in this system. The receiver needs two quadrature LO signals, the first one is generated by a synthesizer and the second one is a fixed frequency, which is easy to be generated. So, only the synthesizer which generates the first quadrature LO is discussed in this work.

2. DESIGN SPECIFICATIONS

Some of the main design specifications and considerations are given as follows.

2.1. Output Frequency Range and Resolution

The output frequency range and resolution of the frequency synthesizer are listed in Table 1.

Table 1: The output frequency range and resolution.

Band	Output frequency range (MHz)	Resolution (kHz)
LF	37–37.3	3
MF	37.4–38.7	1
HF	39.2–64	5
FM	112.9–145	25
III band	210.9–277	64
L band	1488.9–1529	64

2.2. Phase Noise and Spurious Frequencies

Numerical stipulation of phase noise for this design, a typical value of -80 dBc/Hz @1 kHz is chosen. Generally speaking, all sidebands need to be approximately 70 to 80 dB below the main carrier.

2.3. Switching Time

Initial design switching time of less than 100 ms is aimed. Furthermore, generation of quadrature LO-signals is mandatory for low-IF receiver architecture.

3. FREQUENCY SYNTHESIZER ARCHITECTURE DESIGN [1]

Since a direct analog frequency synthesizer (DAS) or a direct digital frequency synthesizer (DDFS or DDS) can provide an arbitrarily small frequency step size, at expense of higher complexity, higher dissipation and a larger die area, and thus they are often not suitable for DRM/DAB receivers, the charge-pump phase locked loop (PLL) frequency synthesizer is widely adopted. To address different application requirements, there are several PLL synthesizer architectures, such as fractional-N architecture, dual-loop architecture, or integer-N architecture. Each has advantages and drawbacks, depending upon the application.

The Fractional-N PLL architecture enables a PLL synthesizer to generate output frequencies with a step size smaller than the reference frequency. But, it suffers from fractional spurs which degrade the spurious-tone performance.

In Multi-Loop PLL Synthesizer [2–4], the basic idea of it is that spectral purity can be separated from the minimum step size specification, with the small tuning step requirement being satisfied with the addition of a second loop to the tuning system. This architecture can improve the tradeoff among phase noise, channel spacing, reference frequency, and locking speed of the synthesizer. Although more circuits are needed, the specifications for each building block are much relaxed [5].

Despite the advance of fractional-N or multi-loop PLL architectures, Integer-N architectures are still the most popular synthesizer architectures used in the industry due to its simple architecture, easy implementation, high reliability, low power, and low-cost in terms of design time. The basic limitation is the fact that the reference frequency is equal to the minimum step size of the PLL, which can lead to quite a few drawbacks including: (a) large division ratios — increased area and power, (b) low bandwidth — large lock times, and (c) reference spurious tones. So, conventional single-loop PLL synthesizers are not able to combine the requirements of small step size, good spectral purity, and wide loop bandwidth [3]. While in single-loop integer-N PLL Synthesizer with a divider shown in Fig. 1 [6–8], an additional frequency divider X is placed at the output of the VCO to allow for smaller frequency steps than the loop's reference frequency and improve the lock time, phase noise, and reference spurs.

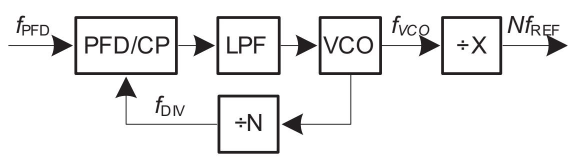

Figure 1: Single-loop integer-N PLL synthesizer with divider.

To address all these needs, 4 frequency synthesizer architectures are given in the following sections.

3.1. Synthesizer Structure 1

The frequency synthesizer architecture 1 given in Fig. 2 has been defined such that all reception bands can be accessed with a single VCO and a single loop filter. The VCO covers the band from 2600 to 3120 MHz. Mapping the frequency of the VCO to the different input bands is achieved by dividing its output frequency by different ratios, depending on the band to be received. A divide-by-2 and -4 circuits are included to generate the desired quadrature LO frequencies. Table 2 presents the frequency synthesizer parameter settings for various reception bands.

In this configuration, $f_{\rm OUT} = (f_{\rm PFD} \times N)/X$. Some consequences for this architecture are given as follows.

a) The minimum step size is indeed smaller than $f_{\rm PFD}$.

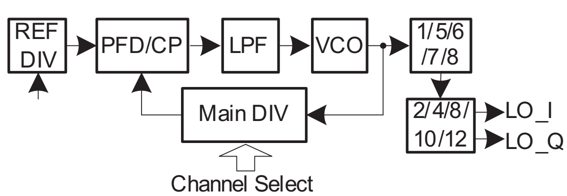

Figure 2: Synthesizer structure 1.

Table 2: Reception bands with corresponding synthesizer Parameters [7].

Band (MHz)	LO (MHz)	$X1$	$X2$	f_{PFD} (kHz)
LF: 0.1485–0.2835	37.0985–37.2355	8	10	240
MF: 0.525-1.710	37.475–38.66	8	10	80
HF: 2.3–27	39.25–43	6	12	360
	43–48	8	8	320
	48–55	7	8	280
	55–63.95	6	8	240
FM: 76–108	112.95–130	6	4	600
	130–144.95	5	4	500
III band: 174–240	210.952-220	7	2	896
	218–260	6	2	768
	260–276.952	5	2	640
L band: 1452–1492	1488.952–1528.952	1	2	256

b) Compared to the use of the standard integer-N architecture, the phase noise performance of this kind of synthesizer is optimized by $10\log(X)$ at the LO output.

c) Reference spurs reduction: In this architecture, at f_{OUT}, the spurious frequencies still exist at the integer multiples of the PFD frequency but they are reduced in amplitude by $20\log(X)$.

d) Shorter lock time due to higher PFD frequency.

The price of this improved performance is the extra cost of the output divider and the extra power consumption of the system as a whole. Thus, the improved performance must be a critical requirement for selecting this architecture.

3.2. Synthesizer Structure 2

Synthesizer structure 2 is shown in Fig. 3. This structure is similar to structure 1, except that f_{PDF}, f_{VCO}, and X is one half of these in structure 1. In other words, f_{VCO} is divided by 40 for LF and MF bands, by 36, 32, 28, or 24 for HF band, by 12 or 10 for FM band, by 7, 6 or 5 for III band, and by 1 for L band. When X is odd number, path I is chosen, in this case a poly-phase filter (PPF) is used to generate the desired I/Q LO frequencies. When X is an even number, path II or III is chosen, a divide-by-2 circuits are included to generate the desired quadrature LO frequencies.

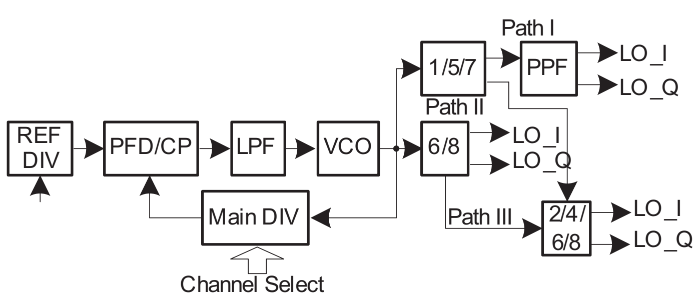

Figure 3: Synthesizer structure 2.

3.3. Synthesizer Structure 3

Synthesizer structure 3 is shown in Fig. 4 [9]. This structure is also similar to structure 1, but f_{PDF}, f_{VCO}, and X is one fourth of the counterpoint in stucture 1. In other words, the VCO covers 650 to 780 MHz, and divided by 20 for LF and MF bands, by 18, 16, 14, or 12 for HF band, by 6 or 5 for FM band, by 3.5, 3 or 2.5 for III band, and by 0.5 for L band. When X is a fraction number, such as 0.5, 2.5, and 3.5, path I is chosen. In this case the Delay-Locked loop (DLL) combines the functions of frequency multiplication and quadrature generation. It consists of a DLL with $2N$

tunable delay cells that can multiply the frequency of the incoming signal with a factor N, while also generating the quadrature LO-signals [10]. When X is an odd number, path I is used, but the DLL is used to generate the desired I/Q LO frequencies only. When X is an even number, path II is chosen, in which a divide-by-2 circuits are included to generate the desired quadrature LO frequencies.

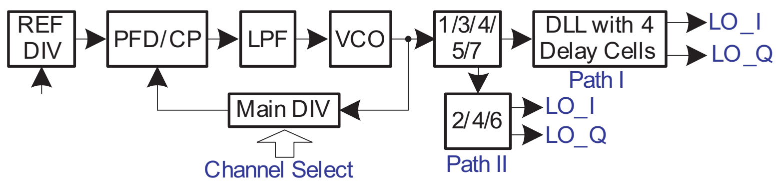

Figure 4: Synthesizer structure 3.

3.4. Synthesizer Structure 4

Another alternative solution is to use a dual-loop architecture shown in Fig. 5. Table 3 presents the VCO frequency and frequency synthesizer parameter settings for various reception bands. The VCO1 covers 37 to 1529 MHz.

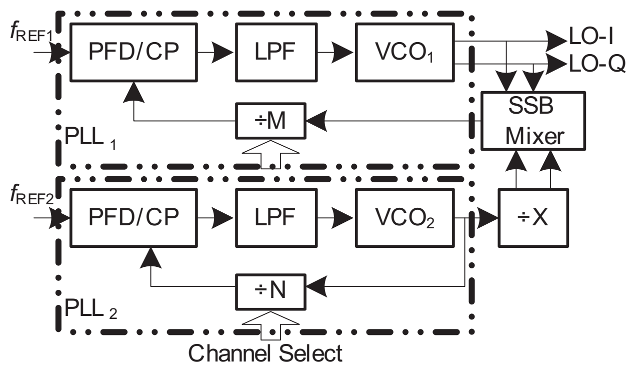

Figure 5: Synthesizer structure.

Table 3: VCO frequency and frequency synthesizer parameter settings for various reception bands.

Band	f_{REF1} (MHz)	M	X	N	f_{VCO2} (MHz)
LF HF	3	12	20	366–887	21.97–53.2
HF	2	19–30	14	1250–3950	17.5–55.3
FM	5	22–27	10 6	590–1990	29.5–60 36–59.7
III band	8	26–33	6 4	118–518	17.7–48 32–51.8
L band	20	74–75	2	139–453	17.9–57.9

3.5. Comparison of These 4 Synthesizer Structures

The total phase noise in a phase locked loop (dB) can be expressed as follows [6]:

$$PN_{\text{tot}} = PN_{\text{floor}} + 20\log N + 10\log f_{\text{REF}} - 20\log X \tag{1}$$

where, PN_{tot} is the total phase noise of the synthesizer, f_{REF} is the incoming PFD frequency of the synthesizer, PN_{floor} is the phase noise due to the PLL synthesizer circuit itself. This provides a figure of merit for the PLL synthesizer circuit itself. For ADF4106, this figure is $-219\,\mathrm{dBc/Hz}$ @1 kHz. $20\log N$ is the increase of phase noise due to the frequency magnification associated with the feedback ratio, $1/N$. $20\log X$ is the improvement of phase noise due to the division with the divider ratio, $1/X$.

On the other hand, the spurious frequencies exist at the integer multiples of the PFD frequency, and they are reduced in amplitude by $20\log X$. Furthermore, shorter lock time due to higher PFD frequency.

So the phase noise of structure 1 is 3 dB, 6 dB better than the counterpart of structure 2 and structure 3 respectively. And the reference spurs of structure 1 is 6 dB, 12 dB better than the counterpart of structure 2 and structure 3, respectively. And the lock time is much shorter than structure 2 and structure 3.

The f_{VCO} of Structure 1 is two and four times of that of the structure 2 and 3, respectively, it needs more power consumption. However, it easier to implement on-chip than that of Structure 2 and 3. Moreover, Structure 2 and 3 need extra PPF or DLL to generate the quadrature LO signals, so they need a more complex circuit, a larger chip area and even more power consumption.

The phase noise, reference spurs and lock time of Structure 4 maybe better than these of other structures, at expense of higher complexity and a larger die area. Especially, the tunable frequency range of VCO_1 and VCO_2 is too large to implement on-chip, and VCO_1 need output quadrature LO signals, and the performance of synthesizer also lies on the perfect single side-band mixer. So this design is not the best solution for DRM/DAB receivers' synthesizer.

Based on the analyses given above, we can know that the synthesizer structure 1 is the most suitable one for DRM/DAB receiver.

4. PERFORMANCE ANALYSIS OF THE SYNTHESIZER STRUCTURES

Suppose that the PN_{floor} of the PLL is better than $-210\,\mathrm{dBc/Hz}$ @1 kHz, we can obtain the performance of the synthesizer structure 1, which is given in Table 4, based on the formula (1) and the experiential formula that the switch time $t_{sw} < 25/f_{\mathrm{PFD}}$.

Table 4: The performance of synthesizer structure 1.

Band	Step Size (kHz)	Phase noise (dBc/Hz@1 kHz)	Ref. spur Reduction (dB)	Switch Time (ms)
LF	3	< -112	38	< 0.1
MF	1	< -107	38	< 0.3
HF	5	< -107	> 33.6	< 0.1
FM	25	< -103	> 26	< 0.05
III band	64	< -99	> 20	< 0.04
L band	64	< -80.4	6	< 0.1

5. CONCLUSIONS

In the quest for true reconfigurable DRM/DAB receiver, four frequency synthesizer architectures are given, enabling the generation of quadrature LO signals over extremely wide frequency ranges. Theoretical analysis shows that structure 1 will be the best one to be used with good performance in phase noise, reference spurs and lock time, at expense of little more power consumption. As we can see from the Table 4, synthesizer structure 1 can meet the design specification, is very suitable for DRM/DAB receivers, need few external components and require no mechanical alignments.

REFERENCES

1. Sinha, S., "Design of an integrated CMOS PLL frequency synthesizer," *Proceedings of 11th Mediterranean Electrotechnical Conference, MELECON 2002*, 220–224, 7–9 May 2002.
2. Leenarts, D. M. W. and C. S. Vaucher, "Frequency synthesizers for RF transceivers," *Proceedings of the 2003 Bipolar/BiCMOS Circuits and Technology Meeting*, 189–196, 28–30 Sept. 2003.
3. Vaucher, C. and D. Kasperkovitz, "A wide-band tuning system for fully integrated satellite receivers," *IEEE Journal of Solid-State Circuits*, Vol. 33, No. 7, 987–997, July 1998.

4. Yan and H. C. Luong, "A 2-V 900-MHz monolithic CMOS dual-loop frequency synthesizer for GSM wireless receivers," *IEEE J. Solid-State Circuits*, Vol. 36, 204–216, Feb. 2001.
5. Razavi, B., "Challenges in the design of frequency synthesizers for wireless applications," *Proceedings of IEEE Custom IC Conference*, 395–402, May 1997.
6. Curtin, M., "Design a direct 6-GHz local oscillator with a wideband integer-N PLL synthesizer," *Analog Dialogue*, Vol. 35, No. 6, 1–4, 2001.
7. Vaucher, C. S., "An adaptive PLL tuning system architecture combining high spectral purity and fast setting time," *IEEE Journal of Solid-State Circuits*, Vol. 35, No. 4, 490–502, April 2000.
8. Luff, G. F., S. Tuncer, N. M. Troop, C. R. Taylor, and D. W. Eddowes, "A compact triple-band Eureka-147 RF tuner with an FM receiver," *Proceedings of 2005 IEEE International Solid-State Circuits Conference, ISSCC 2005*, Vol. 1, 434–608, 6–10 Feb.2005.
9. Van Driessche, J., J. Craninckx, and B. Come, "Analysis and key specifications of a novel frequency synthesizer architecture for multi-standard transceivers," *Proceedings of 2006 IEEE Radio and Wireless Symposium*, 481–484, Jan. 2006.
10. Craninckx, J., V. Gravot, and S. Donnay, "A harmonic quadrature LO generator using a 90° delay-locked loop," *Proceedings of ESSCIRC 2004*, 127–130, 21–23 Sept. 2004.

Path Planning during the Geomagnetic Navigation

Lingling Jiang[1,2] and Lixin Ran[1,2]

[1]Electromagnetics Academy at Zhejiang University, Zhejiang University, Hangzhou 310027, China
[2]Department of Information and Electronic Engineering, Zhejiang University, Hangzhou 310027, China

Abstract— An optimal path planning learned from homing pigeon utilizing geomagnetic distributions on the earth is presented, which depends totally on the geomagnetic environments, without relying on familiar landmarks or information collected along the journey.

1. INTRODUCTIONEARTH'S

magnetic field is discovered to be information for pigeon's homing navigation in Todd E. Dennis's article [1]. Whether pigeons can rely totally on the geomagnetic field for position determination begs more biological experiments. Here we propose a theoretical navigation method similar to pigeons' homing behavior, which depends totally on the geomagnetic environments, without relying on familiar landmarks or information collected along the journey.

2. BACKGROUND

The true axis used by pigeons needs scientists' further experiments. Here we just set up a geomagnetic navigation model, pigeon homing as a paradigm, trying to explain her path planning during flying trajectory.

There must be two or more oblique intersecting coordinates to determine a fixed position on a surface [2]. I have a suggestion here to use paired combinations of the geomagnetic intensity and the declination. Then after released from an unfamiliar site, the pigeon's task is to compare these two factors with that of her home loft to find a way back.

3. MAGNETIC DIPOLE FIELD DECLINATION

The main composition of the geomagnetic field is geocentric magnetic dipole field, thus the systematic distribution of the dipole's declination can reflect that of the real world geomagnetic field to some extent.

Definition:

a Angle between magnetic North Pole and geographic North Pole.

c Magnetic colatitude, ranges from 0 degree to 180 degree.

λ_m Magnetic longitude, ranges from 0 degree to 360 degree, calculated from the half great circle connecting magnetic North Pole and geographic North Pole.

A Magnetic declination.

By calculation referring to Spherical Trigonometry materials [3, 4], we get following equation for A

$$\cos(A) = \frac{\sin(c)\cos(a) - \sin(a)\cos(c)\cos\lambda_m}{\sqrt{\sin^2 a\cos^2 c + \sin^2 c(1 - \sin^2 a^* \cos^2 \lambda_m) - \frac{1}{2}\sin(2c)\sin(2a)\cos\lambda_m}} \tag{1}$$

From Equation (1) we know that the declination varies with c and λ_m.

Plus, the isopleths of magnetic intensity of a Geocentric Dipole lies exactly where c is a constant.

4. PATH PLANNING DURING GEOMAGNETIC NAVIGATION

In Todd E. Dennis's article [1], pigeons showed parallel and perpendicular alignments to isopleths of geomagnetic intensity during homing. One abstraction and generalization of the flying trajectories is to approximate them to be connections of line segments showed in Figure 1, where the junction points are called nodes.

The geomagnetic intensity serves as the first factor. The line segments can be divided into two groups accordingly, the one parallel to isopleths of geomagnetic intensity are labeled as "a" segments; the other perpendicular to them labeled as "e" segments. We define two segments composed of one "a" segment and one "e" segment as one "a_e" pair. Along the way from starting point (or released point) to ending point (or home loft point), these segments are labeled with subscript as 1, 2 ... to n in sequence. The nodes are labeled in sequence too, with starting point as 0.

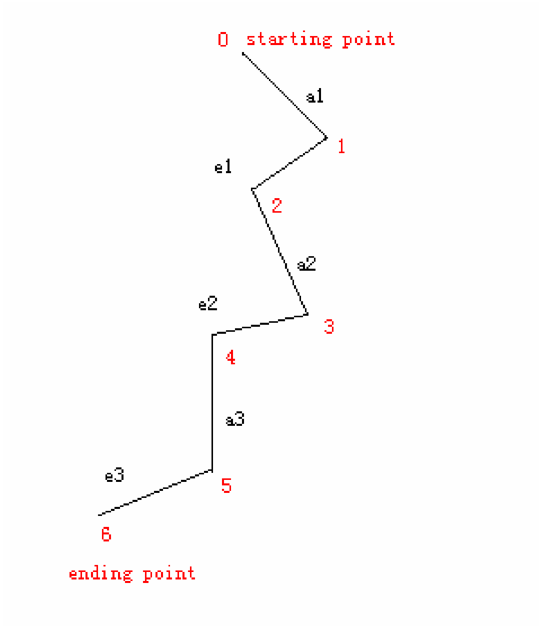

Figure 1: Idealized fly trajectories.

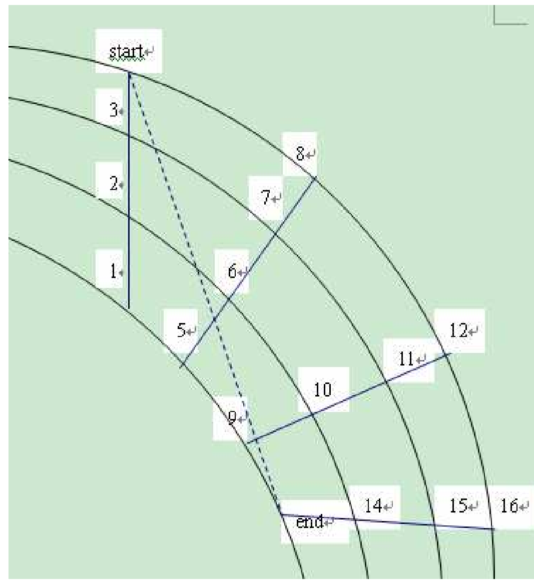

Figure 2: Multi-segments method.

Many pigeon racers discovered that pigeons turn circles in the air both after initially released and before landing to home loft [5]. We think it is the way pigeons finding the slope of the geomagnetic intensity isopleths around the circle center. During a uniform speed circle shape flying, the intensity varies at different rates at different positions. The tangent of the curve at the lowest rate position is parallel to the isopleths, whereas the highest rate designates perpendicular direction.

Each line segment joins two nodes, which can be marked as origin and aim according to the flying order. When pigeon fly along "e" segments, the magnetic intensity varies fastest since the segment is perpendicular to the intensity isopleths. And when it is along "a" segments, the magnetic intensity scalar keeps constant.

But when along "a" segment, another factor such as the geomagnetic declination varies as the second coordinate.

If the isopleths of the two factors are aligned at high angels to each other, then the variation rates will be efficient for homing pigeons.

5. EXPLANATION FOR PIGEON'S OPTIMAL PATH PLANNING BEHAVIOR

At this point, there comes up one doubt: Why don't pigeons fly along one "a" segment until the 2nd factor is the same as home loft before flying along the "e" segment to make the 1st factor equal to the final aim's demand, or these two procedures reversed? Only two segments will be much easier! Why its trajectory consists of so many segments?

Our explanations are as follows:

1) When in "e" segments, intensity varies. But the variation is too fast for pigeons to justify which grade of intensity they have reached, thus they need to turn to "a" segments frequently to make sure if the intensity has been over-varied (increased or decreased too much), or if they have overdo the homing. Since in "a" segments, intensity varies little, pigeons can find out the intensity value easier and compare it with that of the home loft. The comparison will not be time enough when the factor varies too fast.

2) Under the assumption that the pigeons can not pre-know the geomagnetic factor distributions along the homing way, since no information is collected along the journey when pigeons are taken from home to the released points, "multi-segments method" is a better choice to decrease the total distance as much as possible compared with "only two segments method".

An abstract illustration is showed in Figure 2 (warning: this is just a paradigm, not the real world factors' distributions.) Black line segments are isopleths of intensity factors, while blue line segments indicate perpendicular lines to intensity isopleths; numbered nodes indicate their junctions. Suppose pigeons are released at the "start node", its task is to find way back to the "end node". According to the homing decision described above, pigeon will fly along black and blue lines.

Since pigeons can not pre-know these line shapes. If the flying trajectory only consists of two segments, one pair of "a_e", there can be two possible routes: 1st is and the start→1→end and the 2nd is start→16→end, whether they choose the 1st route or the 2nd route depends on probability, obviously the 1st route is much shorter than the 2nd one.

But if "a_e" pairs increase

start→16 →end

starting→8→7→15→end

starting→8→7→11→10→14→end, etc

As the number of "a_e" segment pair increase, the trajectory gradually approximate to the start→end homeward direction (dashed line in Figure 2). Since the beeline connection of two points is the shortest route between them, if the pigeon's velocity is constant, it may be an optimal planning for pigeon navigation to make homing time less when the distribution along the way are unknown.

6. CONCLUSION

An optimal path planning is introduced in this paper, where the position determination is not limited to pigeon's biological behavior but expected to be applicable to human beings' navigations. It only needs acquainting the magnetic data near home and continuous comparing work done during the journey, instead of recording detailed magnetic information of a large scale area in advance (e.g., huge amounts of data required in terrain navigation). Therefore it may be used on the other planets where we do not know detailed magnetic data, as long as these planets have systematic magnetic distributions.

ACKNOWLEDGMENT

This work is supported by the NSFC (Nos. 60531020, 60671003), ZJNSF (No. R105253), the NCET-07-0750, and the Ph.D. Programs Foundation of MEC (No. 20070335120).

REFERENCES

1. Dennis, T. E., M. J. Rayner, and M. M. Walker, "Evidence that pigeons orient to geomagnetic intensity during homing," *Proceedings of the Royal Society B: Biological Sciences*, Vol. 274, No. 1614, 1153–1158, May 2007.
2. Walker, W. M., T. E. Dennis, and J. L. Kirschvink, "The magnetic sense and its use in long-distance navigation by animals," *Current Opinion in Neurobiology*, Vol. 12, No. 6, 735–744, December 1, 2002.
3. http://mathworld.wolfram.com/SphericalTrigonometry.html.
4. http://math.rice.edu/ pcmi/sphere/.
5. http://gdgs.chinaxinge.com/.

Simulation for a Distributed Phase-stable Synchronization System

J. Long[1], **S. Qiao**[3], **J. T. Huangfu**[1,2], **and L. X. Ran**[1,2]

[1]Department of Information Science and Electronic Engineering
Zhejiang University, Hangzhou 310027, China
[2]The Electromagnetics Academy at Zhejiang University
Zhejiang University, Hangzhou 310027, China
[3]City College, Zhejiang University, Hangzhou 310027, China

Abstract— In this paper, a method of providing a phase-stable signal to the remote terminal using a loop system is mentioned. The phase stability is the feature of this system. Two methods of simulation are presented. Excellent results show the great performance of the system.

1. INTRODUCTION

In some fields, such as measurement, microwave sensor, wireless communication and so on, a high precision clock is of great demand to achieve greater performance. In this paper, a distributed phase-stable synchronization system, which is capable of sending a phase-synchronous signal from the master base to several slave bases over a distance using a microwave signal, is presented. Several simulations and their results have been described here.

2. SYSTEM DESCRIPTION

This design is based on the system described in [1, 2], As is shown in Figure 1, the system over a radio link using two antennas separated by a physical, generally varying all the time, distance is composed of 4 modules, upper-sideband generator (USG), lower-sideband generator (LSG), phase-halving block, antennas and transmitting space part. USG and LSG as well as other mixers appearing in the system are the components used to manipulate the phase and frequency. The phase-halving block is a function block which is able to divide not only the frequency but also the phase in half precisely, suggesting using a PLL with the phase error of zero. The transmitting space part and antennas are used here only because this system is used to provide a signal over a distance.

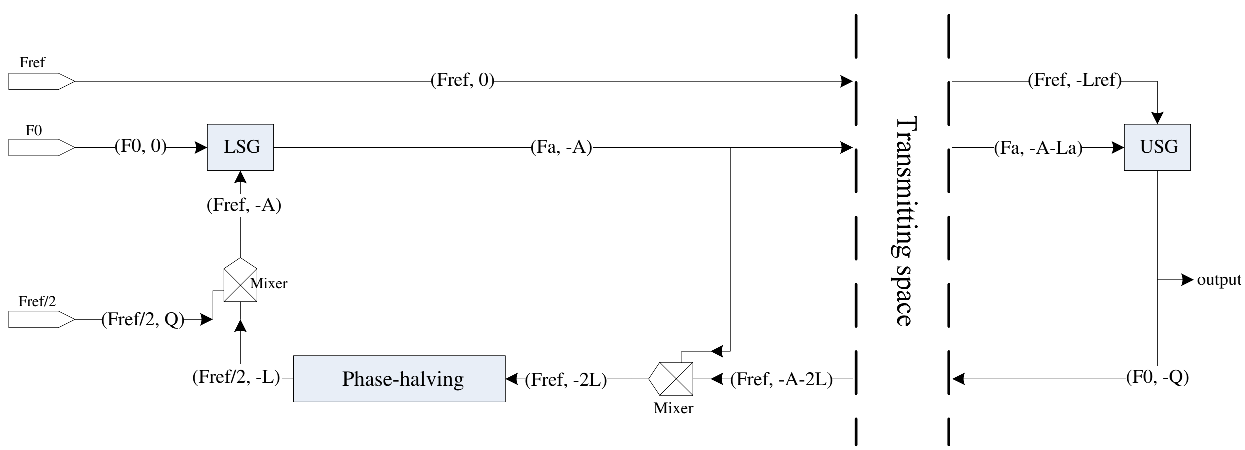

Figure 1: System block diagram.

In Figure 1, $(Fref, 0)$ means a signal with the frequency of $Fref$ and the phase of $0\,\text{rad}$; $Fa = F0 - Fref$, $A = Q - L$; L, $Lref$ and La are the phase delay of $F0$, $Fref$ and Fa separately. From these frequencies and the phases labeled on Figure 1, we can easily see how the signal is locked. The key component is the phase-halving block. It must be able to divide both the phase and frequency in half; otherwise the system can not work properly.

3. NUMERICAL SIMULATION

A simulation with matlab is formulated here. The system is implemented with the method of the mathematic model. As analyzed in the previous section, we simulate the system in phase domain.

As shown in Figure 2, three phase-controlled sources, which are $Fref$, $F0$ and $Fref/2$, are constants. Q is a source controlling the output phase. Distance is a source that varies with time depending on the distance between the master and slave, which is a parameter of the transmission space block. USG and LSG, as well as the mixers in Figure 1, are implemented by the SUM model, which can add or subtract the inputs depending on the configuration settings. Phase-halving block consists of two transfer function blocks, an adder and a gain block, which are put together to form a PLL. The transmission space block is actually an adder. Three components are added here, which are input signal with a time delay, noise and the phase delay due to the distance. Details of the transmission space block are in Figure 3. During the simulation, several types of sources are applied to Q and Distance in order to verify the performance of the system.

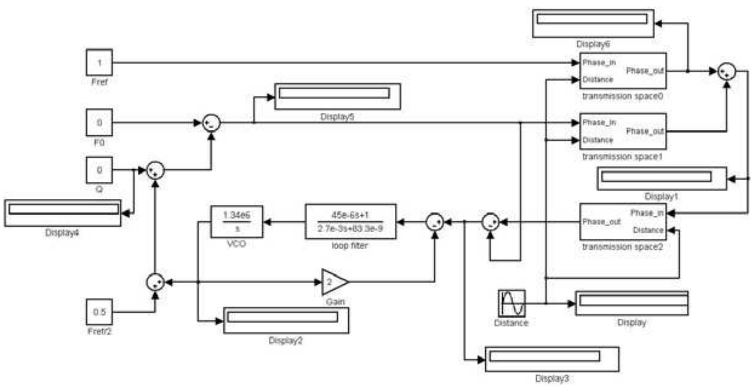

Figure 2: Numerical simulation in matlab.

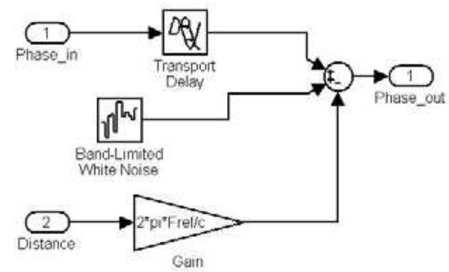

Figure 3: Details of transmission space block.

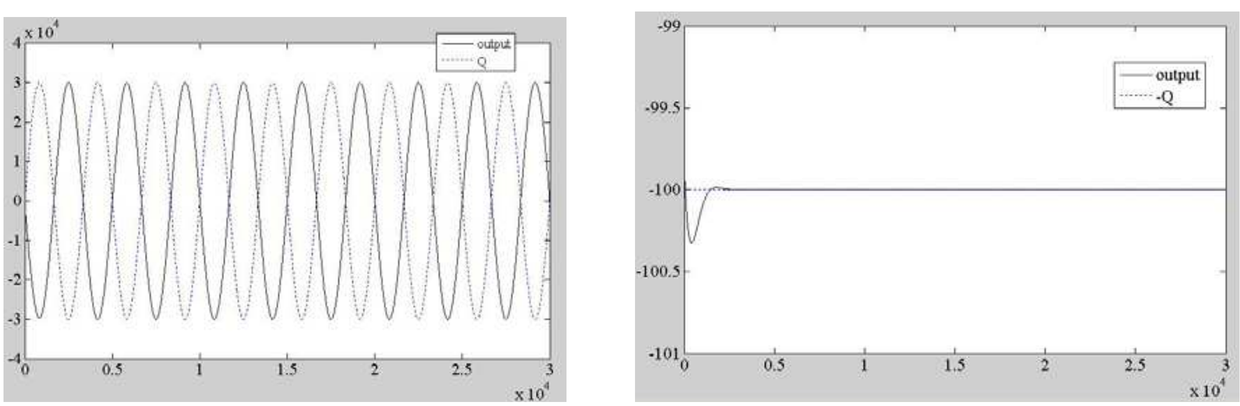

(a) (b)

Figure 4: Simulation result (without noise), (a) Distance is constant and Q is a sine signal, (b) Q is constant and Distance is a sine signal.

When Distance is fixed, we use three waveforms, which are constant, ramp and sine wave, to emulate Q. The result shows that all these three waveforms get a locked signal from the output and the locking time is too short to be distinguished. Figure 4(a) is about the result when a constant Distance and a sine Q are added to the system. When Q is fixed, the same method is applied to Distance. For a ramp signal, the system can be locked quickly. The output can be locked easily if Distance is a sine wave in a low frequency (less than 100 Hz). For a higher frequency, if the amplitude is large enough (we simulated as 30000), the output can not lock to Q. However, this case is impossible to happen. Figure 4(b) is about when a sine Distance and constant Q are added to the system.

In addition, a band-limited white noise is added. The two simulations mentioned above are done again. Results in Figure 5 show that a constant error occurs when a noise is added, but the locking time does not change much. According to the result, it is suggested that the system lock in a very short time. Without the noise, the output is absolutely the same as the input. If a noise is added to the system, the output has a constant error with the value. Therefore, according to the result of numerical simulation, the system is able to lock most types of signals.

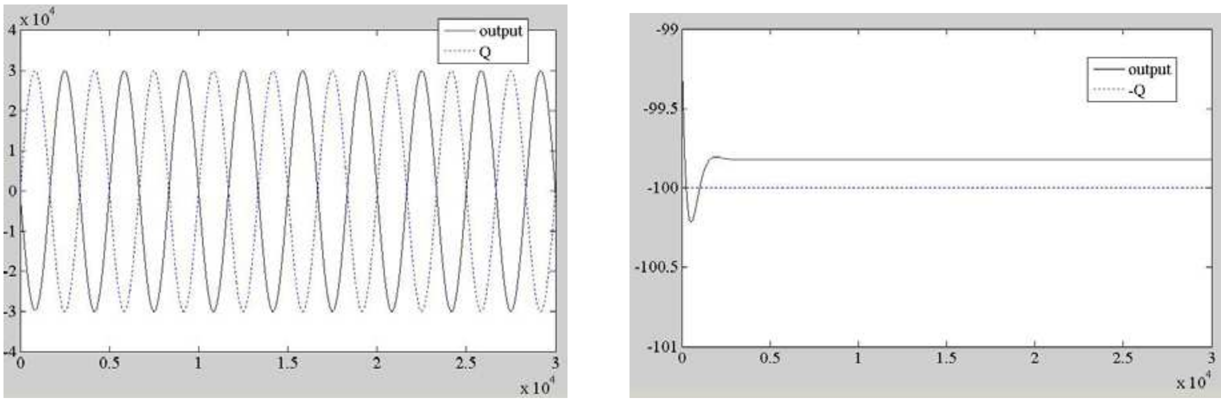

(a) (b)

Figure 5: Simulation result (with noise added into the transmission space block), (a) Distance is constant and Q is a sine signal, (b) Q is constant and Distance is a sine signal.

4. SYSTEM SIMULATION

In this section, we put forward a simulation with ADS (advanced design system) as system simulation. The whole simulation system is plotted in Figure 6. Q, as mentioned above, is integrated into *Half_Fref*. Three signal sources are implemented by sine wave blocks with specified phase and frequency. A mixer and a Butterworth band-pass filter are combined together as USG or LSG. A time delay is regarded as the transmission space. The most complicated part, phase-halving module, is composed of a PLL with low gain active 2 poles. An extra testing module is added in system simulation to evaluate the performance of the system. Since the output phase of the phase-halving block is within the range of 0 to 180°, it has an ambiguity of phase error of 180°. Thus a process on the output phase is necessary. The simplest way is to use a computer to make a judgment whether to add 180° or not.

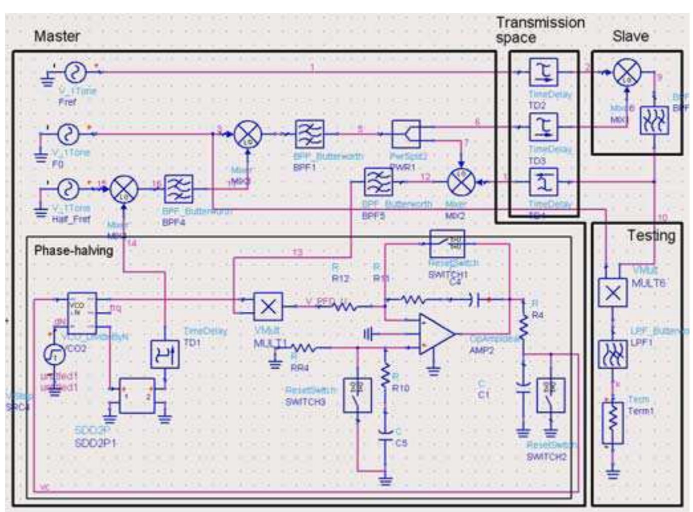

Figure 6: System simulation.

A transient simulation is conducted. We tune the phase of the *Half_Fref* and time delay to see how the phase of the output changes. Figure 7 is the result with the parameter as follows:

Stop time = 205 µs; Time step = 0.1 ns; Phase (this is the phase of *Half_Fref*) = 30 rad; Time delay = 60 µs. From Figure 7 we can definitely see that the input and output frequency and phase. The output of the testing module is almost constant after 100 µs, which demonstrates that the input and output have a constant dephasing and the same frequency.

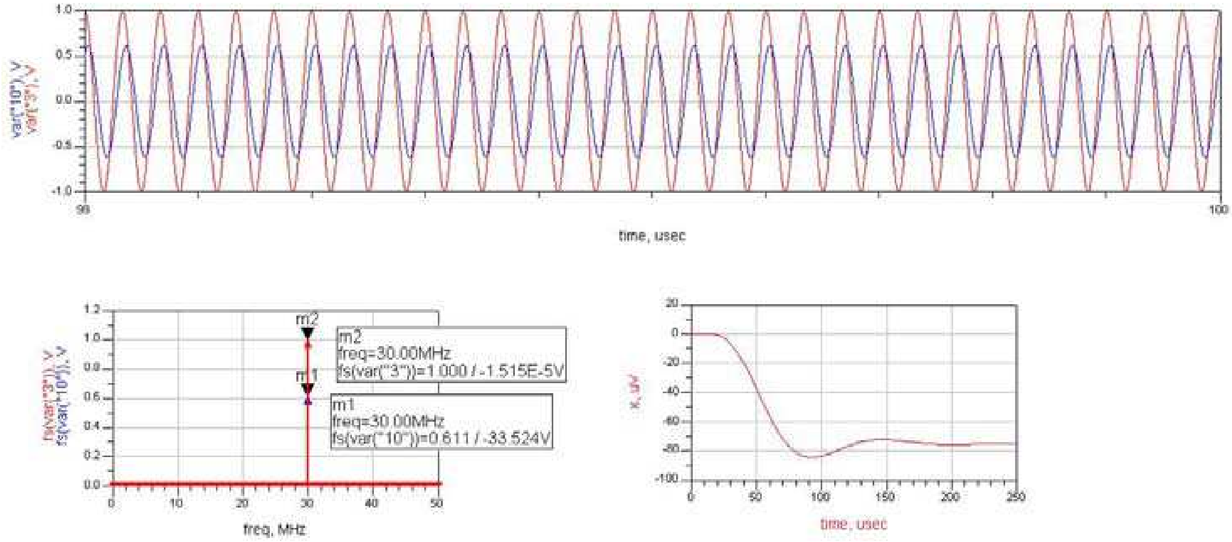

Figure 7: System simulation result.

Further simulation is put forward. Different parameters are applied and the summary is listed in the Table 1 and Table 2. Table 1 shows the performance under the condition of varying time delay. According to the table, with the time delay increasing, the phase difference is able to be controlled by the phase of *Half_Fref*. The average error is 3.025° and the standard deviation is 1.386°. Table 2 shows the case where the controlling phase is different. All the results show that the system can be locked within a small error range.

Table 1: Data collection when increasing the time delay.

No.	**stop time (µs)**	**Step (ns)**	**Phase of *Half_Fref***	**Time delay (ns)**	**Phase of $F0$**	**Output phase**	**Output Processed**	**Error**
1	100	0.1	30	30	$-1.577E-05$	−31.371	31.371	1.371
2	100	0.1	30	40	$-1.577E-05$	−35.276	35.276	5.276
3	100	0.1	30	45	$-1.577E-05$	147.666	32.334	2.334
4	100	0.1	30	50	$-1.577E-05$	146.861	33.139	3.139
5	100	0.1	30	55	$-1.577E-05$	147.119	32.881	2.881
6	205	0.1	30	60	$-1.515E-05$	−33.524	33.524	3.524
7	100	0.1	30	65	$-1.577E-05$	−33.353	33.353	3.353
8	100	0.1	30	70	$-1.577E-05$	−33.586	33.586	3.586
9	100	0.1	30	75	$-1.577E-05$	148.98	31.020	1.020
10	100	0.1	30	80	$-1.577E-05$	148.65	31.350	1.350
11	100	0.1	30	90	$-1.577E-05$	144.67	35.330	5.330
12	100	0.1	30	100	$-1.577E-05$	−33.14	33.140	3.140

Table 2: Data collection when phase is increasing.

No.	**stop time (μs)**	**Step (ns)**	**Phase of *Half_Fref***	**Time delay (ns)**	**Phase of $F0$**	**Output phase**	**Output Processed**	**Error**
1	100 μs	0.1 ns	0	65 ns	$-1.577E-05$	−3.023	3.023	3.023
2	100 μs	0.1 ns	15	65 ns	$-1.577E-05$	−18.637	18.637	3.637
3	100 μs	0.1 ns	30	65 ns	$-1.577E-05$	−33.353	33.353	3.353
4	100 μs	0.1 ns	45	65 ns	$-1.577E-05$	−47.252	47.252	2.252
5	100 μs	0.1 ns	60	65 ns	$-1.577E-05$	−62.101	62.101	2.101
6	100 μs	0.1 ns	75	65 ns	$-1.577E-05$	−77.353	77.353	2.353
7	100 μs	0.1 ns	90	65 ns	$-1.577E-05$	−93.076	93.076	3.076
8	100 μs	0.1 ns	105	65 ns	$-1.577E-05$	−108.689	108.689	3.689
9	100 μs	0.1 ns	120	65 ns	$-1.577E-05$	−123.39	123.390	3.390
10	100 μs	0.1 ns	135	65 ns	$-1.577E-05$	−137.545	137.545	2.545
11	100 μs	0.1 ns	150	65 ns	$-1.577E-05$	−152.098	152.098	2.098
12	100 μs	0.1 ns	165	65 ns	$-1.577E-05$	−167.321	167.321	2.321
13	100 μs	0.1 ns	180	65 ns	$-1.577E-05$	176.977	183.023	3.023

5. CONCLUSION

A method of providing a phase-stable signal to the remote terminal using a loop system is introduced and in order to analyze its performance, two methods of simulation, which are numerical simulation and system simulation, are presented. The results of the simulation are listed and prove the good performance of the system.

ACKNOWLEDGMENT

This work is supported by the NSFC (Nos. 60531020, 60671003), ZJNSF (No. R105253), the NCET-07-0750, and the Ph.D. Programs Foundation of MEC (No. 20070335120).

REFERENCES

1. Landecker, T. L. and J. F. Vaneldik, "A phase-stabilized local-oscillator system for a synthesis radio telescope," *IEEE Trans. Instrum. Meas.*, Vol. 31, 185–192, Sept. 1982.
2. Belostotski, L., "Local oscillator and focal length measurement system for the square kilometre array," *Master of Science*, Jan. 2000.

A 2.5 GHz Voltage Controlled FBAR Oscillator

J. H. Lin[1] and Y. H. Kao[2]

[1]Department of Communication Engineering, National Chiao-Tung University, Hsinchu, Taiwan
[2]Department of Communication Engineering, Chung Hua University, Hsinchu, Taiwan

Abstract— A film bulk acoustic resonator (FBAR) is designed and fabricated in this work. Using this resonator, a 2.5 GHz voltage-controlled FBAR oscillator is designed and realized with hybrid circuits. The electronic tuning range exceeds ±6%. The 2nd harmonics of oscillator is suppressed below 40 dB. The oscillator provides 14.5 dBm of output power and consumes 65 mA from +5 V DC power supply.

1. INTRODUCTION

In high-speed digital communication system, a clock recovery circuit is used for signal integrity. The clock is usually extracted from a phase-look-loop (PLL) circuit with low jitter voltage controlled oscillator (VCO). In optical communications, 2.488 GHz VCO plays an important role in the jitter filter and frequency translator for 40 G system, like OC768.

Due to the availability of high frequency and high quality resonator, the VCOs were mostly fabricated at 622 MHz either by the fourth harmonic of 155 MHz crystal oscillator (VCXO) or directly 622 MHz saw oscillator (VCSO) [1, 2]. Both cases suffer from the increase of floor noise and the degradation factor of $20\log(N)$ =12 dB on the phase noise as applications to OC768 at 2488.32 MHz. Thus, high frequency VCO with high-Q resonator using direct oscillation is required to overcome these disadvantages. For this purpose, Film Buck Acoustic Resonator (FBAR) is the hopeful candidate.

In this paper, a high quality FBAR was designed and fabricated. Using this resonator, a high frequency voltage controlled FBAR oscillator is designed and realized with hybrid circuits.

2. FILM BULK ACOUSTIC RESONATOR

The FBAR device is a three-layer structure with the top and bottom electrodes of aluminum and gold sandwiching a middle layer of oriented piezoelectric aluminum nitride. An air interface is used on both outer surfaces to provide high-Q reflectors at all frequency. When RF signals are applied near the mechanical resonant frequency the piezoelectric transducer excites the fundamental bulk compress wave traveling perpendicular to the films [3].

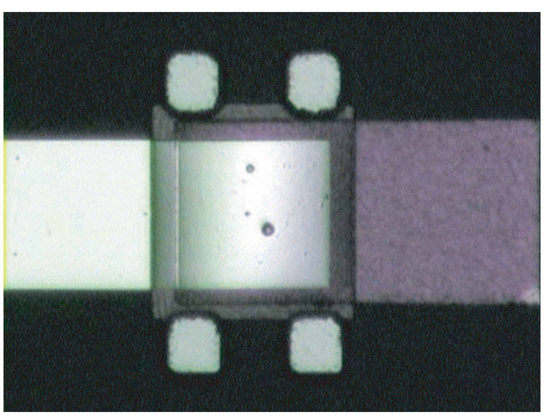

Figure 1: Picture for the film bulk acoustic resonator.

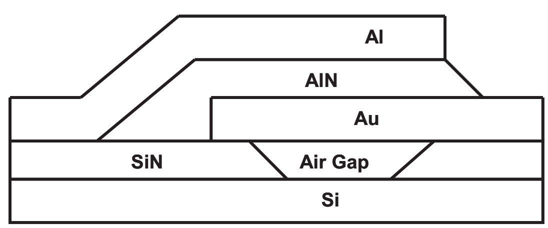

Figure 2: A simplified principal-level cross section of film bulk acoustic resonator.

The picture of FBAR is shown in Fig. 1. The size of the resonator is about 70 × 70 μm. Fig. 2 shows the device geometry for the FBAR. The thickness of aluminum nitride is about 1 μm. The Modified Butterworth VanDyke (MBVD) equivalent circuit model for the resonator is shown in Fig. 3. The typical values for the FBAR, to be described below, at 2.5 GHz are: $Lm = 143$ nH, $Cm = 29$ fF, $Rm = 1$ Ohm, $C0 = 2$ pF, $R0 = 1$ Ohm and $Rs = 1$ Ohm.

3. OSCILLATOR DESIGN

Here, the architecture with a FBAR forming a feedback loop is chosen for proper control of parasitic capacitances and shown in Fig. 4.

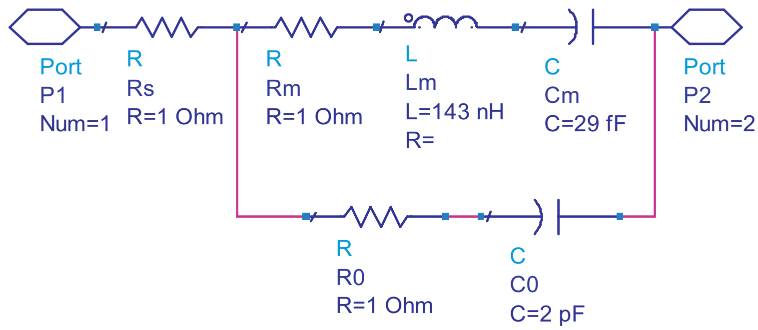

Figure 3: MBVD equivalent circuit model of the resonator.

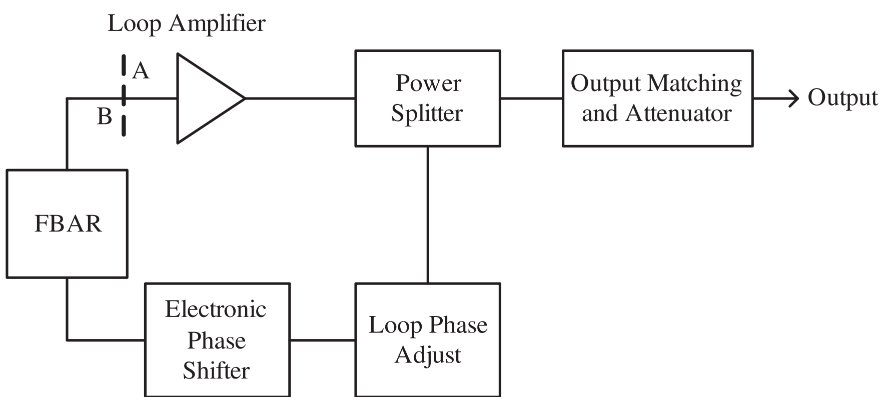

Figure 4: Block diagram of a feedback loop oscillator.

It consists of a single loop amplifier, an electronic phase shifter, a lump element reactive Wilkinson power splitter, a lumped element reactive phase adjusting, and a FBAR resonator. The resonator acts as a short circuit with zero phase-shift at the desired frequency. No output buffer amplifier is used because it may degrade the oscillator's white phase noise floor. The oscillation starts as the closed loop gain satisfies Barkausen's criteria. During design phase, the open loop gain is evaluated by breaking the loop at the appropriate plane with equal input and output impedance, such as line AB noted in Fig. 4.

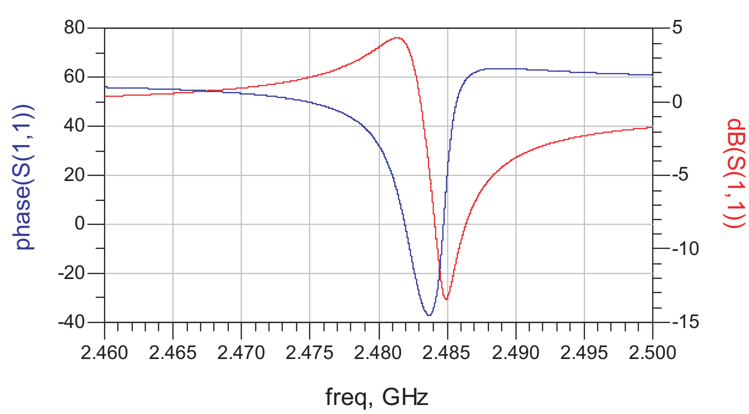

Figure 5: Results of linear simulation using ADS.

The linear simulation result of open-loop frequency response using Agilent Advance Design System (ADS) software is shown in Fig. 5. The linear simulation is used to ensure $|S11| > 1$

(negative resistance) in the desired frequency. The oscillation starts when the phase of $S11$ equal to zero and $|S11| > 1$. The Barkhausen's criteria are satisfied in this moment.

The HBT monolithic amplifier is selected as the loop amplifier because of low noise figure and high dynamic range. The P1 dB is at +17 dBm and the bandwidth is 4 GHz. Its bandwidth was properly selected to prevent high 2nd harmonics. The nominal gain of 17 dB is much greater than that required to overcome the total loop losses to insure the stable oscillation. The magnitude of gain variation over temperature is approximately 0.005 dB/°C and this feature can prevent the AM-PM noise induced with the temperature variation.

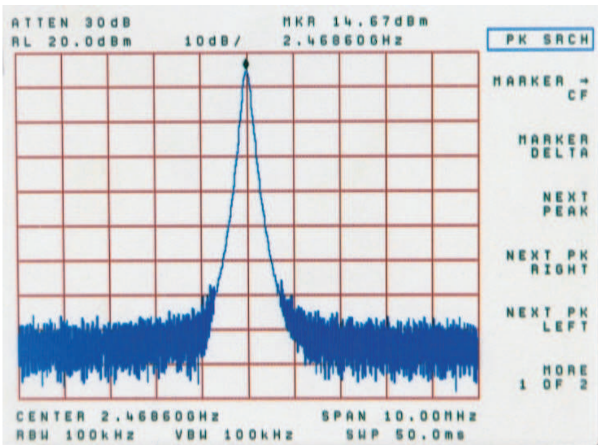

Figure 6: Output spectrum for the oscillator.

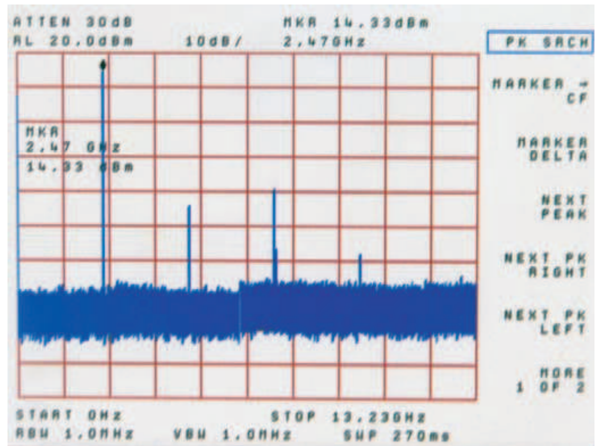

Figure 7: Harmonics spectrum for this oscillator.

Item	Value
Supply Voltage (Volts)	+5.0
Supply Current (mA)	65
Output Power (dBm)	+14.5
Tuning Voltage (Volts)	0–5
Tuning Range	$> \pm 6\%$
Sub Harmonics (dBc)	−40

Table 1: Measured results for the oscillator.

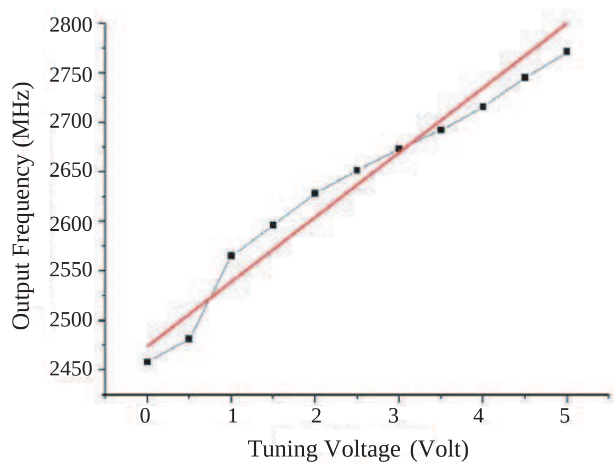

Figure 8: Output frequency vs. tuning voltage.

4. OSCILLATOR PERFORMANCE

The performances of the oscillator with FBAR resonator are measured and summarized in Table 1.

The narrow and wide scan of output spectrum and relative levels of harmonic are shown in Figs. 6 and 7, respectively. The 2nd harmonics of oscillator is suppressed below 40 dB as shown in Fig. 7. The tuning characteristic is shown in Fig. 8 with ±6% range.

5. CONCLUSIONS

A film bulk acoustic resonator is design and fabricated in this work. Using this resonator, a 2.5 GHz voltage controlled oscillator was designed and fabricated in this study. The resonator is operated directly at the specific frequency 2.5 GHz to avoid the degradation of phase noise due to frequency multiplication. The tuning capability achieves ±6%. The 2nd harmonics of oscillator is suppressed below 40 dB. The oscillator provides 14.5 dBm of output power and consumes 65 mA from +5 V DC power supply.

ACKNOWLEDGMENT

This work is supported by Chung Shan Institute of Science and Technology under contract BV95G11P-001P00. The authors would like to thank Dr. P. Y. Chen at Chung Shan Institute of Science and Technology for fabricating the film bulk acoustic resonator.

REFERENCES

1. Ishii, O., H. Iwata, M. Sugano, and T. Ohshima, "UHF AT-CUT crystal resonators operating in the fundmental mode," *IEEE Int. Frequency Control Symposium*, 975–980, 1998.
2. Nomura, N., M. Itagaki, and Y. Aoyagi, "Small packaged VCSO for 10 Gbit Ethernet Application," *IEEE UFFC*, 68–73, 2004.
3. Rubby, R., J. D. Larson, P. Bradley, and Y. Oshmyansky, "Ultra-miniature, high-Q filter and duplexers using FBAR technology," *ISSC*, Feb. 2001.

High Tunable Capacitor Using a Finger Structured Electrode

Young Chul Lee[1] **and Kyung Hyun Ko**[2]

[1]Div. of Marine Electronics and Communication Engineering
Mokpo National Maritime University (MMU), Korea
[2]Department of Materials Science and Engineering, Ajou University, Korea

Abstract— We present a novel tunable metal-insulator-metal (MIM) capacitor with the finger-structure electrode for improving its tunability. The capacitors were fabricated on a low-resistivity Si substrate employing lead zinc niobate (PZN) thin film dielectric. The fabricated capacitor, whose line width and spacing was 2.5 and 2.0 μm, respectively, achieved the effective capacitance tunability of 22.9% at 5.5 V. This achieved tunability is higher value of 10% than that of the conventional rectangular MIM capacitor at 900 MHz.

1. INTRODUCTION

Recently, a great diversity of networks such as cellular network, personal area network (PAN), wireless local area network (WLAN), etc. coexist in the wireless communication market. In order to enable "seamless roaming" reconfigurable intelligent devices are needed to be compatible with various communication standards [1]. Therefore, compact and low-cost tunable devices are indispensable for reconfigurable RF applications satisfying multi-band or multi-mode standards. Tunable dielectric based tunable RF device technology is one of the viable solutions for reconfigurable RF applications, because of a high tunability, compact size, and low cost. In order to realize various reconfigurable devices, tunable capacitors as their basic element have been implemented by using several electric-field tunable dielectrics such as ferroelectric materials or paraelectric materials [2–5].

Representative electric-field tunable dielectrics such as barium-strontium titanate (BST) [6, 7] and bismuth zinc niobate (BZN) [8–10] have been successfully demonstrated for the possibility of the tunable circuits. Using these dielectrics, high-performance capacitors, matching networks, band pass filters [11], and phase shifters [12] have been implemented for tunable system applications. However, although high tunable characteristics were achieved, their operation frequencies were as low as below ~ 100 MHz and the applied bias voltage ranged $20 \sim 50$ V. Therefore, only limited applications are available for low-frequency circuits or high-power systems. Moreover, most research efforts have focused on dielectric materials, metallization [9, 12, 13], or buffer layers [14] for high tunable and low-loss characteristics.

In this paper, a tunable capacitor with a finger-structure electrode is presented in order to improve its tunability and DC bias characteristics. This capacitor was fabricated on a general low-resistivity Si substrate using PbO-ZnO-Nb_2O_5 (PZN) cubic pyrochlore thin film dielectrics. The capacitor is analyzed in terms of the effective capacitance and tunability compared to the conventional one with the rectangle-structure electrode.

2. DESIGN AND FABRICATION

Tunable MIM capacitors operate using electric (E)-fields. Their distribution is linear and uniform between the electrodes and fringes out at the edges. For devices with larger electrodes, the energy of the fringe field is small to the total capacitive energy, but for small devices the fringe field energy comes to dominate [15]. The intensity of the fringe fields at the edge is higher than that of the E-fields between electrodes. Therefore, the purpose of this work is to improve the tunability and DC bias characteristics utilizing fringe fields. The tunable MIM capacitor with the finger-structure electrode is proposed. This proposed tunable capacitor utilizes fringe E-fields for improving tunibility and bias characteristics.

The tunable MIM capacitors were fabricated on the silicon substrate. The substrate resistivity was $1 \sim 30\,\Omega\,$cm. The bottom electrode layer (Pt) of 2300 Å was deposited and patterned using the sputtering and dry etching process, respectively. The PZN thin film of 2000 Å was deposited on a Pt layer by RF-magnetron sputtering. The deposition was carried out from $Pb_6ZnNb_6O_{22}$ target material in an O_2/Ar atmosphere. During reactive RF magnetron sputtering, off-axis type system geometry was used. The base pressure in the process chamber was 3.0×10^{-6} Torr, while the working pressure was maintained at 10 mTorr using a throttle valve. High purity Ar and O_2 (> 99.99%) were used as base and reactive gases, respectively. The plasma discharge was generated at a constant RF power of 150 W and the O_2/Ar flow rate ratio was held at 10% (2/20 SCCM). Using the Inductive Coupled Plasma (ICP) dry etcher the PZN film was patterned to cover the bottom electrodes. After patterning, post-annealing processes were carried out at 600°C for 3 hours in air to crystallize the film. Finally, the Pt layers of 2300 Å for the top electrodes and coplanar-waveguide (CPW)-probe pads were deposited by the sputtering process and patterned by the dry etching process for the top electrode. The line width (L) and spacing (S) of the finger pattern were 2.5 and 2.0 μm respectively, The capacitor areas for the rectangular and finger electrode were 1,200 $(40 \times 30)\,\mu m^2$ and $1{,}170\,\mu m^2$, respectively. Relative dielectric constant of the PZN thin film was 240 at 10 MHz. Fig. 1 shows the photography of the fabricated tunable MIM capacitors in CPW configuration and enlarged finger-type top electrode.

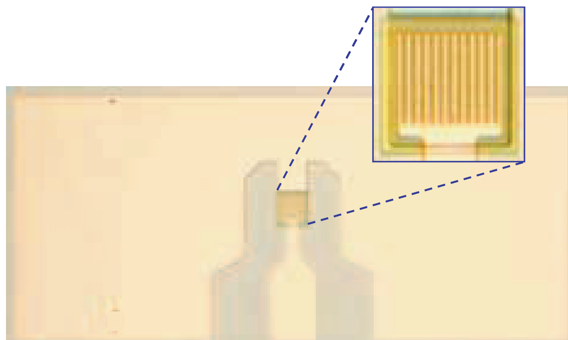

Figure 1: Fabricated MIM tunable capacitors with finger-structure top electrode.

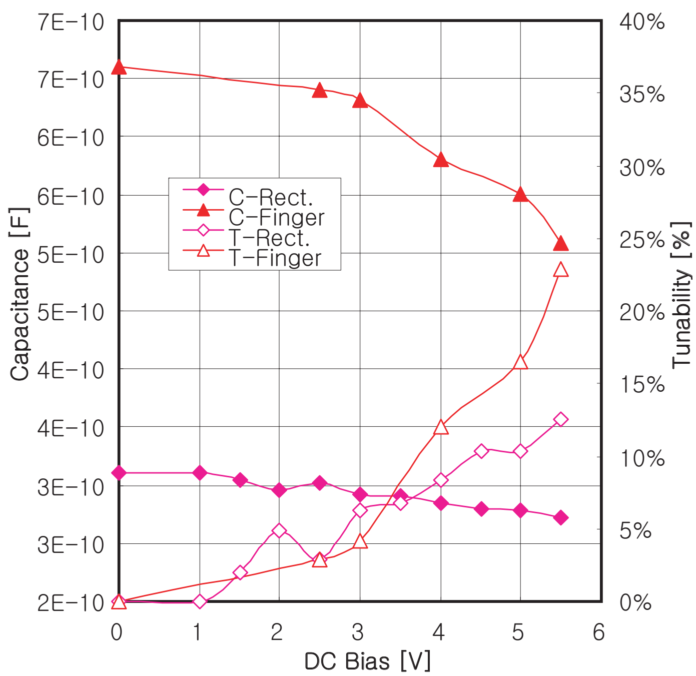

Figure 2: Measured effective capacitance and tunability for the proposed finger structured capacitor at different bias voltages, compared to the conventional capacitor (Rect.: the rectangle structured electrode, C-: the effective capacitance, and T-: the tunability).

3. MEASUREMENTS

The effective capacitance (C_{eff}) and percentage tunability (T) of the fabricated capacitors were analyzed by measuring complex reflection coefficients (S_{11}) with a vector network analyzer (HP 8510C) and a probe station. A thru-reflect line (TRL) calibration was performed with a standard calibration kit. Using the measured S11 data, the effective capacitance (C_{eff}) and tunability (T) are analyzed, as following equations,

$$C_{eff} = -\frac{1}{2\pi \cdot freq \cdot \mathrm{Im}(Z_{11})}[F]$$
$$T = \frac{C_{\max} - C_{\min}}{C_{\max}}[\%]$$

where Z_{11} is the total impedance of the device under test calculated from the measured S_{11}. $C_{\min}$ and $C_{\max}$ are the measured minimum and maximum capacitance, respectively, within the applied bias voltage range.

Figure 2 shows effective capacitance and tunability characteristics of the proposed finger structured capacitor as a function of bias voltages at 900 MHz, compared to the conventional one with the rectangular electrode. Even though the area for two capacitors is nearly the same, each effective capacitance (C_{eff}) is different due to fringe E-fields. The finger electrode makes more fringe fields than the conventional structure one. Therefore its capacitance is increased and its permittivity due to high fringe fields is easily changed. The tunability of 22.9% is achieved for the finger-type capacitor at 5.5 V. this tunability is 10.4% higher value than that of the rectangle-type one.

4. CONCLUSIONS

A tunable MIM capacitor with the finger-structure electrode was proposed and demonstrated in order to improve the tunability characteristics utilizing fringe fields. The capacitors were fabricated on the Si substrate using lead zinc niobate (PZN) thin film dielectric. The fabricated capacitor with the finger structured electrode achieved the effective capacitance tunability of 22.9% at 900 MHz and 5.5 V. In the conventional capacitor with rectangle structured electrode the tunability of 12.5% was measured at the same conditions.

ACKNOWLEDGMENT

This work was supported by the Korea Research Foundation Grant funded by the Korean Government (MOEHRD) (KRF-2006-521-D00328).

REFERENCES

1. Kakerow, R., M. Muller, D. Pienkowski, and R. Circa, "Reconfigurable receiver approach for 4 G terminals and beyond," *IEEE NEWCAS Conference*, 9–12, June 2005.
2. Lu, J. and S. temmer, "Low-loss, tunable bismuth zinc niobate films deposited by rf magnetron sputtering," *Applied Physics Letters*, Vol. 83, No. 12, 2411–2413, 2003.
3. Tombak, A., J.-P. Maria, F. T. Ayguavives, Z. Jin, G. T. Stauf, A. I. Kingon, and A. Mortazawi, "Voltage-controlled RF filters employing thin-film barium-strontium-titanate tunable capacitors," *IEEE Transaction on Microwave Theory and Techniques*, Vol. 51, No. 2, 462–467, 2003.
4. Ouaddari, M., S. Delprat, F. Vidal, M. Chaker, and K. Wu, "Microwave characterization of ferroelectric thin-film materials," *IEEE Transaction on Microwave Theory and Techniques*, Vol. 53, No. 4, 1390–1397, 2005.
5. Jose, K. A., H. Yoon, K. J. Vinoy, P. Sharma, V. K. Varadan, and V. V. Varadan, "Low voltage tunable capacitors for RF MEM filters and antenna applications," *IEEE Antenna and Propagation Society International Symposium*, Vol. 3, 670–673, 2001.
6. Tombak, A., F. T. Ayguavives, J.-P. Maria, G. T. Stauf, A. I. Kingon, and A. Mortazawi, "Low voltage tunable barium strontium titanate thin film capacitors for RF and microwave applications," *MTT-S In. Microwave Symposium Digest*, Vol. 3, 1345–1348, 2000.
7. Fardin, E. A., A. S. Holland, K. Ghorbani, E. K. Akdogan, W. K. Simon, A. Safari, and J. Y. Wang, "Polycrystalline $Ba_{0.6}Sr_{0.4}TiO_3$ thin films on r-plane sapphire: Effect of film thickness on strain and dielectric properties," *Applied Physics Letters*, Vol. 89, 182907-1–182907-3, 2006.
8. Lee, Y. C., Y. P. Hong, D. M. Kim, and K. H. Ko, "Very high tunable inter-digital capacitor using bismuth zinc niobate thin-film dielectrics for microwave applications," *Electron. Lett.*, Vol. 42, 851–853, 2006.

9. Lu, J., S. Schmidt, D. S. Boesch, N. Pervez, R. A. York, and S. Stemmer, "Low-loss tunable capacitors fabricated directly on gold bottom electrodes," *Appl. Phys. Lett.*, Vol. 88, 112905-1–112905-3, 2006.
10. Park, J., J. Lu, S. Stemmer, and R. A. York, "Microwave dielectric properties of tunable capacitors employing bismuth zinc niobate thin films," *Appl. Phys. Lett.*, Vol. 97, 084110-1–084110-4, 2005.
11. Erker, E. G., A. S. Nagra, Y. Liu, P. Periaswamy, T. R. Taylor, J. Speck, and R. A. York, 'Monolithic Ka-band phase shifter using voltage tunale $BaSrTiO_2$ parallel plate capacitors," *IEEE Microw. Guid. Wave Lett.*, Vol. 10, 10–12, 2000.
12. Finstrom, N. H., J. A. Gannon, N. K. Pervez, R. A. York, and S. Stemmer, "Dielectric losses of $SrTiO_2$ thin film capacitors with Pt bottom electrodes at frequencies upto 1 GHz," *Appl. Phys. Lett.*, Vol. 89, 242910-1–242910-3, 2006.
13. Dube, D. C., J. Baborowski, P. Muralt, and N. Setter, "The effect of bottom electrode on the performance of thin film based capacitors in the gigahertz region," *Appl. Phys. Lett.*, Vol. 74, 3546–3548, 1999.
14. Kim, H.-S., H.-G. Kim, I.-D. Kim, K.-B. Kim, and J.-C. Lee, "High-tunability and low-microwave-loss $Ba_{0.6}Sr_{0.4}TiO_3$ thin films grown on high-resistivity Si substrate using TiO_2 buffer layers," *Appl. Phys. Lett.*, Vol. 87, 212903-1–212903-3, 2005.
15. Hegg, M. C. and A. V. Mamishev, "Influence of variable plate separation on fringing electric fields in parallel-plate capacitors." *2004 International Symposium on Electrical Insulation*, 384–387, 2004.

CPW-to-stripline Vertical via Transitions for 60 GHz LTCC SoP Applications

Young Chul Lee
Div. of Marine Electronic and Communication Engineering
Mokpo National Maritime University (MMU), Korea

Abstract— In this work, CPW-to-stripline (SL) vertical via transitions using gradually stepped vias and embedded air cavities are presented for V-band LTCC System-on-Package (SoP) applications. In order to reduce radiation loss due to abrupt via discontinuities, gradual via transitions are proposed and investigated. In addition, in order to reduce increased parasitic shunt capacitance due to stepped via structures, air cavities are embedded below the transition vias. Using a 3-D EM simulation tool, the proposed transitions are designed and analyzed, compared to the conventional transition. Three-segment transmission lines (CPW-SL-CPW) in 7-layer LTCC dielectrics were fabricated and measured. The two stepped via (STV2) transition embedding air cavities shows an insertion and return losses of 1.6 dB and below −10 dB, respectively, over 60 GHz. The transition loss per one STV2 transition is 0.7 dB at 60 GHz.

1. INTRODUCTION

Recently, various wireless communication systems for mm-wave video transmission, wireless-LANs, and wireless Ethernet applications have been constantly proposed and developed [1–4]. In order to implement these systems commercially, technologies for compact and low-cost radio systems are indispensable. The low temperature ceramic co-firing (LTCC) based SoP approach is one of the most promising solutions for integration of the radio system due to its multi-layer integration capability, excellent metal conductivity, low-loss characteristics, and a temperature coefficient of expansion (TCE) close to semiconductors.

For the three dimensional (3-D) integration of mm-wave radio systems, several vertical transitions such as CPW-to-stripline (SL) transition [5, 6], microstrip-to-SL transition [7, 8] and CPW-to-CPW transition [5, 9] are required. These transitions allow the integration of passive and active circuits to be placed in inner layers or mounted on the top layer. Therefore, various interesting methods for the improvement of their RF performance have been presented. They are roughly divided into two categories: impedance matching [6, 7, 9] and parasitic compensation [5, 6]. In order to match the transition impedance, the coaxial-like transition [7, 9] and intermediate ground planes [6] have been investigated. And also, various attempts were tried for reduction of the capacitive effect in the transition region [7] or the inductive effect of vertical vias [6]. However, if the total height of the vertical vias connected in a row is more than one tenth of the wavelength in the mm-wave frequencies, their physical discontinuities can generate a significant amount of radiation as well as reflection.

In this work, CPW-to-SL vertical via transitions using gradually stepped vias and embedded air cavities are presented. The stepped vias are devised for reduction of their structural discontinuities and the embedded air cavities are designed for compensation of the increased shunt capacitive effect of the proposed stepped vias. Transitions are designed in back-to-back configuration and analyzed using a 3-D Finite Integration Technique (FIT) simulator [10] and they are implemented using a 7-layer LTCC dielectric.

2. DESIGN AND ANALYSIS OF CPW-TO-STRIPLINE VERTICAL VIA TRANSITIONS

2.1. Structures of the Vertical Transitions

CPWs and SLs have been used for signal lines and embedded devices, respectively, for the 3-D system integration because they have low-radiation and high-isolation characteristics. The CPW is insensible to interference from several higher surface modes because its ground planes are on the same layer as the signal line. The SL is principally used for miniaturization of passive circuits through vertical deployment of their elements, because it is basically a buried structure, its radiation and dispersion are negligible. However, embedded passive devices based on the SL require vertical via transition for 3-D interconnection with other circuits or in/output ports.

Figure 1(a) shows a cross-sectional structure of the conventional CPW-to-SL vertical via transition in a 7-layer LTCC substrate. The total height of the vertical vias in the transition region is

300 μm. The wavelength (λ) on the LTCC CPW with a relative dielectric constant of 7.0 is 2.56 mm at 60 GHz. Therefore, the rate of the vertical transition to λ is 11% at 60 GHz. It roughly accounts for the degree of the discontinuity. As a result, radiation and reflection can be induced by the physical discontinuity of the vias. In this work, in order to reduce the physical discontinuity, the directly stacked vias are subdivided into small-length elements relative to the wavelength as shown in Fig. 1(b) and (c). Fig. 1(b) and (c) show one and two stepped vertical via transition (STV1 and STV2), respectively. Therefore, the critical dimension, which primarily influences the discontinuity, is decreased from 300 to 200 and 100 μm for the STV1 and STV2, respectively. However, the stepped vias lead to the increase of the shunt capacitance between the vias and SL ground planes. For reduction of the increased shunt capacitance, the embedded air cavities are inserted below the stepped vias.

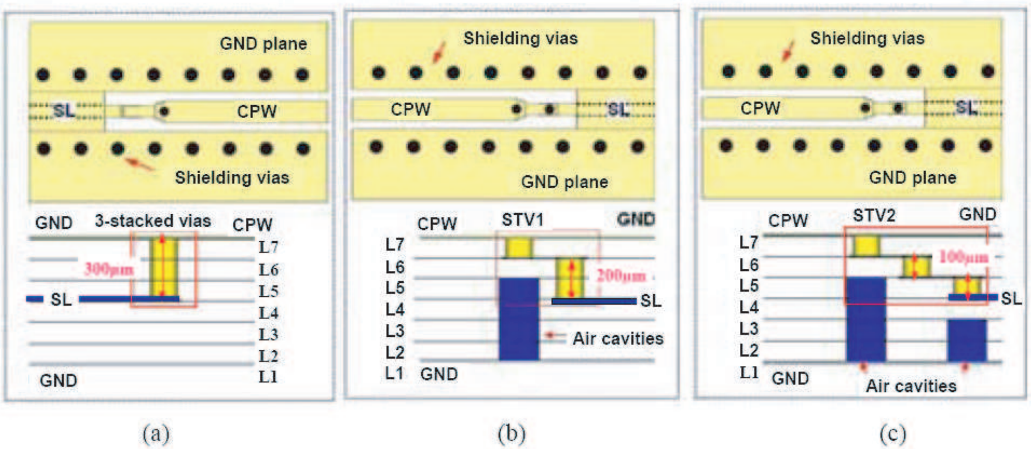

Figure 1: Cross-sectional structures of the CPW-to-SL vertical via transitions. (a) the conventional transition, (b) the novel one-STV1, and (c) the novel one-STV2 (Lx: the number of LTCC layers).

2.2. Design of the Vertical Transitions

For evaluation of the proposed vertical transitions compared to the conventional one, three-segment transmission lines (CPW-SL-CPW) have been designed in back-to-back configuration using the transitions. The ground planes of the CPWs and SL are connected by shielding vias. The STV1 and 2 structures consist of the stepped vias through the 5th and 7th layer. The height and diameter of signal vias are 100 and 135 μm, respectively, and they are connected through lines of 100 μm wide. The CPWs are placed on the top layer, and the SL is placed on the 4th layer. In order to maintain the characteristic impedance of 50 Ω for both CPWs and the SL, the width and gap of the CPWs are 250 and 99 μm, respectively, and the SL is 135 μm in width. The air cavities for the

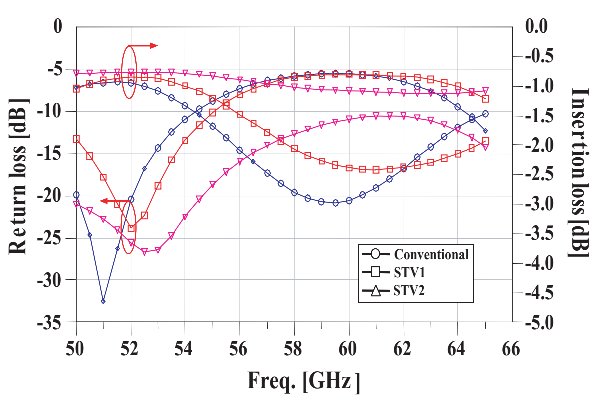

Figure 2: Calculated results of three-segment transmission lines using the conventional vertical transitions, the STV1 ones, and the STV2 ones.

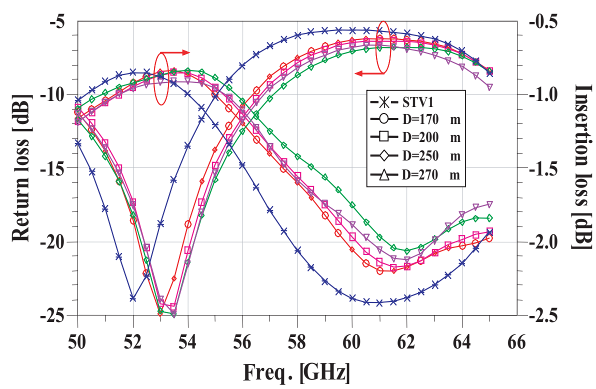

Figure 3: Calculated results of three-segment transmission lines using STV1 transitions with different diameters of embedded air cavities and without them.

STV1 and the STV2 are inserted through the 2nd to 5th layer below the 7th layer via. In addition, they are embedded through the 2nd to 3rd layer below the 5th layer via for the STV2. In the case of the conventional case, two CPW lines of 526 µm are connected at the both ends of the stripline of 2,650 µm. In the case of STV1 and STV2, two CPW lines of 1003 and 526 µm, respectively, are connected at the both end of the SL of 2,050 µm.

2.3. Calculated Results

Figure 2 presents simulated S21 and S22 of the CPW-SL-CPW using the STV1 and STV2 transitions compared to the conventional ones. The proposed transitions, STV1 and STV2, show better S22 and S21 characteristics than the conventional ones. These results come from the reduction of via discontinuity. As the directly stacked vias of 300 µm in the vertical transition region are subdivided into the small elements of 200 and 100 µm for the STV1 and STV2, respectively, their rate of the critical dimension to λ is decreased to 7.8% and 3.9%, respectively, and the structural discontinuities of the vertical via transitions are improved. In the case of the transitions, poles of their S22 shift a little to higher frequencies, due to their increased inductance and shunt capacitance.

Figure 3 shows simulated loss results of the CPW-SL-CPW using STV1 transitions without embedded air cavities and with their different diameters. Compared to the STV1 without embedded air cavities, all of the STV1 with them demonstrate that their integration can reduce the shunt parasitic capacitance in the vertical via transition region. Therefore, S22 and S21 characteristics are improved; as their diameter increases, an insertion and return loss decrease and it is optimized to 250 µm.

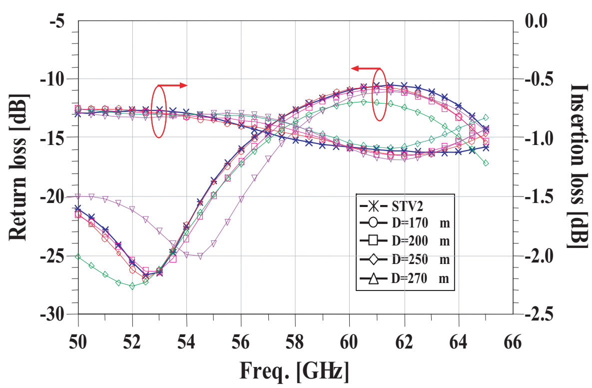

Figure 4: Calculated results of three-segment transmission lines using STV2 transitions with different diameters of embedded air cavities and without them.

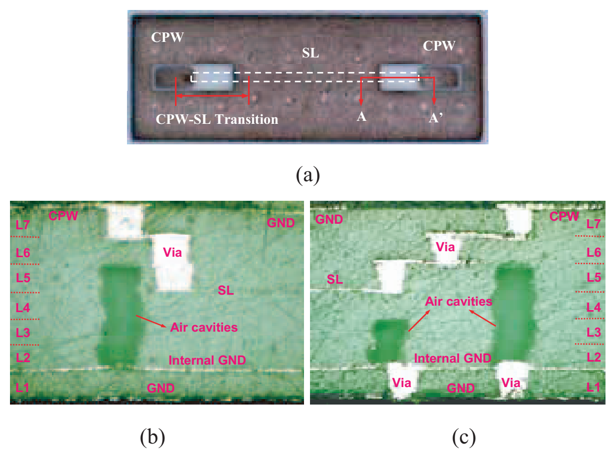

Figure 5: Fabricated CPW-SL-CPW transmission line. (a) and the cross-sectional views of the STV1, (b) and STV2 (c) with embedded air cavities.

Figure 4 displays calculated results of the CPW-SL-CPW using STV2 transitions with a different diameter of air cavities, compared to the transitions without them. For this experiment, the diameter of air cavities below the 7th layer vias was fixed to 170 µm and that below the 5th layer ones were changed from 170 to 270 µm. Unlike the STV1, the effect of the embedded air cavities on the transmission characteristics is very little and the improvements are slight. This result shows that the increased series inductance and shunt capacitance for the STV2 are well matched each other because of reactance cancellation.

3. FABRICATION AND MEASUREMENT

The designed three-segment transmission lines were implemented using seven LTCC dielectric layers with a dielectric constant of 7.0 at 60 GHz and its thickness between the metal layers is 100 µm. The Ag and Ag/Pd conductors were screen-printed on the unfired layers for internal and external conductors, respectively. Signal vias and air-cavities of 150 µm and 190 µm in diameter were formed through the standard mechanical punching process because the design rule between vias was 300 µm in our process, while the optimum diameter of the air cavities for the STV1 was 250 µm. For implementation of embedded air cavities, the metal filing step in punched vias was omitted. The ground planes of the CPWs and stripline are interconnected to each other using shielding vias.

The spacing between ground vias (edge to edge) is 320∼360 μm. Fig. 5(a) shows the fabricated CPW-SL-CPW in back-to-back configuration using CPW-to-SL vertical transitions and their cross-sectional views of the part A-A' of (a) are shown in (b) and (C), respectively, for the STV1 and the STV2. Embedded air cavities were clearly defined and no crack and depression were observed around them.

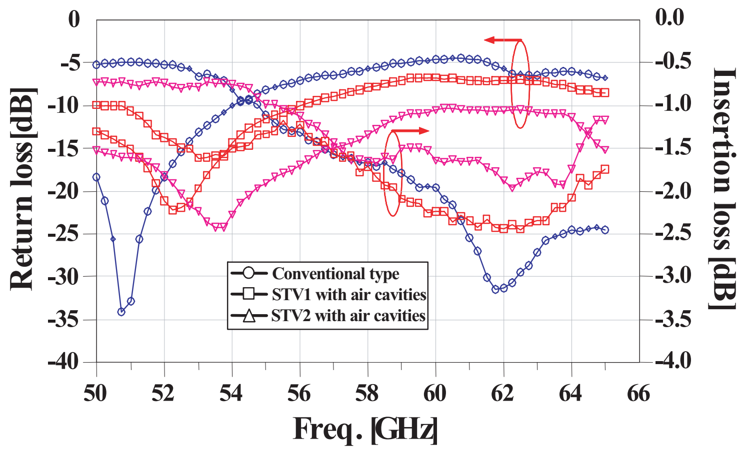

Figure 6: Measured resultss of the fabricated three-segment CPW-SL-CPW transmission lines using the STV1 and STV2 transitions and embedded air cavities in comparison with the conventional transitions.

Figure 6 presents measured S22 and S21 of the fabricated three-segment lines. As the step of the vertical via transition with embedded air cavities increase from the directly stacked vias to one and two stepped via, respectively, their characteristics are improved. In other words, as the critical height in the vertical via transition is decreased, the return loss is also improved. These results imply that a key parameter mainly impacting on the structural discontinuity is the critical dimension rather than total height of the vertical via transition. In the STV2 case, the measured S22 and S21 of the CPW-SL-CPW are less than −10 dB and −2.0 dB, respectively, from 50 to 65 GHz. In particular, its low-S21 of −1.6 dB is achieved at 60 GHz. These values represent all losses along the three-segment transmission lines and the two vertical via transitions. Considering the total loss of transmission lines with −0.19 dB, which is calculated by using a conventional line calculator, the transition loss per a STV transition is 0.7 dB at 60 GHz.

4. CONCLUSION

We present CPW-to-SL vertical via transitions utilizing stepped via structures and embedded air cavities for V-band SoP applications and demonstrate that the STV structures and embedded air cavities reduce discontinuity and parasitic shunt capacitance of the vertical via transition through 3-D EM simulations and the measurements of three-segment transmission lines (CPW-SL-CPW) designed in back-to-back configuration. The fabricated CPW-SL-CPW using two stepped via (STV2) transitions shows an insertion loss of −1.6 dB and return losses of −10 dB at 60 GHz. Compared to the conventional ones using directly stacked vias, an insertion and return loss are improved by 0.4 dB and 5 dB, respectively. The transition loss of 0.7 dB per STV2 transition is achieved at 60 GHz.

REFERENCES

1. Nagatsuma, T., A. Hirata, T. Kosugi, and H. Ito, "Over-100 GHz millimeter-wave technologies for 10 Gbit/s wireless link," *Workshop WM 1 Notes of 2004 IEEE Radio and Wireless Conference*, September 2004.
2. Lee, Y. C., W.-i. Chang, and C. S. Park, "Monolithic LTCC SiP transmitter for 60 GHZ wireless communication terminals," *IEEE MTT-S Int. Microwave Symposium Digest*, June 2005.
3. Ohata, K., K. Maruhashi, M. Ito, S. Kishimoto, K. Ikuina, T. Hashiguchi, K. Ikeda, and N. Takahashi, "1.25 Gbps wireless gigabit ethernet link at 60 GHz-band," *IEEE MTT-S In. Microwave Symposium Digest*, Vol. 1, No. 1, 373–376, June 2003.

4. Lee, J.-H., N. Kidera, G. DeJean, S. Pinel, J. Laskar, and M. M. Tentzeris, "A V-band front-end with 3-D integrated cavity filters/duplexers and antenna in LTCC technologies," *IEEE Trans. on Microwave Theory and Techniques*, Vol. 54, No. 7, 2925–2936, 2006.
5. Panther, A., C. Glaser, M. G. Stubbs, and J. S. Wight, "Vertical transitions in low temperature co-fired ceramics for LMDS applications," *IEEE MTT-S Int. Microwave Symposium Digest*, Vol. 3, 1907–1910, 2001.
6. Lei, S., Y. X. Guo, and L. C. Ong, "CPW to stripline transitions in LTCC for millimeter-wave applications," *IEEE Asia Pacific Microwave Conference (APMC) Proceedings*, 2005.
7. Schmuckle, F. J., A. Jentzch, W. Heinrich, J. Butz, and M. Spinnler, "LTCC as MCM substrate: design of strip-line structures and flip-chip interconnections," *IEEE MTT-S Int. Microwave Symposium Digest*, Vol. 3, 1093–1096, 2001.
8. Yang, T.-H., C.-F. Chen, T.-Y. Huang, C.-L. Wang, and R.-B. Wu, "A 60 GHz LTCC transition between microstrip line and substrate integrated waveguide," *IEEE Asia Pacific Microwave Conference (APMC) Proceedings*, 2005.
9. Heyen, J., A. Gordiyenko, P. Heide, and A. F. Jacob, "Vertical feedthroughs for millimeter-wave LTCC modules," *33rd European Microwave Conference Proceedings*, 411–414, 2003.
10. CST MICROWAVE STUDIO, CST Inc., [Online] Available: http://www.cst.com.

A Novel Ultra Wideband Transformer-feedback LNA

Hui I Wu, Tsung-Ting Lin, Christina F. Jou, Chih-Peng Lin, and Pei-Yuan Chiang
Microwave and Millimeter Wave Laboratory
Institute of Communication Engineering, National Chiao Tung University
Hsinchu, Taiwan

Abstract— A 3–10 GHz wide-band low noise amplifier with novel input matching mechanism is presented in this letter. The proposed circuit uses reactive-feedback and transistor's intrinsic gate-drain capacitor as input matching network to achieve a simulated −10 dB input reflection coefficient from 3.1 GHz to 10.6 GHz. The fabricated wideband LNA achieves a simulated power gain (S21) of about 10 dB from 3.1 G to 10.6 GHz, and noise figure of 2.72–3.26 dB from 3.1 G to 10.6 GHz. The input 1 dB compression point and input IP3 (IIP3) at 3.1 GHz are about −18.5 and −12 dBm, respectively. The DC supply voltage and power consumption is 1.5 V$^-$ and 15 mA, respectively.

1. INTRODUCTION

Ultra wide-band communication techniques have attracted great interests in both academia and industry during the last few years for applications in short-range. A Low-noise amplifier (LNA) is the first stage, after antenna and low-pass filter in the receiver block of a communication system. The UWB LNA face several challenges, such as sufficient power gain through entire bandwidth to suppress the noise of next stage, low noise figure and low power consumption.

In order to connect to an antenna port, the first problem facing is 50 Ohm wide-band input matching. There are several existing matching mechanisms for wideband matching network. However, these topologies have some problems such as high noise figure, large chip area or very complicated matching network. The proposed circuit uses transistor's intrinsic capacitor and reactive-feedback to achieve a simulated −10 dB input reflection coefficient from 3.1 GHz to 10.6 GHz. In addition, the average power gain is abut 10 dB from 3.1–10.6 GHz.

2. CIRCUIT DESIGN

Figure 1 shows the topology of the proposed low noise amplifier designed in 0.18 µm CMOS. This low noise amplifier utilize negative inductive feedback and an added external capacitance to achieve wideband input matching while maintaining the noise of whole circuit over the entire UWB band.

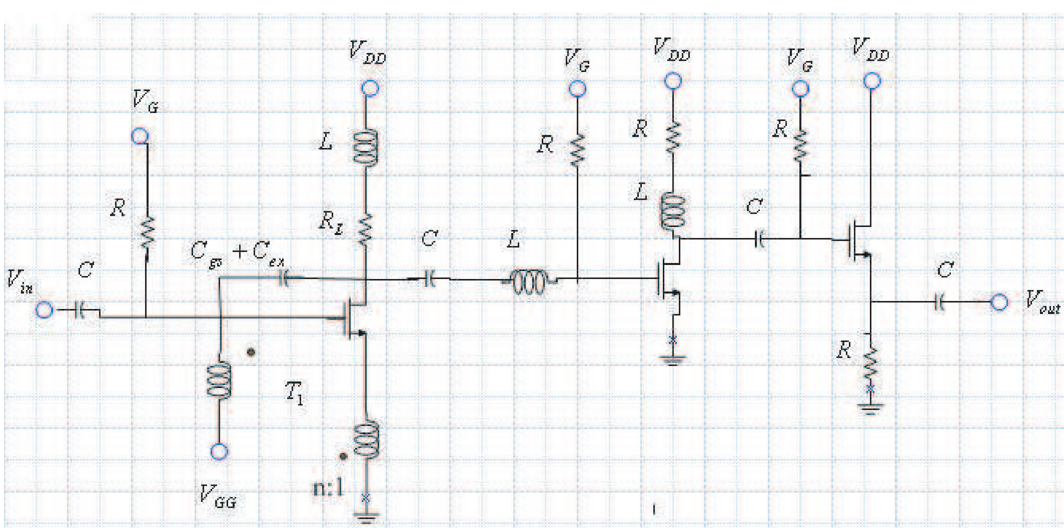

Figure 1: The topology of our proposed low noise amplifier.

Negative inductive feedback [1] allows one to exchange gain for bandwidth, which is useful when designing a UWB amplifier. The input impedance computed from the small-signal equivalent circuit.

$$Z_{in} \approx \frac{A}{(1+\beta)\cdot(1+A\beta)} \cdot \left((\beta^2 r_{sec} + r_{pri}) + \frac{A-1}{g_m \cdot A} + \frac{r_g}{A}\right) \approx \frac{1}{(1+\beta)\cdot\beta\cdot g_m} \tag{1}$$

It depends on the feedback (β) and the transistor transcondutance (g_m). Consequently, the input impedance with feedback is decided by the effective turns ratio of T_1 (n/k) and the transistor transcondutance (g_m) of Q_1. Therefore, one can tune the (n/k) and (g_m) to reach the input matching.

In addition, the wide-band feedback mechanism provided by the transister's intrinsic gate-drain capacitor [2, 3] will develop the wide-band amplifier input matching.

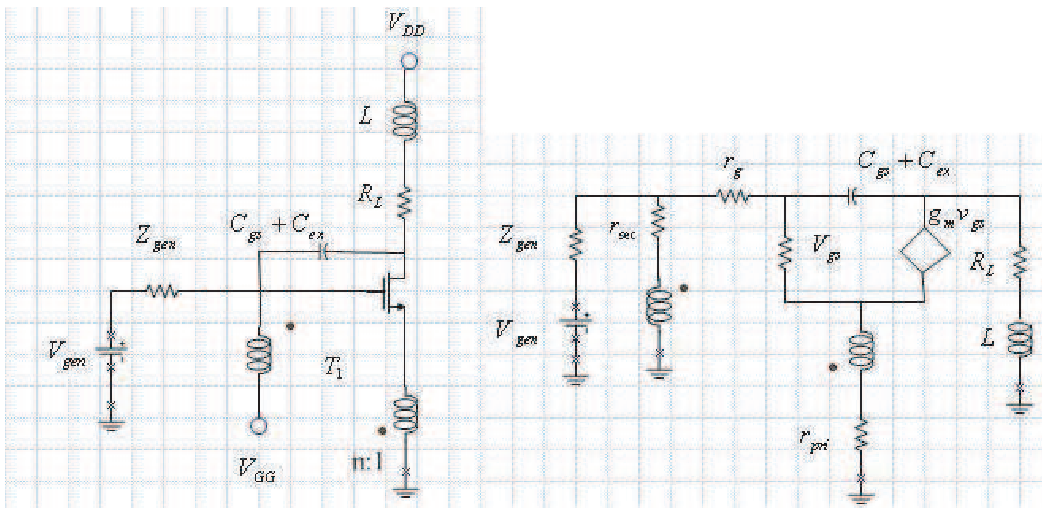

Figure 2: Reactive feedback RF amplifier stage. Schematic and its small-signal equivalent circuit.

The input impedance of the capacitor-loading circuit can be written as

$$Z_{in} = (Y_\alpha + \frac{1}{Z_\beta})^{-1} \tag{2}$$

(Z_β is ignored, because Z_β is much greater than Y_α).

$$Y_\alpha = j\omega C_{gd} + (R_\alpha + \frac{1}{j\omega C_\alpha} + j\omega L_\alpha)^{-1} \tag{3}$$

with

$$\begin{aligned} R_\alpha &= \frac{C_{FB}}{G_m(C_{gd}+C_{ex})} \\ C_\alpha &= G_m R_{ds}(C_{gd}+C_{ex}) \\ L_\alpha &= \frac{L_{FB}C_{FB}}{G_m R_{ds}(C_{gd}+C_{ex})}(1+G_m R_{ds}) \end{aligned} \tag{4}$$

and, n external capacitor C_{ex} is added to lower the R_α to approach 50 Ω.

3. SIMULATION RESULTS

All the simulations are designed with TSMC 0.18 μm Design Kit. The simulated input and output return loss are smaller than −10 dB from 3.1 G to 10.6 GHz, as shown in Fig. 3. The Fig. 4 shows that a flat power gain are about 10 dB from 3.1 G to 10.6 GHz. The noise figure achieves 2.72–3.26 dB from 3.1 G to 10.6 GHz as shown in Fig. 5. The input IP3 (IIP3) and input compression point (P1dB) at 3.1 GHz are −12 and −18.5 dBm respectively, as shown in Fig. 6 and Fig. 7. The DC supply voltage and power consumption is 1.5 V and 15 mA, respectively. The proposed wide-band LNA performance is summarized in Table 1.

Table 1: Summary of the performance of wide-band LNA.

3–10 GHz Wideband LNA (TSMC 0.18 μm)	
Band-width	3.1∼10.6 GHz
Gain (max)	13 (dB)
S11	< -12.83 (dB)
S22	< -14.32 (dB)
NF	2.72∼3.26 (dB)
DC	1.5 V/15 mA
P1 dB	-18.5 dB

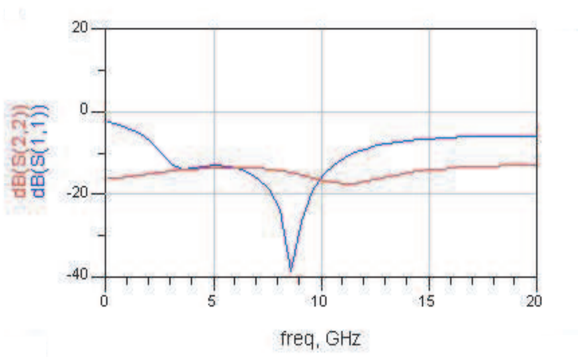

Figure 3: Input and output return loss.

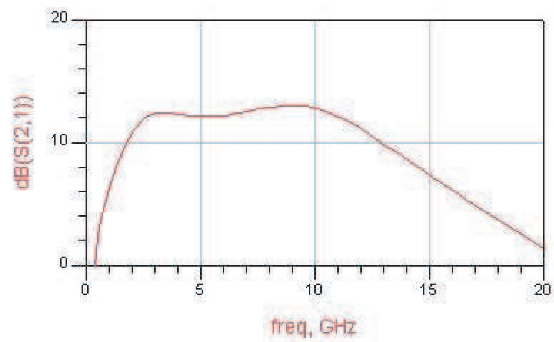

Figure 4: Gain.

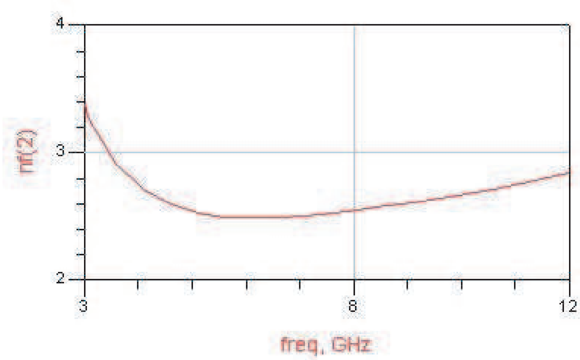

Figure 5: Noise figure.

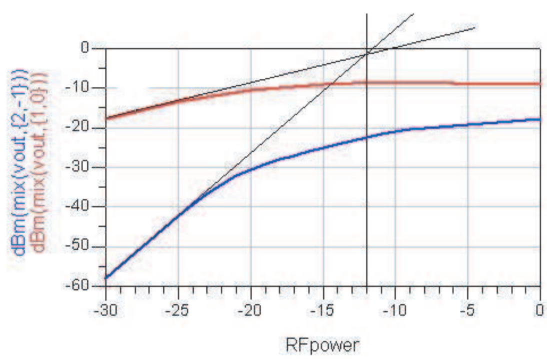

Figure 6: IIP3

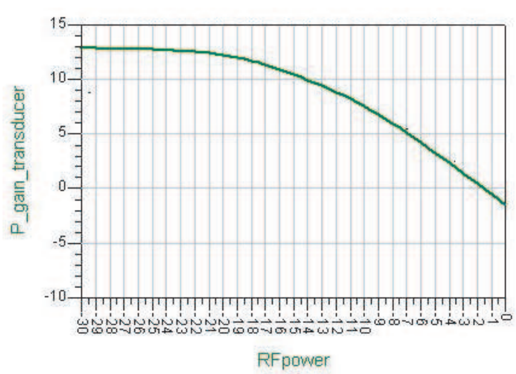

Figure 7: Input 1 dB compression point.

4. CONCLUSION

This letter presents a wideband LNA using cascaded stage to achieve wideband power gain. By way of transistor's intrinsic capacitor Cgd and reactive-feedback as input matching network, wideband input matching can be achieved.

REFERENCES

1. Reiha, M. T., J. R. Long, and J. J. Pekarik, "A 1.2 V reactive-feedback 3.1–10.6 GHz ultrawideband low-noise amplifier in 0.13 µm CMOS," *Radio Frequency Integrated Circuits (RFIC) Symp.*, June 2006.
2. Hu, R., "Wide-band matched LNA design using transistor's intrinsic gate-drain capacitor," *IEEE Transactions on Microwave Theory and Techniques*, Vol. 54, No. 3, March 2006.
3. Hu, R., "An 8-20-GHz wide-band LNA design and the analysis of its input matching mechanism," *IEEE Microwave and Wireless Components Letters*, Vol. 14, No. 11, November 2004.

DDS Based Radar Signal Generator for Microwave Remote Sensing

C. Z. Gu[1], **S. Qiao**[3], **J. T. Huangfu**[1,2], **and L. X. Ran**[1,2]

[1]Department of Information Science and Electronic Engineering
Zhejiang University, Hangzhou 310027, China
[2]The Electromagnetics Academy at Zhejiang University
Zhejiang University, Hangzhou 310027, China
[3]City College, Zhejiang University, Hangzhou 310015, China

Abstract— A system design of a Direct Digital Synthesis (DDS) based radar signal generator is presented. The DDS technique has its inherent disadvantage in noise and spurious suppression, due to the all-digital structure. To overcome these disadvantages, we apply two effective methods of a 3-order low-pass Butterworth filter and the pre-distortion technique to greatly enhance the system performance.

1. INTRODUCTION

Microwave Remote Sensing (MRS) has become a targeted area of intensive research for its great application in diverse situations. Early MRS radar signal generators are analog devices with high-cost, short life, low reliability and low precision. At present, due to the advance of high-speed Very Large Scale Integrated Circuit (VLSI), the technique of Direct Digital Synthesis (DDS) is being widely used to synthesize complex waveforms for applications in MRS. DDS makes it easy to precisely control and adjust the frequency, amplitude and phase of the required Chirp signals that are widely used in MRS. However, DDS technique has its inherent disadvantages in noise and spurious suppression, due to its all-digital structure. This paper presents a system design of a DDS signal generator for MRS. Besides, we put forward two methods to improve the spectrum purity. The first one is to design a low-pass filter to improve the SNR, and the second one is to employ the pre-distortion method to make spectrum within band much flatter.

2. TECHNICAL BACKGROUND

In microwave remote sensing, especially in microwave radar imaging, the transmitted radar signals are supposed to have a wide bandwidth, which helps to acquire high long-distance resolution and trigger other features of the targets. As one of the diverse forms of radar signals, the Chirp signal has a broad application in microwave remote sensing. Since the Chirp signal has a necessarily signal bandwidth, it is also helpful in measuring the generator's signal quality in a certain band. The complex expression of the Chirp signal can be seen as follows:

$$s(t) = u(t)e^{2\pi f_0 t} = \frac{1}{\sqrt{T}}\mathrm{rect}\left(\frac{t}{T}\right)e^{j2\pi(f_0 t + Kt^2/2)} \tag{1}$$

where the complex envelop $u(t)$ is:

$$u(t) = \frac{1}{\sqrt{T}}\mathrm{rect}\left(\frac{t}{T}\right)e^{j\pi Kt^2} \tag{2}$$

In the above equations, T is the pulse width. The instantaneous frequency of the Chirp signal is as below:

$$f_i = \frac{1}{2\pi}\frac{d}{dt}\left[2\pi(f_0 t + Kt^2/2)\right] = f_0 + Kt \tag{3}$$

where $K = B/T$ is the frequency slope, B is the frequency range.

The DDS signal generation technique is theoretically based on Nyquist Sampling Theorem. It could be seen as the inverse process of the signal sampling [2]. The sampling data of the required signals are calculated and stored in a Look-Up-Table (LUP), in which data are reachable by the phase codes. Sampling data are read out of the LUP and converted to analog signals through Digital-to-Analog Converter (DAC). Finally, required radar signal is obtained after the DAC output waves are filtered properly. However, there are some disadvantages for DDS, which degrade the spectrum purity and impose severe restrictions on the performance of the generator. These limitations are noise and spurious suppression, mainly due to the nonlinearity of the logic circuitry such as the DACs, and the Finite Word-length Effect coming from the size limitation of memories and DACs [1].

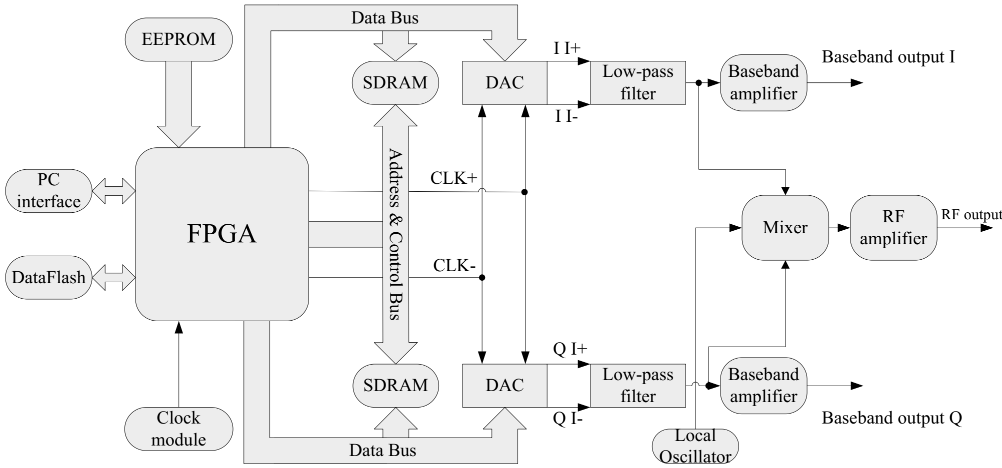

Figure 1: Architecture of DDS radar signal generator.

3. MRS SIGNAL GENERATOR DESIGN

The architecture of the DDS radar signal generator is showed in Figure 1. Waveform data are generated on PC, and DataFlash, a permanent memory, is used as the waveform memory to store these digital data. We apply Xilinx Spartan IIE FPGA as the master chip, fulfilling the communication with PC interface, DataFlash and high-speed SDRAM. Besides, FPGA supplies clock to the DACs. To generate radar signals, waveform data are read out of the DataFlash to the high-speed SDRAM and DACs, with the phase-encoding address sequence generated by FPGA as the address for waveform memory. The DACs convert digital data to analog outputs, which are further filtered to remove undesirable frequency waveforms. The mixer modulates baseband signals to radio frequency (RF) output that is amplified to a required power level for the ultimate radar signal output.

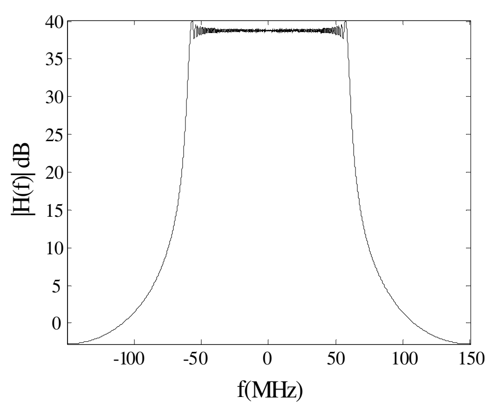

Figure 2: Simulated baseband spectrum.

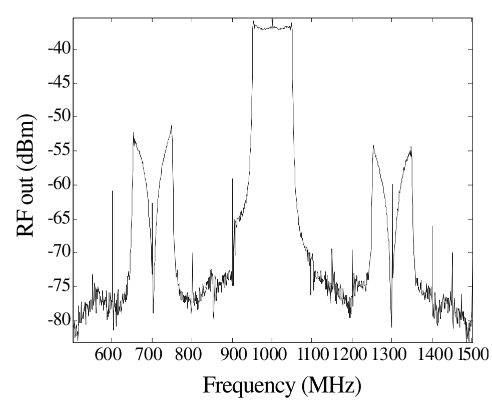

Figure 3: Real spectrum of RF output.

4. ENHANCEMENT OF SPECTRUM PERFORMANCE

According to the analysis in Section 2, we simulate the radar Chirp signal baseband spectrum as in Figure 2. The figured chirp signal is with the pulse width 10 µs, bandwidth 120 MHz, and sampling rate 300 MHz. The SNR is slightly less than 45 dB. There are some regular fluctuations within the band, which could be flat after median filtering. We use Agilent E4407B spectrum analyzer to analyze the real spectrum of the RF output. It is seen as Figure 3, from which we can see clearly that the SNR is degraded to only 20 dB, due to the interference of sideband. In order to increase the SNR, it is necessary to eliminate off-band noise. The simplest way is to insert a properly featured low-pass filter between DAC and mixer. Another parameter measuring the performance within the band is the gain flatness, which refers to the gain range of an amplifier within the whole working frequency band. The gain flatness reflects the linearity of the amplifier within a certain band. The real RF output, in Figure 3, is with a gain variation range of 0.8 dB, much more than the design specification 0.2 dB. To ameliorate the gain flatness, the most direct way is to add a nonlinear circuit before the RF amplifier to offset its nonlinear distortion, that is, the way of pre-distortion.

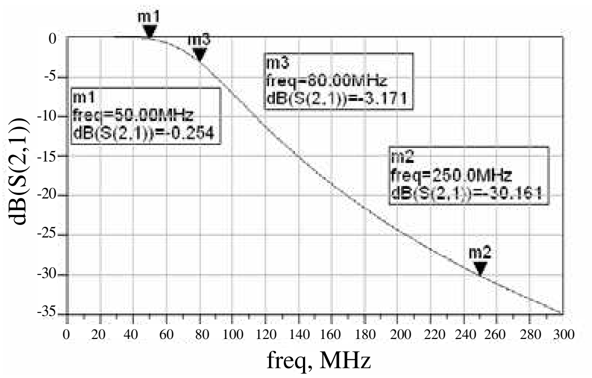

Figure 4: A 3-order low-pass Butterworth filter.

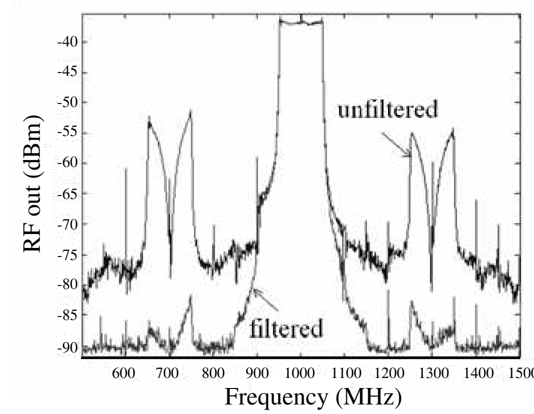

Figure 5: RF spectrum with and without filter inserted.

The clutter noise comes from three aspects: the nonlinearities of logic circuit and devices, especially DACs, the Finite Word-length Effect of memories and DACs, and aliased harmonics predicted by sampling theory [1]. The role of the filter is to remove unwanted signal frequency, or to decline the frequency component below a certain level. The unfiltered signal spectrum is showed in Figure 3. The frequency range 940 MHz to 1.06 GHz must be retained, that is, -60 MHz to 60 MHz in the baseband. So the filter should be a low-pass filter, with the 3 dB cut-off frequency 80 MHz and off band attenuation at 250 MHz no less than 20 dB. For the simplicity of the circuit structure, we choose the passive LC filter. A 3-order low-pass Butterworth filter is designed with components properly selected.

Figure 4 and Figure 5 display respectively the simulation result of a 3-order low-pass Butterworth filter and the RF spectrum with and without the filter inserted. In Figure 5, it is obvious that the designed filter has a good performance in the term of restraining unwanted signals off the band. The SNR is improved to 45 dB or more.

The waveform generation process includes a signal sampling process. So, as long as the amplitude and phase compensation values are made, it is convenient to program and calculate the value after pre-distortion for each sample point. In the system design, we use Agilent E4407B spectrum analyzer, which provides a way to obtain spectrum data through the GPIB (General Purpose Interface Bus) interface. Following are the details of the process of the pre-distortion method: obtain spectrum data from the spectrum analyzer → use filtering algorithm to analyze the spectrum envelop → obtain the pre-distortion compensation coefficient for each sampling point → obtain

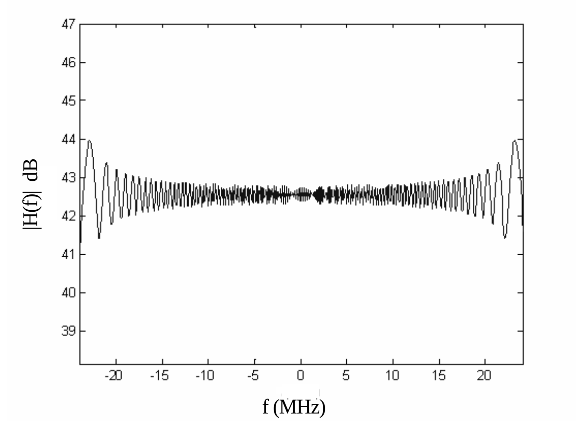

Figure 6: Simulated in-band spectrum.

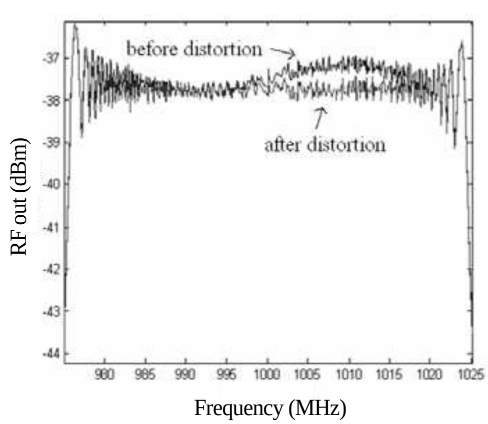

Figure 7: In-band spectrum before/after pre-distortion.

waveform value for each sampling point according to the pre-distortion compensation coefficient → download waveform data. In order to achieve the desired in-band gain flatness, the above process may be repeated several times. Using the pre-distortion method, the system's output signal spectrum in-band flatness is greatly improved. In the experiment, we pre-distort the Chirp signals as mentioned in Figure 3. Then we get the results contrasting the in-band spectrum before and after pre-distortion. Figure 6 displays the simulated in-band spectrum, and Figure 7 shows together the before and after pre-distortion in-band spectrum.

It can be found from the above figures that the pre-distortion method used in this paper leads to very good result in improving the flatness of in-band spectrum. The flatness is improved from original 0.8 dB to present within 0.2 dB.

5. CONCLUSION

We presented a system design of a radar signal generator for microwave remote sensing. Then we proposed two methods to improve the performance of the generator. A 3-order low-pass Butterworth filter is designed to improve the SNR to 45 dB or more. The pre-distortion method is applied to ameliorate the in-band spectrum flatness. Real testing results shows that the designed system has a good performance within in-band spectrum.

ACKNOWLEDGMENT

This work is supported by the NSFC (Nos. 60531020, 60671003), ZJNSF (No. R105253), the NCET-07-0750, and the Ph.D. Programs Foundation of MEC (No. 20070335120).

REFERENCES

1. Endres, T. J., R. B. Hall, and A. M. Lopez, "Design and analysis methods of a DDS-based synthesizer for military spaceborne applications," *Frequency Control Symposium, 1994. 48th. Proceedings of the 1994 IEEE International*, 624–632, June 1–3, 1994.
2. Liu, J. and J. Liu, "Spectrum characteristic analysis of DDS-based RF digital modulation," *Electrical and Electronic Technology, 2001. TENCON. Proceedings of IEEE Region 10 International Conference on*, Vol. 2, 588–591, August 19–22, 2001.

Ambiguity Function of Chaotic Radar with Colpitts Oscillator

Tao Jiang[1,2], **Shan Qiao**[1,3], **Zhi Guo Shi**[1], **and Lixin Ran**[1,2]

[1]Dept. of Information and Electronic Engineering, Zhejiang University, 310027, China
[2]Electromagnetics Academy at Zhejiang University, Zhejiang University, 310027, China
[3]Zhejiang University City college, Zhejiang University, 310027, China

Abstract— The ambiguity function of a kind of chaotic radar uses Colpitts oscillator is investigated and compared from different points of view. The Colpitts oscillator with specific value of capacitance and inductance can generate chaotic signal with frequency band from direct current to several gigahertz. The auto-ambiguity functions show that the chaotic signal of such oscillator is ideal for Radar application with both high range and range rate resolution. The cross-ambiguity functions also indicate the chaotic signal has excellent capabilities in the electronic counter- countermeasures (ECCM).

1. INTRODUCTION

Chaotic and random signal radars have been widely investigated in the recent years. It is known that random signal has high resolution in both range and range rate, making it ideal to radar application. The previous electric circuits generated chaotic signals are all limited by their low and narrow frequency bandwidth for better range resolution. The chaotic signal used in this paper is generated from the Colpitts oscillator. The basic working frequency of the Colpitts oscillator ranged from 1 GHz to 3.5 GHz, with ultra-wide frequency band from direct current to about 10 GHz.

By using the microwave chaotic signals generated from Colpitts oscillator, the advantage of the direct chaotic radar is, by varying the operating condition, the dynamics in a Colpitts oscillator can be easily switched among different states, and the corresponding diverse waveforms with different characteristics are highly desirable, since it provides the property of "multi-user", which is required when a large number of radars with the same scheme co-exist, in applications such as vehicular collision avoidance system.

2. COLPITTS OSCILLITOR CIRCUIT

The basic configuration of the Colpitts oscillator used as the microwave chaotic oscillator source is shown in Fig. 1. It contains a bipolar junction transistor (BJT) as the gain element and a resonant

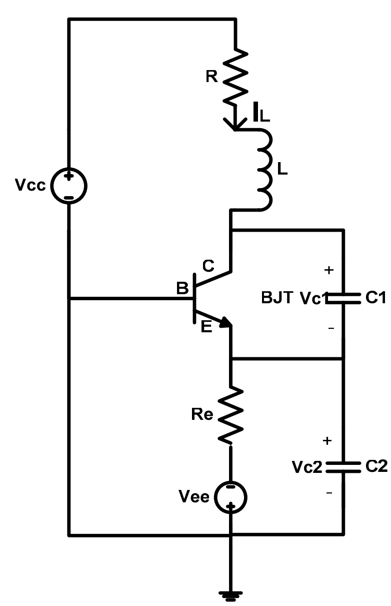

Figure 1: Schematic setup of the Colpitts oscillator circuit.

network consisting an inductor and a pair of capacitors. The state equations for colpitts oscillator as shown in Fig. 1 are:

$$C_1 \frac{dV_{C_1}}{dt} = -f(-V_{C_2}) + I_L \tag{1}$$

$$C_2 \frac{dV_{C_2}}{dt} = I_L - \frac{V_{C_1} + V_{ee}}{Re} \tag{2}$$

$$L \frac{dI_L}{dt} = -V_{C_1} - V_{C_2} - I_L R + V_{CC} \tag{3}$$

where I_L is the current through the inductor L, V_{C_1} and V_{C_2} are the voltages across the capacitors C_1 and C_2. It has been verified with proper value of I_L, C_1 and C_2 list in Fig. 1, the chaotic signal with fundamental frequency more than 1 GHz can be generated. We obtain the chaotic signal both in simulation as shown in Fig. 2. Figs. 2(a) and (b) are the simulation results, where Fig. 2(a) shows the time series which is noise like signal, Fig. 2(b) shows power spectra of the signal V_{C_2}, which is like white noise with frequency band of about 1 GHz. Fig. 3 reveal the chaotic signal with 3.5 GHz fundamental frequency. It is found the fundamental frequency of the Colpitts oscillator can be tuned to be several gigahertz with carefully designed values of C_1, C_2 and I_L.

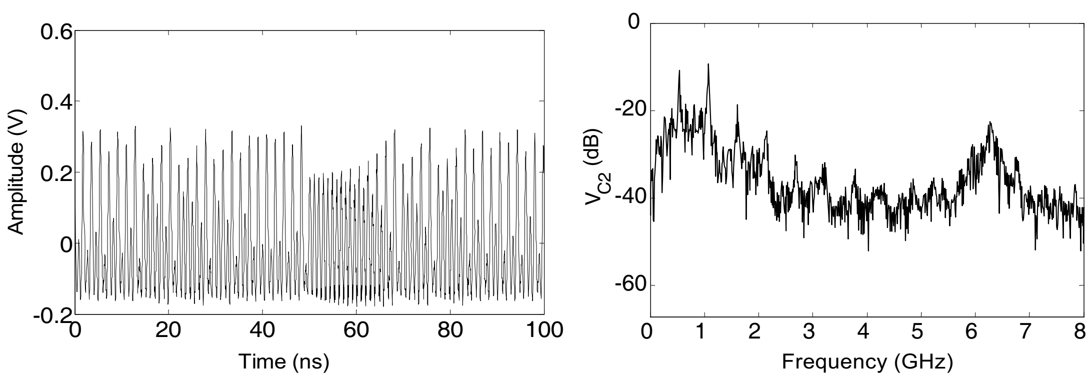

(a) (b)

Figure 2: Simulation results, (a) Time domain waveform of V_{C_2}, (b) Spectrum of V_{C_2}.

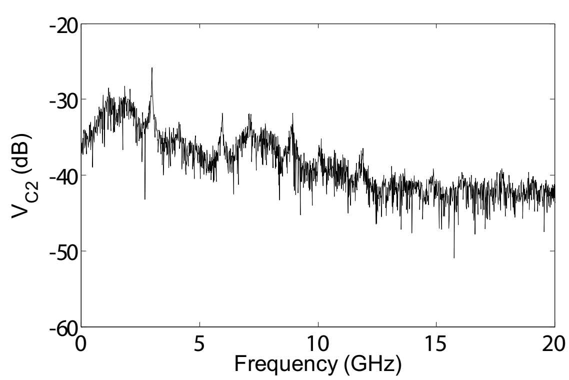

Figure 3: Simulation result for the spectrum of V_{C_2}.

3. AMBIGUITY FUNCTION ANALYSIS OF THE CHAOTIC SIGNAL

3.1. Wideband Chaotic Signal Model

For a point target, suppose $s(t)$ is the reference signal and

$$s_r(t) = s(t - \tau(t)) \tag{4}$$

is the reflected signal from the moving target, where $\tau(t)$ is the delay time between the reference and the received signal, and it can be expressed as

$$\tau(t) = \frac{2R(t)}{c+v} \approx \frac{2R(t)}{c} \tag{5}$$

the velocity of the target is much smaller than the microwave signal, R denotes the distance between the source and the target.

$$s_r(t) = s((1+\alpha)t - \tau_0) \tag{6}$$

where $\alpha = \dfrac{2v}{c}$.

3.2. Ambiguity Function

In the Colpitts oscillator chaotic radar system, the broadband microwave chaotic waveforms are transmitted and received as baseband signals. The ambiguity function is defined as

$$\langle \chi(\tau, \alpha) \rangle = \int_t^{t+T} s(t)s((1+\alpha)t - \tau)dt \tag{7}$$

where T is the correlation interval.

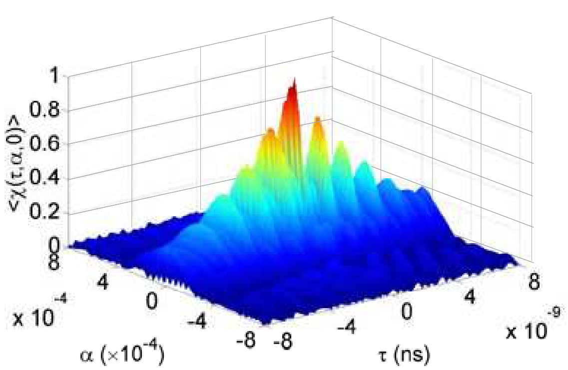

Figure 4: Auto-ambiguity function of the Colpitts oscillator with 1 GHz fundamental frequency.

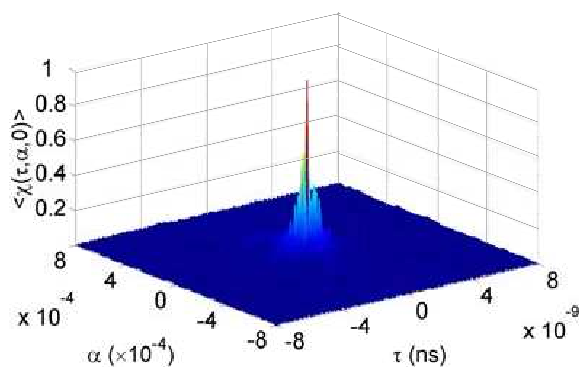

Figure 5: Auto-ambiguity function of the Colpitts oscillator with 3.5 GHz fundamental frequency.

Figure 4 shows the auto-ambiguity function of range and range rate, with correlation internal $T = 10\,\mu\text{s}$, for signal with the fundamental frequency 1 GHz as shown in Fig. 3. As can be seen, the ambiguity function of $\langle \chi(\tau, 0) \rangle$ has many side lobes. This is because the chaotic signal generated by Colpitts oscillator possesses somewhat periodicity essentially, which makes the chaotic signal not ideal random waveform.

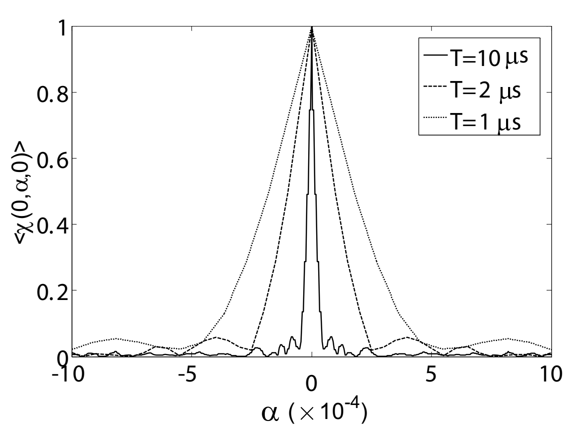

Figure 6: Slices of $\langle \chi(0, \alpha) \rangle$ for different correlation interval T.

Next we investigate the characters of the chaotic signal that affects the ambiguity function. Fig. 6 shows the slices of $\langle\chi(0, \alpha)\rangle_T$ for the chaotic signal with fundamental frequency 3.5 GHz, with $T = 10$, 2, and 1 μs, the widths of the slices narrow when the correlation interval increases. As can be seen from Fig. 8, the FWHM of the slices are inversely proportional to the correlation interval, that means the range rate resolution can be improved linearly with the correlation interval.

Another merit of the chaotic signal of Colpitts oscillator is its sensitivity to initial values of the oscillator parameters, which means the chaotic signals vary greatly with different parameters, this is useful in the multi-users condition such as car collision avoidance. To evaluate the ECCM capability of the Colpitts oscillator, we have calculated the cross-ambiguity function of the signal shown in Fig. 4 with the same circuit parameters but at a different time with a correlation interval $T = 10$ μs in Fig. 7(a), and that of two slight different parameters in Fig. 7(b). One circuit has the same parameters as listed in Fig. 1, the other changes value of R ($R = 27\,\Omega$). The cross-ambiguity function in Fig. 7(a) indicates the chaotic signal of Colpitts oscillator has good randomicity in time domain, thus signal samples at different time have low degree of correlation, the cross-ambiguity function in Fig. 7(b) is due to the sensitivity of chaotic signal of Colpitts oscillator to the circuit's parameters, that means slight change of the parameters will greatly change the character of the chaotic signal. Therefore the chaotic signal of Colpitss oscillator has excellent capabilities in ECCM.

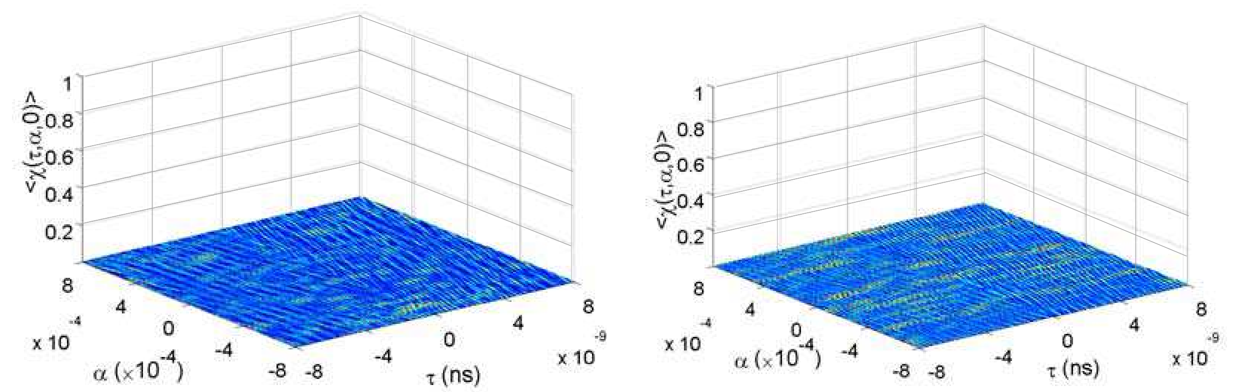

(a) (b)

Figure 7: Cross-ambiguity function of the Colpitts oscillator with 3.5 GHz fundamental frequency, correlation interval $T = 10$ μs. (a) Cross-ambiguity function with different time. (b) Cross-ambiguity function with slight different parameters.

4. CONCLUSION

In this paper, the ambiguity functions of microwave chaotic signal generated by chaotic Colpitts oscillator, have been studied. The time-domain, frequency domain chaotic signal and chaotic attractor of the Colpitts oscillator are presented for illustration. The chaotic signals with fundamental frequency of 1 GHz and 3.5 GHz have been studied and compared. The auto-ambiguity function of chaotic signals shows that the chaotic signal with low frequency possesses periodicity, too many side lobes makes the unambiguous range detection difficult, and the side lobe reduces when the fundamental frequency increases, so that the randomness characteristics of the microwave chaotic signal improves. It should be mentioned that the operating condition of the Colpitts oscillator with more abound dynamic characteristics can help improve the signal spectrum.

The cross-ambiguity functions of the direct radar system have also been investigated to evaluate the ECCM performance and the "multi-user" characteristic when the chaotic signal is used as anti-collision vehicle-borne radar. Rather excellent ECCM capability can be achieved with transmitting chaotic signals generated by circuits with same parameters but at different time or with slightly different circuit parameters.

ACKNOWLEDGMENT

This work is supported by the NSFC (Nos. 60531020, 60671003),ZJNSF (No. R105253), the NCET-07-0750, and the Ph.D. Programs Foundation of MEC (No. 20070335120).

REFERENCES

1. Liu, G. S., H. Gu, and W. M. Su, "The development of randomsignal radars," *IEEE Transactions on Aerospace and Electronic Systems*, Vol. 35, No. 3, 770–777, 1999.
2. Lin, F. Y. and J. M. Liu, "Ambiguity functions of laser-basedchaotic radar," *IEEE Journal of Quantum Electronics*, Vol. 40, No. 12, 1732–1738, 2004.
3. Flores, B. C., E. A. Solis, and G. Thomas, "Assessment of chaosbased FM signals for range-Dopper imaging," *IEEE Proc. Radar Sonar Navig.*, Vol. 150, No. 4, 313–322, 2003.
4. Shi, Z. G. and L. X. Ran, "Microwave chaotic Colpitts oscillator: Design, implementation and applications," *Journal of Electromagnetic Waves and Applications*, Vol. 20, No. 10, 1335–1349, 2006.
5. Qiao, S., Z. G. Shi, K. S. Chen, W. Z. Cui, W. Ma, T. Jiang, and L. X. Ran, "A new architecture of UWB radar utilizing microwave chaotic signals and chaos synchronization," *Progress In Electromagnetics Research*, PIER 75, 225–237, 2007.

A Broadband Low Noise Amplifier Design

Ying Wang, **Yi Fu**, **Wan-Zhao Cui**, **and Wei Ma**

National Key Laboratory of Space Microwave Technology
Xi'an Institute of Space Radio Technology, Xi'an 710100, China

Abstract— Low noise amplifier (LNA), as the first stage of RF and microwave receivers, is a very important element in communication systems. It is imperative to accelerate the production process of the space LNA by developing the broadband LNA with high reliability.

In this paper, a design method for space LNA is proposed. Compared with those LNA's designed by traditional ways using the same low noise element, the LNA's performance obtained here can be improved and 30% bandwidth is achieved in noise factor.

1. INTRODUCTION

At present, the space LNA is made up of the packaged MESFET or HEMT. Because of the parasitic effects in packaged MESFET or HEMT itself, it is difficult for electronic engineers to design broadband LNA.

In this paper, a method for broad band LNA design is shown. Firstly, the resonance network is used as the LNA's input matching network. Secondly, by optimizing elements' values of the resonance network, the port impedance is matched to the optimal noise impedance of the low noise element in a broad band based on simulations and the broadband noise matching is obtained. A C-band two stages broadband LNA is designed on the basis of the authors' method.

The circuit and EM simulation are showed by microstrip elements in Agilent ADS software, which proves the availability and practicality of the method.

2. DESIGN PROCEDURE

2.1. Source-Peaking and Analysis of FET

At the beginning of LNA design, it is necessary to give a thorough analysis of the low noise FET which in the authors' design. Source-Peaking, a feedback method, will be applied. This is a brief introduction of Source-Peaking. Connect an inductor between the source and the ground and select an appropriate value of the inductor. This series process can change the S parameter and Noise parameter of FET (a little change in Noise Figure). These adjusted parameters make the design process easy to implement. We can get low noise and good VSWR simultaneously.

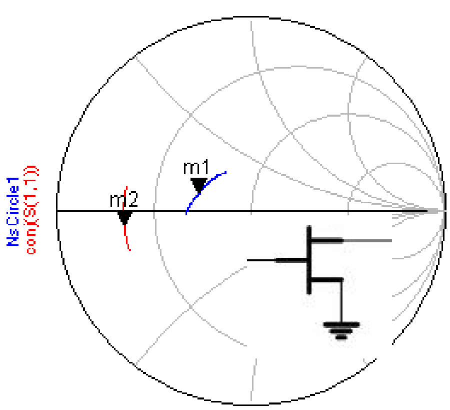

Figure 1: Common source connection.

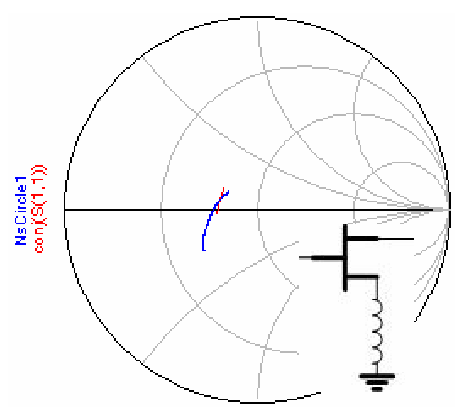

Figure 2: Source-Peaking connection.

Figure 1, Figure 2 show the Optimal Noise Impedance curve and the conjugate S_{11} curve of a packaged FET. Figure 1 shows the common source status and Figure 2 shows the Source-Peaking status.

From the curves in Smith Chart of the two ground methods, it can be seen that the Optimal Noise Impedance curve and the conjugate S_{11} curve is overlapped after Source-Peaking processing. To design a matching network based adjusted parameters can easily achieve the low noise figure and good VSWR. The authors also can get the circuit more stable through Source-Peaking. However, the inductor that connects ground and the source of FET is very small. It is hard to find a lumped inductor with so small value. The authors have to use a fine microstrip line and via hole to achieve an equivalent inductor. Optimize the microstrip line and via hole to make the S parameters of the microstrip circuit to approach the S parameters of schematic circuit (Figure 3).

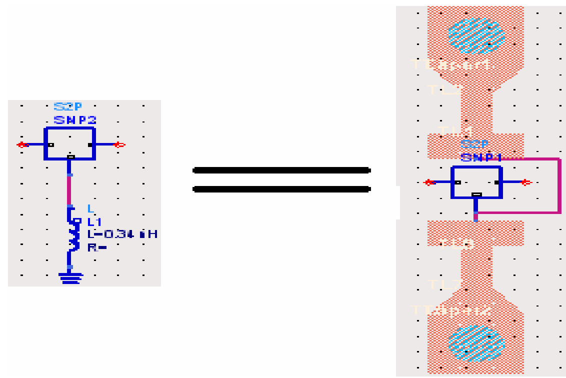

Figure 3: Source-Peaking microstrip line equivalent circuit.

2.2. Input Matching Network Design

As everyone knows, the design of input network is a key process in whole LNA design. If designers want to get broadband performance, it is necessary to match the optimal noise impedance in specified bandwidth. Traditional 'L' matching network always used for narrowband design is hard to implement in broadband applications. Because the frequency respond curve of resonance network can across a curve of certain frequency respond in Smith chart several times. To obtain the broadband performance, the resonance network as the matching network must be used in design.

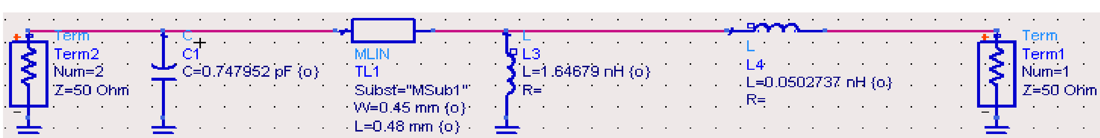

(a)

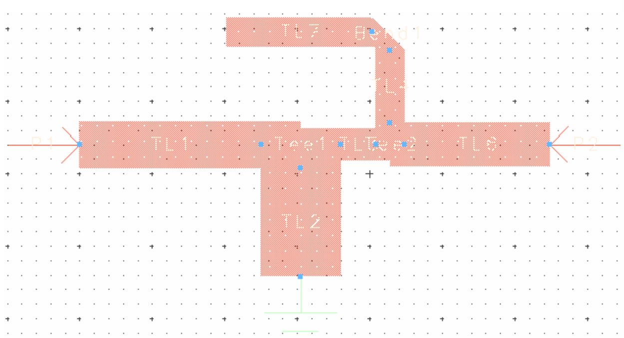

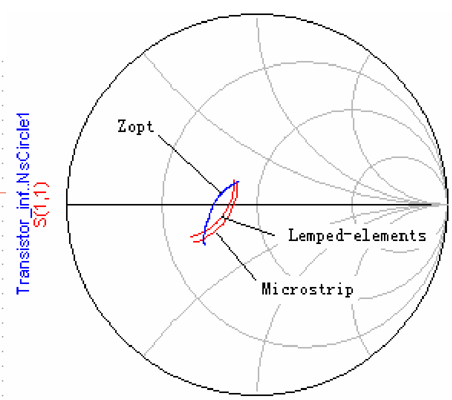

(b) (c)

Figure 4: Input matching network: (a) Input matching network with lumped-elements. (b) Input matching network with microstrip. (c) Simulation results of the input matching network.

Figure 4, Zopt's curve is the curve of optimal noise impedance. The frequency respond curve of resonance network constitutes of lumped elements and microstrip elements across the Zopt's curve at low and upper frequency point. The two curves (Zopt and frequency respond curve of resonance network) must have the same direction. After these processes, the authors get the broadband noise matching. Simultaneous, a good VSWR is achieved by the Source-Peaking technology.

2.3. The Whole LNA Design

After the input matching network design, the key step of LNA design is finished. Then, the inter-matching and output networks are designing. During the inter-matching network design, designers need pay attention to the frequency respond of the LNA. In the other word, the frequency respond of the FET amplifier always drops as frequency increases so the frequency respond of the inter-matching network must be oppositional with the FET's respond.

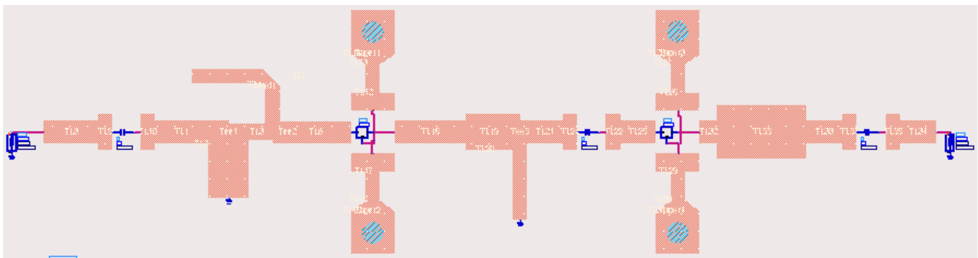

Figure 5: EM simulating circuit.

EM simulation is implemented for the input, inter- and output matching network. Then, the authors simulate the LNA using the EM simulation data and active element s2p file (Figure 5). Simulated results are showed in Figure 6.

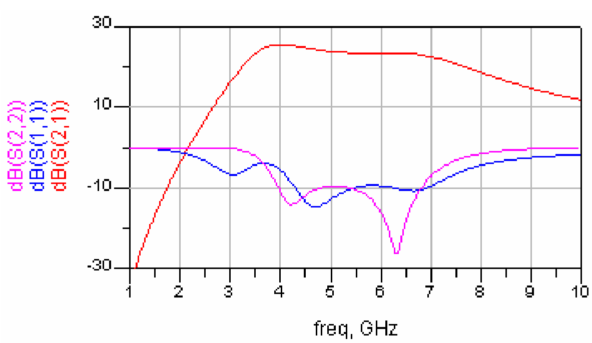

(a)

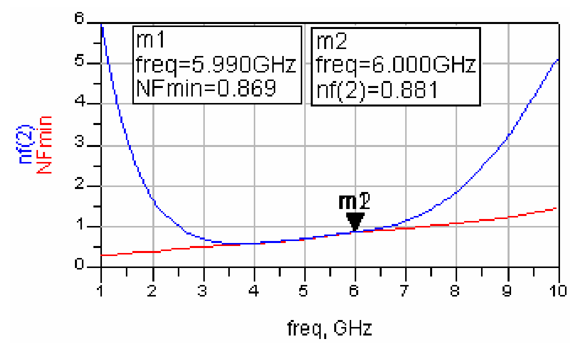

(b)

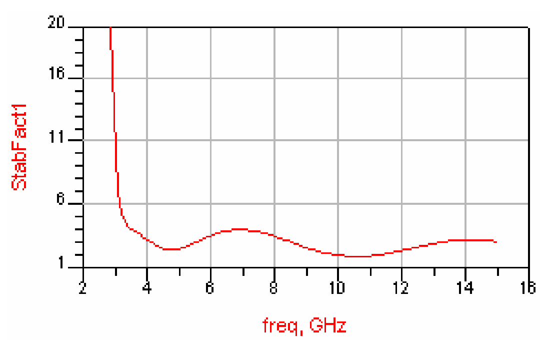

(c)

Figure 6: Simulated results: (a) Gain, S_{11} and S_{22} of the LNA. (b) Comparison of NFmin and simulated NF. (c) Stability factor.

3. CONCLUSION

This paper presents a method for broadband LNA design using resonance network. A C-band two stages broadband LNA is designed with packaged MESFET on the basis of the authors' method. The simulated results show that 30% bandwidth is achieved in noise factor and proved the availability and practicality of the authors' method.

REFERENCES

1. Abbas, T. and M. Bin Ihsan, "Design of a two stage low noise amplifier at Ku band," 0-7803-9262-0/05 @ IEEE 2005.
2. Vendelin, G. D., A. M. Pavio, and U. L. Rohde, *Microwave Circuit Design Using Linear and Nonlinear Techniques*, Wliley, 1990.
3. Bahl, I. and P. Bhartia, *Microwave Solid State Circuit Design 2nd Edition*, John Wiley & Sons, Inc., Hoboken, New Jersey, 2003.

Reducing the Time Steps of FDTD Predictions of High-Q Cavities

Juan Chen[1] **and Jianguo Wang**[1,2]

[1]School of Electronic and Information Engineering, Xi'an Jiaotong University, Xi'an 710049, China
[2]Northwest Institute of Nuclear Technology, P. O. Box 69-15, Xi'an 710024, China

Abstract— Finite-difference time-domain (FDTD) method is an effective tool for shielding effectiveness analysis. But due to the high Q of the cavity considered, the conventional second-order FDTD method requires a very large number of time steps for a pulse excitation to decay to a value that is sufficiently close to zero for accurate Fourier transformation of the time-domain fields into the frequency domain. This paper demonstrates the long FDTD time steps for generating accurate frequency domain parameters can be reduced by introducing an infinite ground plane at the bottom of the enclosure. The ground plane has no effect on the shielding effectiveness, but can improve the calculation efficiency. Compared with the method of introducing of an artificial loss into the solution space, this method has much higher accuracy, which is validated by numerical examples.

1. INTRODUCTION

The penetration of electromagnetic fields into conducting enclosures via apertures is an important EMI issue. Finite-difference time-domain (FDTD) method is an effective tool for shielding effectiveness analysis. But due to the high Q of the cavity considered, the conventional second-order FDTD method requires a very large number of time steps for a pulse excitation to decay to a value that is sufficiently close to zero for accurate Fourier transformation of the time-domain fields into the frequency domain. Particularly when the aperture is small relative to the size of the enclosure, 100,000 time steps may be insufficient [1]. The introduction of a small artificial conductivity can resolve the problem to some extent [1, 2]. But the inclusion of artificial losses, the pulse response of the cavity is altered, and the accuracy of the prediction is degraded, especially in the high frequency range. [3] and [4] combine the FDTD with Prony's methods [5] for reducing the computation time of the calculations.

The required FDTD time response can be efficiently obtained from a relatively short time record by using an extrapolation scheme based upon the Prony's method. This method is complicated and the accuracy of the prediction is also degraded.

This paper introduces an infinite ground plane at the bottom of the enclosure for reducing the FDTD computation time. The ground plane has no effect on the shielding effectiveness, but can improve the calculation efficiency. Compared with the former two methods, this method is simple and with higher accuracy.

2. FDTD PREDICTION

The enclosure is a rectangular box having the dimensions of 30 cm wide by 30 cm deep by 12 cm high. The aperture is centered on the side of the box and is 20 cm wide by 3 cm high. This is one of the geometries considered by many authors [2, 6, 7]. The incident field (Gaussian pulse) is vertically polarized and normally incident on the aperture.

We apply the FDTD technique to analyze shielding effectiveness of this enclosure. Due to the cavity resonances, the time-domain electric field amplitude at the center of the box decays slowly. For getting accurate Fourier transformation of the time-domain fields into the frequency domain, a very large number of time steps are need. For reducing the computation time, an infinite ground plane at the bottom of the enclosure is introduced, as shown in Figure 1.

In Figure 2, the vertical component of the time domain electric field at the center of the enclosure without the infinite ground is plotted with respect to the number of time steps. As shown in the figure, for the field decaying to a value that is sufficiently close to zero for accurate Fourier transformation of the time-domain fields into the frequency domain, the FDTD time steps can't be less than 10,000. If the slot become smaller, for example, $10\,\mathrm{cm} \times 0.5\,\mathrm{cm}$, it is estimated that the FDTD simulation would extend 100,000 time steps before the late-time fields approach zero [1].

In Figure 3, the vertical component of the time domain electric field at the center of the enclosure with the infinite ground is plotted with respect to the number of time steps. For comparison,

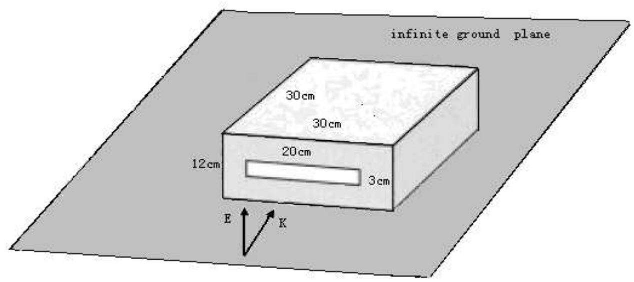

Figure 1: Geometry.

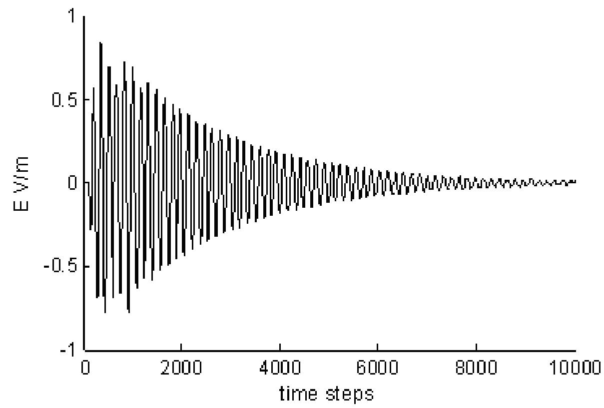

Figure 2: The vertical component of the electric field at the center of the enclosure without the infinite ground.

Figure 3 also gives the time domain electric field of the enclosure when a conductivity of 0.001 S/m is assigned to all of the free-space cells.

As shown in Figure 3, introducing an infinite ground plane at the bottom of the enclosure can fast the FDTD computation. Only after 4,000 time steps, the electrical field already reach a small value close to zero. The effect of the infinite ground plane on the FDTD computation is a little better than that of artificially assignment conductivity of 0.001 S/m to the free-space cells.

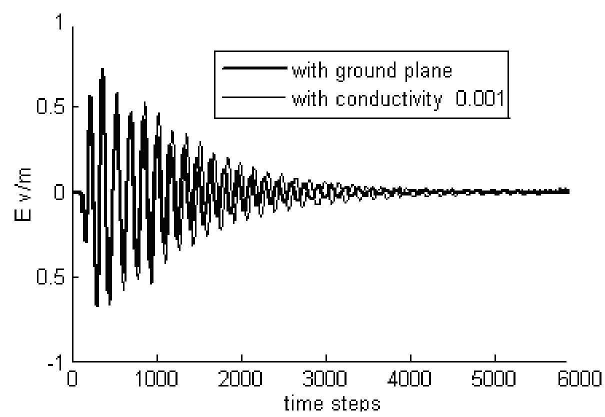

Figure 3: The vertical component of the electric field at the center of the enclosure with an infinite ground plane or a conductivity of 0.001 S/m.

The FDTD-predicted electric field shielding (defined as the ratio of the incident electric field to the field at the center of the box) is plotted in Figure 4. The shielding effectiveness simulated by introducing an infinite ground plane agreed well with the direct FDTD generated result. The ground plane has no effect on the shielding performance of enclosure, except to reduce the computation time. The discrepancy between the direct FDTD result and the result calculated by assigning a conductivity of 0.001 S/m is apparent in the high frequencies. Compared with the introduction of a small artificial conductivity, the introduction of an infinite ground plane has much higher accuracy.

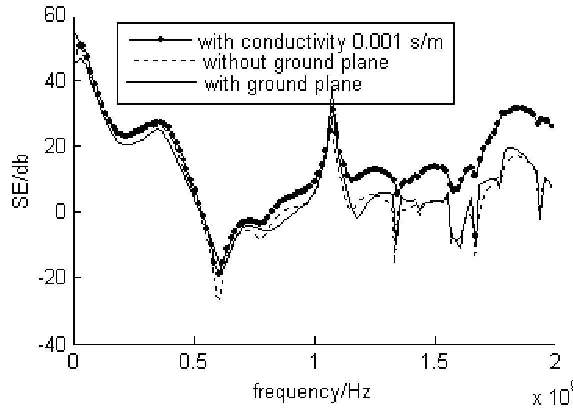

Figure 4: Electric field shielding effectiveness.

3. CONCLUSIONS

Due to the high Q of the cavity considered, the FDTD method requires a very large number of time steps for a pulse excitation to decay to a value that is sufficiently close to zero for accurate Fourier transformation of the time-domain fields into the frequency domain. By introducing an infinite ground plane at the bottom of the enclosure, the transient fields inside the cavity are forced to decay to zero much more rapidly. Compared with the introduction of an artificial loss mechanism into the solution space, this method has much higher accuracy, enabling the accurate Fourier transform of the time-domain fields into the frequency domain.

REFERENCES

1. Birtcher, C., S. Georgakopoulos, and C. A. Balanis, "Artificial loss in FDTD predictions of high-Q cavities," *IEEE APS-3*, 1492–1495, 2000.
2. Georgakopoulos, S. V., C. R. Birtcher, and C. A. Balanis, "HIRF penetration through apertures: FDTD versus measurements," *IEEE Trans. Electromagn. Compa.*, Vol. 43, No. 3, 282–294, 2001.
3. Li, M., S. Radu, and J. Nuebel, "Design of airflow aperture arrays in shielding enclosures," *IEEE ISEMC-2*, 1059–1063, 1998.
4. Li, M., J. Nuebel, J. LDrewniak, et al., "EMI from airflow aperture arrays in shielding enclosures — Experiments, FDTD, and MoM modeling," *IEEE Trans. Electromagn. Compat.*, Vol. 42, No. 3, 265–275, 2000.
5. Ko, W. L. and R. Mittra, "A combination of FD-TD and Prony's methods for analyzing microwave integrated circuits," *IEEE Trans. Microwave Theory Tech.*, Vol. 39, No. 12, 2176–2181, 1991.
6. Azaro, R., S. Caorsi, M. Donelli, et al., "A circuital approach to evaluating the electromagnetic field on rectangular apertures backed by rectangular cavities," *IEEE Trans. Microwave Theory Tech.*, Vol. 50, No. 10, 2259–2266, 2002.
7. Siah, E. S., K. Sertel, J. L. Volakis, et al., "Coupling studies and shielding techniques for electromagnetic penetration through apertures on complex cavities and vehicular platforms," *IEEE Trans Electromagn. Compat.*, Vol. 45, No. 2, 245–256, 2003.

Reduction of EMI and Mutual Coupling in Array Antennas by Using DGS and AMC Structures

A. Mahmoudian[1] **and J. Rashed-Mohassel**[2]
[1]Microwave Lab., Department of Electrical Engineering, Tarbiat Modares University, Tehran, Iran
[2]Center of Excellence on Applied Electromagnetic Systems, School of Electrical and Computer Engineering, University of Tehran, Iran

Abstract— Considering the difficulty of via construction in EBG structures and the cost of lossy materials and absorbers, in this paper, we look for implementing DGS and Artificial Magnetic Conductor to reduce mutual coupling in enclosures and array antennas particularly in CBS antennas. Circular ring defected ground structure and capacitive loaded AMC strips are designed and optimized to have electromagnetic band gaps and incident wave reflection features, respectively, in the resonant frequency band of cavity backed slot (CBS) antenna. The complete structure consists of CBS antenna with circular ring DGS and CLS-AMC. These structures are investigated and enhancement in EMI and the radiation patterns of this antenna is observed.

1. INTRODUCTION

Performance limitations in electronic devices and electromagnetic structures due to mutual coupling between elements is an important aspect which has received much attention. Mutual coupling between different hardware stages such as devices or transmission lines in printed circuit boards is one type of electromagnetic interference (EMI). Moreover, excitation of the surface wave which causes EMI in the printed circuit antenna is another problem of mutual coupling that limits compactness of the structure.

So far, to reduce the effect of mutual coupling various methods have been proposed based on reducing surface waves. Utilizing the lossy material is one of these ways [1]. Using electromagnetic band gap structures (EBG) which reduce surface waves in all directions and in specific frequency bands have been increased in recent years. Decreasing of parallel plate waveguide noise [2] and enhancing antenna characteristics [3, 4] are some application of EBG structures.

In this paper we are focusing on improving the efficiency of cavity backed slot (CBS) antennas by reducing mutual coupling between two cavities through the common plane surface wave. In prior works diverse methods have been suggested for developing EMI in these structures such as implementing lossymaterials [1] or EBG structures constructed from metal patches and vias [5]. In this work, considering the absence of vias, which eases the fabrication process, we are using defected ground structures (DGS) and artificial magnetic conductors (AMC) to achieve this purpose. In addition to the difficulty of via construction, for reducing EMI, two EBG structures is required since each EBG structure with certain dimensions reduces surface waves just in one resonant frequency [5]. The CBS antenna without DGS and AMC structures is first simulated and its working frequencies are derived, then DGS and AMC are designed for this frequency band. Assuming the same dimensions as [5] for CBS antennas, the resonant frequencies of antennas are found to be 7.5 and 12 GHz. Dispersion diagram and the frequency band gap for circular ring DGS is obtained. Next, the transmission coefficient of capacitive loaded AMC strips will be considered and the dimensions of this structure are optimized to act in the operating frequency band of the CBS antenna. Finally, we examine CBS antenna with a circular ring defected ground structure and capacitive loaded strips, and subsequently enhancement in characteristics of the antenna has been observed.

2. CIRCULAR RING DEFECTED GROUND STRUCTURE

Electromagnetic band gap feature of DGS is introduced in [6]. In this paper, we use a circular ring defected ground structure with an internal radius of 2 mm and an external radius of 3 mm with a unit cell length of 8 mm. The circular DGS is constructed below a substrate with thicknesses of 1.575 mm and a permittivity of 10.2. The unit cell of this structure is shown in Fig. 1.

The dispersion or β-f diagram can be calculated from the unit cell. Two dimensional Eigenmode solutions for Maxwell's equations are obtained for the restricted unit cell (or Brillouin zone) under periodic boundary conditions. Algorithms for solving Maxwell's equations under periodic boundary conditions have been implemented using both the Green's function, based on method of moments and the finite element method. In this work we have used a commercially available simulation tool based on finite element method (HFSS).

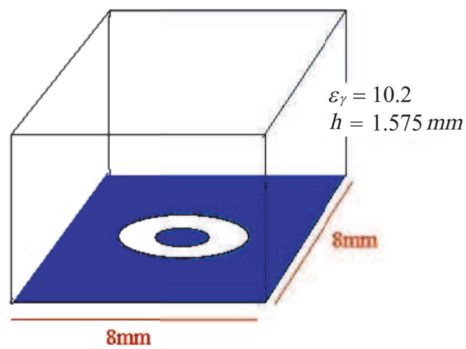

Figure 1: Circular ring DGS showing the unit cell dimensions and the dielectric constant of the structure.

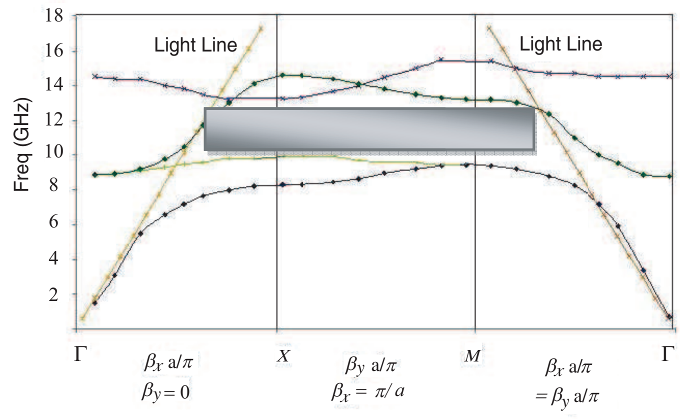

Figure 2: β-f diagram for the circular ring defected ground structure.

The dispersion diagram for this structure is shown in Fig. 2. It is observed that the circular ring DGS with the mentioned dimensions, possesses an omnidirectional surface wave band gap in the range of 10 to 13 GHz.

3. CAPACITIVE LOADED AMC STRIPS

The usage of metallic arrays printed on dielectric substrate in the absence of vias (AMC) has attracted a lot of interest in recent years. Due to reflecting incident waves with a zero degree reflection phase, this surface performs as equivalent artificial magnetic conductors. In this part, we analyze and design a CLS structure. The incident wave reflection properties of this structure has been assessed by using the commercial finite element full wave solver HFSS and the transmission coefficient and reflection phase is obtained. The strip width and length are optimized to attain 7–13 GHz frequency band for reflecting the incident waves. For analyzing this structure with HFSS software, a two port waveguide with two perfect electric conductors is used [7]. The CLS surface is perpendicular to the PEC walls. The size of capacitor gaps are 0.3 mm and every line width is 0.4826 mm. As shown in Fig. 3, every CLS length is 4.3688 mm and the length of one CLS unit cell which consists of three capacitive loaded strips along the axis is 14.605 mm. This structure is constructed on a substrate with 0.254 mm thickness and a permittivity of 2.2. The HFSS calculated magnitudes of S_{11} and S_{21} for a unit cell of CLS in the two ported waveguide is shown in Fig. 3. The strong reflectivity is turning on near 7.6 GHz and lasts up to 13.5 GHz.

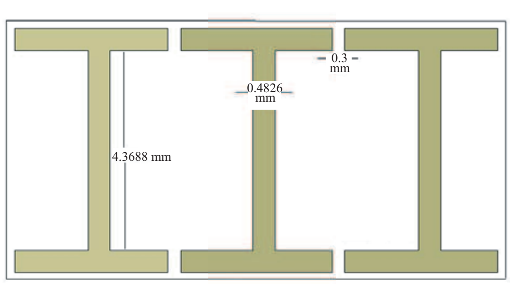

Figure 3: The CLS-AMC geometry.

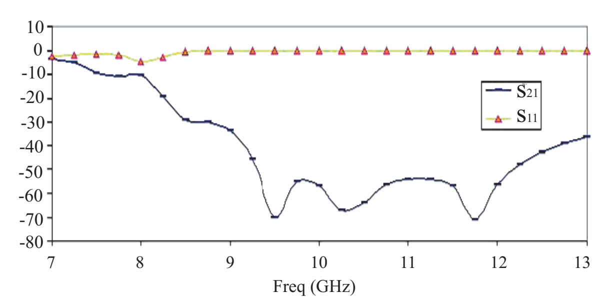

Figure 4: Magnitudes of the HFSS-predicted S parameters for a CLS unit cell.

4. CBS ANTENNA WITH DGS AND AMC

In this part, we combine the cavity backed slot antenna with circular ring DGS and capacitive loaded AMC strips. Dimensions of cavities, coaxial feed and space between the two cavities are the same as [5]. The top and side view of CBS antenna with DGS and AMC is shown in Figs. 5(a) and (b), respectively. The array of circular ring DGS consists of 28 microstrip circular rings forming an array of 4×7 elements. The array period is 8 mm and equals the dimension of the unit cell. This array is placed below the common ground plane between two cavities. Array of 2×12 CLS unit cells is located over the common ground plane. The separation between two CLS unit cells in the x and y directions are 3.175 mm and 4 mm respectively.

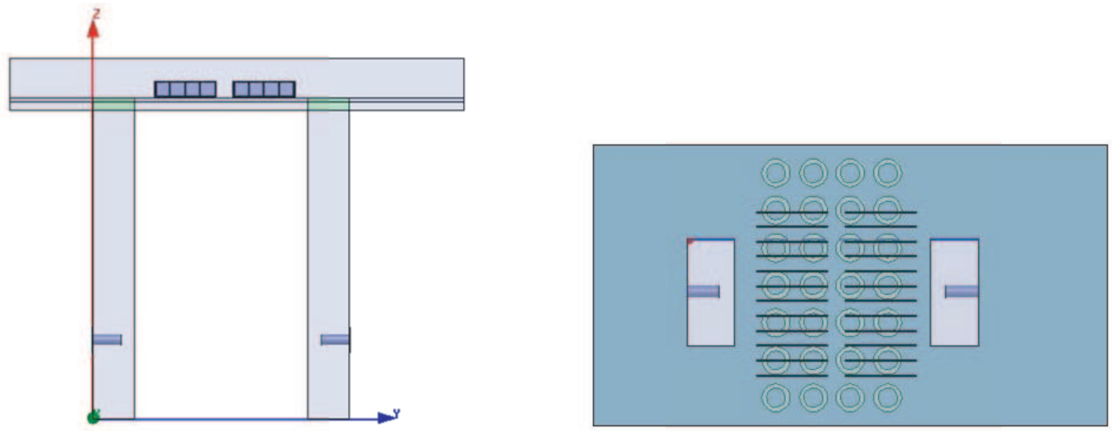

(a) (b)

Figure 5: Side (a) and top (b) views of the CBS antennas demonstrate the placement of the DGS and AMC structures.

The S_{21} (where one antenna is acting as a source and the other as a receiver) of the CBS antennas with and without circular ring DGS and CLS artificial magnetic conductor structures is shown in Fig. 6. These simulations show that significant coupling reduction is achieved, reaching around 40 dB at 11.5–13 GHz frequency band. In the view of the fact that starting frequency of incident waves reflection in the CLS structure was around 7.8 GHz; and the best reduction in mutual coupling occurred over 7.8–8.5 GHz band which has a shift of 0.3 GHz from the resonant frequency.

In view of the reduction of surface waves on the common ground plane and also mutual coupling

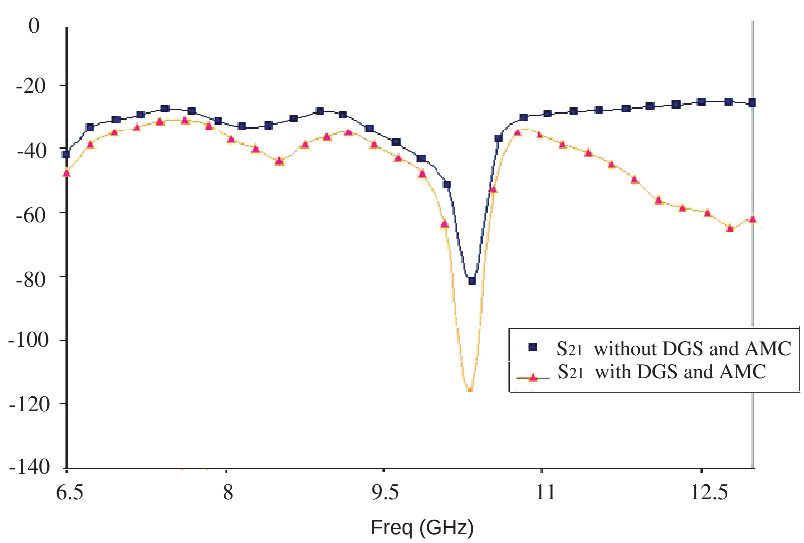

Figure 6: Magnitude of the S_{21} parameter for CBS antenna with and without circular ring DGS and CLS structure.

between the two cavities, we expect the radiation patterns become directive in comparison with CBS antenna without DGS and AMC. The radiation pattern of CBS antenna with and without DGS and AMC is shown in Figs. 7(a) and (b) for $f = 12\,\text{GHz}$. It is clear that the radiation pattern rotates in the direction opposite to the side in which the DGS and AMC structures are located and the gain of the antenna is also increased.. The radiation pattern for $f = 7.5\,\text{GHz}$ is shown in Figs. 8(a) and (b) for both CBS antennas with and without DGS and AMC. The same result in this frequency is preserved as well. We should mention that enhancement of radiation pattern for both 7.5 GHz and 12 GHz are achieved in one structure while in [5] two EBG structures were implemented for enhancing EMI in each resonant frequency and improving of radiation pattern for booth 7.5 GHz and 12 GHz was not accessible at the same time.

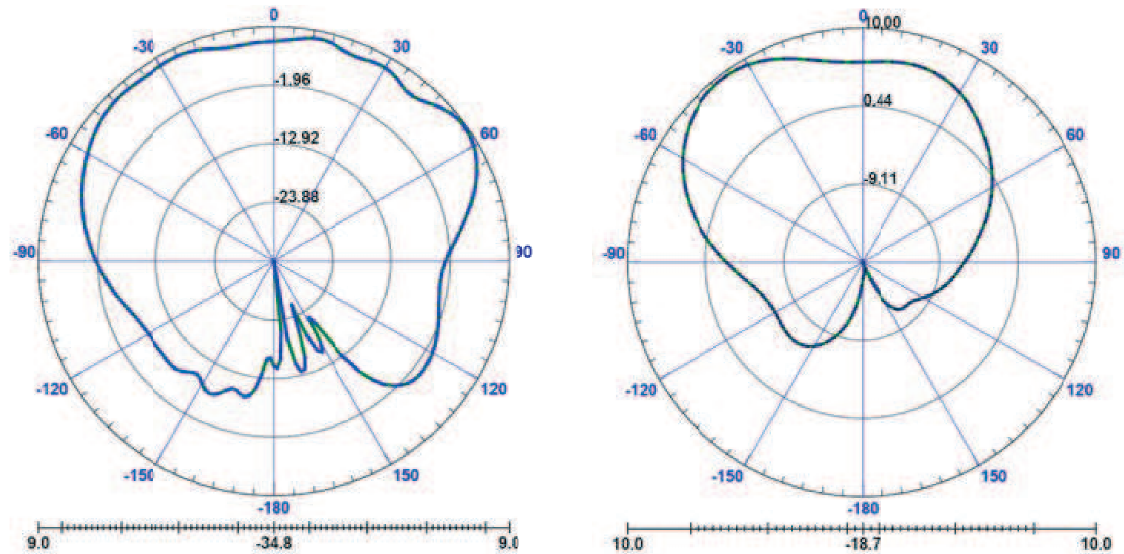

(a) (b)

Figure 7: Radiated field patterns at 12 GHz (a) without and (b) with DGS and AMC structures. The pattern is plotted in the y-z plane (E-plane).

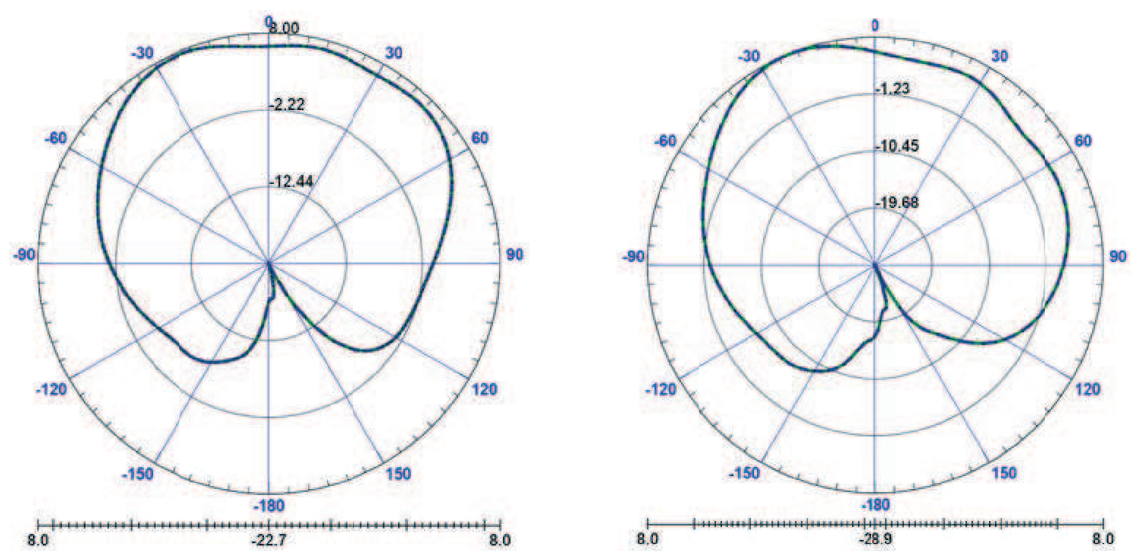

(a) (b)

Figure 8: Radiated field patterns at 7.5 GHz (a) without and (b) with DGS and AMC structures. The pattern is plotted in the y-z plane (E-plane).

5. CONCLUSION

It is demonstrated that DGS and AMC structures can be designed and implemented to reduce the mutual coupling between elements in array structures instead of using two EBG structures with vias that complicate the manufacturing. To derive the dispersion diagram of circular ring DGS and reflection and transmission data for normally incident plane wave illumination in CLS metamaterial HFSS software is used. A set of effective enhancement in decreasing EMI and radiation pattern of the antenna and in the resonant frequency band is observed and discussed.

ACKNOWLEDGMENT

This work was supported by Iran Telecom Research Center under grant TMU-860311.

REFERENCES

1. Georgakopoulos, S. V., C. R. Birtcher, and C. A. Balanis, "Coupling modeling and reduction techniques of cavity-backed slot antennae: FDTD versus measurements," *IEEE Trans. Electromagn. Compat.*, Vol. 43, No. 3, 261–272, Aug. 2001.
2. Abhari, R. and V. Eleftheriades, "Physics-based CAD models for the analysis of Vias in parallel-plate environments," *IEEE Trans. Microw. Theory Tech.*, Vol. 49, No. 10, Oct. 2001.
3. Sievenpiper, D., Z. Lijun, R. F. Broas, N. G. Alexopoulos, and E. Yablonovitch, "High-impedance electromagnetic surfaces with a forbidden frequency band," *IEEE Trans. Microw. Theory Tech.*, Vol. 47, No. 11, 2059–2074, Nov. 1999.
4. Feresidis, P., G. Apostolopoulos, N. Serfas, and J. C. Vardaxoglou, "Closely Coupled Metallodielectric Electromagnetic Band Gap (CCMEBG) structures formed by double layer dipole and tripolearrays," *IEEE Trans. Antennas Propagat.*, Vol. 52, No. 5, 1149–1158, May 2004.
5. Mohajer-Iravan, B. and S. Shahparnia, "Coupling reduction in enclosures and cavities using electromagnetic band gap structures," *IEEE Trans. Electromagn. Compat.*, Vol. 48, No. 2, 292–302, May 2006.
6. Oskouei, H. D. and K. Forooraghi, "Guided and leaky wave characteristics of periodic defected ground structures," *Progress in Electromagnetics Research*, PIER 73, 15–27, 2007.
7. Ziolkowski, R. W., "Design, fabrication, and testing of double negative metamaterials," *IEEE Trans. Antennas Propagat.*, Vol. 51, No. 7, 1516–1529, July 2003.

Facilitating EMI/EMC Modeling by Predicting Voltage Interference in an EMI/EMC Environment by Two Wires as the Pick-up Model of EM Waves

Atanu Roy[1], **Saswati Ghosh**[2], **and Ajay Chakrabarty**[1]

[1]Department of Electronics & Electrical Communication Engineering, IIT Kharagpur, India
[2]Kalpana Chawla Space Technology Cell, IIT Kharagpur, India

Abstract— EMI the silent threat or it may be sfilent killer is present everywhere, inside and outside of all electrical equipments. The successful detection and elimination of EMI require a systematic search for EM1 sources as well as knowledge of interference susceptibilities of the equipment. Familiarity with the environment in which the equipment will work as well as possible alternative environments are fundamental to effective EMI reduction to a required minimum level. In this paper we designed a simple two wire model to predict EMI when this model is illuminated by a distant source antenna. The proposed model is being fabricated at Indian Institute of Technology, India. Measured and simulated results are shown. Simulations were being carried out at Kalpana Chawla Space Technology Cell, IIT Kharagpur, India.

1. INTRODUCTION

The model that we fabricated is a simplified version of the more exact transmission line model, but it will be suitable for prediction purposes. We consider a parallel-wire transmission of length ℓ that has a uniform plane wave incident [1] on it in Fig. 1. The wires are separated by a distance s and have load resistances R_S and R_L. In order to quantify our results, we will place the two wires in the xy plane, with R_S located at $x = 0$ and R_L at $x = \ell$. The wires are parallel to the x axis. Our interest is in predicting the terminal voltages $\hat{V}_S$ and $\hat{V}_L$ [2]. The induced voltage is being contributed by the incident EM field. The component of the incident electric field that is transverse to the line axis, $\hat{E}_t^i = \hat{E}_y^i$ (in the plane of the wires and perpendicular to them and directed upward), and the component of the incident magnetic field that is normal to the plane of the wires, $\hat{H}_n^i = -\hat{H}_z^i$ (perpendicular to the plane of the wires and into the page), as shown in Fig. 1(b). For simulation of the model we used CST Microwave Studio, a 3-D electromagnetic solver [4].

2. FORMULATION OF THE PROBLEM

For the parallel-wire line having wires of radius $\mathrm{r_w}$ the per-unit-length induced sources $\hat{V}_S$ & $\hat{I}_S$ are generated by the incident wave. Faraday's law shows that $\hat{H}_n^i$ will induce an emf in the loop bounded by the wires as shown in Equation (1).

$$\begin{aligned} emf &= j\omega \int\limits_S \hat{B}_n^i \mathrm{d}s \\ &= j\omega \int\limits_S \hat{H}_n^i \mathrm{d}s \\ &= j\omega\mu_0 \Delta x \int\limits_{y=0}^{S} H_n^i \mathrm{d}y \end{aligned} \tag{1}$$

This induced emf can be viewed as an induced voltage source whose polarity, according to Lenz'law, is such that it tends to produce a current and associated magnetic field that opposes any change in the incident magnetic field. Thus, for the incident magnetic field intensity vector, normal to and into the page [3], the positive terminal of the source will be on the left. For a Δx section, the per-unit-length source will be given by dividing the result in by Δx to give

$$\hat{V}_S(x) = j\omega\mu_0 \int\limits_{y=0}^{S} H_n^i \mathrm{d}y \tag{2}$$

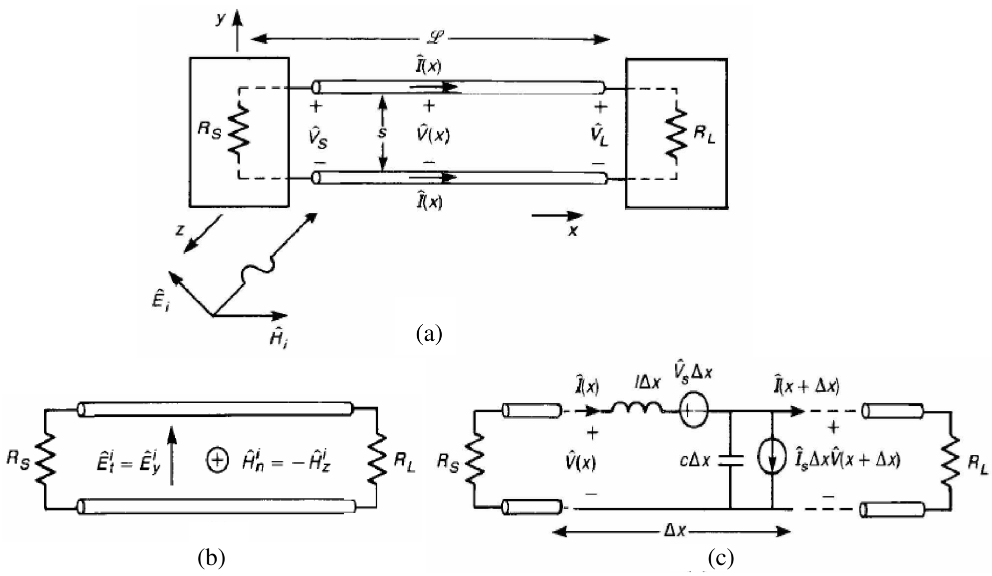

Figure 1: Modeling a two-conductor line to determine the terminal voltages induced by an incident electromagnetic field: (a) problem definition; (b) effects of the transverse electric field component and the normal magnetic field component; (c) a per-unit-length equivalent circuit [1].

The per-unit-length induced current source $\hat{I}_S$ is directed in the $-y$ (downward) direction, and is due to the component of the incident electric field intensity vector that is transverse to the line and directed in the $+y$ direction.

$$\hat{I}_S(x) = j\omega C \int_{y=0}^{S} E_t^i \mathrm{d}y \tag{3}$$

From the per-unit-length equivalent circuit of Fig. 1(c):

$$\hat{V}(x+\Delta x) - \hat{V}(x) = -j\omega l \Delta x \hat{I}(x) - \hat{V}_S(x)\Delta x \tag{4}$$

$$\hat{I}(x+\Delta x) - \hat{I}(x) = -j\omega c \Delta x \hat{V}(x+\Delta x) - \hat{I}_s(x)\Delta x \tag{5}$$

This exact solution is not necessary for estimation purposes, and we will obtain an approximate solution.

Some Approximations

For many cases of practical interest the line length is electrically short at the frequency of interest; this is, $\ell = \lambda_0$. This will be the case of interest here for the purposes of estimating the induced terminal voltages. If the line length is electrically short at the frequency of interest, we may lump the distributed parameters by using one section of the form in Fig. 1(c) to represent the entire line and replacing Δx with ℓ. Thus the per-unit-length elements and sources are multiplied by the total line length ℓ. Although the terminal voltages can be calculated from this model for electrically short lines, we will make a final simplification that provides an extremely simple model that is valid for a wide variety of practical situations. In this model we ignore the per-unit-length parameters of inductance and capacitance. Neglecting the line inductance and capacitance is typically valid so long as the termination impedances are not extreme values such as short or open circuits. In addition, since the wire separation is much less than the wire length, the field vectors do not vary appreciably across the wire cross section, that is, with respect to y. Therefore the integrals in the sources (Equation (2)) and (Equation (3)) with respect to y can be replaced with the wire separation s, giving

$$\hat{V}_S \ell \cong j\omega\mu_0 \hat{H}_n^i A \tag{6}$$

$$\hat{I}_S \ell \cong j\omega c E_t^i A \tag{7}$$

where A is the area of the loop $A = \ell s$.

From this model shown in Fig. 2, it is a simple matter to compute the induced terminal voltages, using superposition, as

$$\hat{V}_S = \frac{R_S}{R_S + R_L} j\omega\mu_0 \ell s \hat{H}_n^i - \frac{R_S R_L}{R_S + R_L} j\omega c \ell s \hat{E}_t^i \tag{8}$$

$$\hat{V}_L = -\frac{R_S}{R_S + R_L} j\omega\mu_0 \ell s \hat{H}_n^i - \frac{R_S R_L}{R_S + R_L} j\omega c \ell s \hat{E}_t^i \tag{9}$$

This is a particularly simple model that will yield useful estimations of the effects of incident fields.

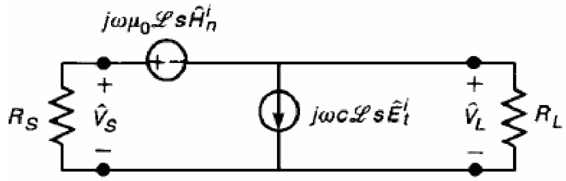

Figure 2: A simplified, lumped equivalent circuit of the pickup of incident fields for a two-conductor line that is electrically short.

3. EXPERIMENTAL SETUP

In this experiment parallel-wire line terminated by 50 ohms impedance at one end and spectrum analyzer with impedance 50 ohms at the other end is studied. The parallel wire line is illuminated by an electromagnetic radiation from a dipole antenna. This incident radiation induces current on the wire surfaces that further produces voltage drop across the impedances connected at both ends. Here the power received by the spectrum analyzer due to the radiated emission from the antenna is studied over a wide frequency range and for 0° angle of incident field direction.

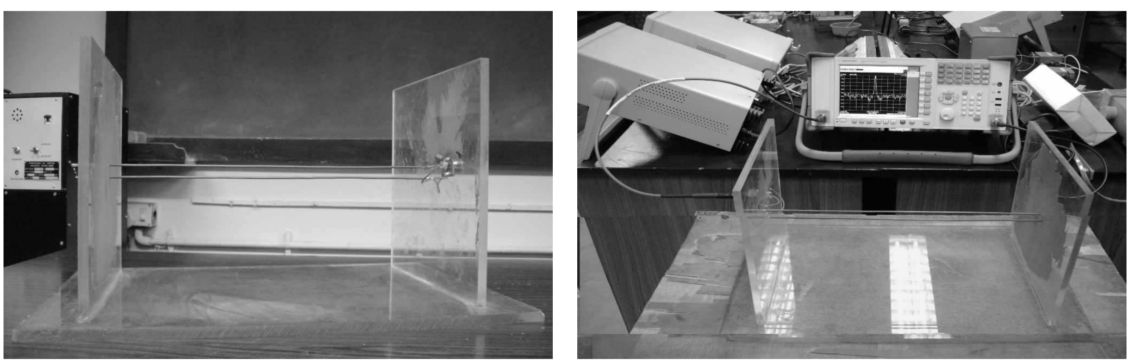

(a) (b)

Figure 3: (a) Fabricated two Wire model of copper wire in homogeneous medium, (b) Receiver side of the experimental setup.

The specifications of the experimental setup are given below:

L = 38 cm (Length of the wire)
S = 1.3 cm (Distance between two wires)
Diameter of the wire = 3.5 mm
Distance between transmitting antenna and two-wire line model = 345 cm

4. RESULTS & ANALYSIS

Figure 4 shows the simulated and measured results of voltage developed across the two wire model when placed in an EM environment. The results shows that both simulated and measured results are following the same pattern, but small difference is there in the values.

We are providing 10 dBm power from the signal generator to exite the dipole transmitting antenna. For the purpose of simulation we are exciting the dipole antenna using discrete port providing 1 watt power for excitation.

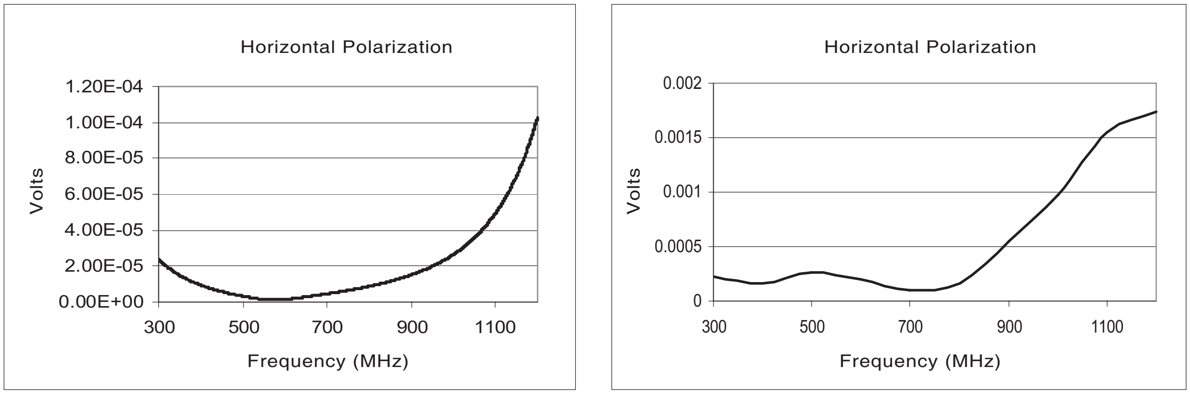

(a) (b)

Figure 4: Voltage pickup when antenna is horizontally oriented w.r.t to ground plane: (a) CST simulated result, (b) Measured result.

Figure 5 shows the simulated and measured results of voltage developed across the two wire model when placed in an EM environment. The results show that both simulated and measured results are following the same pattern, but small difference is there in measured and simulated values. This is because that the whole experiment is performed in Microwave measurement laboratory, IIT Kharagpur where the environment is very much crowded. If the same experiment would have been performed in an anechoic chamber or an OAT site the results would have been quite better.

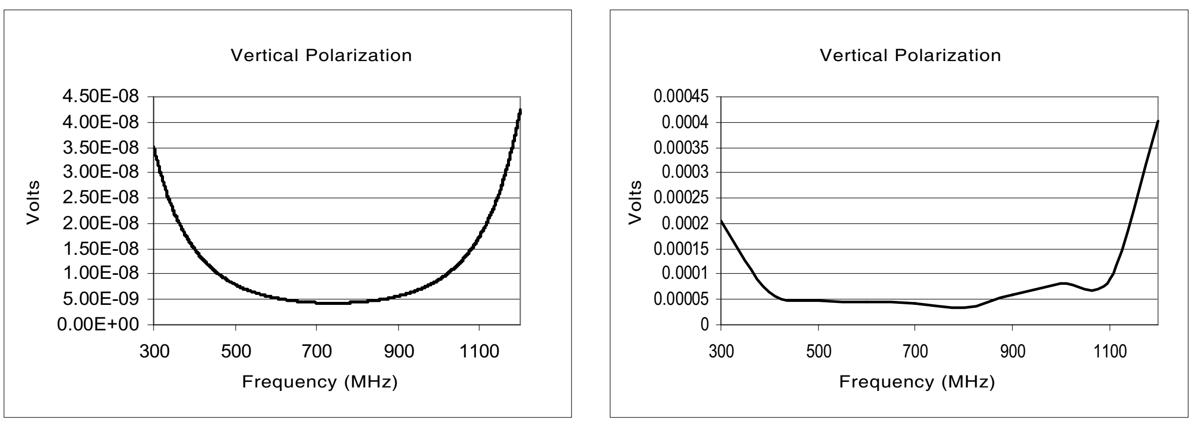

(a) (b)

Figure 5: Voltage pickup when antenna is vertically oriented w.r.t to ground plane: (a) CST simulated result, (b) Measured results.

5. CONCLUSIONS

This paper presents the estimation of the effects of incident fields across the two wire terminals when this model is illuminated by EM wave from some distant antenna thus estimating the effect of EM radiation in an EMI/EMC environment. The results from EMI/EMC stand point of view are very important for system design. Also the study can be extended for PCB lands, shielded wires and bent interconnects. Here we have considered only zero degree angle of incidence of the EM wave. The same experimental setup can be used to measure the induced voltage for different angles of incidence of the EM wave.

REFERENCES

1. Paul, C. R., *Introduction to Electromagnetic Compatibility 2nd Edition*, John Wiley & Sons Inc, New York, 1992.
2. Paul, C. R., "Frequency response of multiconductor transmission lines illuminated by an electromagnetic field," *IEEE Trans. Electromagnetic Compatibility*, Vol. 18, 183–190, 1976.

3. Paul, C. R. and R. T. Abraham, "Coupling of electromagnetic fields to transmission lines," *Proc. IEEE Int. Symp. Electromagnetic Compatibility*, Boulder, CO, Aug. 1981.
4. CST Microwave Studio, Version 5 manual.

Interaction between Magnetoresistor and Magnetotransistor in the Two-dimensional Folded Vertical Hall Devices

Guo-Ming Sung and Chih-Ping Yu
Department of Electrical Engineering, National Taipei University of Technology
1, Sec. 3, Chung-Hsiao E. Rd., Taipei 106, Taiwan, R.O.C.

Abstract— A 2-D folded Hall device, fabricated in a standard 0.35 μm CMOS process, is proposed. By simultaneously altering the bias currents and the polarities of p^+-implant and n^+-implant contacts, the experimental results exhibit that the bulk parasitic magnetotransistor presents either the best magnetosensitivity or the highest induced Hall voltage at the supply bias current 20 mA. A further analyses of the interactions between the Hall device, the lateral magnetotransistor and the vertical parasitic magnetotransistor show that the dominant mechanism evoked by the magnetic induction is the hybrid effect which mixed with the Hall effect and the filament magneto-sensitive effect. By the way, the maximum supply-voltage-related sensitivity of the hybrid effect of vertical magnetoresistor and bulk magnetotransistor is about 68 and 48 times larger than that of the Hall device and the lateral parasitic magnetotransistor, respectively. Note that the maximum induced Hall voltage of the hybrid effect of vertical magnetoresistor and bulk magnetotransistor magnetotransistor is also greater than that of the Hall device and the lateral parasitic magnetotransistor by 136 and 9 times, while the amplification function of the lateral parasitic magnrtotransistor appears at the higher supply bias current. The largest supply-current-related sensitivity is presented with 3.838 (V/A*T).

1. INTRODUCTION

Today a variety of integrated silicon magnetic-field sensors are presented. Among those magnetosensors, magnetotransistors provide some specific advantages such as high sensitivity, easy offset elimination, a wide calibration range and a relatively small temperature drift [1–4], while magnetoresistor or Hall device exhibits better linearity.

For Hall device, there is some novel vertical Hall devices are presented to sense the magnetic field parallel to the device surface. The operation of the vertical Hall device occurs in the active n^+-implant region surrounded by p^+-implant ring. It has been theoretically proven that the sensitivity is invariant with respect to its geometry [5].

For magnetotransistor, the magnetosensitivity is a superposition of the Hall action and the non-equilibrium bipolar conductivity. Many intense researches led us into the unusual sensor's mechanisms in the base region to explain the enhancement on magnetosensitivity. The first one is the electrically controlled polarity of magnetosensitivity (ECPM). The second mechanism is filament magnetosensitivity effect (FME). The third effect is so called magnetogradient effect (MGE). In our study, we design both lateral and vertical BMTs to find the Hall effect between BMTs and Hall device in base region with carrier filament. The vertical MT is fabricated with a standard bulk CMOS technology [6]. That is, we propose a new two-dimensional folded Hall device with two merits, the Hall device inhered with better linearity and the magnetotransistor inherited with higher magnetosensitivity. Many P^+-implant contacts are used as control contacts to alter the trajectories of the majority carriers and to suppress the undesirable sidewall current [7]. The folded style is not only to reduce the offset by shortening the geometric asymmetry, but also to avoid unbalancing on the base current of the parasitic magnetotransistor.

2. EXPERIMENTAL SETUP AND RESULTS

Figure 1 presents the proposed two-dimensional folded Hall Device. In this figure, the symbols, including C, S, t, d and V_H, are the control or bias contact, the sensing contact, the N-well thickness, the width of guard ring, and the induced Hall voltage, respectively. In this paper, we measure the induced Hall voltage, which is got by passing the output current through the surrounding parasitic impedance, in order to comprehend the linear characteristics, not to get the highest magnetosensitivity.

The proposed two-dimensional folded magnetosensor is designed to measure the Hall voltages, V_{HX} and V_{HY}, induced by the applied 2-D magnetic inductions, $-B_X$ and B_Y. If the magnetic induction B_Y is applied in the y-direction, the induced Hall voltage V_{HX} is detected in the x-direction

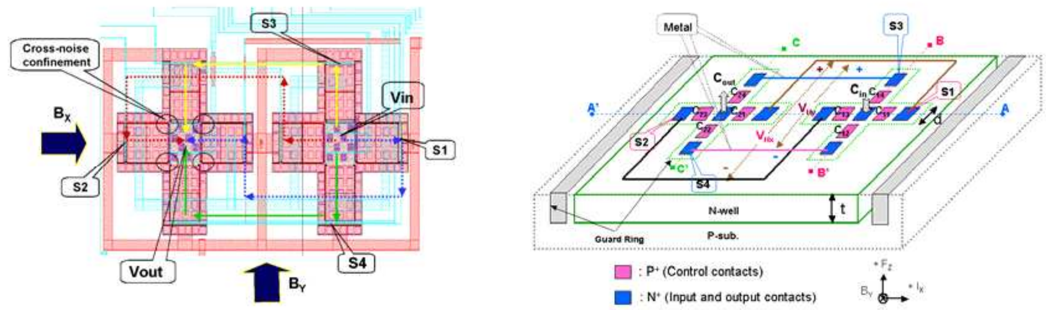

(a) (b)

Figure 1: Detailed structure of the 2-D folded Hall device. (a) Plan view of layout and (b) Geometry configuration.

and the cross-noise V_{HY} is simultaneously caught in the y-direction. Note that the additional P^+-implant contacts are used not only to establish the parasitic lateral magnetotrasistors and bulk magnetotransistors, but also to enhance the magnetosensitivity by lengthening the trajectories of the majority carriers.

Table 1: The experimental setups of the proposed folded magnetic device.

Types	Bias contacts		P^+ implants (Control contacts)	P-substrate	Magnetic effects
	C_{in}	C_{out}	C11∼C24	Bulk	
1	$V+$	$V-$	$V_{\min}$	$V_{\min}$	MR
2	$V-$	$V-$	$V_{\max}$	$V_{\min}$	LMT
3	$V-$	$V-$	$V_{\min}$	$V_{\max}$	BMT
4	$V+$	$V-$	$V_{\min}$	$V_{\max}$	MR+BMT

Table 1 shows the experimental setup to interpret the individual and combined effects of MR, LMT and BMT, the abbreviations MR, LMT and BMT, mean the magnetoresistor, the lateral magnetotransistor, and the bulk magnetoresistor, respectively. It is necessary to note that the signs, $V+$, $V-$, $V_{\min}$ and $V_{\max}$, are the positive voltage of the biased source, the negative voltage of the biased source, the minimum supplied voltage (normally ground) and the maximum supplied voltage (normally 3.5 V for 0.35 µm technology), respectively.

Table 2:

Types	***V_H(mV)***		***S_{RI}(V/A·T)***		***NLE (%)***		***V_{Offset} (mV)***		***I_{bias} (mA)***	***V_{bias} (V)***	***Magnetic effects***
	$V_H(x)$	$V_H(y)$	$S_{RI}(x)$	$S_{RI}(y)$	NLE(x)	NLE(y)	x	y			
1	0.020	0.021	5.28%	5.57%	31.34	43.07	17.29	33.86	10mA	2.7V	MR
2	0.294	0.288	7.83%	7.67%	33.69	39.66	44.66	34.19	100mA	2.6V	LMT
3	1.036	1.051	138.15%	140.15%	2.16	2.32	6.43	1.57	20mA	0.47V	BMT
4	2.704	2.879	360.52%	383.84%	10.21	8.21	12.38	19.47	20mA	0.45V	MR+BMT

Table 2 provides a summary of the measurements of the maximum output Hall voltages in the x-direction and y-direction, $V_H(x)$ and $V_H(y)$, and their relative maximum supply-current-related magnetosensitivities, $S_{RI}(x)$ and $S_{RI}(y)$, the maximum non-linearity errors, NLE, the maximum offsets, V_{offset}, the relative bias currents I_{bias} and bias voltages V_{bias} in the x-axis and y-axis.

All the output Hall voltages are detected by the Electrometer/High Resistance System (KEITHLEY Model: 6517). A supply-current-related sensitivity is defined as [1]

$$S_{RI} = \left| \frac{1}{I_{bias}} \frac{\Delta V_{out}}{\Delta B} \right| [V/A \cdot T] \tag{1}$$

where I_{bias} denotes the supplied bias current, ΔV_{out} is the output Hall voltage and ΔB is the applied magnetic induction paralleled to the chip surface. And that, the non-linearity error (NLE) is defined as

$$NLE = \frac{\Delta V_{out} - \Delta V_{out}^{(0)}}{\Delta V_{out}^{(0)}} \times 100\% \tag{2}$$

where ΔV_{out} is the measured value of the output Hall voltage, and $\Delta V_{out}^{(0)}$ is the calculated value based on the slope of the straight line obtained with best curve fitting the output characteristic [8].

3. DISCUSSION

In types 1 and 2, all the maximum output Hall voltages of folding magnetosensor are inferior to those of longitudinal magnetosensor, but the large non-linearity error and offset seriously damage this merit. In terms of the supply-current-related sensitivity, the measured results of folding magnetosensor are mostly superior to those of longitudinal magnetosensor. The folding magnetosensor integrated with bulk magnetotransistor should be a good design owing to its good magnetosensitivity.

In types 3 and 4, we try to comprehend the interactions between vertical magnetoresistor, vertical magnetotransistor and bulk magnetotransistor. After comparing the maximum output Hall voltage of type 3 with that of type 2 in folding magnetosensor, we conclude that the dominant effect of type 3 is the magnetic function of vertical magnetotransistor.

In the hybrid effect of vertical magnetoresistor and bulk magnetotransistor (type 4), the output Hall voltage is almost proportional to the bias current, I_{bias}, in longitudinal magnetosensor, but it is reversely proportional to the bias current in folding magnetosensor. This important merit of folding magnetosensor manifestly declares that the low power magnetic sensor is possible. The measured result of type 4 shows that the dominant magnetic device is bulk magnetotransistor not only in longitudinal magnetosensor but also in folding magnetosensor.

All the supply-current-related magnetosensitivities are summarized and shown in Table 2. The optimum measured value in type 4, $S_{RI} = 3.838V/A \cdot T$, is better than those in diode device, $S_{RI} = 1.80V/A \cdot T$ [6], and in lateral transistor device, $S_{RI} = 2.00V/A \cdot T$ [7]. In fact, the folding design is not only to obviously improve the non-linearity error, but also to manifestly minimize the offset.

4. CONCLUSION

An experimental analysis is presented to comprehend the interaction of vertical magnetoresistor, vertical magnetotransistor and bulk magnetotransistor in longitudinal and folding magnetosensors fabricated by industrial 0.35 µm technology. On the basis of experimental data generated by individual magnetic device, the proposed folding design will effectively improve the non-linearity error and offset, but the trade-off is low sensitivity. In order to compensate this demerit, a bulk magnetotransistor is put on. Because that the magnetosensitivity of bulk magnetotransistor in folding mganetosensor is over ten times higher than that in longitudinal magnetosensor, we predict this assignment is a good work. The experimental result correctly proves this prediction. After several integrated devices are measured, all the evidences conclude that the dominant magnetic effect is bulk magnetotransistor. Besides, we find that the optimum magnetosensitivity is obtained at high bias current in longitudinal magnetosensor, but it is achieved at low bias current in folding magnetosensor. This discovery in folding magnetosensor makes the implementation of low power magnetic sensor is possible.

Furthermore, if the bulk magnetotransistor integrates with vertical magnetoresistor, the magnetosensitivity will be highly uplifted in both proposed longitudinal and folding magnetosensors. The mechanism is conjectured that the filament current of vertical magnetoresistor is directly injected into the base region of bulk magnetotransistor to increase the minority-carriers and to enhance the magnetosensitivity. So that, the magnetosensitivity is determined by minority-carrier deflection effect for magnetosensor integrated with bulk magnetotransistor. The optimum supply-current-related magnetosensitivity is measured as $S_{RI} = 3.838 \cdot V/A \cdot T$. This result is better than that of diode device, $S_{RI} = 1.80 \cdot V/A \cdot T$, and that of lateral transistor device, $S_{RI} = 2.00V/A \cdot T$.

ACKNOWLEDGMENT

This work was supported by the National Science Council of Taiwan, R.O.C., under contract NSC-90-2218-E-027-020. The authors would also like to thank the CIC, Taiwan, for her assistance.

REFERENCES

1. Ristic, L., T. Smy, and H. P. Baltes, "A lateral magnetotransistor structure with a linear response to the magnetic field," *IEEE Trans. Electron Devices*, Vol. ED-36, 1076–1086, 1989.
2. Nathan, A. and H. P. Baltes, "How to achieve nanotesla resolution with integrated silicon magnetotransistors," *IEDM Tech. Dig.*, 511–514, Washington, DC, 1989.
3. Castagnetti, R., H. P. Baltes, and N. C. Bui, "PNP bipolar magnetotransistor for sensor applications," *Transducer' 91 Digest of Technical Papers*, 1065–1068, IEEE, New York, 1991.
4. Wieder, H. H., *Hall Generators and Magneto-resistors*, Pion Ltd., London, England, 1971.
5. Popovic, R. S., "The vertical Hall-effect devices," *IEEE Electron Device Lett.*, EDL-5, 357–358, 1984.
6. Roumenin, C. S., "Hall-effect in diode structures," *C. R. Acad. Bulg. Sci.*, Vol. 38, 1501–1504, 1985.
7. Roumenin, C. S., "On the performance of a class of lateral magnetotransistors," *C. R. Acad. Bulg. Sci.*, Vol. 38, 579–581, 1985.
8. Baltes, H. P. and R. S. Popovic, "Integrated semiconductor magnetic field sensors," *Proc. IEEE.*, Vol. 74, 1107–1132, 1986.

Multifunctional Piezomagnetic Ferrite Materials and Their Newly Acoustical and Vibration Control Devices

Quanlu Li[1], **Yuan Li**[2], **and Zhaohui Huang**[2]

[1]Institute of Applied Acoustics, School of Physics and Information Technology
Shaanxi Normal University, Xi'an 710062, China
[2]Department of Prevention Medicine, Fourth Military Medical University
♯17, Changlexi Street, Xi'an 710033, China

Abstract— The design, preparation of newly multipurpose ferrites (i.e., a magnetoelectric ceramic materials) $Ba_{6-x}R_{2x}(Nb_{1-x}Fe_{2+x})O_3$, etc, which it exhibiting the piezoelectricity and the piezomagnetic effect, then, preparation and selection of magnetorheological fluids (MRF) have been studied, respectively. The functional integrated devices which is a newly acoustical and vibration control devices combining multipurpose ferrites $Ba_{6-x}R_{2x}(Nb_{1-x}Fe_{2+x})O_3$, etc and magnetorheological fluids, and their applications have been investigated, and, emphasis was given to the applications in acoustics and vibration control, etc, as may be noted.

1. INTRODUCTION

Multifunctional electronic materials and integrated intelligent devices are needed in the development of advanced technologies, especially mechano-electronic integrative units. This work describes the preparation of new type piezomagnetic ferrite materials (i.e., magnetoelectric ceramic materials) and their multifunctional integrated devices which is a newly acoustical and vibration control devices (combining multipurpose ferrites and magnetorheological fluids) and their new applications in this study. Piezomagnetic materials could be used as reversible electroacoustical or electromechanical transducing etc. acoustical devices by piezomagnetic effect [1–3]. This paper briefly reports on multipurpose ferrites (i.e., magnetoelectric ceramic materials) $Ba_{6-x}R_{2x}(Nb_{1-x}Fe_{2+x})O_3$, etc, which it exhibiting the piezoelectricity and the piezomagnetic effect, then, preparation and selection of magnetorheological fluids (MRF) have been studied [4], respectively. And newly functional integrated devices used for acoustics and vibration control.

2. NEW PREPARING METHOD OF THE MULTIFUNCTIONAL PIEZOMAGNETIC FERRITE MONOCRYSTAL

The design, preparation of newly multipurpose ferrites (i.e., a magnetoelectric ceramic materials) $Ba_{6-x}R_{2x}(Nb_{1-x}Fe_{2+x})O_3$, etc, which it exhibiting the piezoelectricity and the piezomagnetic effect that has already been published in paper [5]. In present work, main preparation method of the piezomagnetic ferrite monocrystal which have also tested [6] for the multifunctional piezomagnetic ferrite multicrystal materials, such as: (1) solution technique; crystal growth from solution by the temperature-drop method, (2) vaporation technique; crystal growth from solution evaporation technique, (3) hydro-thermal method, (4) vertical pulling method (that is Czochalski method — CZ method). (5) floating zone method — FZ method, (6) molten-salt growth method, (7) flame melt method; Flame fusion method (that is Verneuil's method), etc. But, in preparation of multifunctional piezomagnetic ferrite, the above technological processes either the method is required conditions to be excessively high, or in the method have gotten the qualified products to be too little. However, these methods are applied in the productions of multifunctional piezomagnetic ferrites are lesser.

3. APPLICATIONS

3.1. General Applications of the Piezomagnetic Ferrites

Piezomagnetic ferrite materials were as piezomagnetic element to be applied in wave filters initially. Recently, applied field of piezomagnetic ferrite materials have greater development. In a word, the applications of piezomagnetic ferrite materials have (1) Magnetostrictor (including transverse length extension vibration mode, thickness- or width-flexure vibration mode, and twist magnetostriction vibration mode etc): Small change in the length of a piece of piezomagnetic material, which is accompanied the process of magnetization. Ferrite bar (rod), ferrite frequency meter, ferrite head, ferrite keeper, ferrite core, ferrite bead, ferrite-filled waveguide, ferrite-plate memory, ferrite-roe antenna, and ferrite-tuning devices, etc. can also made of piezomagnetic ferrite material. (2) More correctly, a magnetostrictive transducer is a device to convert electrical oscillations to mechanical oscillations by employing the property of magnetostriction. It consists in essence of a bar of piezomagnetic magnetic material, anchored at one point, and subjected to an oscillating magnetizing force, i.e., an oscillating current circulating in a coil carried by the magnetic member. The magnetostriction effect (change of length of ferrite with change of magnetization) results in oscillating movement of the free end or ends of the bar. In order to achieve maximum energy transmission, the system must be driven at or near its natural frequency. The oscillating magnetizing current can be derived from a dynamo-electric alternator or from a thermoionic generator. In the latter case the generator must either include an oscillating valve or receive an input consisting of an oscillating current induced in a pick-up coil incorporated in the transducer itself. The direction of the change of length is, in most material, independent of the direction of the applied magnetizing force, and the frequency of the mechanical oscillations is therefore twice the frequency of the field. However, by providing a magnetic bias by means of a superimposed unidirectional field produced by a direct current flowing in the main or in an auxiliary winging, the mechanical oscillation frequency can be made equal to the field frequency. The acoustical transducers are principally employed for producing pressure waves of ultrasonic frequency.

3.2. An Investigation into Multifunctional Integrated Devices

This works were based on the principle theories and related techniques of materials, acoustics, chemistry, physics, electronics, mechanics, etc, which pass the creating and the leaping of the conception and technology, then select be able to accomplishing methods and ways in our laboratory. Starting from the formula, composition and properties testing of the new type multifunctional piezomagnetic ferrite materials which improve on development techniques of the piezomagnetic community, then obtain better properties of the materials and with this materials was made of new acoustic and vibration control devices.

Our investigation into multifunctional piezomagnetic ferrite materials and their applications has shown good progress and results. However, in the development of new multifunctional piezomagnetic ferrites and acoustical devices, there are many parts, which need precision processing techniques, electronics and thermal treatment techniques, and measurement of multifunctional piezomagnetic properties, to be applied, also make the needs for physics, chemistry and engineering etc combining.

In this study, from preparation of material to the analyzes of their properties, from active component to the development of multifunctional integrated devices [such as the model of multifunctional integrated structure with piezomagnetic ferrite and magnetorheological fluid (abbreviated as MRF), the model of the had symmetrical bearing cap and coupling piece (45# steel), and single-leg composite ultrasonic transducer exhibiting piezoelectricity and piezomagnetic effect, etc], we have made good progress, and received qualitative results. The principle properties of the multifunctional piezomagnetic ferrite materials are:

Piezoelectric strain constant $d_{33} \succ 600pC \cdot N^{-1}$,
Piezoelectric voltage constant $g_{33} \succ 34 \times 10^{-3}V \cdot m \cdot N^{-1}$,
Relative dielectric constant $\varepsilon_{33}^{T}/\varepsilon_0 \succ 2500$,
Mechanical factor $Q_m \succ 800$,
Planar electromechanical coupling factor $k_p \succ 0.54$;

And, their magnetic properties are:

Initial permeability $\mu_i = 40000$,
The effective permeability $\mu_Q = 1.25 \times 10^5$ (at ultrasonic frequency range),
(Saturated) magnetic induction $B_s = 5000Gs$,
Magnetostrictive coefficient $\lambda_s$and mechanical strength are higher.

(1). Multifunctional piezomagnetic ferrite materials have been used as an integrated intelligent structure (a new actuator) with piezomagnetic materials (Ni-Zn ferrite or Ni-Cu ferrite) and the composite magnetorheological fluid (abbreviated as MRF [7–10], as it is magnetorheological fluids belong to the group of controllable fluids. Their viscosity may be changed by the external magnetic field. The increase of external magnetic field strength causes the increase of magnetorheological fluid viscosity). In present work were selected and used the composite magnetorheological fluids which made by ourselves and their principle properties are:

Viscosity $> 8P_a \cdot S/10s^{-1}$ (at zero magnetic field),

Response time $< 9\,\mathrm{ms}$.

In proportion to the designed magnetic particles (part-component), whose volume percentage concentration of fluid (the disperse phase) is at $10\% \sim 20\%$,

Anti-precipitate, nonpoisonous and the composite MRF do not contain water.

In the new and unique intelligent structure is shown in Fig. 1 (Schematic diagram of the principle of the model of the integrated intelligent structure with multifunctional piezomagnetic ferrite and MRF). In this intelligent structure (model), when multifunctional ferrite part (piston rod) have a transient pulse force applied to it, that causes the piston rod for a moving along a straight line, then induced change of the magnetic flux in the winding (coil), therefore, a changing current and magnetic field are induced in the winding (coil), at the same time, induced the changing of magnetic field surrounding with the MRE. MER will change from liquid phase to solid therefore to counteract the impulsive forces. Relations between them are given by:

$$B = \mu \cdot \frac{N}{l} \cdot I \tag{1}$$

where

B stands for the magnetic induction of surrounding with MRE,

μ for permeability of multifunctional piezomagnetic ferrite (piston rod),

N for the number of turns of the winding (solenoid),

l for the length of the toroidal solenoid coil,

I for the current through the solenoid coil.

When the piston rod (multifunctional ferrite structure) is subjected the force for moving a straight line inside the solenoid coil, relations between them are given by:

$$L = \mu \cdot \frac{N^2}{l} \cdot S \tag{2}$$

where

L stands for coefficient of self-induction of winding (coil) of the solenoid,

S for the area of the cross-section of pistion rod (multifunctional piezomagnetic ferrite material).

From above formula we have conclusions and results below: when piston rod is perpendicular to the magnetic force lines for moving along a straight line, at same time, the rod certainly will segment (cutting) the magnetic force line, then, caused the changing of the current in toroidal solenoid, while, produced the changing of the magnetic field surround with MER follows the current.

When multifunctional piezomagnetic material elements have been applied a transient time impulsive force and to act rectilinear motion in inside of the coil (winding), therefore, in the coil (winding) could produce changed current and magnetic field, then, the magnetic field (by d-c current) is applied to the magnetorheological fluid in very short duration, where it is simultaneously changed from liquid phase to solid and there to counteract the impulsive force. (a) The first applicable aspects of the integrated intelligent structure will be an effective technique in the vibration control aspect, such as, anti-seismic structure, reducer, damper, and recoilless weapons (equipment), and varied shock-absorber, etc. These applications can be found in fields of national defenses, electronics, aviation-spaceflight, machinery, traffic, chemical industry, robot and medical equipment, nuclear installations, bridge seats, optic engineering, etc; (b) in the acoustic applications, the integrated intelligent structure will be the potential to resist destructiveness of shock wave, and to protect against the perniciousness of infra sound, acoustic shock waves, explosive waves, etc, and, for a collision avoidance system of a future intelligent automobile, the surface protection of modern aircraft to fly at high speeds, etc.

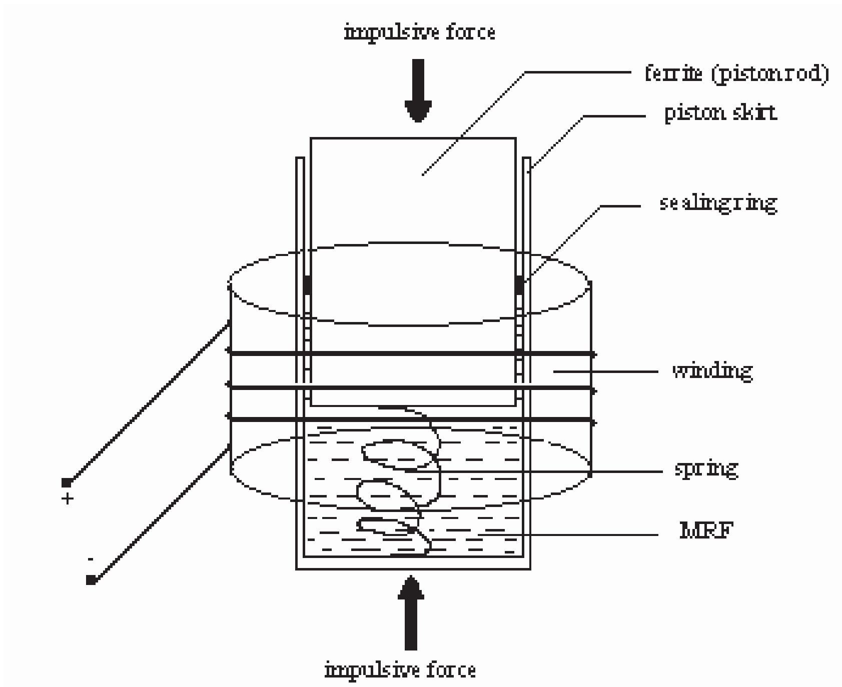

Figure 1: Schematic diagram of the principle of the model of the integrated intelligent structure with multifunctional piezomagnetic ferrite and MRF. ***Notes***: (1) the spring is used to strut the dead weight of the piston rod (at constant magnetic field); (2) the sealing ring is made of insulating rubber; (3) the piston skirt is made of glass fiber reinforced plastic.

4. CONCLUSIONS

4.1 Mention in passing, there is pointed out that piezoelectric and piezomagnetic this two kinds of acoustoelectric transducing materials can't replace each other in some important applications and will be long-term coexistence, but also the both have better compatibility.

4.2 At present, researchers have discovered some analogous multifunctional piezomagnetic ferrite materials (i.e., new magnetoelectric materials) such as follows: Ni(Co, Mn)$Fe_2O_4 - BaTiO_3$, $LiFe_5O_8 - BaTiO_3$, $Pb(Zr_{0.52}Ti_{0.48})O_3 - Tb_{1-x}Dy_xFe_{2-y}$, $Tb_{1-x}Dy_xFe_{2-y}$/Epoxy$-Pb(Zr_{0.52}Ti_{0.48})$ O_3/Epoxy, $DyAlO_3$, $GaFeO_3$, $Y_3Fe_5O_{12}$, etc. For these magnetoelectric materials(which is exhibiting piezoelectricity and piezomagnetic effect), due to magnetic field can produce magnetization and electric polaring strength, or, due to electric field the materials can also produce electric polaring strength and magnetization, therefore, these magnetoelectric materials are possible to make new type magnetic control and electric control devices respectively, or, at same time, it can magnetic control — electric control devices.

4.3 In addition, in chemical industry, piezomagnetic ferrite [11] $Co_xFe_{3-x}O_4$ ($x = 0.1 \sim 0.5$) and ZrO_2 were combined, and prepared a magnetic solid acid catalyst which is possessed of very good catalytical activity and appropriate magnetic properties.

4.4 In this work, the new and unique integrated intelligent structure (a newly acoustical and vibration control devices combining multipurpose ferrites $Ba_{6-x}R_{2x}(Nb_{1-x}Fe_{2+x})O_3$, etc and magnetorheological fluids, see Fig. 1), there are other technological problem that require future research work and solutions to, such as sealing of the piston ring of the MRF, the insulating system of the whole intelligent structure and the standard measuring of the properties of the MRF etc.

4.5 The present research work opens up and suggests further broad applied field for new type multifunctional piezomagnetic ferrites.

REFERENCES

1. Ballato, A., "Modeling piezoelectric and piezomagnetic devices and structures via equivalent networks," *IEEE Transactions on Ultransonics, Ferroelectrics, and Frequency Control*, Vol. 48, No. 5, 1180, 2001.
2. Li, Q., "Research and applications of high-powered acoustoelectric transducing materials," *Technical Acoustics*, Vol. 17, No. 1, 26, 1998 (in Chinese).

3. Nathaway, K. B. and A. E. Clark, *Magnetostrictive Materials*, MRS Bulletin, Vol. 18, No. 4, 34, 1993.
4. Li, Q., "Research and applications of piezoelectric and piezomagnetic acoustoelectric transducer materials," *Piezoelectrics* & *Acoustooptics*, Vol. 17, No. 2, 43, 1995 (in Chinese).
5. Li, Q. and Y. Li. "New type piezomagnetic ferrite materials and their new applications," *Progress in Electromagnetics Research Symposium (PIERS) Proceedings*, 747–751, Beijing, China, March 26–30, 2007.
6. Li, Q., "Research of power ultrasonics and their transducer materials," *Acta Photonica Sinica*, Vol. 27, No. Z3, 47, 1998 (in Chinese).
7. *Proceedings of the 6th International Conference on Electro-Rheological Fluids, Magneto-Rheological Suspensions and Their Applications*, xii+893, 3750, World Scientific, Singapore, 1998.
8. Li, Q., "Research into an integrated intelligent structure — A new actuator combing piezoelectric ceramic and electrorheological fluid," *The Journal of the Acoustical Society of America*, Vol. 111, No. 2, 856, 2002.
9. Zhou, G. Y., "Shear properties of a magnetorheological elastomer," *Smart Materials and Structure*, Vol. 12, 139, 2003.
10. Holdhusen, M. and K. A. Cunefare, "Damping effects on the state-switched absorber used for vibration suppression," *Journal of Intelligent Material Systems and Structure*, Vol. 14, No. 9, 551, 2003.
11. Corma, A., V. Fornes, R. M. Matin-Aranda, et al., *Catalysts*, No. 134, 58, 1992.

Development of Smart Antenna Array Signal Processing Algorithm for Anti-Jam GPS Receiver

Anindya Kundu[1] **and Soham Ghosh**[2]

[1]Kalpana Chawla Space Technology Cell (KCSTC)
Department of Electronics and Electrical Communication Engineering
Indian Institute of Technology, Kharagpur 721 302, West Bengal, India
[2]Department of Electronics Communication Engineering (ECE)
Netaji Subhash Engineering College, Kolkata 700152, West Bengal, India

Abstract— GPS guidance uses low power signals from satellites which are 11000 NMI away. The satellite transmitter power is modest nearly 10 W orders of magnitude. Neither satellite nor receivers have the luxury of very high antenna gain since both entities have significant field of view requirements. These factors result in a very low power density incident on a GPS receiver antenna. The signal received is generally 165 dB down than the thermal noise level. Such signals are notoriously easy to jam either by intentional noise sources (Jammer) or unintentionally from harmonics of broadcasting stations or other out of band sources. Here in this paper we will show how a nulling antenna or controlled reception pattern antenna with adaptive spatial filtering technique efficiently mitigate the intentional and non intentional interferences. A beamforming antenna array is a set of antennas whose outputs are weighted by complex values and combined to form the array output. The effect of the complex valued weights is to steer main lobes of the array pattern to desired directions. These directions may be unknown and so the antenna weights must be adjusted adaptively until some measure of array performance is improved, indicating proper lobe or null placement. An adaptive algorithm to adjust the complex weights of an antenna array is presented that nulls high power signals while allowing reception of GPS signals as long as the signals arrive from different directions.

1. INTRODUCTION

The GPS signals are spread spectrum modulated and have very low average power, on the order of background thermal noise. Simulations of the adaptive algorithm minimize the output power of the array to within 5 dB of the background noise level. The technique which will be adopted to optimize the weight values is steepest descent algorithm and implements an efficient, exact gradient calculation. With M antennas in the array, only M-1 weights are adjustable. It appears that M-1 adjustable antenna weights can null M-1 unwanted signals (jammers). However, in the course of the algorithm development, a few configurations of antennas and jammer arrival directions were found where this is not true. Even when the jammer arrival directions are known, certain configurations are mathematically impossible to cancel out the intentional interferences.

The basic requirements of an adaptive Nulling antenna array are that it should provide enough gain margin to the user (or users) to satisfy the link calculations and at the same time suppressing the interfering signals. To achieve this, the elements of the antenna should have enough gain individually and should be physically configured in such a way as to be able simultaneously to point pattern nulls in the direction of interfering sources. The algorithm is the most crucial in steering the main beam in the direction of the SOI (signal of interest). Incoming signal to the array are of three types 1. GPS Signal 2. Jammer signal 3. Noise The GPS signal and Noise are considered to have low power of the order of background noise level, while Jammers have assumed to have much higher power level. The strategy behind this adaptive nulling aiming on reducing the array output Jammer power to a level comparable to the output GPS signal power, so that the later can be detected with spread spectrum technology.

2. ANTI-JAM ECCM TECHNIQUES

Basic to any AJ receiver design are the abilities to detect the presence of jamming and characterize jamming features. Detection of jamming can be accomplished by comparing signal levels to the noise floor in the receiver, prior to the code correlators. At this stage in the receiver, the GPS signal amplitude is well below the noise floor. Detection of significant signal amplitude at this stage is indicative of the presence of jamming or other interference. Automatic gain control (AGC) measurements can characterize the amplitude of the jamming signal. A discrete Fourier transform

(DFT) provides an effective spectral characterization. Once the presence of jamming is established, a GPS receiver with AJ features can begin to adapt to the jamming environment within which it finds itself. The GPS receiver's next layers of defense, that are aimed at actually reducing the level of jamming contaminating signal processing functions, are embodied in various levels and types of filtering. At the first level, GPS receivers require fixed bandwidth front-end RF filters that pass the L-band frequencies of the spread spectrum satellite signals while simultaneously rejecting out-of-band jamming/interference. Out-of-band jamming would probably not be intended to inhibit GPS users but could incidentally disable receivers if not eliminated early in the receive chain. At the next level, military receivers should have intermediate frequency (IF) adaptive notch filters to counter narrowband noise and CW tone jammers. As described in the previous section, these jamming signals can be located in the frequency domain via DFT measurements performed by the jammer detection process. Once detected and isolated in frequency, various spectral and temporal signal processing techniques can be employed to implement a band rejection (or notch) filter that is adaptively tuned to the narrow frequency interval occupied by the jammer. Such notch filtering techniques can provide 15–30 dB of jamming suppression with only minor distortion/attenuation of the GPS signal, since only a small fraction of the signal's spread bandwidth is affected by the filter. Antenna-based ECCM techniques fall into the basic categories of antenna switching, polarization nulling, and adaptive array processing. Adaptive array processing includes the techniques of beam steering toward satellites, null steering (AKA spatial filtering) toward jammers, and combinations thereof aimed at optimizing the overall signal-to jammer power ratio (SJR). Antenna switching technique employs multiple antennas with narrower main beams than the hemispheric coverage typical of most GPS antennas. In a jamming environment, antennas are selected that have the best combination of gain in the satellite's direction and low side lobes in the jammer's direction — SJR is then maximized for the available set of antennas. However, jammer suppression is relatively marginal for this technique (~ 10 dB) and installation of multiple directional antenna apertures is impractical for some host platforms (especially for Guided Weapons). **Adaptive array processing** techniques attempt to remedy the drawbacks of the antenna switching concept by utilizing arrays of small antenna elements rather than full directional apertures. This makes installation on even small weapon platforms practical. Furthermore, implementation of phased-array processing is the key to significant multiple jammer suppression that can substantially restore GPS receiver operation in extensive jamming environments. Adaptive arrays provide phase control to each element of their multiple element antennas. In the absence of jamming, the individual phases are adjusted

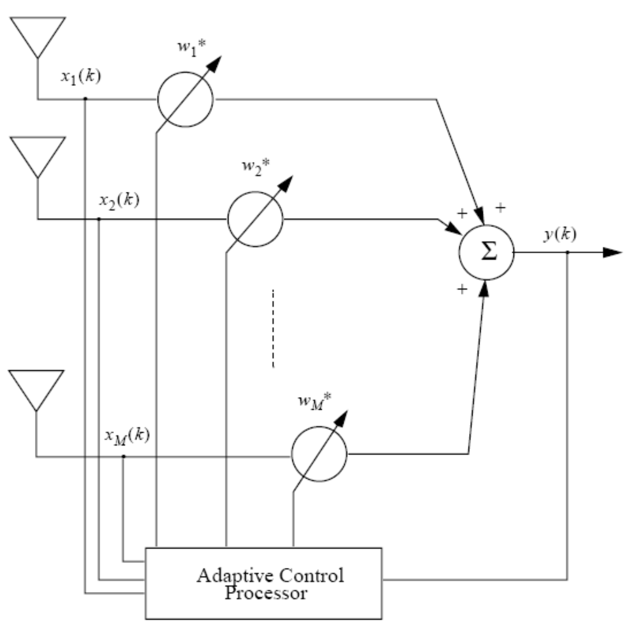

(a)

Anti-Jam Signal Processing Techniques	Jammer Rejection Performance	Cost/ Complexity	Implementation
Pre-correlation Adaptive Nulling Antenna Processing	**30-50 dB**	High	Analog/Digital
Pre-correlation Temporal/ Spec-Tral Processing	20-30 dB	**Very Low**	Digital
Post-correlation Processing	10-15 dB	Low	Digital Hardware/ Software

(b)

Figure 1: Adaptive antenna array with adaptive control processor, (b) comparison of adaptive signal processing technique with respect to performance cost & implementation.

and combined to create hemispheric satellite coverage by the resulting antenna reception pattern. In the presence of jamming, the phases are adjusted to steer high gain beams in the direction of satellites and/or low gain nulls in the direction of jammers. If null steering is implemented exclusively, the adaptive array is referred to as a controlled reception pattern antenna (or CRPA). The number of nulls a CRPA can generate and steer is dictated by the number of antenna elements in the array — the number of nulls being one less than the number of elements.

3. ADAPTIVE ANTENNA ANTI-JAM SIGNAL PROCESSING TECHNIQUE

An adaptive antenna controls its radiation pattern by mixing the received RF signals from multiple antenna elements with controlled complex weights (phase shifters and attenuators) and by summing the resulting signals. The radiation pattern of the final combined signal depends on the radiation pattern of each antenna element, on the geometry of the location of the antenna elements, and on the controlled antenna weights. Jammer suppression is accomplished by generating and using antenna weights so that the resulting radiation pattern minimizes power reception in the direction of the jammer. This system is referred to as a null steering (NS) antenna. Typically, the generation of antenna weights in adaptive NS systems is accomplished by an optimization algorithm which continuously tries to minimize the power of the interference RF signal at the output of the antenna combiner subjected to a suitable constraint (one fixed weight) to ensure signal reception.

Adaptive null steering antennas require, at a minimum, one controlled complex weight for each null in the radiation pattern in addition to one for the first antenna element. For example, we need three antenna elements to suppress two jammers radiating from different directions. These systems are very powerful, in that (1) they do not require the jammer to have distinct signal characteristics compared to the GPS satellite signal and (2) they can provide high processing gain, i.e., improvement in the signal-to-noise ratio (SNR) at the receiver input, often exceeding 30 dB. Unfortunately, adaptive antenna systems are prone to nulling out GPS signals if the direction of arrival of the jamming signal is close to that of the GPS. Also, adaptive antenna systems are very expensive compared to the cost of alternate anti-jamming systems, or even to the cost of the receiver unit itself.

The above two limitations of adaptive RF nulling antenna can be removed by using an optimization criterion (i.e., cost function) which penalizes nulling of a desired signal, such as minimizing J/S where J is the jammer power and S is desired signal, or directly maximizing signal-to-interference-plus-noise power ratio (SINR). The choice of optimization criterion along with the choice of the optimization algorithm determines the performance of the adaptive antenna. The limitation associated with the choice of RF analog implementation for the antenna electronics can be easily removed by employing digital signal processing to effectively implement the antenna gain and phase control and combiner functions.

4. DIRECTION OF ARRIVAL (DOA) ESTIMATION FOR ADAPTIVE PROCESSOR

In array signal processing, the estimation of the direction of arrival angle (DOA) from multiple sources plays an important role, because we need to feed the desired and jamming signal direction to adaptive processor so that it can produce null and steer main lobe towards the desired signal. Usually we employ multiple antenna array elements, and their array signal processing can increase the capacity and throughputs of the system significantly. Estimation of the DOA's of incoming signals can be used to localize the signal sources and characterize them.

Among the various mathematical realization DOA estimation algorithm, like Capon's beamformer, conventional beamformer, MUSIC algorithm, ESPRIT algorithm we choose the last one with some modification in mathematical realization for DOA estimation for Adaptive processor.

5. C-ESPRIT ALGORITHM

Estimation of signal parameters via rotational invariance techniques (ESPRIT) is a signal subspace technique. ESPRIT is a computationally efficient and robust method of DOA estimation. It considers two identical sub arrays consisting of the same number of antenna elements, and each matched pair of elements is called a doublet with an identical displacement vector. In the ESPRIT algorithm, the number of a doublet depends on overlapping between sub arrays. Considering a uniform linear array (ULA) consisting of M elements, then the number of doublets in the case of no overlapping is equal to half the number of elements $M = 2m$, where m is the number of doublets. But if maximum overlapping occurs between the two sub arrays, then the number of doublets becomes $m = M - 1$, compared to the MUSIC algorithm, ESPRIT does not require an exhaustive search through all possible steering vectors to estimate the DOA. Moreover, ESPRIT reduces computational complexity and storage requirements, which makes real time implementation possible. C-ESPIRIT algorithm can provide a more precise DOA estimation and can detect more signals than the well-known classical subspace methods, MUSIC and ESPRIT, for the 1-D and 2-D DOA. The complexity is the same as that of ESPRIT, since the proposed algorithm uses the same array geometry and sub array processing as ESPRIT. The main differences between the proposed and ESPRIT algorithms are as follows: (1) in the proposed algorithm, the number of overlapping array elements between the two sub arrays is equal to M, while in ESPRIT, the maximum number of overlapping elements is M-1, where M denotes the total number of array elements, and (2) the proposed algorithm employs the conjugate of rotation matrix (CRM) Φ^*, while ESPRIT uses Φ with no conjugate for the second sub array geometry.

Considering a uniformly linear array of M elements and assuming K non-coherent and narrowband one dimensional signals are received at uniform linear array(ULA) with different DOA's $\theta_1, \theta_2, \ldots, \theta_k$, the $M*1$ received signal vector can be written as $X(t) = \sum_{k=1}^{K} a(\theta_k) S_k(t) + n(t)$. Where $S_k(t)$ represents the signal from the k th source with DOA equal toθ_k, $a(\theta_k)$ which denotes the $M*1$ array response vector and $n(t)$ is the $M*1$ AWGN vector with each component of mean zero and variance equal to σ^2. The array response vector can be written as $a(\theta_k) = (1, Z_k, Z_k^2, \ldots, Z_k^{M-1})^T$ and $Z_k = \exp(-j\frac{2\pi d\cos(\theta_k)}{\lambda})$ where λ the wave length, d is spacing between elements. $M*K$ array response matrix and $K*1$ signal vector can be written as $A(\theta) = [a(\theta_1), a(\theta_2), \ldots, a(\theta_k)]$, and $S(t) = (S_1(t), S_2(t), S_3(t), \ldots, S_k(t))^T$ respectively. CSPRIT algorithm can estimate either azimuth DOA φ_k or the joint azimuth and elevation DOA (φ_k,θ_k). For the sub-array1 we form column vector $(y_1, y_2, \ldots, y_M)^T$. In fact two separate sub array do not exist they are fully overlapped each sub array processing in a C-SPRIT uses the maximum number of array elements equal to M where as each sub-array processing in ESPRIT can have only $M/2$ elements for the doublet case or M-1 at most, for the maximum overlap case, this is the reason why CSPRIT have better SNR. 1st element in the array is treated as the reference with respect to the other elements. In this case the $M*1$ input vector to sub array can be written as

$$Y_1(t) = A(\theta)S(t) + n_1(t) \tag{1}$$

$A = A(\theta) = \begin{bmatrix} 1 \ldots 1 \\ Z_1 \ldots Z_k \\ Z_1^2 \\ Z_1^{M-2} \ldots Z_k^{M-2} \end{bmatrix}$, $Y_1(t) = [y_1(t), y_2(t), \ldots, y_M(t)]^T$ and $n(t) = [n_1(t), n_2(t), \ldots, n_M(t)]^T$. $A(\theta)$ is the array response matrix with dimension $M*K$, $S(t)$ supposed to be narrowband signal vector with dimension $K*1$, $n_1(t)$ is $M*1$ AWGN vector whose component are zero mean and variance σ^2. Input vectors to sub array 2 is denoted as $Y_2(t) = [y_2^*, y_1, \ldots, y_{M-1}]^T$, if we represent it in terms of $A(\theta)$, $S(t)$, ϕ^* it becomes

$$Y_2(t) = \begin{pmatrix} \sum_{k=1}^{K} S_k Z_k^* + n_2^* \\ \sum_{k=1}^{K} S_k + n_1 \\ \sum_{k=1}^{K} S_k Z_k + n_2 \\ \sum_{k=1}^{K} S_k Z_k^{M-2} + n_{M-1} \end{pmatrix} = A(\theta)\phi^* S(t) + n_2(t). \tag{2}$$

For one dimensional signal $\phi^* = \mathrm{diag}(Z_1^*, Z_2^*, \ldots, Z_k^*)$. Y_1& Y_2 the total output vector Z(t) can be written as,

$$Z(t) = \begin{bmatrix} Y_1(t) \\ Y_2(t) \end{bmatrix} = BS(t) + n(t) \tag{3}$$

$$B = \begin{bmatrix} A \\ A\phi^* \end{bmatrix}, \quad n(t) = \begin{bmatrix} n_1(t) \\ n_2(t) \end{bmatrix}.$$

B is $2M*K$ matrix and both $Z(t)$ and $n(t)$ are $2M*1$ vectors forming $2M*2M$ covariance matrix $Z(t)$.

$$R_{zz} = BR_sB^H + \sigma^2 I \tag{4}$$

$R_s = E[S(t)S(t)^H]$ is a $K*K$ signal covariance matrix. As the signals are uncorrelated and $2M$-K smallest eigen values of R_{zz} are equal to σ^2. The K eigen-vectors corresponds to K largest eigen values can be written in a $2M*K$ matrix $F_s = [e_1, e_2, \ldots, e_k]$. The range space of F_s is equal to B i.e., $R(F_s) = R(B)$, thus a nonsingular matrix T exist such that

$$\begin{aligned} &F_s = BT; \\ &F_s = \begin{bmatrix} F_0 \\ F_1 \end{bmatrix} = \begin{bmatrix} AT \\ A\phi^* T \end{bmatrix} \end{aligned} \tag{5}$$

$\phi^* = T\psi T^{-1}$ Where the Eigen-values of matrix ψ are equal to the diagonal elements of ϕ^* and the columns S of T are the eigenvectors of ψ. To find the DOA steps to be followed may be summarized as

1) Obtain the estimate of R_{zz}.
2) Apply Eigen-value decomposition of R_{zz}. $R_{zz} = F\Lambda_{zz}F^H$.

$$\Lambda_{zz} = \mathrm{diag}(\lambda_1, \lambda_2, \ldots, \lambda_{2M}) \text{ and } F = [e_1, e_2, \ldots, e_{2M}].$$

3) Use multiplicity of K of the smallest Eigen value to estimate the number of signals as $\hat{K} = 2M - K$.
4) Estimate the signal subspace $\hat{F}_s$ using the eigenvector correspond to the largest K Eigen values and decompose F_s into two $M*K$ sub matrices F_0 & F_1.
5) Apply Eigen value decomposition on the matrix formed as $G = \begin{bmatrix} \widehat{F}_0^H \\ \widehat{F}_1^H \end{bmatrix} \begin{bmatrix} \widehat{F}_0 \hat{F}_1 \end{bmatrix} = F\Lambda_G F^H$.

   Partition F into $K*K$ sub matrices as $F = \begin{bmatrix} F_{11}F_{12} \\ F_{21}F_{22} \end{bmatrix}$.
6) Calculate the Eigen value λ_k of ψ When $\psi = -F_{12}F_{22}^{-1}$ then estimate kth diagonal element ϕ_k^*; $\phi_k^* = \lambda_k$.
7) Estimate azimuth DOA $\phi_k^* = \cos^{-1}\left[\frac{\arg(\hat{\phi}_k^*)}{2\pi d/\lambda}\right]$. For realization of joint azimuth & elevation 2D DOA estimation with C-SPRIT we need to collect data from the array elements and Z_K will be function of both elevation DOA θ_k and azimuth DOA ϕ_k and $Z_K = \exp\left(-j\frac{2\pi d\cos\hat{\phi}_k \sin\theta_k}{\lambda}\right)$ and $\hat{\phi}_k^* = \cos^{-1}\left[\frac{\arg(\phi_k^*)}{2\pi d \sin\hat{\theta}_k/\pi}\right]$.

6. SIMULATION RESULT

Assumption is made that $K = 3$, signals are from BPSK sources. ULA of 6 elements separated by distance equal to half wave length of incoming signal employed. The no of data samples per trial at each element output is $N = 200$ and no of total independent trial is 2500. Figure shows the histogram plot of azimuth DOA estimation for DOA at 82°, 90°, 98° and SNR = $[2, 2, 2]$ dB. It becomes clear that proposed algorithm gives the most accurate DOA estimation most of the time all peaks are observed at around 82°, 90°, and 98°.

7. LMS ALGORITHM

This algorithm is based on method of steepest decent. Changes in weight vectors are made along the direction of the estimated gradient vector.

Accordingly,

$$W(j+1) = W(j) + k_s \overset{\wedge}{\nabla}(j) \tag{6}$$

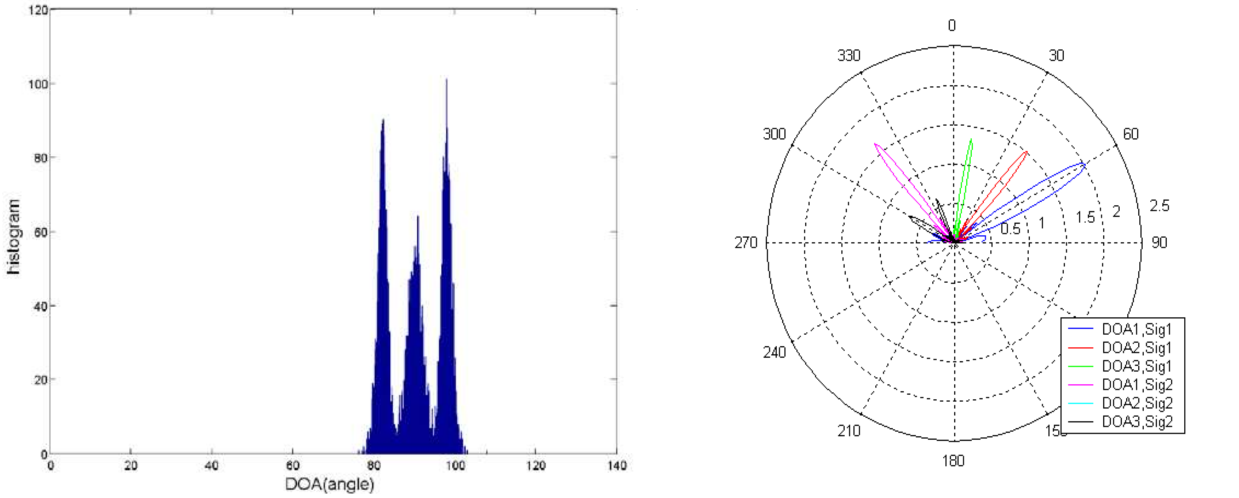

(a) (b)

Figure 2: (a) Histogram of DOA estimations for $K = 3$ sources of DOA at [82°, 90°, 98°], SNR = $[2, 2, 2]$ dB, and $M = 6$ elements for C-SPRIT, (b) adaptive antenna scanning two signals from 60° (with two multipath form 40° & from 10°) &. −40° (with two multipath form −60° & from −20°).

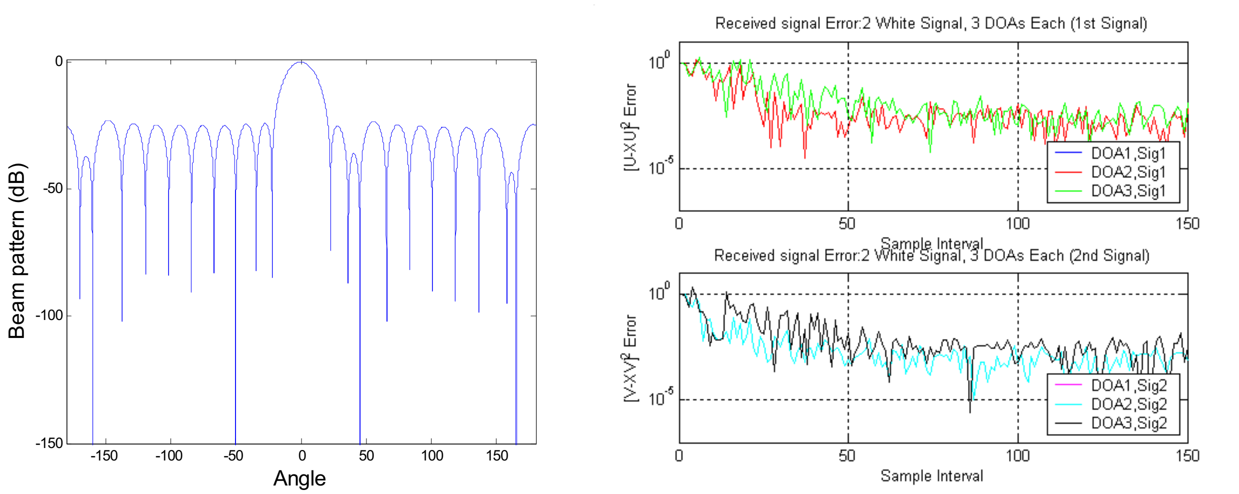

(a) (b)

Figure 3: (a) Multiple null steering desired signal coming from −20° to 20° Jammers are from 45°, 165°, −50° and −160° (4 Jammers), (b) LMS algorithm converging around 49–50 iteration for all signals.

where $W(j)$ = weight vector before adaptation, $W(j+1)$ = weight vector after adaptation, k_s = scalar constant controlling rate of convergence and stability ($k_s < 0$), $\hat{\nabla}(j)$ = estimated gradient vector of $\bar{\varepsilon^2}$ with respect to W. Where the difference between the desired response and the output response forms the error signal $\varepsilon(j) = d(j) - W^T X(j)$. W^T = transpose of the weight vector and $W^T X(j)$ is output at jth sampling instant

$$\begin{aligned}\hat{\nabla}(j) &= \nabla\left[\bar{\varepsilon^2}(j)\right] = 2 * \varepsilon(j) * \nabla(\varepsilon(j)) \\ \nabla(\varepsilon(j)) &= \nabla\left[d(j) - W^T X(j)\right] = -X(j) \\ \hat{\nabla}(j) &= -2 * \varepsilon(j) * X(j)\end{aligned}$$

using the gradient estimation formula the weight iteration rule becomes

$$W(j+1) = W(j) - 2k_s\varepsilon(j)X(j) \tag{7}$$

i.e., the next weight vector is obtained by adding to the present weight vector the input vector scaled by the value of the error. The LMS algorithm is directly usable as a weight adaptation formula for digital systems.

Computer simulations are concluded to ascertain the performance of the proposed LMS adaptive array. The array employed is a 21 element dipole of length $\lambda/2$ and spacing $\lambda/2$. All elements are assumed to be identical and Omni-directional with a unit gain. Here phi $= 0$ and theta is varying desired signal coming from $-20°$ to $20°$. Jammers (4 Jammers) are radiating interference from $45°$, $165°$, $-50°$ and $-160°$.

8. CONCLUSIONS

Techniques for interference suppression and anti-jamming which either dictate certain aspects of, or at least are relevant for, GPS receiver design include the following: (1) adaptive antenna arrays and associated electronics, (2) adaptive digital filters, (3) the addition of sensors (including inertial sensors) and associated hardware, and (2) processor architecture modifications necessitated for signal processing techniques; and adaptive narrowband filters. Adaptive array processing techniques attempt to remedy the drawbacks of the antenna switching concept by utilizing arrays of small antenna elements rather than full directional apertures. This makes installation on even small weapon platforms practical. Furthermore, implementation of phased-array processing is the key to significant multiple jammer suppression that can substantially restore GPS receiver operation in extensive jamming environments. The choice of one algorithm over another is determined by various factors. We are steering the beam in a specific direction. Our objective is fulfilled which reproduce the desired signal accurately as possible. We want the array processor to be very sensitive to the DOA of the signal. Here the issues of concern include (a) the number of operations (i.e., multiplications, divisions, and additions/subtractions) required making one complete iteration of the algorithm, (b) the size of memory locations required to store the data and the program, and (c) the investment required to program the algorithm on a computer or a DSP processor. So we can conclude that this onboard Adaptive antenna processing efficiently mitigate the intentional interference from jammers and keep military GPS receiver accurate.

ACKNOWLEDGMENT

The authors are grateful to Space Application Centre (SAC) Ahmadabad, ISRO for funding this research project.

REFERENCES

1. Mukhopadhyay, M. and B. K. Sarkar, "Adaptive array antenna & LMS algorithm for jamming resistance GPS receiver," *ICAT2005 International Conference on Antenna Technologies*, 2005.
2. Mukhopadhyay, M. and A. Chakrabarty, "Low side lobe adaptive array processing with multipath constraint for anti-jam GPS receiver," *Proc. of URSI GA*, 2005.
3. Sarkar, T. K., M. C. Wicks, M. Salazar-Palma, and R. J. Bonneu, *Smart Antennas*, John Wiley & Sons, 2003.
4. Widrow, B. and S. D. Stearns, *Adaptive Signal Processing*, Prentice Hall, Englewood Cliffs, New Jersey, 1985.
5. Widrow, B., P. E. Mantey, L. J. Grifiths, and B. B. Goode, "Adaptive antenna systems," *Proc. IEEE*, No. 12, 2143–2159, 1967.

Time Domain Studies of Ultra Wideband Dielectric Loaded Monopole Trans-receive Antenna System

Atanu Roy[1], **Saswati Ghosh**[2], **and Ajay Chakrabarty**[1]

[1]Department of Electronics and Electrical Communication Engineering, IIT Kharagpur, India
[2]Kalpana Chawla Space Technology Cell, IIT Kharagpur, India

Abstract— This paper presents the time domain studies of a wideband trans-receive antenna system consisting of a quarter-wave monopole loaded with an annular dielectric resonator antenna. This antenna has recently become attractive to antenna designers due to its broadband characteristics. However, while using this antenna in ultra wideband trans-receive system, the time domain characterization of the whole system is required and investigation on this has not yet been performed by other researchers. In this paper, the transmit antenna is excited by a wideband signal. The time domain waveform of the received voltage developed at the load end of the receiving antenna is presented both for far field and near field position of the receiving antenna. The results are simulated using CST Microwave Studio, version 5.

1. INTRODUCTION

The monopole loaded with dielectric resonator antenna (DRA) has found important application as broadband antenna [1–3]. A very interesting work on the guidelines for the design of this antenna was presented in recent literature [3]. The broadband characteristics of the hybrid antenna both in transmit and receive mode as EMI sensor in frequency domain had already been studied. There has been considerable interest on the studies of different loaded and dielectric resonator antennas for their wideband characteristics [4–7]. However, the authors have not noticed any appreciable work on the time domain analysis of this antenna in a wideband trans-receive antenna system including the mutual coupling between the antenna elements and concentrated on this. In this paper, the time domain studies of the trans-receive antenna system including the medium is presented for far field and also considering the near field coupling between the antennas. The frequency-domain concepts and terminology are commonly used to describe the transmitting and receiving response of an antenna. These are satisfactory for a continuous wave (CW) or narrow band applications. However, for an instantaneous wideband excitation the time-domain analysis of the antenna is necessary. One convenient way of analyzing the trans-receive antenna system in the time domain involves the evaluation of the amplitude and phase of the response over the entire frequency spectrum. For a really wideband antenna the amplitude of the transmitted/received signal will be flat and the phase variation will be linear within the frequency band. The inverse Fourier transform of this signal will represent the time domain waveform which should be identical to the input waveform for a wideband system. Here the equivalent circuit of the trans-receive antenna system is estimated in terms of the equivalent receiving antenna circuit. The transmit antenna is excited by a wideband signal. The electric field radiated by the transmit antenna is considered as the incident electric field on the receive antenna. The voltage developed across the load connected to the receive antenna due to this incident field is evaluated. The time domain waveform is achieved by taking the inverse Fourier transform of the load voltage in frequency domain.

2. THEORY

The general configuration of a trans-receive system consisting of a transmit antenna and another receive antenna is shown in Fig. 1(a). The transmit antenna is driven by a voltage source $V_G(\omega)$ having an internal impedance $Z_G(\omega) = R_G(\omega) + jX_G(\omega)$, while the receive antenna is terminated in load impedance $Z_L(\omega) = R_L(\omega) + jX_L(\omega)$ and has a terminal voltage $V_L(\omega)$. The incident field is the electric field radiated by the transmit antenna excited by the appropriate input voltage. A physical trans-receive system including a DRA-loaded monopole antenna as transmit and receive antenna is shown in Fig. 1(b).

We define a function $\overline{F}_{EG}(\omega)$ which is written in terms of the input voltage and the electric field transmitted by the antenna considering the mutual coupling between the transmit and receive antenna as follows:

$$\overline{F}_{EG}(\omega) = \frac{\overline{E}(\omega)}{V_G(\omega)} \tag{1}$$

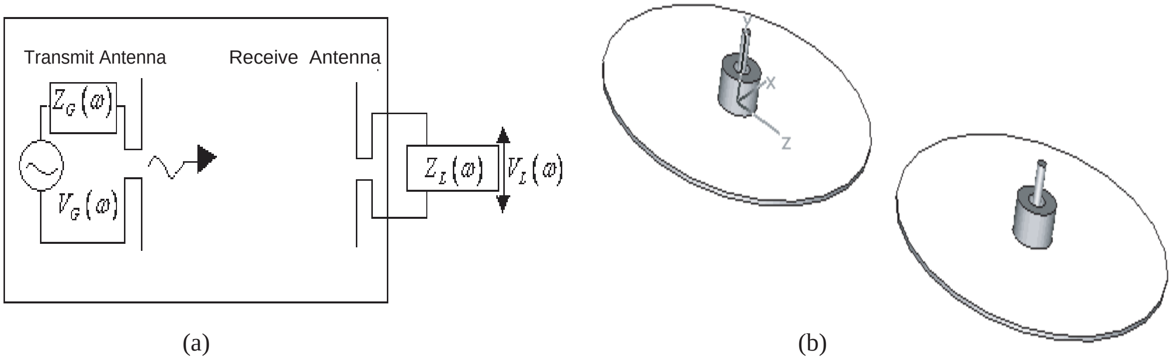

Figure 1: (a) A complete trans-receive antenna system consisting of a transmitting and receiving antenna, (b) A physical trans-receive system using hybrid DRA.

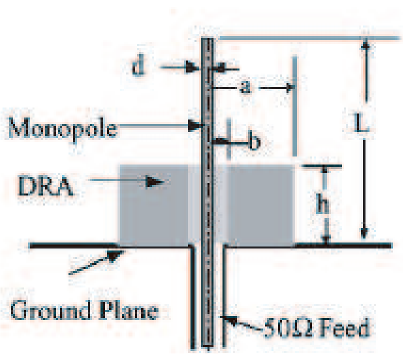

Figure 2: Cross section of hybrid monopole antenna [2].

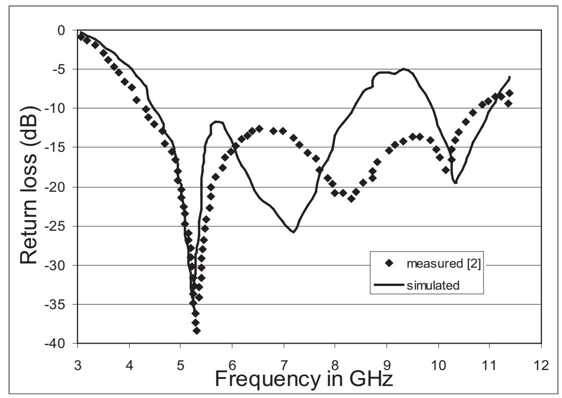

Figure 3: Return loss of a DRA-loaded monopole antenna.

The strong coupling is embedded in the $\overline{F}_{EG}(\omega)$ in Equation (1) and it depends on the distance in the near-field range. Similarly another function $\overline{F}_{EL}(\omega)$ is defined as the ratio of the voltage received at the load end $V_R(\omega)$ to the incident electric field $E(\omega)$ at the surface of the receive antenna due to the transmit antenna.

$$\overline{F}_{EL}(\omega) = \frac{V_R(\omega)}{\overline{E}(\omega)} \tag{2}$$

It should be noted that $\overline{F}_{EL}(\omega)$ depends on the distance between the two antennas in the near field range, however it is same as the transfer function of the receive antenna when they are in far field.

Hence the trans-receive function $\overline{F}_{LG}(\omega)$ of the overall system that relates the receive antenna load voltage to the generator voltage at the transmit antenna is achieved as follows:

$$F_{LG}(\omega) = F_{EG}(\omega) \times F_{EL}(\omega) \tag{3}$$

The inverse Fourier transform of the load voltage gives the time domain waveform of the load voltage due to the suitable excitation. For the simulation the electromagnetic software CST Microwave Studio, version 5 is used [8].

3. GEOMETRY OF THE PROBLEM

The geometry of the antenna studied here is shown in Fig. 2 [2]. The hybrid antenna consists of a thin monopole and an annular DRA, both sharing the same axial reference and mounted on a finite ground plane. The quarter-wave monopole is designed to have a resonance at the lower end of the frequency band, while the DRA is designed to have a resonance near the upper end of the desired spectrum range. The two resonant frequencies are chosen to maintain a minimum return loss of 10 dB throughout the operating frequency range [2]. The dimensions of the hybrid antenna as taken from the literature [2] are as follows:

$L = 15$ mm, $d = 1.3$ mm, $a = 4.5$ mm, $b = 1.2$ mm, $h = 7.2$ mm, Ground plane radius $= 40$ mm, for DRA $\varepsilon_r = 20$.

4. RESULTS AND DISCUSSION

The simulation of the trans-receive system is performed using CST Microwave Studio. The return loss versus frequency of the hybrid DRA loaded monopole antenna is shown in Fig. 3, which is in compliance with the experimental results presented in [2].

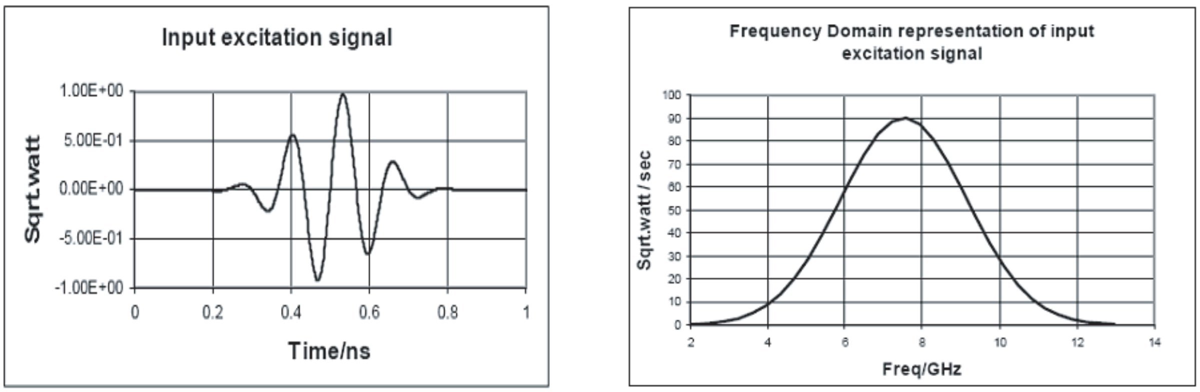

(a) (b)

Figure 4: Input excitation signal of the trans-receive antenna system. (a) Time domain plot, (b) Frequency domain plot.

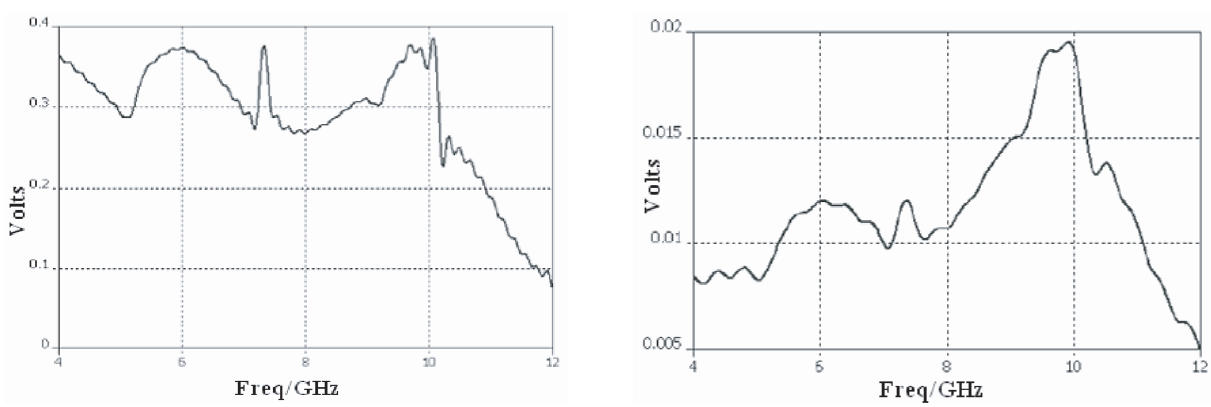

(a) (b)

Figure 5: Plot of the load voltage at the receiving antenna of the trans-receive antenna system. (a) Center to center distance = 90 mm, (b) Center to center distance = 400 mm.

The transmitting antenna of the trans-receive system is excited by a waveguide port. The input signal of excited waveguide port is normalized to 1 sqrt (Watt) peak power and the waveguide port realizes an input power of 1 W over its entire port face. The amplitude of all signals in CST Microwave Studio is normalized to this reference signal. So in case of waveguide ports the excitation is in sqrt (watt). Also the Fourier transform of this normalized input signal, gives the signal in frequency domain with unit sqrt (watt)/sec. The time domain and frequency domain waveform of the excitation voltage applied to the transmit antenna is shown in Fig. 4. The frequency domain plot of the excitation signal (Fig. 4(b)) shows a wideband waveform in the desired frequency range.

The load voltage developed at the load end of the receive antenna is evaluated both in frequency domain and time domain. The transmit antenna and receive antenna are assumed as parallel, radiating in the broadside directions. The results are shown for different distances e.g., 90 mm, 120 mm and 400 mm between the antennas. Applying the conventional far field conditions in the

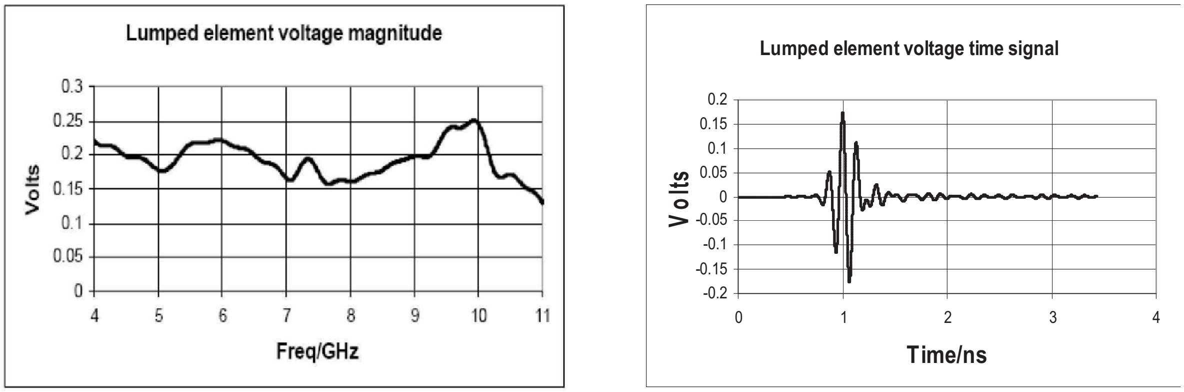

(a) (b)

Figure 6: Plot of the load voltage at the receiving antenna of the trans-receive antenna system (center to center distance = 120 mm). (a) Frequency domain plot, (b) Time domain plot.

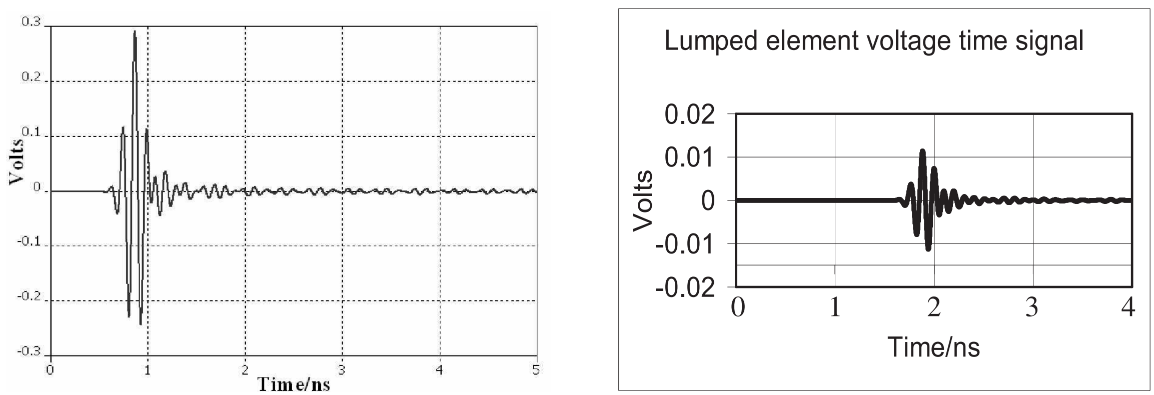

(a) (b)

Figure 7: Time domain waveform of the received voltage at the load of the trans-receive antenna system. (a) Center to center distance = 90 mm, (b) Center to center distance = 400 mm.

entire frequencies of interest, the 90 mm and 120 mm distance is considered in the near field region whereas the 400 mm is considered in the far field region. However, due to the excessively long simulation time for far field simulation, it was not possible to extend the simulation for higher distances in the far field. The frequency domain and time domain plot of the load voltage for various separations between the elements are presented in Figs. 5–7. The received voltage versus frequency plot for the three distances are shown in Figs. 5 & 6(a). The time domain plots of the received voltage for the three cases are shown in Figs. 6(b) & 7. The time for wideband pulses at the receive antenna side indicates the separation between transmit and receive antenna.

5. CONCLUSION

This paper presents the initial investigation on the time domain characterization of a trans-receive antenna system using a hybrid monopole/DRA considering the mutual coupling between the transmit and receive antenna. The time domain waveform of the voltage developed at the load end of the receive antenna is found to be identical to the input waveform for both near field and far field region, which proves the wideband nature of this trans-receive system. This study may find an important application in the ultra wideband technology.

REFERENCES

1. Lapierre, M., Y. M. M. Antar, A. Ittipiboon, and A. Petosa, "A wideband monopole antenna using dielectric resonator loading," *Proceedings IEEE APS North America Radio Science Conference*, Columbus, OH, 22–27, June 2003.
2. Lapierre, M., Y. M. M. Antar, A. Ittipiboon, and A. Petosa, "Ultra wideband

monopole/dielectric resonator antenna," *IEEE Microwave and Wireless Components Letters*, Vol. 15, No. 1, January 2005.

3. Debatosh, G., Y. M. M. Antar, A. Ittipiboon, A. Petosa, and L. David, "Improved design guidelines for the ultra wideband monopole-dielectric resonator antenna," *IEEE Antennas and Wireless Propagation Letters*, Vol. 5, 373–376, 2006.
4. Al-Zoubi, A. S., A. A. Kishk, and A. W. Glisson, "Analysis and design of a rectangular dielectric resonator antenna FED by dielectric image line through narrow slots," *Progress in Electromagnetics Research*, PIER 77, 379–390, 2007.
5. Lu, Y.-Q. and J.-Y. Li, "Optimization of broadband top-loaded antenna using micro-genetic algorithm," *Journal of Electromagnetic Waves and Applications*, Vol. 20, No. 6, 793–801, 2006.
6. Kumar, A. V. P., V. Hamsakutty, J. Yohannan, and K. T. Mathew, "Microstripline fed cylindrical dielectric resonator antenna with a coplanar parasitic strip," *Progress In Electromagnetics Research*, PIER 60, 143–152, 2006.
7. Rezaei, P., M. Hakkak, and K. Forooraghi, "Design of wideband dielectric resonator antenna with a two-segment structure," *Progress In Electromagnetics Research*, PIER 66, 111–124, 2006.
8. *Users' Manual of CST Microwave Studio*, Version 5.

Study and Improvement in Operational Characteristics of Mid Air Collision Aversion System (TCAS)

Vikrant Kumar Sharma

Department of Electronics and Communications
Jaypee Institute Of Information Technology (JIIT)
Noida, Uttar-Pradesh-124001, India

Abstract— The drawbacks in the current system of TCAS are studied in this paper along with the changing needs because of rising air traffic. Improving the maneuvering capability by making a new algorithm for calculating the path, and also by establishing an exclusive communication link enhanced threat handling. It was found that the horizontal steering in a threat situation has to be implied by studying the air traffic in the vicinity. Steering vertically can create a problem when a/c are present above and below. All paths are calculated by taking the distance and climb or decent rate of the individual a/c around the main a/c, which would be necessary to avoid collision with them. This procedure is followed at the other confronting a/c too. The best path which is taken ensures aversion of collision between them and nullifies the possibility of a threat situation with another a/c because of it. These findings were found to be helpful in situations where density of air traffic is high and with them a better probability of collision avoidance is achieved as compared to the present system. It doesn't involve changing the full equipments such as the transponder and the antennae, but some modifications in the processor based on the new algorithm.

1. INTRODUCTION

The TCAS (traffic alert and collision avoidance system) used in aircraft is an instrument, which creates a network of itself in mid-air. Its main objective is to notify and avoid collision with any air borne object. When an aircraft approaches in the periphery of the main aircraft detection and tracking of intruder aircraft is performed via transmission and receptions on a top-mounted TCAS directional antenna and a bottom-mounted TCAS omni directional antenna.

When interrogated, transponders reply after a fixed delay. Measurement of time between interrogation transmission and reply reception allows TCAS to determine range of intruder. If the intruder's transponder is supplied with an altimeter input, TCAS will receive intruder altitude reports in the replies and be able to determine the relative altitude of the intruder. Transmission and reception techniques used on the TCAS directional antennas allow TCAS to determine bearing of intruder.

The vertical maneuvering resolution advisories issued by TCAS can only be determined and generated against intruder aircraft that report altitude data in their transponder replies to TCAS interrogations.

This poses a problem as it only gives a signal of climb or decent as a solution of a possible conflict. If the density of air traffic is more, which is a reality nowadays then this can create another conflict situation in which the crew will get very less time to react to. There is no mechanism of predicting the outcome of the path taken or its implications. Also it doesn't take into consideration the horizontal maneuvering in the adjacent airspace. If a combination of horizontal and vertical steering is considered then many possible "fall-out" paths can arise. From them the best suited for both the confronting aircraft can be chosen. This assures better utilization of the empty airspace and also does not impose danger to other aircraft as a result of the path taken. For better resolution of the threat a voice communication link can also be established using another directional antenna, which can be pointed in the desired direction of the aircraft with which a link has to be made. The pointing can be done without physically moving the antenna. This can be achieved by independently varying the drive level and phase to each of the four elements for four directions contained in the antenna.

Another security feature which can be included in it is transmission of the aircraft registration for the link formation. It will enhance the threat perception. Modifying the network word and including more bits in it can achieve this. The coding used can be VLC,CLC or hamming code which are recognized world wide.

2. TCAS

2.1. Review

The TCAS system is an independent entity for the aircraft. It only needs the desired power supply from the aircraft, which is 115 V at 400 Hz AC or 28 V DC. This is standard supply for all aircraft.

It constantly gets the feed from the altimeter, magnetic heading, pitch and roll attitude and discrete inputs from other important aircraft switched and straps. These inputs are necessary to compute relative altitude, collision course and the direction of the aircraft when compared to the other intruding aircraft.

It consists of the following parts :

- First, TCAS processor.
- Second, transponder which can be a mode S or a mode A/C. the system includes both forward and backward compatibility for any transponder.
- Third, the display information.
- Fourth, the cockpit display unit which has to be digital

The modified algorithm needs the same equipment to operate. Only the specification of the processor and the transponder has to be changed.

2.2. Need

Used for detecting and tracking aircraft in the vicinity of your own aircraft. By interrogating their transponders it analyzes the replies to determine range. Issues visual and audio advisories to the crew for appropriate vertical avoidance maneuver. Display the intruding aircraft relative position and altitude with trend arrow to indicate whether it is climbing or descending.

2.3. Operation

TCAS system forms an INTERNETWORK in the air.

It monitors the air space surroundings aircraft by interrogating the transponder of intruding aircraft and measures:

- Relative bearing to the intruder.
- Range b/w aircraft and intruder.
- Altitude and vertical speed of intruder.
- Closing rate between the intruder and aircraft.

Using this TCAS data, the time to and separation at , and closest point of approach can be determined (CPA). In turn it helps to determine the course of the other aircraft on the basis of which warnings are issued.

TRAFFIC ADVISORY — to alert the crew that traffic is in the vicinity.

RESOLUTION ADVISORY-to obtain or maintain safe vertical separation b/w aircraft and the intruder, it takes 2.5 second for any reaction in case of increase or decrease of RA.

2.4. Processor

It is the nerve center of the TCAS system. It selects directional antenna beams, generates and transfers pulsed 1030 MHz rf interrogation data to the top and bottom antennas. It then examines the reply data and determines threat potential of the intruder. It is responsible for ARINC429 coordination and housekeeping data to mode S transponder subsystem.

It formats and transmits broadcast messages as explained. Which are transmitted at 1030 MHz by each TCAS system to notify others that this aircraft is present in the parameter. It keeps a track of other TCAS equipped aircraft in the broadcast range.

Depending upon the number of interrogations it reduces the power output levels as the TCAS equipped aircraft increases. It reduces the detectable interrogation load on the mode s transponder.

It determines the range, bearing and altitude of the intruder aircraft based on the information received in the reply message on the directional antenna. With these parameters the processor evaluates the threat potential of the aircraft by calculating intruder closing rate and position relative to own aircraft. It listens for squitter messages transmitted by other mode s transponder at 1090 MHz. The directional antenna plays a very important role, as no physical movement is required in it. It works on changing phase of the 4 different arrays present.

2.5. Mode S Transponder

It transmits a1090-MHz mode S reply message when it receives appropriate 1030 MHz mode S interrogation from other TCAS aircraft. It contains aircraft address ID and the only transponder assigned that address will reply. It is basically the transponder i.d and it is not the aircraft registration number. The transponder is connected to the processor by means of a bi-directional bus ARINC 429 data link. Extensive data link communication continuously occurs between the processor and the transponder.

It receives 115 V 400 Hz from an aircraft power source. If the intruder aircraft is TCAS equipped and is declared a threat, a maneuvering coordination data link is established with the intruder. This ensures that the resolution advisories in both TCAS equipped aircraft are coordinated and compatible.

2.6. Display

2.6.1. TA Display

It provides a display of RA, TA or non threat category aircraft. It depicts the threat potential and position of the intruder aircraft. It receives data from the processor via the ARINC 429 bus. Strap inputs are provided to select the vertical speed input source and system variables. The center of the display is a horizontal situation presentation of the traffic around the aircraft including intruder altitude and vertical direction. Traffic is divided into four categories by threat risk and differentiated on the display by symbol color and shape.

2.6.2. RA Display

The RA commands displayed on the TA display are primary indications used for vertical maneuvering guidance. TCAS resolution advisories indicate vertical speeds to be used or avoided in order to maintain or achieve safe vertical separation.

A pointer and vertical speed scale which are a standard feature, indicate the present vertical speed of own aircraft. For TCAS guidance TA displays red and green command arcs on a liquid crystal display for this purpose along with the vertical speed scale and pointer.

The red and green RA command indications provide corrective and preventive resolution advisory maneuvering guidance to the crew, so that the crew within the specified time frame to avoid collision can implement the recommended action.

3. MODIFIED ALGORITHM FOR COLLISION AVOIDANCE

3.1. Defining Proximity Range (PA)

The ranges, which are defined in the current system, are of TA region and RA region. The traffic advisory is issued when an intruder comes in TA region. The boundary of TA range is defined as a point from where an aircraft moving at a speed of 300 kts requires 40 sec to collide with the own aircraft head on. Similarly, the boundary of a RA range is defined as a point from where an aircraft moving at a speed of 300 kts requires 25 sec to collide with the own aircraft head on, as shown in Fig. 1.

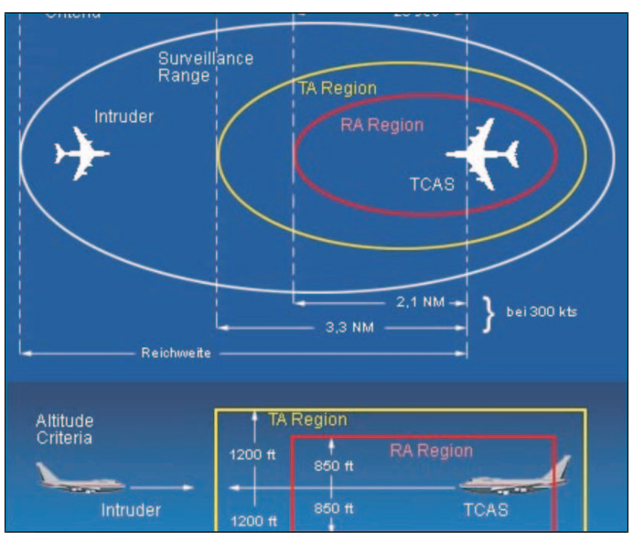

Figure 1: The dipiction of the TA and RA ranges in terms of the collision time and the altitude bracket.

These can also be categorized on the basis of altitude. TA being defined as 1200 ft above and below the aircraft, and RA being defined as 800 ft above and below the aircraft.

Another range has to be defined which is between the TA and the RA range. This range is just for the use of the processor and the transponder. It wont be visible to the crew. The reason being that if will be used for the tracking and path correction for each aircraft, so its relevance will be restricted to the processor only. As giving another criteria on the display can increase the complications at the crew's side.

The distance for the TA and RA ranges are calculated as follows:

TA:

$$\begin{aligned} D &= s * t & (1)\\ S &= 600\,\mathrm{kts/hr}\,(\mathrm{relativevelocity}) & (2)\\ T &= 40\,\mathrm{sec} & (3)\\ D &= 6.66\,\mathrm{kts} & (4)\end{aligned}$$

RA:

$$\begin{aligned} T &= 25\,\mathrm{sec} & (5)\\ D &= 4.16\,\mathrm{kts} & (6)\end{aligned}$$

PA(the new range):

Taking this range to be situated in the middle of these two ranges. So the distance would be 4.9 kts.

$$\begin{aligned} T &= d/s; \\ T &= 29.4\,\mathrm{sec} & (7)\end{aligned}$$

3.2. Omni Directional Maneuvering

Any aircraft entering into the PA range, will lead to the processor finding a path to avert the collision with that particular aircraft. But in this case it would be different as the path will not be restricted to only vertical maneuvering but will take the horizontal airspace in the vicinity into consideration to find the fall out path. As the air traffic in the past has grown by leaps and bounds the density of aircraft per square kts has also increased. So vertical maneuvering can be fatal at times. So a combination of vertical and horizontal movement should be used. For example, an aircraft can climb at a specified rate and at an angle too. This is the most important and essential feature of this algorithm. But to calculate where to maneuver as now the aircraft has the whole sphere around it to move, it is done step by step.

3.2.1. Decision Making

For any aircraft appearing in the PA range, it will be put in the tracking queue by the transponder. All the paths to avoid collision possible with the combination of horizontal and vertical movement are calculated. From these paths those paths are denied which would be leading to collision with other aircraft present in the specified range. So the number of paths in the set gets reduced. Now we are left with those paths which would avoid collision with aircraft A and also avoid collision with any other aircraft in the range.

From these available paths the selection of the path rests on the common path existing for both the aircraft. The processor selects the path which is would need the least deviation from the current course of the aircraft to avoid collision. This path is intimated to aircraft A, so it knows that it cannot take that path as aircraft B is taking it. If aircraft A can only take that path taken by B it tells A to change fall out path, or vice versa.

So by this we have calculated the fall out path for each aircraft in the PA region considering the other traffic present in thee same region and can become a threat. For each aircraft the fall out path will be different, and finalized before the aircraft's enter the RA region.

Any new aircraft entering the PA region is put in the queue and is all the paths already calculated are crosschecked w.r.t to this new aircraft. If any path needs change it is done and proper intimation is done.

This is the relevance of this new region as all the processing and changing is done in this. As the combinational movement requires more intricate decision making rather than just vertical movement.

3.2.2. Path Calculation

The path is calculated on the basis of the altitude, which is constantly reported by the intruder aircraft in its network word. The airspeed and climb/decent rate of own and the other aircraft are known, with this interpolation is done and the collision course is surmised. This same procedure is used to compute the fall out path.

In this the angle of climb or decent is taken into consideration. The aircraft should all be using altitude reporting transponder. Knowing their climb/decent, airspeed and heading is sufficient to predict their path. In turn, it would tell us all the possible paths which would be appropriate to avoid collision with them.

3.2.3. Display

The paths to avoid collision with all the aircraft entering in the RA region have already been calculated in the PA range, subject to the change in the other aircraft's vital data. The aircraft who change course before entering in the RA region are removed from the queue and are no longer tracked. The paths to avoid collision with the specified aircraft in the RA region are shown on the display in terms of climb/decent rate and the angle. So the crew knows the necessary action to take if that aircraft becomes a threat. To their convenience they don't have to look to avoid collision with other aircraft in the region, as it has already been taken into consideration by the processor, while calculating the path.

4. ENHANCED DATA LINK

4.1. Purpose

The purpose of the data link in the existing algorithm is only relevant when the intruder aircraft is in the RA region and has to be intimated that it should take the opposite aversion action as the own aircraft. So it is made at the point where it becomes utterly necessary to establish a distortion free communication channel between the two aircraft. The transponder is responsible for the establishment of this link.

4.2. Modification

One of the drawbacks of the system is that it doesn't send the aircraft registration number, which tells to which country does the aircraft belong. It sends the transponder i.d, which is unique for each transponder. But the aircraft registration number will enhance the threat perception and decrease the time in reacting to a potential situation. This can be attained by encoding the aircraft registration number using variable length coding (VLC) or constant length coding (CLC). It can be transmitted using a pulse code modulation (PCM). The transponder has to be responsible for this. When the aircraft come in the RA region then this link can be formed and the aircraft i.d can be visible on the crew's display. It will enhance the ability of the crew to respond to a situation.

4.3. Voice Transmission

The presence of another directional antenna can allow the formation of a voice link between the two aircraft. HF (high frequency) band can be used to carry out such kind of communication. The aircraft with the highest threat potential in the RA region will be the one with which the link will be formed. This link will include the transmission of aircraft i.d as it has been mentioned above. So at the display unit along with the action to be taken the crew can view the aircraft registration number and a voice link, which can help better analysis and coordination of the situation.

The directional antenna can be aligned in the direction where the aircraft is present. This alignment data is sent by the processor, which knows in which direction the other aircraft is present. When the antenna is aligned then the transmission can take place. When the situation with that aircraft has been averted then the antenna can be directed in any direction as no physical movement is needed, the array in that direction can be energized and it will direct the beam in that direction. So a better switching can be expected with this directional antenna. The band used is HF (high frequency) as the range is less.

The link establishing is only done via the transponder. The matter to be sent is composed by the processor. The vital aircraft statistics are transmitted on a pulse train. Along with them the aircraft i.d is also transmitted. The transponder does the necessary operation to modulate them and send it to the antenna.

5. CONCLUSION

The main points of the modified algorithm are:

1) Maneuvering using a combination of vertical and horizontal movement, which allows a better solution of a threat solution in case of a high air traffic density.

2) Transmitting the aircraft i.d along with the other vital information about the aircraft.

3) Establishing a voice link between the two aircraft in the highest threat zone. This reduces the time needed to take action and also leaves no room for a communication gap between the two aircraft in a sensitive situation.

REFERENCES

1. Allied Signals, Maintenance Manual, CAS-81 Collision Avoidance System, Ref. No. 34-45-00.
2. Honeywell, Collision Avoidance system User's Manual, ACS- 5059, Revision 5, Feb. 2000.
3. Honeywell, EGPWS Overview and Flight Operations, Oct. 2004.
4. Kennedy, H. D., "A new approach to omni directional high-gain wide-band antenna design: The TCI model 540," *Tech. Note 7, Technology for Communication International*, April 1979.
5. Kraus, J. D. and R. J. Marhefka, *Antennas for All Applications*, 3rd ed., Tata McGraw-Hill, New York, 2003.
6. Oppenheim, A. V., A. S. Willsky, and S. H. Nawab, *Signals and Systems*, 2nd ed., Pearson Education, Singapore, 2002.
7. Lathi, B. P., *Modern Digital and Analog Communication System*, 3rd ed., Oxford University Press, New York, 2005.
8. Kennedy, G. and B. Davis, *Electronic Communication Systems*, 4th ed., Mc-Graw Hill, Sept. 1992.

Design of Three-layer Circular Mushroom-like EBG Structures

S. Mahdi Moghadasi[1,2], **A. R. Attari**[1], and **M. M. Mirsalehi**[1]
[1]Electrical Engineering Department, Ferdowsi University of Mashhad, Mashhad, Iran
[2]Communications and Computer Research Center, Ferdowsi University of Mashhad, Mashhad, Iran

Abstract— In this paper two types of three-layer mushroom-like electromagnetic band-gap (EBG) surfaces with circular patches are investigated. One of them consists of a square array of circular patches and the other one consists of a triangular array of circular patches in upper and lower layers. Guidelines for designing a ground plane for low profile antenna applications are presented using the reflection phase characteristics. The effect of some parameters of the three-layer structures on the reflection phase characteristic is studied. The frequency band in which a wire antenna adjacent to the three-layer EBG surface has good matching is determined by investigating the reflection phase characteristics of the EBG ground plane.

1. INTRODUCTION

In recent years, unique properties of electromagnetic band-gap (EBG) structures have made them applicable in many antenna and microwave applications. Two main interesting features associated with EBG structures are suppression of surface waves and in-phase reflection coefficient for plane waves [1–3]. Suppression of surface waves results in higher efficiency, smoother radiation pattern, and less back lobe and side lobe levels in antenna applications [1, 2]. On the other hand, these structures can be used in design of low profile antennas because the radiating current can lie directly adjacent to the ground plane without being shorted [1, 3].

The main reason for using three-layer EBG surfaces is to obtain lower zero-reflection phase frequency in comparison with two-layer structures. This can be shown by computing the reflection phase of the structure when a normal incident plane wave is illuminated to the surface. The relation between the reflection phase characteristic of an EBG surface and the input-match frequency band of a wire antenna placed above the surface is investigated in [3]. It is shown that the frequency region where the EBG surface has a reflection phase between 45° and 135° is very close to the input-match frequency band of the low profile wire antenna witch is placed directly adjacent to the surface. Therefore, one can use the reflection phase curve to identify the input-match frequency band of the antenna. Reflection phase of a periodic surface can be computed using one unit cell of the structure with periodic boundary condition as described in [4].

In this paper we show that a three-layer EBG surface has significantly lower zero-reflection phase frequency comparing to a two-layer structure and then we investigate the effect of the three-layer structures parameters on the reflection phase characteristic. By means of these curves, design guidelines for a three-layer circular mushroom-like EBG ground plane are obtained. Finally, three different configurations for three-layer EBG structures compared based on their reflection phase characteristics.

2. THREE-LAYER CIRCULAR MUSHROOM-LIKE EBG SURFACES

Figure 1 depicts two types of three-layer circular mushroom-like EBG surfaces. Patches radius in the upper and lower layers are r_t and r_b, respectively. In this investigation, the radius of circular patches in both layers have the same values ($r_t = r_b$) and the gap size is represented by g. In Fig. 1(a) the circular patches in both layers are located in a square array while in Fig. 1(b) a triangular array of circular patches forms a three-layer EBG surface. The dielectric constants of the upper and lower substrates are indicated by ε_{r1} and ε_{r2}, respectively. The thicknesses of upper and lower substrates are t and h.

The reflection phase of an EBG surface when a normal incident plane wave illuminates to the surface is investigated. Here, three cases are considered. First, the reflection phase of a two-layer

Table 1: The parameters in design of two- and three-layer EBG structures.

t	h	ε_{r1}	ε_{r2}	$r_t = t_b = r$	g
0.1 mm	3 mm	3.25	4.4	4 mm	0.5 mm

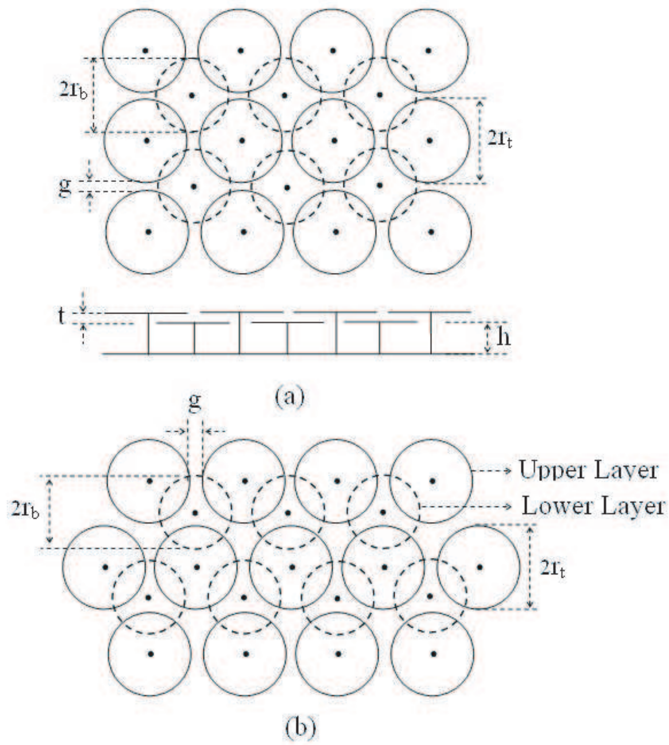

Figure 1: Three-layer mushroom-like EBG surfaces: (a) Square array of circular patches, (b) Triangular array of circular patches.

circular EBG surface is computed and illustrated in Fig. 2(a). Circular patches with radius of r are just printed on the upper layer and the height of patches from the ground plane is $t + h$. The values of parameters for this design are shown in Table 1. The reflection phase characteristics of three-layer EBG surfaces shown in Fig. 1 are illustrated in Fig. 2(b). For both configurations of three-layer EBG structures the radius of circular patches in both layers are the same as the radius of patches in two-layer structure, i.e., r. As can be seen, the zero-reflection phase frequencies of both three-layer structures are significantly lower than that of the two-layer structure. Also, the EBG structure with triangular array of circular patches has lower zero-reflection phase frequency comparing to the EBG structure with square array of circular patches.

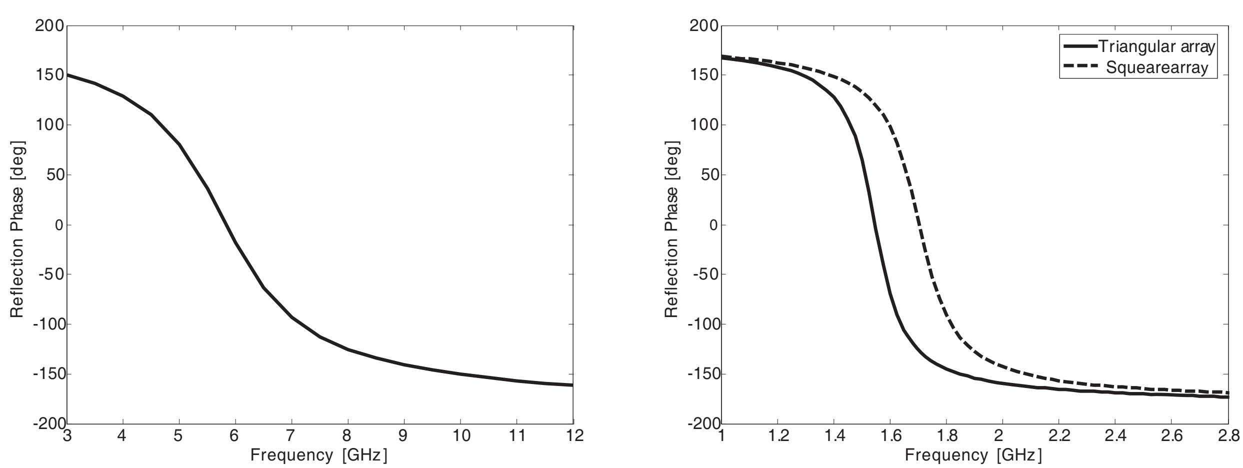

Figure 2: (a) Reflection phase characteristic of a two-layer EBG surface, (b) Reflection phase characteristics of three-layer EBG surfaces.

3. PARAMETRIC STUDY

Effects of various parameters in a two-layer EBG surface on the reflection phase characteristic when a normal incident plane wave illuminates to the surface have been previously studied [3]. Studies on three-layer EBG structures show that, when the dielectric constant or thickness of the lower layer increases the zero-reflection phase frequency would decrease. This behavior can be seen in two-layer structures. Also, when the radius of patches increases or when the gap size decreases, zero-reflection phase frequency of the structure reduces. This is, also, similar to the behavior of

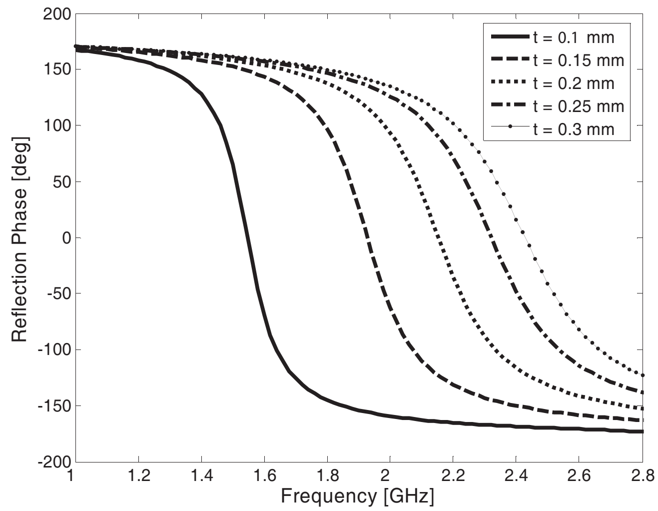

Figure 3: Effect of the upper layer thickness on the reflection phase characteristic.

(a) (b) (c)

Figure 4: EBG surfaces with three different configurations.

two-layer EBG structures. In a triangular array three-layer structure, the effect of the upper layer thickness on the reflection phase characteristic is shown in Fig. 3. This parameter can noticeably change the zero-reflection phase frequency of the structure. As mentioned before, the frequency region where the EBG surface has a reflection phase between 45° and 135° is very close to the input-match frequency band of the low profile wire antenna using the surface as a ground plane. Therefore, to design an EBG surface as a ground plane for an antenna with a specific input-match frequency band, one should consider the reflection phase characteristics of the structure.

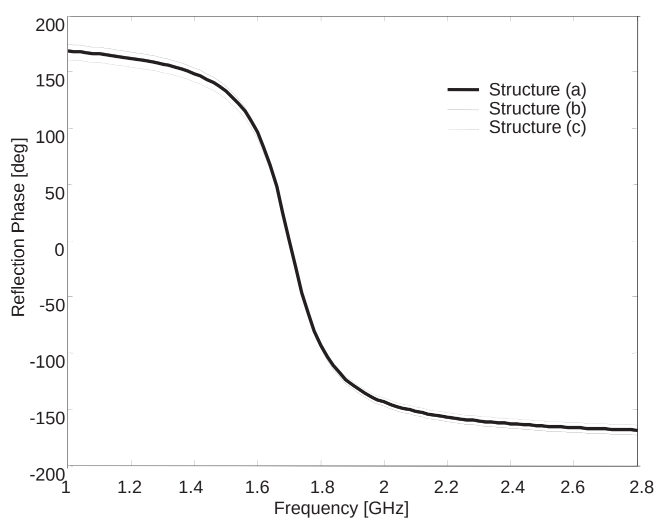

Figure 5: The reflection phase characteristics of EBG surfaces in Fig. 4.

4. THREE CONFIGURATIONS FOR THREE-LAYER EBG SURFACES

Implementation of vias in an EBG structure is not an easy process and reduction in the number of them can decrease the total cost of manufacturing. In Fig. 4 three different configurations for a three-layer EBG structure are illustrated. The number of vias in configurations (b) or (c) is reduced by a factor of two in comparison with the configuration (a). As illustrated in Fig. 5, the reflection phase characteristics of the three structures are similar. Therefore, any of the two configurations (b) or (c) can be used instead of the configuration (a). Although, there are some differences between the three configurations when the band-gap of the structure is considered.

5. CONCLUSIONS

Two low frequency three-layer EBG structures are introduced in this paper and compared with a two-layer EBG structure. One consists of a square array of circular patches in both upper and lower layers. The other one is formed by a triangular array of circular patches. It is shown that both of them have significantly lower zero-reflection phase frequency comparing to a two-layer structure. Also, it is shown that the triangular array structure has lower zero-reflection phase frequency with respect to the square array structure. Parametric study of a three layer structure is presented. Also, two different configurations of the EBG surface for reducing the number of vias are introduced.

REFERENCES

1. Engheta, N. and R. W. Ziolkowski, *Metamaterials Physics and Engineering Explorations*, Wiley, New York, 2006.
2. Sievenpiper, D., L. Zhang, R. F. J. Broas, N. G. Alexopolus, and E. Yablonovitch, "High-impedance electromagnetic surfaces with a forbidden frequency band," *IEEE Trans. Microwave Theory Tech.*, Vol. 47, 2059–2074, Nov. 1999.
3. Yang, F. and Y. Rahmat-Samii, "Reflection phase characterizations of the EBG ground plane for low profile wire antenna applications," *IEEE Trans. Antennas Propag.*, Vol. 51, 2691–2703, Oct. 2003.
4. Remski, R., "Analysis of PBG surfaces using Ansoft HFSS," *Microwave J.*, Vol. 43, No. 9, 190–198, Sept. 2000.

Bandwidth Enhancement of Single-feed Circularly Polarized Equilateral Triangular Microstrip Antenna

Sara Sadat Karimabadi[1], **Yalda Mohsenzadeh**[1]
Amir Reza Attari[1], **and S. Mahdi Moghadasi**[1,2]

[1]Electrical Engineering Department, Ferdowsi University of Mashhad, Iran
[2]Communications and Computer Research Center, Ferdowsi University of Mashhad, Iran

Abstract— This paper presents a novel method of increasing impedance and axial ratio (AR) bandwidth of a single feed circularly polarized tip-truncated equilateral triangular microstrip antenna (ETMSA). Tip-truncated ETMSA has been previously introduced in the literature; in this new method by cutting a small equilateral triangular slot near the modified vertex, the impedance and AR bandwidths are increased more than two times.

1. INTRODUCTION

The main advantage of single-feed circularly polarized microstrip antennas is their simple structures that do not require an external polarizer [1]. Conventional designs of single-feed microstrip antennas for circular polarization (CP) are usually achieved by truncating patch corners of a square patch, using nearly square or nearly circular patches, cutting a diagonal slot in the square or circular patches, protruding or inserting a pair of symmetric perturbation elements at the boundary of a circular patch [1, 2]. Presently, typical designs of circularly polarized triangular microstrip antennas are using a nearly equilateral-triangular patch or an equilateral-triangular patch with a slit inserted at the patch edge [3].

On the other hand, the main weakness of an ordinary microstrip antenna is its narrow bandwidth. There are several ways to overcome this problem. A well known way is based on the introduction of an additional stacked [4, 5] or coupled patch [6, 7]. This makes the configuration more complex. As a consequence the array becomes more costly in production especially in the case of stacked patches. Also the dimension of the array increases. An alternative way consists in the use of specially shaped patches with slits [8, 9] and the rectangular patches with slot [10]. We have considered the slotted tip-truncated equilateral triangular patch because it has a smaller patch size at a given frequency, as compared to square and circular microstrip antennas, and has a good CP operation.

It is shown that by embedding a small equilateral triangular slot near the modified vertex of a tip-truncated equilateral triangular microstrip antenna, an impedance and AR bandwidth enhancement of about two times can be achieved. In the following section, details of the proposed CP designs of slotted triangular microstrip antennas are described and simulation results of the CP performance are presented.

2. ANTENNA CONFIGURATION

The geometry of the present antenna is consisting of a tip-truncated equilateral triangular patch [11] which yields circularly polarization (Fig. 1). The triangular patch with side length of L is printed on a substrate of thickness h and dielectric constant ε_r. By cutting a small equilateral triangular slot of side length b at the triangular patch in the height of h_1 from the bottom side of the patch (Fig. 2), AR bandwidth is improved more than two times.

Also, by further selecting a proper slot length and feeding the patch at a suitable position, two near-degenerate orthogonal resonant modes of equal amplitudes and 90° phase difference, and therefore a CP operation can be obtained. As depicted in Fig. 2, for the feed position at point B, a right-hand CP operation is obtained and by feeding the patch at point A (the mirror image of point B with respect to the centerline of the triangular patch) a left-hand CP is achieved.

3. SIMULATION RESULTS

In this section, simulation results are presented for the geometry shown in Fig. 2. As it will be shown, by using this geometry the AR bandwidth of antenna is increased in comparison to the geometry shown in Fig. 1. First, consider the tip-truncated triangular patch with parameters given in Fig. 1.

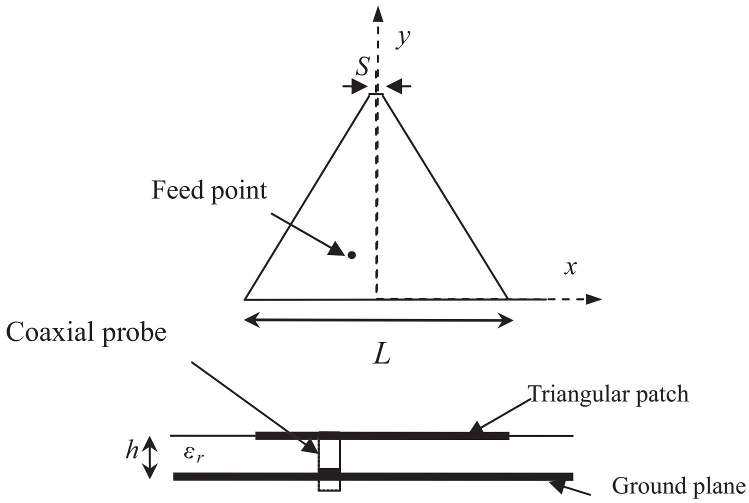

Figure 1: Geometry of circularly polarized tip-truncated equilateral triangular microstrip antenna. ($L = 36$ mm, $S = 2$ mm, $x_f = -3$ mm, $y_f = 7$ mm, $h = 1.52$ mm, $\varepsilon_r = 3.5$, $\tan\delta = 0.00018$)

It is found that by adjusting the inserted slit length (S) to be 2 mm, the CP operation can be obtained. Now, by cutting an equilateral triangular slot with dimensions shown in Fig. 2, a broadband CP operation is achieved. The simulated axial ratio versus frequency is presented in Fig. 3(b). The center frequency, defined as the frequency with a minimum axial ratio, is at 2.895 GHz and the CP bandwidth, determined from −3 dB axial ratio, is about 16.2834 MHz. For comparison, the results are also listed in Table 1 in which the proposed antenna is compared with the reference antenna shown in Fig. 1. The radiation patterns in two orthogonal planes are also computed. Fig. 4 plots the radiation patterns of proposed antenna at 2.895 MHz. As shown in this figure, a good left-hand CP operation is obtained.

Table 1: Comparison between the proposed antenna (with parameters given in Fig. 2) and the reference antenna (with parameters given in Fig. 1).

	Center frequency	Bandwidth VSWR < 2	CP Bandwidth AR $< -3dB$
Proposed antenna	2.895 GHZ	121.1303 MHZ	16.2834 MHZ
Reference antenna	2.902 GHZ	55.99 MHZ	7.7 MHZ

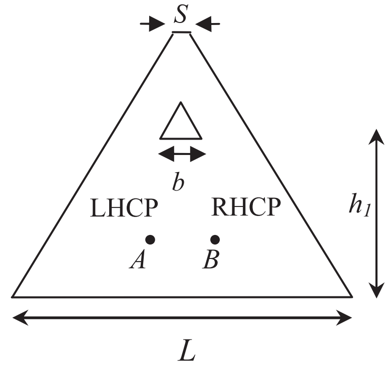

Figure 2: Geometry of the proposed antenna structure for increasing the axial ratio bandwidth. ($b = 4.8$ mm, $h_1 = 22$ mm, $x_f = -3$ mm, $y_f = 7$ mm)

From the simulation result listed in Table 2, it is seen that AR and VSWR bandwidth of proposed antenna decrease with decreasing the slot size. Also, the center frequency for CP operation

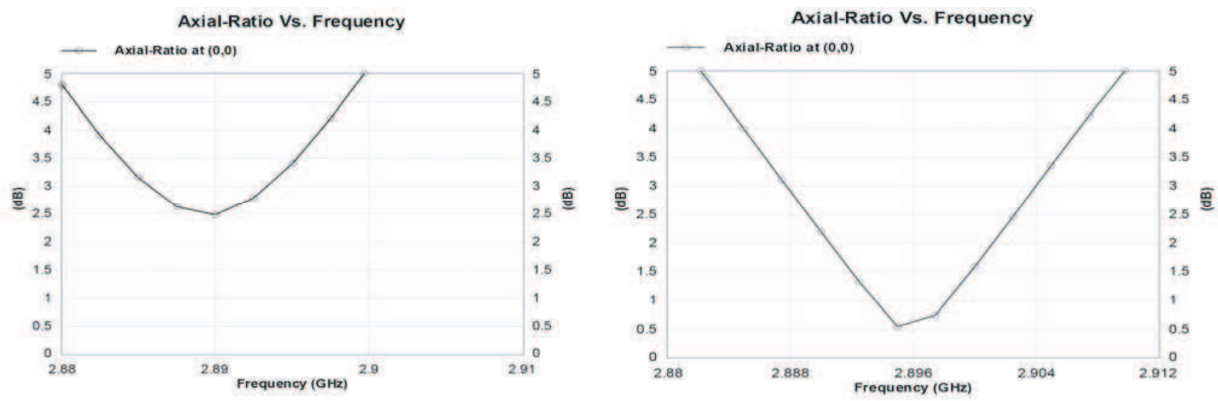

(a) (b)

Figure 3: Simulated axial ratio of (a) reference antenna given in Fig. 1 and (b) proposed antenna shown in Fig. 2.

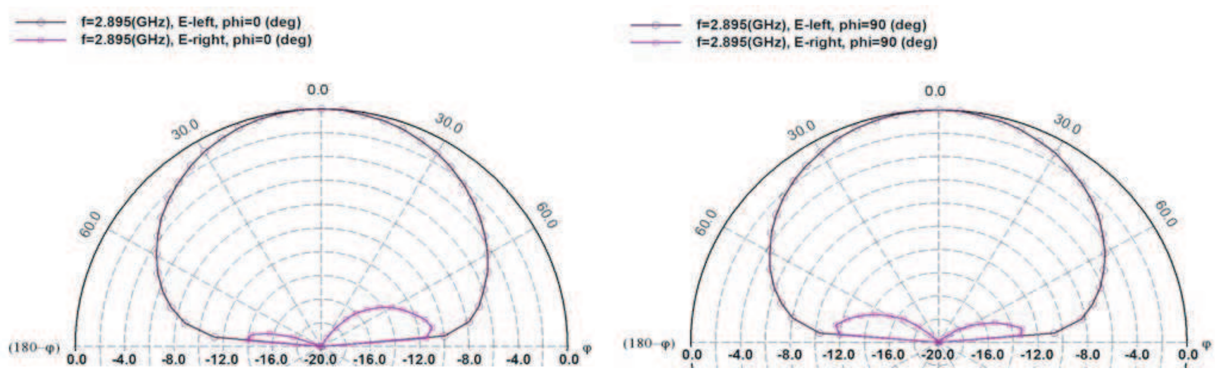

Figure 4: Simulated radiation pattern of proposed antenna in two orthogonal planes at $f = 2.895$ GHz.

of antenna decreases with decreasing h_1. In all these simulations other parameters of proposed antenna, were taken constant.

Table 2: Result of the proposed circularly polarized triangular microstrip antenna with various length and position of the triangular slot (Antenna parameters given in Fig. 1).

b (mm)	Center frequency (GHZ)	VSWR BW (MHZ)	AR BW (MHZ)
5	2.89	72.7122	16.2072
4.8	2.895	71.1303	16.2834
4.6	2.898	68.6034	16.1381
4.4	2.901	66.8675	15.83

h_1 (mm)	Center frequency (GHZ)	VSWR BW (MHZ)	AR BW (MHZ)
22.2	2.9	71.8508	16.2892
22	2.895	71.1303	16.2834
21.8	2.89	69.6429	16.324
21.6	2.884	68.4913	16.0849

4. CONCLUSIONS

A new design of single-feed circularly polarized microstrip antenna using slotted tip-truncated equilateral triangular patch has been proposed. The proposed structure has been simulated by using the IE3D software. The optimum feed position has been determined for good impedance matching. In comparison with an ordinary tip-truncated equilateral triangular patch, the AR bandwidth of our proposed structure is improved more than two times.

REFERENCES

1. Kumar, G. and K. P. Ray, *Broadband Microstrip Antennas*, Artech House, 2003.
2. Sharma, P. C. and K. C. Gupta, "Analysis and optimized design of single feed circularly polarized microstrip antennas," *IEEE Transactions on Antennas and Propagation*, Vol. 31, 949–955, 1983.
3. Lu, J. H., C. L. Tang, and K. L. Wong, "Circular polarization design of a single-feed equilateral-triangular microstrip antenna," *Electron Letters*, Vol. 34, 319–321, 1998.
4. Lee, R. Q., K. F. Lee, and J. Bobinchak, "Characteristics of a two-layer electromagnetically coupled rectangular patch antenna," *Electronic Letters*, Vol. 23, No. 20, 1070–1072, 1987.
5. Croq, F. and D. M. Pozar, "Millimeter-wave design of wide-band aperture-coupled stacked microstrip antennas," *IEEE Transactions on Antennas and Propagation*, Vol. 39, No. 12, 1770–1776, 1991.
6. Kumar, G. and K. C. Gupta, "Directly coupled multiple resonator wide-band microstrip antenna," *IEEE Transactions on Antennas and Propagation*, Vol. 33, No. 6, 588–593, 1985.
7. Celenet, M. and L. Shafai, "Wideband single layer microstrip antenna for array applications," *Electronic Letters*, Vol. 35, No. 16, 1292–1293, 1999.
8. Yang, F., X. X. Zhang, and Y. Samii, "Wide-band E-shaped patch antennas for wireless communications," *IEEE Transactions on Antennas and Propagation*, Vol. 49, No. 7, 1094–1100, 2001.
9. Wong, K. L. and W. H. Hsu, "A broad-band rectangular patch antennas with a pair of wide slits," *IEEE Transactions on Antennas and Propagation*, Vol. 49, No. 9, 1345–1347, 2001.
10. Huynh, T. and K. F. Lee, "Single-layer single patch wideband microstrip antennas," *Electronic Letters*, Vol. 31, No. 16, 1310–1312, 1995.
11. Tang, C. L., J. H. Lu, and K. L. Wong, "Circularly polarized equilateral triangular microstrip antenna with truncated tip," *Electronic Letters*, Vol. 34, 1277–1278, 1998.

Design of Ultra-wideband Monopole Antenna with Band-notched and GPS Circular Polarization Characteristics

Han-Nien Lin[1], **Che-Min Shao**[1], **and Jer-Long Chen**[2]

[1]Department of Communications Engineering, Feng-Chia University, Taiwan, R. O. C.
[2]Department of Electrical Engineering, National Taiwan Ocean University, Taiwan, R. O. C.

Abstract— In this paper, a printed disk monopole antenna with coplanar waveguide (CPW) feeder for ultra-wideband (UWB) system and global positioning system (GPS) application is proposed. The antenna is implemented with the conventional radiating disk element that would have benefit on manufacturing process and thus being cost-effective [5, 6]. In addition, it utilizes annular stub to reduce current distribution of the right-hand side radiating element to achieve the circular polarization (CP) [2] for GPS application around 1.575 GHz. The impedance bandwidth of the proposed antenna can range from 3 GHz to 11 GHz for VSWR < 2 with the band rejection characteristic in the frequency band from 4.8 GHz to 6 GHz. Since the antenna presents a notched band from 4.8 to 6 GHz, it can prevent the RF interference from the wireless local area network (WLAN) 802.11a [1]. This proposed antenna shows a monopole-like radiation pattern with good agreement being obtained between the simulation and experiment results.

1. INTRODUCTION

In recent years, Ultra-wideband (UWB) system has been widely used and attracted much attention for short-range wireless communication systems because of its advantages on manufacturing process, cost-effective, and high data rate. However, the frequency band (between 3.1 and 10.6 GHz) assigned for UWB system by FCC will cause interference to the existing wireless communication systems, such as the wireless local area network (WLAN) of IEEE 802.11a operating in both 5.15–5.35 GHz and 5.725–5.825 GHz bands. Therefore, the ultra-wideband antenna with a band-notched becomes more and more popular. In this paper, the WLAN band-stop characteristic is realized by cutting an inverse U-shape slot on the radiating disk [3, 4].

In addition, the circular polarization characteristics for GPS band will also be designed in the proposed antenna, because the satellite and terrestrial point-to-point communication systems require circular polarization wave propagation to increase long-distance transmission performance [2]. In this paper, a novel circular polarization GPS monopole antenna is presented, and the characteristics of axial ratio (AR) can be optimized by tuning the length of stub and the spacing between the stub and radiating element. The optimal AR will be achieved at 1.575 GHz, while AR < 3 can be obtained for the frequency range from 1.55 to 1.58 GHz. Moreover, since many planar ultra-wideband monopole antennas changed the ground structure and feed to increase impedance bandwidth [1, 3, 4, 8], this proposed antenna is designed to provide an enhanced impedance bandwidth by modifying the edges of the ground. The band-stop characteristic of the antenna is realized by cutting a U-shape slot on the radiating disk and the frequency of stop-band can be adjusted by changing the length and width of the inserted slot. The measured reflection coefficient of the proposed antenna for $S_{11} \leqq -10$ dB ranges from 1.4 GHz to 11 GHz, and the stop-band with $S_{11} \geqq -10$ dB is obtained from 4.8 GHz to 5.98 GHz. This proposed antenna has shown omni-directional pattern over the whole operating bandwidth.

2. ANTENNA DESIGN

The structure of the proposed monopole is shown in Fig. 1. The monopole is printed on a single layer FR-4 substrate with thickness of 1.6 mm (h) and relative permittivity $\varepsilon_r = 4.4$. A 50-Ω CPW transmission line, which consists of a signal strip thickness of 3.5 mm and a gap spacing 0.4 mm between the signal strip and the coplanar ground plane, is used for feeding the antenna. Moreover, to obtain impedance matching between the feeding and the radiation element, the signal strip width of the upper-side will be cut off from radiating disk element. There are two equal finite ground planes with each side of 30.85 mm long and 19 mm wide, but the edges of the ground are modified as an arc with the arc length of 16.23 mm. The radiation element is a disk patch, where R denotes the radius of the circle with value of 25 mm. The gap between the radiation element and the ground plane is 0.52 mm. The dimension of the antenna is 72 mm $\times$ 66 mm.

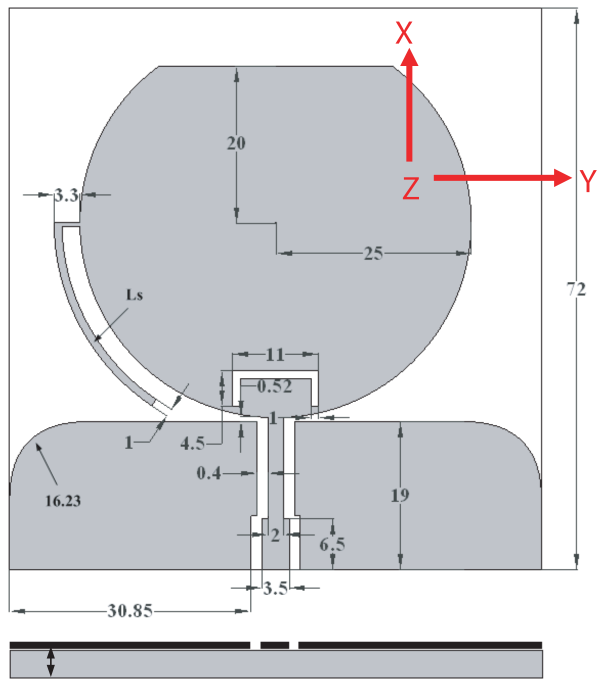

Figure 1: Geometry of proposed ultra-wideband monopole antenna with band-notched and circular polarization characteristics (dimensions: mm).

The annular stub on the right-hand side of radiating element is designed to achieve circular polarization for GPS application at 1.575 GHz. The length of the stub is Ls, and it can be used for tuning optimal circular polarization performance. When the length of the annular stub is 27.65 mm, the A.R. of 0.8 is obtained. The A.R < 3 is required for the GPS frequency range. In this paper we have etched an inverse U-shape slot with mean length L on the UWB antenna to achieve band-notched characteristic. Considering the slot as a half wavelength resonator, the resonant frequency (f_r) can thus be expressed as [7]:

$$f_r = \frac{c}{2L}\sqrt{\frac{2}{\varepsilon_r + 1}} \tag{1}$$

where c is the speed of light in free space, and ε_r is the relative permittivity of the substrate material. The inverse U-shape slot of total length 20 mm is shown in Fig. 1. The frequency of

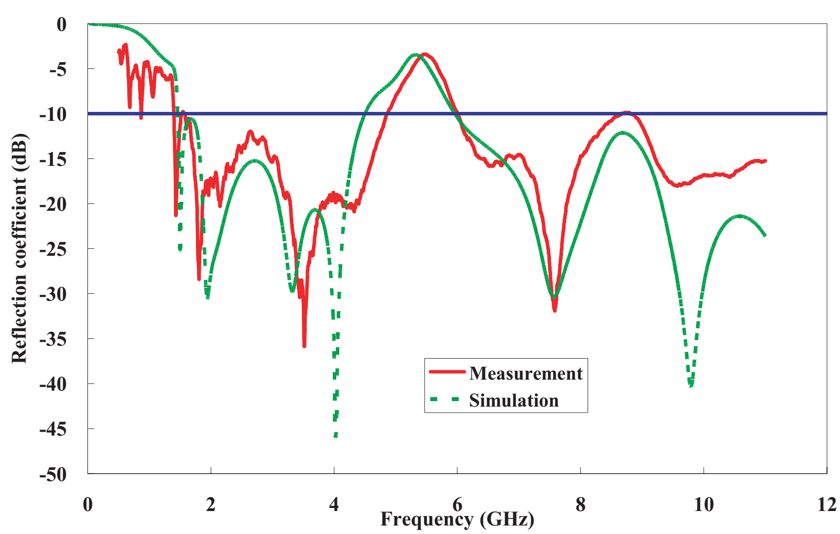

Figure 2: Reflection coefficient of simulation and measurement for the proposed antenna.

band-notched characteristic from 4.8 GHz to 5.98 GHz is obtained from measurement, while the simulation result is from 4.52 GHz to 5.92 GHz. A good agreement has been obtained between both the simulation and measurement results.

3. RESULT AND DISCUSSION

Figure 2 shows the reflection coefficient of the simulation and measurement results for the proposed antenna shown in Fig. 1. Simulation was done by using the IE3D software, while Agilent E8362B network analyzer was used to measure the frequency-domain performances. It is clearly observed that wide operating bandwidth from 1.4 GHz to 11 GHz with reflection coefficient $\leqq -10$ dB is obtained, and band-stop characteristic from 4.8 GHz to 5.98 GHz for reflection coefficient $\geqq -10$ dB is obtained from measurement. The plot shows similar trend between the simulation and measurement results over the whole operating bandwidth, except for slight frequency shift and discrepancy due to the probable deviation on the substrate permittivity at high frequency. Otherwise, a good agreement is achieved.

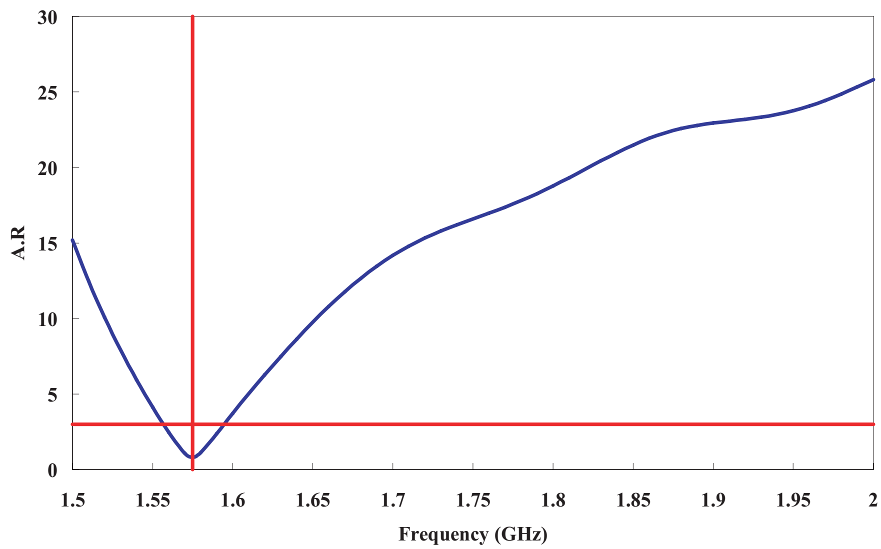

(a)

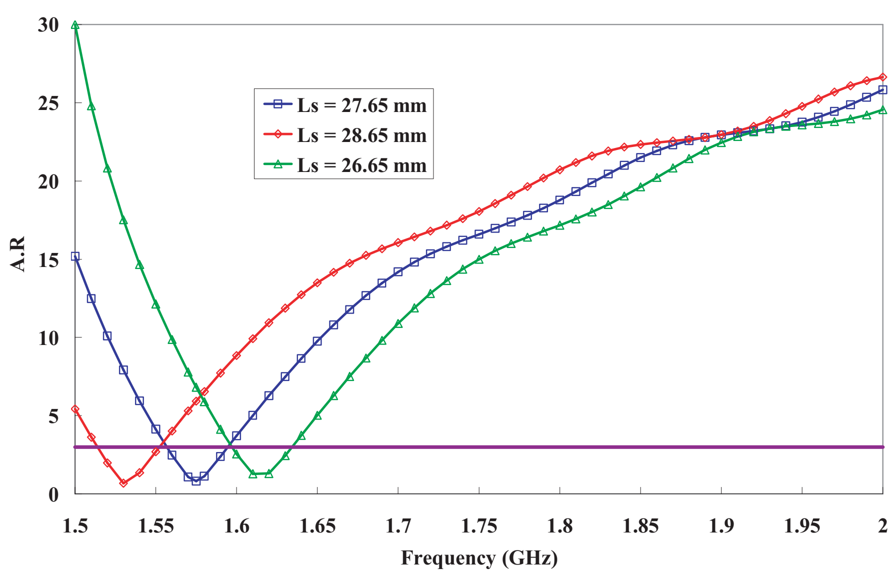

(b)

Figure 3: Simulated A.R for the proposed antenna. (a) Simulated A.R for the proposed antenna with Ls = 27.65 mm. (b) Simulated A.R for the proposed antenna with various length Ls.

Figure 3 shows the effect on A.R by tuning the annular stub on right-hand side of radiating element to Ls = 27.65, 28.65 and 26.65 mm, respectively. The simulated result of A.R. for GPS application at 1.575 GHz about 0.8 is shown in Fig. 3(a). The various length Ls will cause the A.R to change with frequency shift. This is due to the fact that increasing the annular stub of Ls will lengthen the current path, and thus excite the lower resonant mode which does reduce current distributions on right-hand side of radiating element for those lower frequencies. On the other hand, decreasing the annular stub length Ls will reduce the current path, and thus excite the higher resonant mode which does reduce current distribution on right-hand side of radiating element for higher frequency.

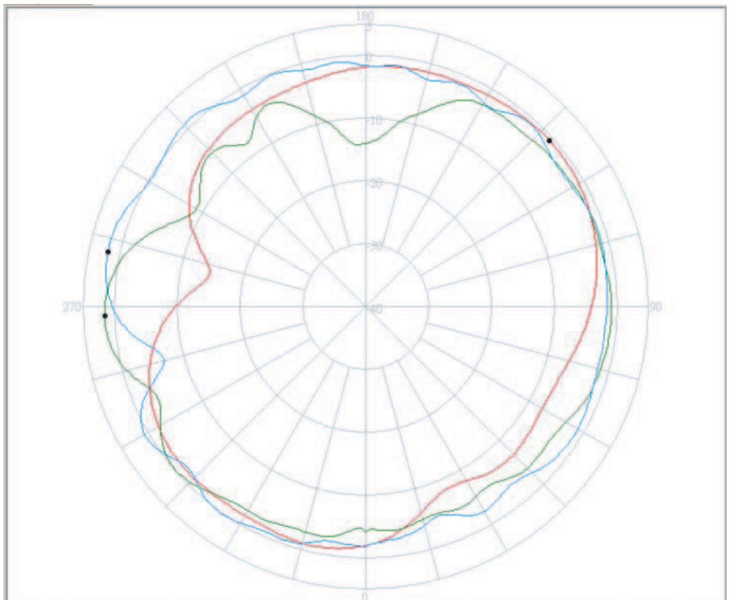

Pattern		Model Name	Test Mode	Freq(MHz)	Peak Gain(dBi)	Peak angle	Avg. Gain(dBi)	Source Polar.	Date	PAG
1		SPV	XY_x-y	1575.00	-0.56	132.00	-3.24	V+H	2007/10/15	-7.14
2		SPV	XZ_z-x	1575.00	1.64	272.00	-2.81	V+H	2007/10/15	-5.71
3		SPV	YZ_y-z	1575.00	2.01	258.00	-1.06	V+H	2007/10/15	-2.23

(a)

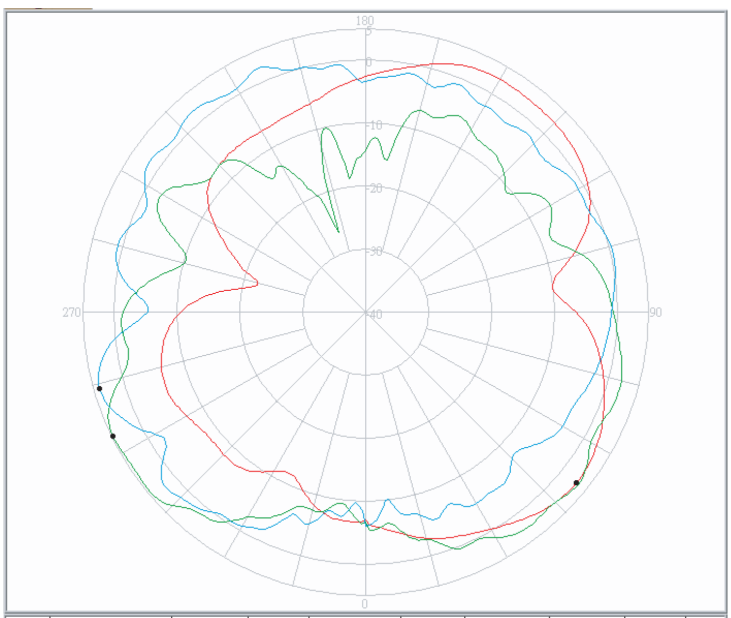

Pattern		Model Name	Test Mode	Freq(MHz)	Peak Gain(dBi)	Peak angle	Avg. Gain(dBi)	Source Polar.	Date	PAG
1		SPV	XY_x-y	3000.00	3.14	51.00	-2.08	V+H	2007/10/15	-8.48
2		SPV	XZ_z-x	3000.00	4.78	296.00	-1.22	V+H	2007/10/15	-8.70
3		SPV	YZ_y-z	3000.00	4.01	286.00	-0.93	V+H	2007/10/15	-5.02

(b)

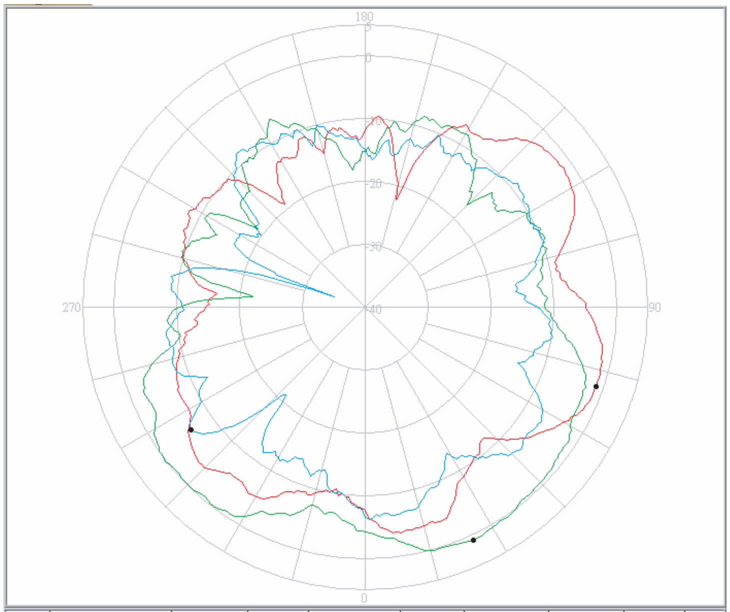

Pattern		Model Name	Test Mode	Freq(MHz)	Peak Gain(dBi)	Peak angle	Avg. Gain(dBi)	Source Polar.	Date	PAG
1		SPV	XY_x-y	5500.00	-1.05	71.00	-6.39	V+H	2007/10/15	-11.64
2		SPV	XZ_z-x	5500.00	0.92	25.00	-4.57	V+H	2007/10/15	-11.93
3		SPV	YZ_y-z	5500.00	-6.07	305.00	-10.34	V+H	2007/10/15	-13.23

(c)

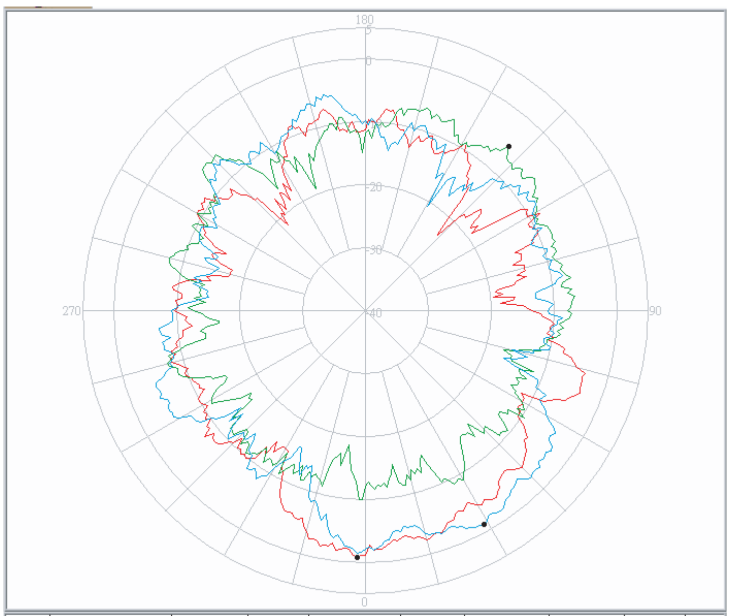

Pattern		Model Name	Test Mode	Freq(MHz)	Peak Gain(dBi)	Peak angle	Avg. Gain(dBi)	Source Polar.	Date	PAG
1		SPV	XY_x-y	8000.00	-0.77	358.00	-7.82	V+H	2007/10/15	-13.57
2		SPV	XZ_z-x	8000.00	-5.31	139.00	-10.08	V+H	2007/10/15	-13.44
3		SPV	YZ_y-z	8000.00	-1.15	29.00	-7.20	V+H	2007/10/15	-12.26

(d)

Figure 4: Measured radiation patterns for proposed antenna in the x-y plane, x-z plane, and y-z plane for different frequencies. (a) 1.575 GHz. (b) 3 GHz. (c) 5.5 GHz. (d) 8 GHz.

Typical radiation characteristics of the frequencies over the whole operating band for the proposed antenna are obtained. The measured radiation patterns are shown in Fig. 4, which include the co-polarization in the x-y plane, x-z plane, and y-z plane for the frequencies of 1.575 GHz, 3 GHz, 5.5 GHz, and 8 GHz, respectively. Similar to a monopole antenna with a good omni-directional pattern in the azimuth plane, the measured patterns of the proposed antenna are all nearly omni-directional in the x-y plane, x-z plane, and y-z plane. The radiation characteristic is degraded around 5.5 GHz (see Fig. 4(c)) as expected because of the resulted band-notched characteristic. While around 8 GHz (see Fig. 4(d)), the undesirable radiation characteristic might be probably due to the deviation of the substrate permittivity and therefore slightly impedance mismatching.

4. CONCLUSION

A novel ultra-wideband monopole antenna with band-notched characteristic and circular polarization characteristics is proposed in this paper. It presents a band-notch performance at the band of WLAN 802.11a, and the circular polarization for GPS application at 1.575 GHz. The circular polarization characteristic can also be tuned by adjusting the length of annular stub Ls. The measured reflection coefficient $\leqq -10$ dB is obtained from 1.4 GHz to 11 GHz, and the band-stop bandwidth for reflection coefficient $\geqq -10$ dB is obtained from 4.8 GHz to 5.98 GHz. The far-field radiation patterns measured are all nearly omni-directional. A good agreement has been achieved between the simulation and measurement results.

REFERENCES

1. Qu, S.-W., J.-L. Li, and Q. Xue, "A band-notched ultrawideband printed monopole antenna," *IEEE Antennas and Wireless Propagation Letters*, Vol. 5, 2006.
2. Toh, B. Y., R. Cahill, and V. F. Fusco, "Understanding and measuring circular polarization," *IEEE Transactions on Education*, Vol. 46, No. 3, August 2003.
3. Lee, C.-M., T.-C. Yo, C.-H. Luo, W.-S. Chen, C.-H. Tu, and Y.-Z. Juang, "Ultra-wideband printed disk monopole antenna with dual-band notched functions," *Wireless and Microwave Technology Conference, 2006, WAMICON '06, IEEE Annual*, 1–4, Dec. 4–5, 2006.
4. Roh, Y., K. Chung, and J. Choi, "Design of a microstrip-fed ultra-wideband monopole antenna having band rejection characteristic," *IEEE Antennas and Propagation Society International Symposium, 2005*, Vol. 2B, 556–559, July 3–8, 2005.
5. Liang, J., L. Guo, C. C. Chiau, and X. Chen, "CPW-fed circular disc monopole antenna for UWB applications," *IEEE International Workshop on Antenna Technology: Small Antennas and Novel Metamaterials, IWAT 2005*, 505–508, March 7–9, 2005.
6. Liang, J., C. C. Chiau, X. Chen, and C. G. Parini, "CPW-fed circular ring monopole antenna," *IEEE Antennas and Propagation Society International Symposium, 2005*, Vol. 2A, 500–503, July 3–8, 2005.
7. Dissanayake, T. and K. P. Esselle, "Design of slot loaded band-notched UWB antennas," *IEEE Antennas and Propagation Society International Symposium, 2005*, Vol. 1B, 545–548, 2005.
8. Wu, Q., R. Jin, J. Geng, and M. Ding, "Compact CPW-fed quasi-circular monopole with very wide bandwidth," *Electronics Letters*, Vol. 43, Issue 2, 69–70, January 18, 2007.

Small Antenna Measurement Facilities

Guan-Yu Chen[1], **Jwo-Shiun Sun**[1], **Cheng-Hung Lin**[2], **Kwong-Kau Tiong**[2], **and Y. D. Chen**[3]

[1]Department of Electronic Engineering, National Taipei University of Technology, Taiwan
[2]Department of Electrical Engineering, National Taiwan Ocean University, Taiwan
[3]Antenna and EMC Laboratory, High Tech Computer Corp. (HTC), Taiwan

Abstract— The mobile phone under test of far-field range testing has been the plan (Fig. 1) at the Cellular Telecommunications & Internet Association (CTIA) certification program test requirements for performing radiated power and receiver performance measurement.

1. SPHERICAL ANTENNA MEASUREMENT

In the US, the Certification Program of the CTIA-The Wireless Association was the first organization to publish a test plan for Over-The-Air (OTA) testing of mobile terminals. During the last few years there has been significant progress towards developing standardized testing methods for wireless devices. A key element in such testing is the accurate evaluation of radiated performance while operating in the respective communications. Such testing is commonly referred to as testing and is becoming a mandatory part of the product certification required by most network operators. In those papers [1–8], facilities of mobile phone measurement have recently commissioned a spherical far-field measurement system (Fig. 2). In this paper describes a spherical antenna measurement system that addresses the challenges in testing antennas for wireless communications. It is a 3D system for measuring low gain antennas and is well matched for PDA Phone or wireless antenna testing. It has effectively demonstrated testing and characterization of far-field performance, CTIA Over-The-Air (OTA) performance data, radiated power (EIRP), and sensitivity (EIS). In passive mode measurements of antennas are performed by a vector network analyzer. It provides radiation pattern data in any polarization, as well as antenna efficiency. In system mode measurements, commonly referred to as OTA Performance Testing, of mobile phones and other cellular terminals can be performed. It is connected to a radio communications tester (Agilent 8960). The communications tester sets up a phone call through the 3D polarization scanning, enabling measurements of radiated transmitter power (EIRP) and receiver sensitivity (EIS) over the entire spherical measurement surface surrounding the mobile phone.

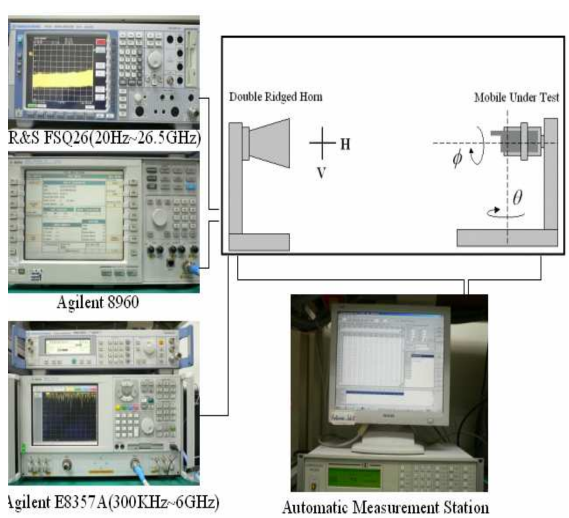

Figure 1: The 3D measurement system and wireless system networking.

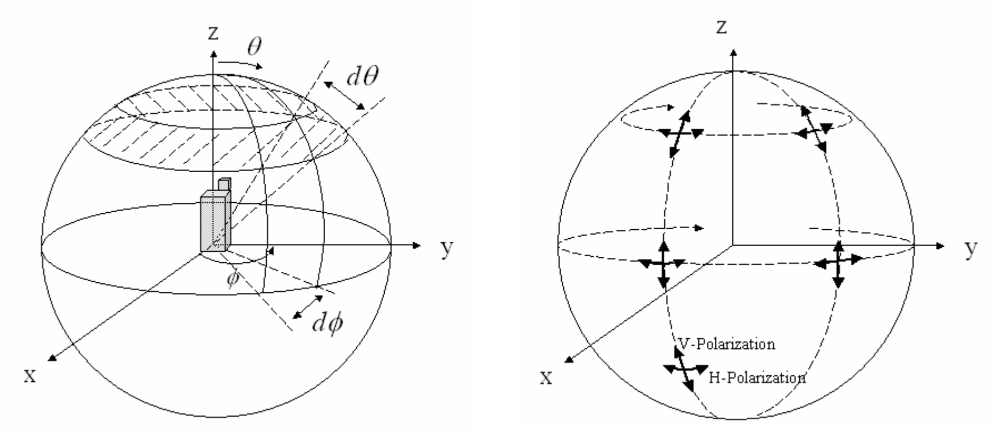

Figure 2: Spherical coordinates and field scanning.

2. CONCLUSIONS

The low profile far-field spherical scan system provides significant advantages over the older far-field testing including elimination of problem of simple theta and phi rotary axis with indoor far-field range testing, complete measurement characterization of the antenna, and improved accuracy. This paper will discuss the antenna and wireless system integration tested with the TRP/TIS and spherical antenna measurement for far-field system, and the results being achieved.

ACKNOWLEDGMENT

The authors acknowledge the Antenna and Wireless System Integration Department of High Tech Computer, Corp. (HTC), Taiwan for sport the wireless technique and measurement environment.

REFERENCES

1. Chen, G. Y., S. Y. Huang, W. F. Yen, J. S. Sun, Y. D. Chen, C. H. Lin, J. Y. Yang, and C. Y. Lin, "The spherical antenna measurement and spherical absorption rate (SAR) for near field radiation evaluation," *2005 Asia Pacific Symposium on EMC (2005 APEMC)*, 128–135, Taipei, Taiwan, Dec. 2005.
2. Chen, G. Y., J. S. Sun, C. J. Huang, S. Y. Huang, Y. T. Chung, K. L. Wu, Y. D. Chen, C. H. Lin, and J. Y. Yang, "The 3D far-field antenna system for total radiation efficiency, mean effective gain and multi-input multi-output measurement operation," *2006 National Symposium on Telecommunications (2006 NST)*, 143, Kaohsiung, Taiwan, Dec. 2006.
3. Chen, G. Y., J. S. Sun, and Y. D. Chen, "The 3D far-field antenna measurement technology for radiation efficiency, mean effective gain and diversity antenna operation," *2006 The 7th International Symposium on Antennas, Propagation, and EM Theory (2006 ISAPE)*, 42–45, Guilin, China, Oct. 2006.
4. Chen, G. Y., J. S. Sun, S. Y. Huang, Y. D. Chen, C. H. Lin, and J. Y. Yang, "Flexible monopole antenna for mobile phone co-design and 3D far-field antenna scanning technique apply to total radiation efficiency and mean effective gain measurement," *2006 China-Japan Joint Microwave Conference (2006 CJMW)*, 89–92, Chengdu, China, Aug. 2006.
5. Chen, G. Y., J. S. Sun, S. Y. Huang, Y. D. Chen, C. H. Lin, and J. Y. Yang, "Manufacture, design, measurement and FPC antennas integration for PDA phone," *2006 China-Japan Joint Microwave Conference (2006 CJMW)*, 416–419, Chengdu, China, Aug. 2006.
6. Chen, G. Y., J. S. Sun, S. Y. Huang, Y. D. Chen, C. H. Lin, and J. Y. Yang, "Mobile handset measurement for wireless system networking," *2006 China-Japan Joint Microwave Conference (2006 CJMW)*, 698–701, Chengdu, China, Aug. 2006.
7. Chen, G. Y., C. H. Lin, J. S. Sun, K. K. Tiong, and Y. D. Chen, "3D far-field antenna scanning technique apply to radiation efficiency and mean effective gain measurement," *IEEE TENCON 2007*, Taipei, Taiwan, Oct. 2007.
8. Chen, G. Y., C. H. Lin, J. S. Sun, K. K. Tiong, and Y. D. Chen, "Mobile handset and radiation power absorption measurement," *IEEE TENCON 2007*, Taipei, Taiwan, Oct. 2007.

Microstrip Antenna Design for Ultra Wideband Application by Using Two Slots

N. Ghassemi[1], **J. Rashed-Mohassel**[2], **and M. H. Neshati**[1]

[1]Electrical Engineering Department, Sistan and Baluchistan University, Zahedan, Iran
[2]Center of Excellence on Applied Electromagnetic Systems, University of Tehran, Tehran, Iran

Abstract— This paper presents a multiresonator microstrip antenna using a rectangular patch located on top of two slots, with different lengths and excited by a U-shaped feed line. The patch and slots are separated by a substrate with low dielectric constant and an air gap. The results show that the bandwidth of the antenna increases by using two slots. Finally an antenna with VSWR < 2 from 9.8 GHz to 22 GHz and 6.1 GHz (42%) gain bandwidth (above 7 dB) is obtained. The simulated gain of the antenna is over 5 dB from 9.8 GHz to 19 GHz and with a maximum gain of 9.16 dB at the frequency of 14 GHz.

1. INTRODUCTION

Increasing the gain and impedance bandwidth of microstrip antennas has been a primary goal of researches in this field [1–3]. For this purpose, techniques such as using multilayer structures, low dielectric constant and air gap between layers have been reported in literature [1–6]. Characteristics of microstrip antennas is closely related to their feeding method and substrate materials. Strip line coupled to the patch through an aperture would be a good choice, especially at higher frequencies, because of the advantages such as: 1) radiation of feed network and radiating elements and design flexibility [6], and 2) avoidance of a coaxial feed and soldering problem [3, 6]. One way of widening the impedance bandwidth of aperture coupled microstrip antennas is to utilize a U-shaped feed line [1, 7].

In this paper a multilayer multiresonator aperture coupled microstrip antenna with a U-shaped feed line and two slots is investigated, based on Method of Moments (MoM). There is a rectangular patch above the slots. The patch and slots are separated by an air gap and a substrate with low dielectric constant, from each other. It is shown that using two slots increases the impedance and gain bandwidth of the structure. An antenna with VSWR < 2 from 9.8 GHz to 22 GHz and 6.1 GHz (42%) gain bandwidth (above 7 dB) is obtained. The simulated gain of the antenna is over 5 dB from 9.8 GHz to 19 GHz and the maximum gain is 9.16 dB at 14 GHz.

2. ANTENNA MODEL

Figures 1(a) and (c) shows an antenna structure with one slot, which is a sandwich of three dielectric layers. D_1 and D_3 are made from a material with the relative permittivity of 2.2. Under the first dielectric layer (D_1) there is a 50 Ω microstrip feed line which is divided into, two 100 Ω feed line, with different lengths, by a two-way microstrip power divider. Between D_1 and D_3 there is an air gap with 2 mm thickness (D_2) and a patch is placed on top of the third dielectric layer (D_3). As it is shown in Fig. 2 the impedance bandwidth of the antenna with one slot is 4.1 GHz (34.5%) and the gain bandwidth is 3.2 GHz (26%).

As it is shown in Fig. 1(b), without changing the dimensions of the patch and feed lines, by using two slots and decreasing the thickness of D_2 and D_3 a new structure is achieved. In the second structure there is one slot above each of the 100 Ω feed lines. The structure has three resonant frequencies. The distance between the slots (S_1), their positions (L_5 and L_6) and their lengths (L_7 and L_8) and the lengths of feed lines (L_3 and L_4) have an important effect on the resonant frequencies and the impedance bandwidth of the antenna. By changing these parameters one can set the resonant frequencies by each other to increase the impedance and gain bandwidth of the antenna. All dimensions of the antenna are shown in Table 1.

Table 1: Dimensions of the Antenna.

W	S, S_2	S_1	L_1	L_2	L_3	L_4	L_5, L_6	L_7	L_8
7 mm	0.2 mm	1 mm	16 mm	9.7 mm	4 mm	5 mm	2.5 mm	8 mm	8.5 mm

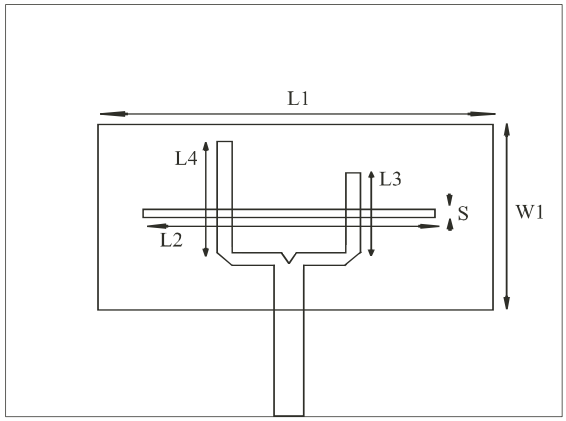

(a)

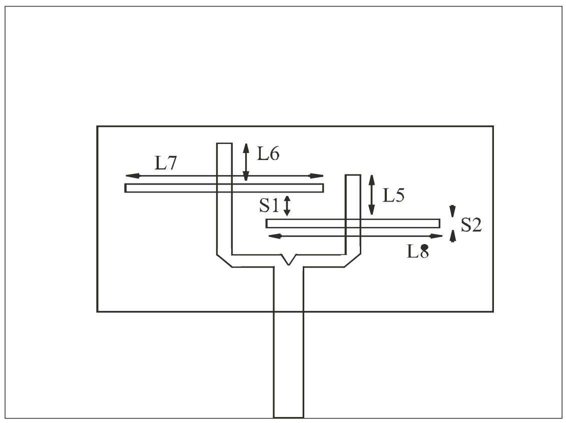

(b)

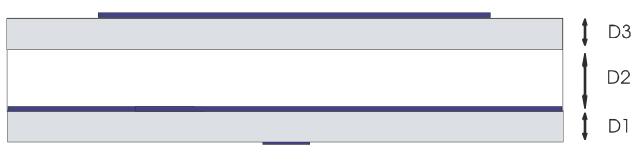

(c)

Figure 1: Antenna structure: (a) Top view of the antenna with one slot, (b) Top view of the antenna with two slots, (c) Side view of the antenna.

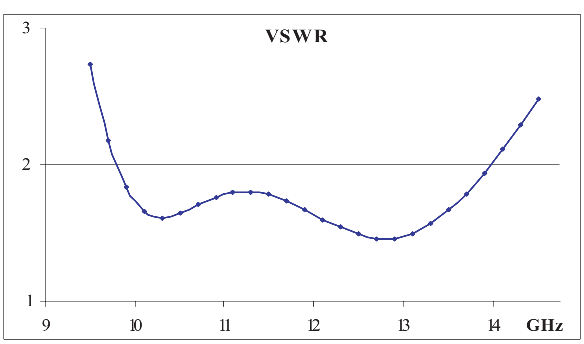

(a)

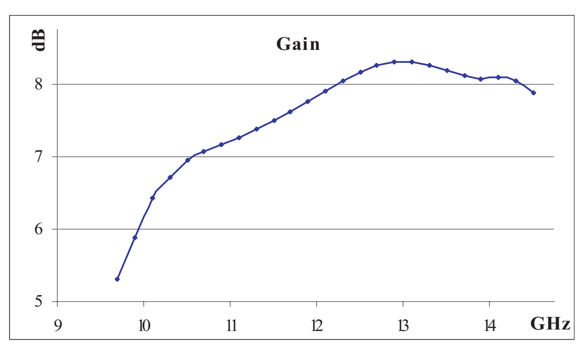

(b)

Figure 2: (a) VSWR, (b) Gain of the antenna with one slot.

Figure 3 shows VSWR and gain of the antenna with two slots. It is clear that the antenna has VSWR $<$ 2 from 9.8 GHz to 22 GHz and 6.1 GHz (42%) gain bandwidth (above 7 dB). The simulated gain of the antenna is over 5 dB from 9.8 GHz to 19 GHz and maximum gain is 9.16 dB at the frequency of 14 GHz. By comparing Figs. 2 and 3 one can understand that, using two slots increase the impedance and gain bandwidth of the antenna.

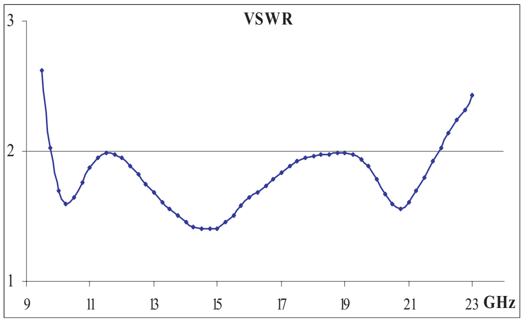

(a)

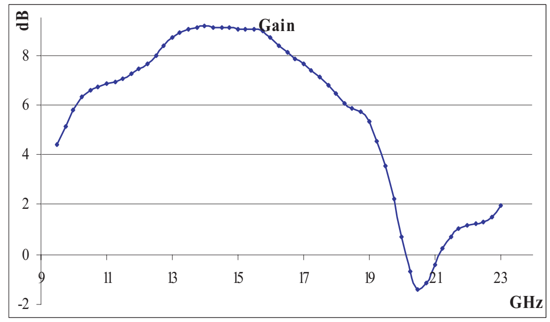

(b)

Figure 3: (a) VSWR, (b) Gain of the antenna with two slots.

3. CONCLUSIONS

This paper presents the design of an ultra wideband multilayer microstrip antenna by using two slots. In this structure there is a rectangular patch and a U-shaped feed line. The slots and patch are separated by a substrate with low dielectric constant and an air gap. This paper shows that using two slots can increase impedance and gain bandwidth of the antenna. Finally an antenna with VSWR < 2 from 9.8 GHz to 22 GHz and 6.1 GHz (42%) gain bandwidth (above 7 dB) is obtained. The simulated gain of the antenna is over 5 dB from 9.8 GHz to 19 GHz and maximum gain is 9.16 dB at the frequency of 14 GHz. However, an optimization procedure is needed to consider other characteristics of the structure such as radiation pattern of the antenna.

ACKNOWLEDGMENT

The authors would like to thank Iran Telecommunication Research Center (ITRC) for its financial supports.

REFERENCES

1. Kumar, G. and K. P. Ray, *Broadband Microstrip Antennas*, Artech House, Boston, 2003.
2. Wong, K. L., *Compact and Broadband Microstrip Antenna*, John Wiley & Sons, New York, 2002.
3. Chai, W, X. Zhang, and J. Liu, "A novel wideband antenna design using U-slot," *Progress In Electromagnetics Research Symposium Proceedings*, 1292–1295, Beijing, China, March 26–30, 2007.
4. Ray, K. P., S. Ghosh, and K. Nirmala, "Multilayer multiresonator circular microstrip antennas for broadband and dual-band operation," *Microwave and Optical Technology Letters*, Vol. 47, No. 5, 489–494, December 2005.
5. Zehforoosh, Y., C. Ghobadi, and J. Nourinia, "Antenna design for ultra wideband application using a new multilayer structure," *Progress In Electromagnetics Research Symposium Proceedings*, 2225–2231, Beijing, China, March 26–30, 2007.
6. Lee, K. F. and W. Chen, *Advances in Microstrip and Printed Antennas*, John Wiley & Sons, New York, 1997.
7. Targonski, S. D., R. B. Waterhouse, and D. M. Pozar, "Design of wide-band aperture-stacked patch microstrip antennaa," *IEEE Transmision on Antennas and Propagation*, Vol. 46, No. 9, 1245–1251, September 1998.
8. Denidni, T. A. and L. Talbi, *High Gain Microstrip Antenna Design for Broadband Wireless Applications*, 511–517, Wiley Periodicals Inc, 2003.

The GPS Antenna Design and Measurement

Kuo-Liang Wu[1], **Guan-Yu Chen**[1], **Jwo-Shiun Sun**[1], **Cheng-Hung Lin**[2]
Kwong-Kau Tiong[2], **and Y. D. Chen**[3]

[1]Department of Electronic Engineering, National Taipei University of Technology, Taiwan
[2]Department of Electrical Engineering, National Taiwan Ocean University, Taiwan
[3]Antenna and EMC Laboratory, High Tech Computer Corp. (HTC), Taiwan

Abstract— This paper accomplished a GPS band for meander inverted-F monopole antenna structure and easy applied mobile cellular phone application. The measured and simulated data including return loss, antenna gain and radiation patterns are presented.

1. INTRODUCTION

GPS as a satellite-based positioning system operated by the United States Department of Defense was officially put into operation in 1995. Using the difference in the radio signal propagation times of at least three of the 24 GPS satellites, a GPS receiver can accurately determine its position worldwide to within a few meters. Signals for civil use are transmitted at a frequency of 1575.42 MHz and bands. The general GPS functions of PDA support the assisted functionality in 2.5/3G wireless networks. Traditional antennas such as monopoles, dipoles and patches are not suitable to meet the requirements of modern wireless communication and highly demanding mobile GPS systems. As a result, there is the need for alternative approaches to small antenna and high performance design. This paper describes a miniaturized meander shorting monopole for integration in modern GPS wireless systems.

2. ANTENNA DESIGN

The resonance mode of a shorting meander wire antenna (Figure 1 and Figure 2) covers the GPS communication bandwidth of 1571.42–1579.42 MHz. The simple wire tuning expansion are introduced to confine the resonance mode region and to facilitate the frequency modes and impedance match expansion easily for antenna and wireless system integration design. This paper proposes meander shorting monopole antenna design for single-band GPS wireless communications, especially for PDA and Smart mobile phones. The single-frequency design for mobile handset mainly utilizes meander line to excite radiation mode. By tuning the dimensions of meander line, the VSWR ratio of the antenna's resonance frequency can be achieved to 2, which makes it very promising for GPS and A-GPS operations.

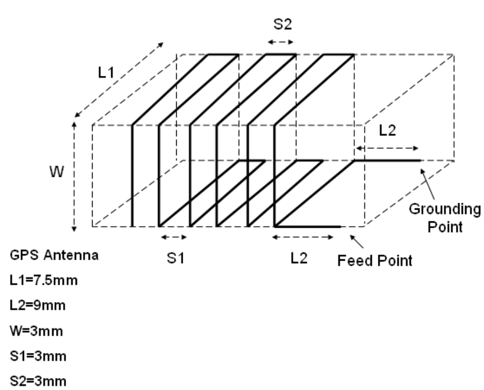

Figure 1: Meander wire antenna design for GPS band and structure layout.

3. MEASUREMENTS

The design requirements for GPS antenna is combined into multiple objective goals, such as simplicity of the antenna geometry, radiation pattern, return loss (Figure 3), antenna impedance (Figure 4) and polarizations. This design in general to a mobile communication apparatus and global positioning system antenna, and more particularly to a mobile communication system, which utilizes a

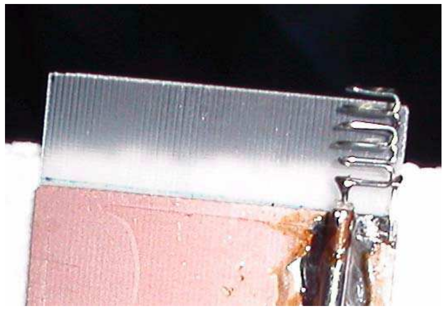

Figure 2: Practical GPS antenna.

small-scale metal for the GPS antenna design. In this paper, the experiment setup (Figure 5) has done [1, 2]. The phase of the two field components is measured relative to the signal generator, and a double ridge horn serves as a source antenna. Equations (1) and (2) may be expanded [3, 4] to give simple expressions that can be inserted into data logging software to provide a direct conversion from dual linear to RHCP and LHCP at each measurement angle(Figure 6 to Figure 8).

$$E_{RHCP} = \frac{1}{\sqrt{2}}(E_H + jE_V) \tag{1}$$

$$E_{LHCP} = \frac{1}{\sqrt{2}}(E_H - jE_V) \tag{2}$$

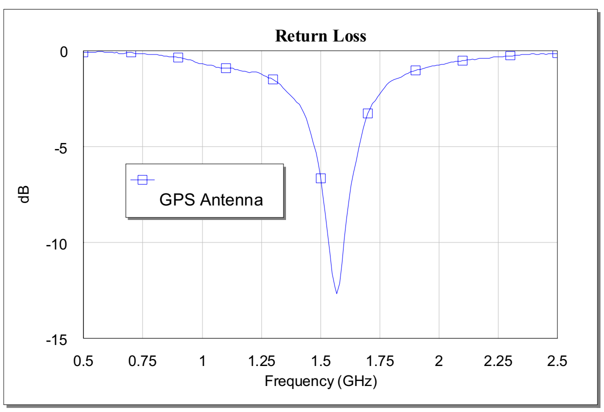

Figure 3: The measured data of return loss.

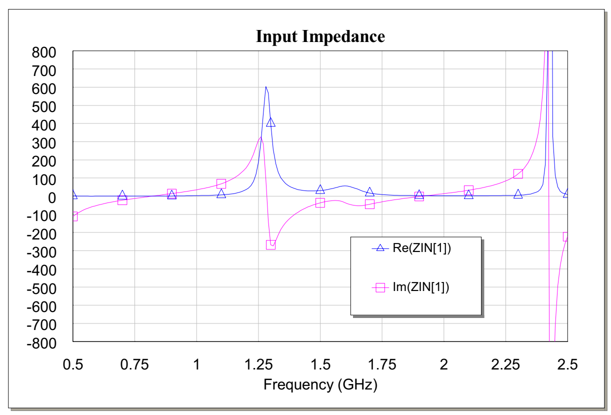

Figure 4: The measured data of antenna impedance.

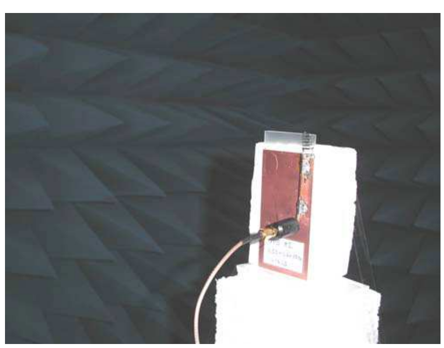

Figure 5: The measurements of RHCP and LHCP with polarization transform method.

4. RESULTS

This article describes a low profile, compact, meander loaded monopole antenna with single feed. A shorting type monopole is used to enhance the impedance matching. This provides a low radiation

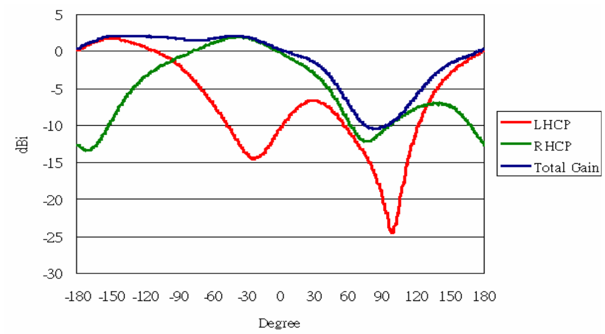

Figure 6: The measured pattern of H-Plane.

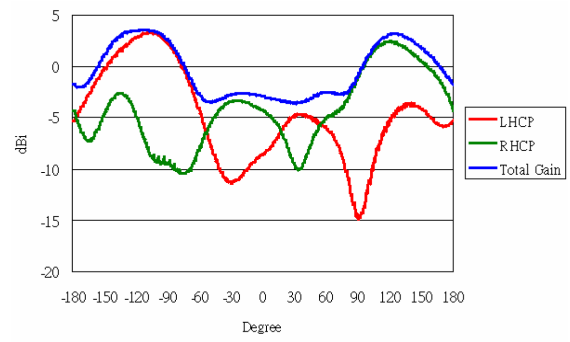

Figure 7: The measured pattern of E1-Plane.

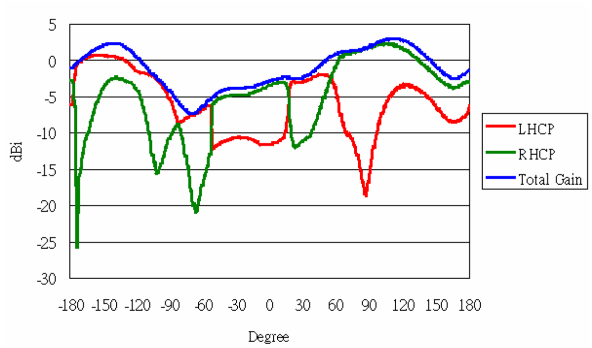

Figure 8: The measured pattern of E2-Plane.

resistance within the GPS band. Shorting meander inverted-F monopole antenna leads to a middle gain. In addition, the meander loading also permits the antennas height and to be reduced antenna size. This antenna also offers a characteristic of high radiation efficiency. Antenna bandwidth of 3.8% (1.53 to 1.59 GHz) was experimentally obtained for a return loss -10 dB. In well known antenna design techniques a matching structure is typically employed to provide matching between the antenna and the GPS circuitry for efficient transfer of energy.

5. CONCLUSIONS

In this paper, a compact and low profile internal meander wire monopole antenna for single band has been proposed. This antenna was designed and measured. A good agreement between measurement and analysis has been obtained. The proposed antenna shows a suitable operating bandwidth and it easy to cover the GPS for location wireless operation and operation of a mobile handset phone, co-design, co-integration and application operations.

ACKNOWLEDGMENT

The authors acknowledge the Antenna and Wireless System Integration Department of High Tech Computer, Corp. (HTC), Taiwan for sport the wireless technique and measurement environment.

REFERENCES

1. Chen, G. Y., J. S. Sun, S. Y. Huang, Y. D. Chen, C. H. Lin, and J. Y. Yang, "Mobile handset measurement for wireless system networking," *2006 China-Japan Joint Microwave Conference (2006 CJMW)*, 698–701, Chengdu, China, Aug. 2006.
2. Chen, G. Y., J. S. Sun, and Y. D. Chen, "The 3D far-field antenna measurement technology for radiation efficiency, mean effective gain and diversity antenna operation," *2006 The 7th International Symposium on Antennas, Propagation, and EM Theory (2006 ISAPE)*, 42–45, Guilin, China, Oct. 2006.
3. Kraus, J. D. and R. J. Marhefka, *Antennas for All Applications*, McGraw-Hill, 2002.
4. Toh, B. Y., R. Cahill, and V. F. Fusco, "Understanding and measuring circular polarization," *IEEE Transactions on Education*, Vol. 46, No. 3, 313–318, Aug. 2003.

Shaping Design of Side-fed Offset Cassegrain Reflector Antennas

S. D. Liu[1,2], S. F. Liu[2], Y. C. Jiao[2], and F. S. Zhang[2]

[1]Xi'an Institute of Space Radio Technology, Xi'an 710000, China
[2]Xidian University, Xi'an 710071, China

Abstract— The purpose of this paper is to improve the scanning performance of the Side-fed Offset Cassegrain (SFOC) reflector antenna by adjusting its reflectors' shape. Firstly the ray-tracing technique is employed to obtain the path lengths and directions of the outgoing rays emanated from two specified feeds. Then the path length and direction errors of these rays are minimized by adjusting the antenna's main- and sub-reflector surfaces. An optimization example of the SFOC antenna is provided for improving its wide-angle scanning performance, and the validity of the method presented is demonstrated.

1. INTRODUCTION

In satellite communication systems, shaped coverage and frequency reuse require satellite antennas to provide multiple high-quality spot beams over the entire 18° field of view. For a given aperture, a reflector antenna is much less expensive than a phased array. However, unless the reflector antenna is mechanically rotatable, its performance is limited to a very small angular range. In order to reduce the scan degradation, much effort has been given to the development of shaping methods for scanning reflector antennas over the last four decades. For example, a bifocal synthesis procedure can be used to obtain improved scan characteristics [1–4]. In order to achieve both low scan losses and low cross polarization when the satellite antenna scans over an 18° conical field of view, Jørgensen has presented a kind of antenna configuration named Side-fed Offset Cassegrain (SFOC) antenna [5]. This kind of antenna has excellent scan properties due to the large length of the main reflector. The paper describes a reflector shaping technique for further improving the scan properties of the SFOC antenna with an optimization algorithm [6, 7].

In this paper, the main- and sub-reflector surfaces of the SFOC antenna are both expressed with the bicubic spline functions. The bicubic spline function can be represented in terms of so-called bicubic splines, $B(x, y)$, and each of them is non-zero over only a part of the reflector which makes the bicubic spline function an efficient choice in reflector shaping.

The paper is organized as follows: In Section 2, the idea of the design method and the used formulae are presented. Numerical results and discussion are given in Section 3, and conclusions are drawn in Section 4.

2. DESIGN METHOD

The geometry of SFOC antenna in the symmetric plane is shown in Figure 1. In the process of the optimization design, the main- and sub-reflector surfaces of the antenna are both expressed by bicubic spline functions, which can be described as

$$z = \sum_{i=1}^{N_x} \sum_{j=1}^{N_y} c_{ij} B_{ij}(x, y), \quad x_{\min} \leq x \leq x_{\max}, \quad y_{\min} \leq y \leq y_{\max} \tag{1}$$

where B_{ij} are so-called bicubic spline, c_{ij} are so-called spline coefficients, and it is assumed that the surfaces are interpolated in a rectangular grid with N_x points equidistantly distributed along x from $x_{\min}$ to $x_{\max}$ and N_y points along y from $y_{\min}$ to $y_{\max}$. Each bicubic spline is non-zero over only a part of the reflector surface which makes the expansion an efficient choice in reflector shaping. The optimization algorithm will shape the reflector surfaces by modifying the z-values of those interpolation points. The program consists of three main functional blocks: a ray-tracing procedure, a fitness function calculation, and the optimization algorithm itself. All of them have been developed in the Fortran 90 environment.

The ray-tracing procedure is capable of determining the path lengths and directions of the rays emanated from specified feeds and reflected by the antenna's sub- and main-reflectors, where the reflect points are used as the interpolation data of the bicubic spline function. The number of rays is the same at each scan angle.

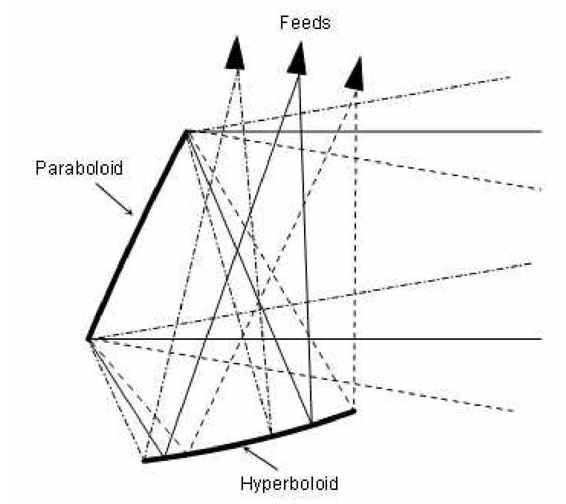

Figure 1: Geometry of the Side-fed Offset Cassegrain system.

It is essential, in shaping the reflector, to calculate not only the path-length errors, but also the varying directions of the outgoing rays. The fitness function should contain both evaluations. Through trial and error, a successful fitness function for kth scan direction was found to be

$$f_k = \sum_{i=1}^{N}(L_k^i - \overline{L_k})^2 + W \cdot \sum_{i=1}^{N}(1.0 - \hat{R}_k^i \cdot \hat{U}_k)^2 \tag{2}$$

where L_k^i represents the path length of a ray emanated from the kth feed position (corresponding to the kth scan direction) and reflected by sub- and main-reflector and finally arriving at the ith sample point on the kth scanning aperture plane, and $\overline{L_k}$ represents the mean path length defined by

$$\overline{L_k} = \frac{1}{N}\sum_{i=1}^{N} L_k^i. \tag{3}$$

Unit vectors $\hat{R}_k^i$ and $\hat{U}_k$ represent the direction of the outgoing ray and the specified kth scan direction, respectively. For example, for the kth scan angle $(\theta_k,\ \varphi_k)$, $\hat{U}_k$ can be written as

$$\hat{U}_k = (\sin\theta_k \cos\varphi_k, \sin\theta_k \sin\varphi_k, \cos\theta_k). \tag{4}$$

W is a weight by which we can adjust the significance of the first summation (path-length error) and the second summation (direction error), and N is the total number of sample points.

Essentially, the value of the first summation and the second summation in Equation (2) corresponds to the level of the path-length error and the direction error of the rays, respectively, and the ideal values of these two summations are zero. For instance, for the parabolic reflector, when the feed is located at the focal point and the corresponding scan angle $(\theta,\ \varphi)$ is $(0°,\ 0°)$, the two summations will have the same value as zero, and then f_k will obtain its minimum.

Then the fitness function for realizing scanning can be defined as

$$f = \sum_{k=1}^{K} w_k f_k \tag{5}$$

by summing the expressions given by Equation (2) for a number of scan directions over the specified scan range, where K is the number of scan directions and w_k is the weighting factor of the kth scan direction which must be specified beforehand by the designer.

For a range of scanning, the optimization algorithm will attempt to generate a reflector shape which makes each $f_k(k = 1,\ 2,\ \ldots,\ K)$ the minimum by adjusting the coordinates of the interpolation points. If this is not possible, then it could be the case where the shaped reflector makes some

f_k minimum, but not the others. There may be other cases where the solutions are a compromise, and these solutions should be more desirable from our design standpoint. Through multiple runs of the program and manual adjustment of the weighting factors, solutions suitable for beam scanning can be obtained.

3. NUMERICAL RESULTS AND DISCUSSION

The antenna's original (unshaped) main- and sub-reflector surfaces are paraboloid and hyperboloid, respectively, and the diameter of the main reflector is 400 wavelengths. Initial synthesis of the SFOC reflector system can be performed with geometrical optics.

In the process of optimization, two scanning angles $-6°$ and $+6°$ (since only 1-D scanning is considered in this paper, the scanning azimuth angle is all zero degree) are considered in the fitness function and the corresponding feed positions are selected as the optimum feed positions (OFPs) [8] of the initial reflectors. By running the developed program, the main- and sub-reflectors suitable for scanning are obtained.

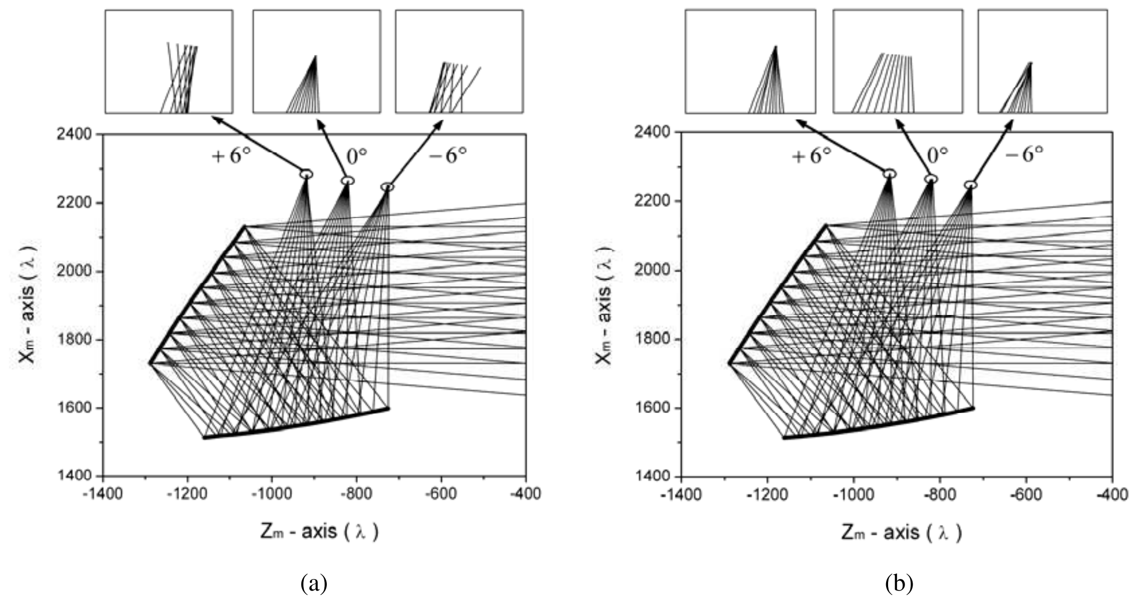

Figure 2: Rays tracing through (a) original antenna and (b) shaped antenna.

In the geometrical optics approximation, the plane wave is generally replaced by a bundle of parallel rays. When the antenna is considered as a receiving system and is illuminated by parallel rays coming from $\pm 6°$ and $0°$, Figures 2(a) and (b) show the ray tracing in the symmetrical plane of the initial and shaped antennas, respectively. It can be seen that for the initial antenna the parallel rays coming from $0°$ are all reflected to a point (focal point of the antenna system), but when the rays come from $\pm 6°$, the caustic region at the feed array plane becomes severe. Comparatively, although the astigmatism is introduced when the rays come from $0°$, the shaped antenna achieves two focal points, one for the rays coming from $-6°$ and the other for the rays from $+6°$. Figure 3 shows the maximum path-length error on the aperture versus the scanning angle when the antenna scans between $-10°$ and $+10°$. It can be seen that the maximum path-length error for the original antenna increases monotonically with the scan angle, whereas the maximum path-length error for the shaped antenna decreases with the scan angle and becomes zero for $\pm 6°$ and then increases monotonically. Given a maximum path-length error of 0.31λ, it can be found from Figure 3 that the scanning ranges of the original antenna and the shaped antenna are $[-5°, +6°]$ and $[-8.5°, +9°]$, respectively. Therefore, the shaped antenna has a scanning range of about 59 percent wider than the original antenna.

When the secondary pattern is computed, a circularly symmetric feed is employed and its E- and H-plane patterns are both approximated by the raised cosine function $\cos^7\theta$. Rays emanated from the feed are traced and induced currents are then integrated over the main reflector, producing the radiation fields of the antenna. Figure 4 shows two-dimensional cross sections in the plane of scan of these patterns. It is seen that, compared with the original antenna, the shaped antenna achieves surprisingly symmetric beams and substantial side lobe reduction for ±6° scanned beams.

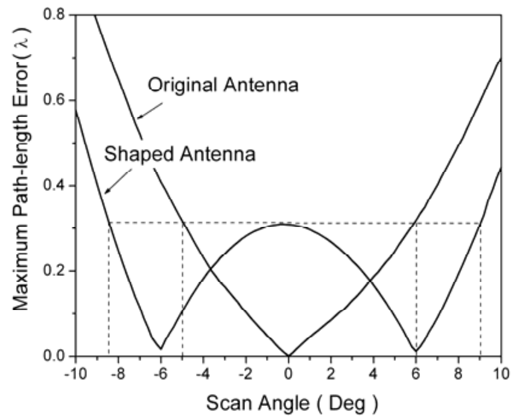

Figure 3: Maximum path-length errors of the original and shaped antennas versus the scanning angle.

In these simulations, due to the relatively small feed size (feed pattern is simulated by the function $\cos^7\theta$) and the small angle subtended by the sub-reflector rim, the feed spillover is large.

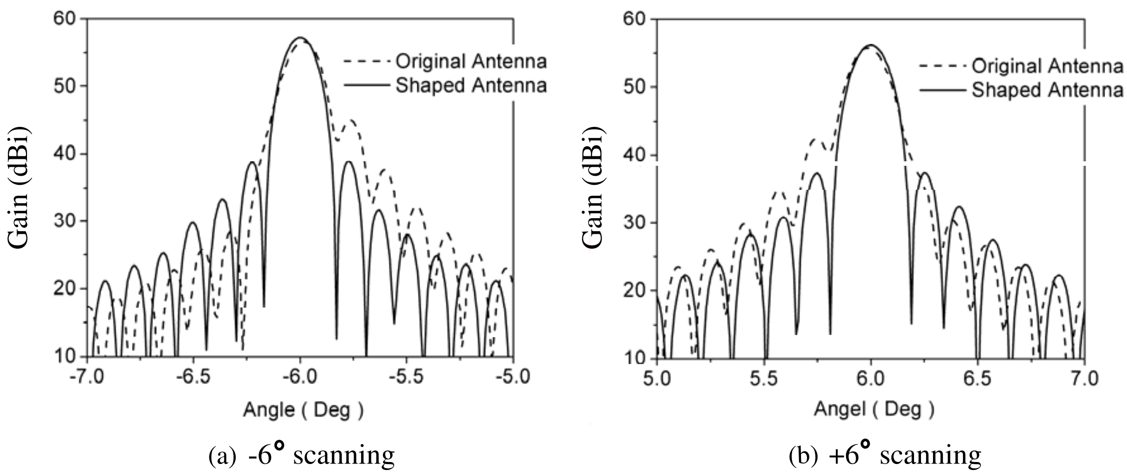

Figure 4: Radiation patterns of the original and shaped antenna in the plane of scan.

4. CONCLUSIONS

In this paper a numerical technique to improve the beam scanning capability of SFOC antenna is introduced. We employ an optimization algorithm to adjust the shape of the reflectors. The rays emanated from the initial feed positions to the corresponding scan directions are redirected. A numerical example was specifically designed with the method presented and its scanning performances are studied, which shows that the original SFOC reflector antenna is transformed into a bi-focal antenna through shaping its main- and sub- reflector surfaces, thus improved scanning characteristics are achieved.

REFERENCES

1. Rao, B. L. J., "Bicollimated Gregorian reflector antenna," *IEEE Trans. Antennas Propagat.*, Vol. 32, 147–158, 1984.
2. Rappaport, C. M., "An offset bifocal reflector antenna design for wide-angle beam scanning," *IEEE Trans. Antennas Propagat.*, Vol. 32, 1196–1203, 1984.
3. Lorenzo, M. E., C. M. Rappaport, and A. G. Pino, "An offset bifocal reflector antenna with Gregorian configuration," *IEEE AP, Society International Symposium 1997*, Vol. 3, 1655–1658, 1997.

4. Detweiler, P. L. and K. M. Pasala, "Wide-angle scanning with reflector antennas: A new design technique," *National Aerospace and Electronics Conference*, 136–145, 2000.
5. Jørgensen, R., P. Balling, and W. J. English, "Dual offset reflector multi-beam antenna for international communications satellite application," *IEEE Trans. Antenna Propagat.*, Vol. 33, 1304–1312, 1985.
6. Rahmat-Samii, Y., D. Gies, and J. Robinson, "Particle Swarm Optimization (PSO): A novel paradigm for antenna designs," The Radio Science Bulletin, 14–22, September 2003.
7. Gies, D. and Y. Rahmat-Samii, "Particle Swarm Optimization (PSO) for reflector antenna shaping," *AP-S International Symposium (Digest)*, Vol. 3, 2289–2292, 2004.
8. Krichevsky, V. and D. F. Difonzo, "Optimum beam scanning in offset single and dual reflector antennas," *IEEE Trans. Antennas Propagat.*, Vol. 33, 179–188, 1985.

Planar Leaky-wave Antenna with Aperture Coupled Feed

A. Mahmoudian, H. Dalili Oskouei, and K. Forooraghi
Microwave Lab., Department of Electrical Engineering, Tarbiat Modares University
Tehran, Iran

Abstract— In this paper we study a new design of a two-dimensional (2-D) planar leaky-wave antenna. The antenna consists of a two dimensional periodic array of square patch which is excited by an aperture coupled feed. Dispersion diagram for a periodic array of patches on top of a grounded dielectric slab is obtained by using the Floquet theorem for periodic structure and by means of HFSS software, then the appropriate frequency band for leaky wave excitation is derived and an aperture coupled design is performed for this frequency band. Finally two high gain radiation patterns at two frequencies are studied.

1. INTRODUCTION

The microstrip line leaky-wave antennas have received much attention in 1990–2000 [1, 2]. In these structures, the microstrip line dimensions, dielectric constant and thickness are derived in order to excite first or second higher order modes in the proper frequency band [3, 4].

In a leaky-wave antenna design proposed by Frezza [5], the structure is excited in low frequencies by dispersion feature for a periodic strip on a grounded dielectric substrate. Unexpected dispersion behaviors appear at low frequency and these behaviors strongly depend on the ratio s/p (i.e., strip width (s) and period (p)). For a basically closed structure (values of s/p close to unity) the bound mode becomes leaky at low frequencies due to radiation from fundamental spatial harmonic ($n = 0$), while for a low values of s/p the proper bound mode becomes improper real at low frequency.

In recent years a novel type of leaky-wave antenna (planar structure) is introduced. The planar leaky wave antenna has various types such as, rectangular slot array [6] and rectangular patch array [7]. The leaky wave antenna design in this structure is based on a leaky parallel-plate waveguide mode, which operates in the $n = 1$ mode. This planar structure has broadside radiation pattern in one frequency and dual beam pattern at other frequencies.

In this paper the planar structures is assumed as periodic square patch array on a grounded dielectric substrate with the array period 'a' and the patch length 'L'. We first investigate normalized phase constant β/k_0 versus frequency for waves on the planar periodic square patch array and recognize the frequency band that the leaky-wave is propagating through the structure, and then we design an aperture coupled feed for this frequency band.

2. ANALYSIS AND DESIGN

The dispersion or β-f diagram can be calculated from the unit cell. Two dimensional Eigen mode solutions for Maxwell equations are obtained for the restricted unit cell (or Brillouin zone) under periodic boundary conditions. Algorithms for solving Maxwell equations under periodic boundary conditions have been implemented using both the Green's function based on method of moments and the finite element method. In the present work we used a commercially available simulation tool based on the victories finite element method (HFSS).

Figure 1 shows the normalized phase constant (β/k_0) versus frequency for a planar array of square patches with a patch length 6 mm and a period 8 mm which are located on the substrate with dielectric constant 10.2 and thickness 1.27 mm. In this figure, we have three leaky-wave regions. The first region is located around 6.5 GHz but in this region the phase constant is increased dramatically and thus we have a short frequency band for leaky-wave excitement. The second region exists in the frequency band 7.8–10.5 GHz. In this region we have two modes, either a fast leaky mode or bound (surface wave) mode; where the ratio $\beta/k_0 \approx 1$ and hence the leaky mode turn in to bound mode as the frequency changes slightly. The third region is located in frequency band 11–11.3 GHz; in this region we have sufficient frequency band to excite the leaky wave.

We choose aperture coupled feed for this structure because of its features such as wider bandwidth and shielding of the radiation patches from the radiation of the feed structure. Since we obtain the leaky wave region (dispersion diagram) for array of periodic square patches on a grounded dielectric substrate, so if we choose another feed structure, it is influenced our dispersion diagram.

Firstly an aperture coupled feed is designed for a leaky wave frequency band (11–11.3 GHz) and then the complete structure (i.e., planar array of square patches and aperture coupled feeds) is optimized by HFSS. For approximately the center frequency of leaky wave band. The longer slot line-fed structure has better efficiency, so we choose longer length slot line for aperture coupled feed.

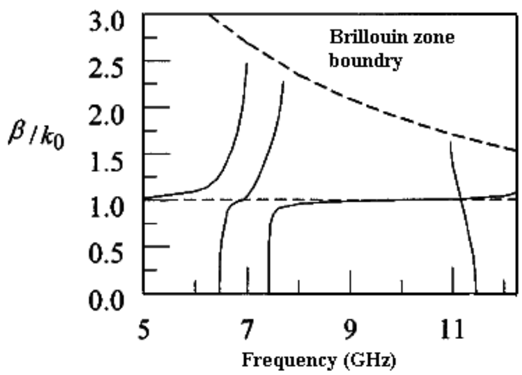

Figure 1: Dispersion diagram for periodic array of square patch. The array period is 8 mm and patch length is 6 mm.

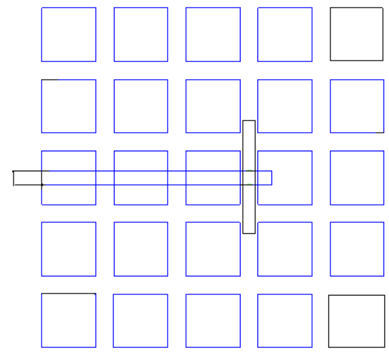

Figure 2: Shematic for periodic array of square patch and aperture coupled feed.

3. SIMULATION AND RESULTS

At first, an aperture coupled feed is designed for a leaky wave frequency band and then the completed structure is optimized for the approximately center frequency of leaky wave band.

The structure is shown in Fig. 2. As it can be seen in figure, the 25 square patches in array of 5×5 have formed the planar array. The patch size is 6 mm and array period is 8 mm in both x and y direction. The dielectric constant and thickness between the slot and planer array are 10.2 and 1.27 mm. The feeding microstrip line has 1.585 mm width and a characteristic impedance of 50 ohms.

We assume that the dielectric constant and the thickness, which is used as substrate for a feeding structure, are 2.2, 0.508 mm respectively. With these values the optimized results for slot length and width are obtained respectively 15.8 mm and 0.3 mm and a tuning length is $lm = 2.5$ mm.The return loss plot for this structure with the optimized values are obtained by means of commercial moment method software (Ensemble$^{\text{TM}}$). As shown in Fig. 3, we see resonance frequency in 11.11 GHz. The bandwidth of radiation is about 0.1 GHz around the resonance frequency. That is enough and proper bandwidth because we just have 0.3 GHz bandwidth (11–11.3 GHz) in dispersion diagram that the leaky wave is propagating.

Figures 4 and 6 show the E-plane radiation patterns for two frequencies. In 11.1 GHz as shown in Fig. 4, we have dual beam pattern at 30° scan angle. These results show that relatively narrow

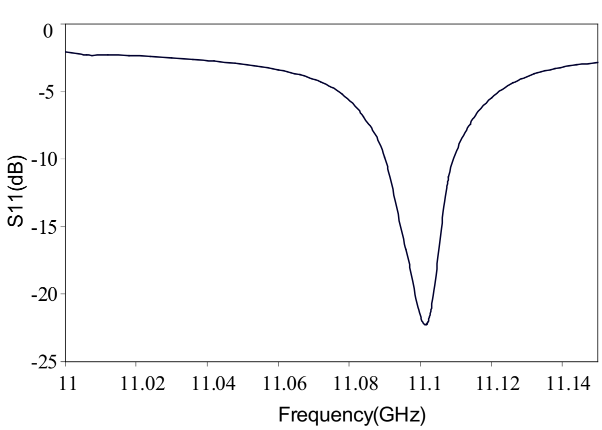

Figure 3: The simulated return loss of the planer planar.

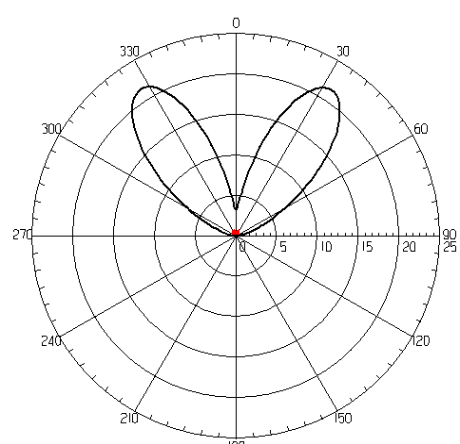

Figure 4: The radiation pattern for a periodic square patch at 11.1 GHz.

pencil beam at 30° scan angle can be achieved from a periodic array of square patch LWA structure. In Fig. 5, the E-plane radiation pattern is plotted for 11.2 GHz for planar array in which the aperture coupled feed is design for 11.2 GHz. the return loss for this case is plotted in Fig. 5. In this case we have a narrow pencil beam pattern at broadside direction. So as can be seen from Fig. 1 and by increasing the frequency β/k_0 is move to the zero and the main beam is placed in the broadside and the gain of the antenna has been increased by changing the frequency from 11.1 to 11.2.

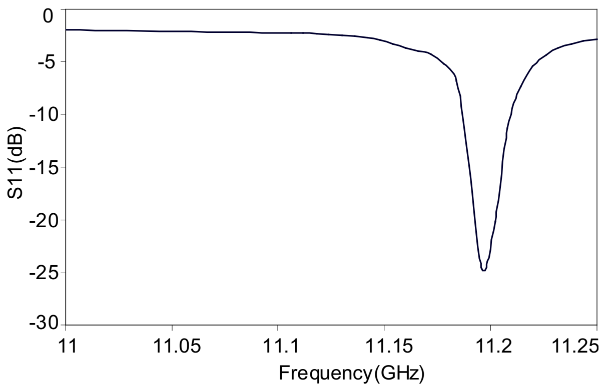

Figure 5: The simulated return loss of the planer array.

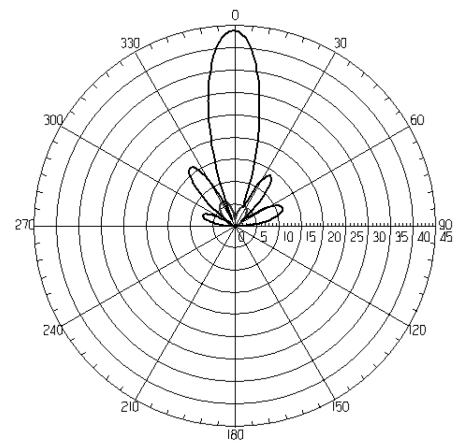

Figure 6: The radiation pattern for a periodic square array at 11.2 GHz.

4. CONCLUSION

This work describes the design of a planar leaky-wave array excited by an aperture coupled feed. First pass dispersion diagram for planar array of square patch on grounded dielectric is derived and appropriate leaky wave region is detected and the aperture coupled feed is designed for this frequency band. The patterns for two frequencies are plotted.

ACKNOWLEDGMENT

This work was supported by the Iran Telecom Research Center under the grant TMU-860311.

REFERENCES

1. Oliner, A., "Leaky-wave antennas," *Antenna Engineerng Handbook*, R. C. Johnson, Ed., 3rd Ed., Ch. 10, New York, Me-Graw Hill, 1993.
2. Hessel, A., "Traveling wave antennas," *Antenna Theory*, R. E. Collin and F. J. Zucker, Eds., Ch. 19, Mc-Graw Hill, New York, 1969.
3. Oliner, A. and K. S. Lee, "The nature of the leakage from higher-ordermodes on microstrip line," *IEEE MTT-S Int. Microwave Symp. Dig.*, 57–60, Baltimore, 1986.
4. Chen, T.-L., "Microstrip-fed microstrip second higher order leaky-mode antenna," *IEEE Trans. Antennas Propag.*, Vol. 49, No. 6, June 2001.
5. Burghignoli, P., "Low-frequency dispersion features of a new complex mode for a periodic strip grating on a grounded dielectric slab," *IEEE Trans. Antennas Propag.*, Vol. 49, No. 12, Dec. 2001.
6. Zhao, T., "2-D periodic leaky-wave antennas — Part II: Slot design," *IEEE Trans. Antennas Propag.*, Vol. 53, No. 11, Nov. 2005.
7. Zhao, T., D. R. Jackson, J. T. Williams, H. Y. Yang, and A. A. Oliner, "2-D periodic Leaky-wave antennas — Part I: Metal patch design," *IEEE Trans. Antennas Propag.*, Vol. 53, No. 11, 3505–3514, Nov. 2005.

Clover Polarimetric Detector — A Novel Design of an Ortho-mode Transducer at 150 and 225 GHz

Philip Mauskopf[1], **Peter Ade**[1], **Stafford Withington**[3], **Jin Zhang**[1], **and Paul Grime**[2]

[1]Astronomy Instrumentation Group, Cardiff University, UK
[2]Experimental Radio Cosmology Group, Oxford University, UK
[3]Cavendish Laboratory, University of Cambridge, UK

Abstract— This paper presents the design of an ortho-mode transducer (OMT) to separate two orthogonal linearly polarized signals traveling in a circular waveguide with frequency channels at 150/255 GHz band. Simulations (in HFSS) are presented to determine the optimal probe geometry and feed impedance to achieve good coupling to the optimized probes over a wide bandwidth with corresponding feed impedances for telescopes operating at 150 and 225 GHz. The results show that at 150 GHz band, the return loss can reach below −20 dB from 126 GHz to 180 GHz with the cross polarization reach below −40 dB. At 225 GHz band, the return loss can reach below −20 dB from 190 GHz to 260 GHz with the polarization isolation more than 32 dB.

1. INTRODUCTION

The existence of primordial gravitational waves in the universe is a fundamental prediction of the inflationary cosmological paradigm, and determination of the level of this tensor contribution to primordial fluctuations is a uniquely powerful test of inflationary models. The project CLOVER is to measure this tensor contribution via its effect on the B-mode polarization of the Cosmic Microwave Background (CMB) down to a sensitivity limited by the foreground contamination due to lensing. This project comprises three independent telescopes operating at 97, 150 and 225 GHz.

OMTs have traditionally been adopted at lower frequencies and measurements of a scale-model OMT has been presented in [1] at 1–2 GHz. This paper presents a design of an OMT to separate two orthogonal linearly polarized signals traveling in a circular waveguide. The design concept compromises two key issues: The first is to design a four-probe OMT that can be integrated with a set of TES detectors, the waveguide needs to be split in order to get he OMT signals out to the detectors. This results in a loss of signal propagating out of the gap between the incoming waveguide and the backshort section. The effect of this waveguide gap has been presented in this paper. The second issue is to design a planar structure that will couple well to the rectangular probes. Microstrip was adopted in this design for two main advantages: the field is confined in a microstrip and therefore the parameters of the waveguide gap has no effect o the microstrip impedance; the microstrip line is the most compact transmission line and therefore the only type that is possible to be used for carrying the signal over the thermally isolating silicon nitride legs of the TES detectors.

2. DESCRIPTION OF THE MODEL

The design concept has been illustrated in Fig. 1 showing four rectangular probes in a circular waveguide. The waveguide has a $\lambda/4$ backshort section behind the probes. The first design challenge is in order to insert the OMT probes and get the signals out to the TES detectors; a break is required in the waveguide which results in a loss of signal propagating out of the gap between the incoming waveguide and the backshort section. The waveguide has been split leaving a total gap of 20 µm between the upper waveguide and the lower waveguide. A thin 1 µm membrane (typical of the SiN membranes used in detector manufacture) which has a solid conducting ground plane starting from the edge of the waveguide wall and extending a distance of $\lambda/4$. The free standing membrane therefore is a circular window of radius 1.32 mm (for 150 GHz channels). The membrane is supported on its silicon frame which is not metallised. The change in impedance from the metallised membrane to the unmetallised membrane/silicon acts as an open circuit for the TEM modes propagating in the gap between the two waveguide sections. This causes modes that correspond to a wavelength λ (2 mm for 150 GHz channels) not to propagate out of the gap. The simulation in HFSS shows the good coupling to the probes and good performance of the system, as shown in Fig. 2.

The second design issue is to design a planar structure that will couple to the rectangular probes. Ideally microstrip line is adopted due to the two main advantages:

1) The field is confined in the microstrip and therefore we do not have to worry about the parameters of the gap between the waveguide affecting the microstrip impedance.
2) Microstrip line is the most compact transmission line and therefore the only type that it is practical to use for carrying the signal over the thermally isolating silicon nitride legs of the TES detectors.

However, the choice of coupling line is limited by constraints on the dimensions of the lines due to the fabrication. A minimum line width of 2 μm was chosen for microstrip signal lines and the maximum thickness of the insulator used in the microstrip design has been limited to be 400 nm. This combined with the dielectric constant of the insulators (SiO_2) as well as the effects of the superconducting penetration depth means that the maximum microstrip line impedance is 27 Ω. Therefore we approached the full design: assume the probes represent ideal 50 Ω source impedance, a $\lambda/4$ section of microstrip with an impedance of 27 Ω to couple to an output microstrip line with an impedance of 25 Ω. It is relatively easy to modify this design to produce an output impedance of 23 Ω which is required by the current CLOVER design output microstrip impedance with little loss of performance. It is noted that the concept designs and to be considered as proof of principle only. The final designs will require additional optimization with the detector fabrication.

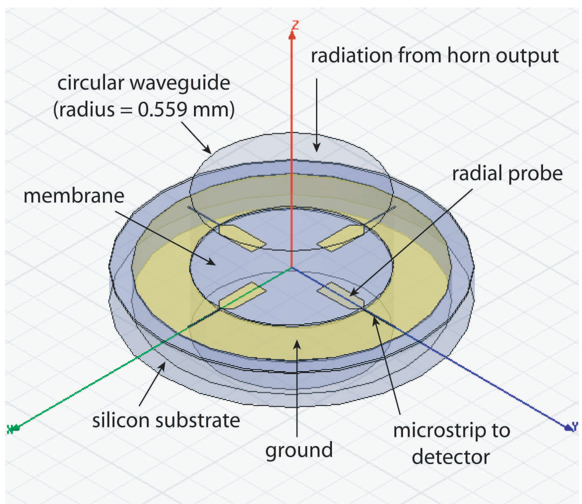

Figure 1: 4-probes OMT in circular waveguide at 150/225 GHz.

3. SIMULATION RESULTS

The simulations have been conducted to evaluate the performance of the designed models for a frequency range of 100–180 GHz for 150 GHz channels and 180–280 GHz for 225 GHz channels where the fabrication requires tight tolerances. Fig. 2 shows the simulation results for 150 GHz channels and for 225 GHz channels results are shown in Fig. 3.

In the simulation, the input is single polarisation aligned with probe 1 and 3. As shown in Fig. 2, S (waveport1,lumpport1) (blue), S (waveport1, lumpport3) (green) represent forward transmission coefficient for the polarised opposite pair probes; S (waveport1, lumpport2) (red), S (waveport1, lumpport4) (pink) represent forward transmission coefficient for the depolarised opposite pair probes; S (waveport1, waveport1) (black) represents the return loss. It can be observed that the two traces of polarised pair probes overlapped perfectly at −3 dB each. The power is divided equally between them. The other two depolarised traces are below −42 dB through the band. The return loss is below −30 dB from 128 to 170 GHz.

For 225 channels, the polarised probe 1 and 3 overlapped perfectly with the power divided equally into the two probes and the other depolarised pair probes are below −50 dB through the band. The return loss is below −30 dB from 187.5 to 252.5 GHz.

4. OPTIMIZATION OF THE 4-PROBES PLANAR OMT

The design of the planar OMT needs to be modified to accommodate fabrication and mounting tolerances. First modification is to increasing the size of the gap between the input waveguide

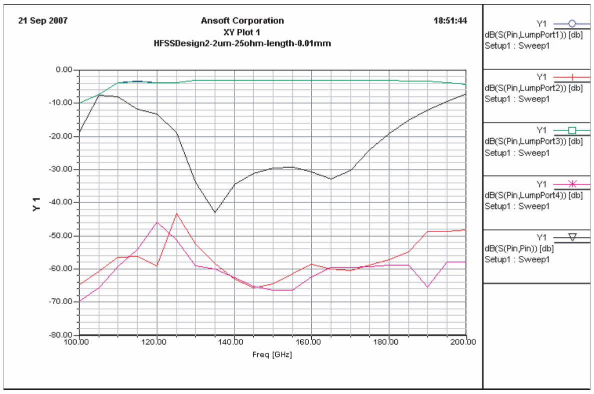

Figure 2: S-parameters for 4-probes OMT for 150 GHz channels.

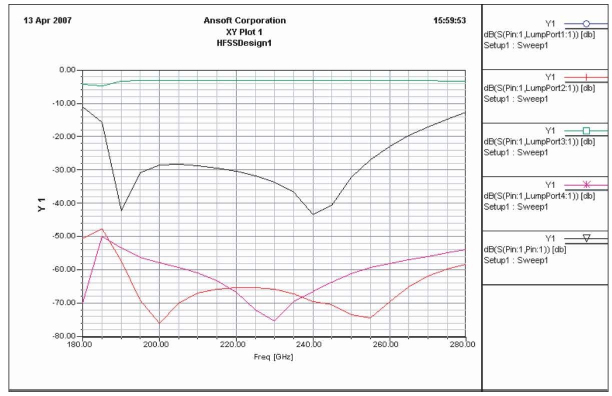

Figure 3: S-parameters for 4-probes OMT for 225 GHz channels.

and the backshort flange from 20 µm to 60 µm to accommodate tolerancing of machining, silicon substrate thickness and mounting of the chip (glue thickness); the other main modification is to add an air gap between the silicon substrate and the metal backshort with a total of 65 µm to accommodate the differential thermal contraction of the silicon and the metal flange and overetching of the silicon during processing. The model with modifications is shown in Fig. 4.

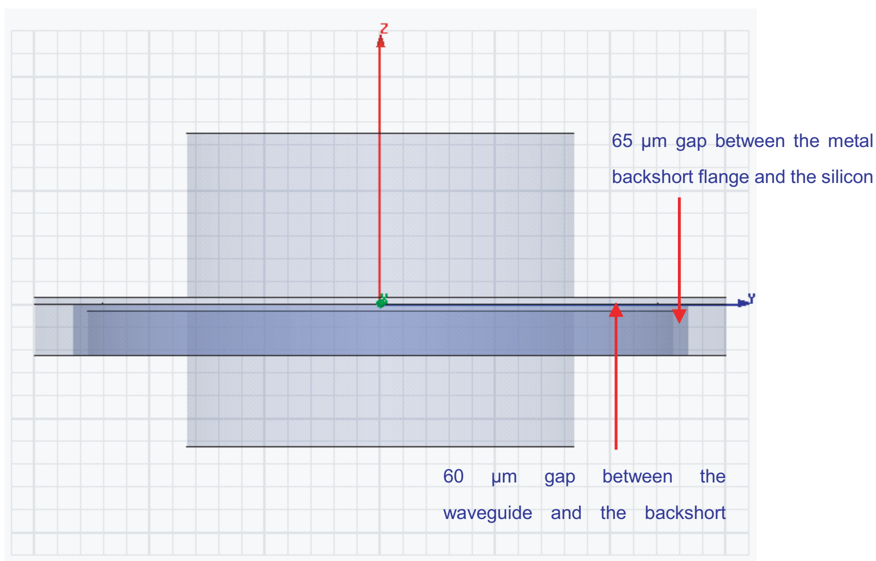

Figure 4: OMT for 150 GHz channels (with modifications).

As a result of scaling the design with fixed manufacture criteria, a higher level of power leaking into the gap was introduced compared with the previous designs. This higher level of power also enhanced a resonant feature at the lower end of the band, for 150 GHz channels as example it is at around 130 GHz. The simulation result is shown in Fig. 5. It can be observed that at 130 GHz there is a resonant feature. The resonance feature appeared due to the area between the waveguide and the silicon acting as a ring resonator. The 3-wavelength mode occurred at 130 GHz and therefore was independent of the dimensions of the silicon and the metal grounding ring on the silicon nitride.

To solve this problem, radial slots were cut in the input waveguide and backshort flange at 45 degree to the probes, as shown in Fig. 6(a). This effectively increases the circumference of the ring resonator and moves the resonance to lower frequency. This also gives a lower in-band reflection than cutting the ground plane. The simulation result is shown in Fig. 6(b). It can be observed that the resonance has shifted from 130 GHz to lower frequency at 115 GHz. The return loss reached below -20 dB in the range of 117.5 to 162.5 GHz. The power leaking through the air gaps is represented by the bright green curve, which is now below -28 dB through the required band.

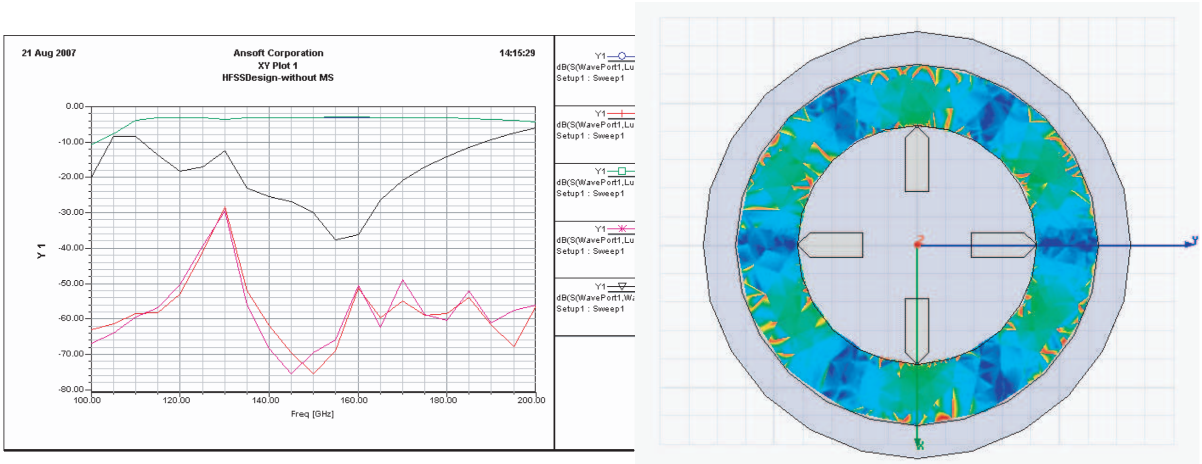

(a) (b)

Figure 5: (a) S-parameters of OMT for 150 GHz with modification. (b) Simulated field in backshort at 130 GHz (top view).

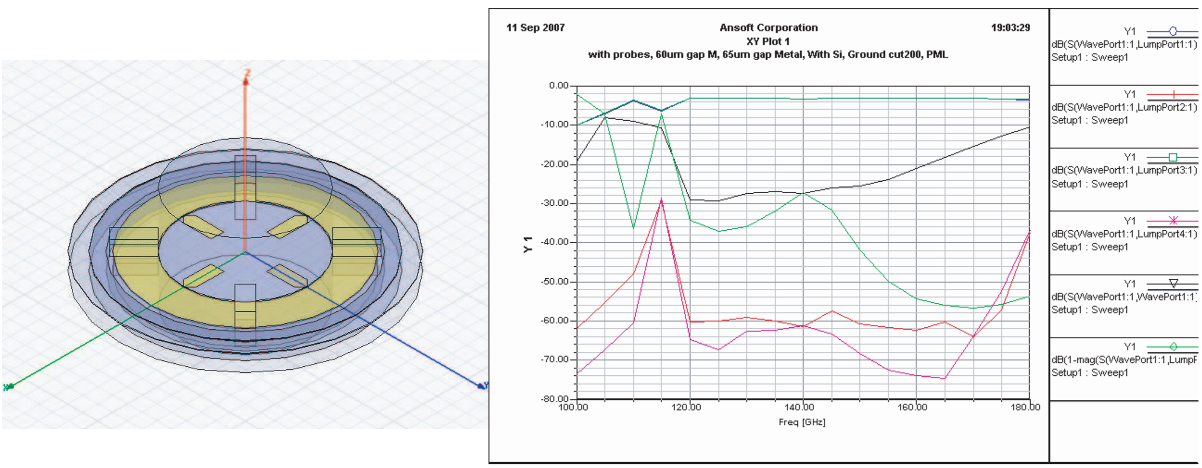

(a) (b)

Figure 6: (a) OMT model for 150 GHz channels with radial slots in the waveguide and backshort flange. (b) Simulated S-parameters of 150 GHz model with radial slots in the waveguide and backshort flange.

5. CONCLUSION

Based on the simulation results from HFSS for both 150 and 225 GHz channels, the microstrip design is seen to yield good performance. The final model for 150 GHz channels has been iterated to test the performance loss due to fabrication and mounting errors and is seen to give acceptable performance over a 75% bandwidth with a return loss below −20 dB. The forward transmission coefficient for the depolarized opposite pair probes, namely S (Waveport1, LumpPort2) and S (Waveport1, LumpPort4) are below −50 dB through the band from 129 GHz to 174 GHz. The power leakage through the air gaps is below −28 dB through the band. The test of prototype devices is currently on going in Cambridge Cavendish Laboratory.

REFERENCES

1. Bock, D., "Measurements of a scale-model ortho-mode transducer", *BIMA Memo*, 74, 1999.

Circular Polarization GPS Patch Antennas with Self-biased Magnetic Films

G. M. Yang[1], **A. Daigle**[1], **N. X. Sun**[1], **and K. Naishadham**[2]

[1]Center for Microwave Magnetic Materials and Integrated Circuits
Department of Electrical and Computer Engineering
Northeastern University, Boston, MA 02115, USA
[2]RF Communications Group, Draper Laboratory, Cambridge, MA 02139, USA

Abstract— Magneto-dielectric substrates with thin magnetic films show great potential in realizing electrically small tunable antennas with improved directivity and higher bandwidth than those realized on dielectric substrates. This paper introduces self-biased magnetic films as a practical means to tune a patch antenna by loading a commercially available dielectric substrate. Novel antenna designs with self-biased metallic magnetic films and ferrite films were investigated. These magnetic patch antennas have improved the axial ratio from 1.57 dB to 0.97 dB with respect to the central frequency ranging from 1.575 GHz to 1.562 GHz, a large radiation frequency tunability of about 40% to 80% of the −10 dB bandwidth, and a significantly enhanced directivity.

1. INTRODUCTION

In recent years, with the continuous growth of wireless communication technology, design and manufacturing low cost microwave components have become critical issues to the development of RF communications systems. As a very important passive component in a wireless communications system, miniaturized antennas with decent gain and bandwidth are receiving considerable attention in both industry and academia [1]. Planar antennas, because of their simple configuration, manufacturing advantages, as well as compactness, are highly desirable for these systems. The substrates of planar antennas play a very important role in antenna miniaturization. In particular, antenna substrates with larger relative permeability can lead to antenna miniaturization, enhanced bandwidth, tunable center frequency, polarization diversity, and beam steering [2–4].

Bulk ferrite materials, composites of ferrite particles in polymer matrix, metamaterials with embedded metallic circuits, etc., have been used as antenna substrates for achieving $\mu_r > 1$. However, these materials or composites are too lossy to be used at frequencies > 500 MHz under self-bias conditions, and large biasing magnetic fields are needed for ferrites to operate at higher frequencies. In order to be practically feasible in miniature circular polarization (CP) antennas [5] for Global Positioning System (GPS) applications, it is important for antenna substrates to be comprised of self-biased magnetic materials, in which no external bias field is applied. However, it has been challenging to achieve self-biased magnetic materials for antenna substrate applications at > 500 MHz frequency range. Magnetic thin films, however, provide a unique opportunity for achieving self-biased magnetic patch antenna substrates with $\mu_r > 1$ at > 1 GHz frequencies [6]. The strong demagnetization field for magnetic thin films, Hdemag $= 4\pi M_s$, allows for a self-biased magnetization with high ferromagnetic resonance (FMR) frequencies up to several GHz, which are essential for microwave devices.

In this paper, a CP patch antenna miniaturized using self-biased ferrite thin films embedded in alumina substrate is presented, thus essentially creating a magneto-dielectric substrate for practical applications. These magnetic patch antennas showed a decrease in axial ratio from 1.57 dB to 0.97 dB with respect to the central frequency ranging from 1.575 GHz to 1.562 GHz, a large radiation frequency tunability of about 40% to 80% of the −10 dB bandwidth, and a significantly enhanced directivity. These magnetic antennas can be made conformably at a low cost near room temperature.

2. DESIGN OF CIRCULAR POLARIZATION PATCH ANTENNA

Figures 1(a) and (b) show the schematic top view and side view, respectively, of the circular polarization patch antenna. This antenna consists of a rectangular patch with seven fingers on each side. Both the patch and the fingers are realized by patterned copper cladding on the top surface of the underlying dielectric substrate. A metallic side-wall is adopted to improve the antenna's directivity, with the same height as the dielectric substrate. A circular ground plane with the radius of 101.6 mm is added at the back of the dielectric substrate. The feed point is located on the 45 degree diagonal, with a distance of 2.54 mm along the x-axis. This structure excites two degenerate orthogonal modes with equal amplitude and 90 degree phase difference, and right hand circular polarization (RHCP) radiation is obtained. The substrate has relative permittivity of 13 and a thickness of 1.52 mm. All the other parameters are listed in the caption of Fig. 1.

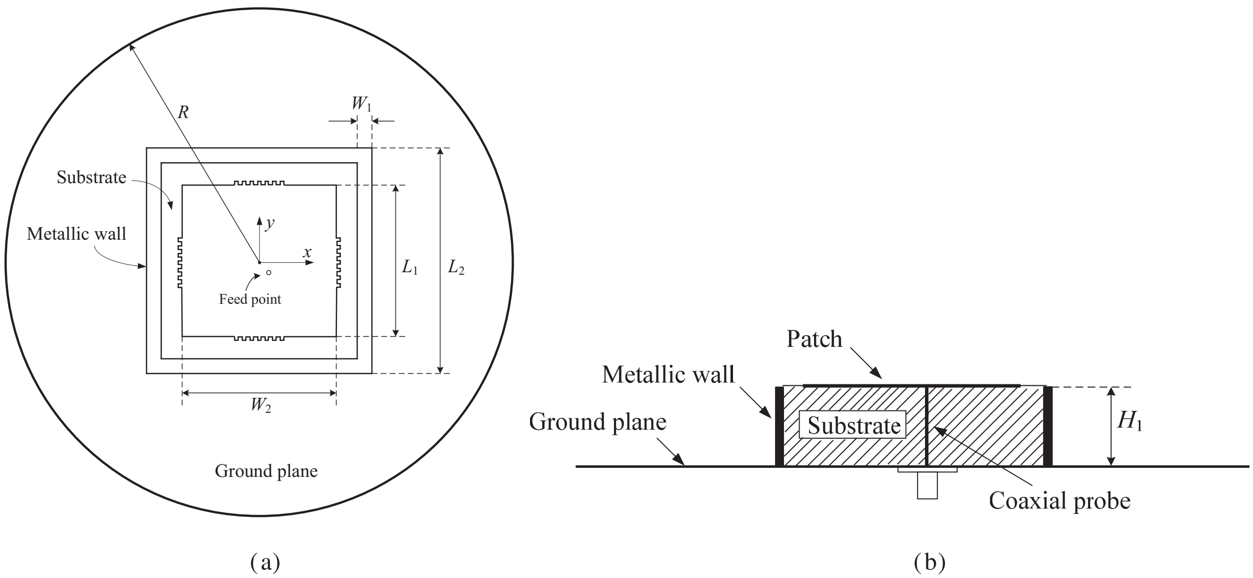

Figure 1: Geometry of the circularly-polarized rectangular patch antenna with fingers. (a) Top view, $W_1 = 2.54$ mm, $W_2 = 25.96$ mm, $L_1 = 25.76$ mm, $L_2 = 32.76$ mm and $R = 101.6$ mm, (b) side view, $H_1 = 1.52$ mm.

3. ANTENNAS WITH MAGNETIC FILMS AND SIMULATED RESULTS

In order to obviate biasing of magnetic substrates by an external field, we propose using self-biased ferrites films with a relatively high in-plane anisotropy. This large anisotropy enables a low loss tangent of the ferrite films at GHz frequencies. The ferrite films used have a relative permittivity of 13 and relative permeability of 10 with zero loss tangent.

Three CP patch antennas with ferrite films are designed as follows. Case I, a ferrite thin film of thickness 2 μm and surface dimensions $L_1 \times W_2$ introduced just below the rectangular patch, as indicated in Fig. 2(a).

For case II, a 2 μm thick ferrite film is added just above the ground plane, as shown in the schematic in Fig. 2(b). In this case, the ferrite film has the same size as the dielectric substrate. Combining the above two cases, we also design an antenna with two ferrite layers in case III. One film is just beneath the rectangular patch, and the other above the ground plane as shown in Fig. 2(c). All these three antenna designs with ferrite films can be readily fabricated.

In order to compare the results with the non-magnetic patch antenna, the return loss, the axial ratio and the radiation pattern of ferrite-loaded patch antenna are plotted and analyzed next. The return loss curves in Fig. 3 are from simulations under the condition that all the geometrical dimensions of the antenna are kept unchanged, and only the ferrite films are added at different layers. All the simulations, including the baseline non-magnetic patch antenna, were carried out with Ansoft's HFSS software.

From Fig. 3 we can see that the central resonant frequency of the non-magnetic patch antenna is about 1.575 GHz, and the −10 dB bandwidth is 16 MHz. When a ferrite film is added below the patch in case I, the resonant frequency shifts down to 1.569 GHz with the magnitude of −15.6 dB. This indicates a tuning range of 6 MHz relative to the non-magnetic patch, or equivalent to approximately 40% of the bandwidth. The bandwidth remains unchanged with addition of the ferrite film. When a ferrite film is added just above the ground plane in case II, we observe that the resonant frequency is still equal to 1.569 GHz, but with a magnitude of −18.4 dB, indicating that case II has better impedance matching than case I. In the third case, two ferrite films are added below the patch and above the ground plane at the same time, which moves the resonant

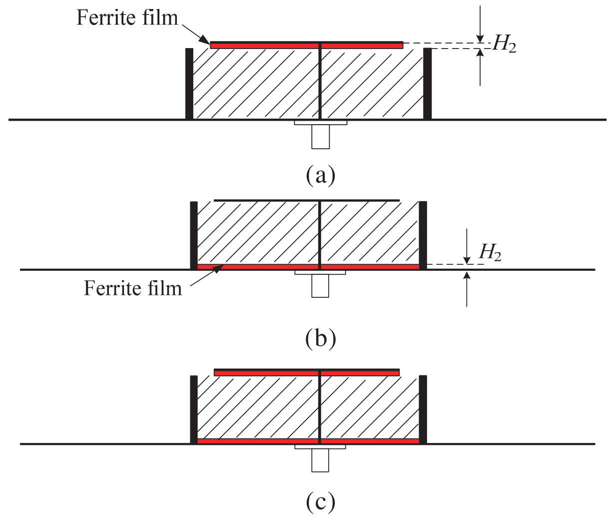

Figure 2: (a) Case I, antenna with ferrite film below the rectangular patch, (b) case II, antenna with ferrite film above the ground plane, (c) case III, antenna with ferrite films both below the rectangular patch and above the ground plane. The thickness of the film is $H_2 = 0.002$ mm.

frequency further down to 1.562 GHz, a shift about 80% of the antenna bandwidth relative to the non-magnetic patch antenna. In summary, we note that the patch antenna loaded with ferrite film can indeed miniaturize the geometrical dimensions effectively (as demonstrated by shifting down the resonance), while the bandwidth remains unaffected. We will show next that the antenna gain is also unaffected by the ferrite film, thus proving that the miniaturization does not compromise either gain or bandwidth.

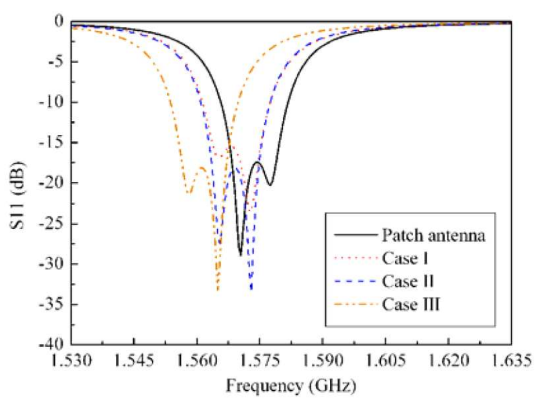

Figure 3: Simulated return loss against frequency for the four different cases.

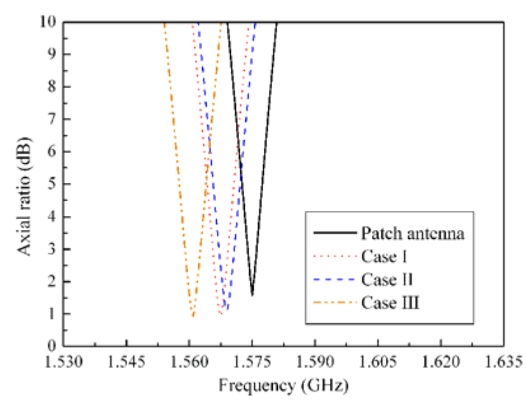

Figure 4: Simulated axial ratio against frequency of the four cases.

The axial ratios of the circular polarization are also computed and presented in Fig. 4, in which the CP bandwidth, determined from 3-dB axial ratio, is found to be about 4 MHz. The axial ratios of these four antennas are 1.57, 1.0, 1.1 and 0.97, respectively. The simulated radiation patterns at the corresponding central frequency are plotted in Fig. 5. Good right hand CP radiation is obtained, with the worst-case cross-polarization isolation at broadside equal to about −15 dB for case I. The isolation for cases II and III is slightly better, at about −17 dB. All the three cases have identical RHCP radiation pattern, with the antenna gain in the broadside direction about 2.8 dBi.

In order to evaluate omni-directionality in the xy-plane of the radiation pattern, the gain of the simulated RHCP radiation patterns for an elevation aspect of 80 degrees is plotted in Fig. 6 against the azimuth angle. The peak-to-peak variation in RHCP gain, a measure of the omni-directionality, is about 1.1 dB for the non-magnetic patch antenna, and 0.8 dB for case I. However, both case II and case III demonstrate smaller peak-to-peak variation in the RHCP pattern, with values about 0.6 dB and 0.4 dB, respectively. Thus, to get the most omni-directional pattern, addition of ferrite

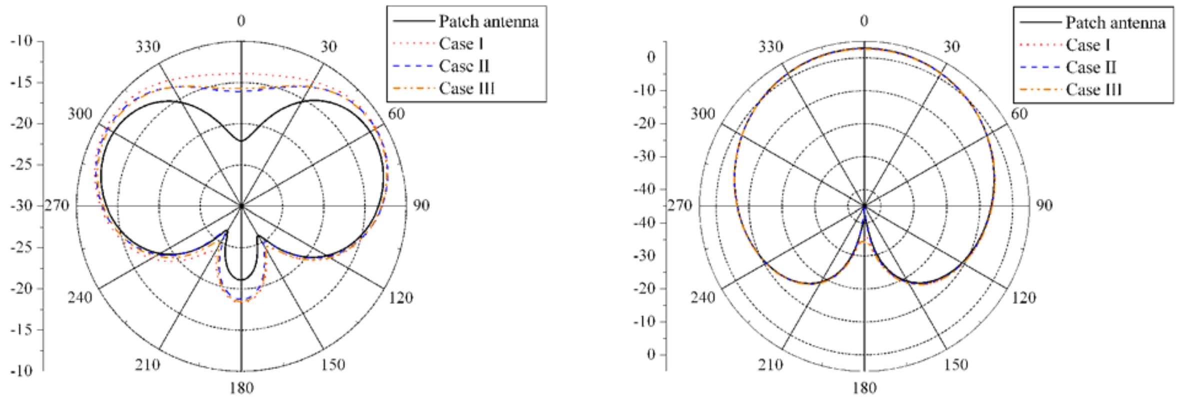

(a) (b)

Figure 5: Simulated radiation patterns with respect to central resonant frequency, (a) LHCP, (b) RHCP.

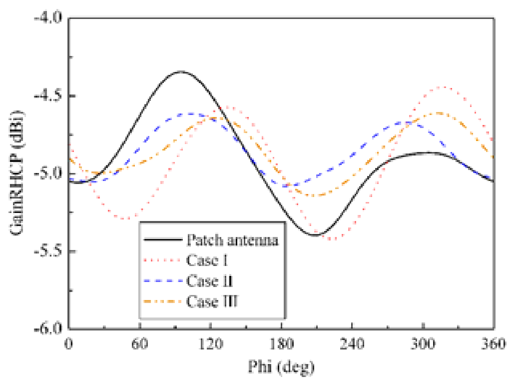

Figure 6: Simulated RHCP radiation patterns at the central resonant frequency ($\theta = 80°$).

films both below the patch and above the ground plane appears to be the best option. We note from Figs. 3 and 4, respectively, that case III also results in the lowest resonant frequency (or the smallest antenna) among the four options, and the lowest axial ratio.

4. CONCLUSIONS

Four circular polarization patch antennas with/without ferrite films are designed and analyzed in this paper. The designed magnetic patch antennas with self-biased ferrite magnetic films can realize a tuning range of 40 to 80% of the antenna bandwidth. The axial ratio can be improved from 1.57 dB to 0.97 dB with respect to the central frequency, which shifts from 1.575 GHz to 1.562 GHz, indicating modest miniaturization. Improvement of omni-directionality in the radiation pattern, without sacrificing peak gain, is also demonstrated with the addition of ferrite films adjacent to both the patch and the ground plane.

REFERENCES

1. Wong, K. L., *Planar Antennas for Wireless Communications*, John Wiley, Hoboken, NJ, 2003.
2. Mosallaei, H. and K. Sarabandi, "Antenna miniaturization and bandwidth enhancement using a reactive impedance substrate," *IEEE Trans. Antennas and Propagat.*, Vol. 52, No. 9, 2403–2414, Sep. 2004.
3. Brown, A. D., J. L. Volakis, L. C. Kempel, and Y. Y. Botros, "Patch antennas on ferromagnetic substrates," *IEEE Trans. Antennas Propagat.*, Vol. 47, No. 1, 26–32, Jan. 1999.
4. Bell, J. M., M. F. Iskander, and J. J. Lee, "UWB hybrid EBG/ferrite ground plane for low-profile array antennas," *IEEE Trans. Antennas Propagat.*, Vol. 55, No. 1, 4–12, Jan. 2007.
5. Huang, C. Y., J. Y. Wu, and K. L. Wong, "Cross-slot coupled microstrip antenna and dielectric resonator antenna for circular polarization," *IEEE Trans. Antennas and Propagat.*, Vol. 47, No. 4, 605–609, Apr. 1999.

6. Sun, N. X., J. W. Wang, A. Daigle, C. Pettiford, H. Mosallaei, and C. Vittoria, "Electronically tunable magnetic patch antennas with metal magnetic films," *Electronics Letters*, Vol. 43, No. 8, 434–435, Apr. 2007.

The Dipole Antenna Array Design with Balun Integration

Guan-Yu Chen[1], **Jwo-Shiun Sun**[1], **Cheng-Hung Lin**[2], **Kwong-Kau Tiong**[2], **and Y. D. Chen**[3]

[1]Department of Electronic Engineering, National Taipei University of Technology, Taiwan
[2]Department of Electrical Engineering, National Taiwan Ocean University, Taiwan
[3]Antenna and EMC Laboratory, High Tech Computer Corp. (HTC), Taiwan

Abstract— In this paper, the array antenna design is suitable for wireless LAN, radio identification, wireless sensor and short rage intelligent wireless communication. In this design, the 1×2 dipole antenna feed network with magic T and divider two wide bandwidth planar tapered balun is studied.

1. INTRODUCTION

In this dipole antenna array design, the dipole antenna feed network with wide bandwidth tapered microstrip balun is studied [1]. The design and experimental results [2] of low profile embedded microstrip dipole antenna with tapered microstrip balun shows fairly good performances. The feed network of the design with wide bandwidth and lower power loss tapered microstrip line to overlap coplanar stripline (CPS) transition that provided unbalanced to balanced line with balanced equal power output of phase difference. The achieved planar embedded ISM band dipole antenna exhibits wider bandwidths at 2.4 GHz center frequency, respectively. Apply full wave EM analyses and shows good agreement with those experimental data. Balanced network feed for dipole antenna not only exhibits equal power magnitude with 180° phase difference but also improves matching capability. Balanced to unbalanced (Balun) transformers is commonly applied in many applications such as balanced mixer, push-pull amplifier, balanced frequency multipliers, phase shifters, matching structures, etc. Double Y balun, Marchand balun, etc. as the antenna feed networks are hard to implement with complex transition problem to solve. A simple and quick method of balun network [1, 2] is proposed as a feeding network for low profile planar dipole antenna. The simple tapered balun for the designed dipole antenna exhibits fairly good performances and compact size. The balanced transmission line with an embedded balun for a half wavelength dipole antenna is shown in Fig. 1 and Fig. 2.

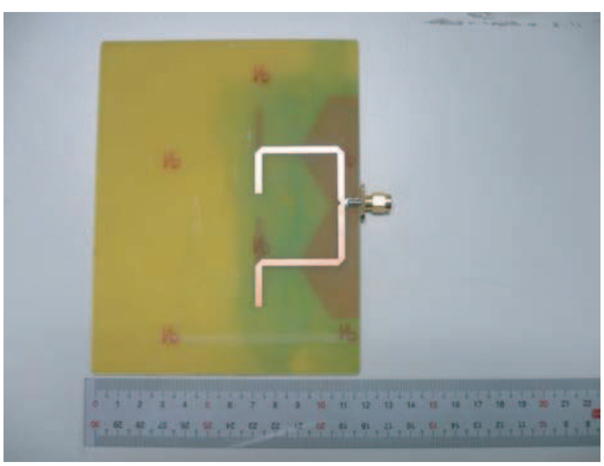

Figure 1: The proposed 1×2 dipole array (top).

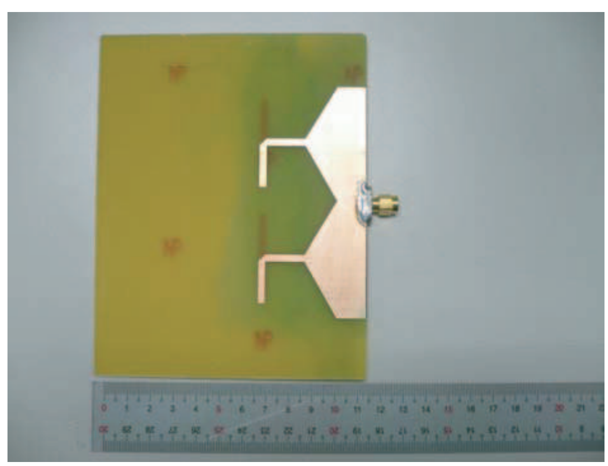

Figure 2: The proposed 1×2 dipole array (bottom).

2. ARRAY ANTENNA DESIGN AND RESULTS

The design and experimental results of low profile embedded dipole antenna array (Fig. 1 and Fig. 2) with tapered balun shows fairly good performances and antenna gain. The feed network of the design with wider bandwidth and lower power loss tapered microstrip line to coplanar stripline (CPS) transition that provided unbalanced to balanced line with balanced equal power output of phase difference. The achieved planar embedded wider band dipole antenna array exhibits antenna

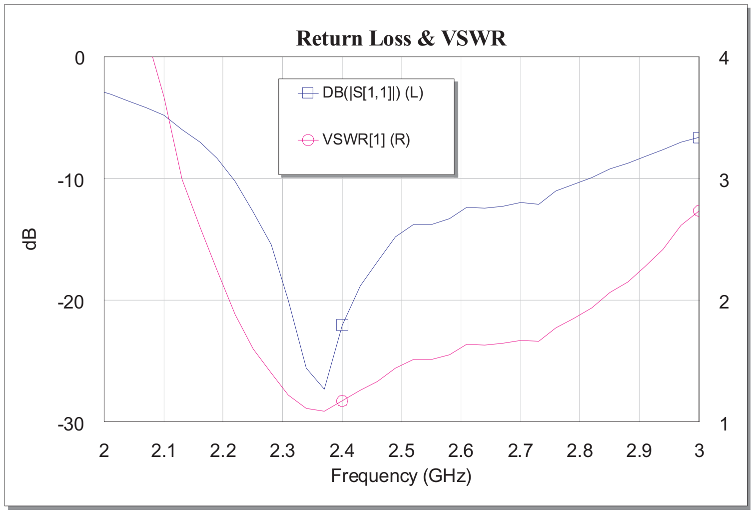

Figure 3: The measured data of return loss and VSWR.

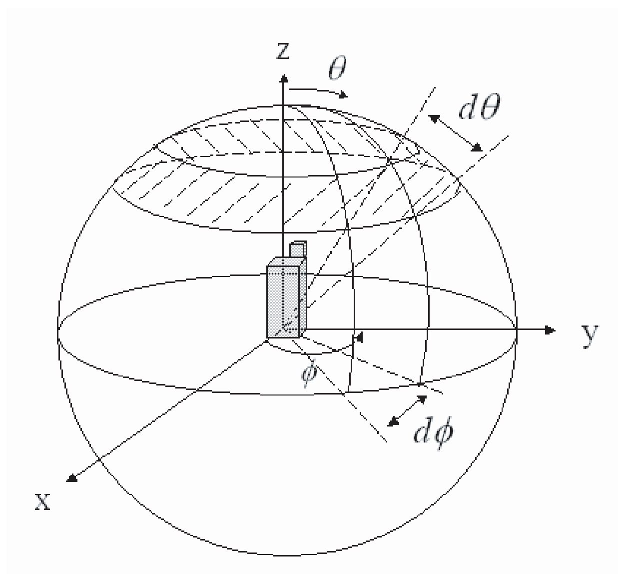

Figure 4: 3D antenna measurements.

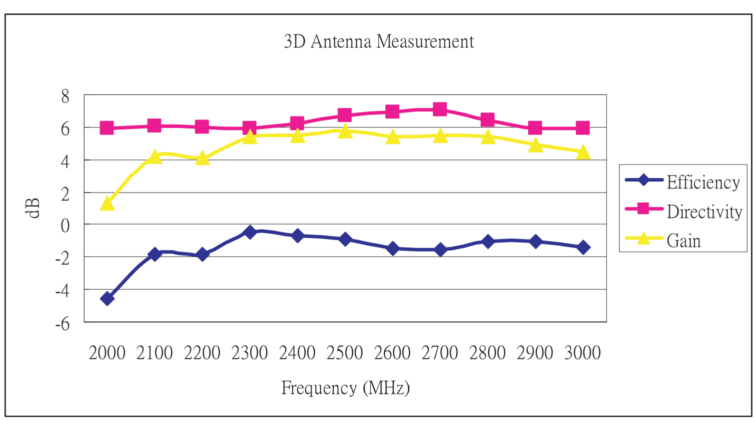

Figure 5: The measured data of 3D antenna performance.

bandwidths (Fig. 3) cover WLAN (IEEE 802.11a/b), RFID (ISM band) and DSRC (IEEE 802.11p), respectively. Apply full wave EM analyses and shows good agreement with those experimental data. The 3D antenna measued method [3–6] and data are shown in Fig. 4 and Fig. 5.

3. CONCLUSIONS

In this wide band dipole design, low profile tapered microstrip line balun feed dipole array antennas with center frequencies at 2.4 GHz is study. The measured results show fairly good performances and fine agreements with those simulated data from full wave EM analyses. The embedded dipole antenna array with matching tapered ground plane exhibits an available bandwidth as well as good impedance matching with a feeding balun. The achieved planar embedded wide band dipole antenna array exhibits wide bandwidths at 2.4 GHz center frequency. The radiation efficiency and return loss of the dipole antenna array fill the bill and anticipation of the design.

ACKNOWLEDGMENT

The authors acknowledge the Antenna and Wireless System Integration Department of High Tech Computer, Corp (HTC), Taiwan for sport the wireless technique and measurement environment.

REFERENCES

1. Chen, G. Y. and J. S. Sun, “A printed dipole antenna with effective microstrip tapered balun,” *Microwave & Optical Technology Letters*, 344–346, Feb. 2004.
2. Chen, G. Y. and J. S. Sun, “Low profile planar dipole antenna,” *IEE Electronics Letters*, 790–792, June 2004.
3. CTIA, http://www.ctia.org/
4. *Test Plane for Mobile Station over the Air Performance*, Revision 2.1, Cellular Telecommunications & Internet Association (CTIA), Washington, D.C., Apr. 2005.
5. Stutzman, L. W., *Antenna Theory and Design*, John Wiley, 1998.
6. Balanis, A. C., *Antenna Theory*, John Wiley, 2005.

Printed Digital Audio Broadcast Antennas

The-Nan Chang and Cheng-Min Jen
Graduate Institute of Communication, Tatung University, Taiwan

Abstract— In this paper, printed antennas were studied for digital broadcast reception. The first one is a meandered loop antenna. Being in a meandered form, it can be made very compact. However, the gain and efficiency are quite low. In our study, the measured gain is only −30 dBi. Aside from low gain, the bandwidth is also narrow. Therefore, this configuration may not be practical in use.

We then studied a bow-tie antenna. Bow-tie antenna is typically considered to have more bandwidth than the meandered configuration. Its gain increases up to 1.85 dBi. Measured bandwidth is around 8%. For DAB reception in upper half of Band III, a required bandwidth of 13% is needed. We found that the bandwidth can be increased by half-sizing the bow-tie antenna without reducing too much of its gain. This half sized bow-tie antenna (HBTA) takes an area of 475 mm by 110 mm. Measured 10 db return loss bandwidth ranges from 192 to 236 MHz, or 21% bandwidth centered at 214 MHz. The gain is 1.78 dBi within the whole band.

1. INTRODUCTION

DAB uses a wide-bandwidth broadcast technology. Its spectrum have been allocated in Band III (174–240 MHz) and L band (1452–1492 MHz). Not every country takes full sectrum of Band III. For example, in Taiwan, we only use uppeer-half band (210–240 MHz, or 13% centered at 225 MHz). The free space wavelength for center frequency of 215 MHz in Band III is 133 cm. In order to have a compact size and take advantage of using printed circuit technique, one may design an antenna with a meandered line configuration. To our best knowledge, the achieved gain is quite low using such a configuration at this low frequency band. In order to increase gain, we try a traditional bow-tie antenna. As is expected, the gain is increased at the cost of a large space. However, we found that the gain is only slightly reduced by half-sizing the previous antenna. The bandwidth, however, can be made broader.

2. MEANDERED ANTENNA

The geometry of the top metal surface of a meandered double-sided loop antenna is shown in Fig. 1. The same metal pattern is also etched on the bottom side of an FR4 substrate, which has a thickness of 1.6 mm. If the thickness goes to zero, the top and bottom surface are overlapped. The path starts at the right feeding point to point B, then goes down to a corresponding opposite point (not shown) at the bottom side via a connecting metal post, en-routing the path on bottom surface to a point opposite to point A and goes up to point A via another connecting post. The

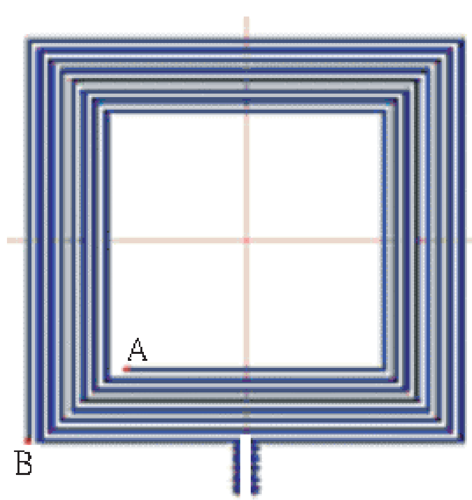

Figure 1: Configuration of a meandered loop antenna.

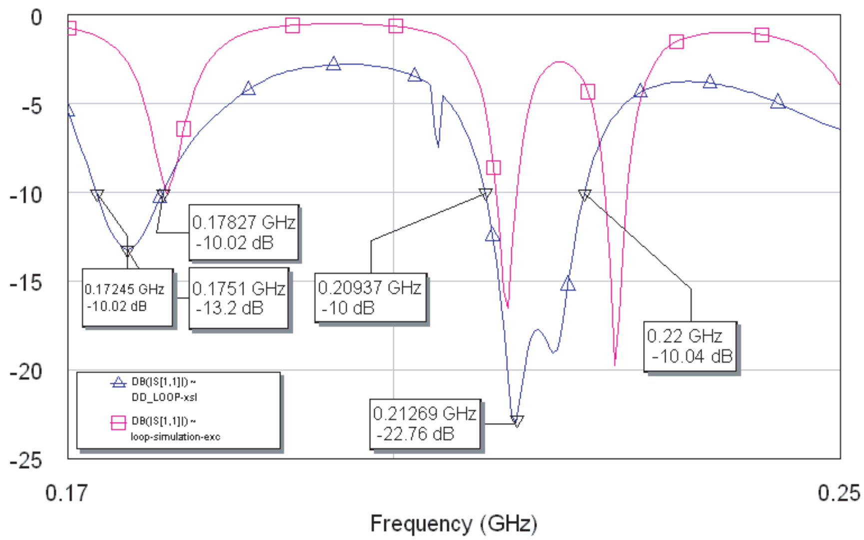

Figure 2: Return loss of a meandered antenna.

dimensions of the antenna are 102 × 87 mm. There are 8 turns. Each turn has a width of 1 mm. Length of each turn varies from 208 mm to 320 mm. Total length of the loop is 2112 mm(single side). The loop antenna is fed by a coaxial cable. No balun was used in our study.

Return losses in Fig. 2 were measured and compared with simulation results by IE3D. Simulation shows that there are three separate frequency bands. In [1], we have studied that multiple resonances can be generated via coupled meander structures. We also pointed out that multi-frequency bands can be brought together by a back-side tuning scheme. In Fig. 2, measured results show that there is a coupling band from 209 to 220 MHz. The coupling effect may be due to the unbalanced feeding. Maximum measured gain at bore sight direction is −30 dBi at 210 MHz. Low gain of this antenna makes it of no practical use. After trying different meandered configurations to boost the gain, we found none can have a gain above −10 dbi with this compact size.

To increase both gain and bandwidth, a planar bow-tie antenna shown in Fig. 3(a) is constructed. It contains two radiating triangle branches; fabricated on FR4 substrate with a thickness of 1.6 mm. Dimensions are 390 mm by 220 mm. Measured 10 db return loss bandwidth is from 207 to 225 MHz, the percent bandwidth is 8% centered at 216 MHz.

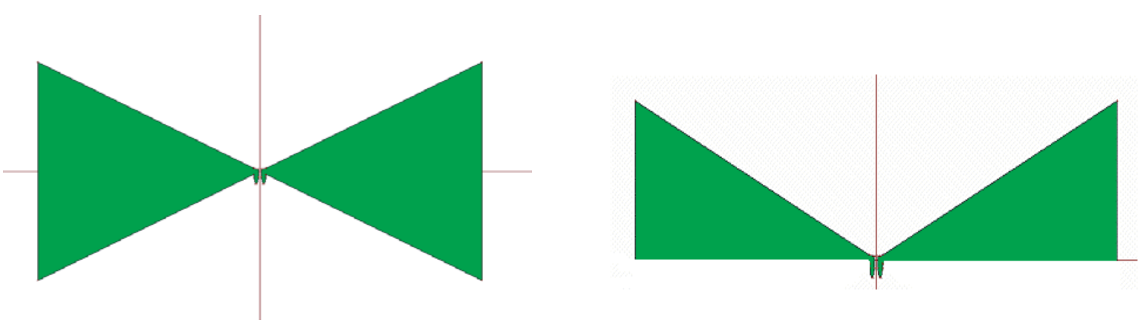

(a) (b)

Figure 3: Geometry of (a) a bow-tie antenna, (b) a half sized bow-tie antenna.

3. HALF-SIZED BOW-TIE ANTENNA (HBTA)

We found most current flows around edges of the planar bow-tie antenna. By half-sizing the bow-tie antenna, we get an HBTA configuration shown in Fig. 3(b). The current still flows around edges for an HBTA. As the effective length of current flow is reduced, we expect that the operating frequency gets higher. For an HBTA with a dimension of 390 mm by 110 mm, 10 dB return loss bandwidth ranges from 234 to 260 MHz. Therefore, the center operating frequency increases from 216 to

247 MHz. We also note that the bandwidth is also increased from 8% to 11% without reducing too much of the gain. Therefore, one easy way to get a 13% bandwidth within the upper half Band III, we may keep the height of an HBTA as 110 mm while increasing its width. Fig. 4 shows simulation results by varying its width from 390 to 450 mm. It is clear that we can get 30 MHz or 14% bandwidth centered at 218 MHz with a width of 450 mm. To have some safe margins, an HBTA antenna with a dimension of 470 mm by 110 mm was constructed. Fig. 5 shows simulated and measured results of this antenna. Measured 10 db return loss bandwidth of the antenna is from 192 to 236 MHz, or 20% centered at 214 MHz. The simulated bandwidth is 34 MHz or 16% centered at 214 MHz. The antenna provides horizontal polarization with a measured maximum gain of 1.78 dBi which is compatible with a gain of 1.85 dBi for the full sized bow-tie antenna.

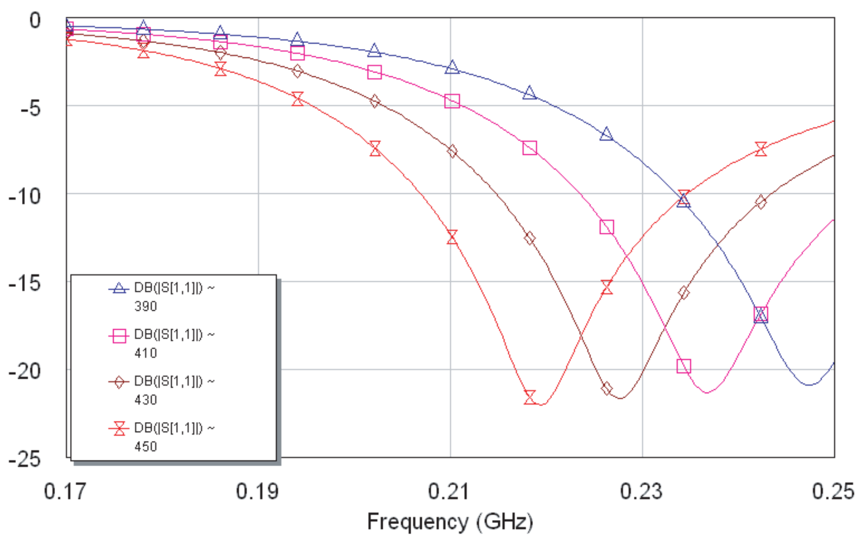

Figure 4: Return losses of HBTA antennas with various widths.

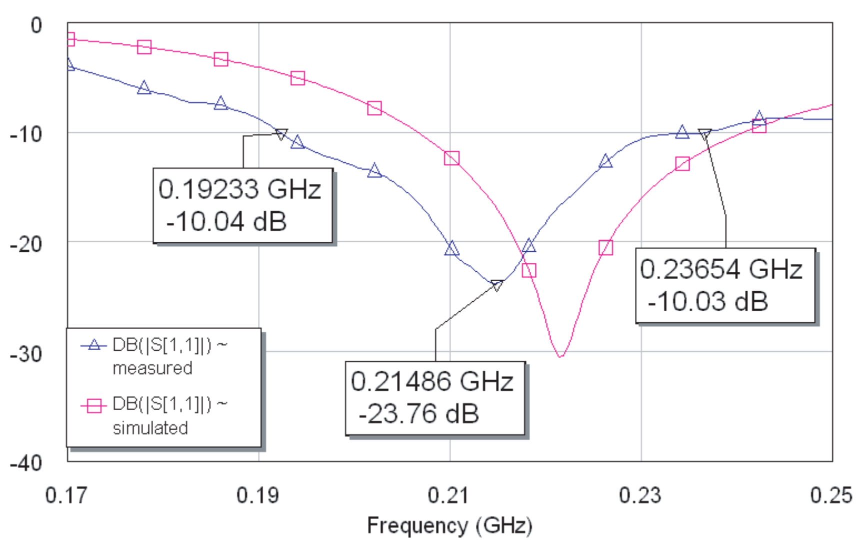

Figure 5: Simulated and measured return losses of an HBTA antenna.

As a comparison, a printed flat dipole with a dimension of 470 mm by 10 mm has a 10 db return loss bandwidth of 24 MHz, or 8.8% centered at 274 MHz. To bring the bandwidth within upper half Band III, a dimension of 602 mm by 10 mm is required, which yields a bandwidth of 20 MHz, or 9% centered at 215 MHz.

4. CONCLUSION

In this paper, printed meandered loop and bow-tie antennas are studied. Meandered loop has a very compact size with a very low gain at DAB band. The bow-tie antenna has a gain of 1.85 dBi and a bandwidth of around 10%. A flat dipole with a wider width (602 mm in width) can provide only 10% bandwidth. To increase bandwidth without sacrificing the gain, an HBTA configuration was introduced. This antenna can provide 16% simulated bandwidth with a dimension of 470 mm by 110 mm. Generally speaking, bandwidth can be increased with a wider width for the same height of either a bow-tie or a HBTA antenna. The limitation is around 16%, which can be judged from Fig. 4. Therefore, it is hard to cover full Band III (174–240 MHz) by the present configuration. However, the HBTA is superior to the traditional bow-tie antenna in terms of occupied space if we limit our bandwidth within half upper Band III.

REFERENCES

1. Chang, T.-N. and C.-C. Kuo, "Meander antenna with backside tuning stubs," *IEEE Transactions on Antennas and Propagation*, Vol. 53, No. 4, April 2005.

Two-layer Variable Slot Length Reflectarray

The-Nan Chang and Chia-Hsin Chung
Graduate Institute of Communication, Tatung University, Taiwan

Abstract— In this paper, a microstrip patch loaded with a co-plane slot and an atop-patch is used to realize a 12 GHz reflectarray on a two-layer substrate. Phase of reflection is adjusted by tuning the length of each slot. Two different lengths of the atop-patch are selected so that we can have a full 360° phase shift range.

1. INTRODUCTION

To design a reflectarray, we usually need to devise a technique to control reflection phase shifts among adjacent elements. Different methods have been proposed. We can use identical patches with different length phase-delay lines or we can use patches with various sizes [1–3]. In [4], an array of patches loaded with slots was proposed. One interesting feature is that phases are controlled by both the length of the patch and the length of the slot aperture. Two kinds of patches with different lengths were etched on top surface of a single layer grounded substrate.

In this paper, we generate the idea of [4] and applied it to a two-layer substrate. On top surface of the first substrate layer, there is a square patch. On bottom surface of it, there is another square patch loaded with a slot. With such a structure, we find that the length of the top patch can also be used as a controlling factor. As the length of the patch is longer than the maximum variable length of the slot, there is very little phase shift tunable by the slot. The reason is that the effect of change in slot length is blocked by the top patch. The shorter the length of the top patch compared with the maximum variable slot length, the more the phase shift can be tuned by the slot. Therefore, we can employ patches with different lengths to control the required phase curve section by section so that a full 360 degrees phase shifts can be achieved.

2. BASIC CELL OF A TWO-LAYER VARIABLE SLOT-LENGTH REFLECTARRAY

Figure 1 shows the unit cell of the proposed structure. We keep values of s, d and s' fixed. S' determines spacing between adjacent elements and s and d are dimensions of the bottom patch. In [4], two different lengths of s were chosen while varying b to cover a 360° phase shift range in a single-layer substrate. Optionally, we can add one top patch. It is studied that two different lengths of patch are required while varying b for a full 360° phase shift control.

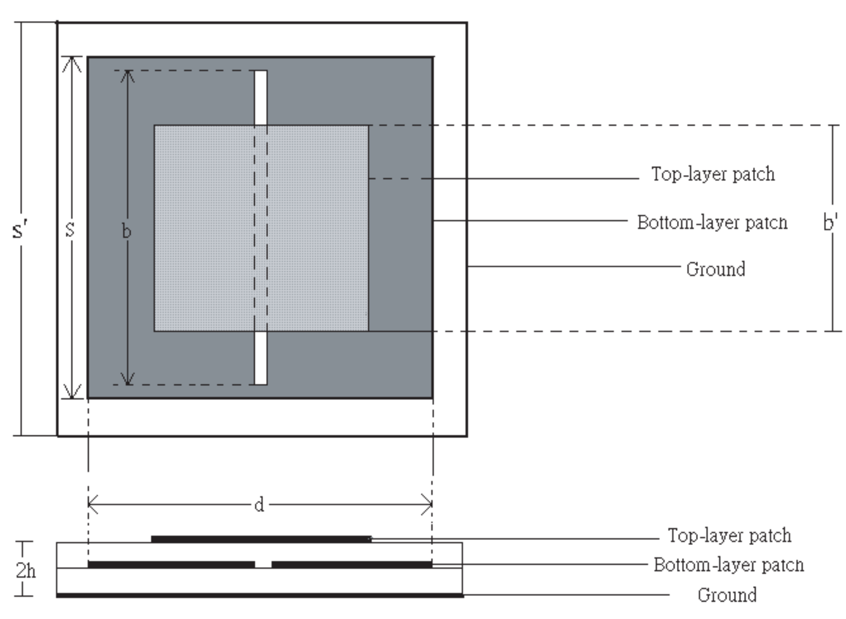

Figure 1: Unit unit cell of the proposed structure.

We etch rectangular slot on the bottom patch. The FR4 substrate is 3.2 mm thick ($h = h_1 + h_2 = 3.2$ mm, $h_1 = h_2$), and the unit cell is $10 \times 10\,\text{mm}^2$ ($s' = 10$ mm). The phase diagram shown in Fig. 2 depends not only on slot length, but also on length b' (or ratio $= b'/s'$) of the top patch. It is shown that a 237° (201° $\sim$ −36°) phase range can be obtained for $0.5 < b < 5.5$ mm and $r = b'/s' = 0.4$; and an 113° (−49° $\sim$ −172°) phase range is reached for $5.5 < b < 7$ mm and $r = 0.6$. By combining these two reflection phase sections, a full 360° phase range can be achieved.

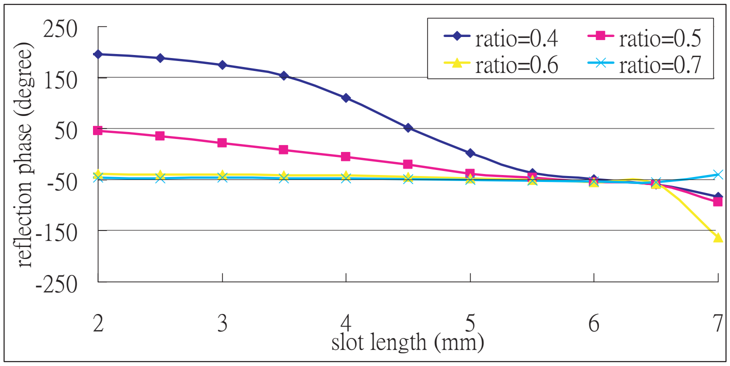

Figure 2: Simulated phase of the reflection coefficient versus slot length.

It is interested to note that three is very little phase change as slot varies for ratio of 0.7. In this case, the top patch length is equal to 7 mm. It is longer than the maximum varied slot length. Therefore, the tuning effect by varying length of the slot is largely blocked by the top patch. It is also noted that the blocked range is from 1 mm to 3 mm for ratio of 0.4 and is from 1 mm to 5.5 mm for ratio of 0.6. Since any curve using a single ratio cannot result in a full 360° phase shift, we need combine two phase sections to complete the full range. Fig. 3 shows phase diagrams at different frequencies. Based on this plot, bandwidth of the reflectarray can cover from 11.8 to 12.4 GHz, or 5% centered at 12.1 GHz.

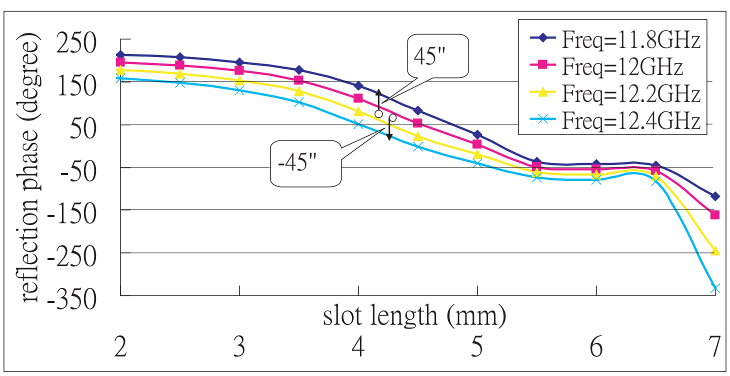

Figure 3: Reflection phase diagrams at different frequencies.

3. EXPERIMENT RESULTS

A reflectarray composed of 504 elements covering an area of 20 cm × 30 cm is constructed. An on-axis feed horn is located 24 cm ahead of the reflect array. Fig. 4 shows the measured gain from 11.6 GHz to 13.2 GHz, where a 1.5-dB bandwidth is 5.93%, from 11.6 to 12.3 GHz.

At 11.8 GHz the maximum gain is 24.39 dBi, the cross-polarization level is bellow −25 dB and the aperture efficiency is 31.4%. Fig. 5 shows the relative gain pattern at 12 GHz.

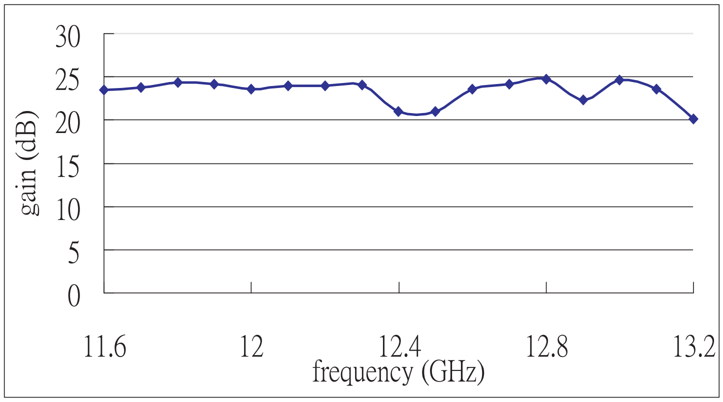

Figure 4: Measured gain versus frequency.

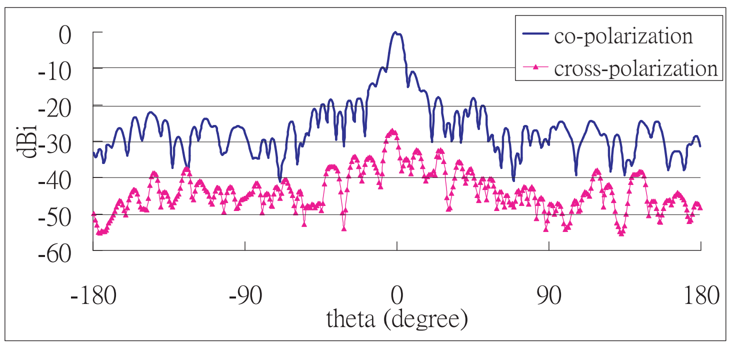

Figure 5: Co and cross polarization measurement at 12 GHz.

4. CONCLUSION

A new radiating cell consisting of a microstrip patch loaded with a co-plane slot and an atop-patch is used to realize a 12 GHz reflectarray on a two-layer substrate. It is found that relative length of the top patch with respect to the maximum variable length of the slot may be used to control the phase diagram. A phase shift range greater than 360° can be achieved by this method. Result of numerical simulations and measurements demonstrate the validity of the design procedure.

REFERENCES

1. Bozzi, M, S. Germani, and L. Perregrini, "Performance comparison of different element shaper used in printed reflectarrays," *IEEE Antennas and Wireless Propagat Letter*, Vol. 2, 219–222, 2003.
2. Encinar, J. A., "Design of two-layer printed reflectarrays using patches of variable size," *IEEE Trans. Antennas Propagat*, Vol. 49, No. 10, 1403–1410, October 2001.
3. Encinar, J. A. and J. A. Zornoza, "Broadband design of three-layer printed reflectarrays," *IEEE Trans. Antennas Propagat*, Vol. 50, No. 7, 1662–1664, July 2003.
4. Cadoret, D., A. Laisne, R. Gillard, L. Le Coq, and H. Legay, "Design and measurement of new reflectarray antenna using microstip patches loaded with slot," *Electronics Letters*, Vol. 41, No. 11, May 26, 2005.

The Planar V-dipole Antenna Fed by Marchand Balun

Cheng-Hung Lin[1], **Guan-Yu Chen**[2], **Jwo-Shiun Sun**[2], **Kwong-Kau Tiong**[1], **and Y. D. Chen**[3]

[1]Department of Electrical Engineering, National Taiwan Ocean University, Taiwan
[2]Department of Electronic Engineering, National Taipei University of Technology, Taiwan
[3]Antenna and EMC Laboratory, High Tech Computer Corp. (HTC), Taiwan

Abstract— The Marchand balun for microwave band as a feeding network structure that effectively excited tapered V-dipole antenna geometry is proposed. The microstrip line to coplanar strip line transition then to fed tapered V-dipole antenna. The designed quasi-tapered TEM horn (V-dipole) antenna has the merits such as wideband, simple feeding network, low profile compact size with fairly good antenna performances such as return loss, peak gain and radiation patterns.

1. INTRODUCTION

The radiation mechanism of a TEM horn antenna is based on traveling wave propagation along the tapered aperture slot, which results in an end-fire antenna. TEM horn or tapered slot antenna (TSA) exhibits some advantages such as wideband, wide scanning, high gain, low cross polarization and symmetrical E and H plane radiation patterns [1] for an array or embedded circuits as antenna radiating elements. Some articles for analyses of tapered slot antenna were studied such as moment method [2], finite difference time domain method [3]. And the applications of TSA were proposed in dual polarized antenna array [4], spatial power combining [5] and waveguide transition [6]. The general feeding structures in a TSA were mentioned with a coaxial cable, a microstrip line or a coplanar waveguide (CPW) [7–9]. A novel design method [10] for a TEM horn antenna is proposed on the basis of parallel plate waveguide theory. An exponentially tapered wideband TEM horn antenna [11] having a balun is designed. The balun is used to improve the impedance characteristic of the TEM horn antenna. The designed antenna can be used not only for EMC measurements, but also for broadband communication systems. A novel stable beamwidth, ultrawide-bandwidth low-scattering antenna [12] is presented. This antenna is a modified version of the conducting slot-line bowtie hybrid antenna with resistive sheets introduced into the guiding structure design. The analytical and design formula [13], based on conformal mapping, for the characteristic impedance of the transverse electromagnetic horn antenna. In this paper, the Marchand balun with a balanced to unbalanced transition is shown good impedance matching and easy to integration and fabrication and the frame of the planar structure on tapered TEM horn (V-dipole) was experimentally investigated. Measured results indicate that effects have significant impacts on the return loss, input impedance, radiation patterns and antenna gain of the TEM horn (V-dipole) antenna.

Figure 1: V-dipole antenna fed by Marchand balun.

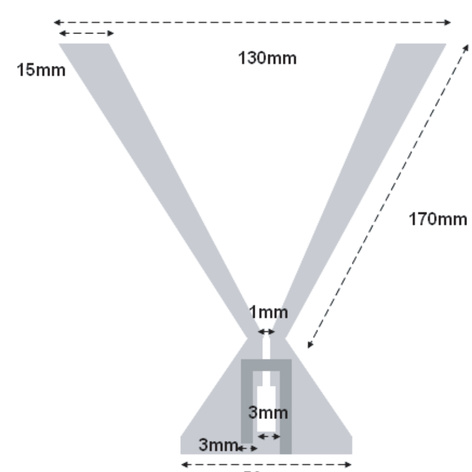

Figure 2: V-dipole antenna structure and size.

2. QUASI-TEM HORN (V-DIPOLE) ANTENNA

The coplanar stripline to feed planar tapered V-shape as quasi-TEM antenna radiator. The V-dipole antenna is a kind of traveling wave antenna that wave propagating along the tapered slot for heading radiation. The basic geometry of the designed TEM horn antenna is like a double ridge as shown in Figure 1. The transition provides wider balanced equal outputs, as well as a matching section for the traveling tapered slot of TEM horn antenna. The FEM software based on full wave frequency domain method [14] was adopted to perform the simulation of the designed low profile and planar TEM horn antenna. The planar quasi-TEM horn was fabricated on the FR4 substrate (dielectric constant = 4.4 and dielectric loss = 0.02) and detail size is shown in Figure 2. The simple quasi-TEM horn antenna structures exhibits broadband and low profile compact structure for UWB and impulse radio applications.

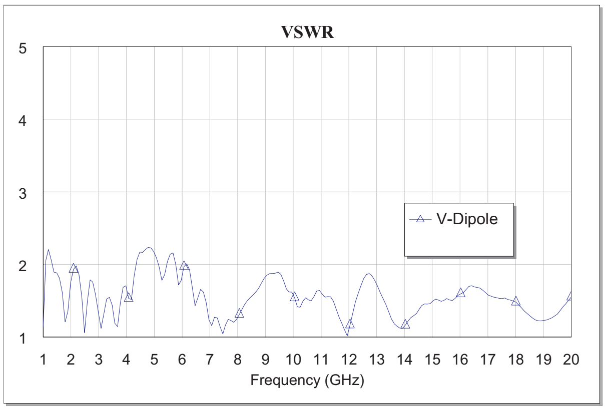

Figure 3: Measured data of VSWR.

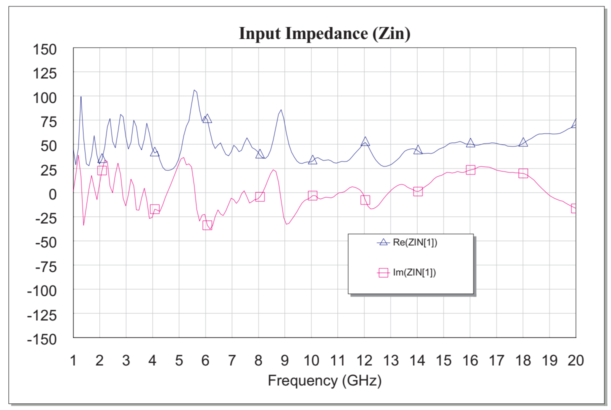

Figure 4: Measured data of input impedance.

3. RESULTS

Figure 2 shows the layout of the quasi-TEM horn (V-dipole) antenna size and structure. The measured VSWR and input impedance of V-dipole antenna (Zin = Rin + jXin) shows good impedance matching based on the transition as shown in Figure 3 and Figure 4. The radiation characteristics of the TEM horn antenna based on the spherical coordinate and 3D chamber system [15] are measured. The measured data of H-plane and E-plane are shown in Figure 5.

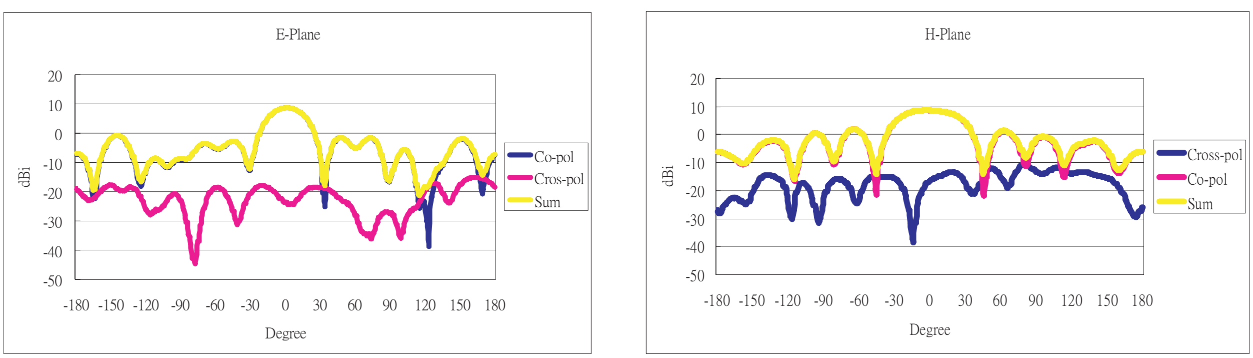

Figure 5: Measured 3 GHz antenna gain pattern of E and H plane.

4. CONCLUSIONS

The designed V-dipole antenna fed by coplanar stripline and the transition is presented. It exhibits the merits of geometric simplicity, wide bandwidth, lightweight, low cross polarization, and high peak gain. This V-dipole antenna is suitable for UWB impulse radio operation and application.

ACKNOWLEDGMENT

The authors acknowledge the Antenna and Wireless System Integration Department of High Tech Computer, Corp (HTC), Taiwan for sport the wireless technique and measurement environment.

REFERENCES

1. Lee, K. F. and W. Chen, "Advances in microstrip and printed antennas," *John Wiley & Sons, Inc.*, 1997.
2. Schaubert, D. H., J. A. Aas, M. E. Cooley, and N. E. Buris, "Moment method analysis of infinite stripline fed tapered slot antenna arrays with a ground plane," *IEEE Trans. Antennas Propagation*, Vol. 42, 1161–1166, Aug. 1994.
3. Thiele, E. and A. Taflove, "FD-TD analysis of vivaldi flared horn antennas and array," *IEEE Trans. Antennas Propagat.*, Vol. 42, 633–641, May 1994.
4. Chio, T. H. and D. H. Schaubert, "Parameter study and design of wide band widescan dual polarized tapered slot antenna arrays," *IEEE Trans. Antennas Propagation*, Vol. 48, 879–886, Jun. 2000.
5. Cheng, N. S., P. Jia, D. B. Rensch, and R. A. York, "A 120-w x-band spatially combined solid-state amplifier," *IEEE Trans. Microwave Theory Tech.*, Vol. 47, 2557–2561, Dec. 1999.
6. Lin, T. H. and R. B. Wu, "CPW to waveguide transition with tapered slotline probe," *IEEE Microwave and Wireless Components Lett.*, Vol. 11, 314–316, Jul. 2001.
7. Kim, J. P. and W. S. Park, "Network analysis of inclined microstrip-slotline transitions," *IEE Proc.-Microw. Antennas Propag.*, Vol. 147, 412–416, Oct. 2000.
8. Simons, R. N. and R. Q. Lee, "New techniques for exciting linearly tapered slot antennas with coplanar waveguide," *IEE Electronics Lett.*, Vol. 28, 620–621, Mar. 1992.
9. Knott, P. and A. Bell, "Coaxially fed tapered tapered slot antenna," *IEE Electronics Lett.*, Vol. 37, 1103–1104, Aug. 2001.
10. Chung, K. H., S. H. Pyun, S. Y. Chung, and J. H. Choi, "Design of a wideband TEM horn antenna," *IEEE Antennas and Propagation Society International Symposium*, 229–232, June 2003.
11. Chung, K. H., S. H. Pyun, S. Y. Chung, and J. H. Choi, "The design of a wideband TEM horn antenna with a microstrip-type balun," *IEEE Antennas and Propagation Society International Symposium*, 1899–1902, June 2004.
12. Chung, L., T. Chang, and W. D. Bumside, "An ultrawide-bandwidth tapered resistive TEM horn antenna," *IEEE Transactions on Antennas and Propagation*, Vol. 48, 1848–1857, Dec. 2000.
13. Lee, R. T. and G. S. Smith, "On the characteristic impedance of the TEM horn antenna," *IEEE Transactions on Antennas and Propagation*, Vol. 52, 315–318, Jan. 2004.
14. Ansoft User's Guide, 2002
15. Chen, G. Y., J. S. Sun, and Y. D. Chen, "The 3D far-field antenna measurement technology for radiation efficiency, mean effective gain and diversity antenna operation," *2006 The 7th International Symposium on Antennas, Propagation, and EM Theory (2006 ISAPE)*, 42–45, Guilin, China, Oct. 2006.

A Single Feed Circularly Polarized Fractal Shaped Microstrip Antenna with Fractal Slot

P. Nageswara Rao and N. V. S. N. Sarma

Department of Electronics and Communications Engineering
National Institute of Technology, Warangal, India

Abstract— A Koch fractal boundary single feed Circularly polarized fractal antenna with a fractal slot is presented. The regular Euclidean shaped square patch antenna's each side replaced by Koch fractal curve of 2nd stage with indentation angle of 20° to increase the overall electrical length of the patch is considered. A 3 dB axial ratio bandwidth of about 1.2% is obtained.

1. INTRODUCTIONFRACTAL

antennas have become a hot topic of interest for the antenna designers because of their unique features like compact size, multiband operation etc [1]. Many articles are found in open literature on fractal antennas. Though different fractal geometries are available, a very few can be used in the design of microsrip antennas. One such geometry is Koch curve. K. J. Vinoy et al. [2] have shown the relation between fractal dimension and indentation angles of Koch curve. The fractal dimension is a measure of the space filling ability of a fractal curve. In the present paper using the concept of this indentation angle of Koch curve applied to square patch to get circular polarization is presented. Several articles are available in the open literature on single feed circularly polarized microstrip antennas. Many of them are based on Euclidean shaped patch antennas like rectangular, triangular or circular. The general method to get circular polarization with single feed is to perturb the regular structure of square patch by truncating the corners or by altering the length to width ratio [3]. This method gives a 6 dB axial ratio bandwidth of not more than 1%. Jui-Han Lu et al. have proposed many techniques to get circular polarization using single feed, like providing a small rectangular slot and a crossed slot at the center of triangular patch [4]. Wen-Shyang Chen et al. proposed a different technique for getting circular polarization with square patch by providing a four slits and truncated corners [5]. Kin Lu Wong et al. have presented another method to get circular polarization with circular patch using a stub [6]. But all of them are Euclidean shaped patches. In the present paper first time a fractal curve is used for the square patch as boundary to get circular polarization.

2. ANTENNA GEOMETRY AND NUMERICAL RESULTS

The proposed antenna can be obtained by replacing each side of square patch by Koch curve of 2nd stage with indentation angle 20° and having fractal slot of same shape as original patch but scaled

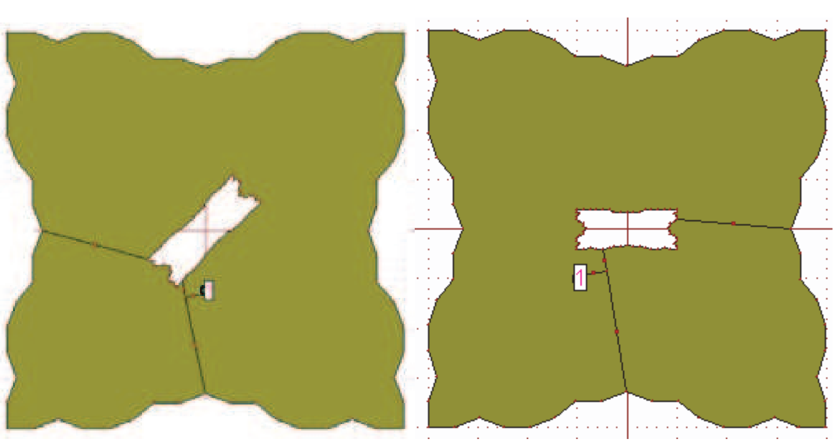

(a) (b)

Figure 1: Geometry of the proposed circular polarized antenna (a) fed along the y-axis (b) fed along the diagonal.

down by a factor 0.31×0.1 at the center. By using fractal boundary the overall area occupied by the patch will be reduced compared to the rectangular patch. The slot is provided in order to produce two orthogonal modes which are 90° out of phase. The slot can be inclined at an angle by 45° and feeding the antenna along the y-axis or if slot is along the x-axis the antenna can be fed along the diagonal. Fig. 1 shows the geometry of the antenna. The axial ratio, and radiation pattern of the proposed antenna are shown in Figs. 2 and 4. The purity of circular polarization can be easily seen from the smith chart, where the variation of input impedance will have a small loop. If the two degenerate modes which are necessary for obtaining circular polarization are very close to each other then the loop area becomes zero as shown in Fig. 3. The antenna is printed on RT Duroid substrate with thickness 3.2 mm and relative permittivity 2.33 and is fed using probe feed. The center frequency of the antenna is 2254 MHz. and gives a 3 dB axial ratio bandwidth of about 1.2% with minimum axial ratio of 0.31 dB. With this method the cross polarization level of about −30 dB is obtained. The end to end dimension of the antenna is 40 mm. The antenna is designed and analyzed using Zeland IE3D simulation software.

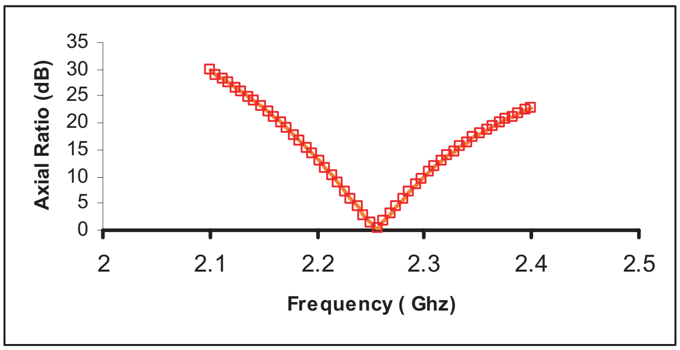

Figure 2: Axial ratio vs frequency of proposed fractal boundary antenna.

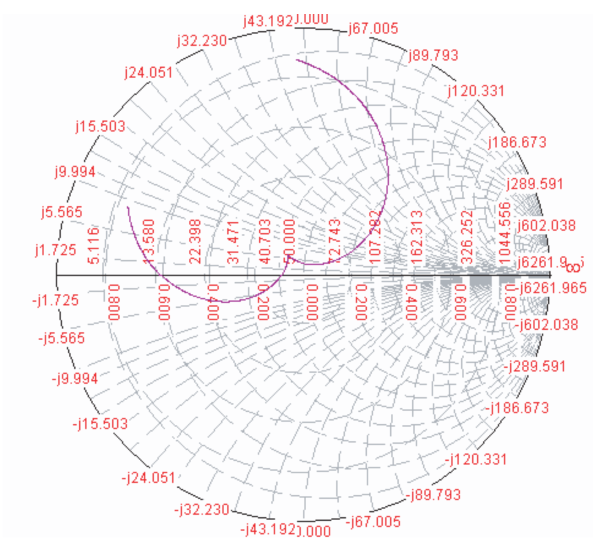

Figure 3: Variation of input impedance with frequency.

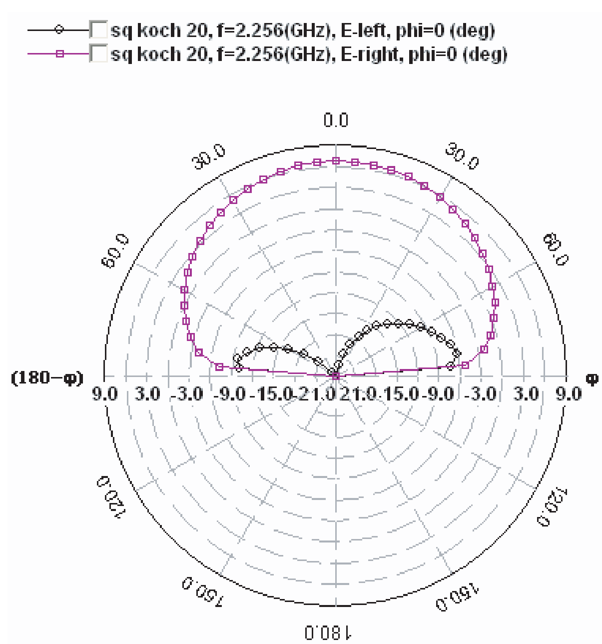

Figure 4: Radiation pattern (co and cross polarization).

3. CONCLUSIONS

Circular polarization with fractal boundary applied to a square patch with fractal slot using a single feed is presented. With this proposed method a 3 dB axial ratio bandwidth of 1.2% with a minimum axial ratio of 0.31 dB is obtained. If further iterations are considered still better compact size antenna can be designed.

REFERENCES

1. Werner, D. H. and S. Ganguly, "An overview of fractal antenna engineering research," *IEEE Antennas and Propagation Magazine*, Vol. 45, No. 1, 38–56, February 2003.
2. Vinoy, K. J., J. K. Abraham, and V. K. Vardan, "On the relationship between fractal dimension and the performance of multi-resonant dipole antennas using koch curves," *IEEE Transactions on Antennas and Propagations*, Vol. 51, No. 9, 2296–2303. September 2003.
3. Sharma, P. C. and K. C. Gupta, "Analysis and optimized design of single feed circular polarized microstrip antenna," *IEEE Transactions on Antennas and Propagation*, Vol. 29, 949–955, 1983.
4. Lu, J.-H., C.-L. Tang, and K.-L. Wong, "Single feed slotted equilateral triangular microstrip antenna for circular polarization," *IEEE Antenna and Propagation*, Vol. 47, No. 7, 1174–1178, July 1999.
5. Chen, W.-S., C.-K. Wu, and K. L. Wong, "Novel compact circularly polarized square microstrip antenna," *IEEE Transactions on Antennas and Propagation*, Vol. 49, No. 3, 340–342, March 2001.
6. Wong, K.-L. and Y. F. Lin, "Circularly polarized microstrip antenna with a tuning stub," *Electronic Letters*, Vol. 34, No. 9, 831–832, April 1998.

Design and Implementation of Aperture Coupled Microstrip IFF Antenna

M. N. Jazi[1], **Z. H. Firouzeh**[2], **H. Mirmohammad-Sadeghi**[3], **and G. Askari**[3]

[1]Institut National de la Recherche Scientifique, Université de Québec, Canada
[2]Department of Electrical Engineering, Amirkabir University of Technology, Iran
[3]Information and Communication Technology Institute, Isfahan University of Technology, Iran

Abstract— Design and implementation procedure of a wideband aperture coupled microstrip antenna in L-band frequency is introduced. To improve radiation performance of the microstrip antenna four structures are proposed. The structure with air substrate has the maximum frequency bandwidth. Experimental results of frequency bandwidth and radiation patterns of the optimum structure agree with the simulation results. The antenna has the gain of 8.5 dB, the frequency bandwidth of greater than 25%, and F/B better than 15 dB. This aperture coupled microstrip antenna can be used as an element of microstrip array antennas in IFF systems.

1. INTRODUCTION

Microstrip antennas (MA) are simple planar structures that have advantages such as low profile, conformal availability, simple fabrication using printed circuit technology, low cost and compatibility with integrated circuits. In spite of limitations such as small bandwidth, low gain and low power handling capability [1], MA offers over than other type of antennas due to their advantages and increasingly used in a variety applications such as military, industry and wireless communication [2]. Different techniques have been used to increase bandwidth such as using thick substrate [3]. This technique improves bandwidth less than 5 percent. Aperture coupled stacked patch microstrip antenna can improve bandwidth more than 50 percent at the expense of increasing in back lobe radiation level. To reduce back radiation, metallic rods or resonance planes are used in the back of the antenna or appropriate cavities are put next to the coupling aperture [5–8]. Aperture coupled microstrip antenna has been used for IFF (or Secondary Surveillance Radar) systems with 6 percent bandwidth for VSWR < 1.5. However, Front to Back (F/B) ratio has been reported 10 dB which is not enough for IFF application [9].

In this paper, both techniques have been used to increase the bandwidth and decrease the back radiation. The design process of the proposed structure is organized as followed. First of all, an aperture coupled microstrip antenna will be designed according to the requirements. Then, four structures will be introduced and compared to each other. After simulation, the best structure will be selected and optimized to fabricate. Finally, the measurements and conclusion will be reported.

2. DESIGN AND SIMULATION

The structure of the aperture coupled microstrip antenna has been depicted in Figure 1. This antenna has been designed to use as an element in the microstrip array antenna for IFF (or SSR) systems. The central frequency is 1060 MHz and the bandwidth is at least 250 MHz. The thickness of patch substrate, h_3 is chosen 20 mm due to the desired bandwidth. The feed substrate is RT/Duroid 5880 with thickness of $h_2 = 0.787$ mm and relative dielectric constant of 2.2. FR4 is used as cover with thickness of $h_4 = 1$ mm and $\varepsilon_{r4} = 4.3$.

According to [1], the preliminary antenna dimensions are designed and calculated at the central frequency of 1060 MHz. [4] recommends that aperture width W_s is the half of its length L_{sl} and T_s is the one-tenth of L_{sl}. The length of the stub, L_{st} is $0.22\lambda_g$, in which λ_g is the wavelength in the feed substrate.

The antenna parameters such as patch dimensions, aperture length, the length of stub, and the distance between feed line and back plane are optimized by use of full wave simulator IE3D until frequency bandwidth greater than 25% and F/B greater than 20 dB will be obtained at the central frequency of 1060 MHz. Four different structures as shown in Figure 2 are designed, simulated and compared to recognize the structure with best performance.

Aperture has been designed to resonate near the resonance frequency of the patch. Aperture shape is very important to control the maximum coupling between the feed line and the patch and also the minimum back radiation. A metallic plane is placed behind of the antenna to reduce back radiation power to −20 dB. Actually, this plane functions as a resonator and generates appropriate current distribution to eliminate undesired radiation fields in the rear of the antenna. The distance between the back plane and the feed line influences on the amplitude of the current distribution but the phase of the current distribution is controlled by the size of the back plane.

The four structures have been simulated and optimized by IE3D software. The graph of their return losses has been depicted in Figure 3. According to Figure 2, structure (a) has the maximum bandwidth. The simulation results indicate that the smallest bandwidth will be achieved when Teflon dielectric is directly beneath the patch. In addition, the frequency center of structure (d) is lower than other structures. The simulation results have been indicated in Table 1 in which f_u and f_l are the low and high frequency corresponding to −10 dB return loss.

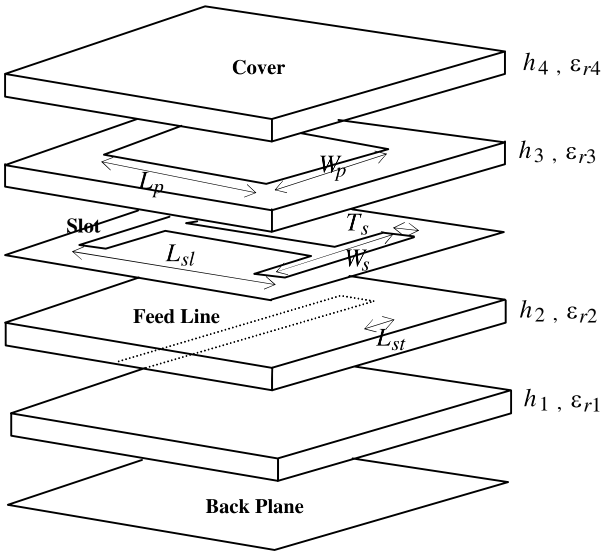

Figure 1: Aperture coupled microstrip antenna structure.

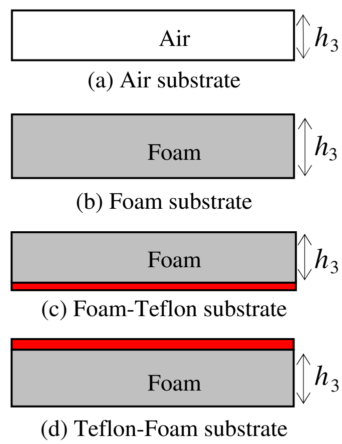

Figure 2: Four different structures of aperture coupled microstrip antenna.

Structure	Central Frequency (MHz) $(f_u + f_l)/2$	Bandwidth (MHz) $f_u - f_l$
(a)	1038	279
(b)	1030	260
(c)	1018	224
(d)	1000	195

Table 1: Simulation results of four different structures as shown in Figure 2.

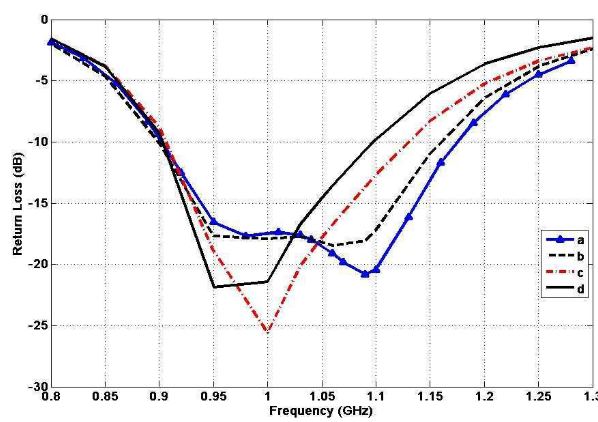

Figure 3: Return losses of four structures simulated by IE3D.

E- and H-plane radiation patterns at 1030 MHz and 1090 MHz have been represented for structure (a) in Figures 4 and 5, respectively. The Front to Back ratio is greater than 20 dB. E- and H-plane Half Power Beam Width (HPBW) at 1030 MHz are 65° and 75°, respectively. At 1090 MHz, E-plane HPBW is 63° and H-plane HPBW is 74°. Figure 6 shows simulated results for gain of four structures. The gain difference between 1030 MHz and 1090 MHz is less than 0.5 dB for four structures. For example, the gain of structure (a) at 1030 MHz is 8.5 dB but at 1090 MHz is 8.8 dB.

After consideration and comparison of the simulation results of four structures show that structure (a) i.e., the antenna with air substrate has the performance to realize the desired antenna.

Consequently, this structure is selected to be fabricated and measured its radiation parameters.

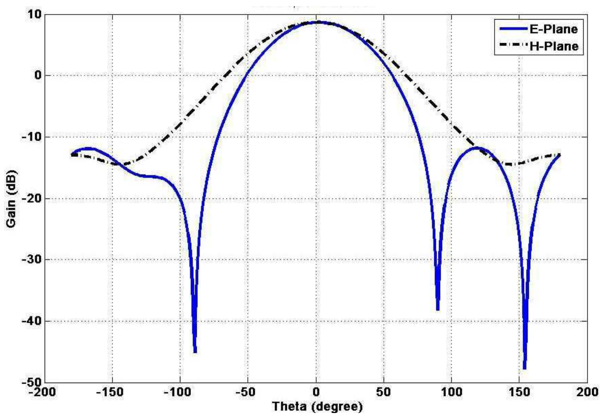

Figure 4: E- and H-plane radiation patterns at 1030 MHz simulated by IE3D.

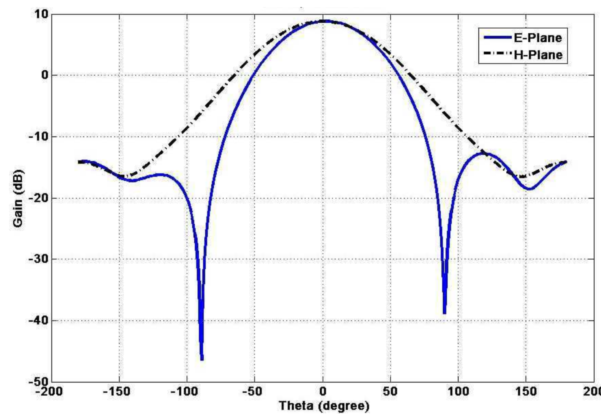

Figure 5: E- and H-plane radiation patterns at 1090 MHz simulated by IE3D.

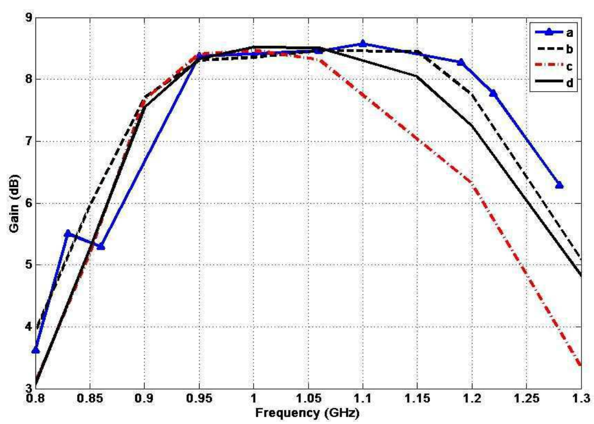

Figure 6: Comparison the gain of four different structures simulated by IE3D.

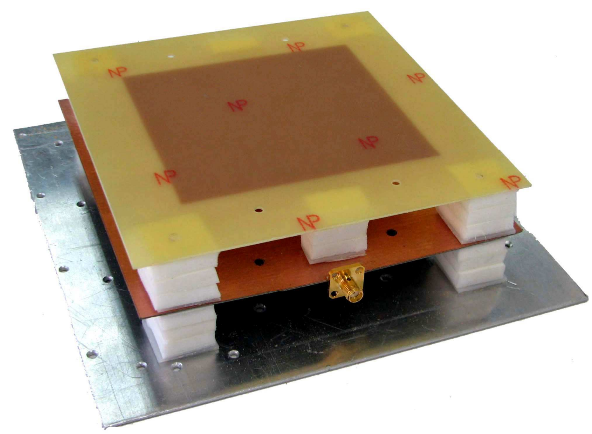

Figure 7: The photo of the fabricated aperture coupled microstrip antenna with air substrate.

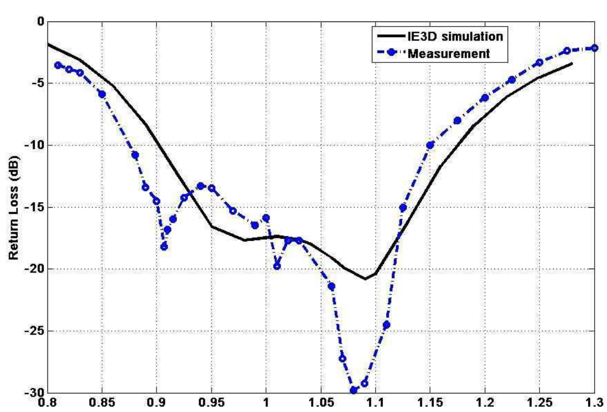

Figure 8: Simulation and measurement results of return loss of the antenna.

3. MEASUREMENT

Figure 7 shows photo of the fabricated aperture coupled microstrip antenna. Return loss of the antenna has been measured and compared with simulation result in Figure 8. A little frequency

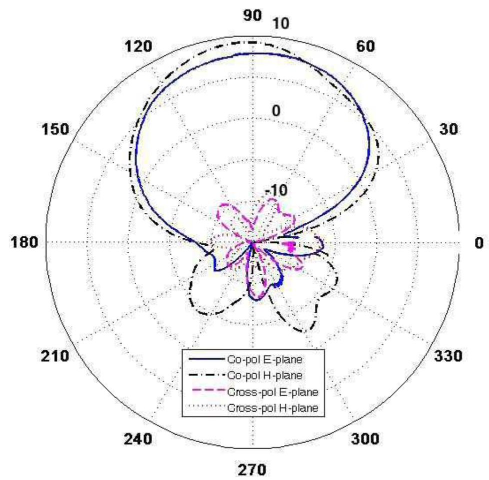

Figure 9: Measurement of co- and cross-polarization radiation patterns at 1030 MHz.

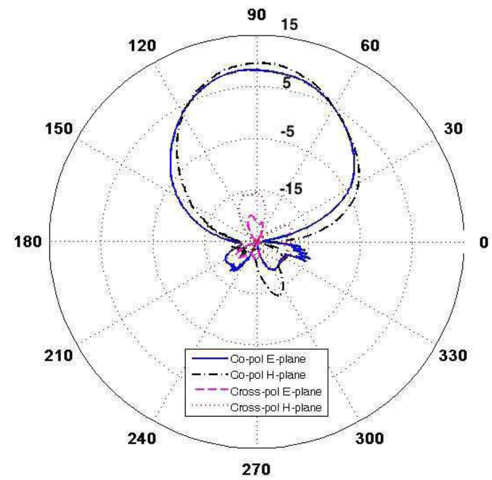

Figure 10: Measurement of co- and cross-polarization radiation patterns at 1090 MHz.

difference between two curves is observed because of simulation accuracy, simulation settings, measurement accuracy and fabrication tolerance. The return loss of the antenna is less than -10 dB in the frequency range of 875 MHz–1150 MHz, i.e., the frequency bandwidth is greater than 25%. Figures 9 and 10 show respectively co- and cross-polarization radiation patterns at 1030 MHz and 1090 MHz. F/B of E- and H-plane radiation patterns are greater than 15 dB and 13 dB at 1030 MHz, respectively. Figure 10 indicates F/B of E-plane radiation pattern is greater than 20 dB but that of H-plane radiation pattern is greater than 15 dB. This difference is due to low accurate measurement of anechoic chamber for this frequency bandwidth. The gain difference of both planes is less than 0.5 dB. This antenna has better performance such as bandwidth and F/B than the antenna reported in [9].

4. CONCLUSIONS

In this paper, four different structures of aperture coupled microstrip antenna have been considered to achieve the maximum bandwidth with good radiation performance in this bandwidth. The air substrate antenna was selected and optimized by IE3D simulator. The simulation and measurement results have the good agreement with each other. The antenna has the gain of 8.5 dB, the bandwidth of greater than 25%, and F/B better than 15 dB. This aperture coupled microstrip antenna can be used as an element of microstrip array antennas in IFF (or SSR) systems.

ACKNOWLEDGMENT

The authors would like to thank the staff of Information and Communication Technology Institute (ICTI), Isfahan University of Technology (IUT), Isfahan, Iran for their co-operator and supporting this work.

REFERENCES

1. Garg, R., P. Bhartia, I. Bahl, and A. Ittipihoon, *Microstrip Antenna Design Handbook*, Artech House, 2001.
2. Pozar, D. M. and D. H. Schaubert, *Microstrip Antenna, the Analysis, and Design of Microstrip Antenna and Arrays*, IEEE Press, New York, 1995.
3. Pozar, D. M., *Review of Aperture Coupled Microstrip Antenna: History, Operation, Development, and Application*, Microwave Online System Company world wide web site, July 1996.
4. Targonski, H. S., R. B. Waterhous, and D. M. Pozer, "Design of wideband aperture stacked patch microstrip antennas," *IEEE Trans. on Antennas and Propagation*, Vol. 46, No. 9, 1245–1251, Sept. 1998.
5. Targonski, S. D., R. B. Waterhouse, and D. M. Pozar, "Reflector elements for aperture coupled microstrip antennas," *Antennas Propag. Symp. Dig.*, 1997.
6. Blefko, M. J. and W. N. Klimczak, "A secondary surveillance radar (SSR) antenna with integrated difference and sidelobe suppression (SLS) channel," *APS International Symposium*, USA, July 1996.

7. Shin, H. S. and N. Kim, "Wideband and high gain-one patch microstrip antenna coupled with H-shaped aperture," *Electronic Letters*, Vol. 38, No. 19, Sept. 2002.
8. Ahmed, Z., M. B. Ihsan, N. Chaudhry, and J. Kiani, "Design of a low sidelobe aperture coupled microstrip antenna array," *IEEE*, 2004.
9. Kreczkowski, A., T. Rutkowski, A. Buda, and S. Kostka, "The microstrip IFF antenna for the airborne radar," *International Conference on Microwaves, Radar and Wireless Communications*, MIKON, 2002.

Design of the Spiral Monopole Antenna for Multi-band Mobile Communication and SAR Analysis

S. M. Park[1], **N. Kim**[1], **S. W. Lee**[1], **H. M. Lee**[2], **and S. W. Park**[1]

[1]Division of Information and Communication Eng., Chungbuk National University, Korea
[2]Department of Bioelectronics, BIT Graduate school, Chungbuk National University, Korea

Abstract— In this paper, the spiral planar monopole antenna mounted on a Cellular/WCDMA handset is designed. Frequency characteristics are optimized with various design parameters. The two spiral lines are adopted in order to implement Cellular frequency bandwidth and WCDMA frequency bandwidth. The bandwidth of the realized antenna is 0.805∼0.892 GHz (10%) and 1.867∼2.302 GHz (21%) for VSWR≦2 which contain the proposed frequency bandwidth. In human head, the simulated value on 1 g and 10 g averaged SAR caused by electromagnetic wave radiated in the designed antenna is compared with the measured value. As a result, the measured values of 1 g and 10 g averaged SAR were similar to the simulated values, which were lower than the SAR guidelines.

1. INTRODUCTION

In modern society, new wireless communication devices and portable electronic devices have been consistently developed with the aid of development in telecommunication technology and wireless communication technology. In particular, rapid development in mobile communication technology has sped up development in functions of related devices and their physical parts. In Korea, new services, including Wibro, WCDMA, DMB have been consistently introduced, and thus it is required to develop a variety of terminals which can stably provide the new services together with existing mobile communication services.

Accordingly, in this paper, there has been designed a dual resonance planar monopole antenna that satisfies a thin-film structure, and cellular and WCDMA bands with the use of a spiral line. The optimization of a proposed antenna was achieved by optimizing parameters affecting the frequency characteristic of the antenna, and the reflection loss and radiation pattern of the proposed antenna were measured by actual manufacturing. A specific absorption rate (SAR) was calculated by considering that it is the cellular phone antenna, and the calculated SAR result was compared with an SAR result measured by attaching the antenna to an actual terminal.

2. STRUCTURE OF ANTENNA

A meander line is used to overcome the defects of a general monopole antenna. The meander line is used as a method for extending the electric length of the antenna, resulting in lowering a resonance frequency more efficiently than antennas having the same length. However, since mutual inductances are reversely formed in the meander line, they can be mutually offset, it is difficult to obtain a comparatively high value of L in proportion to the length of the meander line. In this paper, there a spiral structure in which larger value of L can be obtained was used with a small inductance, to which a magnetic field is added in the same direction. Fig. 1 shows the structure of the proposed antenna.

The overall size of the antenna was designed to $35 \times 80 \times 1\,\mathrm{mm}^3$. An FR-4 substrate having a permittivity of 4.62 was used. A ground plane patch of $35 \times 60\,\mathrm{mm}^2$ is printed on one plane and an antenna patch of $35 \times 20\,\mathrm{mm}^2$ is printed on the other plane. A $50\,\Omega$ microstrip line having the width of 1.74 mm was formed at the center of the substrate by calculating the width of a fitting line after preferentially considering the thickness and permittivity of the substrate, and the thickness of a thin film as variables affecting antenna input impedance matching. In a monopole antenna satisfying a length of $\lambda/4$, the electric length of the antenna for satisfying the frequency band of a CDMA was about 87 mm. Accordingly, in the proposed antenna, the resonance frequency band could be tuned with the use of a spiral line.

3. ANTENNA MANUFACTURING AND MEASUREMENT

Figure 2 shows the concrete image of a manufactured antenna, and Fig. 3 is a graph in which a simulation result and a measurement result of an optimized antenna are compared with each other.

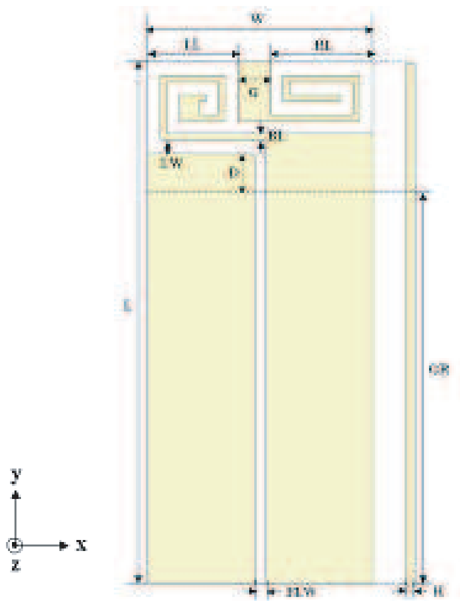

Figure 1: Structure of the proposed planar monopole antenna.

Parameter	Value [mm]
W	35
L	80
H	1
GR	60
FLW	1.74
D	6
LW	2
BL	1
C	15.5
LL	14
RL	16

Table 1: Optimized parameters for the proposed antenna.

In the simulation result, the resonance frequency band was in the range of 0.823∼0.910 GHz and 1.919∼2.232 GHz, while in the measurement result, the resonance frequency band was in the range of 0.805∼0.892 GHz and 1.867∼2.302 GHz. In both results, a result satisfying frequency bands of cellular phone and WCDMA could be obtained. The resonance frequency of the measurement result was slightly different from that of the simulation result, but it was confirmed that the measurement result coincided with the simulation result as a whole.

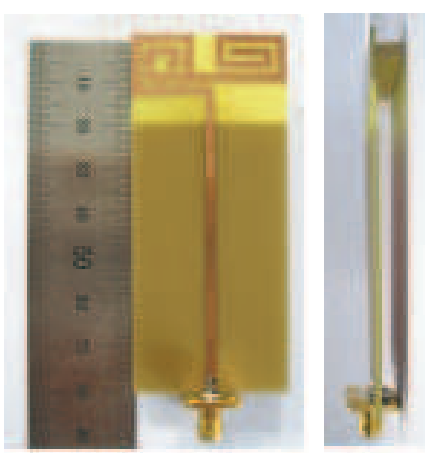

Figure 2: Photograph of the fabricated antenna.

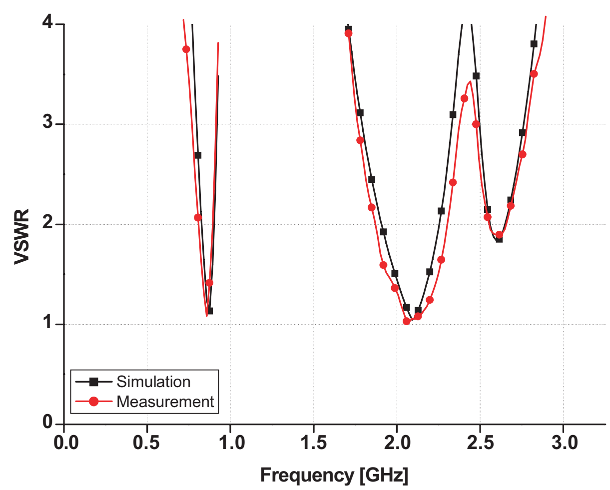

Figure 3: Comparison of the simulated and measured return loss on the optimized antenna.

Figure 4 shows a radiation pattern measured in cellular bands of 0.83 GHz and 0.86 GHz, and a radiation pattern measured in WCDMA bands of 1.90 GHz and 2.10 GHz. In a general monopole antenna, an H-plane characteristic should be isotropic, but in an antenna proposed in this paper, a pattern similar to the isotropic pattern of the monopole antenna could be obtained. We could determine that each transmit frequency band and a receive frequency band of a mobile communication had a generally constant pattern. It was confirmed that the maximum gain of the measurement result was 3.6 dB in the cellular frequency band and 3.9 dB in the WCDMA frequency band.

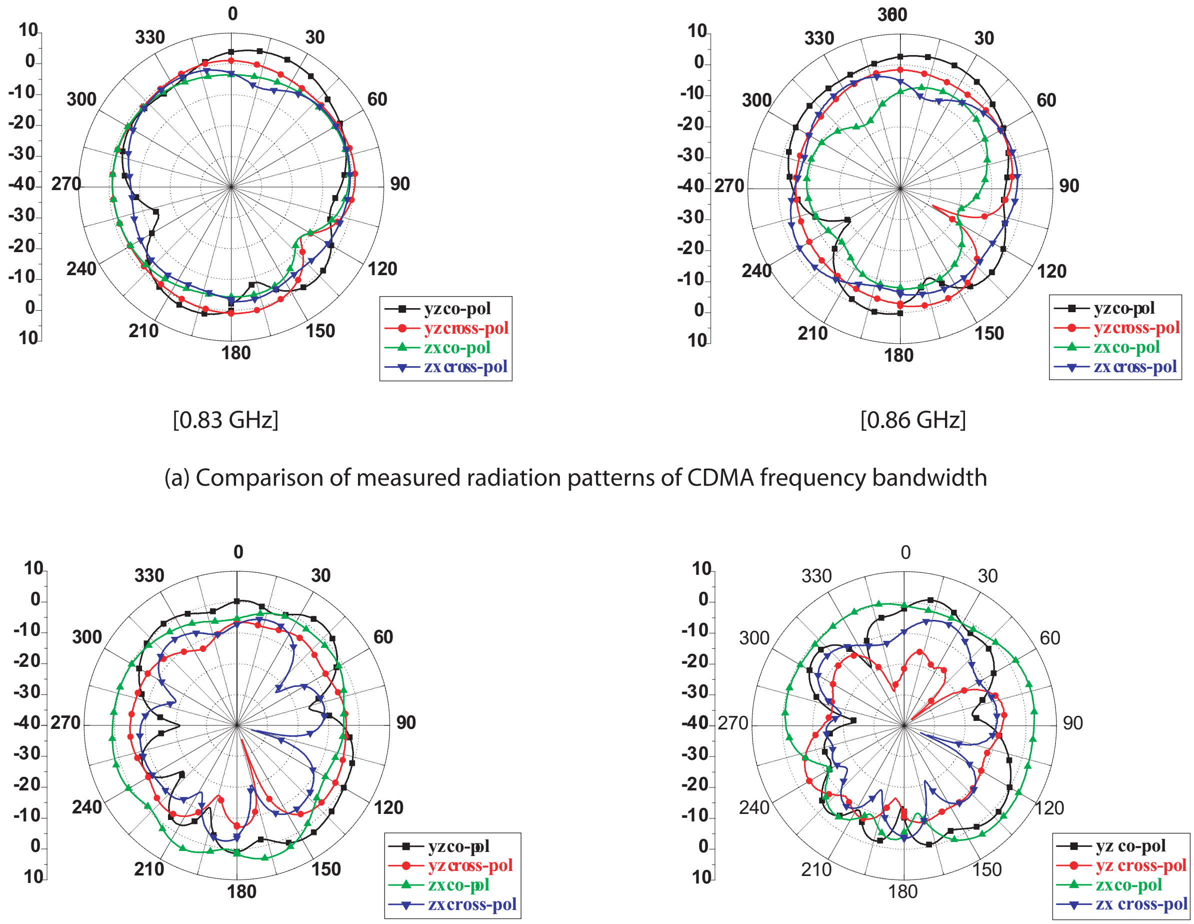

[0.83 GHz] [0.86 GHz]

(a) Comparison of measured radiation patterns of CDMA frequency bandwidth

[1.90 GHz] [2.10 GHz]

(b) Comparison of measured radiation patterns of HSDPA frequency bandwidth

Figure 4: Comparison of the measured radiation patterns for proposed antenna.

4. CALCULATION AND MEASUREMENT OF SAR

In this paper, SAR was calculated by the use of SEMCAD, which is the commercial SAR analysis tool. In order to calculate the value of SAR for the cellular frequency band, SAR was calculated in a frequency of 0.835 GHz and an input power of 0.5 W. The result of the average value of SAR for each of 1 g and 10 g was achieved. Fig. 5 shows the result calculated when the antenna is mounted on the lower part of a folder-type terminal. In this case, the lower part of the terminal was in contact with one point (cheek) on a SAM, and thus the maximum value of SAR was detected on the skin surface of the SAM's cheek. When the input power was 0.5 W, the average SAR value for 1 g was 0.654 W/kg, and the average SAR value for 10 g was 0.435 W/kg. We could find that a separation distance between the antenna and the SAM had a large influence on the SAR value. In this research, the separation distance between the antenna and the dummy located within the terminal was 7.48 mm. According to the result, it is expected that the SAR value at a tilt position will be smaller than that at a contact position.

ESSAY-3, manufactured by EMF Safety INC., is used for the SAR measurement of the antenna. Similarly as in the SAR calculation, the measurement is performed when the input power is 0.5 W. When the input power was 0.5 W, the average SAR value of 1 g was 0.462 W/kg and the average SAR value of 10 g was 0.245 W/kg. We could confirm that this is the result satisfying 1.6 W/kg, which is the SAR limit value in Korea, and 2 W/kg, which is the reference value in the average of 10 g.

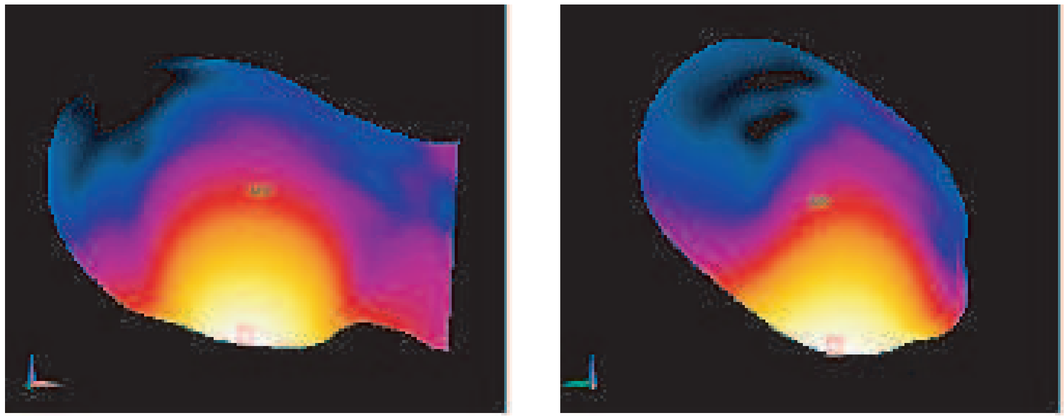

[XZ plane] [YZ plane]

(a) 1 g averaged SAR (0.654 [W/kg])

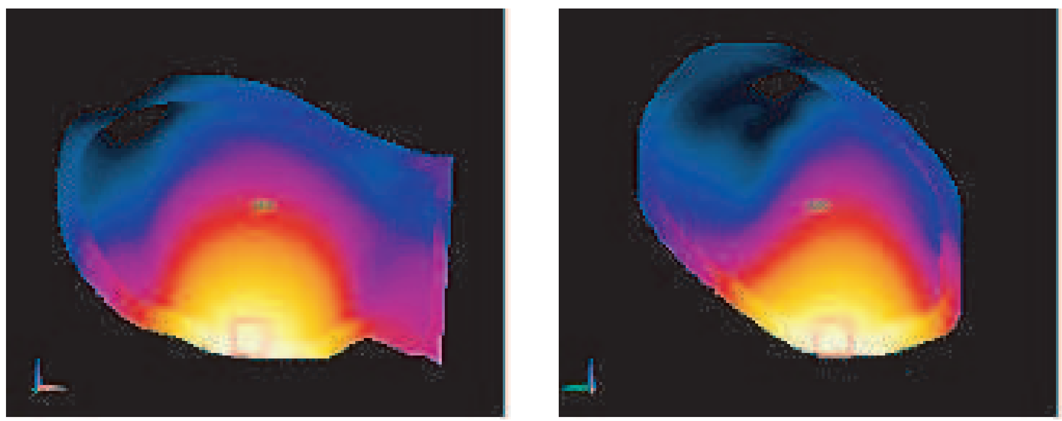

[XZ plane] [YZ plane]

(b) 10 g averaged SAR (0.435 [W/kg])

Figure 5: 1 g and 10 g averaged SARs having the input power of 0.5 W.

5. CONCLUSIONS

In this paper, a spiral monopole antenna operable in the frequency including the cellular and the WCDMA frequency band is designed and manufactured. The proposed antenna satisfied frequency bands of 0.823∼0.910 GHz and 1.919∼2.232 GHz as a result of calculation and satisfied frequency bands of 0.805∼0.892 GHz and 1.867∼2.302 GHz as a result of measurement. We could determine that the antenna gain was 3.6 dB in the cellular frequency band and 2.9 dB in the WCDMA frequency band. SAR was calculated when the cellular frequency band was 835 MHz and the input power was 0.5 W. The average SAR values of 1 g and 10 g for 0.5 W were measured with the proposed antenna mounted on a cellular phone having a folder structure. The measured results were compared with each other.

In this paper, the cellular phone terminal modeled to use in calculating the SAR is obviously different from an actually used terminal in a medium and an environment. In considering that these bring about an error between the calculated value and the measured value, a complement using more actual data is required to calculate the SAR.

ACKNOWLEDGMENT

This research was supported by the MIC (Ministry of Information and Communication), Korea, under the ITRC (Information Technology Research Center) support program supervised by the IITA (Institute of Information Technology Advancement) (IITA-2007-(C1090-0701-0034)).

REFERENCES

1. Kaiser, J. A., "The archimedean two-wire spiral antenna," *IRE Trans. Antennas Propagat.*, Vol. 8, 312–323, 1960.
2. Nurnberger, M. W. and J. L. Volakis, "A new planar feed for slot spiral antenna," *IEEE Trans. Antennas Propagat.*, Vol. 44, No. 1, 130–131, 1996.
3. Oh, D. Y., M. Kim, and I. Park, "Two-arm microstrip spiral antenna with a circular aperture on the ground plane," *Microwave Opt. Tech. Lett.*, Vol. 35, 453–455, 2002.
4. "IEEE recommended practice for determining the peak spatial-average specific absorption rate(SAR) in the human head from wireless communications devices: measurement techniques," *IEEE Std. 1528-2003*, 1–149, 2003.
5. Chavannes, N., R. Tay, N. Nikoloski, and N. Kuster, "Suitability of FDTD-based TCAD tools for RF design of mobile phones," *IEEE Antennas and Propagation Magazine*, Vol. 45, No. 6, 52–66, 2003.
6. Shin, C. S., H. S. Shin, N. Kim, J. I. Choi, and J. D. Park, "Internal monopole antenna design for multiband operation and sar analysis," *The Journal of Korea Electromagnetic Engineering Society*, Vol. 15, No. 12, 1190–1198, 2004.
7. Choi, D. G., H. S. Shin, N. Kim, and Y. K. Kim, "Design of the broadband PIFA with multiband for SAR reduction," *The Journal of Korea Electromagnetic Engineering Society*, Vol. 16, No. 1, 66–77, 2005.

Design and SAR Measurement of the Trapezoidal Shape Antenna

S. W. Lee[1], **S. M. Park**[1], **N. Kim**[1], **S. W. Park**[1], **and S. Y. Rhee**[2]

[1]Chungbuk National University, Korea
[2]Chonnam National University, Korea

Abstract— In this paper, we designed the trapezoidal shape antenna which can be used in WLAN services. The trapezoidal shape would be working in the 2 GHz band and 5.2 GHz, and the small rectangular pieces in the trapezoidal shape were making the frequency shift from 5.2 GHz to 5.7 GHz. In addition, we found out the best values of the antenna parameters by sweeping some characteristics. The designed antenna has occurred resonances of which the first band is 1.65 GHz ∼ 2.36 GHz and the second band is 5.49 GHz ∼ 5.88 GHz below the return loss of −10 dB. Also, we will measure the SAR (Specific Absorption Rate) values for the human body.

1. INTRODUCTION

For the minimized antenna, there are the methods of using the semiconductor, the geometrical structures, and sub-patches [1]. One of research trends is dramatically downsized the antenna using the mictrostrip feeding method and supplemented the radiation using the patch until now, but it would be increased the current density and Q factor (quality factor) by the minimized antenna and seriously decreased the bandwidth of the frequency range. The other way, the impedance would be increased, and then the gain of the antenna should be decreased [2]. CPW (coplanar waveguide) feeding slot antenna is studied various methods for increased the working bandwidth of the antenna, and there are designed several structures by following the application field [3]. CPW feeding slot antenna is smaller the radiation loss and the dispersion than the microstrip method, and we can take the broad bandwidth because the varying of the characteristic impedance is small [4–11].

In this paper, we designed the antenna which makes dual resonances interposed the patch that is the teeth of a saw in the CPW feeding antenna of the trapezoidal shape having the small size and the broadband characteristics. The designed antenna is working the dual band, 1.65 GHz∼2.36 GHz and 5.49 GHz∼5.88 GHz, for the PCS, WCDMA, and WLAN services. In addition, we proved the designed antenna is satisfied the SAR guideline.

2. ANTENNA DESIGN

Figure 1 illustrates the antenna structure of the trapezoidal shape. The size of the designed antenna is 60.0 mm(W)×30.0 mm(L)×1.0 mm(T), and the substrate is FR4 consisted of the copper of 1 mm and dielectric constant of 4.62. The antenna structure is CPW structure of the basic trapezoidal shape, as shown Fig. 1. Usually most of the patch antenna has the rectangular shape, but we proposed the trapezoidal shape antenna showed the broadband characteristics by making the smoothly flowing of the current [5]. Although we can get the broadband characteristics in the trapezoidal shape antenna transformed the rectangular shape, we cannot get the characteristics of the adopted band. So there is deleted the wasted portion without approximately 1 mm of the width in the antenna. Therefore, there are dual resonances in the frequency bands of 2 GHz and 5.2 GHz.

Various parameters shown Figure 1 and Table 1 are changed so that the resonance is formed in the desired frequency band. In the trapezoid patch, the desired band characteristic was obtained in a 2 GHz band, but 5.2 GHz was just obtained in the band for WLAN. Therefore, the frequency band could be manipulated according to the length of the patch by inserting another patch having a rectangular shape in the trapezoid patch. As already know, the wavelength is in an inverse proportion to the frequency, and thus the length of the patch should be shortened in order to increase the frequency. This will be described in detail in "Chapter 3. Antenna Simulation," afterwards, but the frequency band satisfying a PCS service and WCDMA service in the range of 1.65 GHz to 2.36 GHz could be obtained through sweeping the parameters of the antenna, and the frequency band of 5.49 GHz to 5.88 GHz, which satisfies the WLAN service band, could be obtained by adding a saw-like patch.

The parameters shown in Table 1 represent values optimized through sweeping. However, in an initial design stage, the width of the strip line was acquired by the use of factors, including a

Table 1: Parameters of the proposed antenna.

Parameters	Explanation	Value (mm)
po1x	The base of the trapezoid patch	16
po2x	The upper side of the trapezoid patch	26
py	The height of the trapezoid patch 0	14
sh	The size of the sub-patch	1
gx	The width of the ground plane	28.84
gy	The height of the ground plane	4
sx	The width of the feeder	1.8
sy	The length of the feeder	10

permittivity, the thickness of a substrate, the thickness of a metal, a desired frequency band, and an impedance line width between the strip line and a ground was acquired.

Figure 2 shows a simulated result using the optimized values shown in Table 1. On the basis of a return loss of −10 dB or less, a first resonance occurred in the band of from 1.65 GHz to 2.36 GHz, and a second resonance occurred in the band of from 5.49 GHz to 5.88 GHz. Figure 3 shows radiation patterns of the designed antenna in 1.67 GHz and 5.5 GHz. In this thesis, a trapezoid CPW antenna, usable in the PCS, WCDMA and WLAN bands, was designed. The overall size of the antenna was reduced by the use of a CPW structure and its performance was checked through simulation. As a result of the simulation of the designed antenna, we could determine that the dual resonance was formed, and the antenna satisfied the band of 1.65 GHz to 2.36 GHz and 5.49 GHz to 5.88 GHz.

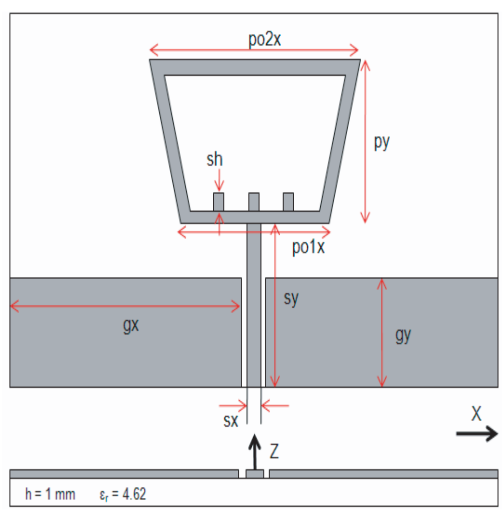

Figure 1: The structure of the proposed antenna.

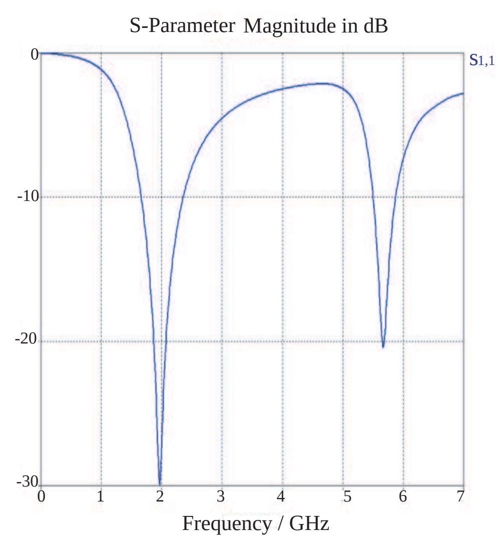

Figure 2: The return loss of the optimized parameters.

3. ANTENNA FABRICATION AND SAR MEASUREMENT

We were fabricated the proposed antenna, as shown Figure 4. For the measuring of the absorption of the electromagnetic wave in the human body, we were doing SAR (specific absorption rate) measurement. The target service is WLAN of 2.45 GHz band, and we have got the results of 1g and 10 g averaged SARs in 2.45 GHz, as shown Figure 5.

As the results of the SAR measurement, 1 g averaged SAR, which the guideline is 1.6 W/kg, is 0.529 W/kg, and 10 g averaged SAR, which the guideline is 2.0 W/kg, is 0.273 W/kg. The SAR values are satisfied the guideline values.

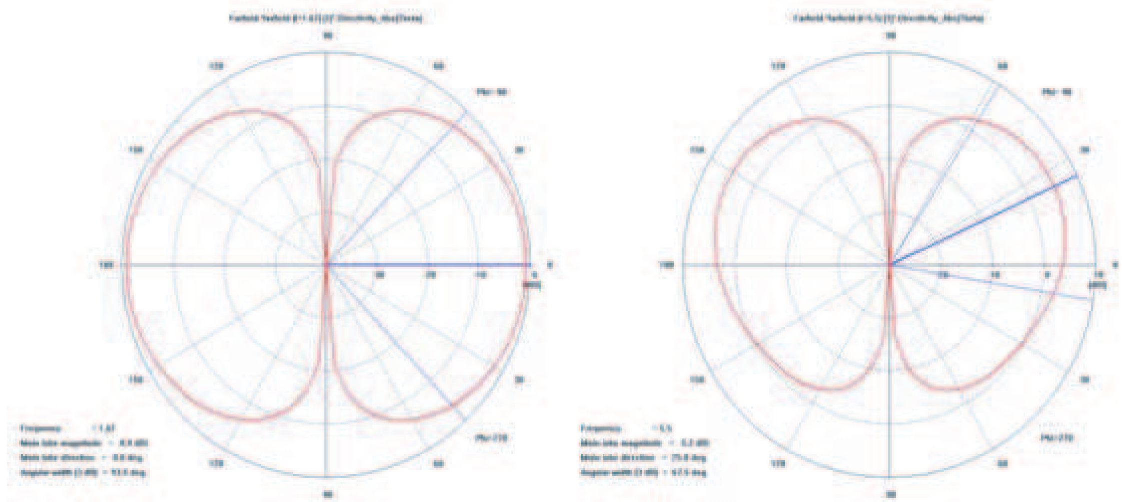

Figure 3: The radiation pattern at 1.67 GHz and 5.5 GHz.

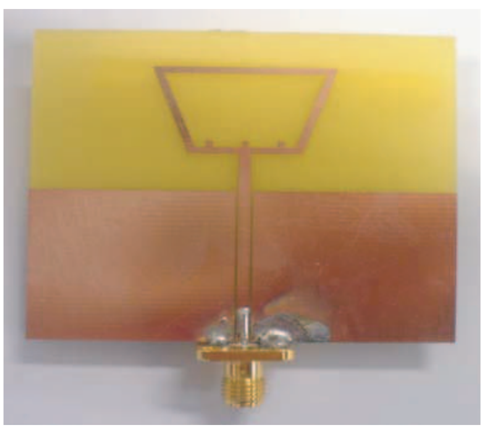

Figure 4: The fabricated antenna.

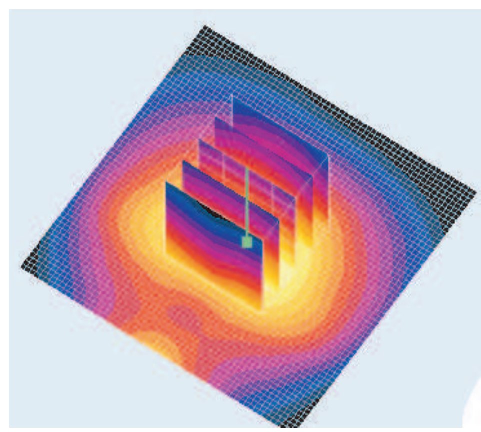

Figure 5: The SAR measurement.

4. CONCLUSIONS

We designed and fabricated the antenna of the trapezoid shape for the PCS, WCDMA, and WLAN bands in this paper. We reduced the antenna size using the CPW structure, and confirmed the performance using the computer simulation firstly. Then we fabricated the proposed antenna having the dual resonance characteristic. In the return loss of -10 dB or less, the antenna was working the 1.65 GHz to 2.36 GHz and 5.49 GHz to 5.88 GHz. In case of SAR measurement, the 1 g and 10 g averaged SARs are satisfied the guideline which is 1.6 W/kg and 2.0 W/kg respectively. As the results, the 1 g and 10 g averaged SARs are 0.529 W/kg and 0.273 W/kg. We proved all results are satisfied the guideline by the experiment test.

ACKNOWLEDGMENT

This research was supported by the MIC (Ministry of Information and Communication), Korea, under the ITRC (Information Technology Research Center) support program supervised by the IITA (Institute of Information Technology Advancement) (IITA-2007-(C1090-0701-0034)).

REFERENCES

1. Hiraswa, K. and M. Haneishi, *Analysis, Design, and Measurement of Small and Low-profile Antennas*, Artech House, London, 1992.
2. Lee, H. J., J. W. Jung, and Y. S. Lim, "A design of wide-band folded dual monopole antennas," *Journal of the Institute of Electronics Engineering of Korea*, Vol. 44, No. 2, 69–75, 2007.

3. Lee, J. N., S. H. Lee, and J. K. Park, "A trapezoidal ultra-wideband antenna design," *Journal of Korea Electromagnetic Engineering Society*, Vol. 16, No. 3, 235–245, 2005.
4. Choi, S. S., J. I. Kim, and Y. Jee, "Design of broadband CPW-fed square slot antenna," *Journal of the Institute of Electronics Engineering of Korea*, Vol. 42, No. 11, 107–116, 2005.
5. Fortino, N., G. Kossiavas, J. Y. Dauvignac, and R. Starai, "Novel antennas for ultra-wideband communications," *Microwave Opt. Tech. Lett.*, Vol. 41, No. 3, 166–169, 2004.
6. Moon, Y. G. and H. S. Kim, "Design and fabrication of a broadband microstrip slot antenna with a fork-shaped feedline," *Journal of the Institute of Electronics Engineering of Korea*, Vol. 41, No. 8, 87–92, 2004.
7. Kim, M. S., K. S. Shin, Y. D. Kim, and H. M. Lee, "Design of wide-band slot antenna with CPW-fed," *Journal of Korea Electromagnetic Engineering Society*, Vol. 15, No. 2, 212–216, 2004.
8. Kim, K. S. and D. K. Park, "CPW fed ultra wide band slot antenna," *Journal of Korea Electromagnetic Engineering Society*, Vol. 14, No. 7, 663–668, 2003.
9. Kim, J. I., W. T. Lee, J. W. Jang, and Y Jee, "Design of ultra waveband coplanar waveguide-fed L-planar type monopole antennas," *Journal of Korea Electromagnetic Engineering Society*, Vol. 18, No. 1, 82–89, 2007.
10. Kim, N., G. B. Son, and S. M. Park, "Sectorial form UWB antenna with a CPW-fed uni-planar," *Journal of Korea Electromagnetic Engineering Society*, Vol. 18, No. 3, 305–314, 2007.
11. Park, G. Y., H. S. Shin, B. C. Oh, and N. Kim, "Uni-planar elliptical UWB antenna with band-notched characteristic and modified ground plane," *Journal of Korea Electromagnetic Engineering Society*, Vol. 16, No. 12, 1194–1205, 2005.

Design of Dual-band PIFA for WLAN

Sung-Keun Jeon[1], **Nam Kim**[2], **Seung-Woo Lee**[2]
Sang-Myeong Park[2], **and Byoung-Jun Jang**[3]

[1]Department of Bioelectron, BIT Graduate School, Chungbuk National University, Korea
[2]Division of Information and Communication Eng., Chungbuk National University, Korea
[3]Collage of Electrical Engineering, Kookmin University, Korea

Abstract— This paper proposed a new dual-band PIFA(Planar Inverted-F Antenna) for WLAN. Two patches were used in order to embody each WLAN band. The shorting strip and meander-type radiation patches were used in order to minimize the size of the antenna. The −10 dB return loss bandwidth of a realized antenna was 1.95 ∼ 2.65 GHz and 5.47 ∼ 6.03 GHz which contains WLAN. The measured bandwidth contain two WLAN band(2.4 ∼ 2.4835 GHz, 5.725 ∼ 5.825 GHz).

1. INTRODUCTION

These days, a mobile communication system has an advantage in that various mobile communication services including voice, data, moving images, and digital TV broadcasting can be easily exchanged free from time and spatial limitations. The number of users has rapidly increased thanks to the convenience of mobile communication, and thus the mobile communication system has rapidly developed. The development of various mobile communication systems including cellular, PCS, IMT-2000, WLAN (Wireless LAN), PDA, and satellite DMB, requires the need for the development of a high-functioning and high-performance personal portable terminal and development of a small, light and thin antenna.

In this thesis, a small dual-band WLAN PIFA having a dual resonance characteristic, which satisfies the requirement, was designed. In the designed antenna, resonance frequencies can be tuned independently of each other and do not affect each other, thereby easily realizing the antenna. The performance of the proposed antenna is verified through manufacturing and measurement.

2. DESIGN AND ANALYSIS OF DUAL-BAND PIFA

2.1. Design of Modified PIFA Having a Dual Band and Its Result

In an antenna proposed in this thesis, the modified dual-band PIFA having a WLAN band was designed, and a characteristic satisfying WLAN band of 2.4 to 2.4835 GHz and 5.725 to 5.825 GHz

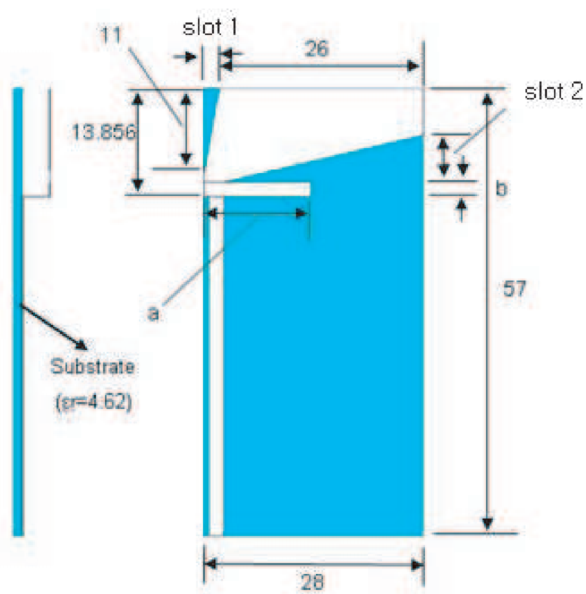

Figure 1: Structure of the proposed PIFA antenna.

were obtained through comparative analysis. The size of the antenna, and the sizes of an FR4 substrate, a ground plane and a short strip were adjusted, and the lengths of slots and the widths between the slots were adjusted in order to acquire the dual characteristic. In particular, it was possible to acquire the desired characteristic of the frequency band by adjusting the length and width of the short strip, the sizes of the FR4 substrate and the ground plane, and the width between the slots [3]. Fig. 1 shows the proposed antenna. The height of the antenna is 3.5 mm to the maximum, and the size of the radiation patch having a thickness of 0.035 mm was $13.856 \times 28 \times 0.035\,\mathrm{mm}^3$. The FR-4 substrate having a size $57 \times 28\,\mathrm{mm}^2$ and a thickness of 1 mm was used as a dielectric as shown in Fig. 1.

Two resonances were acquired by the use of two radiation patches having trapezoid and rectangular patches, respectively. In general, a high-frequency band was adjusted according to the length of the rectangular patch, and the height and width of the short strip and a low-frequency band were adjusted according the widths of the slot and PIFA, the position of a feeding point or the size of the ground plane. The trapezoid radiation patch and the rectangular radiation patch of the proposed antenna each had the WLAN band. The optimization result is shown in Table. 1.

Table 1: Optimized parameters for the proposed antenna.

Parameter	value
Size of Anetnna	$28 \times 13.856\,\mathrm{mm}^2$
Size of Ground	$28 \times 43.144\,\mathrm{mm}^2$
Size of FR4	$28 \times 57\,\mathrm{mm}^2$
H	3.5 mm
W	1.856 mm
slot 1	6 mm
slot 2	2 mm
a	13.7 mm
b	1.856 mm

2.2. Result of Sweeping the Proposed PIFA

Figures 2 and 3 show variation in reflection loss according to the length of each slot. Fig. 4 shows variation according to the length of the patch bringing about radiation in 5 GHz band out of the dual bands. Fig. 2 shows a reflection loss when the slot length of the antenna radiating in 2 GHz band is in the range of 2 to 8 mm. In 2 GHz band, as the length of the slot increased, the overall frequency band moved to a higher frequency band, thereby reducing the reflection loss. In 5 GHz

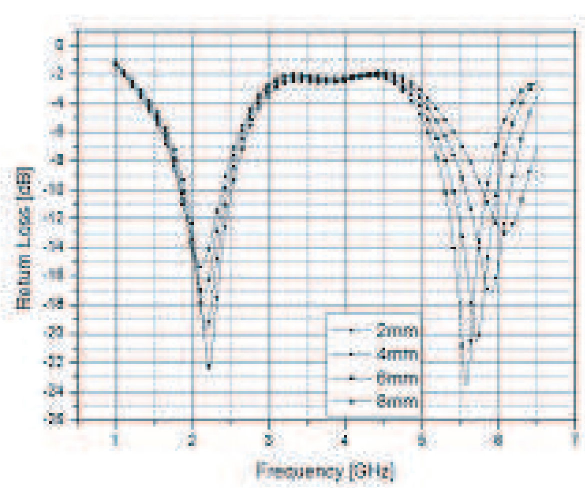

Figure 2: Return loss(slot 1).

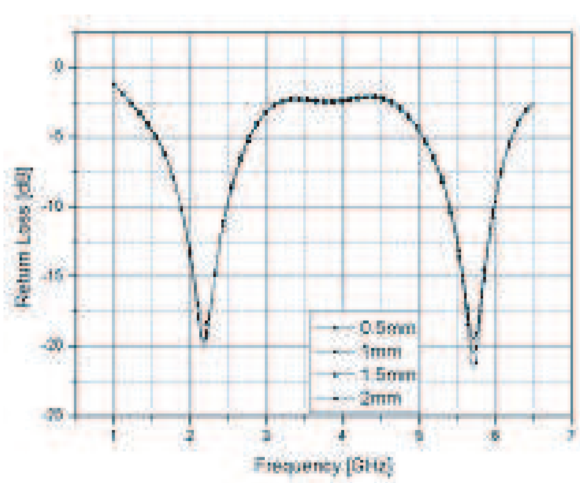

Figure 3: Return loss(slot 2).

band, as the length of the slot increased, the resonance frequency decreased and the reflection loss decreased. Fig. 4 shows the reflection loss when the length of Slot 3 is in the range of 13.5 to 14.1 mm. As the length of Slot 3 increased, the 2 GHz frequency band showed a slight change and the 5 GHz frequency band showed a considerable change. As the length of the slot increased, the reflection loss increased, and the resonance frequency increased. This occurred when the overall current flow increased, as the length of the slot increased. The length of the patch was set to 13.7 mm in order to adjust the frequency band to a wireless LAN band of 5.725 to 5.825 GHz in the 5 GHz band. As the length of the slot increased, the path length of the overall current flow increased. Accordingly, the frequency band decreased.

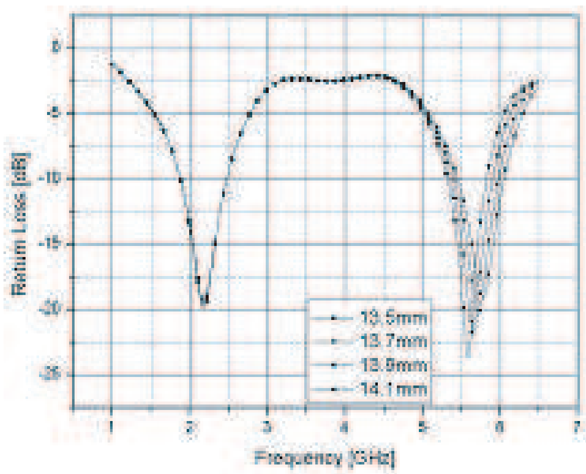

Figure 4: Return loss(slot 3).

Figure 5 shows variation according to the size of the short strip. (a) shows the height of the short strip and (b) shows variation according to the width. (a) shows a reflection loss when the height varied from 2.5 to 4 mm by 0.5 mm and the most suitable frequency band was acquired in case that the height was 3.5 mm. As the height of the short strip increased, the resonance frequency decreased. (b) shows a reflection loss when the width of the short strip varied from 2.3 to 2.6 mm. The desired frequency band was acquired in case that the width was 2.5 mm. As the width of the short strip increased, the resonance frequency decreased.

Figure 6 shows the comparison of the simulation result and the measurement result of the proposed antenna. The measurement result coincided with the simulation result, but the bandwidth

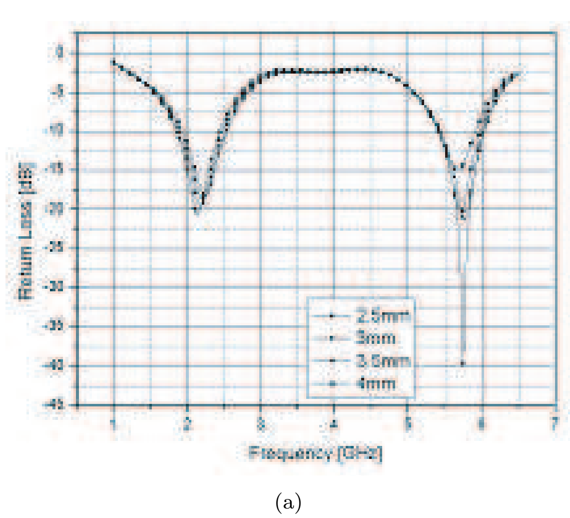

(a)

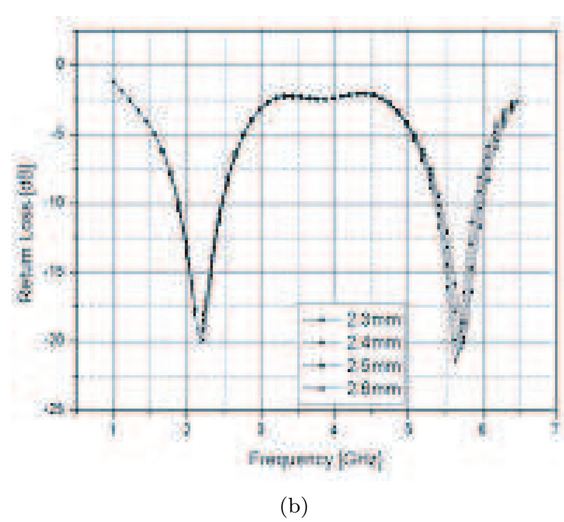

(b)

Figure 5: Return loss(short strip), (a) Return loss(height of the short strip), (b) Return loss(width of the short strip).

in the measurement result was smaller and more efficient than that in the simulation result. It is judged that this is because an accurate antenna satisfying the design value was difficult to manufacture, and the frequency characteristic varies in spite of minute structural different because of an RF characteristic.

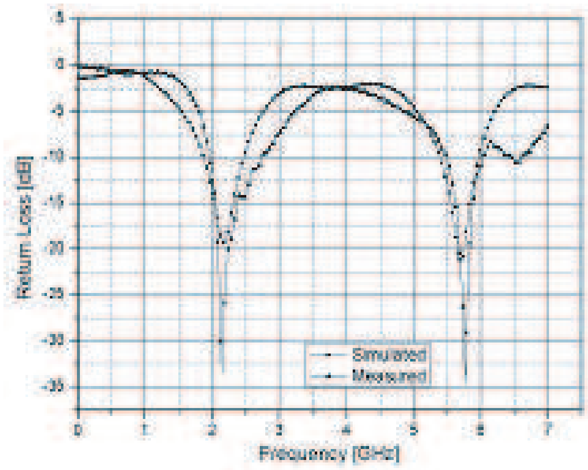

Figure 6: Comparison of the simulated and measured return loss on the optimized antenna.

3. MANUFACTURING AND ANALYSIS

A dual-band PIFA of a meander structure having a standard shown in Table 1 was manufactured on the basis of the simulation result. An FR-4 substrate having a permittivity of 4.62 was used as a dielectric, and a copper plate having a thickness of 0.01 mm was used as a patch. A microstrip cable was used for feeding, and an impedance matching was 50 Ω. Fig. 7 shows the concrete structure of the manufactured antenna.

Figure 8 shows the measurement result of the manufactured antenna. In the measurement result, −10 dB bandwidth of the proposed dual-band PIFA has the dual-band characteristic. For example, it is in the range of 1.95 to 2.65 GHz and in the range of 5.47 to 6.03 GHz. The measured bandwidth satisfied two WLAN bands of 2.4 to 2.4835 GHz and 5.725 to 5.825 GHz.

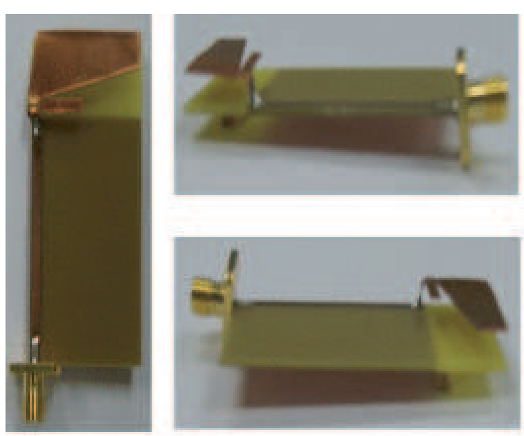

Figure 7: Photograph of the fabricated antenna.

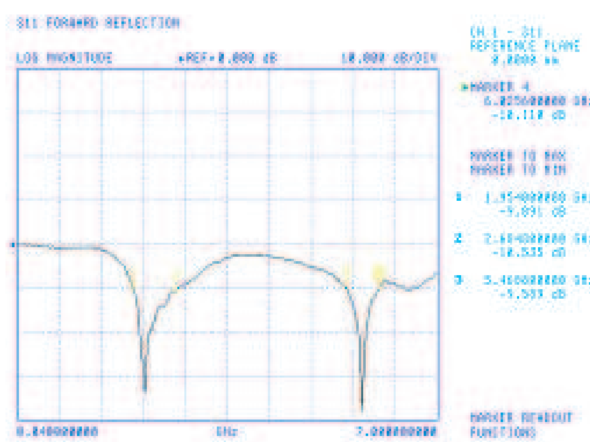

Figure 8: Return loss of fabricated antenna.

4. CONCLUSION

In this thesis, a dual-band antenna having a 2 GHz IMT-2000/WLAN band and a 5 GHz WLAN band was designed. The height and width of the short strip for deciding the size of the antenna were set to 3.5 mm and 2.5 mm, respectively, and the length of the slot was adjusted. Accordingly, the desired frequency band could be obtained.

The antenna was manufactured and measured on the basis of the simulation result. In the measurement result, −10 dB bandwidth of the proposed dual-band PIFA has a dual-band characteristic. For example, it is in the range of 1.95 to 2.65 GHz and in the range of 5.47 to 6.03 GHz.

In this thesis, since the manufactured antenna is suitable for miniaturization and it can be changed by the use of various wideband techniques, it is prospected that the antenna will continue to be studied in the future.

ACKNOWLEDGMENT

This work was supported by the Korea Research Foundation Grant funded by the Korean Government(MOEHRD) (The Regional Research Universities Program/Chungbuk BIT Research-Oriented University Consortium)

REFERENCES

1. Wong, K. L., *Compact and Broadband Microstrip Antennas*, John Wiley & Sons, Inc., New York, 2002.
2. Wong, K. L., *Planar Antennas for Wireless Communications*, John Wiley & Sons, Inc., New Jersey, 2003.
3. Choi, D. G., H. S. Shin, N. Kim, and Y. K. Kim, "Design of the broadband PIFA with multi-Band for SAR reduction," *The Journal of Korea Electromagnetic Engineering Society*, Vol. 16, No. 1, 66–77, 2005.
4. Sim, D. U. and S. O. Park, "An effects of the handset case, battery, and human head on the performance of a triple-band internal antenna," *Antennas and Propagation Society Symposium*, Vol. 2, 1951–1954, June 2004.
5. Chen, W. S., T. W. Chiou, and K. L. Wong, "Compact PIFA for GSM/DCS/PCS triple band mobile phone," *Antennas and Propagation Society International Sym.*, Vol. 4, 528–531, 2002.
6. Taflove, A. and M. E. Brodwin, "Numerical solution of steady-state electromagnetic scattering problems using the time-dependent Maxwell's equation," *IEEE Trans. Microwave Theory Tech.*, Vol. 23, 623–630, Aug. 1975.

12 GHz Planar Array Antenna for Satellite Communication

Adel M. Abdin
Department of Communications, Faculty of Engineering
Shorouk Academy, Shorouk City, Cairo, Egypt

Abstract— A novel microstrip array antenna of 32 elements is designed and built for broadcasting satellite orbital positions. It is working in the 12.43–12.53 GHz band (space-to-Earth). A corporate feeding network is used to give equal amplitude and phase to each element. The theoretical analysis is based on IE3D (Zeland) software and genetic algorithm to optimize the performance of the planar array. A dummy column of elements is assumed around the excited 32 elements. The effect of these dummy elements is tested using IE3D (Zeland) software on the return loss and voltage standing wave ratio (VSWR). The simulation shows the return loss and VSWR decrease as the number of columns of parasitic elements increases. On the other hand the center frequency increases as the number of parasitic elements increases. The return loss and VSWR are measured and compared with the simulated results. They are very close. Both the theoretical and experimental results are presented and discussed.

1. INTRODUCTION

During recent years, microstrip antenna array is widely used due to its several advantages, such as low profile, light weight, and low cost, etc. [1, 2]. In various communications and radar systems, a microstrip array is greatly desired. The designed antenna is suitable for the 12 GHz Broadcasting Satellite Service (BSS) frequency bands. It is working in the frequency band 12.43–12.53 GHz. A single-feed planar antenna can be easily integrated. The antenna consists of 32-elements with corporate feeding network. This feeding was designed to give equal amplitude and phase to each element. The dimension of each patch, spacing between patches, and the width of the feeding line are shown in Figure 1 [3]. The array was fabricated on a dielectric substrate called Teflon with $h = 0.7874$ mm, $\varepsilon_r = 2.2$, area of 91.5×53 mm. The dimension of the patch and the spacing between the elements in x and y directions are 9.5×7.6, 12.0482, and 12.0482 mm respectively. The feeding system includes three different microstrip transmission lines of different impedances and different widths. The impedances are 50 Ω, 71.7 Ω, and 100 Ω and the corresponding widths are 2.377 mm, 1.339 mm, and 0.655 mm respectively.

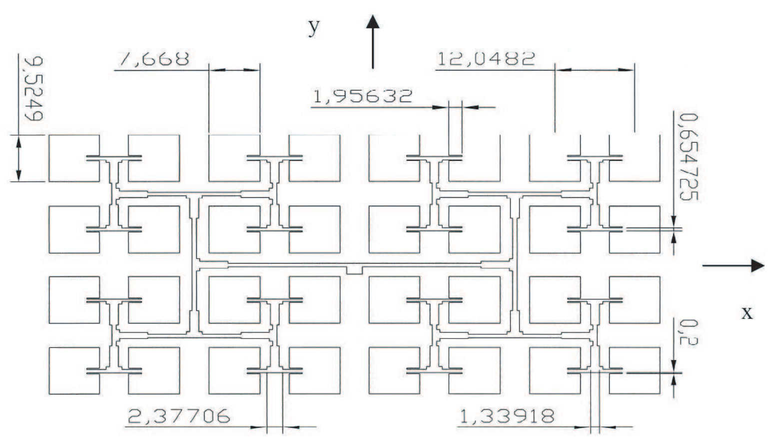

Figure 1: The dimension of the designed antenna and its feeding system.

2. ARRAY ANTENNA

The design of this array and its feeding is discussed in Section 2. The parameter of the antenna shown in Figure 2 is optimized using IE3D (Zeland) software. The simulated and measured return loss (S_{11}) and VSWR of 4×8 antenna array are shown in Figure 3. The simulated and measured results are very close. It can be seen from the figure that S_{11} and VSWR of the fabricated antenna

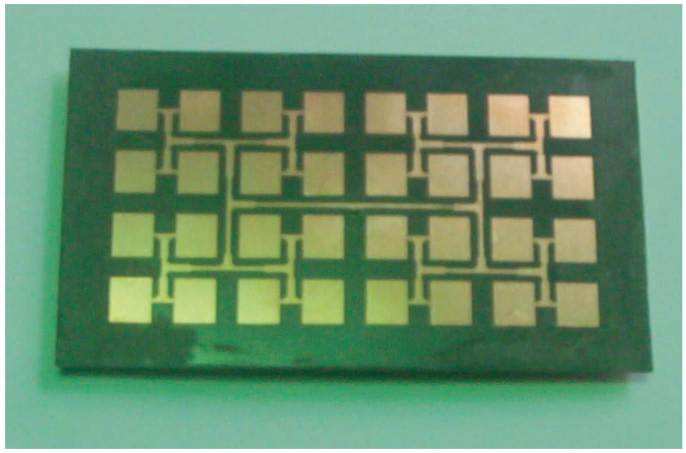

Figure 2: The fabricated array antenna.

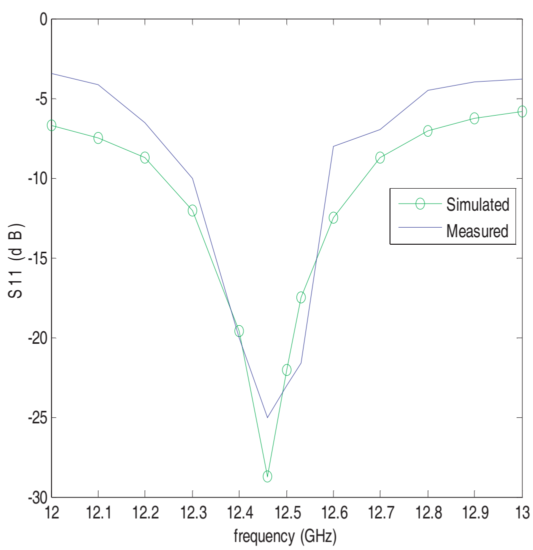

(a)

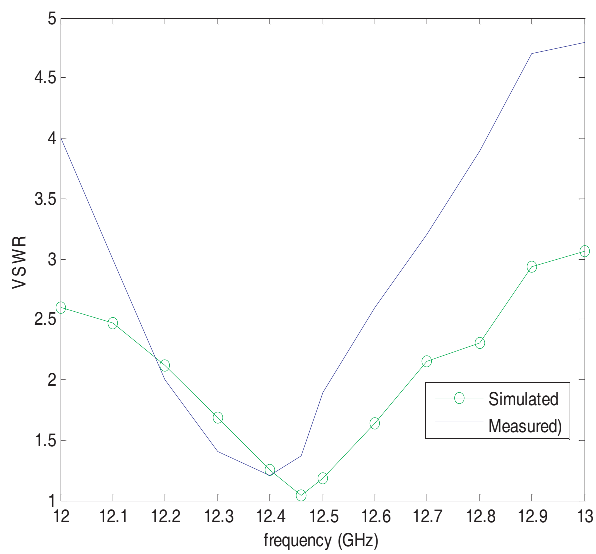

(b)

Figure 3: (a) Simulated and measured return loss. (b) Simulated and measured VSWR.

are -25 dB and 1.2 respectively. On the other hand, the simulated results show that S_{11} and VSWR of the designed antenna are -28.7 dB and 1.0357 respectively.

The impedance smith chart obtained for the designed array is shown in Figure 4. For the plot, it shows that the points are located at the middle of the circle as the frequency becomes nearer to the center frequency. Hence, this indicates that the matching of this antenna is quite good, as the desired location of the points should be in the middle of the circle ($50\,\Omega$).

3. THE EFFECT OF PARASITIC ELEMENTS

A study is done on 4×8 array to investigate the effect of parasitic elements using IE3D (Zeland) software [4]. Figure 5 shows one row and two rows of passive elements on each side of the array antenna.

The simulation results of both S_{11} and VSWR for different cases are shown in Figure 6. The different values of return loss and VSWR and the corresponding frequency for 4×8 array antenna with and without parasitic elements are listed in Table 1. The resonant frequency increases as the number of rows of parasitic elements increases.

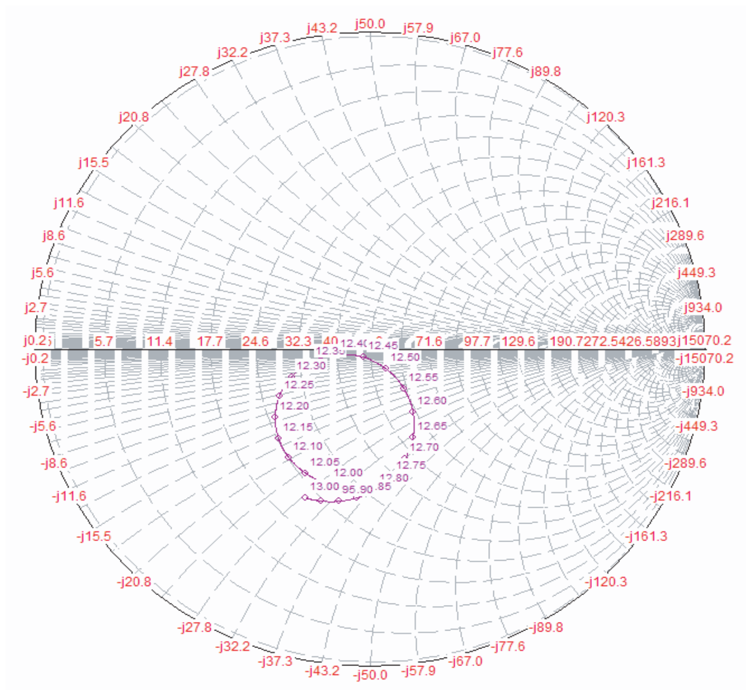

Figure 4: The impedance smith chart obtained for the designed array.

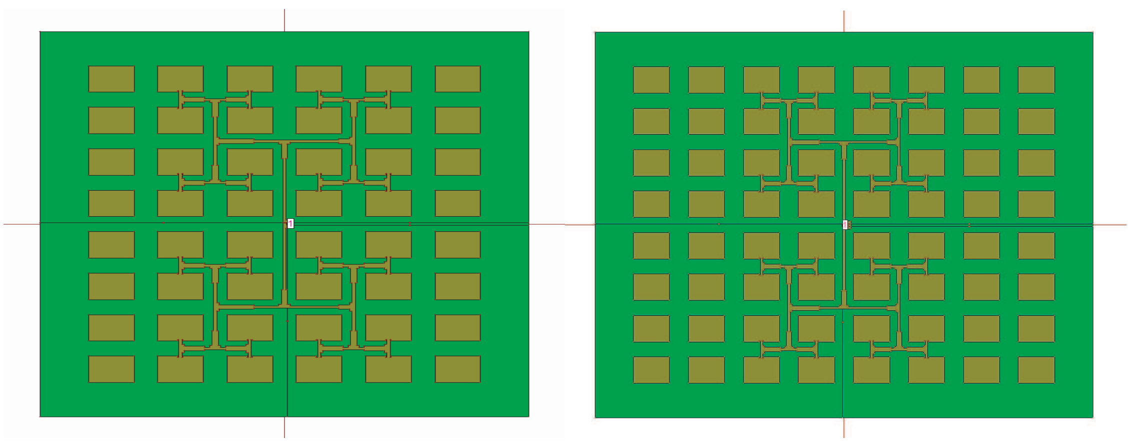

(a) (b)

Figure 5: Passive elements on each side of the array antenna (a) one row (b) two rows.

Table 1: The minimum values of return loss and VSWR and the corresponding frequency for 4 × 8 array antenna with and without parasitic elements.

parameter / Case	F (GHz)	S_{11} (dB)	VSWR
array antenna without parasitic elements	12.46	-28.7	1.0357
array antenna with One row of parasitic elements	12.52	-21.144	1.1785
array antenna with two rows of parasitic elements	12.6	-21.2	1.161

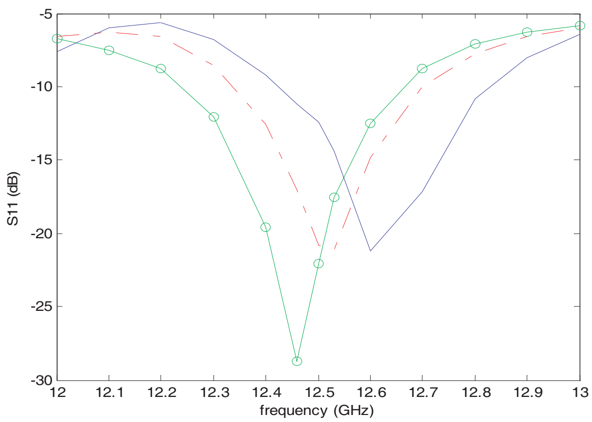

(a)

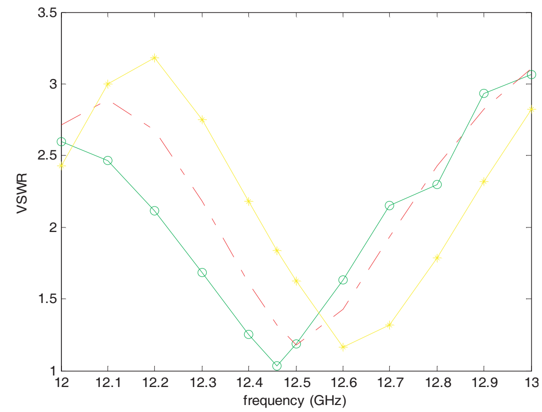

(b)

Figure 6: (a) S_{11} for the array antenna with and without parasitic elements: – o without parasitic elements, –. with one row, and — with two rows. (b) VSWR for the array antenna with and without parasitic elements: – o without parasitic elements, –. with one row, and – * with two rows.

4. CONCLUSIONS

A novel 4×8 microstrip array antenna was developed at 12.46 GHz and presented numerically and experimentally. The parameters of the array such as S_{11}, VSWR, and input impedance are optimized using Zeland software. The measured return loss and VSWR of the designed antenna are is -25 dB and 1.2 respectively, while the simulated values are -28.7 dB and 1.0357 respectively. The simulated and measured results show a reasonably good agreement. The small deviation between them is due to fabrication inaccuracy. The center frequency of the array can be controlled by the number of parasitic elements around it.

REFERENCES

1. Bahl, J. and P. Bhartia, *Microstrip Antennas*, Artech House, Inc., London, 1980.
2. James, J. R. and P. S. Hall, *Handbook of Microstrip Antennas*, Peter Peregronic Ltd., London, 1989.
3. Bhartia, P., et al., *Millimeter-wave Microstrip and Printed Circuit Antennas*, Artech House, Norwood, Mass., 1991.
4. IE3D Software Release 11.5 developed by Zeland Software, Inc.

The Helical Antenna for Handset Design and Phantom Effect

Kuo-Liang Wu[1], **Guan-Yu Chen**[1], **Jwo-Shiun Sun**[1], **Cheng-Hung Lin**[2]
Kwong-Kau Tiong[2], **and Y. D. Chen**[3]

[1]Department of Electronic Engineering, National Taipei University of Technology, Taiwan
[2]Department of Electrical Engineering, National Taiwan Ocean University, Taiwan
[3]Antenna and EMC Laboratory, High Tech Computer Corp. (HTC), Taiwan

Abstract— A high performance wire and patch co-design monopole antenna fabricated using two kinds of folded wire and metal patch as radiator is presented. A prototype of the proposed monopole antenna with a compact area size s implemented, and the antenna shows a wide operating bandwidth of about 300 and 50 MHz for low band and high band bandwidth, making it easy to cover the GSM, EDGE, CDMA, CDMA 2000, W-CDMA and UMTS band for wireless communication and 2.5G/3G dual mode operation of a mobile handset phone.

1. PDA PHONE FOR HELICAL ANTENNA OPERATION

A low profile and compact helical (Fig. 1) antenna with multi-asymmetric helix turns is designed and measured (Fig. 2). The helical antenna, which is placed along the axis of a RF coaxial line fed through the ground plane, can be operated at multi resonant frequencies. The helix wire radiator [1, 2], which is designed to operate at the normal mode radiation performance, is mounted directly on the PDA ground environment. The finite element method (FEM) is used to obtain the numerical solution of far-field radiation patterns, which are found in good agreement compared to the experimental results. The bandwidth performance in multi-frequencies operation would also be explicitly studied. The design of a miniaturized helical antenna is proposed and presented for

Figure 1: The multi-bands for helical antenna operation.

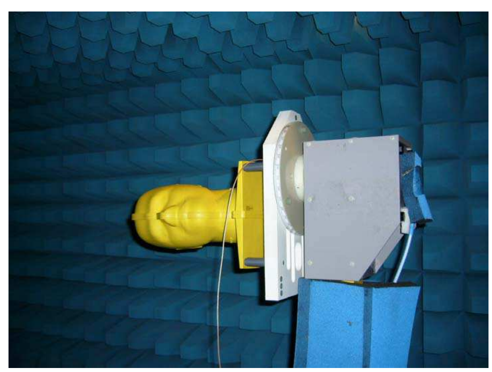

Figure 2: The multi-bands helical antenna for phantom effect.

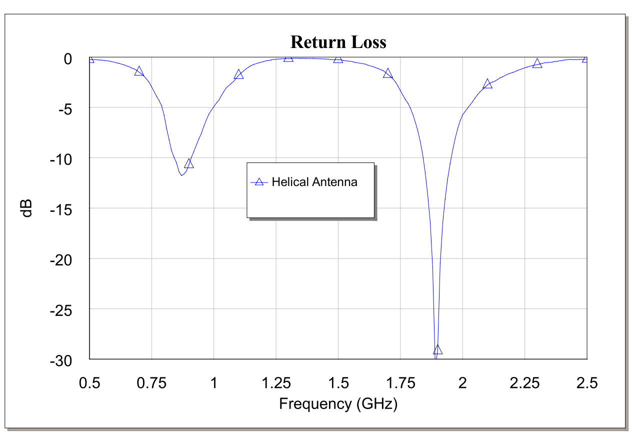

Figure 3: The measured data of helical antenna.

2.5G/3G mobile communication bands. The measured data is shown in Table 1 and Table 2. In this paper, a compact and low profile internal helical antenna for multi-bands has been proposed. This antenna was designed and measured for phantom effect. A good agreement between measurement and analysis has been obtained. The proposed antenna shows a wider operating bandwidth (Fig. 3) and it easy to cover the GSM, EDGE, CDMA, CDMA 2000, W-CDMA and UMTS band for wireless communication and 2.5G/3G dual mode operation of a mobile handset phone, co-design, co-integration and PDA application.

Table 1: The measured antenna gain.

Frequency (MHz)	800	850	900	950	1000	1700
Peak Gain (dBi)	−0.6	−0.4	0.9	−0.15	−0.1	−0.2
Frequency (MHz)	1750	1800	1850	1900	1950	2000
Peak Gain (dBi)	−0.15	−0.3	−0.2	−0.3	−0.25	−1.6

Table 2: The measured antenna gain with phantom effect.

Frequency (MHz)	800	850	900	950	1000	1700
Peak Gain (dBi)	−7.8	−7.3	−6.1	−5.95	−5.9	−3.25
Frequency (MHz)	1750	1800	1850	1900	1950	2000
Peak Gain (dBi)	−3.25	−3.6	−3.8	−3.5	−3.4	−4.25

2. CONCLUSIONS

In this paper, a compact and low profile helical antenna for multi-bands has been proposed. This antenna was designed and measured. A good agreement between measurement and analysis has been obtained. The proposed antenna shows a wider operating bandwidth and it easy to cover the GSM, EDGE, CDMA, CDMA 2000, W-CDMA and UMTS band for wireless communication and 2.5G/3G dual mode operation of a mobile handset phone, co-design, co-integration and application.

ACKNOWLEDGMENT

The authors acknowledge the Antenna and Wireless System Integration Department of High Tech Computer, Corp. (HTC), Taiwan for sport the wireless technique and measurement environment.

REFERENCES

1. Stutzman, L. W., *Antenna Theory and Design*, John Wiley, 1998.
2. Balanis, A. C., *Antenna Theory*, John Wiley, 2005.

MIMO Channel Model and Its Impact on the Channel Capacity

Jun Wang, Quan Zhou, Wei Ma, and Lede Qiu

National Key Laboratory of Space Microwave Technology
Xi'an Institute of Space Radio Technology, Xi'an 710100, China

Abstract— In order to study the impacts of array configuration and channel model parameters including antenna spacing and scattering angle on the channel capacity of an S-MIMO (Satellite Multiple Input Multiple Output) system, a novel method is proposed to explore the channel capacity under flat fading. A novel channel model is constructed based on the fading correlation matrix which depends on the array configuration. And then using the properties of Wishart distribution, closed-form expressions for the upper and lower bounds on the ergodic capacity of N by M MIMO system are presented in detail. The novel method also could be generalized to MIMO-OFDM systems with any number of transmit and receive antennas. Computer simulation results show that for small spacing the UCA yields higher channel capacity than ULA. The channel capacity is maximized when the antenna spacing increases to a certain point, and further more, the larger the scattering angle, the quicker the channel capacity converges to its maximum. And at high SNR, the upper and lower bounds on the ergodic capacity are close to its true value.

1. INTRODUCTION

Multiple Input Multiple Output (MIMO) using multiple antennae simultaneously at both end in a wireless system has been shown to significantly improve spectrum efficiency of communication systems over traditional Single Input Single Output (SISO) systems. Theoretical work of [1] and [2] proved that if the fades between different pairs of transmit-receive antenna elements are independent and identical Rayleigh and receiver knows the channel perfectly, the channel capacity increases linearly with the minimum of the number of transmit and receive antennas.

In satellite systems, how to use the limited resource to increase the system performance is the important problem. Many authors [3, 4] proposed that future land mobile satellite systems can take advantage of MIMO technology to boost data-rates in resource limited allocated spectrum. Although the land mobile satellite channel at low elevation is harsh, a significant increase in capacity can be achieved using space time coding from a single satellite MIMO system.

In real propagation environments, correlation exists between the fades of deferent antenna elements due to the antenna spacing and the surroundings around antenna arrays are insufficient. This can cause the channel capacity of MIMO systems reduce significantly. In [5] the statistical model of the fading correlation is constructed and the asymptotic channel capacity is investigated when the number of antennas is infinite using random matrices theory. According to [6], the closed-form expression of MIMO systems can be derived using the probability density function of eigenvalues of Wishart matrix. But the computational complexity is very high. In [6] and [7] the upper and lower bounds on the ergodic capacity of MIMO system are presented, and the results shown that the upper and lower bounds are close to its real value.

In this paper, we develop a method based on the receive UCA to investigate the channel capacity and analyze the impacts of antenna spacing and scattering angel on the capacity of S-MIMO systems. In addition, we introduce the properties of Wishart distribution to derive the upper and lower bounds in detail, which can reduce the computational complexity significantly. We also investigate the impacts of array configuration and channel model parameters including antenna spacing and scattering angle on the channel capacity of S-MIMO systems.

2. THE CHANNEL MODEL AND CAPACITY OF S-MIMO SYSTEMS

In the following, we assume: (1) M and N denote the number of transmit and receive antennae, respectively. (2) a single user in the system and employ the narrowband Rayleigh MIMO channel. (3) uniform circular antenna or uniform linear antenna is used at the receiver. (4) $\mathbf{H}$ is the matrix channel impulse, $\mathbf{n}$ is the $M \times 1$ zero mean and unit variance additive white Gaussian noise vector. (5) AOA distribution is uniform and the central AOA is denoted as Θ, and the angle of arrival is uniform distribution in $[\Theta - \Delta, \Theta + \Delta]$, the radius of UCA is r, the angle that each element location makes with the horizontal axis is φ_i, the angle spread is Δ.

The spatial fading correlation between the mth and nth antenna element is defined as

$$\begin{aligned} R(m,n) \;=\; & \frac{1}{2\Delta}\int_{-\Delta}^{\Delta}\exp\left(\frac{j4\pi r}{\lambda}\sin\left(\frac{\varphi_n-\varphi_m}{2}\right)\left[\sin z\cos\left(\Theta-\frac{\varphi_n+\varphi_m}{2}\right)\right.\right. \\ & \left.\left. +\cos z\sin\left(\Theta-\frac{\varphi_n+\varphi_m}{2}\right)\right]\right)dz \end{aligned}$$

For the uplink, Δ is usually small. We can approximate $\cos z\approx 1$ and $\sin z\approx z$ which gives

$$R(m,n)=\exp\left(j4\pi r\alpha/\lambda\right)\sin c\left(4r\beta\Delta/\lambda\right) \tag{1}$$

where $\alpha=\sin\left((\varphi_n-\varphi_m)/2\right)\sin\left(\Theta-(\varphi_n+\varphi_m)/2\right)$, $\beta=\sin\left((\varphi_n-\varphi_m)/2\right)\cos\left(\Theta-(\varphi_n+\varphi_m)/2\right)$.

When ULA is used at the receiver, the spatial correlation between two elements a distance d apart can be determined as

$$R(d)=\frac{1}{2\Delta}\int_{\Theta-\Delta}^{\Theta+\Delta}\exp\left(j\frac{2\pi d}{\lambda}\sin(\theta)\right)d\theta=\exp\left(j\frac{2\pi d}{\lambda}\sin(\Theta)\right)\sin c\left(\frac{2\pi d}{\lambda}\cos(\Theta)\Delta\right) \tag{2}$$

The spatial fading correlation matrix $\mathbf{R}$ is constructed based on (1) or (2).

And then the channel matrix can be written as

$$\mathbf{H}=\mathbf{R}^{1/2}\mathbf{U} \tag{3}$$

We assume the channel is perfectly known at the receiver but unknown at the transmitter. The total power of the signal is constrained to P, regardless of the number of transmit antennas. The channel capacity is given by

$$C=\log_2(\det(\mathbf{I}_M+\rho\mathbf{H}\mathbf{H}^T)) \tag{4}$$

where $\mathbf{I}_M$ is $M\times M$ identity matrix, T is denote conjugate transpose, $\rho=P/N$.

Using (3) and factorize $\mathbf{R}$ using the singular value decomposition, we get

$$C=\log_2\left(\det\left(\mathbf{I}+\rho\mathbf{\Lambda}_{\mathbf{R}}^{1/2}\mathbf{W}\mathbf{\Lambda}_{\mathbf{R}}^{1/2}\right)\right) \tag{5}$$

For investigating the mean capacity of MIMO system, it is important to analyze the statistical property of the eigenvalues of $\mathbf{V}=\mathbf{\Lambda}_{\mathbf{R}}^{1/2}\mathbf{W}\mathbf{\Lambda}_{\mathbf{R}}^{1/2}$. It is known to all that $\mathbf{W}\sim\mathbf{W}_M(N,\mathbf{I})$ and using the properties of Wishart distribution, we get $\mathbf{V}\sim\mathbf{W}_M\left(N,\mathbf{\Lambda}_{\mathbf{R}}\right)$. There exists the closed-form expression for the joint probability density of the eigenvalues of $\mathbf{V}$, but it is very difficult to calculate the marginal pdf of the eigenvalues to derive the closed-form expression of the channel capacity. So we will give the closed-form expressions for the upper and lower bounds on the mean capacity and get some useful conclusions.

Noting $\log x$ is concave function in x, so $E\log x\le\log Ex$. Using this property, we can get

$$E(C)\le\log_2 E\left(\det\left(\mathbf{I}+\rho\mathbf{V}\right)\right)\approx M\log_2\left(\rho\right)+\log_2\left(E\left(\det\mathbf{V}\right)\right) \tag{6}$$

Wishart distribution has the property: if $\mathbf{V}$ is $\mathbf{W}_M\left(N,\mathbf{\Lambda}_{\mathbf{R}}\right)$, then $\det(\mathbf{V})/\det(\mathbf{\Lambda}_{\mathbf{R}})$ has the same distribution as $\prod_{k=1}^{M}\chi^2_{N-k+1}$, where the χ^2_{N-k+1} for $k=1,\ldots,M$, denote independent χ^2 random variables. Using this property, we can get

$$E\left(\det\mathbf{V}\right)\;=\;\det\mathbf{\Lambda}_{\mathbf{R}}2^M\Gamma_M\left(\frac{N}{2}+1\right)\Big/\Gamma_M\left(\frac{N}{2}\right) \tag{7}$$

$$E\left(\log_2\left(\det\mathbf{V}\right)\right)\;=\;\left(\sum_{i=1}^{M}\left(\ln\left(\lambda_i\right)+\psi\left(N-i+1\right)\right)\right)\Big/\ln 2 \tag{8}$$

Using (7), then (6) can be written as

$$E(C)\le M\left(\log_2\left(\frac{P}{N}\right)+1\right)+\sum_{i=1}^{M}\log_2\left(\lambda_i\right)+\log_2\left(\Gamma_M\left(\frac{1}{2}N+1\right)\Big/\Gamma_M\left(\frac{1}{2}N\right)\right) \tag{9}$$

where $\Gamma_M(a) = \pi^{M(M-1)/2} \prod_{i=1}^{M} \Gamma(a - i + 1)$.

For a Hermitian matrix $\mathbf{A}$, it is true that: $\det(\mathbf{I} + \mathbf{A}) \geq \det(\mathbf{A})$. From this property, we get

$$E(C) \geq E(\log_2(\det(\rho\mathbf{V}))) \tag{10}$$

using (8), we can lower bound $E(C)$ as

$$E(C) \geq \left(M \ln(\rho) + \left(\sum_{i=1}^{M} (\ln(\lambda_i) + \psi(N - i + 1)) \right) \right) \Big/ \ln 2 \tag{11}$$

where $\psi(x) = \Gamma'(x)/\Gamma(x)$.

3. SIMULATION

Simulation considers the narrowband single user S-MIMO system with $M = 4$ receive and $N = 6$ transmit antennae. The central angle of arrival is $\Theta = \pi/3$, the radius of UCA is r, the receive SNR is 20 dB.

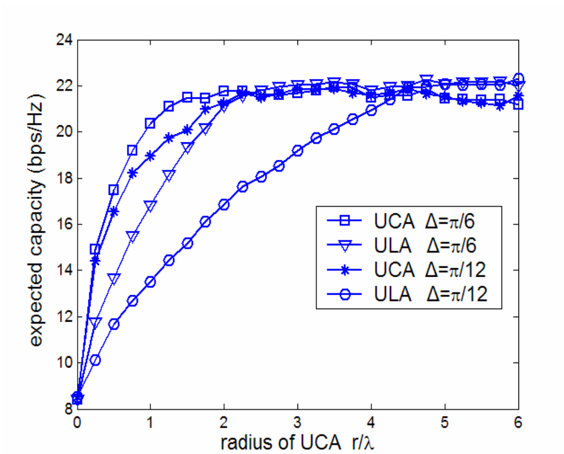

Figure 1: Mean capacity of MIMO for various scattering angels at $\Theta = \pi/3$.

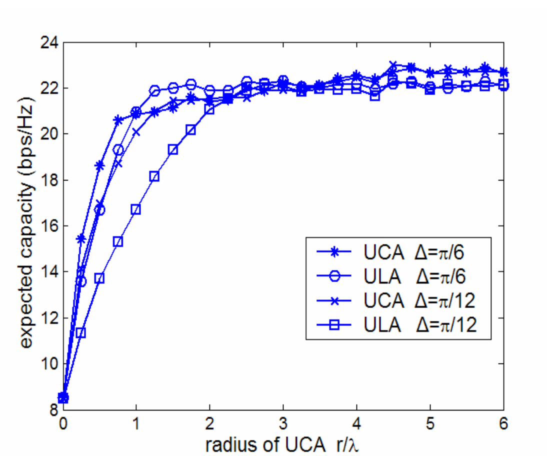

Figure 2: Mean capacity of MIMO for various scattering angels at $\Theta = 0$.

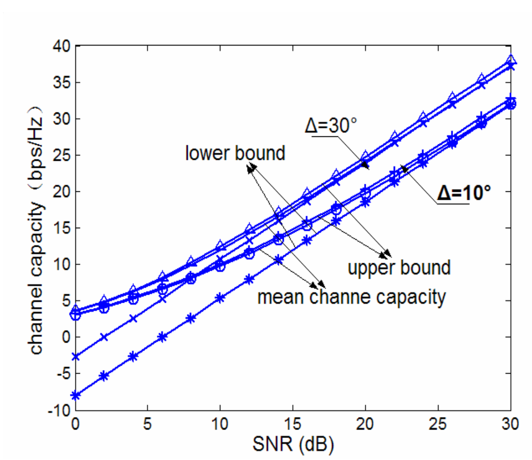

Figure 3: Channel capacity and its upper and lower bounds.

Figure 1 and Fig. 2 show the mean capacity of spatially correlated Rayleigh-fading MIMO channels for different scattering angels. Note that for a four-element linear array, the element spacing is $d = (2/3)r$, while for the UCA, the minimum spacing between elements is $\sqrt{2}r$. As shown, the channel capacity is maximized when the antenna spacing increases to a certain point, and further more, the larger the scattering angle is, the quicker the channel capacity converges to its maximum is. And we also see that for small element spacing, when the scattering angle is determined, the UCA outperforms the ULA.

Figure 3 shows the mean capacity and its upper and lower bounds of correlated Rayleigh-fading MIMO channels. We can see that, at high SNR, the upper and lower bounds on the mean capacity are close to its actual value.

4. CONCLUSIONS

We have constructed the statistical channel model based on fading correlation and developed a method to investigate the capacity of S-MIMO systems. The method using the properties of Wishart distribution to derive the closed-form expressions for the upper and lower bounds on the ergodic capacity based on receive UCA. And we also investigate the impacts of array configuration and channel model parameters including antenna spacing and scattering angle on the channel capacity of a MIMO systems. Simulation results show that for small element spacing, when the scattering angle is determined, the UCA outperforms the ULA. At high SNR, the upper and lower bounds on the mean capacity are close to its actual value.

ACKNOWLEDGMENT

This work was supported by the National Key Laboratory Foundation of China under Grant 9140C5303010703.

REFERENCES

1. Foschini, G. J., "Layered space-time architecture for wireless communication in a fading environment when using multi-element antennas," *Bell Labs Technical Journal*, Vol. 1, No. 2, 41–59, 1996.
2. Foschini, G. J. and M. J. Gans, "On limits of wireless communications in a fading environment when using multiple antennas," *Wireless Personal Communications*, Vol. 6, No. 3, 311–335, 1998.
3. King, P. R. and S. Stavrou, "Land mobile-satellite MIMO capacity predictions," *IEE Electronics Letters*, Vol. 41, No. 13, 749–750, 2005.
4. King, P. R. and S. Stavrou, "Capacity improvement for a land mobile single satellite MIMO system," *IEEE Antennas and Wireless Propagation Letters*, Vol. 5, No. 2, 98–100, 2006.
5. Chuah, C. N., D. Tse, J. M. Kahn, and R. A. Valenzuela, "Capacity scaling in MIMO wireless systems under correlated fading," *IEEE Trans. on Information Theory*, Vol. 48, No. 3, 637–651, 2002.
6. Shiu, D.-S., G. J. Foschini, M. J. Gans, et al., "Fading correlation and its effect on the capacity of multi-element antenna systems," *IEEE Trans. on Communications*, Vol. 48, No. 3, 502–512, 2000.
7. Grant, A., "Rayleigh fading multiple-antenna channels," *EURASIP Journal on Applied Signal Processing (Special Issue on Space-Time Coding (Part I))*, Vol. 2002, No. 3, 316–329, 2002.
8. Muirhead, R. J., *Aspects of Multivariate Statistical Theory*, John Wiley, New York, 1982.

The Influence of the Climatic Peculiarities on the Electromagnetic Waves Attenuation in the Baltic Sea Region

M. Zilinskas[1,2], **M. Tamosiunaite**[2,3], **S. Tamosiunas**[2,3], **and M. Tamosiuniene**[4]

[1]Communications Regulatory Authority of the Republic of Lithuania
Department of Radio Communication, Algirdo 27, LT-03219 Vilnius, Lithuania
[2]Faculty of Physics, Vilnius University, Sauletekio 9, LT-10222 Vilnius, Lithuania
[3]Institute of Materials Science and Applied Research, Vilnius University
Sauletekio 9, LT-10222 Vilnius, Lithuania
[4]Semiconductor Physics Institute, A. Gostauto 11, LT-01108 Vilnius, Lithuania

Abstract— The peculiarities of the climatic conditions in the Baltic Sea Region are reviewed. According to the values of rain rates measured in the Lithuanian Weather Stations with the 10-minute's integration time, a relation between the rain rate and the annual precipitation has been derived. The model for one-minute rain rate calculation on the months starting from May up to September in Lithuania has been presented. The values of the electromagnetic waves attenuation due to the rain have been determined. The cloud attenuation has been computed by using the meteorological data measured at the ground level. The semi empirical method has been used. The values of the specific attenuation under conditions of cloud cover have been determined.

1. INTRODUCTION

Knowledge of the electromagnetic waves attenuation due to rain and clouds is desirable while planning the communication systems, especially at frequencies of 10 GHz and above. Most of the methodologies for the prediction of rain attenuation on radio waves paths require the knowledge of the rain rate R-value. Rain rate data is presented in units of length per unit time (in millimeters per hour), but in practice it is measured over intervals of typically one minute, five minutes, hour or yearlong. In [1], it was mentioned that the integration time Δt (time between the readings of the values of rainfall amount) is important parameter and it can change the R-value. Most of the rain attenuation prediction methods require one-minute rain rate value. One-minute rain rate (mm/h) is the rainfall for one minute (mm/min) multiplied by 60. Rainfall rate is highly variable. Therefore, the rain rate and rain attenuation are analyzed for concrete climatic conditions. However, the electromagnetic waves attenuation due to rain under the Baltic Sea Region climatic conditions has been analyzed not enough [2, 3]. The electromagnetic waves attenuation due the clouds, as far as we know, has been not analyzed under Lithuanian climatic conditions. The main goals of this paper were to determine the one-minute value of rain rate by using ten-minutes rainfall amount data measured in the Lithuanian Weather Stations and to estimate the values of the electromagnetic waves attenuation due to the rain and the clouds.

2. THE PECULIARITIES OF THE CLIMATIC CONDITIONS IN THE BALTIC SEA REGION

The climate of Baltic Sea Region (BSR) is specific. BSR, being in the transition geography zone from Baltic Sea climate to Atlantic and continentals East Europe climate, may be distinguished for its variable climate. The average amount of precipitation in the BSR is 679 mm. The average nebulosity in the region is 50%. The minimal nebulosity (46%) occurs in spring [4]. The increase of nebulosity is going from north to south. In this paper we analyze Lithuanian climate more particularly. The climate of Lithuania is definable as middling cold, with the snowy winters. There are 20–30 thaw days even in mid-winter. In Lithuania, humid weathers predominate all over the year. The annual precipitation in rainy wet year is almost twice higher than in dry year. The values of annual rainfall measured in the localities of Lithuania are presented in Table 1. The showers are observed in the warm period of the year. Such climate is typical climate of the middle part of the East Europe.

The climate of the west part of Lithuania (for example, of Klaipeda) is specified as the moderate warm climate. The average temperature of the coldest month is more than -3°C. Such type of the climate is dominating in the West Europe. Vilnius is one of the cloudiest localities of Lithuania. There are about 100 overcast days in the year.

Table 1: The values of annual rainfall (mm) measured in the Localities of Lithuania in the period of years 1999–2004.

Year / Locality	1999	2000	2001	2002	2004	2005
Vilnius	520	694	653	616	646	720
Klaipeda	770	587	851	645	727	649

3. ELECTROMAGNETIC WAVES ATTENUATION DUE TO RAIN

One of the most accepted methods for prediction of rain attenuation is an empirical procedure based on the approximate relation between specific attenuation α (dB/km) and the rain rate R (mm/h) [5]:

$$\alpha = aR^b \tag{1}$$

where a and b are the functions of frequency f and rain temperature T.

According to the ITU-R (the Radiocommunication Sector of the International Union) Recommendation, the rain rate $R = 22$ mm/h when the rain attenuation is determined in Lithuania and Latvia can be used. In [1] it was mentioned that the ITU-R value $R = 22$ mm/h is too low for prediction of the rain attenuation in Latvia. The events when the rain rate exceeds the value mentioned above were observed in Lithuania as well. We analyze the intense rain events in Vilnius in more detail (see Table 2). The values of very intense rain rates measured in Vilnius Weather Station in the period of years 1970–1996 [6], the integration time and the percent of the time of the year are presented. The values of 10-minutes rain rates $R_{10\,\mathrm{min}\,0.01\%}$ (mm/h), determined by using the data measured in Lithuanian Weather Station in Vilnius in the period of years 1999–2004, and the values converted to one-minute rain rate using method [7] $R_{1\,\mathrm{min}\,0.01\%}$.are presented in Table 3. About 60% of the annual rainfall amount falls in the warm period of the year in Lithuania. This fact must be taken into account when the rain attenuation is predicted in the localities of Lithuania. The review of results measured at the Weather Station in Vilnius shows that relation between the ten-minutes rain rate for 0.01% of time and the annual precipitation can be written as:

$$R_{10\,\mathrm{min}\,0.01} = 3.23(\gamma M_r) \tag{2}$$

where M_r is the annual precipitation (mm) and γ is the coefficient of the warm period ($\gamma = 0.6$ in our case). The average value of the one-minute rain rate for 0.01% is 35.2 mm/h in Vilnius (in the period of years 1999–2004) and it is by 1.6 times higher than the ITU-R value $R = 22$ mm/h.

Table 2: The values of very intense rain rates R measured in Vilnius in the period of years 1970–1996 [6].

$\boldsymbol{R}$ **(mm/h)**	120.0	150.0	72.4	72.5	35.0
$\boldsymbol{\Delta t}$ **(min)**	11	12	30	25	120
% of time	0.0021	0.0023	0.0057	0.0048	0.0228

Table 3: The values of $R_{10\,\mathrm{min}\,0.01\%}$ (mm/h) and ones converted to one-minute rain rate $R_{1\,\mathrm{min}\,0.01\%}$ using (3).

Year	1999	2000	2001	2001	2003	2004
$\mathbf{R_{10\,\mathrm{min}\,0.01\%}}$ **(mm/h)**	45.5	46.7	35.7	26.8	23.1	33.2
$\mathbf{R_{10\,\mathrm{min}\,0.01\%}}$, **(mm/h)**	71.3	78.0	58.0	41.9	35.4	53.4

In [7], the relationship between one-minute rain rate for 0.01% of time and τ-minutes rain rate for 0.01% of time $R\ (\tau\,\mathrm{min})_{0.01\%}$ is expressed as:

$$R_{1\,\mathrm{min}\,0.01\%} = (R(\tau\,\mathrm{min})_{0.01\%})^d \tag{3}$$

with $d = 0987\,(\tau \text{ min})^{0.061}$, where $R\,(\tau \text{ min})_{0.01\%}$ exceeded during 0.01 percent of time for τ-minute integration time.

Analysis of rainfall data in the localities of Lithuania shows that the events of heavy rainfall and showers happen frequently in the months of May–September. During the warm period, the part of convectional precipitation in the general precipitation amount is 0.48 [4]. In light of these facts, the relationship presented in [8] under Lithuanian climatic conditions, may be written as:

$$R(1\,\text{min}) = \frac{[\ln{(0,03 \cdot 0,48 \cdot M_w/t)}]}{0,03} \tag{4}$$

where M_w is amount of rainfall during the months of May–September, and t is the number of hours in a year when the value of rain rate exceeds the value R.

The value of $R_{0.01\%}$ measured with 10-minute's integration time and the value of $R_{0.01\%}$ measured with 20-minute's integration time [4] were used in our calculations. The R (20 min)-value is maximum value of the rain rate on the event of 20 minutes duration when such event is recurring by one time in a year [4]. The values of $R_{1\text{ min }0.01\%}$ determined using relations (3) and (4), and the values of α (for horizontal polarization) determined by using relationship (1), and the values of $R_{1\,\text{min}\,0.01\%}$, mentioned above, are presented in Table 4. It was obtained, that the value of $R\,(1\text{ min}) = 58.9\,\text{mm/h}$ are by 67% higher than the average value of $R\,(10\text{ min}) = 35.2\,\text{mm/h}$.

Table 4: The values of R (1 min) obtained by using relations (3) and (4) and the values of α ($f = 20\,\text{GHz}$).

$\boldsymbol{\Delta t}$ **(min)**	–	10	20
Relation	(4)	(3)	(3)
$\boldsymbol{R}$ **(mm/h)**	58.9	56.4	63.0
$\boldsymbol{\alpha}$ **(dB/km)**	6.62	6.31	7.13

4. ELECTROMAGNETIC WAVES ATTENUATION DUE TO CLOUDS

In [5], the specific cloud attenuation α (dB/km) was expressed as a function of the liquid water content M:

$$\alpha_c = K_c M. \tag{5}$$

The attenuation constant K_c is the function of the frequency f and temperature T. The values of K_c for pure water droplets are presented in [5]. M describes the mass of water drops in the volume units. In the cloud, M varies in the wide range. The knowledge of the liquid water content M is the main problem when using (5). The direct measurements of M at a point in space or averaged over the radio path are problematic. We have been determinating the attenuation due to clouds under Lithuanian climatic conditions for the first time. There was no possibility to measure the specific cloud attenuation as well as the liquid water content and temperature within the clouds. Considering these facts, the method, which required only the meteorological parameters measured at the ground level, was chosen. We used the basic idea of a model [9]: the water vapour in the atmosphere will lead to the formation of clouds whenever there is a possibility for condensation at some height h above ground level. It is mentioned in [9], that the condensation is possible when the water vapour concentration exceeds the saturation density ρ_s at temperature T prevailing at that height. It is assumed in [9], that the water vapour density $\rho(h)$ can be estimated from humidity measurements carried out at ground level. M is estimated as the difference between ρ and saturation density ρ_s at cloud temperature. It is assumed that clouds are formed when $M > 0$. In [9, 10], it was considered that clouds are created starting in the vicinity of the height h of the 0°C isotherm and h (km). Relationship between the ground temperature T_0 (K) and the height h was presented in [9, 10]. The analysis of the cloud cover under the localities of Lithuania data shows that the [10] model can be used only in cases when the middle or high clouds will be formed. The cloud cover data in Vilnius on the April 2007 is presented in Table 5. According the Data of the Weather Station, in most cases the cloud base heights were of 2.0–2.5 km (19 events). It is worth to mention that [10] model was suitable in almost all of the 19 cases mentioned above ($h = 2.0$–2.5 km) whenever temperature at the ground level was $t \leq 10$°C. When $t \geq 10$°C, the values of h determined by using model [10] are over high. However, according to the Weather Station Data (see Table 6), in January 2007, in most cases, the low clouds with the cloud base height of 300–600 m were formed over the localities of Lithuania (16 events); in one case, the humidity of 100% was at the ground level. It is evident that the relation between the h and the ground temperature T_0 presented in [10] is not suitable in the cases mentioned above. If a dew point and the temperature at the ground level are known, the value of h can be obtained by using a temperature lapse rate.

Table 5: The values of the clouds base heights measured on April 2007 in Vilnius.

Cloud base heigh, km	N
0.3–0.6	2
0.6–1.0	5
1.0–1.5	1
1.5–2.0	3
2.0–2.5	19

Table 6: The values of the clouds base heights measured on January 2007 in Vilnius.

Cloud base heigh, km	N
0.0	1
0.2–0.3	6
0.3–0.6	16
0.6–1.0	3
1.0–1.5	2
2.0–2.5	3

Analysis of the cover data over the Lithuania shows, that the low clouds base height is near the height determined from the difference between the temperature at the ground level and the dew point temperature divided by the lapse of temperature (6.5°C). In the frequent events, the cumulonimbus clouds have been formed at the height of 300–600 m; the cumulus clouds occur at the height of 1000–1500 m. The review of data measured in the Weather Station shows that the use of the ITU-R vertical profiles of the atmosphere proposed in Recommendation ITU-R P. 835–3 for calculation of the clouds temperature must be revised before using under the Lithuanian climatic conditions. In our calculations, it was assumed, that the temperature within the cloud is near the dew point temperature. The temperature at height h is the temperature of the cloud in our study. The equation of state, assuming an adiabatic process [9] has been used for determination of the water vapour density $\rho\,(\mathrm{h})$ at the height h. Using the values of the relative humidity H and the temperature at the ground level we have determined the water vapour density at the ground level.

For example, in Vilnius, on 1 October 2007, there was the daily temperature of 3.9°C. The relative humidity at the ground level was $H_0 = 90\%$ on that day. The dew point temperature was $t_d = 2.4$°C. The clouds have been formed at the height of 0.23 km. We obtained, that $M = 0.9\,\mathrm{g/m^3}$. According to data of Meteorological Weather Station, recorded when the stratocumulus clouds were formed over Vilnius, the cloud base height was about 300–600 m. It is known, that the values of M for stratocumulus clouds varied starting from 0.3 up to $1.3\,\mathrm{g/m^3}$ and the value of $M = 0.9\,\mathrm{g/m^3}$ is from the range mentioned above. The values of the α_c, determined using the value $M = 0.9\,\mathrm{g/m^3}$ and relation (5), are presented in Table 7.

Table 7: The values of specific cloud attenuation α_c.

$\boldsymbol{f}$, GHz	10	20	30	40	50	60	70
$\boldsymbol{\alpha}_c$, dB/km	0.09	0.35	0.60	1.25	1.75	2.5	3.0

5. CONCLUSIONS

It is a necessity to take the peculiarities of the Baltic Sea Region climate into account, when determining he values of the specific rain attenuation and cloud attenuation in this region. The ITU-R-value $R = 22$ mm/h is too low for prediction of the rain attenuation in Lithuania. The review of cloud data shows that relationship presented in [10] can be used for determination of the middle and high clouds base height under the Lithuanian climatic conditions.

ACKNOWLEDGMENT

The authors are grateful to the Direction of the Lithuanian Weather-Station for possibility to have a use of the data of the Archives of the Weather Stations.

REFERENCES

1. Ivanovs, G. and D. Serdega, "Rain intensity influence on to microwave line payback terms," *Electronics and Electrical Engineering*, No. 6 (70), 60–64, 2006.
2. Tamosiunas, S., M. Zilinskas, M. Sileika, and M. Tamosiuniene, "Revised model of attenuation of electromagnetic waves due to rain," *Lithuanian Journal of Physics*, Vol. 46, No. 4, 433–436, 2006.
3. Zilinskas, M., S. Tamosiunas, and M. Tamosiuniene, "Calculation of radio signal attenuation using annual precipitation and heavy rainfall data," *Proceedings of 18th International Wroclaw Symposium and Exhibition on Electromagnetic Compatibility*, 490–493, Wroclaw, Poland, June 2006.
4. Pankauskas, M. and A. Bukantis, "The dynamics of the Baltic Sea Region climate humidity in 1950–2004," *Annales Geographicae*, Vol. 39, No. 1, 5–14, 2006.
5. Freeman, R. L., *Radio System Design for Telecommunications*, John Wiley & Sons, Inc., NewYork, Chichester, Weinheim, Brisbane, Singapore, Toronto, 1997.
6. Bukantis, A., *The Unusual Natural Phenomena in the Territory of Lithuania in the 11th–20th Centuries*, Vilnius, 1998 (in Lithuanian).
7. Moupfouma, F. and L. Martin, "Modelling of the rainfall rate cumulative distribution for the design of satellite and terrestrial communication systems," *International J. of Satellite Comm.*, Vol. 13, No. 2, 105–115, 1995.
8. Rice, P. L. and N. R. Holmberg, "Cumulative time of surface-point rainfall rates," *IEEE Trans. on Communications*, Vol. 21, No. 10, 1131–1136, 1973.
9. Dintelmann, F. and G. Ortgies, "Semiempirical model for cloud attenuation prediction," *Electronics Letters*, Vol. 25, No. 22, 1487–1488, 1989.
10. Ito, S., "Dependence of 0°C isotherm height on temperature at ground level in rain," *Trans. IEICE*, Vol. E72, No. 2, 98–100, 1989.

OFDM System Location Determination with 4-element Antenna Array Using Frequency Domain Matrix Pencil (FDMP) Method

Mohamed A. Labib and Hassan M. Elkamchouchi
Department of Electrical Engineering, Alexandria University, Alexandria, Egypt

Abstract— A 3D location determination method using only four elements antenna is proposed for OFDM systems which are commonly used in the 4G. A group of frequencies is received from the transmitter (on mobile phone) or returned signals (Radar). The Matrix Pencil method is used to identify the length of each path. Depending on the geometrical distribution of the four elements, the phase shifts are determined for each path. Knowing the phase shift between the elements helps to find the Direction of Arrival (DOA) for each path. Small dipole antennas are used in the numerical examples to clarify this location determination method in the presence of complex noise in the OFDM systems.

1. INTRODUCTION

As known the OFDM is a multi-carrier technique that has recently received considerable attention for high speed wireless communication. Most WLAN systems currently use the IEEE802.11b standard, which provides a maximum data rate of 11 Mbps. Newer WLAN standards such as IEEE802.11a and HiperLAN are based on OFDM technology and provide a much higher data rate of 54 Mbps. However systems of the near future will require WLANs with data rates of greater than 100 Mbps, and so there is a need to further improve the spectral efficiency and data capacity of OFDM systems in WLAN applications. For cellular mobile applications, we will see in the near future a complete convergence of mobile phone technology, computing, Internet access, and potentially many improved multimedia applications such as high quality video and audio. In fact, some may argue that this convergence has already largely occurred, with the advent of being able to send and receive data using a notebook computer and a mobile phone. The use of frequency diversity, within the framework of narrowband signals for identification of multipaths can be used for distance determination. Based on this technique, DOA and location determination using only four elements are achieved. The procedure depends on sending a group of narrowband tones and sub-carriers from the mobile set to the base station then using the MP method [1–4] for distance determination. This procedure is applied to four small dipole antennas to get the location determination in the OFDM.

2. FUNDAMENTAL CONCEPTS OF OFDM

OFDM [5] has been accepted as the standard for Digital Audio Broadcast (DAB) and Digital Video Broadcast (DVB) in Europe. It has also been established as one of the techniques for the IEEE 802.11a wireless LAN standard. OFDM has emerged as one of the primary candidates for 4G wireless communication systems and high speed ad hoc wireless networks. The basic principle of OFDM is to split the data into multiple parallel streams and employ orthogonal sub-carriers to each of these streams. The sub-carriers are allowed to overlap but they are still *orthogonal* to each other. This makes the OFDM spectrally efficient compared to a conventional multi-carrier system. Each OFDM symbol consists of a sum of sub-carriers that are modulated by PSK or QAM. The kth sample of an OFDM symbol can be written as

$$x_k = \sum_{m=0}^{M-1} X_m \exp\left\{\frac{j2\pi km}{M}\right\}, \quad 0 \le k \le M-1 \tag{1}$$

where M is the number of sub-carriers and X_m is the data symbol, PSK or QAM modulated, on the mth sub-carrier. Equation (1) is identical to the expression of an M point Inverse Discrete Fourier Transform (IDFT). Therefore the sub-carrier multiplexing can be efficiently performed with the help of Inverse Fast Fourier Transformation (IFFT) operation. This is one of the most attractive features of OFDM since the transmitter can multiplex data symbols onto sub-carriers by employing the computationally efficient IFFT operation. Therefore the frequency division multiplexing can be achieved by baseband processing rather than band-pass filtering. Fig. 1 shows a simple OFDM transmitter. Obviously an OFDM receiver can perform the demodulation with a simple FFT operation. This eliminates the banks of sub-carrier oscillators and coherent demodulators required by conventional frequency division multiplexing systems.

3. RECEIVED SIGNAL MODEL WITHOUT SPATIAL DIVERSITY

Consider the case of a wireless communication system as illustrated in Fig. 1. The transmitter, located at position A, is transmitting a signal in all directions. The receiver is located at position B and receives the direct ray from A and the multipaths from the existing obstacles [6].

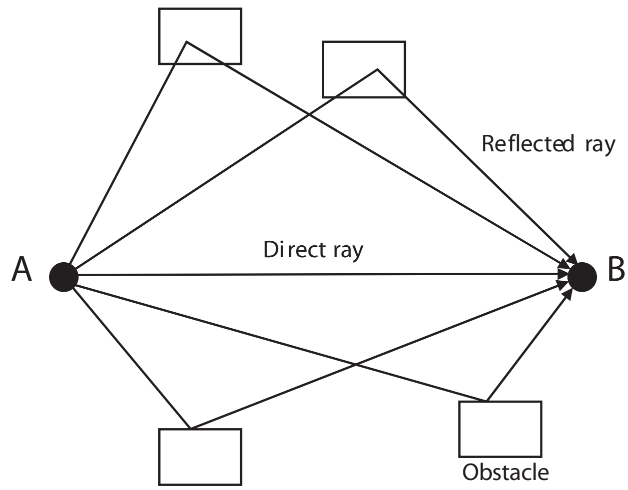

Figure 1: Direct and multipaths effects in communication system with obstacles.

The measured signal at B is

$$y(f_0) = C \exp\left\{\frac{j2\pi d f_0}{c}\right\} + \sum_{i=1}^{M} \alpha_i C \exp\left\{\frac{j2\pi d_i f_0}{c}\right\} + noise \tag{2}$$

where $y(f_0)$ is the complex narrowband signal that is received, C and f_0 are the amplitude and frequency of the transmitted signal, respectively, c is the velocity of the light, d is the path length of the direct ray, M is the number of multipaths, α_i is the reflection coefficient and d_i is the length for the ith path. For Location determination, we send N tones at the same time which are shifted by Δf from each other from the OFDM target transmitter. At the receiver, the values of the signals at all expected frequencies are measured.

$$y_q(f) = y\left\{f_0 + \left(q - \frac{N-1}{2}\right)\Delta f\right\}, \ldots \quad q = 0,\, 1,\, \ldots,\, N-1 \tag{3}$$

N is assumed to be an odd number. Also Δf is resized according to the predicted estimated distance between the transmitter and the receiver. The predicted distance is estimated by sending a message from the base station receiver to the transmitter and measuring the time for replying which gives certain d_j, this procedure is repeated J times then the mean value is taken as a reference for the estimated path length.

$$\overline{d} = \frac{1}{J}\sum_{j=1}^{J} d_j \tag{4}$$

The predicted distance $\overline{d}$ is used to optimize the Δf which can be a group of sub-carriers or tones of one or group of sub-band Fig. 2. This predicted distance is used only in the beginning of the transmitter path tracing. The determination of all signal paths is to be done by the MP method. It has been shown in [1, 2] that this method has a very low variance for estimating the exponents and its residues in the presence of noise and it works with the correlated signals.

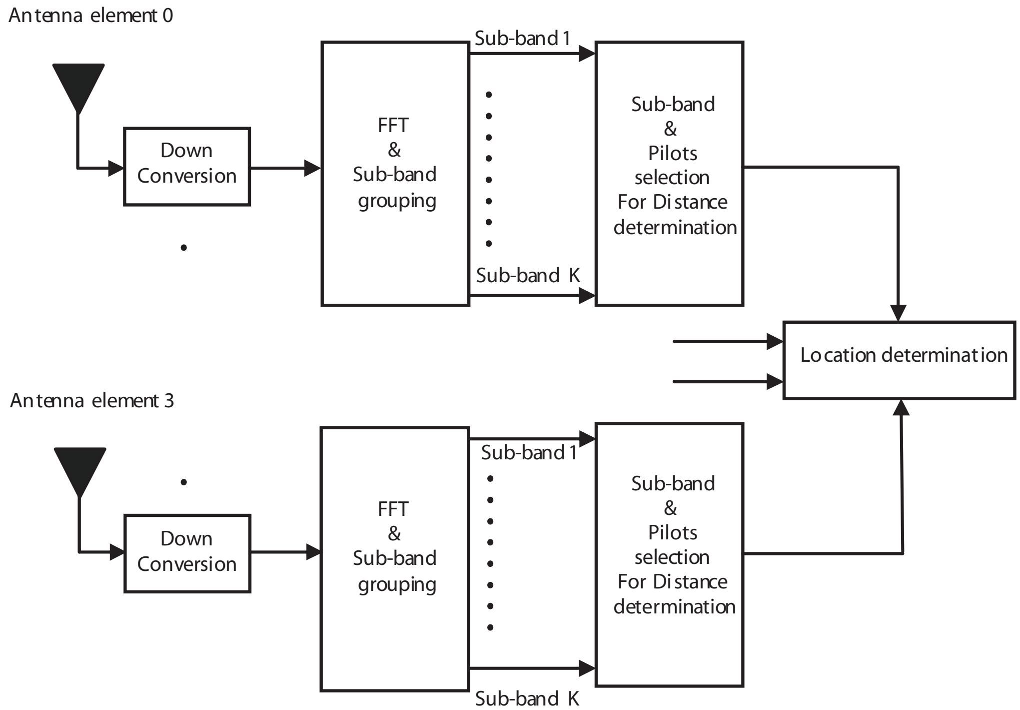

Figure 2: The proposed OFDM receiver for location determination.

4. MP METHOD FOR IDENTIFICATION OF MULTIPATH COMPONENTS

The received signal of the required OFDM signal in this case is

$$y_q = \sum_{i=1}^{M+1} \alpha_i C \exp\left\{\frac{j2\pi d_i}{c}\left(f_0 + \left(q - \frac{N-1}{2}\right)\Delta f\right)\right\} + n_q \quad q = 0, \ldots, N-1 \tag{5}$$

$\alpha_1 = 1$ and $d_1 = d$, for the direct path and n_q is the additive noise component. The required aim of MP is to find the values of d_i, s which are the distances between the transmitter and receivers for each ray path.

Consider two matrices $[Y]_1$ and $[Y]_2$ formed using the received voltages.

$$[Y]_1 = \begin{bmatrix} y_0 & y_1 & \cdots & y_L \\ y_1 & y_2 & \cdots & y_{L+1} \\ \vdots & \vdots & \vdots & \vdots \\ y_{N-L-1} & y_{N-L} & \cdots & y_{N-2} \end{bmatrix}_{(N-1)\times(L+1)}$$

$$[Y]_2 = \begin{bmatrix} y_1 & y_2 & \cdots & y_{L+1} \\ y_2 & y_3 & \cdots & y_{L+2} \\ \vdots & \vdots & \vdots & \vdots \\ y_{N-L} & y_{N-L+1} & \cdots & y_{N-1} \end{bmatrix}_{(N-1)\times(L+1)} \tag{6}$$

where L is the pencil parameter, and (5) can be written as

$$y_q = \sum_{i=1}^{M+1} w_i z_i^q + n_q, \quad q = 0, \ldots, N-1 \tag{7}$$

where

$$w_i = \sum_{i=1}^{M+1} \alpha_i C \exp\left\{\frac{j2\pi d_i}{c}\left(f_0 - \left(\frac{N-1}{2}\right)\Delta f\right)\right\} \tag{8}$$

and

$$z_i = \exp\left\{\frac{j2\pi d_i}{c}(\Delta f)\right\} \tag{9}$$

z_i can be estimated from the M largest eigenvalues of the MP $([Y]_2, [Y]_1)$ [7], which are the eigenvalues of $[Y]_1^+[Y]_2$ where $[Y]_1^+$ is the pseudo-inverse of the matrix $[Y]_1$. Once the exponents z_i are estimated, the multipaths lengths d_i are given by the following

$$d_i = \frac{\arg(z_i)c}{2\pi\Delta f} \tag{10}$$

5. PROPOSED LOCATION DETERMINATION METHOD

Consider an OFDM system with a data rate of 20 Mbps. We employ 16-QAM modulation scheme which means that the bandwidth of the OFDM signal is 5 MHz. The number of sub-carriers for each OFDM symbol is 512. The location determination requires pilot symbols as reference signal. While inserting pilot symbols into the data stream, one has to consider the coherence time [8] of the channel. The pilot symbols are an overhead for the system and it should not reduce the throughput significantly. We define a transmitted frame which consists of 107 OFDM symbols. If using four elements as illustrated in Fig. 3, each element is receiving a set of frequencies from the mobile transmitter. Thus the received signal is

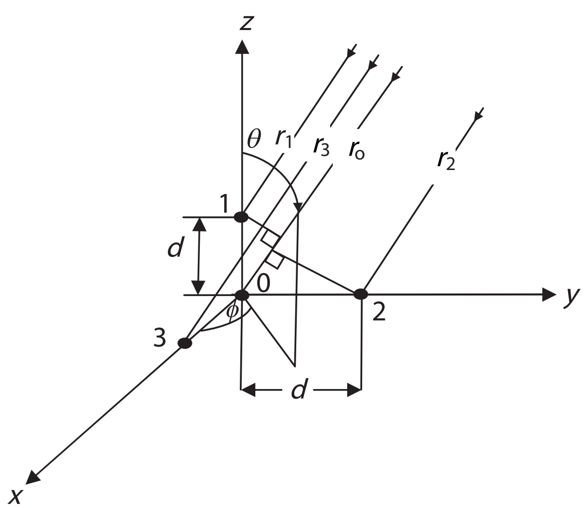

Figure 3: Four elements with uniform distribution.

$$y_q(k) = \sum_{i=1}^{M+1} \alpha_i C \exp\left\{\frac{j2\pi(D_i + \Delta D_i(k))}{c}\left(f_0 + \left(q - \frac{N-1}{2}\right)\Delta f\right)\right\} + n_{q,k} \tag{11}$$

where Di is the ith path distance between the transmitter and the centered element of the receiver, ΔD_i is the phase shift between the received signal by the centered element and the adjacent elements, i.e.,

k is the element index where
$k = 0$, for the centered element.
$k = 1$, for the element on the z-axis.
$k = 2$, for the element on the y-axis.
$k = 3$, for the element on the x-axis.

Equation (11) can be written as

$$\begin{aligned} y_q(k) = \sum_{i=1}^{M+1} \alpha_i C \Big(&\exp\left\{\tfrac{j2\pi(D_i)}{c}\left(f_0 + \left(q - \tfrac{N-1}{2}\right)\Delta f\right)\right\} \\ &\cdot \exp\left\{\tfrac{j2\pi(\Delta D_i(k))}{c}\left(f_0 + \left(q - \tfrac{N-1}{2}\right)\Delta f\right)\right\}\Big) + n_{q,k} \end{aligned} \tag{12}$$

This can be written as

$$y_q(k) = \sum_{i=1}^{M+1} [w_i z_i^q] + n_{q,k} \tag{13}$$

where

$$w_i = \sum_{i=1}^{M+1} \alpha_i C \exp\left\{\frac{j2\pi(D_i + \Delta D_i(k))}{c}\left(f_0 - \left(\frac{N-1}{2}\right)\Delta f\right)\right\} \tag{14}$$

$$z_i = \exp\left\{\frac{j2\pi(D_i + \Delta D_i(k))}{c}(\Delta f)\right\} \tag{15}$$

$n_{q,k}$ is the noise at each frequency.

Once the $D_i + \Delta D_i(k)$ is determined for each element as in (10), then the phase shift $\Delta D_i(k)$ is calculated. For the reference element ($k = 0$), $\Delta D_i(0) = 0$ so the path length D_i for the ith path is determined.

For the element on the z-axis ($k = 1$)

$$\Delta D_i(1) = d \cos\theta_i \tag{16}$$

For the element on the y-axis ($k = 2$)

$$\Delta D_i(2) = d \sin\theta_i \sin\phi_i \tag{17}$$

For the element on the x-axis ($k = 3$)

$$\Delta D_i(3) = d \sin\theta_i \cos\phi_i \tag{18}$$

then the direction of arrival for each path is estimated as,

$$\theta_i = \cos^{-1}\left(\frac{\Delta D_i(1)}{d}\right) \tag{19}$$

$$\phi_i = \cos^{-1}\left(\frac{\Delta D_i(3)}{d \sin\theta_i}\right) \tag{20}$$

or by using,

$$\phi_i = \tan^{-1}\left(\frac{\Delta D_i(2)}{\Delta D_i(3)}\right) \tag{21}$$

$$\theta_i = \sin^{-1}\left(\frac{\Delta D_i(3)}{d \cos\phi_i}\right) \tag{22}$$

To overcome any ambiguity, we determine the reception region depending on the phase shift which differs according to the DOA for each element. As considered above the centered element $k = 0$ is taken as the reference element so the reception sector is as in Table 1.

Table 1: Signs of elements phase shifts and reception sectors.

$\Delta D_i(1)$	$\Delta D_i(2)$	$\Delta D_i(3)$	Reception sector		
			x-axis	y-axis	z-axis
−	−	−	+	+	+
−	−	+	−	+	+
+	−	−	+	+	−
+	−	+	−	+	−
−	+	−	+	−	+
−	+	+	−	−	+
+	+	−	+	−	−
+	+	+	−	−	−

The error in the determination of the DOA is

$$E(\theta) = \sum_{i=1}^{M} |\theta_{i,a} - \theta_{i,c}| \tag{23}$$

where

$\theta_{i,a}$ is the actual received angle of the ith path.
$\theta_{i,c}$ is the determined received angle of the ith path.

$$E(\phi) = \sum_{i=1}^{M} |\phi_{i,a} - \phi_{i,c}| \tag{24}$$

where

$\phi_{i,a}$ is the actual received angle of the ith path.
$\phi_{i,c}$ is the determined received angle of the ith path.

6. NUMERICAL EXAMPLES

In case of using small vertical dipole antennas arranged as in Fig. 3. $f_0 = 2.4\,\text{GHz}$, $l = \lambda/10$. The numerical examples are simulated using MATLAB R13.

A) The proposed multipaths distances, where the azimuth and elevation angles are as in Table 2, $\Delta f = 0.0005 f_0 = 1.2\,\text{MHz}$, The transmitted set of pilots are $N = 111$.

The results are as shown in Table 3 for SIR $= 0$, SNR $= 20\,\text{dB}$ and Table 4 for SIR $= 0$, SNR $= -20\,\text{dB}$.

Table 2: The proposed distances and angles.

Multipath	Distance (m)	Azimuth (degree)	Elevation (degree)
1 (direct path)	100	110	0
2	102	111	10
3	103	115	15
4	104	140	20

Table 3: Numerical results using small dipole antennas SNR = 20 dB.

Multipath	Distance (m)	Azimuth (degree)	Elevation (degree)
1	100	110	0
2	102	111	10
3	103	115	15
4	104	140	20

Table 4: Numerical results using small dipole antennas SNR = −20 dB.

Multipath	Distance (m)	Azimuth (degree)	Elevation (degree)
1	100	110.0	0.0108
2	102	111.0001	9.9996
3	103	115.0004	14.9991
4	104	140.0002	19.9993

Table 5: The proposed distances and angles.

Multipath	Distance (m)	Azimuth (degree)	Elevation (degree)
1 (direct path)	100	110	0
2	120	111	10
3	150	115	15
4	190	140	20

Table 6: Numerical results using small dipole antennas SNR = 20 dB.

Multipath	Distance (m)	Azimuth (degree)	Elevation (degree)
1	99.95	110.09	0.42
2	120	110.85	10.04
3	150	114.9	15.1
4	190	140.1	19.9

Table 7: Numerical results using small dipole antennas SNR = −20 dB.

Multipath	Distance (m)	Azimuth (degree)	Elevation (degree)
1	99.999	110.07	0.4
2	120	110.78	10.028
3	150	114.998	15.012
4	190	140	19.9986

Table 8: The proposed distances and angles.

Multipath	Distance (m)	Azimuth (degree)	Elevation (degree)
1 (direct path)	10000	110	0
2	10020	111	10
3	10030	115	15
4	10040	140	20

Table 9: Numerical results using small dipole antennas SNR = -20 dB.

Multipath	Distance (m)	Azimuth (degree)	Elevation (degree)
1	10000	110.0135	0.0
2	10020	111.78	9.2260
3	10030	115.1995	14.8086
4	10040	139.6468	21.1473

Table 10: Numerical results using small dipole antennas SNR = 20 dB.

Multipath	Distance (m)	Azimuth (degree)	Elevation (degree)
1	10000	109.9996	0.5502
2	10020	111.0059	10.3767
3	10030	115.0203	15.4640
4	10040	139.9957	20.1105

B) The proposed multipaths distances, where the azimuth and elevation angles are as in Table 5, $\Delta f = 0.00005 f_0 = 0.12$ MHz. The results are as shown in Table 6 for SIR = 0, SNR = 20 dB, $N = 61$ and Table 7 for SIR = 0, SNR = -20 dB, $N = 111$.

C) The proposed multipaths distances, the azimuth and elevation angles are as in Table 8, $\Delta f = 0.000005 f_o = 12$ kHz. The results are as shown in Table 9 for SIR = 0, SNR = -20 dB, N = 891 and Table 10 for SIR = 0, SNR = 20 dB, $N = 591$.

7. CONCLUSION

Location determination can be achieved with only four elements antenna using a band of frequencies for distance determination which are enough to calculate the incident angles (azimuth, elevation). As the number of used pilot optimized, the performance enhances and can overcome the complex noise effects and the mutual coupling. Numerical examples are simulated using MATLAB R13 (version 6.5) with small dipoles elements antenna. The results show high accuracy in determining the location of the target. This idea can be used for mobile communications 4G, WiBro, HIPERMAN.

REFERENCES

1. Hua, Y. and T. K. Sarkar, "Matrix pencil method for estimating parameters of exponentially damped/undamped sinusoids in noise," *IEEE Transactions on Acoustics, Speech, and Signal Processing*, Vol. 38, No. 5, 814–824, May 1990.
2. Sarkar, T. K. and O. Pererira, "Using matrix pencil method to estimate the parameters of a sum of complex exponentials," *IEEE Antennas and Propagation Magazine*, Vol. 37, No. 1, 48–55, Feb. 1995.
3. Medouri, A., A. Gallego, D. P. Ruiz, and M. C. Carrion, "Estimation one and two direction of arrival in an incoherent/coherent source environment," *IEICE Transactions on Communications*, Vol. E80-B, No. 11, 1728–1740, Nov. 1997.
4. Hua, Y. and T. K. Sarkar, "Generalized pencil of function method for extracting poles of an EM system from its transit response," *IEEE Antennas and Propagation Magazine*, Vol. 37, No. 2, Feb. 1989.
5. Alam, F., "Space time processing for third generation CDMA systems," 121–126, 2002.
6. Sarkar, T. K., M. C. Wicks, M. Salazar, and R. Bonneau, *Smart Antennas*, Ch. 10, 319–324, Wiley-interscience Press, 2003.
7. Golub, G. H. and C. F. V. Loan, *Matrix Computation*, Johns Hopkins University Press, 1983.
8. Rappaport, T. S., *Wireless Communications: Principles and Practice*, Prentice Hall PTR, Upper Saddle River, NJ, 1996.

WCDMA 3D Location Determination with 3D Polarization Using Four 3-element Arrays

Mohamed A. Labib and Hassan M. Elkamchouchi
Department of Electrical Engineering, Alexandria University, Alexandria, Egypt

Abstract— A 3D location determination method uses only four 3-element arrays, each 3-element array consists of three orthogonal dipoles to achieve the vertical, horizontal and orthogonal one to both of them. The non line-of-sight path would change the polarization at the receiver which can affect the quality and the strength of the received signal. This method is proposed for WCDMA mobile systems which are commonly used in the 3G. The receiver RAKE is used to identify the multipath and the time delay between the elements for each polarization state. Depending on the geometrical distribution of the four arrays, the phase shifts are determined for each path. Knowing the phase shift between the elements helps to find the Direction of Arrival (DOA) for each path. The path distance is determined via the traveling time of the message response between the transmitter and the receiver. The received signals of the antenna elements are combined on the MRC for signal maximization also.

1. INTRODUCTION

Due to reflections from obstacles a radio channel can consist of many copies of originally transmitted signals having different amplitudes, phases and delays. Multipath can occur in a radio channel in various ways such as reflection, diffraction and scattering. The WCDMA RAKE receiver uses a multipath diversity principle. It rakes the energy from the multipath propagated signal components. M-ray multipath model can be used. Each of the M paths has an independent delay and an independent complex time-variant gain. RAKE receiver utilizes multiple correlators to separately detect M strongest multipath components. Each correlator detects a time-shifted version of the original transmission, and each finger correlates to a portion of the signal, which is delayed by at least one chip in time from the other fingers. Using an antenna with four positions each one has three elements antennas orthogonal to each other to achieve the vertical, horizontal and orthogonal one to both of them. The polarization is considered where the base station can receive the radio signal of the same polarization as the transmitted signal only in line-of-sight communication, but as the radio signal may be reflected, each reflection could change the polarization state. This means that the base station with non line-of-sight (NLOS) path would receive the signal with a randomly polarized state [1, 2]. Experimental data taken at different places indicate that the difference in cross coupling between two polarized waves in the mobile radio field is only about 4∼6 dB [3]. When the mobile transmits vertical polarization, the received vertical polarization at the base is about 6 dB stronger than that of the horizontal polarization. When the mobile transmits horizontal polarization, the received horizontal polarization is again found to be about 6 dB stronger than the vertical signal. The multipath detection time delay on each element with respect to the centered one is the base of DOA. The path distance is determined via a common method which is the travelling time of the message response between the transmitter and the receiver.

2. WCDMA RACK RECEIVER CONCEPTS

Radio propagation in the land mobile channel is characterized by multiple reflection, diffraction and attenuation of the signal energy. These are caused by natural obstacles such as buildings, hills, and so on, resulting in so called multipath propagation. There are two effects resulting from the multipath propagation. It can sometimes destroy signal through fast fading. However, these multipath components can be used as a multipath diversity also called RAKE combining in WCDMA system. The RAKE diversity receiving technology improves the reception performance by combining the individual paths after they were received separately among multiple paths. In WCDMA, the chip duration at 3.84 Mcps is 0.26 µs. If the time delay difference of the multipath components is at least 0.26 µs, the WCDMA receiver can separate those multipath components and combine them coherently to obtain multipath diversity. The 0.26 µs delay can be obtained if the difference in path lengths is at least 78 m (= speed of light m/s ÷ chip rate Mcps = 3.0×10^8 m/s ÷ 3.84 Mcps). With the chip rate of about 1 Mcps, the difference in the path lengths of the multipath components must be about 300 m which cannot be obtained in small cells. Therefore, it is easy to see that the 5 MHz WCDMA can provide multipath diversity in small cells. The use of a wider band carrier can improve the capability to separate these multiple paths, which consequently reduces the required transmitter power. This makes it possible to lower the transmitter power of mobile stations, and at the same time brings down the interference power, which leads to further improve the spectrum utilization efficiency and system capacity. Assume that the multipath spread is of the order of a few chip intervals $\mathrm{T_c}$ and, since the signal is band-limited to $\mathrm{B} = 1/\mathrm{T_c}$, the tap delay line model has taps spaced at chip intervals $\mathrm{T_c}$. The channel baseband equivalent impulse response is

$$h(t, \tau) = \sum_{i=0}^{M-1} c_i(t)\delta(\tau - \tau_i) \tag{1}$$

where $c_i(t) = a_i(t)e^{j\phi_i(t)}$, $a_i(t)$ is path attenuation, $\phi_i(t)$ is path phase, τ_i is path delay, and M is the number of resolvable multipaths. The channel parameters c_i and τ_i are assumed known in the despreading and demodulation process, although in practice the impulse response of the channel is typically estimated using pilot symbols or pilot channel. Hence, suppose the output of the matched filter matching to the pulse shaping filter in the transmitter is $z_k(i)$, then the output of each finger is given after channel matched and correlating as in Fig. 1,

$$y_i = \sum_{j=1}^{PG} c^*_{k,m}(i)s^*_{k,j}(i)z_k(i) \tag{2}$$

$c^*_{k,m}(i)$ is the complex conjugate estimate of the channel's impulse response, $s^*_{k,j}(i)$ is the complex conjugate of chipmatched sampled signature sequence of the user of interest. $\hat{s}_k(i)$ is the user k signature sequence, the zero-padded spreading sequence for symbols transmitted by user k, $\hat{c}_{k,m}(i)$ denotes the channel coefficients over the mth multipath for the i^{th} symbol generated by user k, L is the total number of the data symbols sent by every active users, K is the total number of active users sending data , $\hat{M}$ is the maximum delay spread normalized to sampling interval, and M is the number of resolvable multipath components per user data sequence.

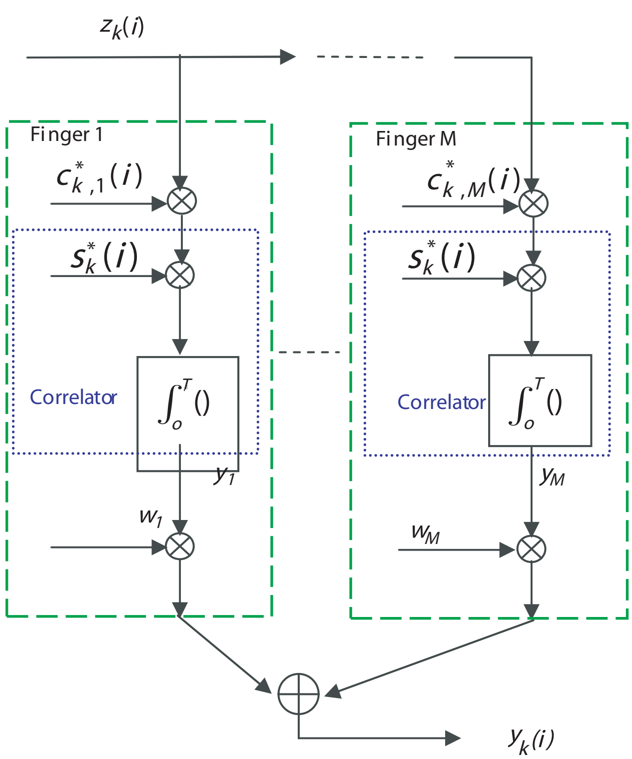

Figure 1: RAKE receiver with M fingers.

3. RAKE RECEIVER BLOCKS

In Fig. 2, the RAKE receiver [4] consists of a matched filter (impulse response measurement, largest peaks to RAKE fingers, timing to delay equalizer, tracks and monitors peaks with a measurement rate depending on speeds of mobile station and on propagation environment), code generators (PN codes for the user or channel), correlator (despreading and integration of user data symbols), channel estimator (channel state estimate, channel effect corrections), phase rotator (phase correction), delay equalizer (compensates delay for the difference in the arrival times of the symbols in each finger) and combiner (adding of the channel compensated symbol multipath diversity against fading). The RAKE receiver has to know the multipath delays for time delay synchronization, Phases of the multipath components for carrier phase synchronization, amplitudes of the multipath components for amplitude tracking and number of multipath components for RAKE allocation. The time delay synchronization is based on correlation measurements (delay acquisition, delay-locked loops). Due to fading channels conventional phase-locked loop (PLL) cannot be used in carrier and amplitude tracking. The number of available fingers depends on the channel profile and the chip rate. The higher the chip rate, the more resolvable paths there are. A very large number of fingers lead to combining losses and practical implementation problems. The main challenges for RAKE receivers operating in fading channels are in receiver synchronization. High bandwidth (5 MHz in WCDMA) and dynamic interference inherent to WCDMA requires that RF and IF parts have to operate linearly with large dynamic range. In practical RAKE receivers synchronization sets some requirements such as automatic gain control (AGC) loop which is needed to keep the receiver at the dynamic range of the A/D converter. AGC must be fast and accurate enough to keep receiver at the linear range. Frame-by-frame data range change may set higher AGC and A/D converter requirements. The high sampling rates of few tens of MHz and high dynamics of the input signal (80 dB) require fast A/D converters and high resolution.

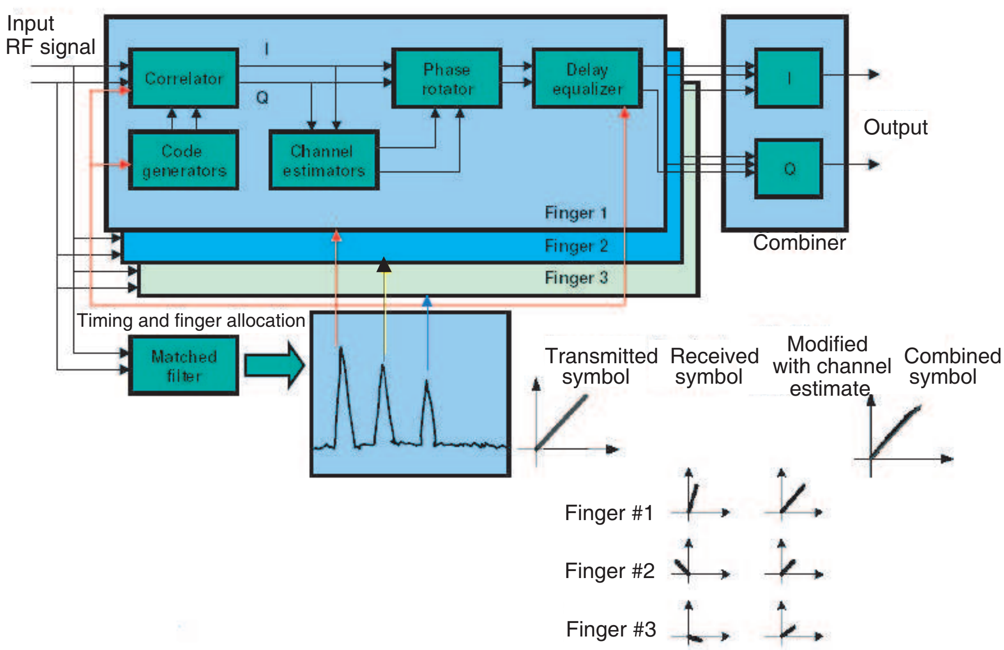

Figure 2: The RAKE receiver.

4. PROPOSED LOCATION DETERMINATION METHOD

The WCDMA RAKE receiver detects the multipath delays and its time arrival in each finger. Using spatial combination of antennas, there is a time difference of arrival for multipath detection in each antenna RAKE. These different delays are used for DOA [5]. The Structure in Fig. 3 performs spatial RAKE MRC on the signals at different antenna elements that have the same temporal delay. The contribution form different multipath components are then combined to exploit the temporal diversity.

The NLOS affects the strength of the received signal and its polarization. Suppose the received first signal path with horizontal polarization, the second path is vertical polarization with strength $-3\,\mathrm{dB}$ than the first and the receiver antenna is vertically installed. The DOA on each path

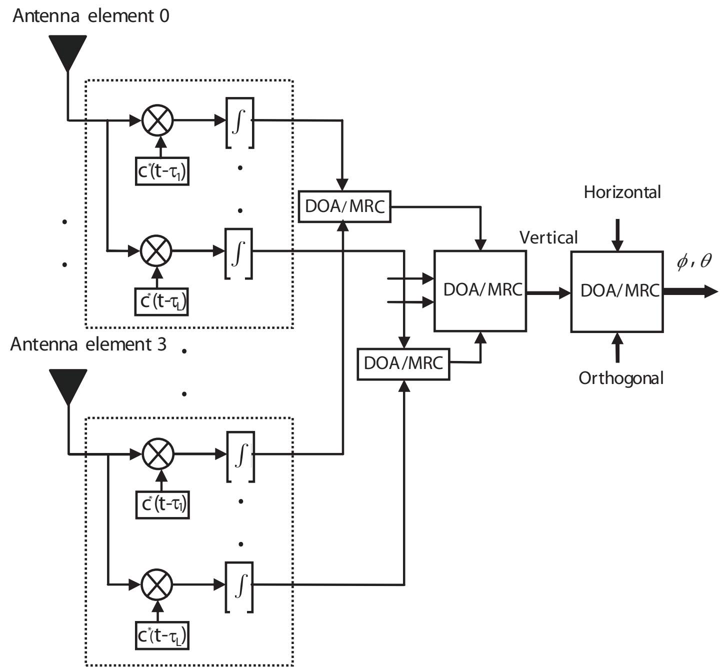

Figure 3: The proposed location determination with MRC.

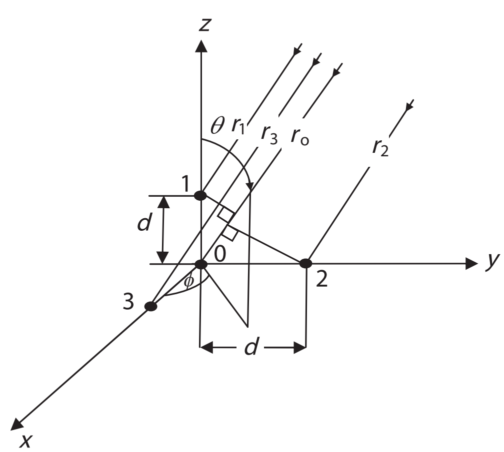

Figure 4: Four elements with uniform distribution.

is determined but the assumed actual DOA is the first path of arrival. Since the second is of larger strength than the first and can lead to ambiguous results. To overcome this ambiguity the polarization state is considered. The received signals of polarization, spatial and multipath, are combined for MRC as in Fig. 3 besides the DOA detection. The path length, which is considered as the distance between the mobile and the base station, is estimated by sending a message from the base station to the mobile and measuring the time for replying which gives certain τ_j, this procedure is repeated J times then the mean value is taken as a reference for the estimated path length.

$$D_i = \frac{1}{J}\sum_{j=1}^{J} c\tau_{i,j} \tag{3}$$

where c is the velocity of light, D_i the ith path distance between the transmitter and the centered element of the receiver and ΔD_i is the phase shift between the received signal by the centered element and the adjacent elements, as in Fig. 4, i.e.,

k is the element index where
$k = 0$, for the centered element position.
$k = 1$, for the element position on the z-axis.
$k = 2$, for the element position on the y-axis.
$k = 3$, for the element position on the x-axis.

Each element position consists of three element installed with different polarizations (vertical, horizontal and orthogonal to both of them).

The phase shift $\Delta D_i(k, l)$ is determined by the time delay between each element and the centered one where l is the index of polarization type.

$$\Delta D_i(k, l) = c\Delta\tau(k, l) \tag{4}$$

For the reference element ($k = 0$), $\Delta D_i(0, l) = 0$ so, for the element on the z-axis ($k = 1$)

$$\Delta D_i(1, l) = d\cos\theta_i \tag{5}$$

For the element on the y-axis ($k = 2$)

$$\Delta D_{i,l}(2, l) = d\sin\theta_{i,l} \sin\phi_{i,l} \tag{6}$$

For the element on the x-axis ($k = 3$)

$$\Delta D_{i,l}(3, l) = d\sin\theta_{i,l} \cos\phi_{i,l} \tag{7}$$

then the direction of arrival for each path is estimated as,

$$\theta_{i,l} = \cos^{-1}\left[\frac{\Delta D_i(1, l)}{d}\right] \tag{8}$$

$$\phi_{i,l} = \cos^{-1}\left[\frac{\Delta D_i(3, l)}{d\sin\theta_i}\right] \tag{9}$$

or by using,

$$\phi_{i,l} = \tan^{-1}\left[\frac{\Delta D_i(2, l)}{\Delta D_i(3, l)}\right] \tag{10}$$

$$\theta i,\, l = \sin^{-1}\left[\frac{\Delta D_i(3, l)}{d\cos\phi_i}\right] \tag{11}$$

Table 1: Signs of elements phase shifts and reception sectors.

$\Delta D_i(1, l)$	$\Delta D_i(2, l)$	$\Delta D_i(3, l)$	Reception sector		
			x-axis	y-axis	z-axis
−	−	−	+	+	+
−	−	+	−	+	+
+	−	−	+	+	−
+	−	+	−	+	−
−	+	−	+	−	+
−	+	+	−	−	+
+	+	−	+	−	−
+	+	+	−	−	−

To overcome any ambiguity, we determine the reception region depending on the phase shift which differs according to the DOA for each element. As considered above the centered element $k = 0$ is taken as the reference element so the reception sector is as in Table 1.

Error in the determination of DOA for each polarization state is

$$E(\theta) = \sum_{i=1}^{M} |\theta_{i,a} - \theta_{i,c}| \tag{12}$$

where

$\theta_{i,a}$ is the actual received angle of the ith path.
$\theta_{i,c}$ is the determined received angle of the ith path.

$$E(\phi) = \sum_{i=1}^{M} |\phi_{i,a} - \phi_{i,c}| \tag{13}$$

where

$\phi_{i,a}$ is the actual received angle of the ith path.
$\phi_{i,c}$ is the determined received angle of the ith path.

5. NUMERICAL EXAMPLES

a) Using small vertical dipole antennas in WCDMA distributed as in Fig. 4 versus the proposed method where the four 3-small dipole arrays are used. The received signal of each path for the different polarization states is shown in Table 2. The small vertical dipole antennas simulation results that the predicted DOA is the 1st path. The proposed method simulation results that the predicted DOA is the 6th path.

Table 2: Signs of elements phase shifts and reception sectors.

Path	Vertical polarization	Horizontal polarization	Orthogonal polarization	ϕ, θ
1	-2	-8	-10	$30, 30$
2	-3	-8	-12	$40, 50$
3	-8	-3	-13	$50, 40$
4	-4	-10	-15	$10, 20$
5	-10	-5	-16	$60, 20$
6	-6	0	-10	$20, 40$

Table 3: Signs of elements phase shifts and reception sectors.

Path	Vertical polarization	Horizontal polarization	Orthogonal polarization	ϕ, θ
1	0	-5	-10	$30, 30$
2	-2	-8	-12	$40, 50$
3	-3	-7	-11	$50, 40$
4	-5	-2	-10	$10, 20$
5	-8	-3	-11	$60, 20$
6	-6	-4	-12	$20, 40$

b) Using small horizontal dipole antennas in WCDMA distributed as in Fig. 4 versus the proposed method where the four 3-small dipole arrays are used. The received signal of each path for the different polarization states is shown in Table 3. The small horizontal dipole antennas simulation results that the predicted DOA is the 4th path. The proposed method simulation results that the predicted DOA is the 1st path.

6. CONCLUSION

Location determination can be achieved with the proposed method using only four 3-element arrays, each 3-element array consists of three orthogonal dipoles to achieve the vertical, horizontal and orthogonal one to both of them, these distributed dipoles achieve spatial, temporal and polarization fingers in the RACK receiver. These fingers are enough to determine the incident angles (azimuth, elevation) with higher accuracy. Numerical examples are simulated using MATLAB R13 (version 6.5) with small dipoles elements antenna. The results show high accuracy in determining the location of the target in contrary of using only one polarization state. This idea can be used for WCDMA mobile communications.

REFERENCES

1. Lee, W. C.-Y. and Y. S. Yeh, "Polarization diversity system for mobile radio," *IEEE Transactions on Communications*, Vol. 20, No. 5, 912–93, Oct. 1972.
2. Lukama, L., K. Konstantinou, and D. J. Edwards, "Three-branch orthogonal polarization diversity," *Electronics Letters*, Vol. 37, No. 20, 1258–1259, Sept. 2001.
3. Mao, X.-P. and J. W. Mark, "On polarization diversity in mobile communications," *Communication Technology, 2006. ICCT '06. International Conference*, 1–4, Nov. 2006.
4. Heikkila, T., "RAKE receiver," S-72.333 Postgraduate Course in Radio Communications, 8, 2004.
5. Alam, F., "Space time processing for third generation CDMA systems," 157–158, 2002.

Location Determination for 2G/3G/4G Using Time Delay Matrix Pencil (TDMP) Method

Mohamed A. Labib and Hassan M. Elkamchouchi
Department of Electrical Engineering, Alexandria University, Alexandria, Egypt

Abstract— A 3D location determination method using only four elements antenna is proposed depending on a Time Delay Matrix Pencil (TDMP) method. A group of signal symbols in time variant domain is received from the transmitter (on mobile phone 2G/3G/4G) or returned signals (Radar), then transferred to the frequency domain using FFT. The Matrix Pencil method is applied to identify the length of each path. Depending on the geometrical distribution of the four elements, the phase shifts are determined for each path. Knowing the phase shift between the elements helps to find the Direction of Arrival (DOA) for each path. Small dipole or small circular loop antennas are used in the numerical examples to clarify this location determination method in the presence of complex noise for GSM, WCDMA and OFDM systems.

1. INTRODUCTION

Position location is a technique that determines the position of a mobile device, often in conjunction with some additional mapping or direction information, in a wireless communication system. Detecting the time and angle of the signal arrival via the direct path between a mobile transmitter and base station receiver is the most important basis for the majority of technologies developed for location-based services. A precise time and DOA measurement results in more accurate location estimation. Regardless of the wireless system deployed, the performance of a location technology depends on accuracy, consistency, reliability and the speed of the measurements of time and angle of signal arrival. In this paper, the location determination using only four elements are achieved with FFT/MP method. The procedure depends on receiving a group of signal symbols from the mobile set to the base station then using the FFT to be applied on MP method [1–4] for distance determination. This procedure is applied to four small loop antennas or small dipole antennas to get the location determination for the different generations of mobile systems in the presence of complex noise. The MP is a super-resolution parameter estimation technique for position location estimation. It has some advantages over the other super-resolution methods for parameter estimation such as MUSIC [5, 6]. The superior performance of MP has been documented in previous works. The performance of MP DOA estimation in CDMA cellular networks is compared to the MUSIC algorithm in [5]. In [6], Dharamdial compared MP to the MUSIC method in recovering the paths delays of a wireless multipath channel. Nowadays, there are two generation of mobile communication 2G like GSM and 3G like WCDMA in the markets and it is expected to find the 4G in 2010 which will depend on Orthogonal Frequency Division Multiplexing (OFDM). This paper shows the adaptation of this new proposal for the three generations.

2. FFT/MP METHOD FOR IDENTIFICATION OF MULTIPATH COMPONENTS

Consider the case of a wireless communication system as illustrated in Fig. 1. The transmitter, located at position A, is transmitting a signal in all directions. The receiver is located at position B and receives the direct ray from A and the multipaths from the existing obstacles [7].

Consider the following sequence of data of length N described by

$$h(\tau) = \sum_{m=1}^{M} \alpha_m \delta(t - \tau_m) + n(\tau_m) \tag{1}$$

where α_m is the complex amplitudes of the mth signal of a total of M signals and τ_m is the propagation delay of the received signal.

The FFT/MP method is used for the estimation of the path delays which is the guide of finding the distances (the path lengths) between the transmitter and the receiver. A training sequence of length N and symbol period T are used for channel training. The base station (receiver) sends a message to the mobile (transmitter) to send a sequence of symbols with a certain symbol rate. The channel is considered to be slowly fading meaning its components stay constant for the duration of the training sequence. That can be achieved easily where T is taken in the range of 10^{-6} to 10^{-8} s,

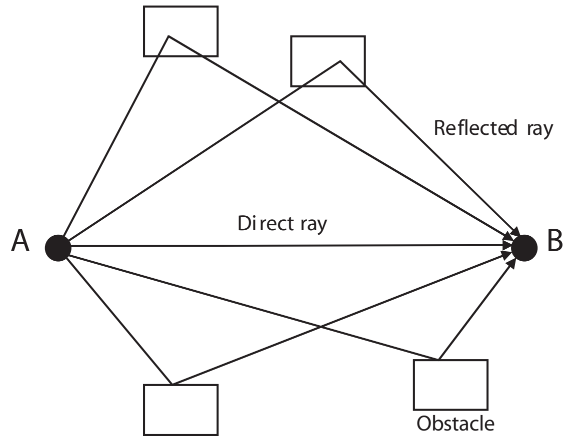

Figure 1: Direct and multipaths effects in communication system with obstacles.

so if $N = 100$, the symbol periods take about 10^{-4} to 10^{-6} s which is a very short time for channel fading or moving mobile transmitter. The discrete frequency channel representation is [8]

$$H_n = \sum_{m=1}^{M} \alpha_m z_m^{(n-1)} + noise_n, \quad z_m = \exp(-j\omega_o \tau_m) \tag{2}$$

where $H_n = H(n\omega_o)$ and $\omega_o = \frac{2\pi}{NT}$

This transfer function consists of the sum of M discrete exponential frequency components. Therefore, the MP technique can be applied to estimate the z_m'^{s}.

Consider two matrices $[Y]_1$ and $[Y]_2$ formed using the received voltages.

$$[Y]_1 = \begin{bmatrix} y_0 & y_1 & \cdots & y_L \\ y_1 & y_2 & \cdots & y_{L+1} \\ \vdots & \vdots & \vdots & \vdots \\ y_{N-L-1} & y_{N-L} & \cdots & y_{N-2} \end{bmatrix}_{(N-1)\times(L+1)}$$

$$[Y]_2 = \begin{bmatrix} y_1 & y_2 & \cdots & y_{L+1} \\ y_2 & y_3 & \cdots & y_{L+2} \\ \vdots & \vdots & \vdots & \vdots \\ y_{N-L} & y_{N-L+1} & \cdots & y_{N-1} \end{bmatrix}_{(N-1)\times(L+1)} \tag{3}$$

where L is the pencil parameter, and $y_n = H_n$.

z_m can be estimated from the M largest eigenvalues of the MP ($[Y]_2$, $[Y]_1$) [9], which are the eigenvalues of $[Y]_1^+ \, [Y]_2$ where $[Y]_1^+$ is the pseudo-inverse of the matrix $[Y]_1$. Once the values of z_m s are estimated and the c is the light velocity, the length of each signal path is

$$d_m = \mathrm{Img}(-\frac{\ln(z_m)}{2\pi} NT) \quad c \tag{4}$$

3. THE LOCATION DETERMINATION METHOD

If using four elements as illustrated in Fig. 2, each element is receiving a set of symbols from the mobile transmitter. Thus the frequency domain received signal is

$$y_q(k) = \sum_{i=1}^{M+1} \alpha_i C \quad \exp\left\{\frac{j2\pi(D_i + \Delta D_i(k))}{c}((q-1)f_0)\right\} + n_{q,k} \tag{5}$$

where f_0 is the symbol rate, q is the symbol index, D_i is the ith path distance between the transmitter and the centered element of the receiver, ΔD_i is the phase shift between the received signal by the centered element and the adjacent elements, i.e.,

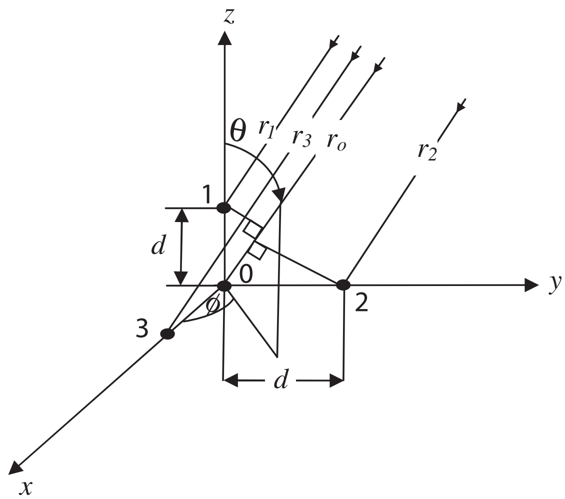

Figure 2: Four elements with uniform distribution.

k is the element index where

$k = 0$, for the centered element

$k = 1$, for the element on the z-axis

$k = 2$, for the element on the y-axis

$k = 3$, for the element on the x-axis

This can be written as

$$y_q(k) = \sum_{i=1}^{M+1} \left[w_i z_i^{(q-1)} \right] + n_{q,k} \tag{6}$$

$$w_i = \alpha_i C \tag{7}$$

$$z_i = \exp\left\{ \frac{j2\pi(D_i + \Delta D_i(k))}{c} (f_0) \right\} \tag{8}$$

$n_{q,k}$ is the noise at each receiving element. Once the $D_i + \Delta D_i(k)$ is determined for each element as in (4), then the phase shift $\Delta Di(k)$ is calculated. For the reference element ($k = 0$), $\Delta D_i(0) = 0$ so the path length D_i for the ith path is determined.

For the element on the z-axis ($k = 1$)

$$\Delta D_i(1) = d \cos\theta_i \tag{9}$$

For the element on the y-axis ($k = 2$)

$$\Delta D_i(2) = d \sin\theta_i \sin\phi_i \tag{10}$$

For the element on the x-axis ($k = 3$)

$$\Delta D_i(3) = d \sin\theta_i \cos\phi_i \tag{11}$$

then the direction of arrival for each path is estimated as,

$$\theta_i = \cos^{-1}\left(\frac{\Delta D_i(1)}{d} \right) \tag{12}$$

$$\phi_i = \cos^{-1}\left(\frac{\Delta D_i(3)}{d \sin\theta_i} \right) \tag{13}$$

or by using,

$$\phi_i = \tan^{-1}\left(\frac{\Delta D_i(2)}{\Delta D_i(3)}\right) \tag{14}$$

$$\theta_i = \sin^{-1}\left(\frac{\Delta D_i(3)}{d\cos\phi_i}\right) \tag{15}$$

To overcome any ambiguity, we determine the reception region depending on the phase shift which differs according to the direction of arrival for each element. As considered above the centered element $k = 0$ is taken as the reference element so the reception sector is as in Table 1.

The error in the determination of the DOA is

$$E(\theta) = \sum_{i=1}^{M} |\theta_{i,a} - \theta_{i,c}| \tag{16}$$

where $\theta_{i,a}$ is the actual received angle of the ith path, and $\theta_{i,c}$ is the determined received angle of the ith path.

$$E(\phi) = \sum_{i=1}^{M} |\phi_{i,a} - \phi_{i,c}| \tag{17}$$

where $\phi_{i,a}$ is the actual received angle of the ith path, and $\phi_{i,c}$ is the determined received angle of the ith path.

Table 1: Signs of elements phase shifts and reception sectors.

$\Delta D_i(1)$	$\Delta D_i(2)$	$\Delta D_i(3)$	Reception sector		
			x-axis	y-axis	z-axis
−	−	−	+	+	+
−	−	+	−	+	+
+	−	−	+	+	−
+	−	+	−	+	−
−	+	−	+	−	+
−	+	+	−	−	+
+	+	−	+	−	−
+	+	+	−	−	−

4. PERFORMANCE ENHANCEMENT IN TDMP

The multipath delays may have huge or small variations depending on the surrounding obstacles. According to these variations an optimization is required for the symbol period T which is taken of the order of the inverse of one tenth the carrier frequency. If the multipath delays have small variation, then the suggested T is optimum but if the multipath delays have large variations, the T has to be increased. The applied method to decide the accuracy of T is to send a message to the mobile and measure the time of the replying which gives certain d_j, this procedure is repeated J times then the mean value is taken as a reference for the estimated path length.

$$\bar{d} = \frac{1}{J}\sum_{j=1}^{J} d_j \tag{18}$$

Comparing the reference estimated path length with the FFT/MP estimation results at a symbol rate of one tenth the carrier frequency, if there is a significant error i.e., tens of meters, T has to be optimized. This mostly distinguished in case of the distance is more than hundreds of meters.

Another optimized number is the used number of samples N which is used to overcome the complex noise, the compensation of the mutual coupling and increasing the accuracy of the path length estimation.

5. NUMERICAL EXAMPLES

(A) In case of using small circular loops with centers at 0, 1, 2 and 3 and planes parallel to the xz -plane as in Fig. 2. The transmitted set of samples is $N = 21$, $T = 10^{-7}$ s with WCDMA and $a = \lambda/10$. The proposed multipaths distances, the azimuth and elevation angles are as in Table 2. The multipaths are considered to be of the same amplitude as the direct path (SIR = 0 dB) and the complex noise is taken to be below the signal by 20 dB i.e., (SNR = 20 dB). The results are as shown in Table 3.

Table 2: The proposed distances and angles.

Multipath	Distance (m)	Azimuth (degree)	Elevation (degree)
1 (direct path)	100	110	0
2	120	111	10
3	150	115	15
4	190	140	20

Table 3: Numerical results with small circular loop antennas.

Multipath	Distance (m)	Azimuth (degree)	Elevation (degree)
1	100	110	0
2	120	111	10
3	150	115	15
4	190	140	20

(B) In case of using small vertical dipole antennas arranged as in Fig. 2, the transmitted set of samples are $N = 15$, $T = 10^{-7}$ s with WCDMA and $l = \lambda/10$. The proposed multipaths distances, the azimuth and elevation angles are as in Table 2. The multipaths are considered to be of the same amplitude as the direct path (SIR = 0 dB) and the complex noise is taken to be below the signal by 20 dB i.e., (SNR = 20 dB).

The numerical examples are simulated using MATLAB R13 version 6.5. The results are as shown in Table 4.

Table 4: Numerical results using small dipole antennas.

Multipath	Distance (m)	Azimuth (degree)	Elevation (degree)
1	100	110	0
2	120	111	10
3	150	115	15
4	190	140	20

Table 5: The proposed distances and angles.

Multipath	Distance (m)	Azimuth (degree)	Elevation (degree)
1 (direct path)	100	110	0
2	102	111	10
3	103	115	15
4	104	140	20

(C) In case of using small vertical dipole antennas arranged as in Fig. 2, the transmitted set of samples are $N = 111$, $T = 10^{-8}$ s with WCDMA & GSM and $l = \lambda/10$. The proposed multipaths distances, the azimuth and elevation angles are as in Table 5. The multipaths are considered to be of the same amplitude as the direct path (SIR = 0 dB) and the complex noise is taken to be above the signal by 20 dB i.e., (SNR= −20 dB).

The WCDMA results are as shown in Table 6. The GSM results are as shown in Table 7.

Table 6: WCDMA numerical results using small dipole antennas.

Multipath	Distance (m)	Azimuth (degree)	Elevation (degree)
1	100	110	0.1568
2	102	110.9982	9.9903
3	103	115	14.9473
4	104	140.001	19.9878

Table 7: GSM numerical results using small dipole antennas.

Multipath	Distance (m)	Azimuth (degree)	Elevation (degree)
1	100	110	0
2	102	111.0015	10.0143
3	103	115.0014	15.0108
4	104	139.9997	19.9989

(D) In case of using small vertical dipole antennas arranged as in Fig. 2, the transmitted set of samples are $N = 111$, $T = 10^{-7}$ s with WCDMA and $l = \lambda/10$. The proposed multipaths distances, the azimuth and elevation angles are as in Table 8. The multipaths are considered to be of the same amplitude as the direct path (SIR = 0 dB) and the complex noise is taken to be above the signal by 20 dB i.e., (SNR = −20 dB). The results are as shown in Table 9.

Table 8: The proposed distances and angles.

Multipath	Distance (m)	Azimuth (degree)	Elevation (degree)
1(direct path)	1000	110	0
2	1020	111	10
3	1030	115	15
4	1040	140	20

Table 9: Numerical results using small dipole antennas.

Multipath	Distance (m)	Azimuth (degree)	Elevation (degree)
1	1000	109.9983	0.4026
2	1020	111.0052	9.8747
3	1030	115.0818	14.6748
4	1040	140.0241	19.8977

(E) In case of using small vertical dipole antennas arranged as in Fig. 2, the transmitted set of samples are $N = 111$, $T = 10^{-8}$ s with OFDM at the carrier frequency 2.4 GHz and $l = \lambda/10$.

The proposed multipaths distances, the azimuth and elevation angles are as in Table 5. The multipaths are considered to be of the same amplitude as the direct path (SIR = 0 dB) and the complex noise is taken to be above the signal by 20 dB i.e., (SNR= −20 dB). The results are as shown in Table 10.

Table 10: Numerical results using small dipole antennas.

Multipath	Distance (m)	Azimuth (degree)	Elevation (degree)
1	100	110.0002	0
2	102	110.9969	9.9969
3	103	114.9931	15.0420
4	104	139.9999	20.0088

Table 11: The proposed distances and angles.

Multipath	Distance (m)	Azimuth (degree)	Elevation (degree)
1 (direct path)	10000	110	0
2	10010	111	10
3	10020	115	15
4	10030	140	20

(F) In case of using small vertical dipole antennas arranged as in Fig. 2, the transmitted set of samples are $N = 111$, $T = 10^{-8}$ s with WCDMA and $l = \lambda/10$. The proposed multipaths distances, the azimuth and elevation angles are as in Table 11. The multipaths are considered to be of the same amplitude as the direct path (SIR = 0 dB) and the complex noise versus the estimated DOA is shown in Fig. 3 and Fig. 4.

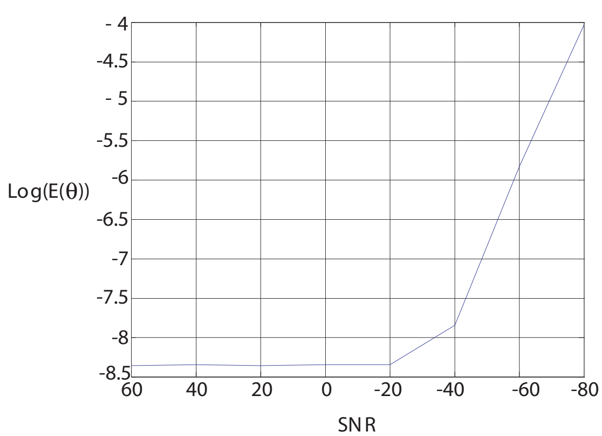

Figure 3: SNR vs. the error in determining $E(\theta)$ at $N = 111$ with complex noise (in case F).

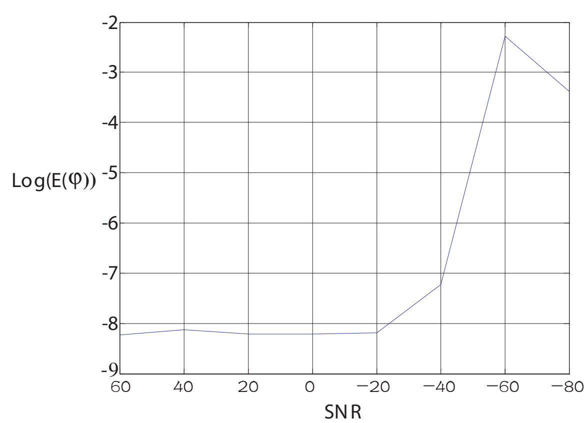

Figure 4: SNR vs. the error in determining $E(\phi)$ at $N = 111$ with complex noise (in case F).

6. CONCLUSION

Location determination can be achieved with only four elements antenna using a group of the signal symbols for distance determination which are enough to calculate the incident angles (azimuth, elevation). As the number of used samples and the symbol rate are optimized, the performance enhances and can overcome the noise effects and the mutual coupling. Numerical examples are simulated using MATLAB R13 with small dipoles or small circular loop elements antenna for GSM, WCDMA and OFDM. The results show high accuracy in determining the location of the target even with high complex noise and long distances. This idea can be used for mobile communications, Radar systems and for buried pipeline locators.

REFERENCES

1. Hua, Y. and T. K. Sarkar, "Matrix pencil method for estimating parameters of exponentially damped/undamped sinusoids in noise," *IEEE Transactions on Acoustics, Speech, and Signal Processing*, Vol. 38, No. 5, 814–824, May 1990.
2. Sarkar, T. K. and O. Pererira, "Using matrix pencil method to estimate the parameters of a sum of complex exponentials," *IEEE Antennas and Propagation Magazine*, Vol. 37, No. 1, 48–55, Feb. 1995.
3. Medouri, A., A. Gallego, D. P. Ruiz, and M. C. Carrion, "Estimation one and two direction of arrival in an incoherent/coherent source environment," *IEICE Transactions on Communications*, Vol. E80-B, No. 11, 1728–1740, Nov. 1997.
4. Hua, Y. and T. K. Sarkar, "Generalized pencil of function method for extracting poles of an EM system from its transit response," *IEEE Antennas and Propagation Magazine*, Vol. 37, No. 2, Feb. 1989.
5. Lau, C. K. E., R. S. Adve, and T. K. Sarkar, "Mutual coupling compensation based on the minimum norm with applications in direction of arrival estimation," accepted for publication, *IEEE Trans. on Antennas and Propagation*, Aug. 2004.
6. Dharamdial, N., R. S. Adve, and R. Farha, "Multipath delay estimation using matrix pencil," *Wireless Communications and Networking*, Vol. 1, 632–635, Mar. 2003.
7. Sarkar, T. K., M. C. Wicks, M. Salazar, and R. Bonneau, *Smart Antennas*, Ch. 10, 319–324, Wiley-interscience Press, 2003.
8. Bayat, K. and R. S. Adve, "Joint TOA/DOA wireless position location using matrix pencil," *Vehicular Technology Conference, 2004.*, VTC2004-Fall, 2004 IEEE 60th, Vol. 5, 3535–3539, 2004.
9. Golub, G. H. and C. F. Van Loan, *Matrix Computation*, Johns Hopkins University Press, 1983.

A General Method for Cloaking Design

Yu Luo[1], **Jingjing Zhang**[1], **Hongsheng Chen**[1,2], **Lixin Ran**[1,2], **and J. A. Kong**[1,2]

[1]The Electromagnetics Academy at Zhejiang University, Zhejiang University, China
[2]Research Laboratory of Electronics, Massachusetts Institute of Technology
Cambridge, MA 02139, USA

Abstract— The idea of using the coordinate transformation approach to design a cloak of invisibility has received much attention. Up to now, most of the discussions on cloaking are based on the linear transformation. If different transformations are adopted, cloaks with different performances can be achieved. This paper gives an analytical field solutions on a spherical cloak created with a general class of transformation functions. The analytical expressions of the electromagnetic field in the whole space are calculated, and the field distributions of cloaks with different parameters are analyzed. This analytical full wave method is a very computational efficient validation method compared with numerical simulations. It also provides a better physical insight into the effect of the transformation function on the performance of devices.

1. INTRODUCTION

Recently, the idea of using the coordinate transformation approach to design a cloak of invisibility has received much attention. J. Pendry et al., [1] first suggested that an obstacle can be protected from detection by surrounding it with a coating consisting of an exotic material. D. Schurig et al., verified the idea by calculating the material properties associated with a coordinate transformation and used these properties to perform ray tracing [2]. Full wave numerical simulations on cylindrical cloaking were presented by S. Cummer [3]. The interactions of electromagnetic wave with the cloaks have also been analytically studied, yielding a better physical interpretation [4, 5].

Up to now, most of the discussions on cloak are base on the transformation presented by J. Pendry [1]. If different transformations are adopted, the cloaks with different performances can be obtained. In this paper, a general idea of designing cloaks using a full wave Mie scattering model is proposed. The analytical expressions of the electromagnetic field in the whole space are calculated, and the field distributions of cloaks with different parameters are analyzed.

2. FOMULATIONS

Consider the three dimensional case (the following idea is also applicable to two dimensional cylindrical case): a general coordinate transformation between two spherical coordinate systems (r', θ', φ') and (r, θ, φ) is described by

$$r' = f(r,\theta,\varphi), \quad \theta' = g(r,\theta,\varphi), \quad \varphi' = h(r,\theta,\varphi), \tag{1}$$

where r', θ', φ' represent the coordinates in the original coordinate system and $f(\bullet)$, $g(\bullet)$, $h(\bullet)$ can be arbitrary monotonic differentiable functions. Following the transformation approach proposed in Ref. [1], Maxwell equations still remain its form invariance in the new space (r, θ, φ) but the permittivity and permeability will turn into distributed, or space dependent tensors,

$$\bar{\bar{\varepsilon}} = \varepsilon_0 \bar{\bar{T}}^{-1}, \quad \bar{\bar{\mu}} = \mu_0 \bar{\bar{T}}^{-1}, \tag{2}$$

where ε_0 and μ_0 represent the scalar permittivity and permeability of free space in the original space before transformation. The matrix T is defined by $T = \bar{\bar{J}}^T \bar{\bar{J}} \Big/ \det\left(\bar{\bar{J}}\right)$, where $\bar{\bar{J}} = \frac{\partial(f,g,h)}{\partial(r,\theta,\varphi)}$ is the Jacobian matrix. According to the Mie scattering theory, for source free cases, we can decompose the fields into TE and TM modes by introducing the vector potential $\bar{A}_{\mathrm{TE}}$ and $\bar{A}_{\mathrm{TM}}$ in the new space and express the fields as

$$\begin{cases} B_{\mathrm{TM}} = \nabla \times \left(\bar{A}_{\mathrm{TM}}\right) \\ D_{\mathrm{TM}} = \frac{i}{\omega}\left[\nabla \times \left(\bar{\bar{\mu}}^{-1} \cdot \nabla \times \left(\bar{A}_{\mathrm{TM}}\right)\right)\right] \\ D_{\mathrm{TE}} = -\nabla \times \left(\bar{A}_{\mathrm{TE}}\right) \\ B_{\mathrm{TE}} = \frac{i}{\omega}\left[\nabla \times \left(\bar{\bar{\varepsilon}}^{-1} \cdot \nabla \times \left(\bar{A}_{\mathrm{TE}}\right)\right)\right] \end{cases}, \tag{3}$$

where B and D represent the magnetic flux density and electric displacement, respectively. Since the media described by $\bar{\bar{\varepsilon}}$ and $\bar{\bar{\mu}}$ is no longer isotropic, the directions of $\bar{A}_{\mathrm{TE}}$ and $\bar{A}_{\mathrm{TM}}$ will not always be along the r direction. For mathematical convenience, we let

$$\begin{aligned}\bar{A}_{\mathrm{TM}} &= \left(\frac{\partial f}{\partial r}\hat{r} + \frac{\partial f}{r\partial\theta}\hat{\theta} + \frac{\partial f}{r\sin\theta\partial\varphi}\hat{\varphi}\right)\Phi_{\mathrm{TM}} \\ \bar{A}_{\mathrm{TE}} &= \left(\frac{\partial f}{\partial r}\hat{r} + \frac{\partial f}{r\partial\theta}\hat{\theta} + \frac{\partial f}{r\sin\theta\partial\varphi}\hat{\varphi}\right)\Phi_{\mathrm{TE}}\end{aligned}, \tag{4}$$

where Φ_{TM} and Φ_{TE} are scalar potentials for TE and TM cases, respectively. Note that if $f(\bullet)$ is only a function of r, for example, a linear function like $f(r) = \frac{R_2}{(R_2-R_1)}(r-R_1)$, then the two vector potential $\bar{A}_{\mathrm{TE}}$ and $\bar{A}_{\mathrm{TM}}$ will be along the r direction, and it will be reduced to the case studied in Ref. [4]. Substituting Equation (4) into Equation (3), we obtain the partial differential equation for Φ_{TE} and Φ_{TM}:

$$\left[\frac{\partial^2}{\partial f^2} + \frac{1}{f^2\sin g}\frac{\partial}{\partial g}\left(\sin g\frac{\partial}{\partial g}\right) + \frac{1}{f^2\sin^2 g}\frac{\partial^2}{\partial h^2} + k_0^2\right]\Phi = 0, \tag{5}$$

which takes the same form as the Helmholtz equation, so one of its special solution is

$$\Phi = \hat{B}_n(k_0 f)\,P_n^m(\cos g)\,(A_m\cos mh + B_m\sin mh), \tag{6}$$

where $\hat{B}_n(\xi)$ is Riccati-Bessel function, P_n^m is the nth orders of the associated Legendre polynomials of degree m, and A_m and B_m are undetermined coefficients. Using Equation (4), we can obtain the vector potentials $\bar{A}_{\mathrm{TE}}$ and $\bar{A}_{\mathrm{TM}}$ as follows:

$$\begin{aligned}\bar{A}_{\mathrm{TM}} &= \sum_{m,n} a_{m,n}^{\mathrm{TM}}\left(\frac{\partial f}{\partial r}\hat{r} + \frac{\partial f}{r\partial\theta}\hat{\theta} + \frac{\partial f}{r\sin\theta\partial\varphi}\hat{\varphi}\right)\hat{B}_n(k_0 f)\,P_n^m(\cos g)\,(A_m\cos mh + B_m\sin mh) \\ \bar{A}_{\mathrm{TE}} &= \sum_{m,n} a_{m,n}^{\mathrm{TE}}\left(\frac{\partial f}{\partial r}\hat{r} + \frac{\partial f}{r\partial\theta}\hat{\theta} + \frac{\partial f}{r\sin\theta\partial\varphi}\hat{\varphi}\right)\hat{B}_n(k_0 f)\,P_n^m(\cos g)\,(A_m\cos mh + B_m\sin mh)\end{aligned}, \tag{7}$$

where the coefficients $a_{m,n}^{\mathrm{TM}}$ and $a_{m,n}^{\mathrm{TE}}$ can be determined by applying corresponding boundary conditions. Thus all the components of the total fields can be obtained by substituting Equation (7)

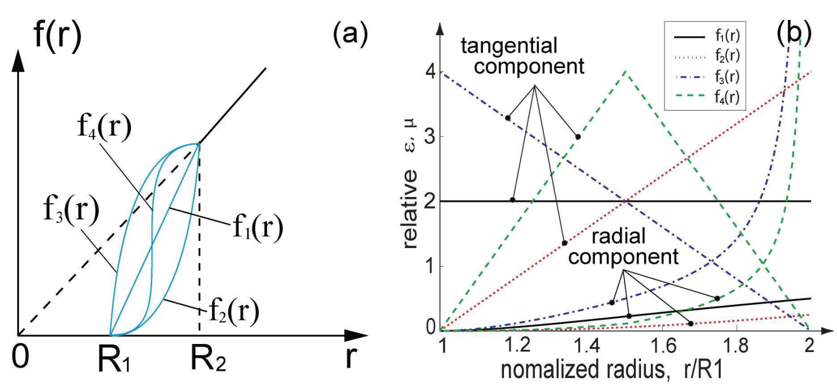

Figure 1: (a) Schematic figure of the transformation functions $f(r)$ in four cases: (Case I) $f_1(r) = \frac{R_2}{(R_2-R_1)}(r-R_1)$, (Case II) $f_2(r) = \frac{R_2}{(R_2-R_1)^2}(r-R_1)^2$ with $f_2'(R_1) = 0$, (Case III) $f_3(r) = -\frac{R_2}{(R_2-R_1)^2}(r-R_2)^2 + R_2$ with $f_3'(R_2) = 0$, and (Case IV) $f_4(r)$ with $f_4'(R_1) = 0$ and $f_4'(R_2) = 0$. (b) The permittivity and permeability components calculated from the corresponding four cases.

into Equations (3), and take the following forms

$$\begin{aligned}
E_r &= \frac{i}{\omega\mu_0\varepsilon_0}\left[\frac{\partial f}{\partial r}\left(\frac{\partial^2}{\partial f^2}+k_0^2\right)+\frac{\partial g}{\partial r}\frac{\partial^2}{\partial f\partial g}+\frac{\partial h}{\partial r}\frac{\partial^2}{\partial f\partial h}\right]\Phi_{\mathrm{TM}} \\
&\quad +\frac{1}{\varepsilon_0}\left(\sin g\frac{\partial h}{\partial r}\frac{\partial}{\partial g}-\frac{1}{\sin g}\frac{\partial g}{\partial r}\frac{\partial}{\partial h}\right)\Phi_{\mathrm{TE}}, && \text{(8-1)}\\
E_\theta &= \frac{i}{\omega\mu_0\varepsilon_0 r}\left[\frac{\partial f}{\partial \theta}\left(\frac{\partial^2}{\partial f^2}+k_0^2\right)+\frac{\partial g}{\partial \theta}\frac{\partial^2}{\partial f\partial g}+\frac{\partial h}{\partial \theta}\frac{\partial^2}{\partial f\partial h}\right]\Phi_{\mathrm{TM}} \\
&\quad +\frac{1}{\varepsilon_0 r}\left(\sin g\frac{\partial h}{\partial \theta}\frac{\partial}{\partial g}-\frac{1}{\sin g}\frac{\partial g}{\partial \theta}\frac{\partial}{\partial h}\right)\Phi_{\mathrm{TE}}, && \text{(8-2)}\\
E_\varphi &= \frac{i}{\omega\mu_0\varepsilon_0 r\sin\theta}\left[\frac{\partial f}{\partial \varphi}\left(\frac{\partial^2}{\partial f^2}+k_0^2\right)+\frac{\partial g}{\partial \varphi}\frac{\partial^2}{\partial f\partial g}+\frac{\partial h}{\partial \varphi}\frac{\partial^2}{\partial f\partial h}\right]\Phi_{\mathrm{TM}} \\
&\quad +\frac{1}{\varepsilon_0 r\sin\theta}\left(\sin g\frac{\partial h}{\partial \varphi}\frac{\partial}{\partial g}-\frac{1}{\sin g}\frac{\partial g}{\partial \varphi}\frac{\partial}{\partial h}\right)\Phi_{\mathrm{TE}}, && \text{(8-3)}\\
H_r &= \frac{1}{\mu_0}\left(\frac{1}{\sin g}\frac{\partial g}{\partial r}\frac{\partial}{\partial h}-\sin g\frac{\partial h}{\partial r}\frac{\partial}{\partial g}\right)\Phi_{\mathrm{TM}} \\
&\quad +\frac{i}{\omega\mu_0\varepsilon_0}\left[\frac{\partial f}{\partial r}\left(\frac{\partial^2}{\partial f^2}+k_0^2\right)+\frac{\partial g}{\partial r}\frac{\partial^2}{\partial f\partial g}+\frac{\partial h}{\partial r}\frac{\partial^2}{\partial f\partial h}\right]\Phi_{\mathrm{TE}}, && \text{(8-4)}\\
H_\theta &= \frac{1}{\mu_0 r}\left(\frac{1}{\sin g}\frac{\partial g}{\partial \theta}\frac{\partial}{\partial h}-\sin g\frac{\partial h}{\partial \theta}\frac{\partial}{\partial g}\right)\Phi_{\mathrm{TM}} \\
&\quad +\frac{i}{\omega\mu_0\varepsilon_0 r}\left[\frac{\partial f}{\partial \theta}\left(\frac{\partial^2}{\partial f^2}+k_0^2\right)+\frac{\partial g}{\partial \theta}\frac{\partial^2}{\partial f\partial g}+\frac{\partial h}{\partial \theta}\frac{\partial^2}{\partial f\partial h}\right]\Phi_{\mathrm{TE}}, && \text{(8-5)}\\
H_\varphi &= \frac{1}{\mu_0 r\sin\theta}\left(\sin g\frac{\partial h}{\partial \varphi}\frac{\partial}{\partial g}-\frac{1}{\sin g}\frac{\partial g}{\partial \varphi}\frac{\partial}{\partial h}\right)\Phi_{\mathrm{TM}} \\
&\quad +\frac{i}{\omega\mu_0\varepsilon_0 r\sin\theta}\left[\frac{\partial f}{\partial \varphi}\left(\frac{\partial^2}{\partial f^2}+k_0^2\right)+\frac{\partial g}{\partial \varphi}\frac{\partial^2}{\partial f\partial g}+\frac{\partial h}{\partial \varphi}\frac{\partial^2}{\partial f\partial h}\right]\Phi_{\mathrm{TE}}, && \text{(8-6)}
\end{aligned}$$

where E and H represent the electric and magnetic fields, respectively.

It should be pointed out that in the cases that the functions are non-monotonic or non-differentiable at some points we can decompose the definition domain into several monotonic and differentiable domains, in which the above method can be applied. And the boundary points of the separate domains can be treated with boundary conditions.

3. SPHERICAL CLOAKS

The above formulas are firstly applied to the spherical cloaks. Any continuous function $f(\bullet)$, $g(\bullet)$, $h(\bullet)$ that satisfy $f(R_2, \theta, \varphi) = R_2$, $g(R_2, \theta, \varphi) = \theta$, $h(R_2, \theta, \varphi) = \varphi + \varphi_0$ (where φ_0 is a definite constant) and $f(R_1, \theta, \varphi) = 0$ (these conditions can be directly obtained from the partial differential equations by setting the scattering coefficients T_n^{TM} and T_n^{TE} to be zero at the outer boundary) can be used to achieve a coating the field inside which is always matched with the outer free space at the outer boundary R_2 and the potential is uniform everywhere at the inner boundary R_1. The coating with this quality can realize a perfect spherical invisibility cloak. Detailed illustration on it is out of the scope of this article and further discussion, with general theoretical analysis and numerical simulations will be given in our other paper. Here we only consider one simple case when $r' = f(r)$, $\theta' = \theta$, $\varphi' = \varphi$. The associated permittivity and permeability tensors are then given by:

$$\bar{\bar{\varepsilon}} = \varepsilon_r(r)\,\hat{r}\hat{r} + \varepsilon_t(r)\,\hat{\theta}\hat{\theta} + \varepsilon_t(r)\,\hat{\varphi}\hat{\varphi}, \quad \bar{\bar{\mu}} = \mu_r(r)\,\hat{r}\hat{r} + \mu_t(r)\,\hat{\theta}\hat{\theta} + \mu_t(r)\,\hat{\varphi}\hat{\varphi},$$

where

$$\varepsilon_t = \varepsilon_0 f'(r), \quad \varepsilon_r = \varepsilon_0\frac{f^2(r)}{r^2 f'(r)}, \quad \mu_t = \mu_0 f'(r), \quad \text{and} \quad \mu_r = \mu_0\frac{f^2(r)}{r^2 f'(r)} \tag{9}$$

For an arbitrary differentiable transformation function $f(r)$, we will show in detail that these parameters yield a perfect invisibility as long as $f(R_2) = R_2$ and $f(R_1) = 0$ are satisfied.

Suppose an E_x polarized plane wave with a unit amplitude $E_i = \hat{x}e^{ik_0 z}$ is incident upon the coated sphere along the z direction. With the solution of Equation (4), the vector potentials for the incident fields ($r > R_2$), the scattered fields ($r > R_2$), and the fields inside the cloak layer ($R_1 < r < R_2$) can be written in the following forms respectively:

$$\begin{aligned} \bar{A}^i_{\mathrm{TM}} &= \hat{r}\frac{\cos\varphi}{\omega}\sum_n a_n \psi_n(k_0 r) P_n^1(\cos\theta) \\ \bar{A}^i_{\mathrm{TE}} &= \hat{r}\frac{\sin\varphi}{\omega\eta_0}\sum_n a_n \psi_n(k_0 r) P_n^1(\cos\theta) \end{aligned}, \tag{10-1}$$

$$\begin{aligned} \bar{A}^s_{\mathrm{TM}} &= \hat{r}\frac{\cos\varphi}{\omega}\sum_n a_n T_n^{\mathrm{TM}} \zeta_n(k_0 r) P_n^1(\cos\theta) \\ \bar{A}^s_{\mathrm{TE}} &= \hat{r}\frac{\sin\varphi}{\omega\eta_0}\sum_n a_n T_n^{\mathrm{TE}} \zeta_n(k_0 r) P_n^1(\cos\theta) \end{aligned}, \tag{10-2}$$

$$\begin{aligned} \bar{A}^c_{\mathrm{TM}} &= \hat{r}\frac{\cos\varphi}{\omega}\sum_n f'(r)(d_n^{\mathrm{TM}}\psi_n(k_0 f(r)) + f_n^{\mathrm{TM}}\chi_n(k_0 f(r)))P_n^1(\cos\theta) \\ \bar{A}^c_{\mathrm{TE}} &= \hat{r}\frac{\sin\varphi}{\omega\eta_0}\sum_n f'(r)(d_n^{\mathrm{TE}}\psi_n(k_0 f(r)) + f_n^{\mathrm{TE}}\chi_n(k_0 f(r)))P_n^1(\cos\theta) \end{aligned}, \tag{10-3}$$

where $a_n = \frac{(-i)^{-n}(2n+1)}{n(n+1)}$, $n = 1, 2, 3, \ldots$, $\eta_0 = \sqrt{\frac{\mu_0}{\varepsilon_0}}$; T_n^{TM}, T_n^{TE}, d_n^{TM}, d_n^{TE}, f_n^{TM} and f_n^{TE} are unknown expansion coefficients; $\psi_n(\xi)$, $\chi_n(\xi)$, $\zeta_n(\xi)$ represent the Riccati-Bessel function of the first, the second, and the third kind, respectively [6]. Since $f(R_1) = 0$, $\chi_n(0)$ is infinite, the finitude of the field at the inner boundary R_1 requires that $f_n^{\mathrm{TM}} = f_n^{\mathrm{TE}} = 0$ [4]. By applying the boundary conditions at the boundary of $r = R_2$, we can get other unknown coefficients:

$$T_n^{\mathrm{TM}} = T_n^{\mathrm{TE}} = -\frac{\psi_n'(k_0R_2)\psi_n(k_0 f(R_2)) - \psi_n(k_0R_2)\psi_n'(k_0 f(R_2))}{\zeta_n'(k_0R_2)\psi_n(k_0 f(R_2)) - \zeta_n(k_0R_2)\psi_n'(k_0 f(R_2))}, \tag{11-1}$$

$$d_n^{\mathrm{TM}} = d_n^{\mathrm{TE}} = \frac{ia_n}{\zeta_n'(k_0R_2)\psi_n(k_0 f(R_2)) - \zeta_n(k_0R_2)\psi_n'(k_0 f(R_2))}, \tag{11-2}$$

Since $f(R_2) = R_2$, the above equations can be simplified as

$$T_n^{\mathrm{TM}} = T_n^{\mathrm{TE}} = 0, \quad d_n^{\mathrm{TM}} = d_n^{\mathrm{TE}} = a_n, \tag{12}$$

The fact that coefficients T_n^{TM} and T_n^{TE} are exactly equal to zero indicates a reflectionless behavior of a perfect cloak. Substituting Equations (10) into Equations (8), after some algebraic manipulations, the summation $\sum\limits_n$ can be written in closed forms. As a result, all components of the electric field are expressed as (Note that the parameters for free space can be regarded as $f(r) = r$, therefore the fields can still be written in the following forms):

$$E_r = f'(r)\sin\theta\cos\varphi e^{ik_0 f(r)\cos\theta}, \tag{13-1}$$

$$E_\theta = \frac{f(r)}{r}\cos\theta\cos\varphi e^{ik_0 f(r)\cos\theta}, \tag{13-2}$$

$$E_\varphi = -\frac{f(r)}{r}\sin\varphi e^{ik_0 f(r)\cos\theta}, \tag{13-3}$$

Therefore, from Equations (12) and (13), we confirmed that as long as $f(R_2) = R_2$ and $f(R_1) = 0$, any spherical shell with parameters defined by Equation (9) can yield a perfect invisibility. Different $f(r)$ in the region $R_1 < r < R_2$ will only cause different field distribution in the cloak layer, but will not disturb the field outside.

The distribution of the field in the cloak shell $R_1 < r < R_2$ and the sensitivity of the cloak to the perturbations at the boundary are determined by the transformation function $f(r)$. We investigate four types of cloak created with four different transformation functions: (Case I) $f_1(r) = \frac{R_2}{(R_2-R_1)}(r - R_1)$, (Case II) $f_2(r) = \frac{R_2}{(R_2-R_1)^2}(r - R_1)^2$ with $f_2'(R_1) = 0$, (Case III)

$f_3(r) = -\frac{R_2}{(R_2-R_1)^2}(r-R_2)^2 + R_2$ with $f_3'(R_2) = 0$, and (Case IV) $f_4(r)$ with $f_4'(R_1) = 0$ and $f_4'(R_2) = 0$. Fig. 1(a) displays the curves of the four transformation functions. Fig. 1(b) shows the corresponding tangential and radial components of ε and μ of the four different cloaks calculated from Equation (9). Fig. 2 depicts the calculated E_x fields distributions and Poynting vectors due to E_x polarized wave incidence onto these four different cloaks, respectively. All the cloaks have a same size of $R_1 = 0.1$ m, and $R_2 = 0.2$ m. The wavelength in free space is 0.15 m. All the quantities are normalized to unity in this and the following calculations.

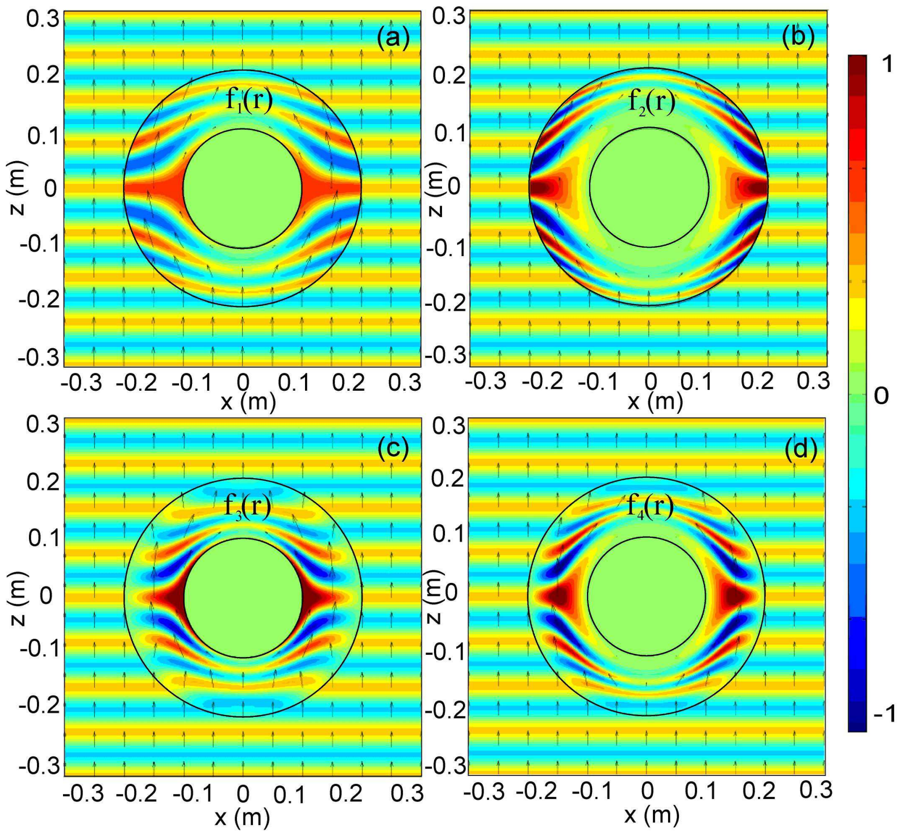

Figure 2: (a), (b), (c), and (d) show the E_x fields distribution and Poynting vectors due to E_x polarized wave incidence onto a cloak created with the four different transformation functions $f_1(r)$, $f_2(r)$, $f_3(r)$, and $f_4(r)$, respectively.

With different transformations, the fields inside the cloaks are differently distributed while the wave propagating in the outer region of the cloak remains undisturbed. In Fig. 1(c), the field is nearly uniformly distributed in the cloak shell with linear function $f_1(r) = \frac{R_2}{(R_2-R_1)}(r-R_1)$ (transformation function used in Ref. [1]) between R_1 and R_2. From the result we can find that this kind of cloak, which can be called linear-transformed cloak, is sensitive to perturbations both at the inner boundary R_1 and outer boundary R_2; In Fig. 1(d), the field is mainly distributed near the outer boundary in the cloak with the convex transformation function $f_2(r)$. And this so called convex-transformed cloak is not sensitive to the perturbations at the inner boundary but much more sensitive to perturbations at the outer boundary; In Fig. 1(e), the field is mainly distributed close to the inner boundary in the cloak with a concave transformation function $f_3(r)$. This so called concave-transformed cloak is not sensitive to the perturbations at the outer boundary, but it is sensitive to tiny perturbations at the inner boundary. In a word, the field inside the cloak is larger in the position where the differential of the function$f(r)$ is larger. Thus by choosing a function like $f_4(r)$, the differential of which is zero at both R_1 and R_2, we can get a cloak in which the field is mainly distributed near the central region of the coating and approaches to zero at both boundaries. In fact, if we choose a transformation function $f(r)$ that satisfies $f'(R_1) = 0$ and $f'(R_2) = 1$, the cloak will be insensitive to perturbations at neither the outer boundary nor the inner boundary, however, it will be sensitive to the perturbations in the central region of the cloak.

4. CONCLUSION

In this paper, we summarized a generalized formulation on how to use the transformations to obtain different cloak by combining the merits of both coordinate transformation and the Mie scattering solutions. We show by mathematical analysis that the coordinate transformation to the Maxwell equations can be in a generalized form: any continuous functions can be adopted in the transformation, and different type of functions will bring different characteristic of the EM behaviors in the transformed space. Starting from the formulation deduced in this paper, invisibility cloaks can be easily obtained by simply selecting different scalar transformation functions, and the internal field distributions in the cloaks can also be controlled by tuning the shapes of the functions. Various examples for the design of cloaks are given to demonstrate the validity of the formulation and the very high computational efficiency. Our paper presents a very useful tool in the analysis and design for EM devices.

ACKNOWLEDGMENT

This work is sponsored by the Chinese National Science Foundation under Grant Nos. 60531020, 60671003 and 60701007, the NCET-07-0750, the ZJNSF (R105253), the Ph.D. Programs Foundation of MEC (No. 20070335120), the ONR under Contract No. N00014-01-1-0713, and the Department of the Air Force under Air Force Contract No. F19628-00-C-0002.

REFERENCES

1. Pendry, J. B., D. Schurig, and D. R. Smith, *Science*, Vol. 312, 1780, 2006.
2. Schurig, D., J. B. Pendry, and D. R. Smith, *Opt. Express*, Vol. 14, 9794, 2006.
3. Cummer, S. A., B.-I. Popa, D. Schurig, D. R. Smith, and J. B. Pendry, *Phys. Rev. E*, Vol. 74, 036621, 2006.
4. Chen, H., B.-I. Wu, B. Zhang, and J. A. Kong, *Phys. Rev. Letts.*, Vol. 99, 063903, 2007.
5. Luo, Y., H. Chen, J. Zhang, L. Ran, and J. A. Kong, *Phys. Rev. B.*, eprint ArXiv: 0712. 2027, 2007, (to be published).
6. Van de Hulst, H. C., *Light Scattering by Small Particles*, Dover, New York, 1957.

Waveguide Structures for Generation of Terahertz Radiation by Electro-optical Process in GaAs and $ZnGeP_2$ Using 1.55 μm Fiber Laser Pulses

T. Yang, S. Song, H. Dong, and R. Ba
College of Precision Instruments and Opto-electronics Engineering
Laboratory of Optoelectronics Information Technical Science, Educational Ministry of China
Center for Terahertz Waves, Tianjin University, China

Abstract— By discussing the basic schemes of the terahertz generation methods based on the 1550-nm ultrafast lasers briefly, GaAs and $ZnGeP_2$ are likely to be promising nonlinear optical crystals for terahertz waves generation by using optical rectification process. However, the mismatches of velocities between the terahertz waves and optical pulses are so large that the phase-matching coherent lengths are quite short, for example, the coherent length of 0.7 mm for GaAs and 0.5 mm for $ZnGeP_2$ at 2 THz around, respectively. That limited extremely the applications of these bulk excellent nonlinear optical crystals in terahertz regime. In this paper, we demonstrated theoretically that the dielectric planar waveguide could be used to enhance the coherent length of optical rectification process in THz regime. And for the first time, a dielectric planar THz waveguide that has potential applicable value in THz generation by optical rectification method was proposed. We predicted that the effective coherent length could be extended to 4 mm at 2 THz in a GaAs/$ZnGeP_2$ dielectric planar waveguide during optical rectification process pumped by ultrafast optical pulses at wavelength of 1550 nm.

1. INTRODUCTION

Recent advances in the ultrafast-pulse-laser technique have spurred the rapid development of the generation and detection of the terahertz (THz) electromagnetic pulse, which has led to various applications, such as material characterization, time-domain spectroscopy, and imaging. The THz emitter, based on ultrafast laser, is a potential candidate that has a wide THz bandwidth. But the Ti: Sapphire solid state laser that is currently being used as a pump source, is too expensive and bulky. Hence, developing a compact, low cost THz field source and detection technique, based on 1550-nm fiber laser, is a necessity. The present research trend suggests a shift of the pump wavelength from 810 to 1550 nm of ultrafast fiber laser to use cheaper components for optical communication wavelength [1]. And fiber laser also has the advantages of compact, low cost, free of water-cooling, etc.

There exist two schemes for THz pulse generation by tabletop devices. These are photoconductive switches illuminated by ultrashort laser pulses, and optical rectification of ultrashort laser pulses in nonlinear crystals. To realize photoconductive switches operable with 1550-nm light, the band gap of the material should be reduced so as to enable efficient photoexcitation. Though low-temperature-grown (LTG) $In_xGa_{1-x}As$ $(0.4 < x < 0.53)$ has been shown to work at 1560-nm excitation [2], there is no well established photoconductive material suitable for 1550-nm excitation yet. A nonresonant electro-optical (EO) process is the simplest method for both THz generation with optical rectification and detection using EO sampling methods because the optimization of nonlinear crystal is well established even in the long wavelength region. Optical rectification of femtosecond laser pulses in nonlinear crystals is a proven way to generate THz radiation. The earliest optical rectification experiments were performed by Yang et al. in a $LiNbO_3$ nonlinear optical crystal. Later, other groups applied the optical rectification technique to different nonlinear crystals such as $LiTaO_3$, GaAs, GaSe and others, and used femtosecond laser pulses to increase the generated THz bandwidth [3]. Recently, 10 μJ ultrashort THz pulses have been generated by optical rectification in a lithium niobate crystal based on a 10 Hz Ti: sapphire laser [4]. However, there is rare successful examples of THz pulses generation by optical rectification in a nonlinear crystal based on an ultrafast fiber laser at a wavelength of 1550-nm. The main reason is that matching between the optical group velocity and THz phase velocity is crucial for efficient optical rectification. For a large set of well known nonlinear crystals with low absorption in THz band, such as GaAs, GaSe, GaP, ZnTe and $ZnGeP_2$, their phase matching conditions are not satisfied at 1550 nm, resulting in quite small coherent length. So the enhancement of coherence length of the nonlinear process is crucial way to improve the THz radiation efficiency. In this paper, we are intent on designing a planar waveguide configuration to reduce the degree of mismatching between the optical group velocity and THz phase velocity.

There several groups have demonstrated the planar waveguide structures in THz generation. They all aimed on confining the THz radiation in a metallic planar waveguide effectively in which the THz field is forced to be a fundamental guide mode of transverse electromagnetic (TEM) mode [5–7]. The phase velocity of TEM mode in a metallic planar waveguide is the same as electromagnetic waves in free space. That means that the metallic waveguide structure would not be effective to narrow the velocity gap between the optical pulses and THz radiation. Normally, the phase velocity of THz wave is smaller than the group velocity of the near infrared ultrashort pulse in nonlinear optical crystals. In this paper, we try to establish a dielectric planar waveguide for THz waves in which the fundamental mode is transverse magnetic (TM) mode of which effective propagation velocity is larger than TEM mode in a metallic planar waveguide. This is the first time, to our knowledge, to establish a dielectric planar waveguide for THz waves to enhance the coherent length of optical rectification of ulrashort optical pulse at a wavelength of 1550-nm for THz wave generation.

2. COHERENT LENGTH

The phase matching condition for the optical rectification process (collinear difference frequency mixing) is given by

$$\Delta k = k\left(\omega_{\text{opt}} + \omega_{\text{THz}}\right) - k\left(\omega_{\text{opt}}\right) - k\left(\omega_{\text{THz}}\right) = 0 \tag{1}$$

where ω_{opt} and ω_{THz} are the optical and THz wave frequencies, respectively, and ω_{opt} and $(\omega_{\text{opt}} + \omega_{\text{THz}})$ lie within the spectrum of the optical pulse. If we neglect dispersion in the optical spectral range, we can express the coherence length $lc(= \pi/\Delta k)$ as

$$l_c = \frac{\pi c}{\omega_{\text{THz}} \left|n_{\text{opt,phase}} - n_{\text{THz}}\right|} \tag{2}$$

Here, c is the speed of light and $n_{\text{opt,phase}}$ and n_{THz} are the optical and THz wave refractive indexes of bulk crystals, respectively. For an ultrashort optical pulse, the dispersion in the optical refractive index may be used to obtain collinear, noncritical phase matching over a broad bandwidth in the THz band. For a medium with dispersion at optical frequencies, the phase matching condition of Eq. (1) may be rewritten as [8]

$$\frac{k(\omega_{\text{THz}})}{\omega_{\text{THz}}} \approx \left(\frac{\partial k}{\partial \omega}\right)_{\text{opt}} \tag{3}$$

This relation implies that phase matching is achieved when the phase of the THz wave travels at the velocity of the optical pulse envelope (i.e., the optical group velocity, v_g). The corresponding coherence length for difference frequency mixing is now

$$l_c = \frac{\pi c}{\omega_{\text{THz}} \left|n_{\text{opt,group}} - n_{\text{THz}}\right|} \tag{4}$$

where $n_{\text{opt,group}}$ is the group index at the optical pump frequency in the bulk nonlinear optical crystal and can be determined by the dispersion property of the optical crystal as following expression

$$n_{\text{opt,group}} = n_{\text{opt,phase}} - \lambda_{\text{opt}} \left.\frac{dn_{\text{opt,phase}}}{d\lambda_{\text{opt}}}\right|_{\lambda_{\text{opt}}} \tag{5}$$

where λ_{opt} is the center-wavelength of pumping ultrashort optical pulse.

Using published values [9–11] for the relevant optical parameters, we have calculated the $n_{\text{opt,group}}$ at optical wavelength of 1550 nm and n_{THz} at 2 THz for a set of well known nonlinear crystals. The results are shown in Table 1.

From the Table 1 we can see that the coherent length is quite small for optical rectification process because of the difference between the $n_{\text{opt,group}}$ and n_{THz}, and n_{THz} is normally larger than $n_{\text{opt,group}}$. So we have to reduce the n_{THz}, or increase the phase velocity of THz wave by introducing appropriate waveguide structure to enhance the coherence length if the $n_{\text{opt,group}}$ is kept unchangeable in that waveguide structure.

Table 1: The group index at the optical pump frequency and the phase index at THz frequency of well known nonlinear crystals.

	GaAs [9]	$ZnGeP_2$ [10, 11]	GaP [11]	ZnTe [9]
$n_{\text{opt,phase}}$@ 1550 nm	3.3767	3.1697	3.0543	2.7330
$n_{\text{opt,group}}$@ 1550 nm	3.5174	3.2745	3.1705	2.8065
n_{THz}@ 2 THz	3.61	3.420	3.3494	3.22
$\lambda_{\text{opt,phase-maching}}$ @ 2 THz [nm]	1330	1191	1000	800
l_c@ 1550 nm [mm]	0.78	0.5155	0.42	0.1

3. DIELECTRIC PLANAR WAVEGUIDE FOR THZ WAVES

We set up a dielectric planar waveguide (See Fig. 1) for THz waves other than a metallic planar waveguide because the electromagnetic waves could travel faster in dielectric planar waveguides than in a bulk counterpart dielectric medium.

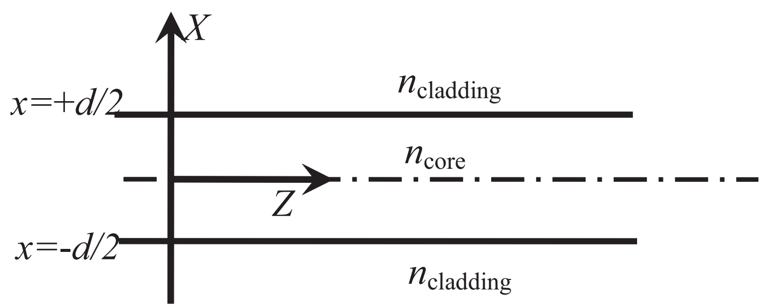

Figure 1: Dielectric planar waveguide geometry.

The solution of TM modes for the electric field may be written [12]

$$E_x = E_y = 0, \quad E_z = \begin{cases} -\dfrac{\alpha_x}{i\omega n_{\text{cladding}}^2} B e^{-\alpha_x x} e^{-i\beta z} & x > \dfrac{d}{2} \\ -\dfrac{k_x}{i\omega n_{\text{core}}^2} A \sin k_x x e^{-i\beta z} & |x| < \dfrac{d}{2} \\ -\dfrac{\alpha_x}{i\omega n_{\text{cladding}}^2} B e^{\alpha_x x} e^{-i\beta z} & x < -\dfrac{d}{2} \end{cases} \tag{6}$$

where k_x is the transverse propagation number and β is the longitudinal propagation number which is equal to the propagation number of TM mode in the core range, α_x is the transverse parameter of mode section, ω is the angular frequency of electromagnetic field, n_{core} and n_{cladding} are the refractive indices of core medium and cladding medium of the planar waveguide, respectively.

By matching the boundary conditions at $x = d/2$, we can have the determinantal equation

$$\frac{k_x}{i\omega n_{\text{core}}^2} \tan \frac{k_x d}{2} = \frac{\alpha_x}{i\omega n_{\text{cladding}}^2} \tag{7}$$

The longitudinal propagation number, β, and the transverse propagation number of k_x can be determined by combining the relations (8) as following derived from wave equations with Eq. (7).

$$\begin{aligned} \beta^2 - \alpha_x^2 &= \omega^2 \mu_0 n_{\text{cladding}}^2 = k_{\text{cladding}}^2 \\ \beta^2 + k_x^2 &= \omega^2 \mu_0 n_{\text{core}}^2 = k_{\text{core}}^2 \end{aligned} \tag{8}$$

where k_{core} and k_{cladding} are the propagation numbers in unbounded mediums of which indices are n_{core} and n_{cladding}, respectively.

The propagation number β is smaller than k_{core}, thus indicating that the phase velocity of mode is greater than the speed of an infinite plane wave in a medium with a uniform index n_{core}. This situation can not be happened in a metallic planar waveguide in which the fundamental mode is TEM mode which electric field can be written

$$E_x = \begin{cases} 0 & x > \dfrac{d}{2} \\ E_0 e^{-i\beta z} & |x| < \dfrac{d}{2}, \\ 0 & x < -\dfrac{d}{2} \end{cases} \quad E_y = 0, \quad E_z = 0 \tag{9}$$

where β is the propagation number of the TEM mode and is equal to the k_{core} if the medium with refractive index of n_{core} is sandwiched between two metallic films or plates.

We finally choose two kinds of nonlinear optical crystals which have high effective nonlinear coefficients for optical rectification process and low absorption in THz regime, GaAs and $ZnGeP_2$, after examining a large set of well known nonlinear crystals. We designed three different planar waveguide structures by using different crystals and calculated the propagation number β of TM_0 mode, the fundamental mode, and the effective index, $n_{\text{THz,eff.}}$, at a frequency ω of 2 THz according to the Eq. (10). The results are summarized in Table 2.

$$\beta_{TM_0}^2 = \omega^2 \mu_0 n_{\text{THz,eff.}}^2 \tag{10}$$

The coherence length for difference frequency mixing in waveguide configuration is becoming now

$$l_{\text{c,eff.}} = \frac{\pi c}{\omega_{\text{THz}} \left| n_{\text{opt,group}} - n_{\text{THz,eff.}} \right|} \tag{11}$$

where $n_{\text{opt,group}}$ could be still the group index at the optical pump frequency in the bulk nonlinear optical crystal because the effects of waveguide are quite weak for optical wave of which optical wavelength is much smaller than the thickness of the planar waveguide. Thus we considered that optical pulses pass the waveguide in such a way that it travel in an unlimited uniform medium.

Table 2: Three different planar waveguide structures and their coherence lengths.

	Core medium: GaAs Cladding medium: $ZnGeP_2$	Core medium: $ZnGeP_2$ Cladding medium: Si	Core medium: $ZnGeP_2$ Cladding medium: GaP
Thickness of planar waveguide [µm]	60	500	100
n_{THz} in core medium @ 2 THz	3.61	3.42	3.42
$n_{\text{THz,eff.}}$ of TM_0 mode @ 2 THz	3.5335	3.4190	3.3922
l_c @ 1550 nm [mm]	0.78	0.5155	0.5155
$l_{\text{c,eff.}}$ with waveguide @ 1550 nm [mm]	4.0	0.5191	0.637

The best result is the GaAs/$ZnGeP_2$ dielectric planar waveguide in which the effective coherent length enhances to 4 mm from 0.78 mm without waveguide structure. For GaAs/$ZnGeP_2$ waveguide, the maximum thickness of single mode planar waveguide is about 65 µm and the absorption coefficients at THz regime are 0.5 cm^{-1} and 0.1 cm^{-1} for GaAs and $ZnGeP_2$, respectively.

4. CONCLUSIONS

In summary, we demonstrated theoretically that the dielectric planar waveguide could be used to enhance the coherent length of optical rectification process in THz regime. And for the first time, a dielectric planar THz waveguide that has potential applicable value in THz generation by optical rectification method was proposed. We predicted that the effective coherent length could be extended to 4 mm at 2 THz in a GaAs/$ZnGeP_2$ dielectric planar waveguide during optical rectification process pumped by ultrafast optical pulses at wavelength of 1550 nm.

ACKNOWLEDGMENT

This work is supported partly by the National natural science foundation of China (NSFC) under the project which number is 60578022.

REFERENCES

1. Gong, Y. D., M. Y. W. Chia, and B. Luo, "Terahertz spectroscopy technology trendy using 1550-nm ultrafast fiber laser," *Micro. Opt. Tech. Letts.*, Vol. 49, No. 2, 439–443, 2007.
2. Takazato, A., M. Kamakura, T. Matsui, J. Kitagawa, and Y. Kadoya, "Detection of terahertz waves using low-temperature-grown InGaAs with 1.56 μm pulse excitation," *Appl. Phy. Letts.*, Vol. 90, No. 17, 101119, 2007.
3. Planken, P. C. M, C. E. W. M. van Rijmenam, and R. N. Schouten, "Opto-electronic pulsed THz systems," *Semicond. Sci. Technol.*, Vol. 20, S121–S127, 2005.
4. Yeh, K.-L., M. C. Hoffmann, J. Hebling, and Keith A. Nelson, "Generation of 10 μJ ultrashort terahertz pulses by optical rectification," *Appl. Phy. Letts.*, Vol. 90, No. 17, 171121, 2007.
5. Mendis, R. and D. Grischkowsky, "Undistorted guided-wave propagation of subpicosecond terahertz pulses," *Opt. Letts.*, Vol. 26, No. 11, 846–848, 2001.
6. Mendis, R., "Nature of subpicosecond terahertz pulse propagation in practical dielectric-filled parallel-plate waveguides," *Opt. Letts.*, Vol. 31, No. 17, 2643–2645, 2006.
7. Cao, H., R. A. Linke, and A. Nahata, "Broadband generation of terahertz radiation in a waveguide," *Opt. Letts.*, Vol. 29, No. 15, 1751–1753, 2004.
8. Nahata, A., A. Aniruddha, S. Weling, and T. F. Heinz, "A wideband coherent terahertz spectroscopy system using optical rectification and electro-optic sampling," *Appl. Phys. Letts.*, Vol. 69, No. 16, 2321–2323, 1996.
9. Nagaia, M., K. Tanaka, H. Ohtake, T. Bessho, T. Sugiura, T. Hirosumi, and M. Yoshida, "Generation and detection of terahertz radiation by electro-optical process in GaAs using 1.56 mm fiber laser pulses," *Appl. Phys. Letts.*, Vol. 85, No. 18, 3974–3976, 2004.
10. Kumbhakar, P., T. Kobayashi, and G. C. Bhar, "Sellmeier dispersion for phase-matched terahertz generation in $ZnGeP_2$," *Appl. Opt.*, Vol. 43, No. 16, 3324–3328, 2004.
11. Palik, E. D., *Handbook of Optical Constants of Solids*, Academic Press, London, 1985.
12. Haus, H. A., *Waves and Fields in Optoelectronics*, Prentice-Hall Inc., New Jersey, 1984.

The Role of Non-resonant Effect in Terahertz Transmission through Subwavelength Holes

Jiaguang Han[1,2], **Xinchao Lu**[1], **Abul K. Azad**[1], **Mufei Gong**[1], **and Weili Zhang**[1]
[1]School of Electrical and Computer Engineering, Oklahoma State University
Stillwater, Oklahoma 74078, USA
[2]Department of Physics, National University of Singapore, 2 Science Drive 3, 117542, Singapore

Abstract— We study the role of non-resonant effect in enhanced transmission of terahertz pulses through periodic array of subwavelength holes. The measured terahertz transmission spectra exhibit a characteristic evolution with various hole widths. The peak transmission approaches a maximum value at a critical hole width, while monotonic linewidth broadening and blueshift are observed when the hole width increases. The physical mechanism responsible for such transmission properties is closely associated with the coupling between discrete resonant excitation of surface plasmons and continuum non-resonant transmission through the holes.

1. INTRODUCTION

Recently, extraordinary transmission in two-dimensional array of subwavelength holes has been widely investigated in a broad spectral range of electromagnetic waves [1–3]. It has also demonstrated attractive interdisciplinary applications such as in photonics, optoelectronics, bioengineering, and nanofabrication. Generally, the enhanced, higher-than-unity transmission was attributed to the resonant excitation of surface plasmons (SPs) set up by the periodicity of the metallic hole array, where the light is coupled to SPs on the incidence surface of the array and reemit from the second surface afterwards. SPs are collective excitations for quantized oscillations of electrons. The resonant interaction between electron-charged oscillations near the surface of metal and the electromagnetic field creates SPs and results in rather unique properties. Recent studies in the visible spectral region have revealed that besides SPs, localized modes also make contributions to the extraordinary transmission in periodic subwavelength holes [8–10].

The recent advance focusing on this topic has been obtained in the far-infrared terahertz region by use of terahertz time-domain spectroscopy (THz-TDS). The highly conductive nature of metals at terahertz frequencies generates unique interest in extraordinary transmissions of the far infrared terahertz pulses. Experimentally, the role of the hole shape, polarization, dielectric properties of metal and substrate, and thickness of the arrays on SP-enhanced terahertz transmission have been studied [4–6]. The characteristic terahertz SPs enhanced transmission research provides us a broader and further extended understanding to the physical mechanism of this effect.

In order to better understand such transmission enhancement in the terahertz regime, here we study a series of subwavelength hole arrays with various hole widths that correspond to filling fractions of metal ranging from 81.3% to 34.4%. The measured hole width-dependent transmission spectra present a characteristic evolution, including well-regulated change in transmittance, linewidth broadening, and blueshift of peak frequencies. Such characteristic evolution can be attributed to the coupling between discrete resonant excitation of SPs and continuum non-resonant transmission through the holes; this agrees well with the numerical analysis based on the Fano model and the measured angle-resolved transmission [4, 7].

2. SAMPLE FABRICATION AND THZ-TDS EXPERIMENTS

Hexagonal arrays of rectangular subwavelength holes are 180-nm-thick Al film fabricated on a silicon wafer (0.64-mm-thick, p-type resistivity 20 Ω cm, inset of Fig. 1) by conventional photolithography. Each array, with dimensions of 15 mm × 15 mm, has holes of a fixed length 120 μm and various widths from 40 to 140 μm with a 20-μm interval, and a constant lattice period of 160 μm. The THz-TDS system used in this experiment employs photoconductive switch-based terahertz transmitter and receiver in an 8-F configuration [4]. Both the amplitude and phase information of the transmitted terahertz electrical pulses can be acquired in a single THz-TDS scan. While both transmitter and receiver are driven with an average optical pump power of 10 mW from the output of a self-mode-locked Ti: sapphire femtosecond laser of 26 fs, 86 MHz pulses, the system can generate and detect a broad band terahertz signal with a usable bandwidth extending from 0.1 to 4.5 THz. The 8-F configuration is accomplished by using an additional pair of off-axis paraboloidal mirrors of focal length 50 mm placed midway between the two major paraboloidal mirrors. As a result, a frequency independent 3.5-mm-diameter terahertz beam waist is obtained, which is smaller than the dimensions of the samples. The array is placed midway between the photoconductive transmitter and receiver in the far field at the beam waist that covers more than 370 holes. A blank silicon slab identical to the array substrate is used to obtain the reference terahertz pulses. The p-polarized terahertz electric field is perpendicular to the fixed axis of the holes. The absolute transmittance is defined as $T(\omega) = |t(\omega)|^2 = |E_{\text{out}}(\omega)/E_{\text{in}}(\omega)|^2$, where $|t(\omega)|$ is the amplitude transmission, $E_{\text{out}}(\omega)$ and $E_{\text{in}}(\omega)$ are the amplitudes of terahertz pulses through the sample and reference, respectively. The coherent measurement also provides the corresponding phase change as: $\phi(\omega) = \arg[t(\omega)]$.

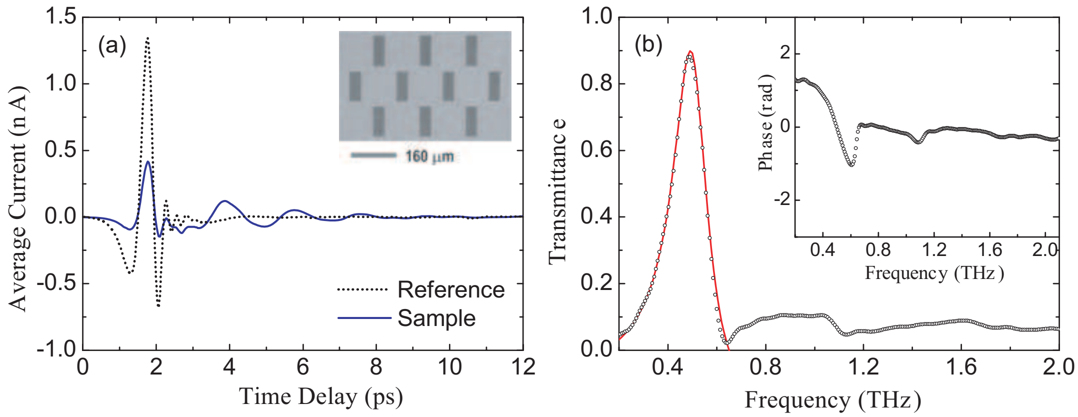

Figure 1: (a) Measured transmitted terahertz pulses through the reference and the 120 μm × 40 μm hole array. The inset shows a scanning electron microscopy (SEM) image of the array. (b) Measured (open circles) and theoretical fit by the Fano model (solid curve) of the frequency-dependent transmittance. The inset illustrates the corresponding data of phase change.

3. RESULTS AND DISCUSSION

Figure 1(a) illustrates the measured transmitted terahertz pulses through the reference and an array with hole dimensions of 120 μm×40 μm. The extracted frequency-dependent absolute transmittance is illustrated as open circles in Fig. 1(b), while the inset shows the corresponding phase change. The well-defined maximum observed around 0.49 THz in the transmittance spectrum is generally attributed to the resonant excitation of SPs at the metal-dielectric interface. In such hole arrays, SPs can be resonantly excited at the Al-Si interface by conserving the momentum match: $\mathbf{k_{sp}} = \mathbf{k}_{||} + \mathbf{G}$, where $\mathbf{k_{sp}}$ is the wave vector of SPs, $\mathbf{k}_{||}$ is the in-plane wave vector with $\mathbf{k}_{||} = (\omega/c)\sin\theta$, $\mathbf{G}$ is the reciprocal lattice vectors, and θ is the incidence angle [1]. At normal incidence, the in-plane wave vector becomes zero; the resonant frequency in the THz region can be approximately given as $\omega_{SP}^{m,n} \cong cG_m\varepsilon_d^{-1/2}$, [1, 3] where $G_{mn} = 4\pi\left(m^2 + n^2 + mn\right)^{1/2}/\sqrt{3}L$ is the grating momentum wave vector for hexagonal hole arrays, L is the lattice constant, m and n are the integer mode indices, ε_d is the dielectric constant of the medium, here $\varepsilon_d = 11.68$ for silicon; the contribution of the imaginary dielectric constant of lightly doped silicon can be negligible.

The measured transmittance is analyzed by the Fano model that involves two types of scattering processes: one refers to the continuum direct scattering state, and the other is the discrete resonant state [4, 7, 11]. For an isolated resonance, the Fano model can be written as $T_{fano(\omega)} = |t(\omega)|^2 = T_a + T_b(\varepsilon_v + q_v)^2/(1 + \varepsilon_v^2)$, where $\varepsilon_v = (\omega - \omega_v)/(\Gamma_v/2)$, T_a is a slowly varying transmittance, and $|T_b|$ is the contribution of a zero-order continuum state that couples with the discrete resonant state. The resonant state is characterized by the resonance frequency ω_v, the linewidth Γ_v, and the Breit-Wigner-Fano coupling coefficient q_v. Considering that such transmission behavior is resulted from two contributions: the resonant excitation of SPs as the discrete resonant state and the direct continuum state, namely the non-resonant terahertz transmission, the Fano model provides a consistent fit (solid curve) to the measured transmittance shown in Fig. 1(b), with a single resonance at $\omega_v/2\pi = 0.49$ THz and linewidth $\Gamma_v/2\pi = 0.16$ THz.

To understand clearly the coupling between SPs and non-resonant transmission, we have characterized arrays with various hole widths from 40 to 140 μm. The measured peak transmission frequencies and the corresponding linewidths of these arrays shown in Fig. 2(a) reveals a char-

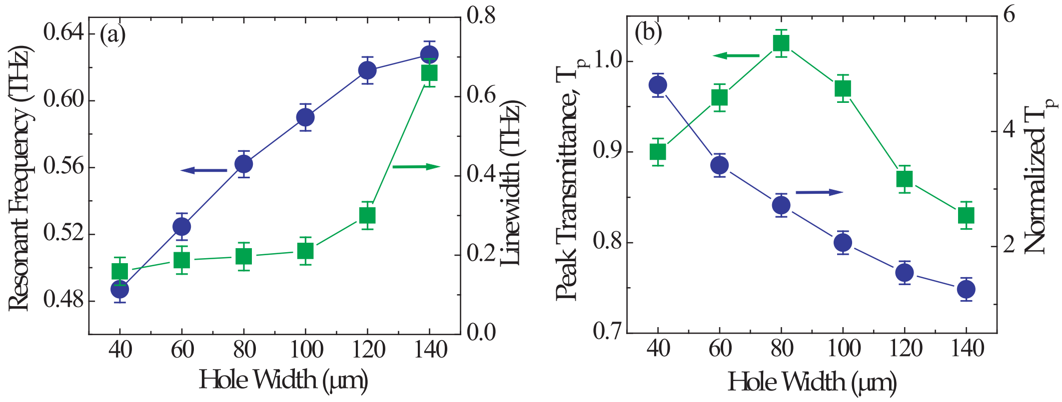

Figure 2: (a) Measured peak transmission frequencies (dots) and the corresponding linewidths (squares) of the hole arrays with fixed hole length of 120 μm and various hole widths from 40 to 140 μm with an interval of 20 μm. (b) Absolute (squares) and normalized (dots) peak transmittance as a function of hole width. The solid lines are the guide to the eye.

acteristic evolution with respect to hole widths. The resonance frequency and the corresponding linewidth exhibit monotonic changes. As the hole width increases from 40 to 140 μm, the peak transmission is shifted from 0.49 to 0.63 THz, while the corresponding linewidth is broadened from 0.16 to $\sim$ 0.66 THz. As shown in Fig. 2(b), the peak absolute transmittance T_p (squares) is enhanced with increasing hole width of up to 80 μm, however, the further increase in hole width beyond 80 μm gives rise to a monotonic decay in T_p. At hole width of 40 μm, T_p has a value of 0.9, whereafter it is enhanced to $\sim$ 1.0 at 80 μm, and then is reduced to 0.83 at 140 μm. This suggests that there exists an optimal hole width, at which T_p approaches a maximum value.

Taking the contribution of in-plane wave vector $k_{||} = (\omega/c)\sin\theta$ into account, the resonance frequency of SPs exhibits dependence on incidence angle θ, whereas the non-resonant transmission is angle independent. As shown by Fig. 3(a), even for the 120 μm × 80 μm holes, the angle-dependent transmission can be seen clearly denoting a main role of SPs. For the 120 μm × 120 μm holes, the scattering state becomes dominant. This agrees well with the experimentally observed angle-resolution measurements as shown in Fig. 3(b). The angle-dependent low-frequency peak near 0.54 THz is originated from SPs, while the angle-independent peak at 0.63 THz is due to the effect of direct scattering. Further details can be seen from the measured full bandstructure sketched in the inset of Fig. 3(b). An energy gap of $\sim$ 0.36 meV between the two peaks is clearly resolved at incident angle above 9°.

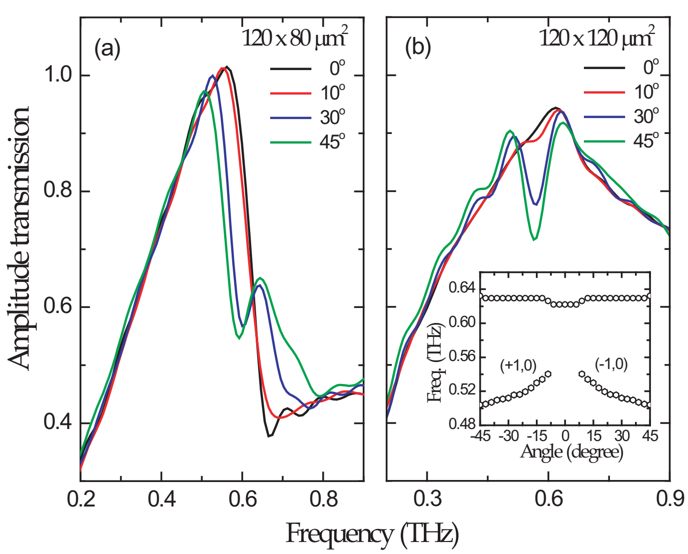

Figure 3: The incident angle dependent amplitude transmission for the arrays with (a) 120 μm × 80 μm holes, and (b) 120 μm × 120 μm holes. The inset of (b) sketches the detailed angle-resolved bandstructure.

The coupling strength between SPs and non-resonant transmission for arrays with different hole widths at normal incidence is calculated based on the Fano Hamiltonian, $\hat{H} = \hat{H}_{SP} + \hat{H}_{NRT} + \hat{H}_{Coupling}$. With increasing hole width the coupling strength is enhanced monotonically from $|\chi|^2 = 1.22 \times 10^{-3}$ at $40\,\mu$m to $|\chi|^2 = 6.21 \times 10^{-3}$ at $140\,\mu$m. This further explains the measured characteristic evolution in the transmission spectra of these arrays. The increase in hole width, that corresponds to reduced aspect ratio of holes and lower filling fraction of metal, not only leads to increased direct transmission through the holes, but also enhances the coupling between SPs and non-resonant transmission. This in turn gives rise to an increased damping of SPs and thus the linewidth broadens and shifts to higher frequencies towards the peak of non-resonant transmission.

4. CONCLUSION

We present THz-TDS studies of transmission properties of periodic subwavelength holes of various widths. Frequency-dependent transmittance in the terahertz regime is characterized by two processes: resonant excitations of SPs and non-resonant transmission through the holes. The coupling between these two processes is enhanced with increasing hole width, leading to a characteristic evolution in transmittance, linewidth, and peak frequency. An optimal hole width exists, at which the peak transmittance approaches a maximum value. This is essential in design of terahertz plasmonic devices; in particular, when control of transmission and linewidth is needed, such as for bandpass terahertz filters.

ACKNOWLEDGMENT

This work was partially supported by the National Science Foundation of USA.

REFERENCES

1. Ebbesen, T. E., H. J. Lezec, H. F. Ghaemi, T. Thio, and P. A. Wolff, "Extraordinary optical transmission through sub-wavelength hole arrays," *Nature*, Vol. 391, 667–669, London, 1998.
2. Ghaemi, H. F., T. Thio, D. E. Grupp, T. W. Ebbesen, and H. J. Lezec, "Surface plasmons enhance optical transmission through subwavelength holes," *Phys. Rev. B*, Vol. 58, 6779–6782, 1998.
3. Qu, D., D. Grischkowsky, and W. Zhang, "Terahertz transmission properties of thin subwavelength metallic hole arrays," *Opt. Lett.*, Vol. 29, 896–898, 2004.
4. Han, J. G., A. K. Azad, M. F. Gong, X. C. Lu, and W. Zhang, "Coupling between surface plasmons and nonresonant transmission in subwavelength holes at terahertz frequencies," *Appl. Phys. Lett.*, Vol. 91, 071122–1–3, 2007.
5. Azad, A. K., M. He, Y. Zhao, and W. Zhang, "Effect of dielectric properties of metals on terahertz transmission in subwavelength hole arrays," *Opt. Lett.*, Vol. 31, 2637–2639, 2006.
6. Azad, A. K. and W. Zhang, "Resonant terahertz transmission in subwavelength metallic hole arrays of sub-skin-depth thickness," *Opt. Lett.*, Vol. 30, 2945–2947, 2005.
7. Genet, C., M. P. van Exter, and J. P. Woerdman, "Fano-type interpretation of red shifts and red tails in hole array transmission spectra," *Opt. Commun.*, Vol. 225, 331–336, 2003.
8. Degiron, A. and T. W. Ebbesen, "The role of localized surface plasmon modes in the enhanced transmission of periodic subwavelength apertures," *J. Opt. A: Pure Appl. Opt.*, Vol. 7, S90–S96, 2005.
9. Molen, K., K. Koerkamp, S. Enoch, F. Segerink, N. Kulst, and Kuipers, "Role of shape and localized resonances in extraordinary transmission through periodic arrays of subwavelength holes: Experiment and theory," *L. Phys. Rev. B*, Vol. 72, 045421–1–9, 2005.
10. Ruan, Z. and M. Qiu, "Enhanced transmission through periodic arrays of subwavelength holes: The role of localized waveguide resonances," *Phys. Rev. Lett.*, Vol. 96, 233901–1–4, 2006.
11. Zhang, W., A. K. Azad, J. G. Han, J. Xu, J. Chen, and X.-C. Zhang, "Direct observation of a transition of a surface plasmon resonance from a photonic crystal effect," *Phys. Rev. Lett.*, Vol. 98, 183901–1–4, 2007.

Terahertz Response of Bulk and Nanostructured ZnO

Jiaguang Han[1, 2], **Wei Chen**[3], **J. Zhang**[4]
Mingxia He[1, 5], **A. K. Azad**[1], **S. Ray**[1], **Y. Zhao**[6], **and Weili Zhang**[1]

[1]School of Electrical and Computer Engineering, Oklahoma State University
Stillwater, Oklahoma 74078, USA
[2]Department of Physics, National University of Singapore, 2 Science Drive 3, 117542, Singapore
[3]Department of Physics, University of Texas at Arlington, Arlington, TX 76019, USA
[4]College of Chemistry and Chemical Engineering, Inner Mongolia University
Hohhot, Inner Mongolia 010021, China
[5]Center for Terahertz waves and College of Precision Instrument and Optoelectronics Engineering
Tianjin University, Tianjin 300072, China
[6]Department of Physics and Astronomy, University of Georgia, Athens, GA 30602, USA

Abstract— We present experimental characterization of far-infrared optical and dielectric properties of single-crystal ZnO and nanostructured ZnO of different morphologies by terahertz time-domain spectroscopy. Frequency dependent complex dielectric function, power absorption, and refractive index of single-crystal, nanowire, tetrapod, tubular, and prismlike ZnO structures are experimentally measured in the terahertz regime, respectively. The experimental results are analyzed and well fit with dielectric theories and effective medium models.

1. INTRODUCTION

As an II-VI semiconductor, Zinc oxide (ZnO) with a room-temperature wide band gap 3.37 eV, has attracted much attention because of their unique properties and large span of promising applications in electro-optic, acousto-optic, optoelectronic devices, ultraviolet (UV) light emitters, chemical sensors, and piezoelectric materials [1–4]. The increasing interest not only focus on bulk crystal, but also much more on the nanocrystalline ZnO. ZnO nanostructures have potential applications for piezoelectric transduction, optical emission, catalysis, actuation, drug delivery, and optical storage with promising photoelectronic, photochemical, and catalytic properties [4]. In the terahertz regime, ZnO possesses a number of advantages in terms of device applications, such as ease in fabrication, wide band gap, rather high mobility and resistivity, and transparent in a broad terahertz frequency range [5–7]. It thus is essential to explore the detailed optical and dielectric properties of ZnO in the broad terahertz frequency region. Here, we present far-infrared optical properties and the complex dielectric function of high-resistivity bulk crystal and nanostructured ZnO, including wire, tetrapod, tubular, and prismlike structures characterized by terahertz time-domain spectroscopy (THz-TDS). The measured refractive index, power absorption, and complex dielectric function are well fit by appropriate theoretical models.

2. SAMPLE PREPARATION AND THZ-TDS EXPERIMENTS

The single-crystal ZnO is an undoped, 5 mm×5 mm×0.5-mm-thick, <0001>-oriented slab with c-axis perpendicular to the surface (MTI Corporation, USA). Hydrothermal growth method was used to fabricate the wurtzite, high-resistivity ZnO with purity higher than 99.99%. The detailed fabrication processes of the nanostructured ZnO as shown in Fig. 1 were described elsewhere [8–11]. The ZnO samples are characterized by use of a photoconductive switch-based THz-TDS system with a useful bandwidth of 0.1–4.5 THz and a signal to noise ratio (S/N) of $>1.5\times10^4 : 1$ [11].

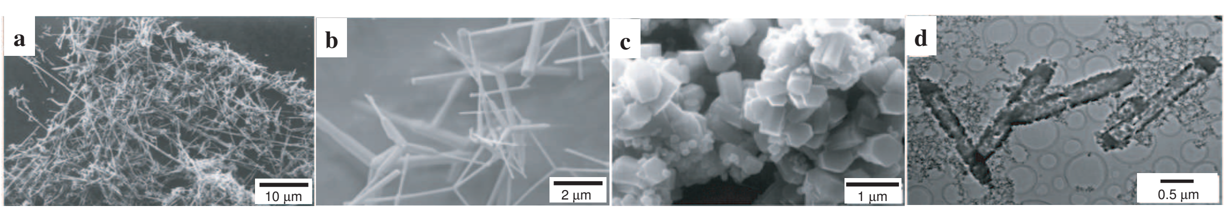

Figure 1: Scanning electron microscopic images of (a) nanowire, (b) tetrapod, (c) tubular, and (d) prismlike ZnO structures.

3. RESULTS AND DISCUSSIONS

3.1. Single-crystal ZnO

The measured power absorption $\alpha(\omega)$ and the refractive index $n(\omega)$of single-crystal ZnO are shown in Figs. 2(a) and 2(b). The power absorption increases with increasing frequency and no prominent absorption peaks are observed below 3.5 THz. This can be verified by the refractive index which shows no remarkable features as well. Employing the measured data of power absorption and refractive index, we obtain the frequency-dependent complex dielectric function through the relation: $\varepsilon(\omega) = (n_r + in_i)^2$, where the imaginary part of the refractive index n_i is related to the power absorption as $n_i = \alpha\lambda/4\pi$. The filled circles shown in Figs. 2(c) and 2(d) represent the recorded data of complex dielectric constant. Generally, optical absorption of ionic crystals in the terahertz region originates from lattice vibrations. The interaction of a radiation field with the fundamental lattice vibration results in absorption of electromagnetic wave due to creation or annihilation of lattice vibration. In the frame of the classical theory of independent pseudo-harmonic approximation, such process can be described below, considering the phonon contribution to dielectric function [12]: $\varepsilon_m(\omega) = \varepsilon_\infty + (\varepsilon_0 - \varepsilon_\infty)\omega_{TO}^2/(\omega_{TO}^2 - \omega^2 - i\gamma\omega)$, where ε_∞ is the high-frequency dielectric constant, ε_0 is the low frequency dielectric constant, ω_{TO} is the frequency of the transverse optical (TO) phonon mode, and γ is the damping constant. Three parameters are used to fit the experimental data: $\varepsilon_0 = 7.77$, $\omega_{TO}/2\pi = 12.42$ THz and $\gamma/2\pi = 0.82$ THz. Given the high-frequency dielectric constant $\varepsilon_\infty = 3.705$, the frequency-dependent complex dielectric constant is obtained. This theoretical calculation gives well fit on the data measured by THz-TDS, as shown by solid curves in Fig. 2.

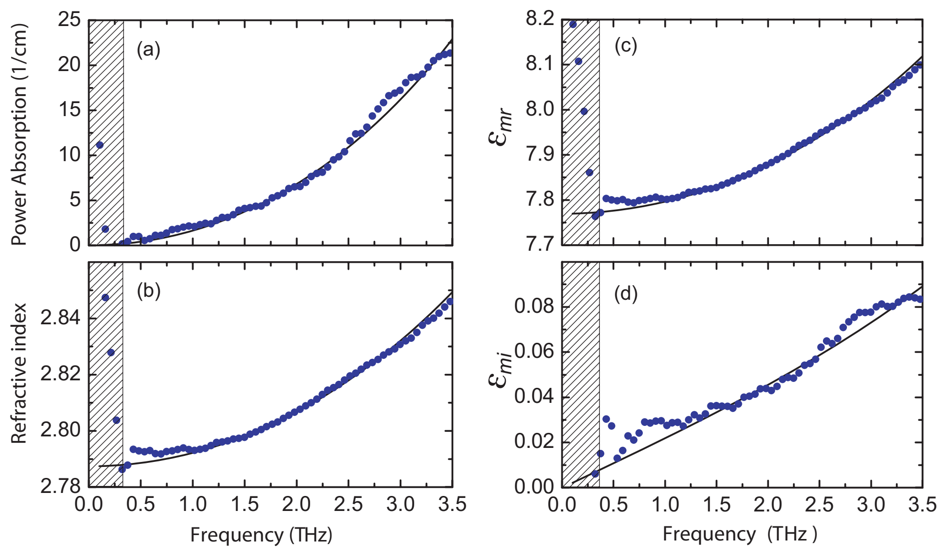

Figure 2: Comparison of THz-TDS data (filled circles) with theoretical fitting (solid curves) for (a) power absorption, (b) refractive index, (c) real part of dielectric constant ε_{mr}, and (d) imaginary dielectric constant ε_{mi}.

3.2. ZnO Nanowires and Tetrapods

In Fig. 3, we present THz-TDS results on ZnO nanowires and tretrapods. The measured absorption coefficients are represented by filled circles in Figs. 3(a) and 3(b), and the index of refraction is shown in Figs. 3(c) and 3(d), respectively, for nanowires and tetrapods. These two nanostructures exhibit a similar absorption behavior, which increases steadily with increasing frequency. The extracted real and imaginary parts of complex dielectric function are depicted by the filled circles in Figs. 3(e)–3(h). Because the measured samples are composites of nanostructures and air, the given complex dielectric constant is called effective dielectric constant that consists of contributions from both pure ZnO nanostructures and air. The effective dielectric function can be treated by simple effective medium theory, $\varepsilon_{eff}(\omega) = f\varepsilon_m(\omega) + (1-f)\varepsilon_h$, where the dielectric function of pure ZnO nanostructures ε_m is calculated based on the pseudo-harmonic model. The filling factor f defines the volume fraction of pure nanostructures and was measured directly in the experiment; ε_h is dielectric constant of the host medium, giving $\varepsilon_h = \varepsilon_{air} = 1.0$ for air. The absorption responses of pure ZnO nanowires and tetrapods are mainly attributed to lattice vibration, which is well described theoretically by the classical pseudo-harmonic phonon model. The good agreement between the experimental data and theoretical fitting, as shown by the solid curves in Fig. 3, implies that the absorption of both nanowires and tetrapods are dominated by the transverse optical mode localized at $\omega_{TO}/2\pi = 12.41 \pm 0.2\,\mathrm{THz}$, with linewidths $\gamma/2\pi = 12.5 \pm 0.2\,\mathrm{THz}$ and $\gamma/2\pi = 21.0 \pm 0.2\,\mathrm{THz}$, respectively. This feature is quite consistent with what has been observed in bulk single-crystal ZnO. This indicates that ZnO nanowires and tetrapods exhibit similar dielectric properties as those for bulk ZnO.

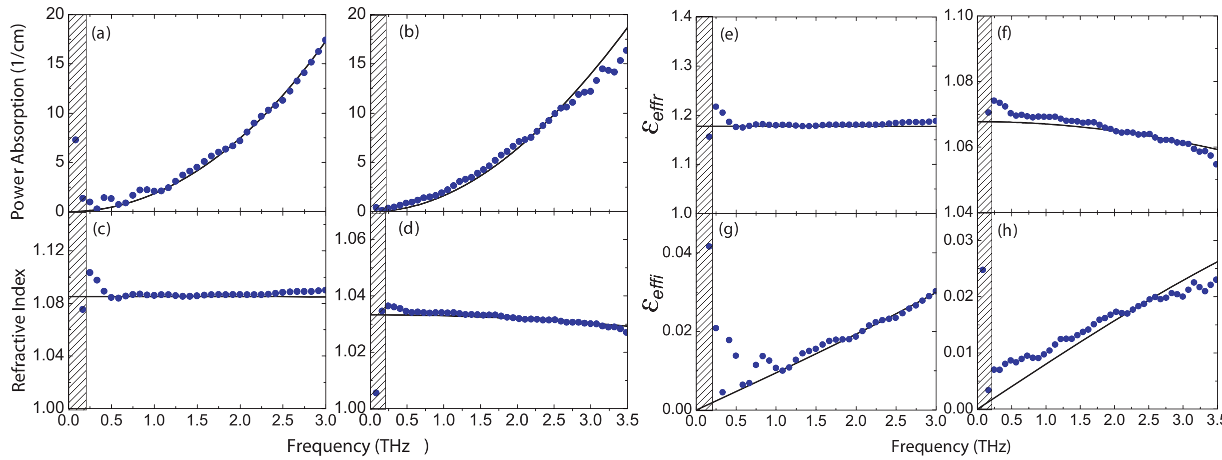

Figure 3: Comparison of THz-TDS measurements (filled circles) and theoretical fitting (solid curves) of ZnO nanowires and tetrapods for power absorption: (a) nanowires and (b) tetrapods; refractive index: (c) nanowires and (d) tetrapods; real dielectric constant ε_{effr}: (e) nanowires and (f) tetrapods; imaginary dielectric constant ε_{effi}: (g) nanowires and (h) tetrapods.

3.3. Tubular and Prismlike ZnO

The filled circles in Fig. 4 illustrate the measured data for tubular and prismlike ZnO structures. The absorption behavior shown in Figs. 4(a) and 4(b) appears very similar to those observed in nanowires and tetrapods and it steadily increases with frequency. However, it can be seen clearly that both the tubular and prismlike structures have significant higher absorption than those of nanowires or tetrapods. At 1.0 THz, the power absorptions for both samples are higher than $200\,\mathrm{cm}^{-1}$. The refractive index, as shown in Figs. 4(c) and 4(d), exhibits a monotonic decrease with increasing frequency. These prominent distinctions than those for nanowires and tetrapods due to morphology implicate that different response mechanism is involved in the absorption process in tubular and prismlike ZnO samples. The real and imaginary parts of complex dielectric constants, as shown in Figs. 4(e)–4(h), further indicate that diverse mechanisms are responsible for the dielectric properties of tubular and prismlike structures.

It is well known that for most metals and semiconductors, optical absorption is caused by the interaction of incident light with free carriers. The most commonly used model to describe such dielectric response process is the Drude model, $\varepsilon_m(\omega) = \varepsilon_{mr} + i\varepsilon_{mi} = \varepsilon_\infty - \omega_p^2/(\omega^2 + i\gamma\omega)$. Taking the contribution of free electrons through the Drude model and the contribution of air from Bruggeman effective medium theory [11, 13]: $f\lfloor(\varepsilon_m - \varepsilon_{eff})/(\varepsilon_m + 2\varepsilon_{eff})\rfloor + (1-f)\lfloor(\varepsilon_h - \varepsilon_{eff})/(\varepsilon_h + 2\varepsilon_{eff})\rfloor = 0$ into account, we obtain good fits to the THz-TDS data of tubular and prismlike ZnO samples. As shown by solid curves in Fig. 4, the measured power absorption, index of refraction, and the corresponding complex dielectric constant are well reproduced. From our results, we clearly see that ZnO nanostructures exhibit quite different characteristics due to various morphologies. In fact, besides morphologies, many factors have influences on the optical and dielectric properties of ZnO nanostructures as well, such as growth conditions, environment, impurities, defects, and so on. Therefore, it is not surprising that the mechanism for terahertz absorption response of ZnO nanowires and tetrapods, similar to that in single-crystal ZnO, is mainly dominated by the interaction of incident light with lattice vibrations, while it is ascribed to the contributions from free electrons for tubular and prismlike structures.

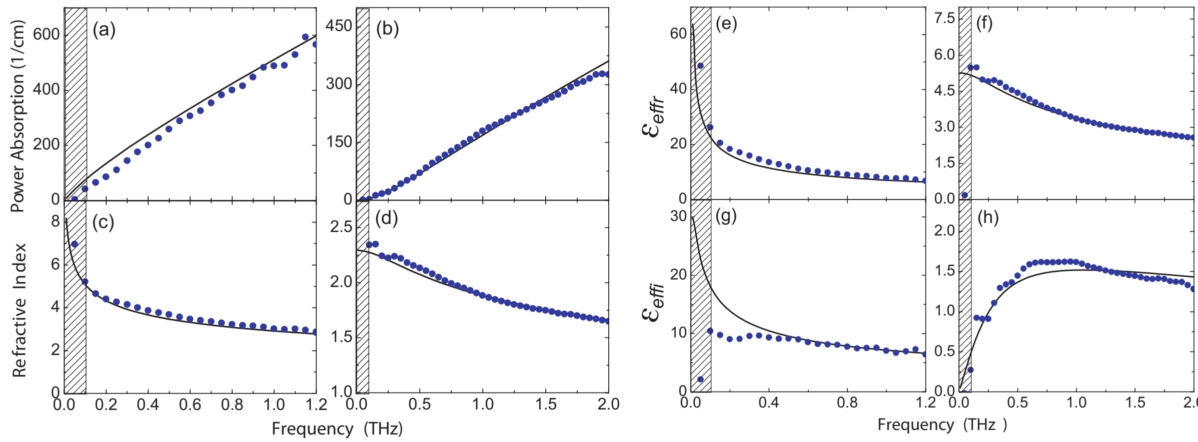

Figure 4: Comparison of THz-TDS measurements (filled circles) and theoretical fitting (solid curves) of tubular and prismlike ZnO for power absorption: (a) tubes and (b) prisms; refractive index: (c) tubes and (d) prisms; real dielectric constant ε_{effr}: (e) tubes and (f) prisms; imaginary dielectric constant ε_{effi}: (g) tubes and (h) prisms.

4. CONCLUSION

We have studied the far-infrared dielectric and optical properties of bulk and nanostructured ZnO. The THz-TDS data for power absorption, refractive index, and complex dielectric function of these samples are well fit by dielectric models combined with the effective medium theories. Our THz-TDS characterization implicates that the dielectric function of ZnO nanowires and tetrapods, similar to those in bulk ZnO, is related to the E_1(TO) phonon mode at 12.41 THz. However, the tubular and prismlike structures exhibit the Drude behavior due to the dominant role of free electrons in terahertz dielectric response. The dissimilar and similar properties of different ZnO nanostructures are related to morphologies, growth processes, defects, and impurities.

ACKNOWLEDGMENT

This work was partially supported by the National Science Foundation and the Oklahoma EPSCoR for the National Science Foundation

REFERENCES

1. Wang, Z. L., "Zinc oxide nanostructures: growth, properties and applications," *J. Phys: Condens. Matter*, Vol. 16, R829–R858, 2004.
2. Fang, Z. and J. G. Lu, "Zinc oxide nanostructures: synthesis and properties," *J. Nanosci. Nanotech.*, Vol. 5, 1561–1573, 2005.
3. Özgür, Ü., Y. I. Alivov, C. Liu, A. Teke, M. A. Reshchikov, S. Doğan, V. Avrutin, S. J. Cho, and H. Morkoç, "A comprehensive review of ZnO materials and devices," *J. Appl. Phys.*, Vol. 98, 041301-1-103, 2005.
4. Tian, Z. R., J. A. Voigt, J. Liu, B. Mckenzie, M. J. McDermott, M. A. Rodriguez, H. Kngishi, and H. Xu, "Complex and oriented ZnO nanostructures," *Nature Mater.*, Vol. 2, 821–826, 2003.
5. Ono, S., H. Murakami, A. Quema, G. Diwa, N. Sarukura, R. Nagasaka, Y. Ichikawa, E. Oshima, H. Ogino, A. Yoshikawa, and T. Fukuda, *Technical Digest of CLEO'2005*, MD (CD ROM), Paper CThX6, 22–27, Baltimore, May 2005.
6. Baxter, J. B. and C. A. Schmuttenmaer, "Conductivity of ZnO nanowires, nanoparticles, and thin films using time-resolved terahertz spectroscopy," *J. Phys. Chem. B*, Vol. 110, 25229–25239, 2006.
7. Han, J. G., Z. Y. Zhu, S. Ray, A. K. Azad, W. Zhang, M. He, S. Li, and Y. Zhao, "Optical and dielectric properties of ZnO tetrapod structures at terahertz frequencies," *Appl. Phys. Lett.*, Vol. 89, 031107-1-3, 2006.
8. Zhang, J., L. D. Sun, H. Y. Pan, C. S. Liao, and C. H. Yan, "ZnO nanowires fabricated by a convenient route," *New Journal of Chemistry*, Vol. 26, 33–34, 2002.
9. Zhang, J., L. D. Sun, C. S. Liao, and C. H. Yan, "A simple route towards tubular ZnO," *Chem. Commun.*, Vol. 3, 262–263, 2002.

10. Zhang, J., L. D. Sun, J. L. Yin, H. L. Su, C. S. Liao, and C. H. Yan, "Control of ZnO morphology via a simple solution route," *Chemistry of Materials*, Vol. 14, 4172–4177, 2002.
11. Han, J. G., W. Zhang, W. Chen, S. Ran, J. Zhang, M. X. He, A. K. Azad, and Z. Y. Zhu, "Terahertz dielectric properties and low-frequency phonon resonances of ZnO nanostructures," *J. Phys. Chem. C*, Vol. 111, 13000–13006, 2007.
12. Balkanski, M., *Optical Properties of Solids*, edited by F. Abelès (North-Holland, New York, 1972), Chap. 8.
13. Weissker, H., J. Furthmuller, and F. Bechstedt, "Validity of effective-medium theory for optical properties of embedded nanocrystallites from *ab initio* supercell calculations," *Phys. Rev. B*, Vol. 67, 165322-1-5, 2003.

Terahertz Time-domain Spectroscopy Signature of Animal Tissues

Mingxia He[1], **Meng Li**[1], **and Weili Zhang**[1,2]

[1]Center for Terahertz Waves, College of Precision Instrument and Optoelectronics Engineering
Tianjin University, Tianjin 300072, China
[2]School of Electrical and Computer Engineering, Oklahoma State University
Stillwater, Oklahoma 74078, USA

Abstract— The terahertz time-domain spectroscopy becomes a promising technology in studies of biological tissues, genetic analysis, and cancer diagnosis. Due to the fact that biological tissues possess high level of hydration, it results in strong absorption at terahertz frequencies. Here, we present terahertz time-domain spectroscopy characterization of animal tissues, including skin, fat, and muscles from porcine and rat samples. The experimental data reveal different frequency-dependent responses to terahertz radiation for difference types of tissues from these two animals. As being consistent with the estimation from the time-domain transmitted pulses and the corresponding spectra, the absorption coefficient of skin tissue is obviously lower than that of muscle by an average of 10%. Compared to skin and muscle, the fat tissue shows extremely low absorption at terahertz frequencies due to very low water content. At 0.5 THz, the power absorption coefficients of skin and lean pork are all above $100\,\mathrm{cm}^{-1}$, while it is only $15\,\mathrm{cm}^{-1}$ for porcine fat.

Owing to the non-ionizing, non-invasive, coherent quasi-optic, and phase sensitive properties, terahertz radiation has wide range applications in spectroscopy, imaging, and sensing. There has been an increasing interest in using terahertz time-domain spectroscopy (THz-TDS) in biology, chemistry and medicine research, such as disease diagnostics, recognition of DNA and bimolecules, and quality control of drugs [1–7, 14].

Since many protein and DNA molecules have distinct signatures in the terahertz spectral region, THz-TDS has been used to identify various types of DNA from low frequency vibrational modes toward label free genetic diagnosis. Recently, various terahertz imaging techniques have been developed and demonstrated in the diagnosis of human and animal tumors. Terahertz pulse imaging (TPI) has been applied to identify human skin cancer, basal cell carcinoma (BCC) both *in vitro* and *in vivo* [8, 9]. By analyzing the image data from both time and frequency domain, the border zone between normal and diseased tissue can be well determined by TPI. Terahertz dark-field imaging of canine cancerous tissue has also been reported which also demonstrated the promising capability of terahertz imaging in tumor detection and diagnosis [3].

As well known that water shows strong absorption at terahertz frequencies ($\alpha = 200\,\mathrm{cm}^{-1}$ at 1.0 THz) [10, 11]. Biomedical tissues with different water content have different response to terahertz radiation. The application of terahertz imaging in cancer diagnosis is based on the fact that THz-TDS is capable to differentiate between diseased and normal tissue owing to the variation in water content. Since cancerous tissue has higher hydration compared to healthy tissue, it shows increased absorption in the terahertz spectral region. This enables tumor diagnosis using terahertz imaging modality with reasonably high contrast.

Theoretical simulation has also confirmed that water plays a major role in distinction between diseased and normal tissue [10]. Different type of normal tissues, however, has different water content as well. By looking at the transmission properties, one can obtain terahertz signatures of various biomedical tissues. In this paper, we present terahertz transmission characterization of animal tissues taken from pork and rat. The power absorption data derived from THz-TDS measurements reveal clear distinction between different types of tissues.

In the THz-TDS experimental setup, the generation and detection of terahertz electromagnetic pulses employ photoconductive switching transmitter and receiver. Femtosecond, 800-nm optical pulses generated from a self-mode-locked Ti:Sapphire laser are used to gate the photoconductive switches. The terahertz setup has four parabolic mirrors arranged in an 8-F confocal geometry [12]. This 8-F confocal system not only ensures excellent beam coupling between the transmitter and receiver but also compresses the terahertz beam to a frequency independent diameter of 3.5 mm. The THz-TDS system has a useful bandwidth of 0.1 to 4.5 THz (3 mm–67 μm) and a signal to noise ratio (S/N) of $> 10000 : 1$.

Two groups of animal samples are characterized. Group I includes skin, fat and lean tissue of pork; group II includes skin and lean tissue of rat. Prior to the THz-TDS measurements, the tissues were sliced into thin and parallel slabs with area dimensions of 10 mm × 10 mm after being frozen for few hours. In order to accurately determine the sample thickness, as well as the power absorption coefficient, the thawed tissue was gently placed in between two 636-μm-thick high-quality silicon slabs with a p-type resistivity of 20 Ω cm. The tissue thickness was obtained by measuring the thickness of the silicon-tissue-silicon sandwich using a Mitutoyo table-top micrometer and each thickness data was an average of 10 measurements. In the THz-TDS experiments, a silicon-air-silicon sandwich with identical thickness was used as a reference.

Figure 1 shows the schematic diagram of the reference- and sample-silicon sandwiches. $E_{ref}(\omega)$ and $E_{tis}(\omega)$ represent the Fourier transformed spectra of the transmitted terahertz pulses from the reference and tissue sample, respectively. The transmitted time-domain terahertz pulses and the corresponding spectra of the reference and the pork tissues are shown in Fig. 2. The tissue samples characterized here include fat, skin and lean tissues of pork with thickness of 1.10 mm, 1.14 mm and 1.09 mm, respectively. As the results of optical dispersion and the frequency-dependent absorption, the terahertz pulses shown in Fig. 2(a) have different level of broadening, phase shift and amplitude attenuation as propagated through the tissue samples. Due to high water content the skin and lean tissues show very weak terahertz signals that are multiplied by 700 to compare with the amplitude signal of reference. The fat tissue, however, owing to very low level of hydration, shows strong transmission signal which is more than two orders of magnitude higher than that from skin and lean tissues. On the other hand, we observe that the terahertz signal from skin tissue is obviously stronger compared to that from lean tissue, which is also resulted from the difference of water content. As water absorption increases with increasing terahertz frequency, the transmission spectra of skin and lean tissue plotted in Fig. 2(b) show very narrow bandwidth, indicating that such tissue with 1-mm-thickness is nearly opaque to terahertz radiation at frequencies above 0.7 THz.

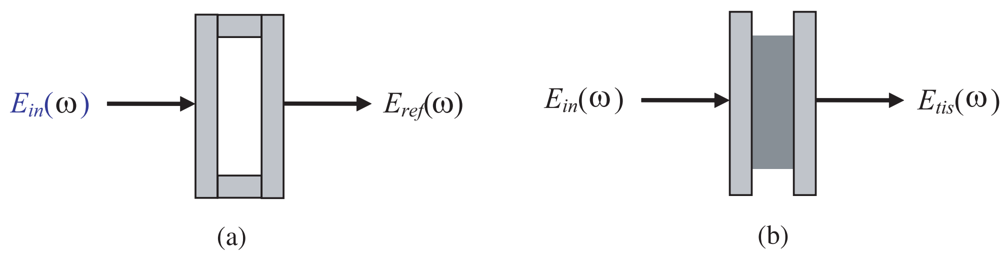

Figure 1: (a) Reference silicon cell made of silicon-air-silicon sandwich, (b) Identical silicon cell filled with animal tissue.

The power absorption of the animal tissues is extracted based on the transmitted pulses. Because of the clear separation in time domain between the transmitted and the first reflected pulse, the multiple reflection effect of the sandwiches is ignored in the data analysis. The complex transmission spectra of the reference $E_{ref}(\omega)$ and the tissue sample $E_{tis}(\omega)$ are given by

$$E_{ref}(\omega) = E_{in}(\omega)t_{sa}t_{as}(ik_0d) \tag{1}$$
$$E_{tis}(\omega) = E_{in}(\omega)t_{st}t_{ts}(ikd)(-\alpha d/2) \tag{2}$$

where $E_{in}(\omega)$ is the incident pulse spectrum, $k_0 = 2\pi/\lambda_0$ and $k = 2\pi n_t/\lambda_0$ are the wave vectors for air and sample, respectively; n_t is the refractive index of the tissue sample, d is the sample thickness, λ_0 is the free-space wavelength, and α is the power absorption coefficient of the tissue; t_{sa}, t_{as}, t_{st}, and t_{ts} are the Fresnel transmission coefficients of the terahertz pulses propagating through silicon-air, air-silicon, silicon-tissue, and tissue-silicon interfaces, respectively, which are given by $t_{sa} = 2n_s/(1+n_s)$, $t_{as} = 2/(1+n_s)$, $t_{st} = 2n_s/(n_s+n_t)$, and $t_{ts} = 2n_t/(n_s+n_t)$. The t_{st} and t_{ts} are the complex, frequency-dependent coefficients related to the tissue samples.

Figure 3(a) shows the power absorption coefficients of the pork samples. Among different type of pork tissues, lean pork shows the highest absorption and the frequency-dependent value is compatible with the previous measurement of pork-muscle tissue [13]. As being consistent with the estimation from the time-domain transmitted pulse and the corresponding spectra, the absorption coefficient of skin tissue is obviously lower than that of lean pork by an average of 10%. Compared to skin and lean pork, the fat tissue shows extremely low absorption at terahertz frequencies due

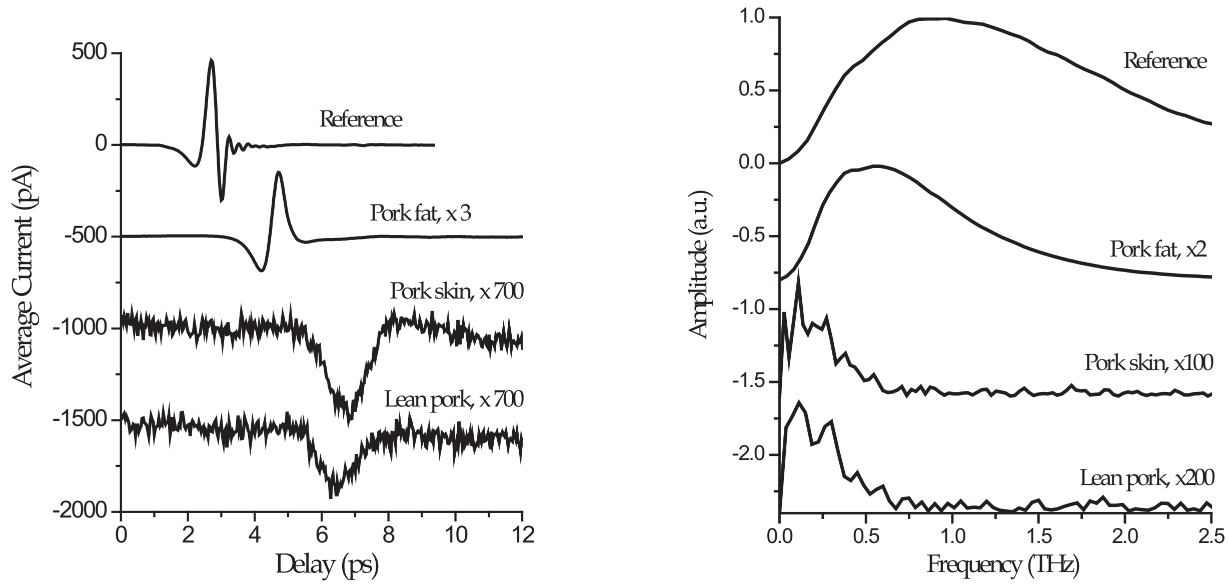

(a) (b)

Figure 2: THz-TDS curves of pork tissues. (a) Transmitted terahertz pulses of reference, fat, skin and lean tissue of pork, (b) The corresponding Fourier-transformed spectra. The thickness of the measured samples is 1.10 mm (fat), 1.14 mm (skin) and 1.09 mm (lean pork), respectively. The curves are vertically displaced for clarity.

to very low water content. At 0.5 THz, the power absorption coefficients of skin and lean pork are all above $100\,\mathrm{cm}^{-1}$, while it is only $15\,\mathrm{cm}^{-1}$ for pork fat. Clearly, the power absorption coefficient provides a quantitative response of the tissue samples to terahertz radiation, which enables the differentiation of various types of biological tissues using terahertz spectroscopy technique.

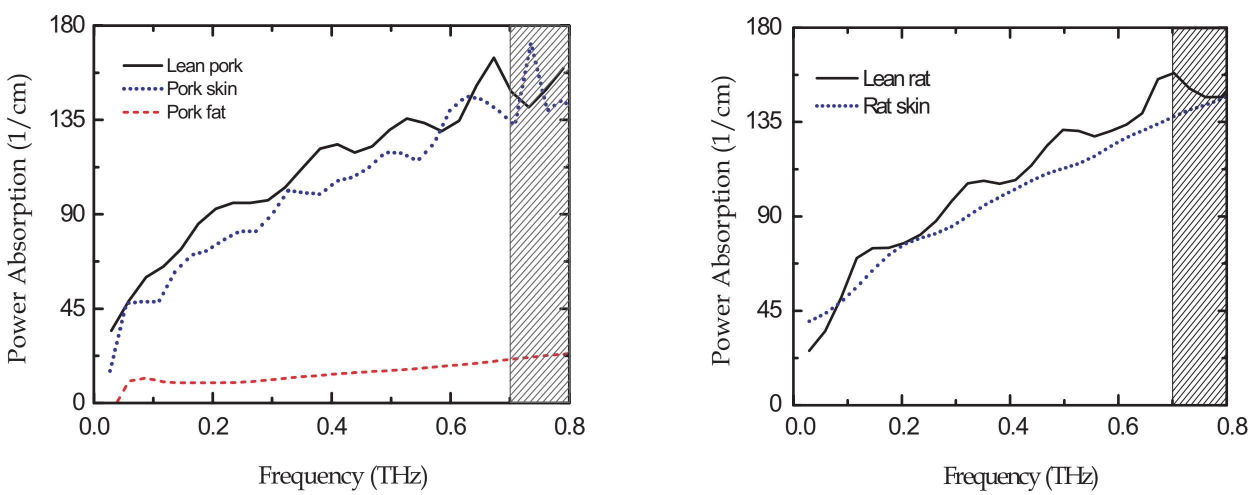

(a) (b)

Figure 3: (a) Power absorption coefficients of rat tissues. The thickness of the skin and lean rat tissues is 0.65 mm and 0.96 mm, respectively. (b) Power absorption coefficients of rat tissues. The thickness of the skin and lean rat tissues is 0.65 mm and 0.96 mm, respectively.

We have also carried out THz-TDS characterization of rat tissues. The experimental procedure was essentially the same as described above. The tissues were measured within 24 hours of the euthanasia of the six-month-old rats. The skin and lean tissues with thickness of 0.53 mm and 0.96 mm, respectively, were characterized. As shown in Fig. 3(b), the power absorption coefficients of the rat tissues have very similar values compared to the results obtained in pork tissues.

In conclusion, the THz-TDS transmitted time-domain pulses, the Fourier transformed spectra, and the derived power absorption coefficients enable the differentiation between different types of animal tissues. The same type tissue of different animals, however, shows similar terahertz response. The measured lean tissue of pork and rat has similar value of frequency-dependent power absorption which is also consistent with the previous data on pork-muscle. The obvious terahertz signatures observed for different type of animal tissues further demonstrate the feasibility of using terahertz technology in the biomedical applications [14, 15].

ACKNOWLEDGMENT

This work was partially supported by the 111 Project China, Program Number: B07014.

REFERENCES

1. Ferguson, B. and X.-C. Zhang, *Nature Materials*, Vol. 1, 26, 2002.
2. Woodward, R. M., B. E. Cole, V. P. Wallace, R. J. Pye, D. D. Arnone, E. H. Linfiled, and M. Pepper, *Phys. Med. Biol.*, Vol. 47, 3853, 2002.
3. Löffler, T., T. Bauer, K. J. Siebert, and H. G. Roskos, *Optics Express*, Vol. 9, 616, 2001.
4. Markelz, A. G., A. Roitberg, and E. J. Heilweil, *Chem. Phys. Lett.*, Vol. 320, 42, 2000.
5. Walther, M., B. Fischer, M. Schall, H. Helm, and P. U. Jepsen, *Chem. Phys. Lett.*, Vol. 332, 389, 2000.
6. Brucherseifer, M., M. Nagel, P. H. Bolivar, H. Kurz, A. Bosserhoff, and R. Büttner, *Appl. Phys. Lett.*, Vol. 77, 4049, 2000.
7. Nishizawa, J., T. Sasaki, K. Suto, T. Yamada, T. Tanabe, T. Tanno, T. Sawai, and Y. Miura, *Opt. Commun.*, Vol. 244, 469, 2005.
8. Woodward, R. M., V. P. Wallace, R. J. Pye, B. E. Cole, D. D. Arnone, E. H. Linfiled, and M. Pepper, *J. Invest. Derm.*, Vol. 120, 72, 2003.
9. Cole, B. E., R. M. Woodward, and D. Crawley, *Proc. SPIE*, Vol. 4276, 1, 2001.
10. Pickwell, E., B. E. Cole, A. J. Fitzgerald, V. P. Wallace, and M. Pepper, *Appl. Phys. Lett.*, Vol. 84, 2190, 2004.
11. Zhang, J. and D. Grischkowsky, *Opt. Lett.*, Vol. 29, 1617, 2004.
12. Thamizhmani, L., A. K. Azad, J. Dai, and W. Zhang, *Appl. Phys. Lett.*, Vol. 86, 131111, 2005.
13. Han, P. Y., G. C. Cho, and X.-C. Zhang, *Opt. Lett.*, Vol. 25, 242, 2000.
14. Liu, H.-B., Y. Chen, and X.-C. Zhang, *J. Pharmaceutical Sciences*, Vol. 96, 927, 2007.
15. Fischer, M., M. Walther, and P. U. Jepsen, *Physics in Medicine and Biology*, Vol. 47, 3807, 2002.

Interferometric ISAR Imaging on Squint Model

Changzheng Ma[1,2], **Tat Soon Yeo**[1], **Hwee Siang Tan**[1], **and Guangyue Lu**[3]

[1]Department of Electrical and Computer Engineering, National University of Singapore, Singapore
[2]School of Electric and Information Engineering, Zhongyuan University of Technology, China
[3]Telecommunication Engineering Department, Xi'an Institute of Post and Telecommunications, China

Abstract— Conventional interferometric inverse synthesis aperture radar three dimensional imaging only consider broadside imaging condition. In this paper, squint model imaging configuration is discussed and the coordinate transform equation is given. The ISAR range profile envelope alignment problem among different antennas are also discussed. Simulation results show the effectiveness of our proposed method.

1. INTRODUCTION

Inverse Synthesis Aperture Radar (ISAR) imaging has received much attention in the past three decades [1–6]. Its high range resolution is attained by transmitting a wideband signal while it's cross range resolution is dependent on the relative rotation between the radar and the target. It is difficult to obtain a good quality ISAR image if the targets are noncooperating and/or maneuvering [3–6]. For non-cooperative targets, the targets' rotation angle cannot be obtained and therefore, the cross range scale is not known. And for maneuvering targets, the rotational axis and the rotational speed of the target relative to the radar is time varying, which means that the Doppler is time varying, and therefore, time frequency analysis must be used to coherently integrate the signals to form a fine ISAR image. On the other hand, the range-Doppler plane may not coincide with the target's conventional range and cross-range plane, and this induces difficulty for target identification.

To overcome the above drawbacks, 3-D interferometric ISAR imaging known as InISAR are proposed [7–12].

Generally three antennas are used and the target is assumed to be located at the broadside of the antennas. The phase difference of a scatterer between two different antennas can be used to determine its cross range position. For slant range target, it is assumed that the antennas rotate mechanically to steer the antenna beam towards the target and maintain the broadside assumption. Some times, it may not be practical or convenient to rotate the antenna. In this paper, we discuss the three dimensional imaging of a slant range target.

2. SIGNAL MODEL

In this paper, a vector is denoted by a small bold letter or a letter with an overhead arrow, while scatterer's position and coordinate system are denoted by capital letters. The geometry of the three dimensional ISAR imaging based on three antennas is shown in Fig. 1. The origin of the three dimensional coordinate system (X', Y', Z') is denoted as O', the transmitting antenna also acts as a receiving antenna and is located at the origin. The other two receiving antennas A, B are located in the X and Y axis and denoted as antenna 1 and antenna 2 respectively, and the distance from both A and B to O' is d.

A local coordinate system (X, Y, Z) on the target parallel to the radar coordinate system is taken with reference, where the local origin is denoted as O. Point P located in (x, y, z) is expressed as $\mathbf{p} = \overrightarrow{OP}$.

Let the transmitted signal from the antenna O' be $\tilde{s}(t) = \exp(j2\pi ft)$. The back scattered signals from scatterer P received at antennas O' and A are

$$s_{p0}(t) = \exp\left(j2\pi f\left(t - \frac{2r_{p0}}{c}\right)\right), \tag{1}$$

and

$$s_{p1}(t) = \exp\left(j2\pi f\left(t - \frac{r_{p0} + r_{p1}}{c}\right)\right), \tag{2}$$

respectively, where $r_{p0} = |\overrightarrow{O'P}| = |\overrightarrow{O'O}+\overrightarrow{OP}| = |\mathbf{r}+\mathbf{p}|$, $r_{p1} = |\overrightarrow{AP}| = |\overrightarrow{AO'}+\overrightarrow{O'O}+\overrightarrow{OP}| = |\mathbf{r}+\mathbf{p}-\mathbf{d}|$, c is the speed of light, f is the carrier frequency. Let the signal from the receive antenna 0 be the

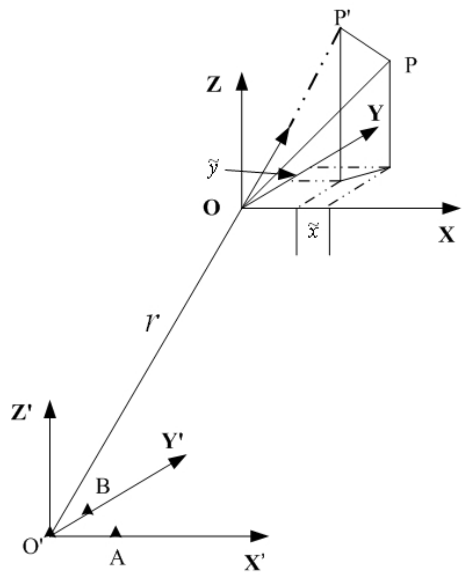

Figure 1: Geometry of the radar and the target.

reference signal, then we have

$$s_{p0}^*(t)s_{p1}(t) = \exp\left(j2\pi f\frac{r_{p0}-r_{p1}}{c}\right). \tag{3}$$

The differene between r_{p0} and r_{p1} is

$$\begin{aligned}\Delta r = r_{p0} - r_{p1} &= |\mathbf{r}+\mathbf{p}| - |\mathbf{r}+\mathbf{p}-\mathbf{d}| \\ &= \frac{(\mathbf{r}+\mathbf{p})^T(\mathbf{r}+\mathbf{p}) - (\mathbf{r}+\mathbf{p}-\mathbf{d})^T(\mathbf{r}+\mathbf{p}-\mathbf{d})}{r_{p0}+r_{p1}} = \frac{2(\mathbf{r}+\mathbf{p})^T\mathbf{d} - \mathbf{d}^T\mathbf{d}}{r_{p0}+r_{p1}}.\end{aligned} \tag{4}$$

For simplicity, the received signals of the two antennas are expressed in an array representation as

$$\mathbf{s}_p = s_{p0}(t) \times \left[1,\ e^{j2\pi\frac{2(\mathbf{r}+\mathbf{p})^T\mathbf{d}-\mathbf{d}^T\mathbf{d}}{\lambda(r_{p0}+r_{p1})}}\right]^T. \tag{5}$$

Let Q be another scatterer located at the origin of the target local coordinate system. The array signal back scattered from scatterer Q is

$$\mathbf{s}_q = e^{-j4\pi\frac{r_{q0}(t)}{\lambda}} \times \left[1,\ e^{j2\pi\frac{2\mathbf{r}^T\mathbf{d}-\mathbf{d}^T\mathbf{d}}{\lambda(r_{q0}+r_{q1})}}\right]^T. \tag{6}$$

Let Q be the focussing point and after compensation using $\mathbf{s}_q$, $\mathbf{s}_p$ becomes

$$\hat{\mathbf{S}}_p(t) = \mathbf{s}_q^*(t) \odot \mathbf{s}_p(t) = e^{-j4\pi\frac{r_{p0}(t)-r_{q0}(t)}{\lambda}} \times \left[1,\ e^{j2\pi\left(\frac{2(\mathbf{r}+\mathbf{p})^T\mathbf{d}-\mathbf{d}^T\mathbf{d}}{\lambda(r_{p0}+r_{p1})} - \frac{2\mathbf{r}^T\mathbf{d}-\mathbf{d}^T\mathbf{d}}{\lambda(r_{q0}+r_{q1})}\right)}\right]^T, \tag{7}$$

where $\odot$ express element wise product. Now let's consider simplifying the phase in the above array signal.

$$\begin{aligned}\Delta r_{QP} &= \frac{2(\mathbf{r}+\mathbf{p})^T\mathbf{d}-\mathbf{d}^T\mathbf{d}}{(r_{p0}+r_{p1})} - \frac{2\mathbf{r}^T\mathbf{d}-\mathbf{d}^T\mathbf{d}}{(r_{q0}+r_{q1})} = \frac{\left(2(\mathbf{r}+\mathbf{p})^T\mathbf{d}-\mathbf{d}^T\mathbf{d}\right)(r_{q0}+r_{q1}) - (2\mathbf{r}^T\mathbf{d}-\mathbf{d}^T\mathbf{d})(r_{p0}+r_{p1})}{(r_{p0}+r_{p1})(r_{q0}+r_{q1})} \\ &\approx \left(2\mathbf{r}^T\mathbf{d}(r_{q0}+r_{q1}-r_{p0}-r_{p1}) + 2\mathbf{p}^T\mathbf{d}(r_{q0}+r_{q1}) + \mathbf{d}^T\mathbf{d}(r_{p0}+r_{p1}-r_{q0}-r_{q1})\right)/(4\tilde{r}^2),\end{aligned} \tag{8}$$

where $\tilde{r} \approx r_{p0}$.

We also have

$$\frac{2\mathbf{r}^T\mathbf{d}(r_{q0}+r_{q1}-r_{p0}-r_{p1})}{4\tilde{r}^2} \approx -\mathbf{n}_0^T\mathbf{d}\mathbf{p}^T\mathbf{n}_0/\tilde{r}, \tag{9}$$

$$\frac{2\mathbf{p}^T\mathbf{d}(r_{q0}+r_{q1})}{4\tilde{r}^2} = \frac{\mathbf{p}^T\mathbf{d}}{\tilde{r}}, \tag{10}$$

and

$$\frac{\mathbf{d}^T\mathbf{d}(r_{p0}+r_{p1}-r_{q0}-r_{q1})}{4\tilde{r}^2} = \frac{\mathbf{d}^T\mathbf{d}\mathbf{p}^T\mathbf{n}_0}{2\tilde{r}^2}, \tag{11}$$

here we use the approximation $\mathbf{r}/\tilde{r} \approx \mathbf{n}_0$, $r_{q0}-r_{p0} \approx -\mathbf{p}^T\mathbf{n}_0$ and $r_{q1}-r_{p1} \approx -\mathbf{p}^T\mathbf{n}_0$. Therefore,

$$\Delta r_{QP} = \frac{-\mathbf{n}_0^T\mathbf{d}\mathbf{p}^T\mathbf{n}_0+\mathbf{p}^T\mathbf{d}}{\tilde{r}} + \frac{\mathbf{d}^T\mathbf{d}\mathbf{p}^T\mathbf{n}_0}{2\tilde{r}^2} \simeq \frac{(\mathbf{p}-\mathbf{p}^T\mathbf{n}_0\mathbf{n}_0)^T\mathbf{d}}{\tilde{r}} \tag{12}$$

Here we have assumed the target to be small and that the antenna array configuration satisfies $\mathbf{d}^T\mathbf{d} = \tilde{r} << 1$. Therefore, the array signal can be simplified to

$$\hat{\mathbf{s}}_p(t) = e^{-j4\pi\frac{r_{p0}(t)-r_{q0}(t)}{\lambda}} \times \left[1,\, e^{\frac{j2\pi(\mathbf{p}-\mathbf{p}^T\mathbf{n}_0\mathbf{n}_0)^T\mathbf{d}}{\lambda\tilde{r}}}\right] \tag{13}$$

It should be noted that the above Equation (13) holds only when (1) the target is located in far field and the size of the target is small, (2) the motion of the target in the range direction is small.

3. THREE DIMENSIONAL IMAGING ALGORITHMS

The position of scatterer P relative to Q along X direction can be obtained by comparing the phase of the antenna 1 and antenna 0's received signal. Similarly, position of P relative to Q along the Y direction can also be obtained. Together with the range information obtained by wide band pulse compression, the three dimensional position of the scatterer P relative to O can be obtained. The phase of the signal of P can be obtained by first carrying out ISAR imaging of the three antennas signal. What we need to pay more attention on is to retain the phase information during the ISAR imaging process as this can be used to deduce the scatterer's position.

In ISAR imaging, the first step is envelope alignment. Because the delays r_{p0} et al. are time varying, the echo's envelope are shifted with time. Cross range signal processing can only be done after the signals' envelopes are aligned. For a three-antenna cases, compared to one antenna ISAR imaging, what we need to know is that at any time instant, whether the different antenna's one dimensional range profile is aligned or not. For slant range imaging condition, it is obvious that envelope alignment is needed as the distance of the target to the three antennas is different, and as the difference in distance is comparable to range resolution, therefore range alignment is needed for the signal from the different antennas.

According to (13), the phase difference φ_x between antenna 0 and antenna 1 is

$$\varphi_x = \frac{2\pi(\mathbf{p}-\mathbf{p}^T\mathbf{n}_0\mathbf{n}_0)^T\mathbf{d}}{\lambda\tilde{r}}, \tag{14}$$

and this can be obtained by ISAR imaging. Similarly, the phase difference φ_y between antenna 0 and antenna 2 can also be obtained. Denote $\overrightarrow{P'P} = \mathbf{p}-\mathbf{p}^T\mathbf{n}_0\mathbf{n}_0 = \{\tilde{x},\, \tilde{y},\, \tilde{z}\}$, $r = \mathbf{p}^T\mathbf{n}_0$, and $\mathbf{p} = \{x,\, y,\, z\}$, then we have

$$\tilde{x} = \varphi_x\frac{\lambda\tilde{r}}{2\pi d}, \tag{15}$$

$$\tilde{y} = \varphi_y\frac{\lambda\tilde{r}}{2\pi d}, \tag{16}$$

$$\tilde{x} = x - rn_x, \tag{17}$$

$$\tilde{y} = y - rn_y, \tag{18}$$

According to $\mathbf{p}^T\mathbf{n}_0 = r$, it is easy to obtain

$$x = \tilde{x} + rn_x \tag{19}$$

$$y = \tilde{y} + rn_y \tag{20}$$

$$z = \frac{r - xn_x - yn_y}{n_z} \tag{21}$$

As the period of phase is of modulo 2π in order to ensure that there exists an unique relationship between $\tilde{x}$ and φ, one should ensure that $\left|\frac{2\pi\tilde{x}d}{\lambda\tilde{r}} < \pi\right|$. Therefore, the maximum cross range non-ambiguous width is

$$\tilde{x} \in X = \left[-\frac{\lambda\tilde{r}}{2d}, \frac{\lambda\tilde{r}}{2d}\right]. \tag{22}$$

In the above discussion, we have also assumed that the radar line of sight vector $\mathbf{n}_0$ is obtained by other system.

4. SIMULATION RESULTS

In our simulation, the distance of the target to the antennas is 20 km, the transmitted signal's wavelength is $\lambda = 0.08$ m, the signal bandwidth is 300 MHz corresponding to a range resolution of 0.5 m. The distance between antenna 0 and antenna 1 is 1.5123 m. The cross unambiguous distance is 105.8 m. The target is composed of 69 scatterers and is placed on $[1, 1, 1]$ direction. Fig. 2, Fig. 3, Fig. 4 and Fig. 5 depict the three projection images and three dimensional image of the original target. The target moves with a velocity of $[3,32,-32]$ m per second. The data collection time is 5 s, therefore the angle of rotation is 0.4584° which results in a nominal cross range resolution of about 0.3536 m. An isolated scatterer is used to do motion compensation and the ISAR image of antenna 0 is shown in Fig. 6. The reconstructed three projection images and three dimensional image are shown in Fig. 7, Fig. 8, Fig. 9 and Fig. 10. It can be seen that the reconstructed three dimensional image is similar to that of the original target image.

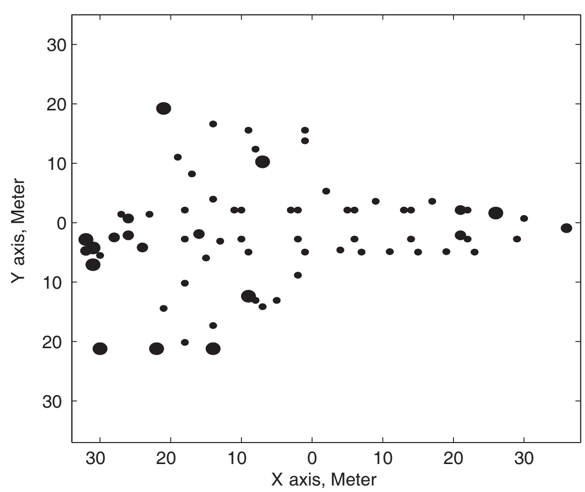

Figure 2: Original target's image on XY plane.

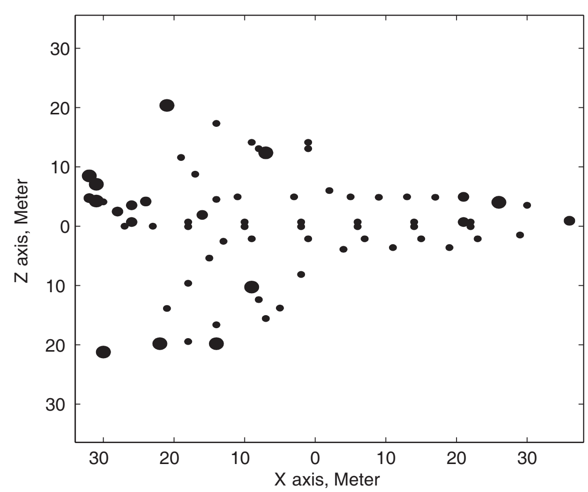

Figure 3: Original target's image on XZ plane.

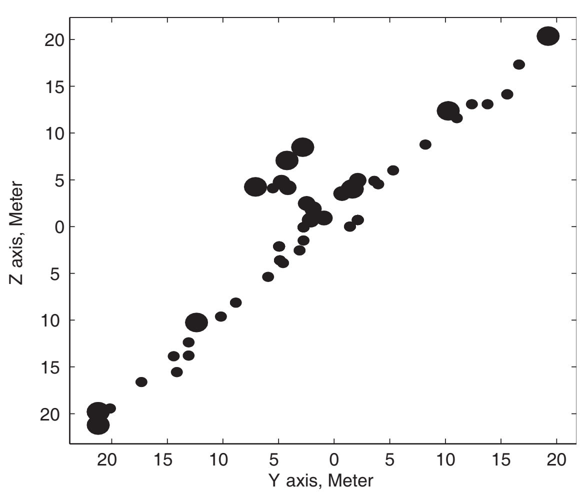

Figure 4: Original target's image on YZ plane.

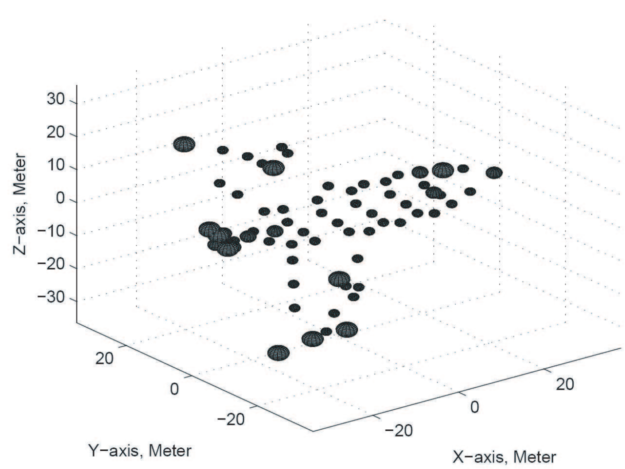

Figure 5: Original target's image on XYZ plane.

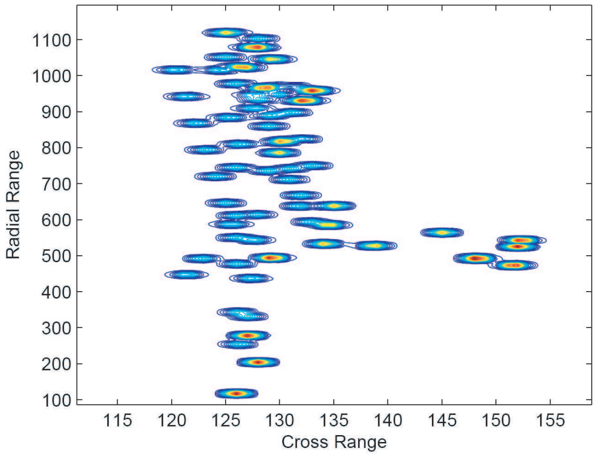

Figure 6: Target's ISAR image.

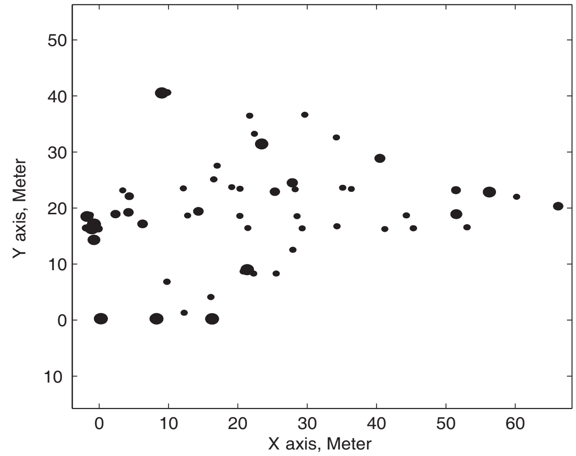

Figure 7: Constructed target's image on XY plane.

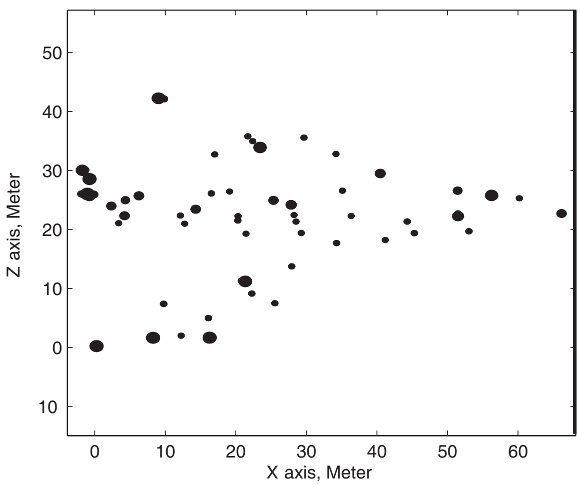

Figure 8: Constructed target's image on XZ plane.

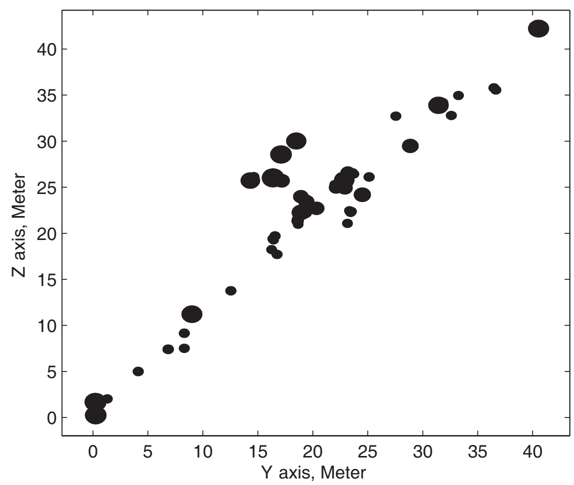

Figure 9: Constructed target's image on YZ plane.

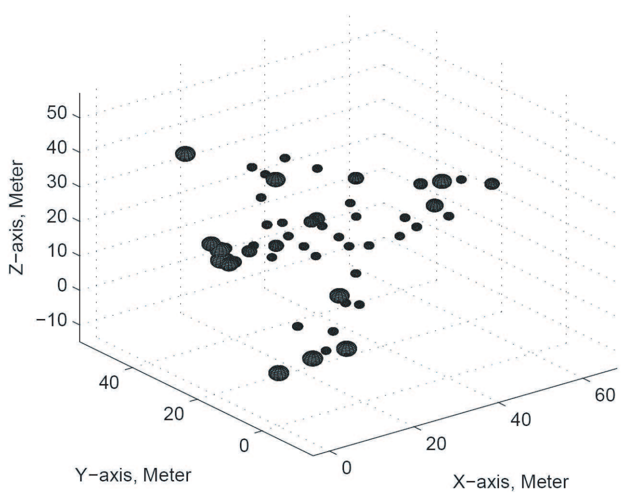

Figure 10: Constructed target's image on XYZ plane.

5. CONCLUSIONS

In this paper, we have derived a three dimensional imaging formula for slant range targets. Generally, envelope alignment between different antennas is needed. Simulation results show the effectiveness of our proposed method.

ACKNOWLEDGMENT

This work is partly supported by Henan Intelligent Youngster Science Agency under Grant No. 0512000500 and NSFC under Grant No. 60472087.

REFERENCES

1. Chen, C. C. and H. C. Andrews, "Target-motion-induced radar imaging," *IEEE Trans. Aerosp. Electron. Syst.*, Vol. 16, 2–14, Jan. 1980.
2. Walker, J. L., "Range-Doppler imaging of rotating objects," *IEEE Trans. Aerosp. Electron. Syst.*, Vol. 16, 23–52, Jan. 1980.
3. Bao, Z., G. Y. Wang, and L. Luo, "Inverse synthetic aperture radar imaging of maneuvering targets," *Opt. Eng.*, Vol. 37, 1582, 1998.
4. Wang, G. Y. and Z. Bao, "ISAR imaging of maneuvering targets based on chirplet decomposition," *Opt. Eng.*, Vol. 38, 1534–1541, 1999.
5. Wang, Y., H. Lin, and V. C. Chen, "ISAR motion compensation via adaptive joint time-frequency techniques," *IEEE Trans. Aerospace and Elec. Sys.*, Vol. 34, No. 2, 670–677, 1998.
6. Chen, V. C. and S. Qian, "joint time-frequency transform for radar range doppler imaging," *IEEE Trans. Aerospace and Elec. Sys.*, Vol. 34, No. 2, 486–499, Feb. 1998.
7. Ma, C. Z., "Research on radar three dimensional imaging techniques," PhD thesis, Xidian University, 1999.
8. Wang, G. Y., X. G. Xia, and V. C. Chen, "Three dimensional ISAR imaging of maneuvering targets using three receivers," *IEEE Trans. Image Processing*, Vol. 10, 436–447, Mar. 2001.
9. Xu, X. J. and R. M. Narayanan, "Three-dimensional interferometric ISAR imaging for target scatterering diagnosis and modeling," *IEEE Trans. Image Processing*, Vol. 10, 1094–1102, July 2001.
10. Zhang, Q., C. Z. Ma, T. Zhang, and S. H. Zhang, "Research on radar three dimensional imaging techniques based on interferometric techniques," *Journal of Electronic and Information*, Vol. 23, 890–898, Sept. 2001.
11. Zhang, Q., T. S. Yeo, G. Du, and S. H. Zhang, "Estimation of three-dimensional motion parameters in interferometric ISAR imaging," *IEEE Trans. Geosci. Remote Sensing*, Vol. 42, 292–300, Feb. 2004.
12. Zhang, Q. and T. S. Yeo, "Three-dimensional SAR imaging of a ground moving target using the InISAR technique," *IEEE Trans. Geosci. Remote Sensing*, Vol. 42, No. 9, 1818–1828, Sep. 2004.

Avian Detection and Monitoring Using Frequency-stepped Chirp Signal Radar

Q. Zhang[1,2], Y. Luo[1], D. L. Hu[3], B. F. Luo[3], and Y. S. Zeng[1]
[1]Institute of Telecommunication Engineering, AFEU, Xi'an 710077, China
[2]Key Laboratory of Wave Scattering and Remote Sensing Information (Ministry of Education)
Fudan University, Shanghai 200433, China
[3]Naval University of Engineering, Wuhan 430033, China

Abstract— The bird aircraft strike hazard (BASH) is a worldwide problem to aviation, which deprives lots of properties and lives every year. Avian radar systems are necessary to be developed for avian surveillance and early warning. In this paper, the frequency-stepped chirp signal radar is utilized to obtain high range resolution for micro-Doppler features extraction by means of synthetic bandwidth. The micro-Doppler features provide important information for avian detection and monitoring. The micro-Doppler effect in frequency-stepped chirp radar is analyzed in the paper and some micro-Doppler feature extraction methods are introduced.

1. INTRODUCTION

Along with the flourish of the aviation, the bird strikes are reported annually and the bird aircraft strike hazard (BASH) becomes a worldwide problem. Statistics suggested that about 10,000 bird strike accidents happened all around the world per year, and 90 percent occurred during take-off and landing in the vicinity of airports. It is necessary to develop avian radar system for avian detection and monitoring, which makes early warning be possible. Experiments illustrate that 3-centimeter wavelength surveillance radar (e.g., BIRDRAD) can detect the departure of migrants from different types of habitat within a range of 6 kilometers of the radar, and the Doppler weather surveillance radar (WSR-88D) can measure the density of birds in the radar beam as they begin a migratory movement within 60 kilometers [1], but trying to identify the type of bird is problematical. The abilities to distinguish the types of targets (birds, insects or aircraft with small size, such as Unmanned Aerial Vehicle), identity types of birds, and determine flock sizes are considered to be important goals for future research and development [2].

The radar imaging with high resolution is a potential technique to solve the problems. To explore the movement features of birds, the ultra-large-wideband signal is necessary to be utilized for high range resolution. In this paper, the frequency-stepped chirp signal [3, 4] is applied to synthesize a signal with a bandwidth of 3 GHz for a range resolution of 5 cm. The range resolution is high enough to explore the micro-Doppler information of birds. The rotating structures in a radar target or mechanical vibrations of the target body may induce additional frequency modulation on returned signals and generate side-bands about the center frequency of the body Doppler frequency, called micro-Doppler effect [5]. Micro-Doppler feature can be regarded as an important signature of the target, and provides additional information for target detection, recognition and identification. The beating of bird's wings can also cause micro-Doppler phenomenon, which offers a new approach to identify the birds: transmit frequency-stepped chirp signals to the birds, and then extract the micro-Doppler information from the echoes.

2. IMAGING PRINCIPLE OF FREQUENCY-STEPPED CHIRP SIGNAL

Frequency-stepped chirp signal is made up of a series of bursts, each of which consists of a sequence of chirp subpulses of stepped carrier frequency. The frequency variation in a burst is shown in Fig. 1. The i-th subpulse in a burst is written as (assume the initial time of the signal at $-T_1/2$)

$$U(t) = u_1(t - iT_r)\exp\left(j2\pi\left(f_0 + i\Delta f\right)t + \theta_i\right), \quad 0 \le i \le N-1 \tag{1}$$

where $u_1(t) = rect\left(t/T_1\right) \cdot \exp\left(j\pi\mu t^2\right)$ is the chirp subpulse, μ is the frequency slope, T_1 is the duration of the chirp subpulse, T_r is the subpulse repetition time, $f_0 + i\Delta f$ is the carrier frequency of the i-th subpulse, Δf is the step size, θ_i is the initial phase of the subpulse, and N is the number of subpulses in a burst. Assuming a target of a point-scatterer, the echo of the i-th subpulse from the target is

$$S_i(t) = rect\left(\frac{t - iT_r - 2R/c}{T_1}\right) \cdot \exp\left(j\pi\mu\left(t - iT_r - 2R/c\right)^2\right) \cdot \exp\left(j2\pi\left(f_0 + i\Delta f\right)\left(t - 2R/c\right) + \theta_i\right) \tag{2}$$

where R is the distance between the target and the radar, c is the wave propagation velocity. The reference signal can be written as

$$S_{i0}(t) = rect\left(\frac{t - iT_r - 2R_0/c}{T_{ref}}\right) \cdot \exp\left(j\pi\mu\left(t - iT_r - 2R_0/c\right)^2\right) \cdot \exp\left(j2\pi\left(f_0 + i\Delta f\right)\left(t - 2R_0/c\right) + \theta_i\right) \tag{3}$$

where R_0 is the distance between the reference point and the radar, T_{ref} is the duration of the reference signal which is a little larger than T_1. After dechirping processing, it yields

$$\begin{aligned} S_{ic}(t) = S_i(t)S_{i0}^*(t) \; &= \; rect\left(\frac{t - iT_r - 2R/c}{T_1}\right) \cdot \exp\left(-j\frac{4\pi\mu}{c}\left(t - \frac{2R_0}{c}\right)R_\Delta\right) \\ &\cdot \exp\left(-j\frac{4\pi}{c}\left(f_0 + i\Delta f\right)R_\Delta\right) \cdot \exp\left(j\frac{4\pi\mu}{c^2}R_\Delta^2\right) \end{aligned} \tag{4}$$

where $R_\Delta = R - R_0$. Replace $(t - 2R_0/c)$ by t', then take the Fourier transform to Eq. (4) with respect to t' and remove the Residual Video Phase (RVP), it yields

$$S_{ic}(\omega) = T_1 \mathrm{sinc}\left(T_1\left(\omega + \frac{4\pi\mu}{c}R_\Delta\right)\right) \cdot \exp\left(-j\frac{4\pi}{c}\left(f_0 + i\Delta f\right)R_\Delta\right) \tag{5}$$

It can be found that the peak value of $|S_{ic}(\omega)|$ appears at $\omega = -4\pi\mu R_\Delta/c$, and in fact, it is the coarse range profile of the point-target created by the i-th subpulse exactly. N subpulses will create N coarse range profiles. Let $\omega = -4\pi\mu R_\Delta/c$, and take Fourier transform of these coarse range profiles, it can be obtained

$$S\left(k\right) = C \cdot \mathrm{sinc}\left(k + 4\pi\Delta f R_\Delta/c\right) \cdot \exp\left(-j4\pi f_0 R_\Delta/c\right) \tag{6}$$

where C is a constant. From Eq. (6) it can be found that the peak value of $S(k)$ appears at $k = -4\pi\Delta f \cdot R_\Delta/c$, therefore, the high-resolution range profile (HRRP) is obtained. Each burst creates a HRRP; by transmitting a number of bursts and taking the Fourier transform to the HRRPs with respect to slow-time, the ISAR image of the target can be obtained.

Generally, the size of bird is between 0.1m and several meters. To achieve the range resolution high enough to identify birds, we synthesize a signal with a bandwidth of 3 GHz for a range resolution of 5 cm.

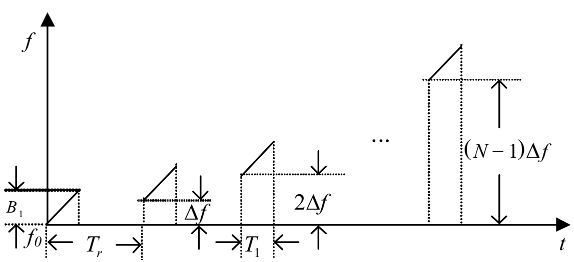

Figure 1: Frequency variety in a burst.

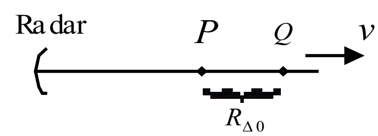

Figure 2: The micro-motion of target.

3. MICRO-DOPPLER EFFECT

If the target is a rigid body, after the motion compensation, the HRRPs obtained from each burst will be similar to each other. But in many cases, the radar target can't be regarded as a rigid object, for example, the helicopter with rotating rotors and bird with wings beating. This kind of micro-motions may induce micro-Doppler effect, which provides abundant structure and motion information of the object for identification.

As shown in Fig. 2, point P is the reference point, Q is a micro-motional point with velocity v along the radar line of sight (LOS). The distance between P and Q at the initial time is $R_{\Delta 0}$. Because of the movement of Q, R_Δ in Eq. (4) should be expressed as follow:

$$R_\Delta = R_{\Delta 0} + iT_r v \tag{7}$$

Generally, the displacement of Q in a burst can't exceed a coarse range cell. Eq. (5) can be rewritten as

$$S_{ic}(\omega) = T_1 \mathrm{sinc}\left(T_1\left(\omega + 4\pi\mu R_{\Delta 0}/c\right)\right) \cdot \exp\left(-j4\pi\left(f_0 + i\Delta f\right)\left(R_{\Delta 0} + iT_r v\right)/c\right) \tag{8}$$

Thus, the HRRP peaks at

$$k = \Phi'(i) = -\frac{4\pi}{c}\Delta f \cdot R_{\Delta 0} - \frac{4\pi}{c} f_0 T_r v - \frac{8\pi}{c}\Delta f i T_r v \tag{9}$$

Observing Eq. (9), the first term denotes the initial location of the point Q, the second term demonstrates that the location of Q has an offset proportional to v. Compared with the first and second terms, the last term of Eq. (9) is quite small and negligible, but this term may make the peaks of the HRRP expanded, especially serious when v is quite large. Ignoring the last term, Eq. (9) is rewritten as

$$k = -\frac{4\pi}{c} f_0 T_r v - \frac{4\pi}{c}\Delta f \cdot R_{\Delta 0} \tag{10}$$

It is obvious that the displacement of Q in the HRRP $-4\pi f_0 T_r v/c$ is proportional to its micro-motion velocity. Because the HRRP is obtained by N-point Fourier transform, the value range of k is defined in $[-\pi, \pi]$. If v is too large, k in Eq. (9) may exceed this scope, and the peak of the HRRP may wrap and appear at the other side of the reference point. Assuming $f_0 = 94\,\mathrm{GHz}$, $R_{\Delta 0} = 0$, the absolute velocity v must be smaller than about $20\,\mathrm{m/s}$ to avoid the wrapping phenomenon. As shown in Fig. 3(a) and Fig. 3(b), four points are all located at the reference point but with different velocities. We can see that the locations of them in the HRRP are related to their velocities. When the absolute value of v varies from $8\,\mathrm{m/s}$ to $25\,\mathrm{m/s}$, the location of according peak varies from the left side of the HRRP to the opposite side, and the peak becomes more and more expanded along with the increasing of v. According to the fact that the maximal velocity of bird's beating is generally lower than $20\,\mathrm{m/s}$, the wrapping phenomenon can be avoided.

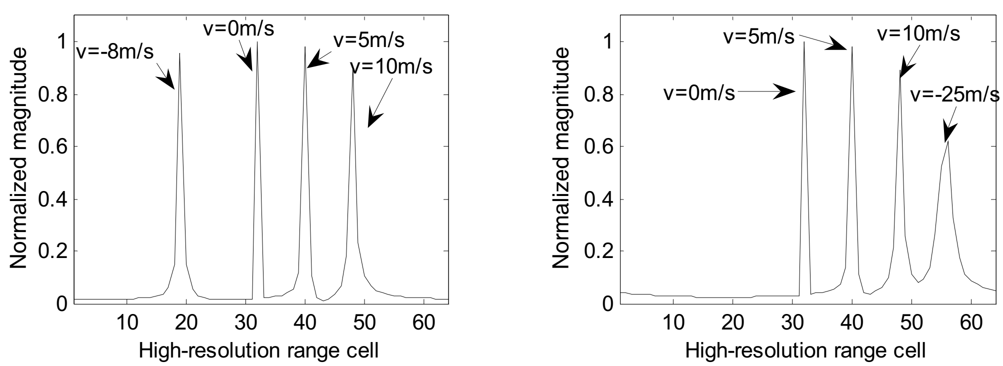

(a) (b)

Figure 3: The micro-Doppler effect.

Different micro-motions will cause different shapes of HRRPs, therefore, the spectrogram, which is defined as the module of the matrix having the HRRPs as vectors, includes the micro-motion information of the object. It provides a new approach to target identification. A bird model is shown in Fig. 4(a) and the spectrogram is shown in Fig. 4(b) when the flapping rate is 2 Hz.

4. EXTRACTION OF MICRO-DOPPLER INFORMATION

The micro-Doppler information contains the micro-motion information of the object, which is regarded as an important characteristic useful for target recognition. The extraction of the micro-Doppler information is an important work to achieve this goal.

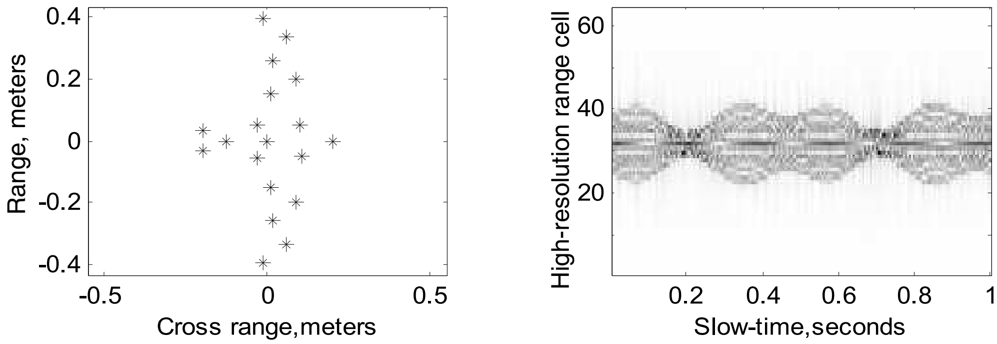

(a) (b)

Figure 4: The spectrogram of the bird model.

As shown in Fig. 4(b), the spectrogram appears to be periodic due to the periodicity of the bird's beating. That is to say, the period of the spectrogram is the same with the period of the bird's beating. As is known, the larger is the size of the bird, the lower its flapping frequency is. Many birds with large size, such as glede and crane, even don't beat their wings in a long time, but hover in the updraft for hours. Therefore, the frequency of the beating is important information to distinguish birds with different size, which can be obtained easily from the spectrogram using the image processing techniques such as autocorrelation.

The shape of the spectrogram also provides the characteristics of the bird's motion useful for identification. The tiny difference of the movement manners can induce the difference in the spectrograms. Much more work has to do to make use of the shape characteristics because it is necessary to build a template database of all kind of birds for bird identification.

To explore the fine flying characteristic of the birds, many methods can be used, such as the time-frequency analysis and the Hough Transform. High-resolution time-frequency technique is considered as a nice modus for the extraction of micro-Doppler information and some references have taken profound discussions about it [5, 6]. The Hough Transform is utilized to extract the micro-motion characteristics of objects with rotating parts such as rotating frequency and radius in [7].

5. CONCLUSIONS

This paper proposes a new approach to the avian detection and identification for the prevention of bird strike in aviation. The frequency-stepped chirp signal radar is utilized to obtain the high range resolution for extraction of micro-Doppler features. The micro-Doppler features are very useful for bird identification. It has to be mentioned that we obtain the spectrogram based on the accurate motion compensation which is a difficult problem to resolve in the future work.

ACKNOWLEDGMENT

This work is supported by the National Natural Science Foundation of China (60672032) and the Natural Science Foundation of Shaanxi Province (2007F28).

REFERENCES

1. Gauthreaux, Jr., S. A. and C. G. Belser, "Radar ornithology and the conservation of migratory birds," USDA Forest Service Gen. Tech. Rep. PSW-GTR-191, 871–875, 2005.
2. Weber, P., T. J. Nohara, and S. Gauthreaux, Jr., "Affordable, real-time, 3-D avian radar networks for centralized north American bird advisory systems," *Bird Strike 2005 Conference*, Vancouver, B.C., Canada, August 14–18, 2005.
3. Long, T., E. K. Mao, and P. K. He, "Analysis and processing of modulated frequency stepped radar signal," *Acta Eletronica Sinica*, Vol. 26, No. 12, 84–88, 1998.
4. Zhang, Q. and Y. Q. Jin, "Aspect of radar imaging using frequency-stepped chirp signals," *EURASIP Journal on Applied Signal Processing*, Vol. 2006, Article ID 85823, 1–8, 2006.
5. Chen, V. C., "Analysis of radar micro-Doppler signature with time-frequency transform," *Proc. Statistical Signal and Array Processing*, 463–466, 2000.

6. Thayaparan, T., G. Lampropoulos, S. K. Wong, et al., "Application of adaptive joint time-frequency algorithm for focusing distorted ISAR images from simulated and measured radar data," *IEE Proc. Radar Sonar Navig.*, Vol. 150, No. 4, 213–220, August 2003.
7. Zhang, Q., H. Guan, Y. Guo, et al., "Separation of micro-Doppler signal using an extended hough transform," *2006 International Conference on Communications, Circuits and Systems Proceeding*, 361–365, China, June 2006.

Model of Man-made Target beneath Foliage Using PolInSAR

Bin Zou, **Hongjun Cai**, **Lamei Zhang**, **and Maoliu Lin**
Harbin Institute of Technology, No. 92 West Dazhi Street, Harbin 150001, China

Abstract— Polarimetric SAR Interferometry can be used for parameter inversion of ground. An appropriate model is of most importance for parameters inversion. This paper derives a series of scattering model that can be used for parameter inversion of forestry area, such as RV, RVoG, OV and OVoG. These models can reveal the characteristics of forestry area as well as establish the relationship between observed data and parameters of test area. Finally, a multi-layer random scattering model that can be used for parameter inversion of forestry area containing a man-made target is derived. An improved model is examined by the simulated data of the single-baseline polarimetric SAR interferometry. The result turns out that the improved RVoG scattering model is correct.

1. INTRODUCTION

Polarimetric SAR interferometry (PolInSAR) is not only sensitive to space distribution of vegetation and vegetation height in interferometric SAR, but also to distribution and shape of vegetation scatterers in polarimetric SAR. Hence, PolInSAR is more advantageous and precision than either polarimetric or interferometric SAR alone in extracting information of vertical vegetation structure. The coherent optimization of PolInSAR provides the optimum separation of the effective phase centers of different scattering mechanisms [1].

PolInSAR is widely regarded as a powerful tool for remote sensing application. One useful application is ground scatterer parameters inversion, especially in the forestry and vegetated areas. During the inversion process, a coherent model of the scattering process that relates the measurables to the desired physical parameters is required. In the case of vegetation area, several models, random volume (RV) scattering model, random volume over ground (RVoG) scattering model, oriented volume (OV) scattering model, and oriented volume over ground (OVoG) scattering model, have been developed [2–5]. However, these inversion models based on PolInSAR are mainly suitable for forest area, model of man-made target beneath foliage have not been studied. In this paper, a new model will be developed and analyzed, which can be used for forestry area in which more scattering centers will be considered.

For this, Section 2 introduces a generalized coherent scattering model suitable for the description of interferometric and polarimetric behavior of the vegetation area and discusses the scattering model in detail. Section 3 extends coherent scattering model suitable for the description of interferometric and polarimetric behavior of the vegetation area to the vegetation area contained man-made target. The validity of the model is demonstrated using simulated PolInSAR data in Section 4. Finally, in Section 5, some conclusions are drawn.

2. GENERALIZED COHERENCE SCATTERING MODEL

The vegetation model was derived first in [2] and extended for fully polarimetric interpretation in [3]. A generalized interferometric coherence for vegetation including random volume and oriented volume is shown in Eq. (1).

$$\tilde{\gamma} = e^{i\phi_0} \frac{\tilde{\gamma}_v(\vec{\omega}) e^{i\phi_c} + m(\vec{\omega})}{1 + m(\vec{\omega})} \tag{1}$$

where ϕ_0 and ϕ_c are the phase centers of the ground topography and tree trunk respectively; $\tilde{\gamma}_v$ and m are the complex coherence for the volume alone and object (ground or man-made target)-to-volume amplitude ratio accounting for the attenuation through the volume respectively as shown in Eqs. (2) and (3).

$$\tilde{\gamma}_v(\vec{\omega}) = \frac{I(\vec{\omega})}{I_0(\vec{\omega})}, \begin{cases} I = \int\limits_0^{h_v} e^{\frac{2\sigma(\vec{\omega})z'}{\cos\theta}} e^{ik_z z'} dz' \\ I_0 = \int\limits_0^{h_v} e^{\frac{2\sigma(\vec{\omega})z'}{\cos\theta}} dz' \end{cases} \tag{2}$$

$$m(\vec{\omega}) = \frac{2\sigma(\vec{\omega})}{\cos\theta \left(e^{2\sigma(\vec{\omega})h_v/\cos\theta} - 1\right)} \frac{\vec{\omega}^{*T} T_O \vec{\omega}}{\vec{\omega}^{*T} T_V \vec{\omega}} \tag{3}$$

where $\vec{\omega}$ is a three-component unitary complex vector defining the choice of polarization, σ the mean wave extinction in the medium and relates to polarization when vegetation layer is oriented volume, k_z the vertical wavenumber of the interferometer and θ the mean angle of incidence. T_v is the 3×3 diagonal coherency matrix for the volume scattering and T_O the object scattering coherence matrix.

The scattering model can be characterized as RV model and OV model depending on relationship between scatter center and polarization. As shown in Fig. 1, in RV model scatter has the same scattering center in different polarization; while in OV model scatter has the different scattering centers in different polarization.

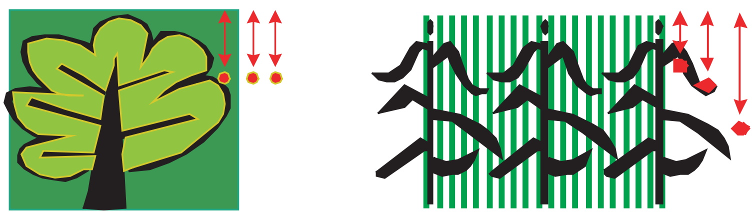

(a) (b)

Figure 1: Scattering center of different type of vegetation in different polarization. (a) Random volume. (b) Oriented volume.

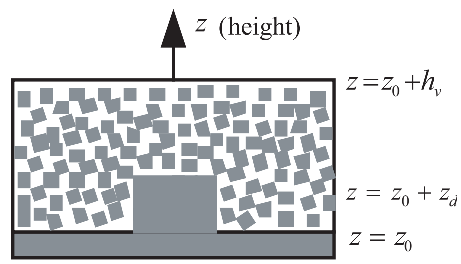

Figure 2: Schematic representation of the MTBRV model.

We can obtain forms of different scattering model by using different condition from Eq. (1). For example, in the case of two-layer random volume over ground, Eq. (1) is written as

$$\tilde{\gamma}_{RVoG} = e^{i\phi_0} \frac{\tilde{\gamma}_v + m(\vec{\omega})}{1 + m(\vec{\omega})} \tag{4}$$

where $\tilde{\gamma}_v$ is the complex coherence for the volume alone and independent of polarization.

3. MODEL OF MAN-MADE TARGET BENEATH RANDOM VOLUME (MTBRV)

The RVoG scattering model, which is derived in the case of natural vegetation, is not correct to the area with man-made target. In realistic scenario, man-made targets, such as houses and vehicles, can also exist in the forest area. If a man-made target is placed in the two-layer vegetation, and supposed that the size of object is comparable with resolution cell, that is, this object can be treated like a point target. When the electromagnetic wave penetrates the canopy and it is scattered, the point target is main scatter. So there is a strong scattering center in the position of the point target. In order to separate this point scatter from background clutters, a novel model is developed. Assuming the man-made target over the ground is located at z_d as shown in Fig. 2.

In the RVoG scattering model, the components related with ground scatterers are

$$\begin{aligned} I_1^G &= \int_0^{h_v} \delta(z') \, e^{\frac{2\sigma z'}{\cos\theta}} T_g dz' = T_g \\ I_2^G &= T_g \end{aligned} \tag{5}$$

Because of the existing man-made target on the ground, scattering center moves to z_d from z_0, thus the component related with man-made target scatterers can be described as

$$\begin{aligned} I_1^G &= \int_0^{h_v} \delta(z' - z_d) \, e^{\frac{2\sigma z'}{\cos\theta}} T_g dz' = e^{\frac{2\sigma z_d}{\cos\theta}} T_g \\ I_2^G &= \int_0^{h_v} \delta(z' - z_d) \, e^{\frac{2\sigma z'}{\cos\theta}} e^{ik_z z'} T_g dz' = e^{ik_z z_d} I_1^G \end{aligned} \tag{6}$$

Therefore, the complex interferometric coherence of Man-made Target beneath Random Volume (MTBRV) can be derived as

$$\tilde{\gamma}_{MTBRV} = e^{i\phi_0} \frac{\tilde{\gamma}_v + e^{ik_z z_d} m(\vec{\omega})}{1 + m(\vec{\omega})} \tag{7}$$

Compared Eq. (4) with Eq. (7), the information of point target is related with $m(\vec{\omega})$ and $e^{ik_z z_d}$. So we can estimate the height of man-made target besides the target-to-volume amplitude ratio. The relationship between the complex interferometric coherence $\tilde{\gamma}$ and man-made target height z_d is shown in Fig. 3.

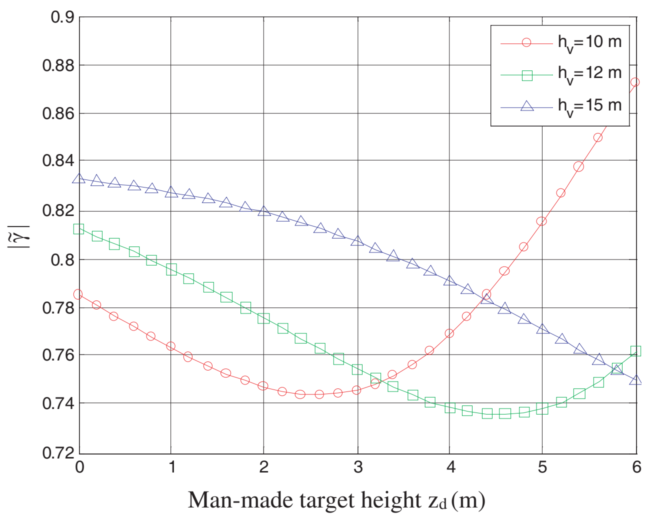

Figure 3: Coherence $\tilde{\gamma}$ variation against man-made target height in MTBRV model.

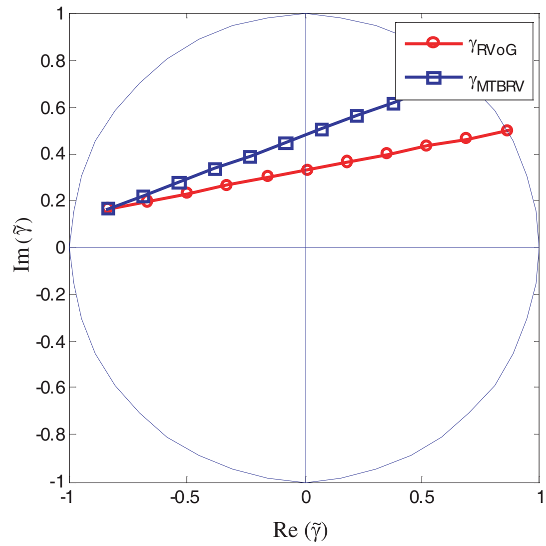

Figure 4: Coherence $\tilde{\gamma}$ variation against $m(\vec{\omega})$ in RVoG and MTBRV model.

Figure 3 gives the relationship between the complex interferometric coherence and the height of man-made target in a resolution cell. When man-made target is high enough compared with the thickness of canopy, the complex interferometric coherence is mainly influenced by man-made target, thus man-made target has stronger scattering characterisitcs.

RVoG model and MTBRV model can be rewritten as the equation of a straight line in the complex plane as

$$\begin{aligned} \tilde{\gamma}_{RVoG} &= e^{i\phi_0} \left[\tilde{\gamma}_v + \mu(\vec{\omega})(1 - \tilde{\gamma}_v)\right] \\ \tilde{\gamma}_{MTBRV} &= e^{i\phi_0} \left[\tilde{\gamma}_v + \mu(\vec{\omega})\left(e^{ik_z z_d} - \tilde{\gamma}_v\right)\right] \end{aligned} \tag{8}$$

where

$$0 \leq \mu(\vec{\omega}) = \frac{m(\vec{\omega})}{1 + m(\vec{\omega})} \leq 1$$

The comparison of RVoG scattering model with MTBRV scattering model is shown in Fig. 4. Seen from Fig. 4, the volume coherence are the same in the MTBRV scattering model and RVoG scattering model, but the ground phase ϕ_0 has phase-shift because of man-made target. So far an improved RVoG scattering model has been derived.

4. EXPERIMENTAL RESULTS

A simplified three-level scattering model is used to generate the simulation data [1, 7]. The mean vegetation height is assumed 18m and the man-made target height 5 m. The ground has small slope.

Firstly, the optimized coherence coefficients are obtained by the polarimetric interferometric principle of coherence optimization (PIPCO) based on modeling data [1]. Secondly, the Treuhaft's RVoG scattering model is used in the vegetation region without man-made target and the improved RVoG model in vegetation region placed man-made target. Finally, based on the scattering model,

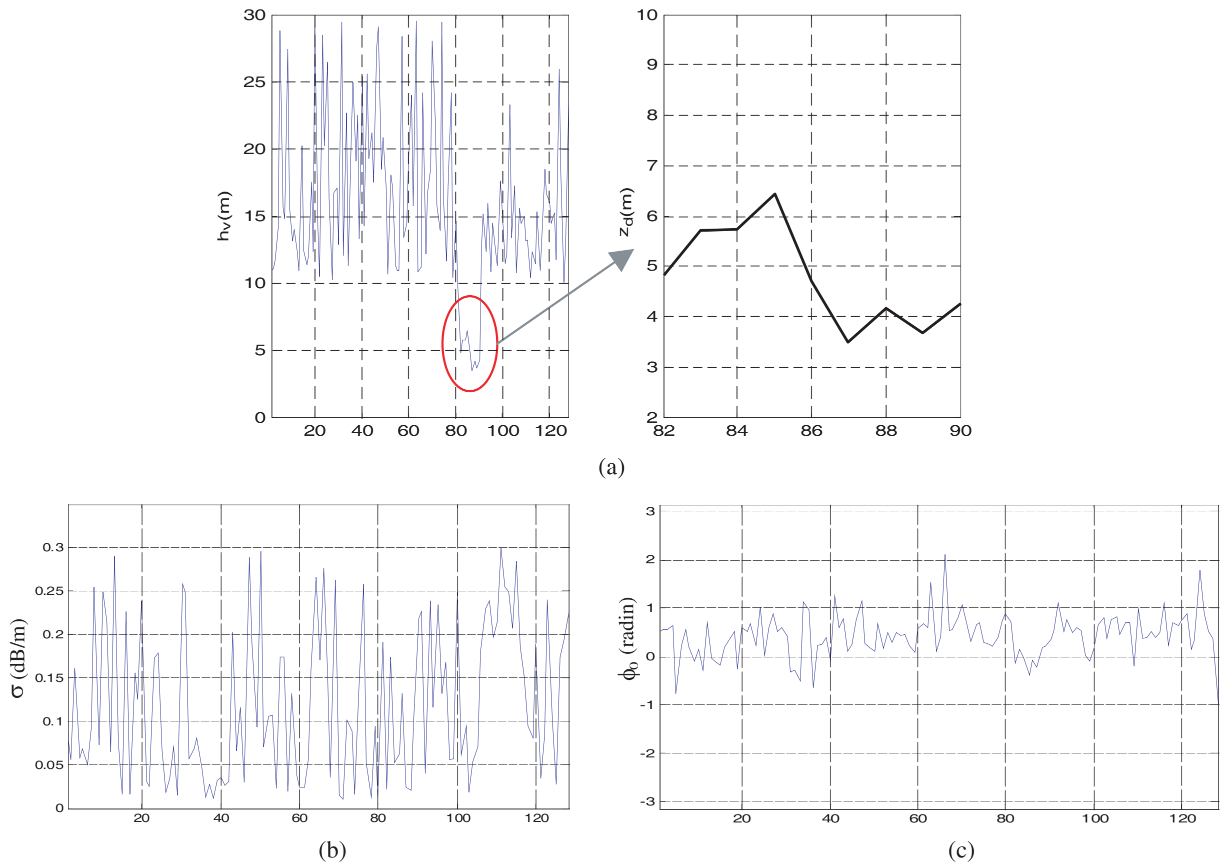

Figure 5: Inversion physical parameters of forest and man-made target. (a) Profile of the extracted forest+ man-made target height values of the 87th row. (b) Profile of the extracted mean extinction values of the 87th row. (c) Profile of the extracted ground topography values of the 87th row.

coherence coefficients and genetic algorithms (GA) [8, 9], the extracted forest and man-made target parameters are shown in Fig. 5.

Seen from the Fig. 5(a), most of forest height ranges from 12 to 25 m, and the volume extinction coefficient ranges from 0.05 to 0.2 dB/m. In the Fig. 5(c), most of phase related to the ground topography ranges from −0.5 to 1 (in radians). Fig. 6 shows a 3-D perspective view of the estimated forest height for the whole scene. The mean forest height and man-made target height are 17.6 m and 5.5 m, respectively. In Fig. 6, only the man-made target height is shown in man-made target area beneath the forest.

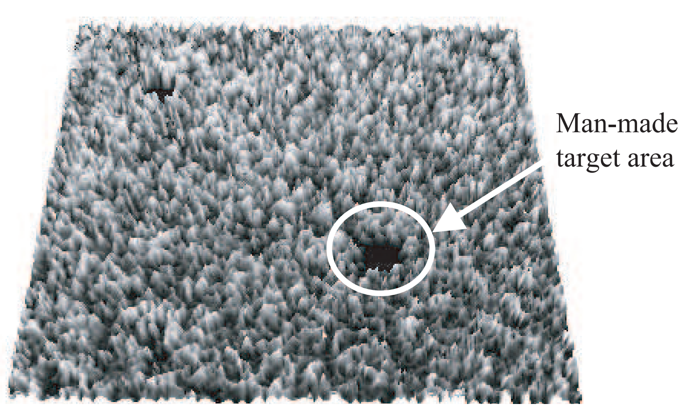

Figure 6: 3-D perspective view of the estimated forest height for the test site.

Compared modeling parameters and experimental results, the improved two-layer RVoG scattering model should be correct.

5. CONCLUSIONS

In this paper, a generalized interferometric coherence for vegetation scattering model including random volume and oriented volume is derived. Based on RVoG scattering model, an extended RVoG scattering model containing man-made target is derived. This new model is evaluated by simulated polarimetric interferometric data. Compared inversion parameter with simulation parameter, the new scattering model is correct. In the vegetation region placed man-made target, this new model can be used to extract physical parameters of man-made target beneath the vegetation.

ACKNOWLEDGMENT

This work is supported by National Natural Science Foundation of China, No. 60672091.

REFERENCES

1. Cloude, S. R. and K. P. Papathanassiou, "Polarimetric SAR interferometry," *IEEE Trans. GRS*, Vol. 36, No. 5, 1551–1565, 1998.
2. Treuhaft, R. N., "Vertical structure of vegetated land surfaces from interferometric and polarimetric radar," *Radio Sciences*, Vol. 35, No. 1, 141–177, 2000.
3. Papathanassiou, K. P. and S. R. Cloude, "Single-baseline polarimetric SAR interferometry," *IEEE Trans. GRS*, Vol. 39, No. 11, 2352–2363, 2001.
4. Treuhaft, R. N. and S. R. Cloude, "The structure of oriented vegetation from polarimetric interferometry," *IEEE Trans. GRS*, Vol. 37, No. 5, 2620–2624, 1999.
5. Hajnsek, I. and S. R. Cloude, "Pol-InSAR for agriculture vegetation parameter estimation," *Proceedings of IEEE. IGARSS'04*, 1224–1227, Alaska, USA, September 2004.
6. Cloude, S. R. and K. P. Papathanassiou, "Three-stage inversion process for polarimetric SAR interferometry," *IEE Proc. — Radar. Sonar Navig*, Vol. 150, No. 3, 125–134, 2003.
7. Cloude, S. R. and K. P. Papathanassiou, "Polarimetric radar interferometry," *SPIE'S 42nd Annual Meeting Proc. Windband Interferometry Sensing and Imaging Polarimetry*, Vol. 3120, 1551–1565, 1997.
8. Haupt, R. L., "An introduction to genetic algorithms for electromagnetics," *IEEE A P*, Vol. 37, No. 2, 7–15, 1995.
9. Zou, B., L. Zhang, W. Wang, and D. Sun, "Forest parameters inversion using PolInSAR data based on genetic algorithm," *Proceedings of IEEE. IGARSS'06*, 2651–2654, Colorado, USA, August 2006.

Comparison of Methods for Target Detection and Applications Using Polarimetric SAR Image

Lamei Zhang, Junping Zhang, Bin Zou, and Ye Zhang
Harbin Institute of Technology, No. 92 West Dazhi Street, Harbin 150001, China

Abstract— Polarimetric SAR (PolSAR) is sensitive to the orientation and characters of object and polarimetry could yield several new descriptive radar target detection parameters and lead to the improvement of radar detection algorithms. Target decomposition theory has been used for information extraction in PolSAR, and it can also explore the phase message in PolSAR data. In this paper, a comparison of polarimetric target decomposition methods is proposed. We generate a validity test for these methods using DLR ESAR L-band full polarized data. Results show that among many target decomposition algorithms, the coherent and incoherent formulations are quite comparable in distinguishing natural targets and man-made buildings. Pauli decomposition, Cameron decomposition and Freeman decomposition are suitable for the detection of natural targets. On the other hand, SDH decomposition, OEC decomposition, and Four-component model, in particular, are very useful for man-made target extraction.

1. INTRODUCTION

Target detection using Synthetic Aperture Radar (SAR) has attracted much attention for both civilian and military applications. Polarimetric SAR (PolSAR) is a well established technique, which allows the identification and separation of scattering mechanisms in the polarization signature for purposes of classification and parameter estimation. PolSAR is sensitive to the orientation and characters of object and polarimetry could yield several new descriptive radar target detection parameters and lead to the improvement of radar detection algorithms.

The polarimetric information of target echo can reflect the geometry structure and physical characteristic of target, and polarimetric target decomposition theorem expresses the average mechanism as the sum of independent elements in order to associate a physical mechanism with each component. Unlike method using SAR for information process, target decomposition explores phase message contained in PolSAR data. Polarimetric target decomposition theorems can be used for target classification or recognition.

Polarimetric SAR data are coherent by nature of the principle of operation, however, most often incoherent approaches are chosen for the post-processing in order to apply conventional averaging and statistical method. At present, two main classes of decomposition can be identified. One, called coherency decomposition, deals with decomposition of the scattering matrix, while another, called incoherent decomposition, deals with decomposition of coherency or covariance matrices.

The main purpose of this paper is to examine the possibilities of target detection using PolSAR data and to compare the effectiveness of target decomposition algorithms using full polarized SAR image.

2. EXPERIMENTAL DATA

The DLR ESAR L-band full polarized image of Oberpfaffenhofen Test Site Area (DE) of Germany, obtained on September 30th, 2000, was used to validate the comparison of the decomposition methods. Its spatial resolution is $3\,\text{m} \times 3\,\text{m}$. The optical image and HH channel image are shown in Fig. 1(a) and (b) respectively. The test area, composed of 2816×1540 pixels, mainly includes forest, several kinds of farmland, bituminous macadam, and man-made buildings.

3. COHERENT TARGET DECOMPOSITION

In this category, we have study three main coherent decomposition theorems, commonly referred to as Pauli decomposition, SDH (Sphere, Diplane, Helix) decomposition, and SSCM (Symmetric Scattering Characterization Method), respectively.

3.1. Pauli Decomposition

The most common known and applied coherent decomposition is Pauli decomposition. Whereby the scattering matrix $[S]$ can be written as:

$$[S] = \alpha \begin{bmatrix} 1 & 0 \\ 0 & 1 \end{bmatrix} + \beta \begin{bmatrix} 1 & 0 \\ 0 & -1 \end{bmatrix} + \gamma \begin{bmatrix} 0 & 1 \\ 1 & 0 \end{bmatrix} \tag{1}$$

(a)

(b)

Figure 1: Test data of ESAR, (a) HH channel image, (b) optical image.

where $\alpha = (s_{hh} + s_{vv})/\sqrt{2}$, $\beta = (s_{hh} - s_{vv})/\sqrt{2}$, and $\gamma = \sqrt{2}s_{hv}$ are the complex quantities representing, respectively, single-bounce, double-bounce, and 45° rotated double-bounce scattering components. Fig. 2 is Pauli decomposition of the test data. Seen from Fig. 2, Pauli decomposition can distinguish natural target well, however, this method cannot detect man-made target.

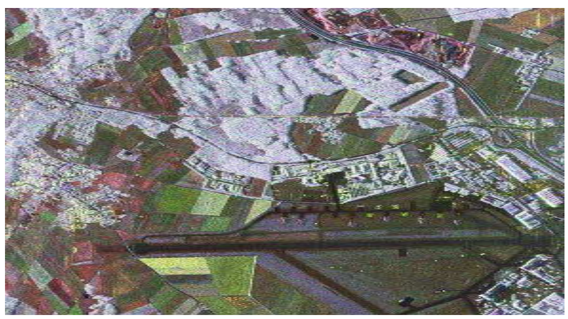

Figure 2: Pauli decomposition, the image is colored by α (red), β (green), and γ (blue).

3.2. SDH Decomposition

According to Krogager, the complex symmetric scattering matrix can be decomposed into three components on the circular basis, which corresponding to a sphere, a diplane and a right- or left-wound helix, respectively [1]:

$$\left[S_{(r,l)}\right] = e^{j\varphi}\left\{e^{j\varphi_s}k_s\left[S_s\right] + k_d\left[S_d\right] + k_h\left[S_h\right]\right\} \tag{2}$$

The coefficients are easily obtained from the elements in the circular basis. Thus, $k_s = |s_{rl}|$, for the left-wound, $k_d^+ = |s_{ll}|$, $k_h^+ = |s_{rr}| - |s_{ll}|$, while for the right-wound, $k_d^- = |s_{rr}|$, $k_h^- = |s_{ll}| - |s_{rr}|$. Because helix scattering is general scattering mechanism, which appears in an urban area whereas disappears for almost all natural distributed scattering, SDH decomposition can distinguish man-made target from natural target well. However, SDH cannot divide one kind of man-made target from another kind. Fig. 3 is SDH decomposition of the test data.

Figure 3: SDH decomposition, the image is colored by k_s (red), k_d (green), and k_h (blue).

3.3. Cameron Decomposition and SSCM

Under reciprocity conditions, coherent scattering can be decomposed into a maximized symmetric component and an asymmetric component by using Cameron's decomposition theory [2]

$$\vec{S} = A\left[\cos\tau\vec{S}_{sym}^{\max} + \sin\tau\vec{S}_{sym}^{\min}\right] \tag{3}$$

The maximum symmetric component $\vec{S}_{sym}^{\max}$ is characterized by the two complex entities α and ε, which represent the distribution of the largest symmetric scattering component on the basis of the orthogonal vectors,

$$\vec{S}_{sym}^{\max} = \alpha\vec{S}_a + \varepsilon\vec{S}_b \tag{4}$$

where $\vec{S}_a$ and $\vec{S}_b$ are trihedral and dihedral scattering vectors respectively.

R. Touzi proposed SSCM to improve Cameron decomposition. Then $\vec{S}_{sym}^{\max}$ can be expressed as [3],

$$\vec{S}_{sym}^{\max} = \exp^{j\phi_{S_a}} \cdot \sqrt{|\alpha|^2 + |\varepsilon|^2} \cdot \left[\cos(\eta)\cdot\vec{S}_a + \sin(\eta)\exp^{j(\phi_{S_a}-\phi_{S_b})}\cdot\vec{S}_b\right] \tag{5}$$

where, $\eta \in [0, \pi/2]$ characterizes the direction of scattering vector on the $\vec{S}_a - \vec{S}_b$ basis. Under coherent conditions, it provides information about the type of scattering of the maximized symmetric component. $\phi_{S_b} - \phi_{S_a} \in [-\pi, \pi]$ is the phase difference of $\vec{S}_a - \vec{S}_b$ channel. It can provide useful information about the illuminated target if the channel coherence is high. Both the magnitude and phase of the channel coherence are worth investigating target scattering characterization.

Figures 4(a) and (b) is the distribution of η and $\phi_{S_b} - \phi_{S_a}$, respectively. Different kinds of farmlands have distinct difference in $\phi_{S_b} - \phi_{S_a}$ around $-3\pi/4$ and $3\pi/4$, forest area and man-made buildings concentrated on $-\pi/4$. Therefore the phase difference can be used to distinguish natural targets from man-made targets. The same to SDH decomposition, this method cannot distinguish forest and buildings, either.

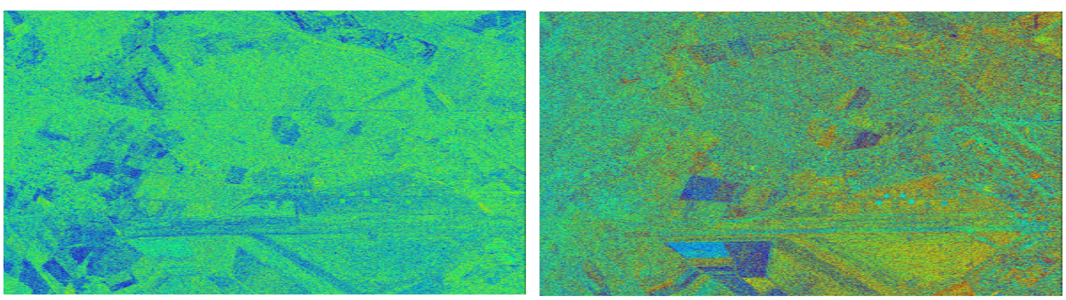

(a) (b)

Figure 4: Distribution of η and $\phi_{S_b} - \phi_{S_a}$ in SSCM, (a) distribution of η, (b) distribution of $\phi_{S_b} - \phi_{S_a}$.

4. INCOHERENT TARGET DECOMPOSITION

In this category, we discuss three incoherent decomposition theorems, there as, Freeman decomposition, OEC decomposition, and Four-component model, respectively.

4.1. Freeman Decomposition

Freeman proposed a three-component scattering model in which covariance matrix $[C]$ of polarimetric SAR data is decomposed for information extraction [4]. Freeman decomposition describes scattering mechanisms as due to three physical mechanisms, namely surface scattering, double-bounce scattering and volume scattering:

$$[C] = f_s[C_{surface}] + f_d[C_{double}] + f_v[C_{volume}] \tag{6}$$

According to this model, the measured power P may be decomposed into three quantities:

$$\begin{array}{l} P_s = f_s(1+|\beta|^2), \quad P_d = f_d(1+|\alpha|^2), \quad P_v = \frac{8}{3}f_v \\ P = P_s + P_d + P_v \end{array} \tag{7}$$

The three-component scattering model based on covariance matrix has been successfully applied to decompose PolSAR image under the reflection symmetry condition $\langle s_{hh}s_{hv}^*\rangle \approx \langle s_{vv}s_{hv}^*\rangle \approx 0$. This method is based on simple physical scattering mechanisms (surface scattering, double-bounce scattering, and volume scattering), just as shown in Fig. 5, the contributions of each of the three scattering mechanisms to the total power are shown for each pixel, with surface scattering colored blue, volume scattering green, and double-bounce scattering red. Result in Fig. 5 shows that volume scattering meets the observation for forest very well. Farmland has surface scattering and double-bounce scattering dominant. This can be interpreted as indication that the longer wavelengths can penetrate the relatively short vegetation in farmland area and the backscatter is mostly from the underlying ground. Therefore, Freeman decomposition can describe different natural targets very good and is powerful for PolSAR image decomposition for natural distributed target areas. However, man-made buildings are also present the volume scattering, thus this model cannot distinguish forest and man-made buildings.

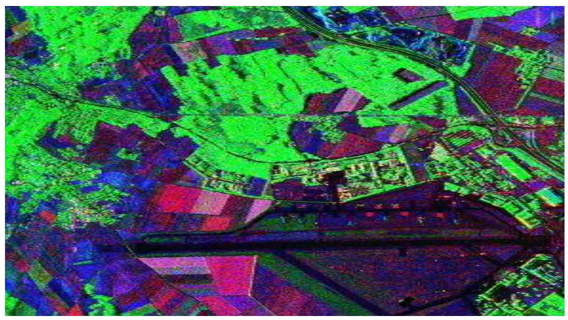

Figure 5: Freeman decomposition, the image is colored by P_d (red), P_v (green), and P_s (blue).

4.2. OEC Decomposition

For urban area, the reflection symmetry condition does not hold, it is necessary to take the effect of $\langle s_{hh}s_{hv}^*\rangle \neq 0$ and $\langle s_{vv}s_{hv}^*\rangle \neq 0$ into account. In 2005, Moriyama proposed a model for urban area information extraction [5]. The model decomposes the covariance matrix into three kinds of scattering mechanisms: odd-bounce scattering; even-bounce scattering and cross scattering:

$$[C] = f_{odd}[C_{odd}] + f_{even}[C_{even}] + f_{cross}[C_{cross}] \tag{8}$$

where f_{odd}, f_{even} and f_{cross} represent the weight of odd bounce scattering, even bounce scattering, and cross scattering, respectively. $[C_{odd}]$, $[C_{even}]$ and $[C_{cross}]$ represent the corresponding covariance base, respectively. Then the power of each term P_{odd}, P_{even} and P_{cross} can be calculated respectively. P is the total power of the three scattering.

$$\begin{aligned} &P_{odd} = f_{odd}(1 + |\beta|^2) \\ &P_{even} = f_{even}(1 + |\alpha|^2) \\ &P_{cross} = f_{cross}(1 + |\gamma|^2 + 2\,|\rho|^2) \\ &P = P_{odd} + P_{even} + P_{cross} \end{aligned} \tag{9}$$

In urban area, buildings have strong even-bounce scattering characteristics, and their information can be easily extracted from even-bounce scattering component. Fig. 6 shows OEC decomposed image. Comparing Fig. 6 with Fig. 1(b), we can find most of farmlands are mainly even-bounce scattering and some farmlands in the middle are mainly odd-bounce scattering. Fig. 6 shows that even-bounce scattering is the dominant scattering mechanism in urban areas. Therefore, this model is suitable to extract polarimetric feature of urban areas. The forest area has a mixed color which means odd scattering and even scattering are contained. The analysis shows that different targets may have dissimilar scattering components. Because the longer wavelengths can penetrate canopy and the backscatter is mostly double-bounce from the ground-trunk interaction. So at L band, forest also indicates even scattering in OEC decomposition. As known buildings are mainly even scattering, therefore, OEC decomposition cannot distinguish forest and buildings well.

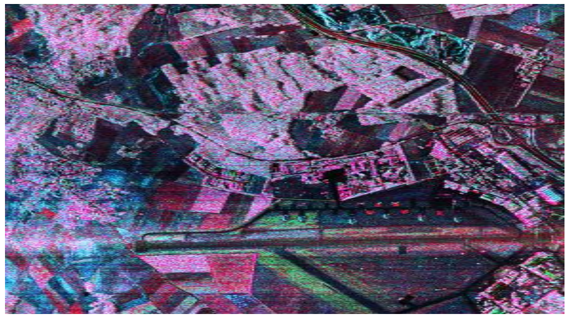

Figure 6: OEC decomposition, the image is colored by P_e (red), P_c (green), and P_o (blue).

4.3. Four-component Scattering Model

Yamaguchi proposes a four-component scattering model based on Freeman's three-component model, in which, covariance matrix $[C]$ or coherency $[T]$ can be denoted as four scattering mechanisms [6, 7]:

$$[C] = f_s[C_{surface}] + f_d[C_{double}] + f_v[C_{volume}] + f_c[C_{helix}] \tag{10}$$

where f_s, f_d, f_v and f_c are the expansion coefficients to be determined. $[C_{surface}]$ and $[C_{double}]$ are identical with those in Freeman decomposition, $[C_{volume}]$ is modified with $10\log\left(\langle|s_{hh}|^2\rangle/\langle|s_{vv}|^2\rangle\right)$, and $[C_{helix}]$ is introduced for encountering the helix scattering power contribution. The scattering powers, P_s, P_d, P_v and P_c corresponding to surface, double bounce, volume and helix contributions, respectively, are obtained as:

$$\begin{array}{l} P_s = f_s(1+|\beta|^2) \quad P_d = f_d(1+|\alpha|^2) \\ P_v = f_v \quad P_c = f_c \\ P = P_s + P_d + P_v + P_c \end{array} \tag{11}$$

Compared with three-component scattering model, the helix scattering power, corresponding to $\langle s_{hh}s_{hv}^*\rangle \neq 0$ and $\langle s_{vv}s_{hv}^*\rangle \neq 0$, is introduced for more general scattering mechanism as the fourth component, which often appears in complex urban areas whereas disappears in almost all natural distributed scenarios. This term is essentially caused by the scattering matrix of helices and is relevant for the complicated shapes of man-made structures, which are predominant in urban areas. Furthermore, the volume scattering component for vegetation is modified by a change of the probability density function for the associated orientation angles, and the choice between the symmetric and the asymmetric covariance can be determined by $10\log\left(\langle|s_{hh}|^2\rangle/\langle|s_{vv}|^2\rangle\right)$ of the image.

The decomposed result of the covariance matrix with P_s (blue), P_d (red), and P_v (green) is shown in Fig. 7(a). It is seen in Fig. 7(a) that P_v (green) is especially strong in the forest area. Most farmland in blue indicates that there is no other scattering mechanism except single bounce scattering. Some farmland in pink indicates that both surface scattering and double-bounce scattering exist. Overall, the decomposition result is acceptable. In urban area, when orientation of building blocks is not parallel to the flight path, these areas with skew-oriented buildings produce a

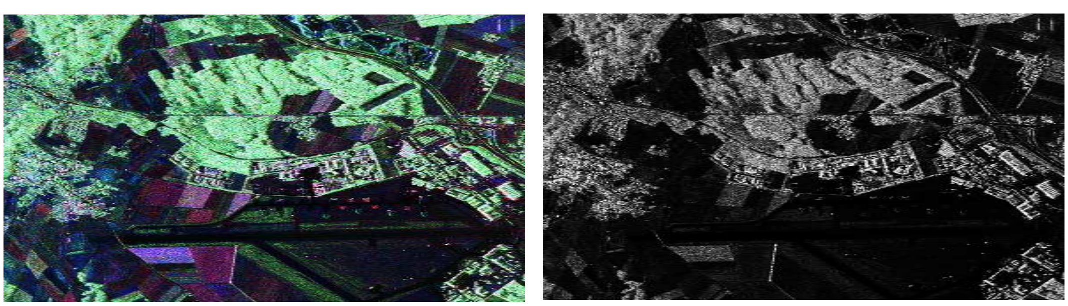

(a) (b)

Figure 7: Four-component decomposed image, (a) the image is colored by P_d (red), P_v (green), and P_s (blue), (b) helix scattering power P_c.

rather predominant HV component. Therefore, the helix scattering component P_c appears strong in these areas as shown in Fig. 7(b).

Table 1: Comparison of coherent and incoherent polarimetric decomposition.

Type of decomposition model		Merits	Demerits
Coherent	Pauli	can distinguish natural target well	cannot detect man-made target
	SDH	can distinguish man-made target from natural target well	cannot divide one kind of man-made target from another kind
	Cameron and SSCM	better exploit the information provided by the maximized symmetric scattering component of coherent targets	not suitable for complex scenario containing a lot of asymmetric targets
Incoherent	Freeman	can describe different natural targets very good and suitable for analyzing the natural distributed target areas	cannot distinguish forest and man-made buildings
	OEC	effective to extract polarimetric feature from urban areas	cannot distinguish forest and buildings well
	Four-component	more general scattering model for both natural targets and man-made targets	

5. DISCUSSION AND CONCLUSION

Table 1 gives a comparison of coherent and incoherent polarimetric decomposition. It can be found that the coherent and incoherent decomposition models have quite comparable results in distinguishing natural targets and man-made buildings. Pauli decomposition, Cameron decomposition and Freeman decomposition are suitable for description of natural targets. On the other hand, SDH decomposition, OEC decomposition, and Four-component model, in particular, are better in describing man-made targets, since they take helix scattering mechanism into consideration, which is a general scattering in urban area. Since the result is obtained only with one test data, the conclusion has certain limitation. A general preference for these methods in other test should therefore be further challenged by follow-on studies.

ACKNOWLEDGMENT

This work is supported by National Natural Science Foundation of China, No. 60672091.

REFERENCES

1. Krogagar, E. and Z. H. Czyz, "Properties of the sphere, diplane, helix (target scattering matrix decomposition)," *Proc. JIPR-3*, J. Saillard, et al., Eds., 106–114, Nantes, France, March 21–23, 1995.
2. Cameron, W. L., N. N. Youssef, and L. K. Leung, "Simulated polarimetric signatures of primitive geometrical shapes," *IEEE Trans. on GRS*, Vol. 34, No. 3, 793–803, 1996.
3. Touzi, R. and F. Charbonneau, "characterization of target symmetric scattering using polarimetric SARs," *IEEE Trans. on GRS*, Vol. 40, No. 11, 2507–2516, 2002.
4. Freeman, A. and S. L. Durden, "A three-component scattering model for polarimetric SAR data," *IEEE Trans. on GRS*, GRS-36(3), 963–973, 1996.
5. Moriyama, T., T. Uratsuka, S. Umehara, T. et al., "Polarimetric SAR image analysis using model fit for urban structures," *IEICE Trans. Commun.*, E88-B(3), 1234–1242, 2005.
6. Yamaguchi, Y. and T. Moriyama, "Four-component scattering model for polarimetric SAR image decomposition," *IEEE Trans. on GRS*, Vol. 43, No. 8, 1699–1706, 2005.
7. Yamaguchi, Y., Y. Yajima, and H. Yamada, "A four component decomposition of polsar images based on the coherency matrix," *IEEE GRSL*, Vol. 3, No. 3, 292–296, 2006.

Localization in Near Field with Wideband Signal: Trade-off between Bandwidth and Number of Sensors

H. He, Y. Wang, and J. Saillard

Laboratoire IREENA, Polytech'Nantes, University of Nantes, France

Abstract— In this article, we present an analysis on resolution of source localization in near field, which concerns mainly the influences on spatial resolution from bandwidth and number of sensors. The resolution is quantified by false estimation rate for a system to separate two sources. Based on simulation results, the trade-off between bandwidth and number of sensors is found approximately. With this relation, we can define an optimal localization system by choosing the best repartition.

1. INTRODUCTION

Source localization in near field has drawn a lot of interests during last few decades. Compared to far field, localization in near field is much more challenging because the wave front is no longer a plan wave when the sources are located near the arrays. The sub-space methods [3] like MUSIC, ESPRIT ... etc. are often used in far-field source localization, however, only the classical MUSIC method can be applied to near field [4]. In near-field, the sources may be close to each other so that to establish localization system with high resolution is very important. There are usually two ways to improve the resolution [3]: to increase the number of sensors and to increase the number of samples. Increasing the number of sensors enlarges the antenna aperture, while increasing number of samples allows better estimates of the covariance matrix of the received signal. Using a wideband signal is an equivalent way to increase the number of samples. By taking summation of the covariance matrices estimated in each frequency, the equivalent number of samples is greatly increased.

Usually, there are two ways to sum the covariance matrices [2]: incoherent summation and coherent summation. The performance of coherent summation is better because the noise factor decreases when taking the coherent summation, but this method brings also errors because the summation is based on a pre-estimated data which is not accurate.

The spatial resolution of localization system depends on a lot of parameters, such as the Signal to Noise ratio, the number of sensors, the number of samples and the number of frequencies. To compare the influences on resolution from the parameters, we quantify the resolution by false estimation rate which is the possibility of failure for a system to separate two sources. We can find the trade-off between these parameters for a defined resolution capacity, and then an optimal system can be found by choosing the best repartition.

In this article, we present the main idea of quantification of spatial resolution. The trade-off between the parameters can be found from simulations.

2. QUANTIFICATION OF RESOLUTION

The resolution is usually quantified as the 3 dB beamwidth [1] of the pseudo-frequency for conventional beamforming method. Since the calculation of this beamwidth depends on the eigenstructure of the covariance matrix, it is very difficult to obtain an accurate result.

The resolution of localization refers to the capacity to separate two sources which are located close to each other. In this article, we define a method to quantify the resolution. The principal of this method is to calculate the possibility of false localization under a certain condition.

We suppose two sources which locate at (ρ_1, θ_1) and (ρ_2, θ_2). The distance between these two sources is:

$$d = \sqrt{\rho_1^2 + \rho_2^2 - 2\rho_1\rho_2 \cos(|\theta_1 - \theta_2|)} \tag{1}$$

The two estimated positions of sources are $(\hat{\rho}_1, \hat{\theta}_1)$ and $(\hat{\rho}_2, \hat{\theta}_2)$.

If the two estimates satisfy these two conditions:

$$\sqrt{\rho_1^2 + \hat{\rho}_1^2 - 2\rho_1\hat{\rho}_1 \cos(|\theta_1 - \hat{\theta}_1|)} \leq d/2 \quad \text{and} \quad \sqrt{\rho_2^2 + \hat{\rho}_2^2 - 2\rho_2\hat{\rho}_2 \cos(|\theta_2 - \hat{\theta}_2|)} \leq d/2$$

it is a correct estimation, or it is a false estimates.

The false estimation rate is then calculated by carrying out Monte-Carlo experiment under the same conditions.

$$P_e = \frac{\text{number of false estimates}}{\text{total number of estimates}} \tag{2}$$

3. CONCLUSIONS

We have defined a method to quantify spatial resolution in this article. The trade-off between the parameters of a localization system can be found from simulations. With this relation, we can optimize our localization system by choosing the best repartition. The future work of this research will be the theoretical analysis on the influence from the parameters.

REFERENCES

1. Scharf, L. L. and P. H. Moose, "Information measures and performance bounds for array processors," *IEEE Transactions on Information Theory*, Vol. 22, No. 1, 11–21, January 1976.
2. Marcos, S., "Les méthodes à haute résolution — traitement d'antenne et analyse spectrale," HERMES, Paris, 1998.
3. Saidi, Z. and S. Bourennane, "Cumulant-based coherent signal subspace method for bearing and range estimation," *EURASIP Journal on Advances in Signal Processing*, Vol. 2007, Article ID 84576, 9 pages, doi:10.1155/2007/84576, 2007.
4. Stoica, P. and A. Nehorai, "MUSIC, maximum likelihood, and Cramer-Rao bound," *IEEE Trans. Acoust., Speech, Signal Processing*, Vol. 37, No. 5, 720–741, 1989.
5. Williams, M. I. Y., G. Dickins, R. A. Kennedy, and T. D. Abhayapala, "Spatial limits on the performance of direction of arrival estimation," *Proceedings of the 6th Australian Communications Theory Workshop 2005*, 189–194, February 2–4, 2005.

Investigation of Novel Surface Acoustic Wave (SAW) Gas Sensor Used in Sensor Network

Mitsutaka Hikita, Keiya Minami, Koki Takimoto, and Yasushi Hiraizumi
Kogakuin University, Nishi-Shinjuku, Shinjuku-ku, Tokyo, Japan

Abstract— Mobile communications, e.g., cellular phones, have become very widespread. A new concept called "Sensor Network" has been proposed with the development of such communications system. Sensed signals from many sensor nodes installed in a wide area are gathered to a center node by technology similar to that used in mobile communications. Home/office circumstance control, environment monitoring and protection can be conducted based on the collected data. We propose a new SAW subtle-gas sensor, which can be used in these sensor nodes. The new sensor structure removes a limited selection for piezoelectric crystal substrates, while only Quartz crystal substrates have been used in conventional SAW gas sensors. The sensing dynamic range was widely extended by utilizing both fundamental and 3rd-harmonic frequency SAWs. Moreover, our sensors are also designed to be combed with 2.4-GHz ZigBee, which has been regulated by IEEE802.15.4, and ZigBee Alliance as a wireless-communications medium for the "Sensor Network". It is predicted that our network system will possibly provide hydrogen-gas leakage sensing for future fuel-cell cars and environmental-pollution gas sensing.

1. INTRODUCTION

In the last half of the twentieth century, mobile communications by means of the cellular-phone system have spread all over the world. Recently, a sensor network has been investigated to control the circumstances at homes, offices and public places. In this system, simple radio communications network is installed in a certain area to connect many distributed sensors by similar technology to that used in cellular-phone system. The sensor network is treated as a new concept which will have a big impact on our lives and grow to a giant industry like the cellular-phone system. It will also contribute to future ecology, i.e., energy saving and environment preservation. In our laboratory, we have been studying the sensor network to achieve comfortable living circumstances by home/office sensing and control [1]. As shown in Fig. 1, many sensor nodes with various sensors will be arranged within homes and offices, where nodes can communicate one another via simple radio network. Sensed signals from all nodes are gathered to a center node. The center node not only supervises sensor nodes and processes collected data but also sends control signals to other installations.

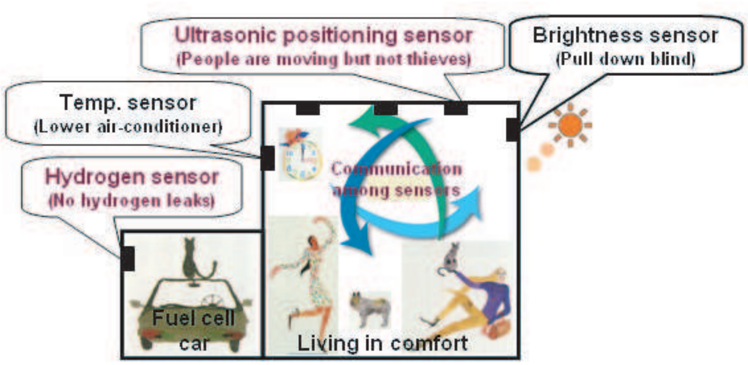

Figure 1: Sensor network with various sensors.

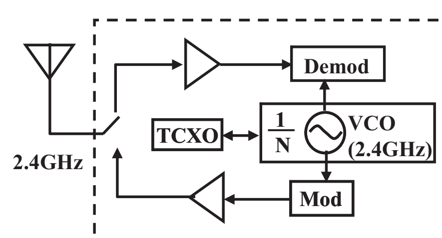

Figure 2: Block diagram for ZigBee node.

In this paper, we propose a new sensor-node structure and a novel SAW (Surface Acoustic Wave) gas sensor which can operate within the sensor node. One of the most successful SAW gas-sensors is a SAW GC (gas chromatography) invented by E. J. Staple, et al. [2, 3]. However, it has a rather complicated structure using not only a SAW sensor but also a trap tube and a column tube to separate gases according to their molecule weight. Due to the rather large size and the high power consumption, it can not be adopted in sensor network. Moreover, only Quartz crystal substrates have been used in these kinds of conventional SAW gas sensors, because conventional SAW sensors require very good temperature characteristics for the piezoelectric substrates. We have invented a novel SAW gas sensor, which can remove such a limited selection for piezoelectric crystal substrates.

ZigBee has been regulated by IEEE 802.15.4 [4] and ZigBee Alliance as a wireless-communications medium for the sensor network. One important feature required for ZigBee is the extreme low-power consumption, which provides several-year operation with a single battery. In ZigBee, 2.4 GHz is used to connect sensor nodes mutually in the sensor network. They can provide not only conventional star-link but also new mesh-link types of network topology. Our sensor is also designed to be combined with 2.4-GHz ZigBee. Sensing signals with several hundred MHz are generated by division and multiplication of 2.4-GHz signal, which can remove the necessity of a SAW feedback oscillator used in the conventional SAW sensors [5, 6]. Moreover, the dynamic range of our sensor is expanded by using not only fundamental but also 3-rd harmonic frequency SAWs to detect gasses. For example, 150 MHz obtained from 2.4 GHz divided by 16 is used in coarse sensing, while 450 MHz i.e., 150 MHz multiplied by 3 is used in fine sensing. The proposed sensor not only can be assembled within the sensor node but also provides self-temperature-compensated characteristics. We will give an illustration of the 2.4-GHz ZigBee-based sensor node in the 2nd Section and present a detail explanation about the SAW gas sensor in the 3rd Section. These sensor nodes with gas sensors installed in the sensor network will be used for sensing hydrogen gas leaked from fuel-cell cars as well as other pollution gases in the future.

2. NEW ZIGBEE-BASED SENSOR-NODE STRUCTURE

ZigBee which uses 2.4 GHz has been regulated by IEEE802.15.4 as one of radio standards for low data-rate communications media such as a sensor network [4]. As a block diagram is shown in Fig. 2, the conventional ZigBee-based sensor node consists of 2.4-GHz VCO (Voltage-Controlled Oscillator) locked to TCXO (Temperature-Compensated Xtal Oscillator) and other circuit components.

We have proposed a new sensor-node structure which is constructed with not only Fig. 2's circuits but also a SAW gas sensor as shown in Fig. 3. In our configuration, sensing RF signals e.g., 150-MHz and 450-MHz signals which are supplied to the SAW sensor are generated from 2.4-GHz signal in the ZigBee circuit. These frequencies are obtained from 2.4 GHz divided by 16 and from 150 MHz multiplied by 3, respectively. As will be explained in the next Section, 150 MHz corresponds to a fundamental SAW, while 450 MHz to a 3rd-harmonic SAW. Both of them can be excited by a single IDT (Interdigital Transducer). When the concentration of hydrogen-gas molecule is very subtle, the 450-MHz 3rd-harmonic SAW is used for sensing with high sensitivity. On the other hand, the 150-MHz fundamental SAW is used for coarse sensing of dense concentration. Therefore a wide sensitivity dynamic range can be achieved by changing two frequencies.

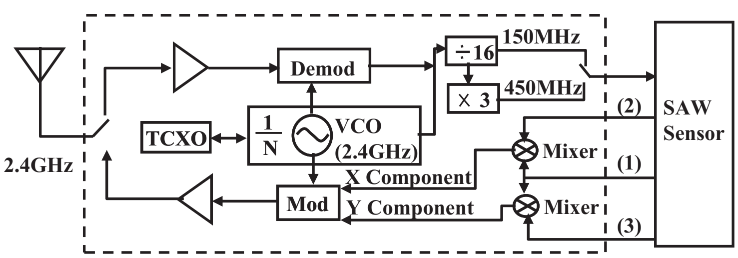

Figure 3: New sensor node with SAW sensor based on ZigBee.

3. NOVEL SAW GAS SENSOR

3.1. Basic Configuration of Sensor

We use three SAW delay lines in our sensor as shown in Fig. 4. Each delay line has input and output IDTs, between which thin film reactive to specific gas molecule is formed. In the case of palladium (Pd) thin film, hydrogen molecule reacts with Pd to produce small mass loading along the SAW propagation path, which results in phase shift of the received SAW. As shown in Fig. 4, the propagation length between input and output IDTs for the delay line of D-1 is defined as L. Other lengths for D-2 and D-3 are $L - \lambda_o/8$ and $L + \lambda_o/8$, respectively, where λ_o is a SAW wavelength. The D-1 is used as a sensing delay line. The D-2 and D-3 are isolated from air and provide standard phases determined by SAW propagation lengths between IDTs.

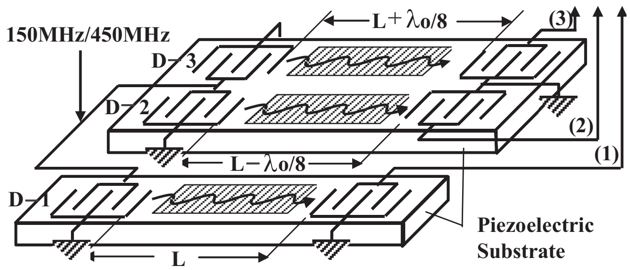

Figure 4: Fundamental configuration for novel SAW gas sensor.

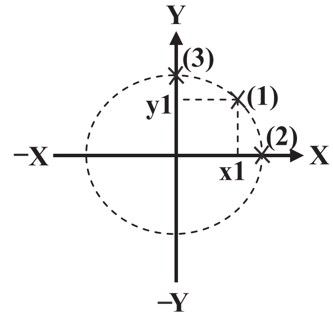

Figure 5: Phase relations for three output signals.

First we assume that the 150-MHz signal which corresponds to a fundamental SAW is providing from the sensor-node circuit shown in Fig. 3. The signal is supplied to all input IDTs of three delay lines, and the received signals from output IDTs are numbered from (1) to (3) in order according to the delay lines from D-1 to D-3 as shown in Fig. 4. Phase relations of three output signals from (1) to (3) are shown in Fig. 5. If the output signal (2) is assumed to be a standard signal with 0-rad phase and to exist on X axis, the output signal (3) is located on Y axis with $\pi/2$-rad phase due to $\lambda_o/4$-propagation path difference. With no concentration of sensing gas, location of the sensor output signal (1) is in the middle point between two output signals (2) and (3) as shown in Fig. 5, because the delay-line length of D-1 is in-between for both D-2 and D-3. With increase of gas concentration signal (1) moves along Fig. 5's circle. This phase shift for propagating SAW is produced due to mass loading effect of sensing gas. It also can be measured based on $x1$ (in-phase) and $y1$ (quadrature-phase) components given by projected values to X and Y axes respectively as shown in Fig. 5. Moreover the delay lines D-2 and D-3 are isolated from the sensing gas, therefore they can provide standard in-phase (I) and quadrature-phase (Q) signals unrelated to gas concentration. The $x1$ and $y1$ can be obtained by mixing the sensor signal (1) with the standard signals (2) and (3) respectively as shown in Fig. 3.

3.2. Self-temperature-compensation Characteristics

SAWs propagating along the general piezoelectric substrates, e.g., LiNbO3, LiTaO3, LBO have velocities with negative temperature coefficients for rising temperature. Their values are from 20 to 100 ppm/°C, which can not be negligible when considering wide temperature range from −40° to 100°C required for the sensor network especially for use within a garage. The phase relations between sensor signal (1) and the standard signals (2)/(3) at room temperature are shown in Fig. 6(a)'s constellation, which are same as in Fig. 5. When the temperature rises the velocity of SAW is decreased, which results in increase of each delay line's phase delay. This corresponds to counter-clockwise rotation in the constellation for each output signal as shown in Fig. 6(b). The more rises the temperature, the further increases the rotation-angle as shown in Fig. 6(c). However, the temperature change has same influence to all three SAW delay lines, which keeps unchanged relative phase relations among three output signals. Therefore, if we introduce new axes of X' and Y', the values projected to X' and Y' can offer same I and Q components as $x1$ and $y1$ at room temperature. This means that the novel sensor structure provides self-temperature-compensation characteristics. The actual phase shift only due to the gas concentration can be obtained independent of the environmental temperature condition.

3.3. Sensing Characteristics with 3rd-harmonic SAW

An IDT can excite both fundamental and 3rd-hamonic SAWs in principle as shown in Fig. 7. However, a problem is low excitation efficiency for the 3rd-haomonic SAW. We have been investigating finger shape of IDT electrodes versus excitation efficiency focusing on the 3rd-harmonic SAW. Various kinds of combination between Fig. 7's electrode finger width W(M) and space width W(S) are possible. We have found that some combinations can provide good excitation efficiency for the 3rd-harmonic SAW as well as reasonable efficiency for the fundamental SAW. These results will be published in other paper.

Almost same excitation efficiency for both fundamental and 3rd-harmonic SAWs are assumed, which provides phase relations between the output signal (1) and the output signals (2)/(3) for the 3rd-harmonic SAW as shown in Fig. 8's constellation. In this case, if we take the output signal (2)

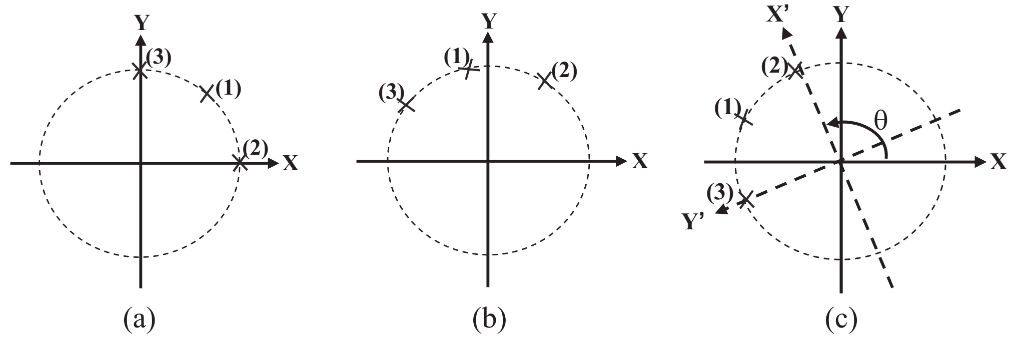

Figure 6: Phase rotations due to temperature change, (a) Room temperature; (b) Counter-clockwise rotation due to temperature rising; (c) New axes, X' and Y'.

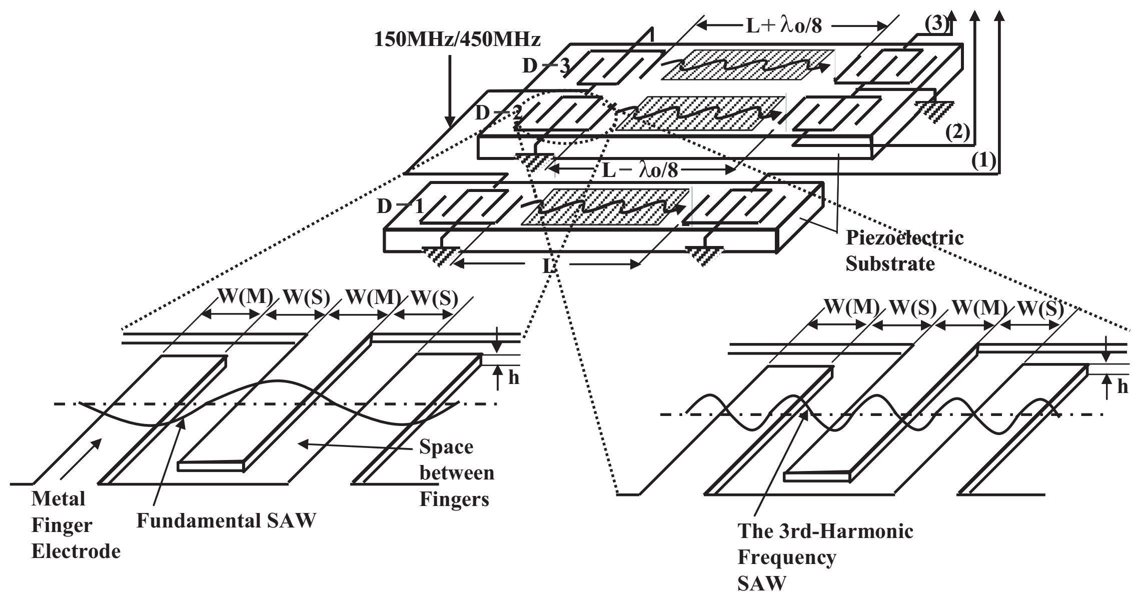

Figure 7: Excitation of fundamental and 3rd-harmonic frequency SAWs.

as a standard signal on X axis with 0-rad phase, the output signal (3) is on $-Y$ axis with $3\pi/2$-rad phase because the quarter-wavelength path difference for fundamental SAW corresponds to three-quarter-wavelength path difference for the 3rd-harmonic SAW. The sensor output signal (1) for the 3rd-harmonic SAW is located in the middle point between (2) and (3). Therefore, changing the sign of the output (3), which is equivalent to changing sign of the mixer output signal obtained from mixing between (1) and (3) shown in Fig. 3, ensures that same procedures as used in the fundamental SAW can be applied to the 3rd–harmonic SAW. The phase shift of the output signal (1) which can

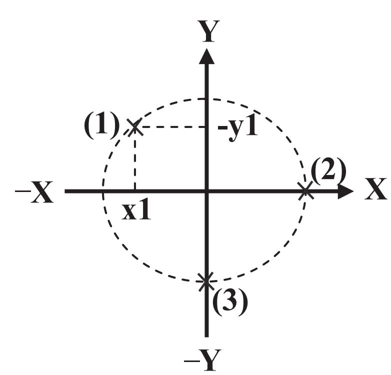

Figure 8: Phase relations for three output signals at 3rd-harmonic frequency.

be monitored by $x1$ and $-y1$ provides amount of gas concentration, whose sensitivity is three times higher than that of the fundamental SAW.

4. CONCLUSION

"Sensor Network" has been investigated as a small-sized radio-communications infrastructure. We have been studying such sensor network as a method to improve home/office circumstances. In this paper, we have proposed a new sensor-node configuration based on 2.4-GHz ZigBee and a novel SAW sensor. Features of our SAW sensor are as follows: (1) Sensing RF signals are generated from the ZigBee circuit, (2) Temperature coefficients of piezoelectric substrates do not need to be considered due to self-temperature-compensation characteristics of the sensor, (3) Wide sensing dynamic range can be achieved by using both fundamental and 3rd-harmonic SAWs. The sensor and sensor node installed in the 2.4-GHz ZigBee-based sensor network will be very useful for future home/office-circumstance control.

REFERENCES

1. Home Page of Kogakuin University, http://www.ns.kogakuin.ac.jp/∼wwa1022/.
2. Staples, E. J., "Dioxin/Furan detection and analysis using a SAW based electronic nose," *IEEE Ultrason. Symp. Proc.*, 521–525, 1998.
3. Electronic Sensor Technology HP, "Chemical sensor for the 21 century," http://www.estcal.com/.
4. IEEE Standard 802.15.4: Wireless Medium Access Control (MAC) and Physical Layer (PHY) Specifications for Low Rate Wireless Personal Area Networks (LR-WPANs), 2003.
5. Yamanaka, K., S. Ishikawa, N. Nakaso, N. Takeda, T. Mihara, and Y. Tsukahara, "Ball SAW devices for hydrogen gas sensor," *IEEE Ultrason. Symp. Proc.*, 229–302, 2003.
6. Kogai, T. and H. Yatsuda, "Liquid sensor using SAW and SH-SAW on Quartz," *IEEE Ultrason. Symp. Proc.*, 552–555, 2006.

Anisotropic Ultrafast Dynamics in Doped $Y_{1-x}Ca_xBa_2Cu_3O_{7-\delta}$ Superconducting Thin Films

C. W. Luo[1], K. H. Wu[1], J.-Y. Lin[2], T. M. Uen[1], Y. S. Gou[3], and J.-Y. Juang[1]

[1]Department of Electrophysics, National Chiao Tung University, Hsinchu, Taiwan, R.O.C.
[2]Institute of Physics, National Chiao Tung University, Hsinchu, Taiwan, R.O.C.
[3]Department of Physics, National Taiwan Normal University, Taipei, Taiwan, R.O.C.

Abstract—The anisotropic dynamics of photoinduced quasiparticle in the $Y_{1-x}Ca_xBa_2Cu_3O_{7-\delta}$ (YCBCO) is revealed by using the orientation-resolved femtosecond reflection spectroscopy. This bulk-sensitive spectroscopy, combining with the well-textured (110)- and (100)- YCBCO thin films, serves as an effective probe to quasiparticle relaxation dynamics along different crystallographic orientations. Since the temperature at which the peak of temperature-dependent relaxation time (τ) manifested in the transient reflectance ($\Delta R/R$) measurements is believed to intimately relate to the opening of superconducting gap, the results reported here should shed some light on the issue of the competing order scenarios for over-doped high-T_c superconductors.

1. INTRODUCTION

The doping-dependent symmetry of superconducting gap and pseudogap of the cuprate superconductors has been a crucial but yet unsettled ingredient for unveiling the high-T_c superconductivity. Another issue of interest is concerning the role played by the pseudogap; a precursor or a competitor? [1, 2] In particular, whether or not the pseudogap will disappear in the overdoped regime after both gaps merged in the vicinity of optimal doping remains an issue of extensive debate.

Unlike other spectroscopic studies used extensively in revealing the density of states near the anisotropic Fermi surface [3–6], the time-domain spectroscopy essentially delineates the electronic states *a priori* to superconductivity and, hence, could potentially provide information on the possible connections between the pseudogap above T_c and the superconducting gap below T_c [7–9]. It is generally agreed by both theoretical and experimental communities that *the amplitude and relaxation time of the transient reflectivity in picosecond scale below T_c are directly associated with the opening of the superconducting gap* and the results are bulk in nature. In this scenario, the significant anisotropies in both the magnitude of the characteristic relaxation time and the photoinduced transient reflectivity changes observed in the *bc*-, *ab*-diagonal-*c* and *ab*-planes should imply that the nature of relaxation channel might be intrinsically anisotropic in different planes and along different orientations of the CuO_2 (*ab*) planes. Previously, we had successfully combined the polarized pump-probe beam with $YBa_2Cu_3O_{7-\delta}$ (YBCO) thin films grown in specific orientations to study the gap evolution and anisotropy in the under-doped to optimally doped regime [12]. Here, we report a continuous effort along the line, albeit some deviations have been evidently observed in the over-doped regime.

2. EXPERIMENTS

2.1. Preparation of (100) and (001) $Y_{1-x}Ca_xBa_2Cu_3O_{7-\delta}$ Thin Film

All of the well characterized thin films with various orientations used in this study were prepared by pulsed laser deposition (PLD). It has been suggested that a $PrBa_2Cu_3O_{7-\delta}$ (PBCO) buffer layer can facilitate the *a*-axis nucleation [11] on K_2NiF_4 type (100) $LaSrGaO_4$ (LSGO) substrates [12]. However, due to the low substrate temperature required to form the *b*-axis oriented PBCO layer, the YBCO films thus obtained all suffered from significant degradation in T_c. To overcome this problem, we developed a modified deposition process, which could produce well-aligned *a*-axis oriented YBCO films [10]. Briefly, a 50-nm-thick PBCO template was deposited on a LSGO substrate at lower temperature ($\sim$660 °C) in 0.1 Torr of O_2. Then, without interrupting the deposition of the PBCO layer, the substrate temperature was raised at a rate of 20 °C/min until it reached 780 °C. The target was switched to YBCO and the oxygen pressure was raised to 0.28 Torr immediately. Finally, a 300-nm-thick YBCO was deposited on the PBCO template. After the deposition, the film was cooled in 600 Torr of oxygen to room temperature with the heater off. This process not only has successfully grown the nearly full in-plane alignment (100) YCBCO but also improved the T_c significantly.

For (001) YCBCO thin films, the deposition conditions were relatively loose, e.g., without a buffer layer, many available substrates, and wide-range of deposition temperatures. Briefly, a KrF excimer laser operating at a repetition rate 3–8 Hz with an energy density of 2–4 J/cm^2 was used. The oxygen partial pressure during deposition was maintained at 0.25 Torr. The substrate temperature was kept at 780–790 °C for 300-nm-thick (001) YCBCO films deposited on a (100) STO substrate. After the deposition, the film was cooled in 600 Torr of oxygen to room temperature with the heater off.

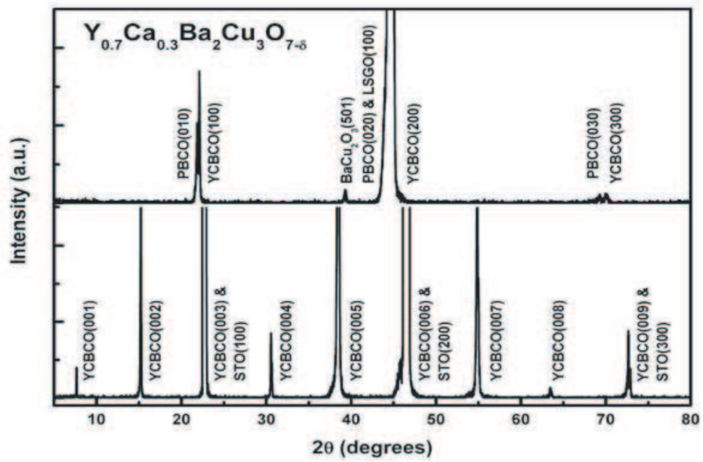

Figure 1: The x-ray diffraction (XRD) pattern of the 30% Ca-doped (100)-YCBCO (the upper panel) and (001)-YCBCO (lower panel) films. Notice the excellent orientation purity and crystallinity quality of the films obtained by the present processes.

Figure 1 shows the x-ray diffraction results for the 30% Ca-doped (100)- and (001)-YCBCO films obtained by using the deposition conditions described above. It is evident that, despite of a minute trace of $BaCu_2O_3$ impurity phase existing in the (100)-YCBCO film, both films exhibit well-oriented characteristics. The ϕ-scan of (102) peak of the (100)-oriented films (not shown here) showed an essentially 180° (two-fold) symmetry with an in-plane alignment better than 95%, as estimated by the ratio between the peak intensities at $\phi = 0°$ and $\phi = 90°$, $I_{\psi=0°}/\left(I_{\psi=0°} + I_{\psi=90°}\right)$. On the other hand the (001)-oriented films displayed the usual four-fold symmetry indicating the a-b axes mixed characteristic.

2.2. Setup for Quasiparticle Dynamics Measurements

The details of the experimental setup used in this study can be found elsewhere [10, 12]. Briefly, the femtosecond pulses from the Ti: sapphire laser was pre-chirped by two prisms before split into pump and probe beams. Both pump and probe beams went through two acousto-optic modulators (AOM), respectively. The spatial overlap of pump and probe beams on the sample was monitored by the CCD camera. The reflection of the probe beam was received by the photodiode. The multimeter and the lock-in amplifier took the DC (R) and AC (ΔR) components in the signal, respectively. We utilized the computer to control the delay stage (delay time, t) and measured the

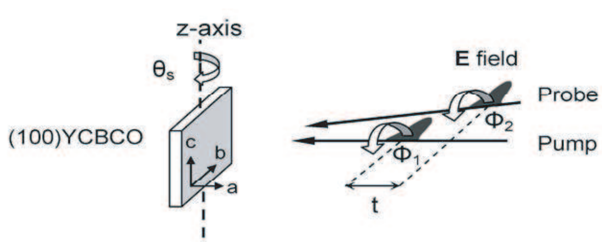

Figure 2: The polarized pump-probe experimental setup. $\Phi_1(\Phi_2)$ is the angle between the b-axis and the pump (probe) pulses. θ_s: the angle between the surface of samples and the polarization of the pump (or probe) pulses. t: the time delay between the pump and probe pulses.

data $[\Delta R/R(t)]$. Moreover, the $\Delta R/R(t, \Phi_1, \Phi_2, \theta_s)$ curves along various directions on the surface of the sample could be obtained by rotating the polarization of pulses (Φ_1, Φ_2) at nearly normal incidence, $\theta_s \sim 0°$ (actually, $\theta_{s,pump} = 4°$ and $\theta_{s,probe} = 1.5°$), as schematically depicted in Fig. 2. In this way, one should be able to measure the responses $[\Delta R/R(t, 0, 0, \theta_s)]$ along various directions in the ab-plane by changing the angle θ_s. The temperature was controlled by mounting the samples on the cold finger of a Janis cryostat connected with transfer tube through a needle valve and an additional 25 Ω resistive heater. The variable temperature range was between 10 and 300 K with a resolution better than 0.1 K. Furthermore, there are four quartz windows with $\Phi = 50$ mm on the vacuum jacket allowed the optical pulses into and out of the low temperature chamber.

3. RESULTS AND DISCUSSION

Figure 3 shows the typical $\Delta R/R$ traces as a function of temperature obtained in (100)-YCBCO (left panel) and (001)-YCBCO (right panel) films with $T_c = 61$ K and 62 K, respectively. As can be seen in both panels, the amplitude of $\Delta R/R$ displays several features. First, the amplitude starts to have noticeable changes at temperatures significantly higher than the film transition temperatures determined by transport measurements and its magnitude appear to increase gradually with decreasing temperature. Secondly, the response is much stronger along the b-axis than within the ab-plane, indicating that superconductivity may be more relevant in b-axis as generally expected. Finally, unlike the underdoped $YBa_2Cu_3O_{7-\delta}$ (YBCO) and slightly (10%) Ca-doped YCBCO samples [10, 12] where the one-component transient was observed to have different temperature dependence for $T < T_c$ (A-type) and $T > T_c$ (B-Type), there appears to have two components in the $\Delta R/R$, the negative and positive transient changes, in the current films. In explaining the similar phenomena observed in the slightly overdoped $Y_{1-x}Ca_xBa_2Cu_3O_7$, Demsar et al. [9] attributed the A-type temperature dependence of $\Delta R/R$ to the opening of the superconducting gap, while claiming the B-type temperature dependence as being governed by the pseudogap.

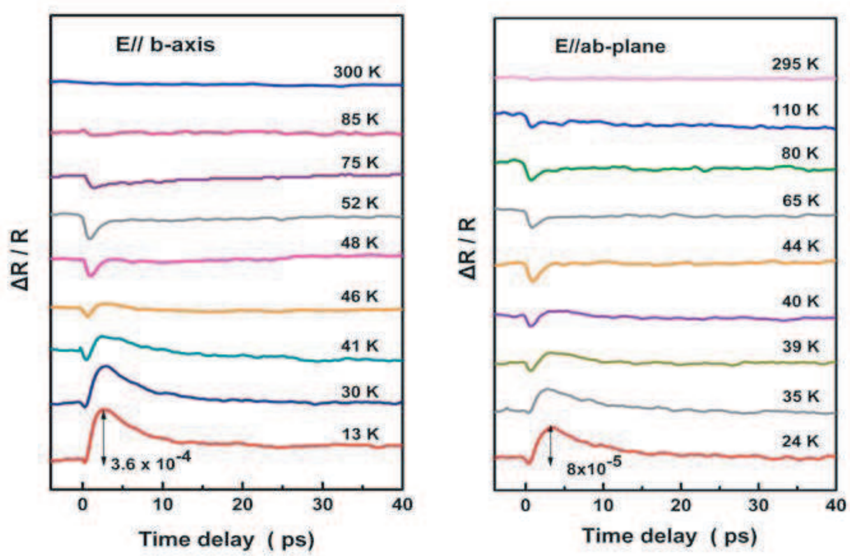

Figure 3: The temperature dependence of $\Delta R/R$ for (100)-YCBCO film ($T_c = 61$ K, left panel) and (001)-YCBCO film ($T_c = 62$ K, right panel). Notice that the changes start to appear at temperatures much higher than the resistive critical temperature of the films.

In order to make a more detailed comparison, we plot the amplitude change and relaxation time of $\Delta R/R$ as a function of temperature in Fig. 4. We note that the relaxation behavior of photoinduced quasiparticle in the present further overdoped samples exhibited a dramatically different behavior as that observed in slightly overdoped samples of $Y_{0.9}Ca_{0.1}Ba_2Cu_3O_{6.92}$. For the amplitude change (left panel of Fig. 4), the additional negative component emerging at temperatures near T_c appears to be expended by the growth of the positive component as the temperature is further lowered. Also, there is an anomalous change in the positive component of $\Delta R/R$ arising around $0.6T_c$ which is apparently significantly lower than its resistive T_c. Although precise physical

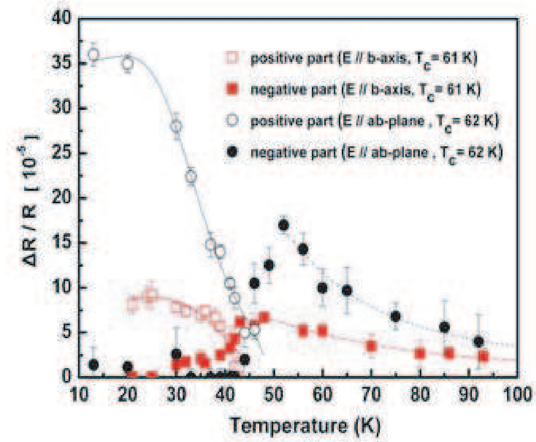

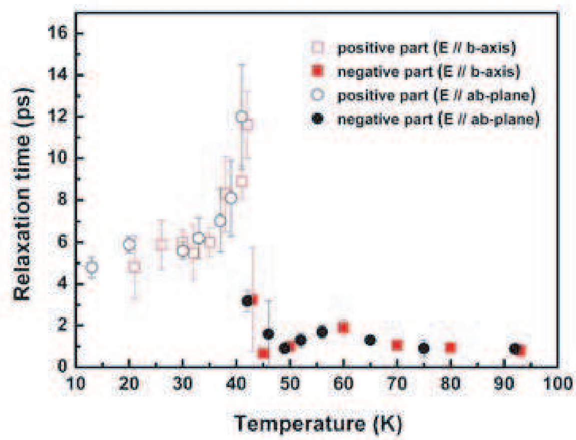

Figure 4: The temperature dependence of the amplitude (left panel) and relaxation time of $\Delta R/R$ as derived from the data shown in Fig. 3. The solid and open symbols represent the positive and negative components displayed in Fig. 3, respectively.

origin of these observations is not clear at present, it may imply that the negative component is a kind of competing order which effectively suppresses the superconductivity above $0.6T_c$. This speculation could be further demonstrated by the temperature dependence of relaxation time of $\Delta R/R$ (right panel of Fig. 4). In general, the relaxation time of $\Delta R/R$ will diverge near T_c, signifying the opening of superconducting gap. In the present case, the superconducting gap opening implied by the amplitude change discussed above is quite consistent with the relaxation divergence peaking around $0.6T_c$. We note that, very recently, a competing order coexistent below T_c with the superconducting gap has been observed in $Tl_2Ba_2Ca_2Cu_3O_y$ (Tl-2223) Chia et al. [13].

4. CONCLUSIONS

In summary, we have demonstrated a method which combines both polarized femtosecond spectroscopy and orientation-specific YCBCO thin films to directly reveal the anisotropy of photo-induced quasiparticle relaxation behaviors. By using the (100)- and (001)-oriented YCBCO thin films, the spatial anisotropy of photoinduced quasiparticle relaxation dynamics in major crystalline axes were disclosed, especially in the heavily overdoped regime. We demonstrated that there, probably, two order parameters coexisting and competing to each other when temperature is below resistive T_c of the sample. Investigations of further details of the orientation dependence of these order parameters are in progress.

ACKNOWLEDGMENT

This work was supported by the National Science Council of Taiwan, R.O.C. under grant: NSC95-2120-M-009-011, NSC95-2112-M-009-011-MY3, NSC96-2923-M-009-001-MY3, and by the Grant MOE ATU Program at NCTU.

REFERENCES

1. Anderson, P. W., P. A. Lee, M. Randeria, T. M. Rice, N. Trivedi, and F. C. Zhang, *J. Phys.: Condens. Matter*, Vol. 16, R755, 2004.
2. Timusk, T. and B. Statt, *Rep. Prog. Phys.*, Vol. 62, 61, 1999.
3. Wollman, D. A., D. J. Van Harlingen, W. C. Lee, D. M. Ginsberg, and A. J. Leggett, *Phys. Rev. Lett.*, Vol. 71, 2134, 1993.
4. Tsuei, C. C. and J. R. Kirtley, *Rev. Mod. Phys.*, Vol. 72, 969, 2000.
5. Dessau, D. S., Z.-X. Shen, D. M. King, D. S. Marshall, L. W. Lombardo, P. H. Dickinson, A. G. Loeser, J. DiCarlo, C.-H. Park, A. Kapitulnik, and W. E. Spicer, *Phys. Rev. Lett.*, Vol. 71, 2781, 1993.
6. Shen, Z.-X. and D. S. Dessau, *Physics Reports*, Vol. 253, 1, 1995.

7. Kabanov, V. V., J. Demsar, B. Podobnik, and D. Mihailovic, *Phys. Rev. B*, Vol. 59, 1497, 1999.
8. Kaindl, R. A., M. Woerner, T. Elsaesser, D. C. Smith, J. F. Ryan, G. A. Farnan, M. P. McCurry, and D. G. Walmsley, *Science*, Vol. 287, 470, 2000.
9. Demsar, J., B. Podobnik, V. V. Kabanov, T. Wolf, and D. Mihailovic, *Phys. Rev. Lett.*, Vol. 82, 4918, 1999.
10. Luo, C. W., P. T. Shih, Y.-J. Chen, M. H. Chen, K. H. Wu, J. Y. Juang, J.-Y. Lin, T. M. Uen, and Y. S. Gou, *Phys. Rev. B*, Vol. 72, 092506, 2005.
11. Wu, K. H., M. C. Hsieh, S. P. Chen, S. C. Chao, J. Y. Juang, T. M. Uen, Y. S. Gou, T. Y. Tseng, C. M. Fu, J. M. Chen, and R. G. Liu, *Jpn. J. Appl. Phys.*, Vol. 37, 4346, 1998.
12. Luo, C. W., K. H. Wu, J. Y. Juang, J.-Y. Lin, T. M. Uen, Y. S. Gou, and T. Kobayashi, unpublished.
13. Chia, E. E. M., J.-X. Zhu, D. Talbayev, R. D. Averitt, A. J. Taylor, K.-H. Oh, I.-S. Jo, and S.-I. Lee, *Phys. Rev. Lett.*, Vol. 99, 147008, 2007.

Growth of Carbon Nanotubes and Its Applications in Quantum Transport Behavior and Hydrogen Storage

H. Y. Miao[1], **L. W. Chang**[2], **and J. T. Lue**[3]

[1]Department of Electrical Engineering, Tunghai University, Taichung, Taiwan
[2]Department of Electrical Engineering, National Tsing Hua University, Hsin Chu, Taiwan
[3]Departments of Physics, National Tsing Hua University, Hsin Chu, Taiwan

Abstract— Carbon nanotubes (CNTs) were successfully grown on alloy substrates made of copper and iron groups by hot-filament chemical vapor deposition method with self-bias induced by a radio-frequency-field. Carbon nanotubes were also directly grown on the ends of micro-electrodes that were fabricated by photolithography. The sample with a single CNT across nickel electrodes was tediously selected by a scanning electron microscope (SEM) to measure the I-V characteristic by a closed cycle He refrigerator. A discontinuous quantum step of the I-V curve was observed at low temperatures as the current is above certain values. We also developed a one-dimensional transport theory for conductors that can qualitatively portray the quantum behavior of the I-V characteristic. The ability of hydrogen uptake of several carbonize material experiments have been carried out and compared. Purified Single-wall and Multi-wall carbon nanotubes (MWCNTs) produced by arc discharge and microwave (MW) CVD, Taiwan bamboo charcoal with MWCNTs on it are compared and discussed. Because of high hydrogen storage capacity, low production cost and high mass production speed, Taiwan bamboo charcoal shows excellent results irrespective of to be pretreated with or without alkali or acid solvent.

Up to now, quantum dot (QD) behaviors of carbon nanotubes (CNTs) have been extensively investigated by numbers of authors [1–4]. The coulomb blockade effect in nanostructure expresses the electrons transfering from source to drain electrodes on account of the electrostatic effect. Owing to the capacitance of the quantum dot system, single electron tunneling is prohibited below certain temperatures when the charging energy $E_C = \frac{e^2}{2C_\Sigma}$ exceeds the thermal energy K_BT. In this work we propose an experimental exploration of a laterally grown CNT directly on electrodes by the microwave plasma-enhanced chemical vapor deposition (MPECVD) method. Lowering down the measuring temperatures, we can observe a nonlinear change of current-voltage curves under various gate voltages. The measured data consist with the theoretical estimation developed for a model of quantum dot structure. Additionally, we also investigate the hydrogen storage of SWCNTs, MWCNTs and Taiwan bamboo charcoal, respectively. Our results indicate that Taiwan bamboo charcoals have high efficiency for hydrogen storage.

We propose a simple model of quantum dot system to illustrate the structure composing of a carbon nanotube for the gate and metallic dots for electrodes, respectively. The calculation of capacitances in this quantum dot structure is based on conventional electromagnetism, which includes three segments C_{S1}, C_{S2} and C_G, as shown in Fig. 1,

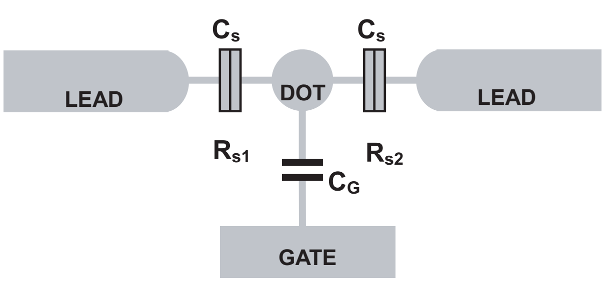

Figure 1: The schematic diagram of quantum dot structure.

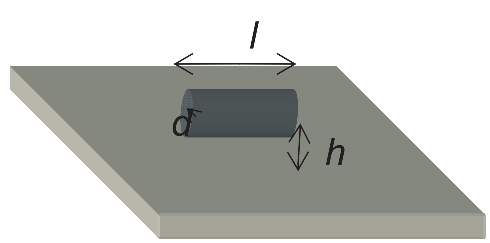

Figure 2: Physical model of a single CNT structure.

where the C and R represent the capacitance and the resistance between the metal-island and lead electrodes, respectively. Here we may calculate the capacitance of a single CNT across the adjacent electrodes by analogy to a charged cylindrical rod and the infinite conducting plane as shown in Fig. 2. The total capacitance is then defined as $C_{total} = C_{S1} + C_{S2} + C_G$.

The structure was prepared by photo lithography and lift-off processes to create several adjacent electrodes. The temperature was with slightly increase the microwave power to obtain 640°C $\sim$ 660°C and then grow MWCNTs across two metal electrodes. A single MWCNT, the electrodes was selected tediously by a SEM, which delineates a nonlinear conductance when it was measured at 20 K by sweeping the source-drain voltage V_{DS} with different gate voltages. A single MWCNT directly grown from the side of pure catalyst electrodes of Ni-Fe as shown in Fig. 3 where some peculiar electronic characteristics were detected at low temperature under various gate voltages.

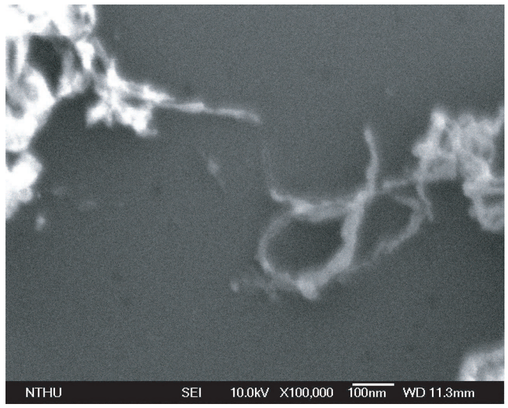

Figure 3: A single MWCNT across Ni-Fe catalyst electrodes.

The electronic characteristics of sample A was measured under fixed gate voltage with DC bias from source and drain. The nonlinear current-voltage characteristics present no charge transfer with almost horizontal curve near source-drain voltage $V_{DS} = 0$ at low temperature as shown in Fig. 4. Increasing the source-drain voltage, the current sharply increase on account of electrons with more energy to tunnel through the barriers. It appeals that the plateau-like curve disappears as the gate voltage varying with the zero conductance. However, the source-drain voltage does not increase usually with the increase of gate bias as dictated in Fig. 4. A possible reason for that behavior is that the fluctuation of conductance may be arisen from resonant tunneling. The similar of coulomb oscillation at low source-drain voltage and low temperature have been studied by many reports [5, 6].

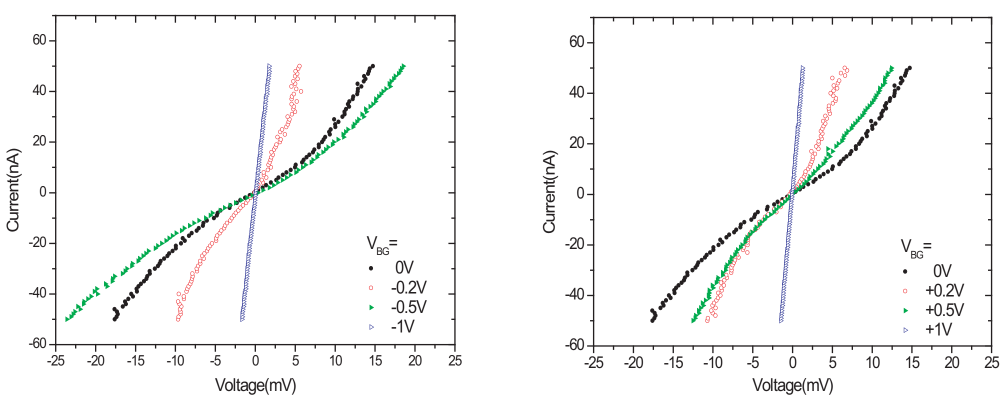

(a) (b)

Figure 4: The manifestation of individual MWCNT quantum dot showing for non-linear I-V curves measured at T = 20 K (a) with negative gate voltages, and (b) with positive gate voltages, respectively at T = 20 K.

Through our developed model, we can estimate that the capacitance of the sample A is $C_{S1} = C_{S2} = 1.48 \times 10^{-17}$(F) and the charging energy $\mathrm{E} = \frac{e^2}{2C_\Sigma} \cong 2.69$ (meV) is slightly larger than the thermal energy $\mathrm{E} = \mathrm{K_B T} = 1.72$ (meV) at T = 20 K. The theoretical calculation also indirectly indicates the emersion of the coulomb blockade behavior at low source-drain voltage and temperature in sample A.

After long time measurement, the insulating oxide layer may be broken by current injection and I-V curve gradually approaches a linear curve, as shown in Fig. 5. Figs. 5(a) and 5(b) demonstrate the resistance change with the duration of the electrical measurements. This finding seems to show that the tunneling barriers are diminished by current flowing process so that the resistance decreases from $1.29\,\mathrm{M\Omega}$ to $14.91\,\mathrm{K\Omega}$ after repeatedly measurements.

Table 1 shows the hydrogen storage of carbonize materials. The hydrogen storage of SWCNTs is the highest value among these materials and the MWCNTs presents the lowest value. However, the hydrogen storage of carbonize materials are all enhanced by the acid and alkali erosion on account of the elimination of amorphous carbon and fullerence inside the materials. The hydrogen storage of Taiwan bamboo charcoal with carbon nanotubes on it does not show apparent changes so that the Taiwan bamboo charcoal is the proper material to store hydrogen gas in the future.

Table 1: The comparison of hydrogen storages in SWCNTs, MWCNTs and Taiwan bamboo charcoal.

Carbon nanotubes	SWCNTs	~0.668wt%
	MWCNTs(Grown by Arc discharge)	~0.219wt%
	MWCNTs(Grown by Arc discharge and purified)	~0.588wt%
Taiwan bamboo charcoal	Virgin	~0.431wt%
	Pretreatment by 70% nitric acid after 24 hr	~0.522wt%
	Pretreatment by 6 M KOH after 24 hr	~0.569wt%
	Bamboo with CNTs grown by Arc discharge	~0.462wt%
	Bamboo with CNTs grown by MPECVD	~0.520wt%

The hydrogen storage of Taiwan bamboo charcoal is excellent to SWCNTs and MWCNTs owing to the advantages of cost and mass production. The implementation of Taiwan bamboo charcoal is limited to increase the efficiency of hydrogen storage. To investigate the marvelous phenomena and salient features of hydrogen storage in Taiwan bamboo charcoals will be highly debated in future.

REFERENCES

1. David, M. B., H. Cobaden, P. L. M. Nasreen, G. Chopra, A. Zettl, A. Thess, and R. E. Smalley, *Science*, Vol. 275, 1922, 1999.
2. Postma, H. W. C., T. Teepen, Z. Yao, M. Grifoni, and C. Dekker, *Science*, Vol. 293, 76, 2001.
3. Coskun, U. C., T. C. Wei, S. V. hveshwara, P. M. Goldbart, and A. Bezryadin, *Science*, Vol. 21, 1132, 2004.
4. Minot, E. D., Y. Yaish, V. Sazonova, and P. L. Mceuen, *Nature*, Vol. 428, 536, 2004.
5. Coskun, U. C., T, C. Wei, S. Vishveshwara, P. M. Goldbart, and A. Bezryadin, *Science*, Vol. 21, 1132, 2004.
6. Ishikuro, H. and T. Hiramoto, *Appl. Phys. Lett.*, Vol. 74, 1126, 1999.

Conductivities for Direct Current and Microwaves with Domain Wall Scattering for Ni-Fe Alloy Thin Films

Yi-Chen Yeh[1] **and Juh Tzeng Lue**[2]

[1]Institute of Photonics Technologies, National Tsing Hua University, Hsin Chu, Taiwan
[2]Department of Physics, National Tsing Hua University, Hsin Chu, Taiwan

Abstract— Stripe domain characteristic for Permalloy thin film under external magnetic field are observed with the variation of applying magnetic field measured. The DC resistivity for currents conducting parallel to domain walls (CIW) is significantly smaller than that of the perpendicular (CPW) case as inspected by a magnetic force microscopy (MFM). As the applied frequencies approach the microwave frequency no difference in conductivities for CPW and CIW is observed. This can be expressed that when the signal frequency is up to microwaves, the electron spin scattering with the magnetic domain walls is diminished by the turn-around of carriers before they arrived next domain walls as measured by a T-junction micro-strip line resonator.

Recent researches in domain wall resistivities have grown dramatically owing to the great advances in fabrication technologies and the large demands of magnetic memory devices. There are many researches related to the magneto resistance while measuring the electron transport characteristic under the applying external magnetic field [1, 2]. However, it worth mentioned that the domain wall configuration of the ferromagnetic thin film could vary with the applying magnetic field [3]. Measurement of resistivities for currents conducting parallel (CIW) and perpendicular (CPW) to DW's that plays an essential role of MR property was investigated in our previous report [4].

Microwave microstrip techniques allow noncontact measurements of the temperature dependence [5, 6] and magnetic field dependence [7] on the conductivity of thin magnetic films. The large demand in communication and video applications also suggests us an impetus to expand the use of monolithic microwave micro-strip circuits.

Since the wall scattering between domains in ferromagnets are the additional source of resistivity for current flowing across the domains. Several excellent reviews concerning the domain-wall scattering of magneto resistance were reported [8]. However, all previous researches were accomplished and measured under direct currents. This work, we endeavor to study the variation of resistivities with the domain wall configurations on nickel and cobalt films under applied signals at DC and microwave frequencies. In the case of a high frequency current, the frequency is compared with two characteristic times. The phase velocity of microwave current can be expressed through the skin depth, which is compared to the DW width.

The magnetic domain wall structure was observed by a multimode Seiko SPI 300 operated under a vacuum of 1.33×10^{-4} pa. The MFM system is running in dynamic, non-contact mode under

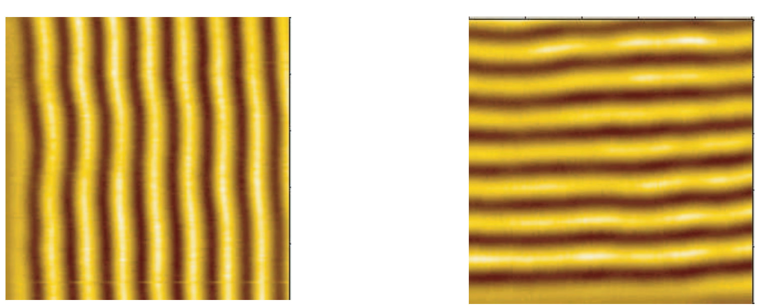

(a) (b)

Figure 1: The domain patterns within an area of $5\,\mu\text{m} \times 5\,\mu\text{m}$ for a 320 nm-thick $Ni_{81.2}Fe_{18.8}$ film under various direction of magnetic field for (a) $H = 0$, the stripe domain structure being a straight line along the y-direction, and (b) $H = 1.2\,\text{T}$ along the x-direction ($\Rightarrow$) where the stripe domain direction is changed to the x-direction, respectively.

high vacuum condition to enhance the image sensitivity. The formation of magnetic domain walls crucially depends on the magnetic anisotropy energy, the magneto static energy and the mechanical stress of the magnetic films. The structure of the magnetic domain changes in complying with the applied external field to balance the increment of the work due to domain wall displacement.

The detail experiment process could Fig. 1(a) and 1(b) show the MFM images of the $Ni_{81.2}Fe_{18.8}$ thin film of thickness 320 nm deposited on SiO_2 substrate without and with applying a 1.2 Tesla magnetic filed perpendicular to the domain wall, respectively. With the straight stripe domain configuration, the magnetization is perpendicular to the plane. As mentioned in our previous paper, the stripe domain period $d = d_{up} + d_{down}$ is proportional to the square root of the ferromagnetic thin film thickness l. As shown in Fig. 3 the relationship between applied magnetic field B and film thickness l, where a and b are the material parameter.

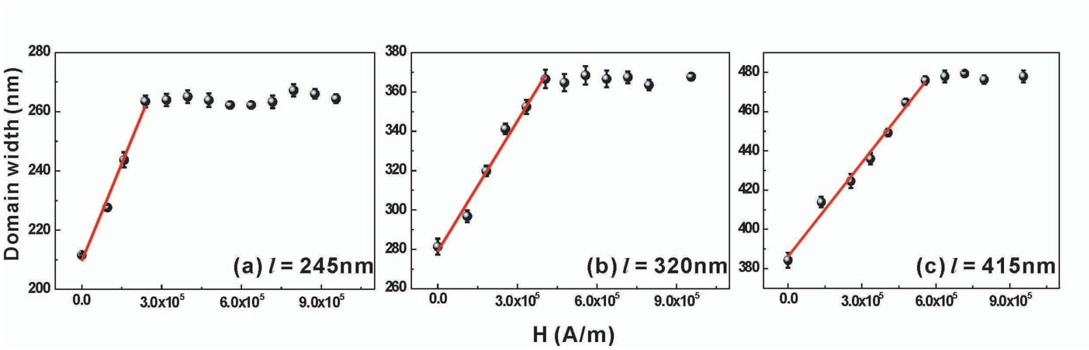

Figure 2: The domain width for $Ni_{81.2}Fe_{18.8}$ thin films of (a) 245, (b) 320, and (c) 415 nm thickness as a function of the applied magnetic field for 0.3 T, 0.5 T, and 0.7 T, respectively.

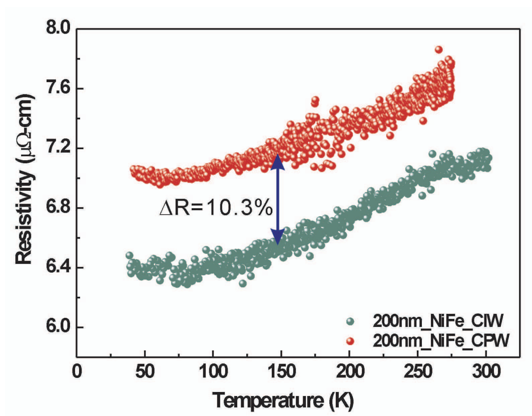

Figure 3: The R-T curves of the 280 nm thick $Ni_{81.2}Fe_{18.8}$ film with R_{CPW}-R_{CIW} = 10.3% measured at 150 K.

linear relation between the applied magnetic field and the film thickness before reaching the saturation as shown in Fig. 3.

Furthermore, the electron transport for the $Ni_{81.2}Fe_{18.8}$ thin film owing to domain wall effect was also investigated. The resistivities of conduction currents parallel to (CIW) and perpendicular to the domain wall (CPW) has been explored by many groups. Fig. 3 illustrates the temperature dependences on DC resistivities (R-T) for the CIW and CPW of the Permalloy thin film, which behaves metallic conductors as being attributed to the mechanism of electron-phonon scattering.

Figure 4(a) and (b) represented the temperature dependences on DC resistivities (RT) for the CIW and CPW of Co and Ni films,respectively. Furthermore, the dependence of conductivity on frequency for the ferromagnetic Co films with thickness of 600 nm and 800 nm measured at 300 K as the microwave current conducts from parallel to perpendicular to the domain walls were illustrated in Fig. 5. This could be elucidated that the fast input signal making the electrons to turn back before they arriving the opposite walls results in dispersing the spin scattering between the electrons.

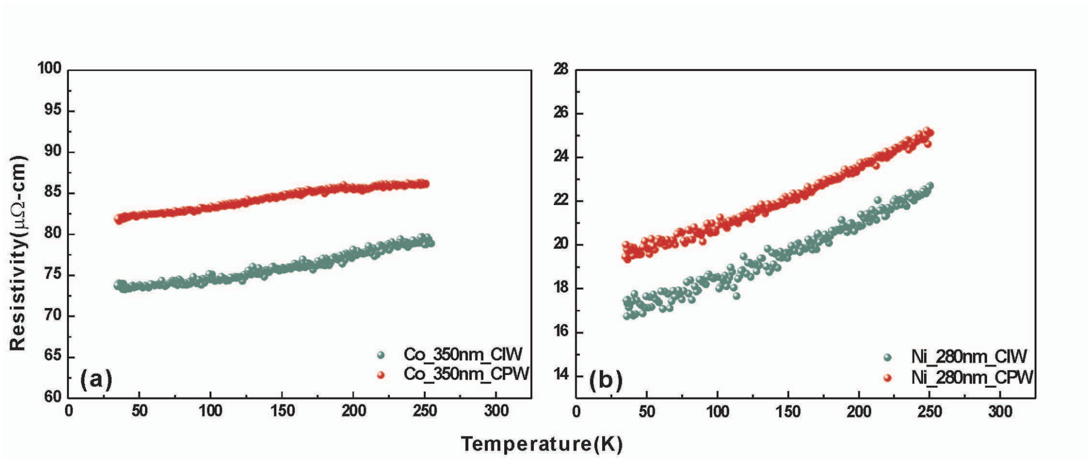

Figure 4: The R-T curves of the (a) 350 nm-thick Co film and (b) 280 nm-thick Ni film The R_{CPW}-R_{CIW} is 12.8% and 11.9% measured at 100 K for Co and Ni films, respectively.

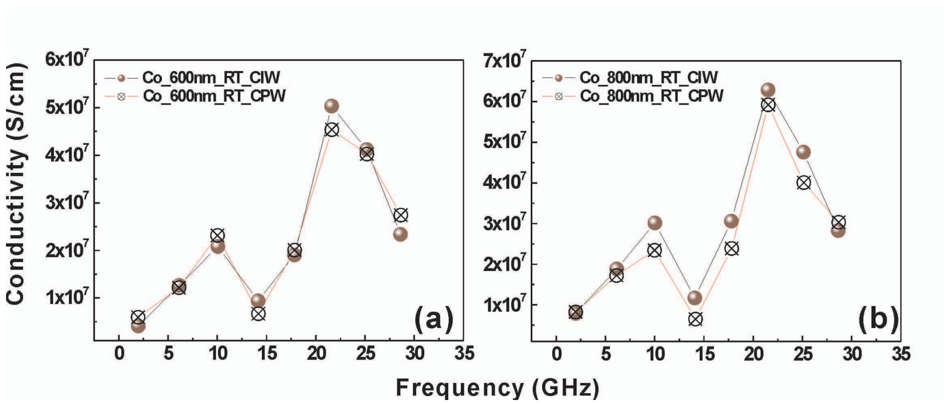

Figure 5: The frequency dependence of T-junction Co micro-strips for CPW and CIW configurations at thicknesses of (a) 600 nm and (b) 800 nm.

The ferromagnetic resonance occurring at microwave frequency causing magnetoresistivities by electron precession motion depends on the anisotropic and saturation magnetization largely. At low fields the magnetization is broken up into randomly oriented magnetic domains which are swept away by the fields. The anisotropic scattering provided by spin-orbit coupling must be invoked to account for the anisotropic magnetoresistance while the magnetic susceptibility plays no role in measuring the dc resistivity. The coexistence of FMR and structure mode resonance of a microwave T-microstrip express that the surface resistance subjects to change with the intensity of the applied magnetic field whilst not with domain configurations.

ACKNOWLEDGMENT

This work was supported from the National Science Council of the Republic of China under the contract NSC-96-2112-M007.

REFERENCES

1. Biehler, A., et al., *Phys. Rev. B*, Vol. 75, 184427, 2007.
2. Leven, B. and G. Dumpich, *Phys. Rev. B*, Vol. 71, 064411, 2005.
3. Pilet, N., et al., *J. Magn. Magn. Mater.*, Vol. 316, e583, 2007.
4. Yeh, Y. C., J. T. Lue, T. Y. Chen, and J. H. Liu, *J. Magn. Magn. Mater.*, Vol. 304, e134, 2006.
5. Lue, H. T., J. T. Lue, and T. Y. Tseng, *IEEE Trans. Instrum. Meas.*, Vol. 51, 433, 2002.
6. Liu, J. H., Y. C. Lin, J. T. Lue, and C. J. Wu, *Meas. Sci. Technol*, Vol. 13, 1132, 2002.
7. Bonalde, I., B. D. Yanoff, M. B. Salamon, D. J. Van Harlingen, E. M. E. Chia, Z. Q. Mao, and Y. Maeno, *Phys. Rev. Lett.*, Vol. 85, 4775, 2000.
8. Berger, L., *J. Appl. Phys.*, Vol. 49, 2156, 1978.

Analysis of Equivalence of Standing-wave Dipole Model and Traveling-wave Monopole Model

Shi-Wei Dong, **Wei Ma**, **Wan-Zhao Cui**, **She Shang**, **Hong-Tai Zhang**, **Hong Chen**
National Key Laboratory of Space Microwave Technology
Xi'an Institute of Space Radio Technology, Xi'an, China

Abstract— The standing-wave dipole model and the traveling-wave monopole model are often employed in time-domain radiation research of wire antenna. The two models are introduced firstly. Then they are demonstrated to be equivalent theoretically from the view point of radiated fields. It should be noted that the field point can be freely located in the space outside the models, which is different from references [1, 2].

1. INTRODUCTION

Standing-wave dipole model and traveling-wave monopole model have both found extensive employment in research of transient radiation of wire antenna [4–9]. When the former is applied, only current density distribution is needed. But when the latter is applied, both current density distribution and charge distribution are needed [1–3].

M. Rubinstein, M. A. Uman, A. Safaeinili and M. Mina have demonstrated the equivalence of standing-wave dipole model and traveling-wave monopole model. But strict limitation was imposed on, that is the equivalent field point must be located on the perpendicular halving plane of the dipole [1, 2]. This paper releases the limitation and deduces the generalized demonstration. The field point can be selected freely in the space outside the models and so the equivalence is more authentic.

2. STANDING-WAVE DIPOLE MODEL

If the current propagation path in free space is as shown in Fig. 1, it can be regarded as a wire antenna. When the current density distribution keeps uniform along the path, we have

$$J(z,t) = \begin{cases} cons\tan t & -L/2 \le z \le L/2 \\ 0 & \text{else} \end{cases}. \tag{1}$$

Thus standing wave comes into being, which is the case considered in [4–6, 9] using standing-wave dipole model with current reflection at its ends. The standing-wave dipole model is portrayed in Fig. 2. It is employed widely in transient radiation study. Using this model only temporal and spatial current density distribution is needed to educe the radiated fields. Formulae given in [6] can be rewritten as follows:

$$E_\theta = \frac{\eta_0}{2\pi\rho}[J(t-r/c)+J(t-L/c-r/c)-J(t-L/2/c-R_1/c)\cos\alpha_1-J(t-L/2/c-R_2/c)\cos\alpha_2] \tag{2a}$$

$$E_r = \frac{\eta_0}{2\pi\rho}[J(t-L/2/c-R_1/c)\sin\alpha_1 - J(t-L/2/c-R_2/c)\sin\alpha_2] \tag{2b}$$

$$H_\varphi = \frac{1}{2\pi\rho}[J(t-r/c)+J(t-L/c-r/c)-J(t-L/2/c-R_1/c)-J(t-L/2/c-R_2/c)] \tag{2c}$$

When $r \to \infty$, far zone fields of standing-wave dipole would be obtained.

3. TRAVELING-WAVE MONOPOLE MODEL

Sometimes (1) no longer holds and current distribution along the transmission path should be regard as a traveling wave. The traveling-wave monopole model would be introduced here which is illustrated in Fig. 3. Its transient radiated fields were formulized by Rothwell [9] and can be

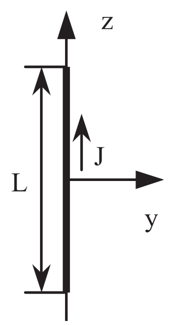

Figure 1: Current propagation path.

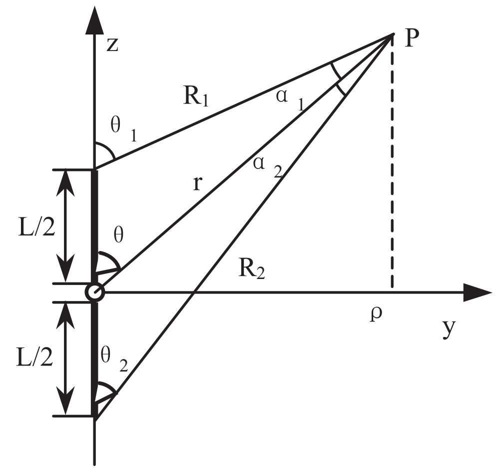

Figure 2: Standing-wave dipole model.

rearranged as followings:

$$\begin{aligned} E_\theta &= \frac{\eta_0}{4\pi}\left[J(t-z_1/c-R_1/c)\frac{\cot\frac{\theta_1}{2}\cos\alpha_1}{R_1}-J(t-z_2/c-R_2/c)\frac{\cot\frac{\theta_2}{2}\cos\alpha_2}{R_2}\right] \\ &\quad -\frac{\eta_0 c}{4\pi}\left[q(t-z_1/c-R_1/c)\frac{\sin\alpha_1}{R_1^2}-q(t-z_2/c-R_2/c)\frac{\sin\alpha_2}{R_2^2}\right] \end{aligned} \tag{3a}$$

$$\begin{aligned} E_r &= \frac{\eta_0}{4\pi}\left[-J(t-z_1/c-R_1/c)\frac{\cot\frac{\theta_1}{2}\sin\alpha_1}{R_1}+J(t-z_2/c-R_2/c)\frac{\cot\frac{\theta_2}{2}\sin\alpha_2}{R_2}\right] \\ &\quad -\frac{\eta_0 c}{4\pi}\left[q(t-z_1/c-R_1/c)\frac{\cos\alpha_1}{R_1^2}-q(t-z_2/c-R_2/c)\frac{\cos\alpha_2}{R_2^2}\right] \end{aligned} \tag{3b}$$

$$H_\varphi = \frac{1}{4\pi}\left[J(t-z_1/c-R_1/c)\frac{\cot\frac{\theta_1}{2}}{R_1}-J(t-z_2/c-R_2/c)\frac{\cot\frac{\theta_2}{2}}{R_2}\right] \tag{3c}$$

where

$$q(t)=\int_{-\infty}^{t}J(t')dt' \tag{4}$$

When $r\to\infty$, far zone fields of the traveling-wave monopole would be obtained.

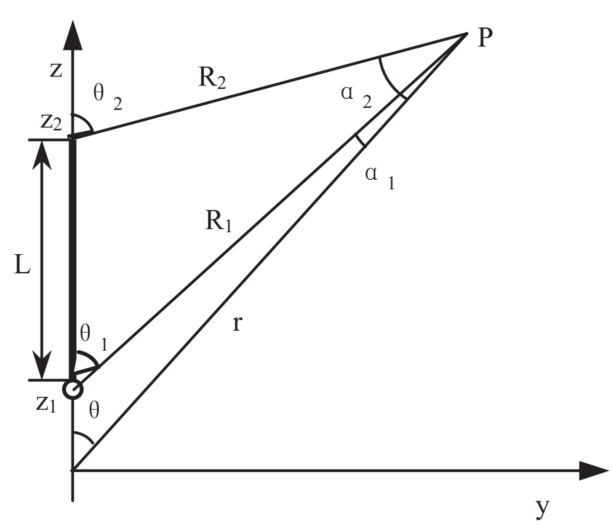

Figure 3: Traveling-wave monopole.

4. EQUIVALENT OF STANDING-WAVE DIPOLE MODEL AND TRAVELING-WAVE MONOPOLE MODEL

While studying radiation of sinusoidal traveling current, W. S. Bennett replaced the dipole with 4 monopoles. As pointed out by G. S. Smith, this idea can be introduced into time domain [10, 11]. Detailed demonstration will be given with deep understanding of the two models.

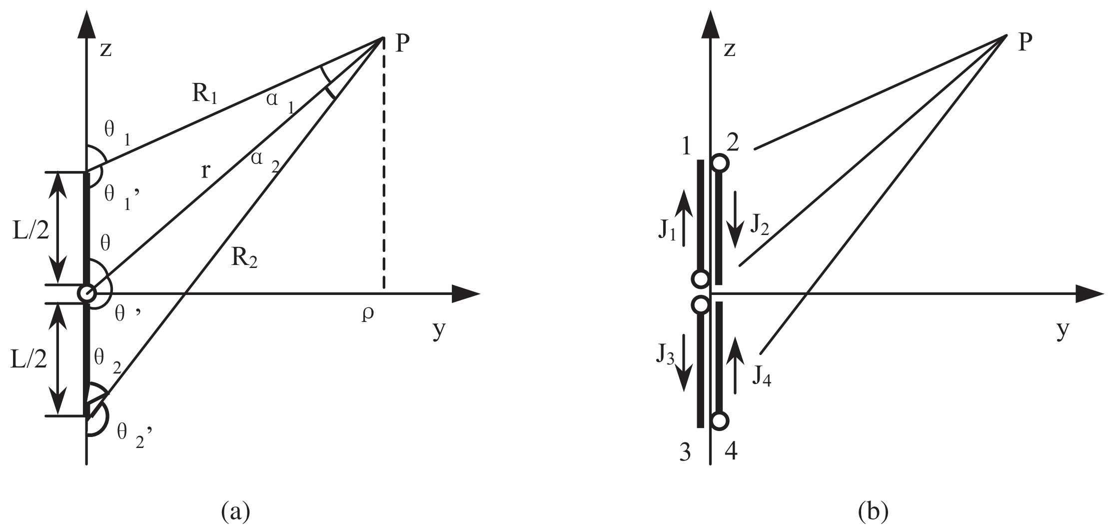

Figure 4: The standing-wave dipole and its equivalent traveling-wave monopoles.

As illustrated in Fig. 4, the standing-wave dipole in (a) is equivalent to 4 monopoles traveling-wave monopoles in (b). Rothwell's hypothesis is met at the load end of the monopoles that the current is absorbed and the charges accumulate. Currents respectively at soured end and load end of monopole 1 are

$$J_{1s} = J(t - r/c), \tag{5a}$$

and

$$J_{1t} = J(t - L/2/c - R_1/c). \tag{5b}$$

For monopole 2, 3 and 4 we have

$$\begin{aligned}
J_{2s} &= J(t - L/2/c - R_1/c) && (5c)\\
J_{2t} &= J(t - L/c - r/c) && (5d)\\
J_{3s} &= -J(t - r/c) && (5e)\\
J_{3t} &= -J(t - L/2/c - R_2/c) && (5f)\\
J_{4s} &= -J(t - L/2/c - R_2/c) && (5g)\\
J_{4t} &= -J(t - L/c - r/c). && (5h)
\end{aligned}$$

Substituting (5) into (3a) we get electrical fields of these 4 monopoles as

$$E_\theta^1 = \frac{\eta_0}{4\pi}\left[\frac{J(t-r/c)}{r}\cot\frac{\theta}{2} - \frac{J(t-L/2/c-R_1/c)}{R_1}\cot\frac{\theta_1}{2}\cos\alpha_1\right] + \frac{\eta_0 c}{4\pi}\frac{q(t-L/2/c-R_1/c)}{R_1^2}\sin\alpha_1 \tag{6a}$$

$$E_\theta^2 = \frac{\eta_0}{4\pi}\left[-\frac{J(t-L/2/c-R_1/c)}{R_1}\cot\frac{\theta_1'}{2}\cos\alpha_1 + \frac{J(t-L/c-r/c)}{r}\cot\frac{\theta'}{2}\right] - \frac{\eta_0 c}{4\pi}\frac{q(t-L/2/c-R_1/c)}{R_1^2}\sin\alpha_1 \tag{6b}$$

$$E_\theta^3 = \frac{\eta_0}{4\pi}\left[\frac{J(t-r/c)}{r}\cot\frac{\theta'}{2} - \frac{J(t-L/2/c-R_2/c)}{R_2}\cot\frac{\theta_2'}{2}\cos\alpha_2\right] + \frac{\eta_0 c}{4\pi}\frac{q(t-L/2/c-R_2/c)}{R_2^2}\sin\alpha_2 \tag{6c}$$

$$E_\theta^4 = \frac{\eta_0}{4\pi}\left[-\frac{J(t-L/2/c-R_2/c)}{R_2}\cot\frac{\theta_2}{2}\cos\alpha_2 + \frac{J(t-L/c-r/c)}{r}\cot\frac{\theta}{2}\right] - \frac{\eta_0 c}{4\pi}\frac{q(t-L/2/c-R_2/c)}{R_2^2}\sin\alpha_2 \tag{6d}$$

According to law of superposition, the synthetic field at any point outside the models is

$$\begin{aligned}
E_\theta &= \sum_{i=1}^{4} E_\theta^i \\
&= \frac{\eta_0}{4\pi}\left[\frac{J(t-r/c)}{R}(\cot\frac{\theta}{2}+\cot\frac{\theta'}{2}) + \frac{J(t-L/c-r/c)}{R}(\cot\frac{\theta}{2}+\cot\frac{\theta'}{2})\right. \\
&\quad \left.-\frac{J(t-L/2/c-R_1/c)}{R_1}(\cot\frac{\theta_1}{2}+\cot\frac{\theta_1'}{2})\cos\alpha_1 - \frac{J(t-L/2/c-R_2/c)}{R_2}(\cot\frac{\theta_2}{2}+\cot\frac{\theta_2'}{2})\cos\alpha_2\right] \\
&= \frac{\eta_0}{4\pi}\left[\frac{2J(t-r/c)}{R\sin\theta}+\frac{2J(t-L/c-r/c)}{R\sin\theta}-\frac{2J(t-L/2/c-R_1/c)}{R_1\sin\theta_1}-\frac{2J(t-L/2/c-R_2/c)}{R_2\sin\theta_2}\right] \\
&= \frac{\eta_0}{2\pi\rho}[J(t-r/c)+J(t-L/c-r/c)-J(t-L/2/c-R_1/c)\cos\alpha_1-J(t-L/2/c-R_2/c)\cos\alpha_2] \quad (7a)
\end{aligned}$$

In the like manner we have

$$E_r = \sum_{i=1}^{4} E_r^i = \frac{\eta_0}{2\pi\rho}[J(t-L/2/c-R_1/c)\sin\alpha_1 - J(t-L/2/c-R_2/c)\sin\alpha_2] \quad (7b)$$

and

$$H_\varphi = \sum_{i=1}^{4} H_\varphi^i = \frac{1}{2\pi\rho}[J(t-r/c)+J(t-L/c-r/c)-J(t-L/2/c-R_1/c)-J(t-L/2/c-R_2/c)] \quad (7c)$$

The absolute agreement of (7) with (2) show that the same results can be obtained using both the standing-wave dipole and its equivalent traveling-wave monopoles. Far zone fields can also be demonstrated to be coincident of these two models. So it safe to say they are equivalent. It should be noted that during the foregoing deduction the field point can be freely located in the space outside the models, not limited to $z = 0$ as in [1, 2].

It is easy to see the radiation effect of charges q_{1s} at source end of monopole 1 counteracts that of charges q_{3s} at source end of monopole 3, the same to q_{1t} and q_{2s}, q_{3t} and q_{4s}, q_{2t} and q_{4t}. So equal number of charges of reverse polarity leave at the source ends of monopole 1 and 3; equal number of charges of identical polarity leave and arrive respectively at the load end of monopole 1 and the source end of monopole 2; equal number of charges of identical polarity leave and arrive respectively at the load end of monopole 3 and the source end of monopole 4; equal number of charges of reverse polarity leave at the load ends of monopole 2 and 4. This is the inherent reason why no charge accumulates both at the source point located at the center of the dipole and at the 2 open ends.

5. CONCLUSIONS

The equivalence is theoretically demonstrated of standing-wave dipole model and traveling-wave monopole model. During the demonstration the field point can be selected freely in the space outside the models. That's to say the 2 models are equivalent in the whole space.

REFERENCES

1. Rubinstein, M. and M. A. Uman, "Methods for calculating the electromagnetic fields from a known source distribution: Application to lightning," *IEEE Trans. Electromag. Compat.*, Vol. 31, No. 2, 183–189, 1989.
2. Safaeinili, A. and M. Mina, "On the analytical equivalence of electromagnetic fields solutions for a known source distribution," *IEEE Trans. Electromag. Compat.*, Vol. 33, No. 1, 69–71, 1991.
3. Wu, D.-L. and C.-L. Ruan, "Transient radiation of traveling-wave wire antennas," *IEEE Trans. Electromag. Compat.*, Vol. 41, No. 2, 120–123, 1999.
4. Chen, Z. Q., "Thoeretical solutions of transient radiation from traveling-wave linear antennas," *IEEE Trans. Electromag. Compat.*, Vol. 30, No. 1, 80–83, 1988.
5. Liu, F. and W. B. Wang, "An analysis of the transient field of linear antennas," *IEEE Trans. Electromag. Compat.*, Vol. 31, No. 4, 404–409, 1989.

6. Podosenov, S. A., Y. G. Svekis, and A. Sokolov, "Transient radiation of traveling waves by wire antennas," *IEEE Trans. Electromag. Compat.*, Vol. 37, No. 3, 367–383, 1995.
7. Pantoja, M. F., A. R. Bretones, and R. G. Martin, "Time-domain analysis of thin-wire loaded antennas using integral equations," *IEE Proc. — Microw. Antennas Propag.*, Vol. 147, No. 3, 203–206, 2000.
8. Martin, R. G., A. R. Bretones, and S. G. Garcia, "Some thoughts about transient radiation by straight thin wire," *IEEE Antennas and Propagation Magazine*, Vol. 41, No. 3, 24–33, 1999.
9. Rothwell, E. J., M. J. Cloud, and P. Ilavarasan, "Transient field produced by traveling-wave wire antenna," *IEEE Trans. Electromag. Compat.*, Vol. 33, No. 3, 172–178, 1991.
10. Smith, G. S. and T. W. Hertel, "On the transient radiation of energy from simple current distributions and linear antennas," *IEEE Antennas and Propagation Magazine*, Vol. 43, No. 3, 49–63, 2001.
11. Smith, G. S., "Teaching antenna radiation from a time-domain perspective," *Am. J. Phys.*, Vol. 69, No. 3, 288–300, 2001.

Research on the Electromagnetic Interference of Antennas on the Satellite

Bin Zhou[1], **Qizhong Liu**[2], **and Xinyang He**[1]

[1]Research Office of Microwave Technology
Xi'an Institute of Space Radio Technology, Xi'an 710100, China
[2]National Laboratory of Antennas and Microwave Technology
Xidian University, Xi'an 710071, China

Abstract— The electromagnetic interference of the antenna system on the satellite is analyzed by the approximate algorithm-Uniform Geometrical Theory of Diffraction (UTD), associated with China Academy of Space Technology pre-research projects. The radiation patterns of the antennas on the satellite and the isolation between transmit antennas and receive antennas are investigated in detail, which provide the scientific proof of the position and frequency setting of antennas on the satellite. So, the mentioned method is widely applied to the engineering calculation, especially for the objects large in electrical size.

1. INTRODUCTION

The antennas on the satellite would interfere each other due to the complex framework of the satellite and the considerable quantity, the similar structure, the adjacent location, the superposed working frequency of antennas. The mutual influence between antennas and satellite, and the interference among the antennas would be inevitable. So, it is urgent for the antennas working normally under the complex electromagnetic interference conditions.

It would consume huge computing resource with low efficiency to analyze the radiation field of the satellite with electrically large size by full wave method, for example MoM and FEM. In 1970s, the patterns and the isolation of the antennas on the airplane were analyzed by UTD and UAT in Ohio State University and Illinois University, which had been applied to the military and civil aviation successfully. The error between the measured results and the calculated results is 3.76 dB. At present, the position of the antennas is decided by the experience and the repeating tests mostly at home, which would be difficult to realize optimization and would consume a lot of manpower and material resources.

In this paper, the approximate algorithm-UTD [1] with advantage of distinct conception and convenient calculation is adopted to analyze the electromagnetic interference of antennas on the satellite (Figure 1), associated with China Academy of Space Technology pre-research projects.

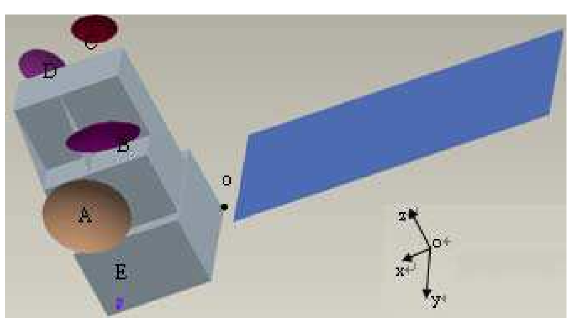

Figure 1: Equivalent model of the satellite and Cartesian coordinates.

2. UNIFORM GEOMETRICAL THEORY OF DIFFRACTION [1]

The problem about the radiation of the point source is solved by UTD. The antennas could be equivalent to the point sources with the same patterns as the antennas', which are located the phase center of the practical antennas. The paraboloid antennas in Figure 1 would be equivalent to the point source, which would bring some errors. The paraboloid antennas could also be equivalent to the combination of many point sources, and the radiation field of the antenna would be the vector superposition of the fields of many point sources. However, this superposition model has the disadvantages of low computation speed and huge computer memory. So, according to the calculating precision and computer hardware, the equivalent model of antennas could be chosen. In this paper, the antennas in Figure 1 are equivalent to the point sources.

2.1. Incidence Field

The incidence field (Figure 2) is defined as the radial field from the source point to the observed point directly. Thus, in the shadow, the incidence field would be zero. We express the incidence field as

$$\vec{\boldsymbol{E}}^i(\vec{r}) = \vec{\boldsymbol{E}}^i(\vec{r}_0)\sqrt{\left(\frac{\rho_1^i}{\rho_1^i + s^i}\right)\left(\frac{\rho_2^i}{\rho_2^i + s^i}\right)}e^{-jks^i} \tag{1}$$

s^i represents the distance along incidence radial, and $\vec{\boldsymbol{E}}^i(\vec{r}_0)$ is the field-strength when $s^i = 0$, and ρ_1^i, ρ_2^i are the curvature radius of the incidence wave front.

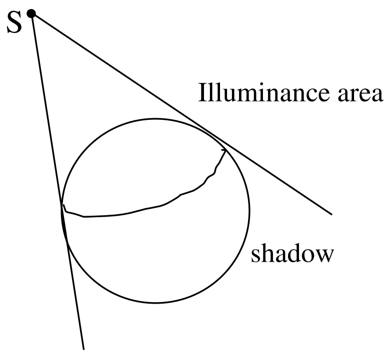

Figure 2: Incidence field.

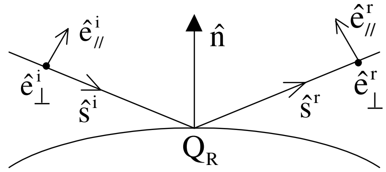

Figure 3: Reflective field.

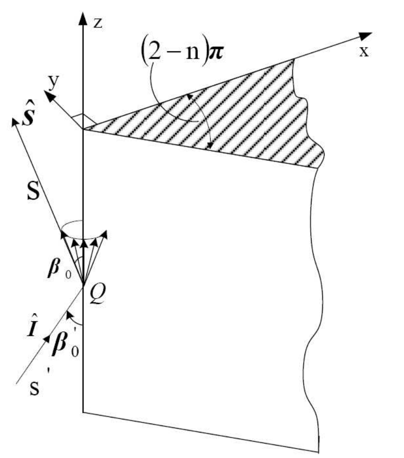

Figure 4: Edge diffraction field.

2.2. Reflective Field

The reflective field (Figure 3) is defined as the radial field reflected by the conductor surface, in radial coordinate system which could be given by

$$\vec{\boldsymbol{E}}^r(P) = \vec{\boldsymbol{E}}^i(Q_R) \cdot \overline{\overline{\boldsymbol{R}}}\sqrt{\rho_1^r\rho_2^r/(\rho_1^r + s)(\rho_2^r + s)}e^{-jks} \tag{2}$$

Q_R is the reflective point, and $E_i(Q_R)$ is the incidence field at Q_R, and s represents the distance from the reflective point to the observed point, and ρ_1^r, ρ_2^r are the curvature radius of the reflective wave front, and $\overline{\overline{\boldsymbol{R}}}$ is the matrix of the reflection coefficient.

2.3. Edge Diffraction Field [7]

As shown in Figure 4, when the conductor edge is irradiated by the electromagnetic wave, the diffraction field would occur at the edge. In radial coordinate system, the edge diffraction field could be written as

$$E^{ed}(P) = E^i(Q) \cdot \overline{\overline{D}}\sqrt{\rho_c/\left(S \cdot (S + \rho_c)\right)}e^{-jks} \tag{3}$$

$E^i(Q)$ is the incidence field at the diffraction point Q, $\overline{\overline{D}}$ is the edge diffraction coefficient, ρ_c represents the difference between the two curvature radius of the diffraction wave front.

2.4. Surface Diffraction Field [2]

When the incidence wave sweeps past the curved surface, there would be surface diffraction wave on the curved surface, which could be express as

$$E^{sd}(P_s) = E^i(Q_1) \cdot \overline{\overline{T}}(Q_1, Q_2)\sqrt{\rho_2^d/S^d \cdot (S^d + \rho_2^d)}e^{-jks_d} \tag{4}$$

As shown in Figure 5, Q_1 and Q_2 are the two surface diffraction points, and $\overline{\overline{T}}(Q_1, Q_2)$ is used to show the emission of the surface diffraction field from Q_1, and the attenuation of the surface diffraction field from Q_1 to Q_2, and the diffraction field at Q_2.

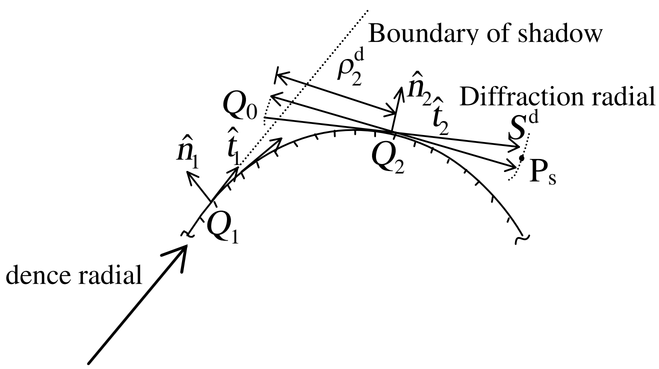

Figure 5: Surface diffraction field.

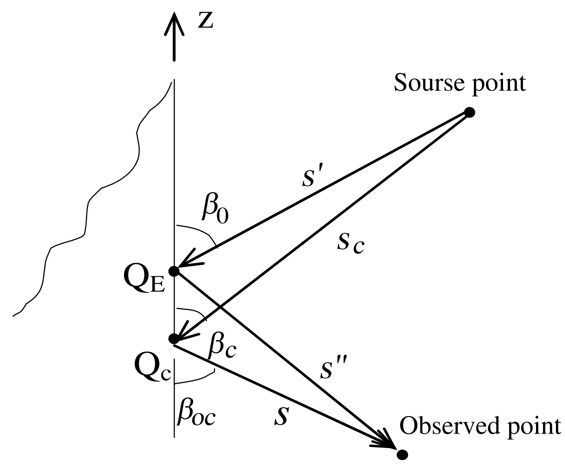

Figure 6: Corner diffraction field.

2.5. Corner Diffraction Field [4]

The corner diffraction field is equal to the sum of the diffraction field of every edge composed the corner. The experiential result was given by Sikta and Burnside, which was proved successful in practice.

$$E^{dc}(P) = \vec{\boldsymbol{E}}^i(Q_c) \cdot \overline{\overline{D}}_{s,h}^c \sqrt{s'/\left(s''(s'+s'')\right)} \sqrt{s\left(s+s_c\right)/s_c} \frac{e^{-jks}}{s} \tag{5}$$

where $D_{s,h}^c$ is the coefficient of the corner diffraction.

2.6. Total Field

After seeking the traces of the radials and judging whether the radials are obstructed or not, the total field would be equal to the vector sum of the fields mentioned above.

$$\begin{bmatrix} E_x \\ E_y \\ E_z \end{bmatrix} = \delta_i \begin{bmatrix} E_x^i \\ E_y^i \\ E_z^i \end{bmatrix} + \delta_r \begin{bmatrix} E_x^r \\ E_y^r \\ E_z^r \end{bmatrix} + \delta_{ed} \begin{bmatrix} E_x^{ed} \\ E_y^{ed} \\ E_z^{ed} \end{bmatrix} + \delta_{sd} \begin{bmatrix} E_x^{sd} \\ E_y^{sd} \\ E_z^{sd} \end{bmatrix} + \delta_{dc} \begin{bmatrix} E_x^{dc} \\ E_y^{dc} \\ E_z^{dc} \end{bmatrix} \tag{6}$$

where δ is the factor of obstruct.

3. NUMERICAL RESULTS

Compared with the full wave method, the accuracy and the validity of this approach mentioned above is explained in [3]. In view of the complexity of the satellite and the condition of the computer hardware, the model of point source is adopted on account of the observed points being far field

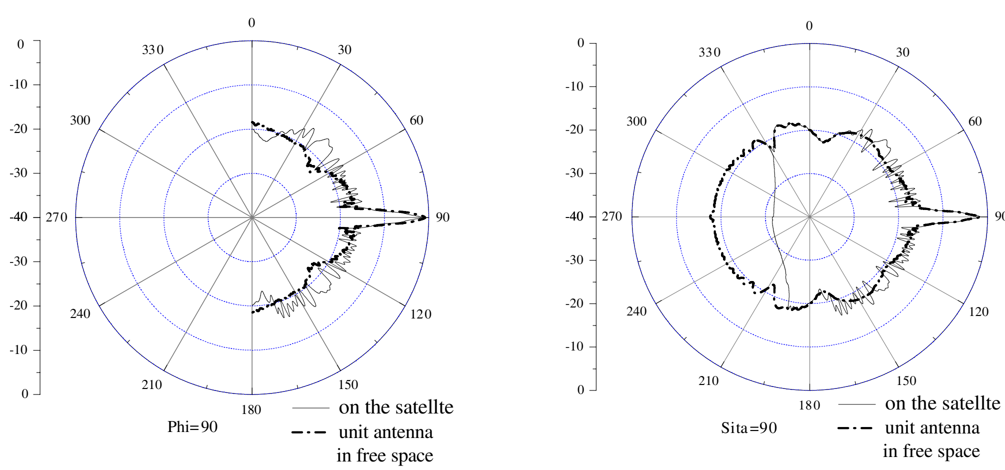

Figure 7: Patterns of antenna A in the pitching plane and the rolling plane.

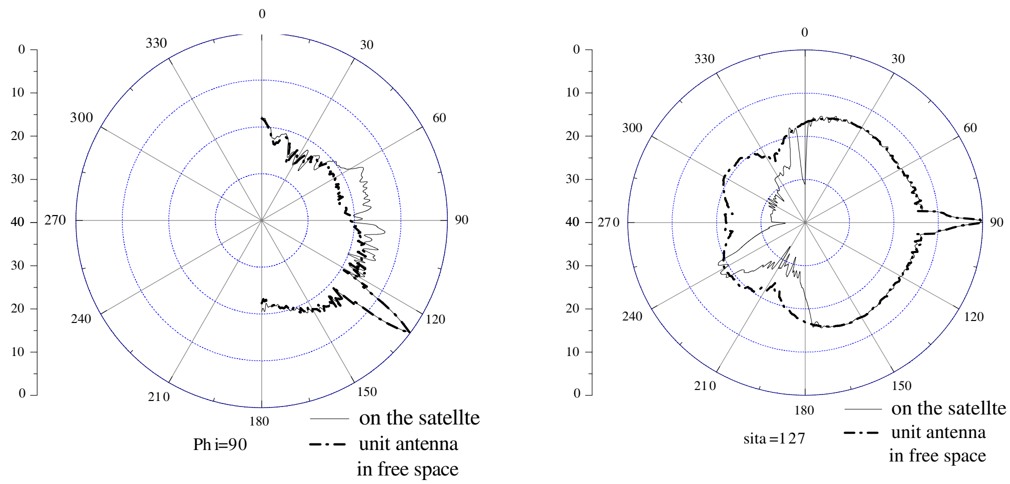

Figure 8: Patterns of antenna B in the pitching plane and the rolling plane.

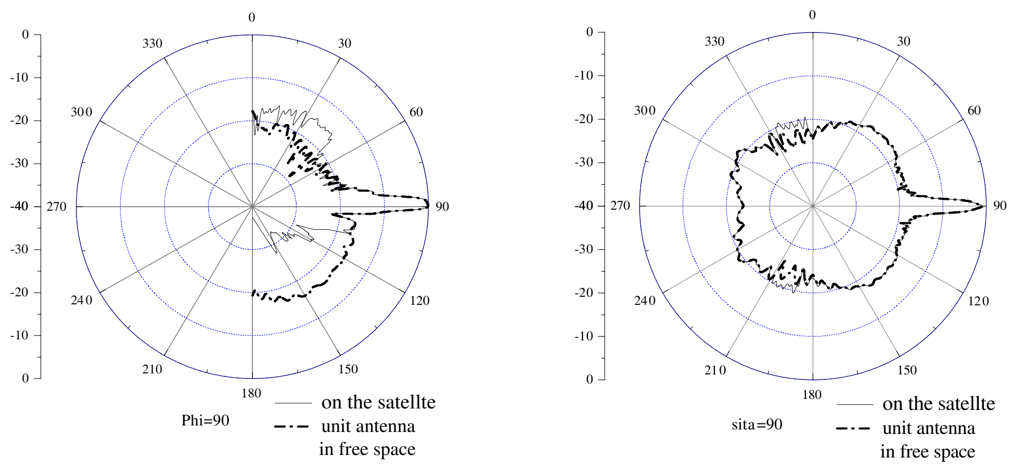

Figure 9: Patterns of antenna C in the pitching plane and the rolling plane.

points relative to the work wavelength. The pattern of the unit antenna in free space would have been solved by the software, which is the pretreatment to analyze the patterns of the antennas on the satellite according to the Equation (6). The antennas A, B and C in Figure 1 would be taken as examples.

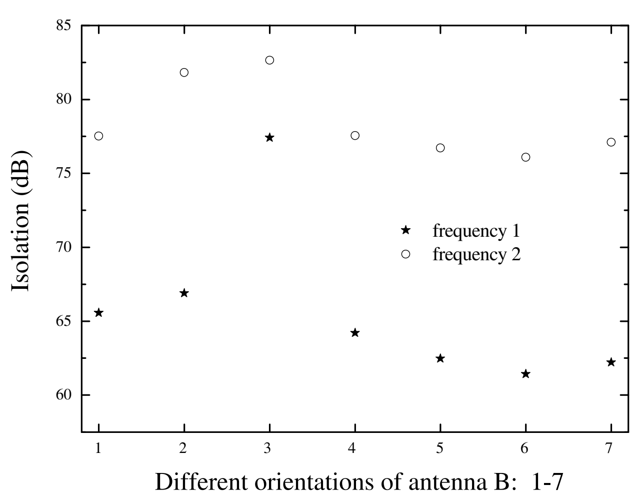

Figure 10: Isolations between antenna A and B.

Seen from Figure 7∼Figure 9, whether the antennas are assembled on the satellite or not, there is little difference in the main lobe of the radiation pattern. Because of the influence of the satellite and the other antennas, the effect of the reflective field and the diffraction field on the side lobes is clear, and in some direction, the radiation is weakened due to the obstruction.

According to the total field of the antennas on the satellite by UTD, the isolation between transmit antennas and receive antennas could be calculated by followed equation,

$$(INS)_{dB} = 10\lg(P_t/P_r) \tag{7}$$

where, P_t is the output power of the transmit antennas, and P_r is the interference power received by receive antennas, which is solved by UTD. The isolations between A and B at two frequencies would be analyzed.

So, the relative position and orientation of antenna A and B could be determined by above results. Consequently, the position and frequency setting of antennas on the satellite could be optimized.

4. CONCLUSION

With the valid equivalent models of the satellite and antennas, the method mentioned in this paper is the effective technique to forecast the patterns and the isolations of the antennas on the satellite, which would be of great value in practice.

ACKNOWLEDGMENT

This work was supported by the National Key Laboratory Foundation of China (No. 9140C53040207 04, 9140C5306010708).

REFERENCES

1. Wang, M., Geometrical Theory of Diffraction, Xidian University, 1994.
2. Pathak, P. H. and R. J. Marhefka, "A uniform GTD analysis of the diffraction of electromagnetic waves by a smooth convex surface," *IEEE Trans. Antennas Propag.*, Vol. 28, No. 5, 631–642, September 1980.
3. Zhou, B. and Q. Liu, "The electromagnetic characteristics of the antennas system in a complex environment," *Journal of Microwaves*, s1, 44–47, 2006.
4. Sikta, F., W. Burnside, and T.-T. Chu, "First-order equivalent current and corner diffraction scattering from flat plate structures," *IEEE Trans. Antennas Propag.*, Vol. 31, No. 4, 584–589, July 1983.
5. Zhou, B., "Research on broadband omnidirectional antennas and the electromagnetic interference of antennas on the satellite," doctoral dissertation, Xidian University, 2006.
6. Keller, J. B., "Geometrical theory of diffraction," *J. Opt. Soc. Am.*, Vol. 52, 116–130, February 1962.
7. Kouyoumijan, R. G. and P. H. Pathak, "A uniform theory of diffraction for an edge in a perfectly conducting surface," *Proc. IEEE*, Vol. 62, No. 11, 1448–1461, November 1974.
8. Pathak, P. H., "New techniques for analysis/synthesis of electrically large satellite antennas," *Microwave and Optoelectronal Conference, 1999. SBMO/IEEE MTT-S, APS and IEOS-IMOC'99. International*, Vol. 2, 475–477, 1999.
9. Munk, P. and P. H. Pathak, "A UTD analysis of the radiation and mutual coupling associated with antennas on a smooth perfectly conducting arbitrary convex surface with a uniform material coating," *IEEE AP-S, Digest*, Vol. 1, 21–26, July 1996.

New Method of Amplitude Modulation for Detection of Multipaction

Yan Ping Li and Yi Ming Ma
Xi'an Institute of Space Radio Technology, Xi'an 710100, China

Abstract— A new global method of amplitude modulation for detection of multipaction in microwave communication systems is presented. Theory demonstrate the potential and usefulness of the method. After experiments, the article gives the practical result.

1. INTRODUCTION

Multipaction is a radio frequency (RF) field-driven resonant discharge in vacuum on the surface between two metal or a single surface of dielectric. A free electron inside a microwave device is accelerated by the electric field and at impact with one of the device walls, secondary electrons are emitted and multipaction take place. Condition of the multipactor break down is different according to different multipaction. To the metal of double surface, it takes place under conditions of vacuum when the mean free path of electrics is larger than the gap between the walls guiding the flow of RF power and electrons average transmit time is odd times half cycle of the RF field. To a single surface of dielectric, the field strength of the DC field bringing by emitted electrons can drive the free electron to come back and hit the surface [1, 4, 6].

As the space technology developed, high power microwave communication being used people find multipaction have become a important point to restrict space technology development. Widely and systemic research about multipaction is needed. It is now urgently task to find out how the multipaction take place, what is the right multipaction threshold of the satellites devices and how to avoid multipaction. Reviewing the history on multipaction researches mostly are based on lots of experiments, ECSS draft on multipaction design and test, it is stated that a test set up should include at least two detection methods and at least one of these methods shall be a so-called "global" method. More attentions must cast on the research of method of multipaction [2, 5].

Several different methods of detection are available and they can be divided into two fairly distinct groups — global and local methods. The global methods are characterized by being able to discern whether or not a multipaction is present somewhere in the system. It can, however, not pinpoint the location of the multipactor. For flight hardware, where the goal is to completely avoid multipaction, the global methods are the methods of preference. In some cases, especially during the hardware development phase, it may be of interest to find out where the multipaction appears in order to identify the parts which require redesign. In such cases, a local method is better, which can monitor a certain area inside a device or a system without taking the entire system into account. Each method has its merit and defect limited by multipaction direction of research and test of device and instruments.

The present work introduces a new global method of amplitude modulation for multipaction detection. The crucial point of the method is the fact that if a small amplitude modulation is superimposed on the microwave signal, the amplitude modulation signal harmonic will not be discernible in the noise spectrum unless a multipaction is present. The underlying physical processes are discussed and the results of experiments, demonstrating the new detection method, are presented.

2. NEW METHOD OF AMPLITUDE MODULATION

The new method test setup are shown in Figure 1. A small amplitude modulation is superimposed on the microwave signal is used as test signal. Because the amplitude modulation depth is so low that only carrier spectrum and side frequency can be see clearly in frequency spectrum before multipaction is present. When multipaction is present, the energy of signal of carrier and side frequency transfer to close-to-carrier noise. The close-to-carrier noise increase due to multipaction non-linear and the harmonic of side frequency increase greatly. From the changed frequency spectrum of multipaction we can get in focus change of the harmonious of side frequency, we can detect the multipaction by this change phenomenon.

Figure 1, amplitude modulation signal from the signal generator is magnified before send to device under test (DUT). The isolator is used to protect the traveling-wave tube amplifier (TWTA).

The output signal from DUT in the vacuum chamber is send to spectrum by directional coupler. The other port is joined to load to absorb the mainly power. Next we will give theoretical analysis to demonstrate this method.

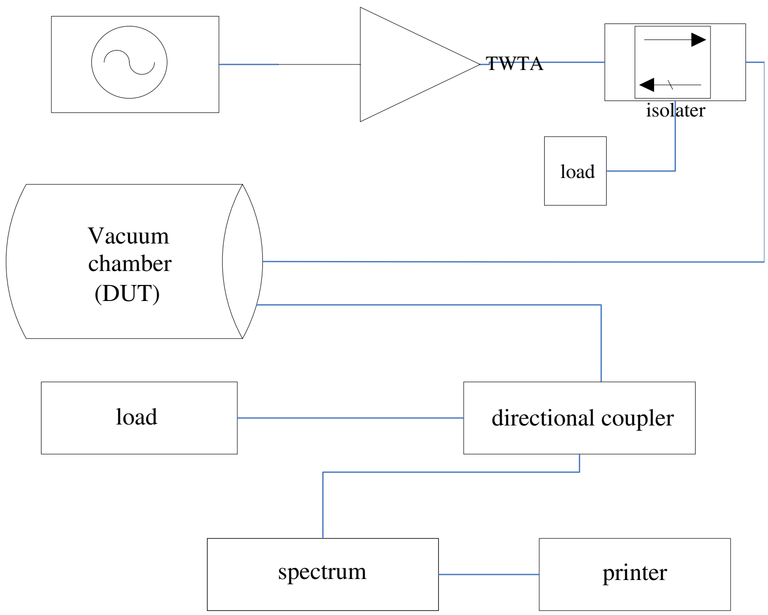

Figure 1: Test setup for multipaction of amplitude modulation method.

3. THEORETICAL ANALYSIS

3.1. Amplitude Modulation Signal Spectrum Variance in a Multipaction Discharge

Multipaction discharge is a non-linear course. When signal pass the non-linear device, signal is transferred, one of this transfer is coming up new frequency. If the transfer function of the nonlinear component can be represented by n-order polynomial power series, the follow is true:

$$V_{out} = aV_{in} + bV_{in}^2 + cV_{in}^3 + \dots \tag{1}$$

Here V_{out} is the output voltage and a, b, $c \dots$ are coefficients depending on the properties of the nonlinear components [3].

Assuming the nonlinear course is excited by a amplitude modulation signal, an expression its input voltage can be written as:

$$\begin{aligned} V_t &= V(1 + m_a \cos \Omega t) \cos \omega_c t \\ &= V \cos \omega_c t + \frac{1}{2} m_a V \cos(\omega_c + \Omega)t + \frac{1}{2} m_a V \cos(\omega_c - \Omega)t \end{aligned} \tag{2}$$

m_a : coefficients of amplitude modulation $m_a < 1$;

ω_c : carrier frequency;

Ω : amplitude modulation frequency.

Finally, making substitution Eq. (2) into Eq. (1) and solving for all intermodulation and harmonic components of V_{out}, we get the expression:

$$V_0 = \frac{3}{4}a_2V^2+\left(a_1V+\frac{3}{4}a_3V^3\right)\cos\omega_ct+\frac{3}{4}a_2V^2\cos 2\omega_ct+\left(\frac{3}{4}a_3V^3+\frac{1}{4}a_3V^3m_a^3\right)\cos 3\omega_ct+a_2V^2m_a\cos\Omega t$$
$$+\frac{1}{4}a_2V^2\cos 2\Omega t+\left(\frac{1}{2}a_1Vm_a+\frac{3}{4}a_3V^3m_a+\frac{9}{32}a_3V^3m_a^3\right)\left[\cos\left(\Omega+\omega_c\right)+\cos\left(\Omega-\omega_c\right)\right]$$
$$+\frac{1}{2}a_2V^2m_a\left[\cos\left(\Omega+2\omega_c\right)+\cos\left(\Omega-2\omega_c\right)\right]+\frac{1}{8}a_2V^2\left[\cos 2\left(\Omega+\omega_c\right)+\cos 2\left(\Omega-\omega_c\right)\right]$$
$$+\left(\frac{1}{4}a_3V^3m_a+\frac{3}{32}a_3V^3m_a^3\right)\left[\cos(\Omega+3\omega_c)+\cos(\Omega-3\omega_c)\right]$$
$$+\frac{3}{8}a_3V^3m_a^2\left[\cos(2\Omega+\omega_c)+\cos(2\Omega-\omega_c)\right]+\frac{1}{8}a_3V^3m_a^2\left[\cos\left(2\Omega+3\omega_c\right)+\cos\left(2\Omega-3\omega_c\right)\right]$$
$$+\frac{3}{32}a_3V^3m_a^3\left[\cos(3\Omega+\omega_c)+\cos(3\Omega-\omega_c)\right]+\frac{1}{32}a_3V^3m_a^3\left[\cos 3(\Omega+\omega_c)+\cos 3(\Omega-\omega_c)\right]+\dots \quad (3)$$

We get the new frequency, $\omega_c \pm 2\Omega$ and $\omega_c \pm 3\Omega$ is the harmonic of $\omega_c + \Omega$ and $\omega_c - \Omega$, this new frequency lying near carrier, can not be filtered and can be modulated by noise close to carrier during the multipaction.

3.2. Amplitude Modulation Signal Power Variance in a Multipaction Discharge

The noise generated by the multipaction will normally not be a simple function of the input power. There are many different factors, which will affect the behavior of the noise as the power is increased. Using the classical multipaction model, one can see that the acceleration of the electrons is proportional to the amplitude of the input signal. The amplitude of the input signal is proportional to the square root of the input power. According to Larmor's formula [2].

$$P = \frac{2e^2a^2}{34\pi\varepsilon_0C^3} \quad (4)$$

P: the power generated by an accelerated charge, e: the charge, ε_0: dielectric constant, C: light speed 3×10^8 m/s, a: the acceleration of the charge.

The power generated by an accelerated charge in the nonrelativistic case, is proportional to the square of the acceleration. Assuming constant electron density, this leads to the conclusion that the close-to-carrier noise power is directly proportional to the input signal power. However, the electron density is most likely not constant, rather it will increase with increased input power. Furthermore, when the amplitude increases, the region within the cavity that will fulfill the resonance condition will increase and, thus, a larger volume of the cavity will be involved in the multipactor resulting in a larger number of multipacting electrons. Even though the electrons within this added region

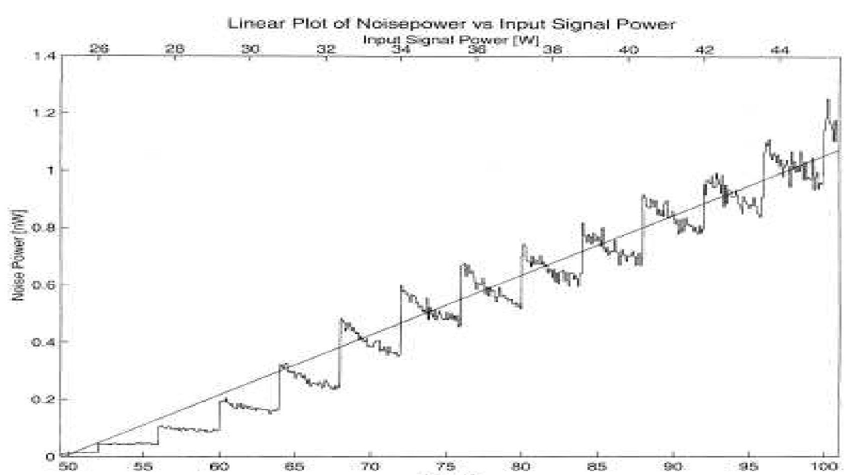

Figure 2: Averaged noise power versus input signal power (top x axis) with linear scales on both axes.

will be less energetic as they are accelerated by an amplitude which is lower than in the middle, the increased number of electrons should result in a nonlinear, exponential increase in noise power.

This is multipactor generated detuning and loading of the cavity. The loading will lead to a lowered-value and a concomitant reduction in electric field strength, which will reduce the impact velocity of the electrons and decrease the region within the cavity that fulfils the resonance condition. Detuning further enhances this effect by allowing less power to enter the cavity. The significance of each of the described effects will be different in each case making an assessment of the relation between noise power and input power a rather difficult problem. In this specific case, measurement data is available and a linear plot of noise power versus input power reveals that there is an approximately linear relation between noise power and input power [2].

$$\begin{gathered} P_{noise} = k(P_{input} - P_{th}) \quad P_{input} \geq P_{th} \\ k = 5.3 \times 10^{-11} \quad P_{th} = 25.2\,\mathrm{W} \end{gathered} \tag{5}$$

No multipaction noise is generated until the threshold power is reached. After the threshold has been reached, the noise power increases linearly as a function of the input signal power. An interesting point is that the noise power is proportional to the difference between the input power and the multipaction threshold power, which makes it sensitive to a modulating signal when the threshold has been barely reached.

From this analysis, we get the result during multipaction: first the harmonic frequency $\omega_c \pm 2\Omega$ and $\omega_c \pm 3\Omega$ are generated and modulated by noise, second the power of noise transferred to the harmonic frequency, the transfer of the power is acutely, its is a sensitive method to detection multipaction.

4. TESTING RESULT

The experimental runs were performed at pressure on the order of 7.0×10^{-4} mm Hg and the temperature is $21° \sim 27°$ in the vacuum. The under test device are chamber filters; the frequency band is 1643.5 MHz±2 MHz. The experimental schematic is Figure 3. In order to produce sufficient electron radioactive source Cesium 137 was used.

To contrast the method of amplitude modulation with other method. The experiment were performed with method of nulling of forward/reverse power detection and second harmonic detection.

The experiment result as theory analysis, the method of amplitude modulation detection multipaction is sensitive to detect multipaction. When multipaction occurred, carrier power dropped

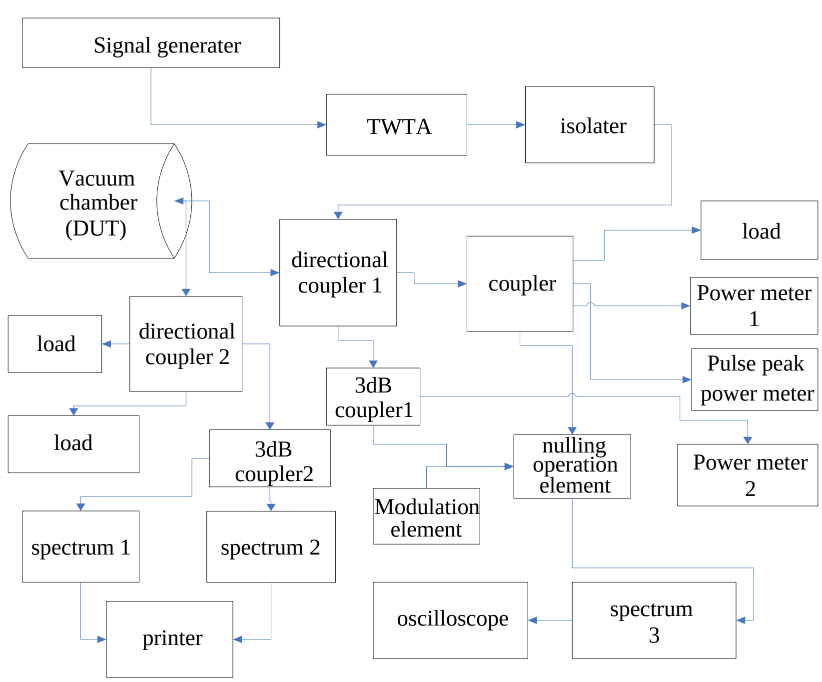

Figure 3: The block diagram of the experiment of three methods.

and the amplitude modulation signal harmonic appeared at the same time raised. the amplitude modulation signal harmonic magnitude variation relate to variation of multipaction.

Figure 4, Before multipaction break down, we can see the frequency of carrier and AM and AM harmonic are so low as to can not be discern in the noise. Thirty minutes should be stay in each test power level till breakdown occurred. We can get result from Figure 4. the energy of signal transferred to AM frequency harmonic. Carrier power dropped and changed 15.24 dB, and also the AM changed 6.85 dB, as the same time the AM frequency second harmonic raised 20.42 dB, third harmonic raised 10 dB. This due to multipaction break down. The AM frequency harmonics changed greatly. So this method is sensitive to detect multipaction.

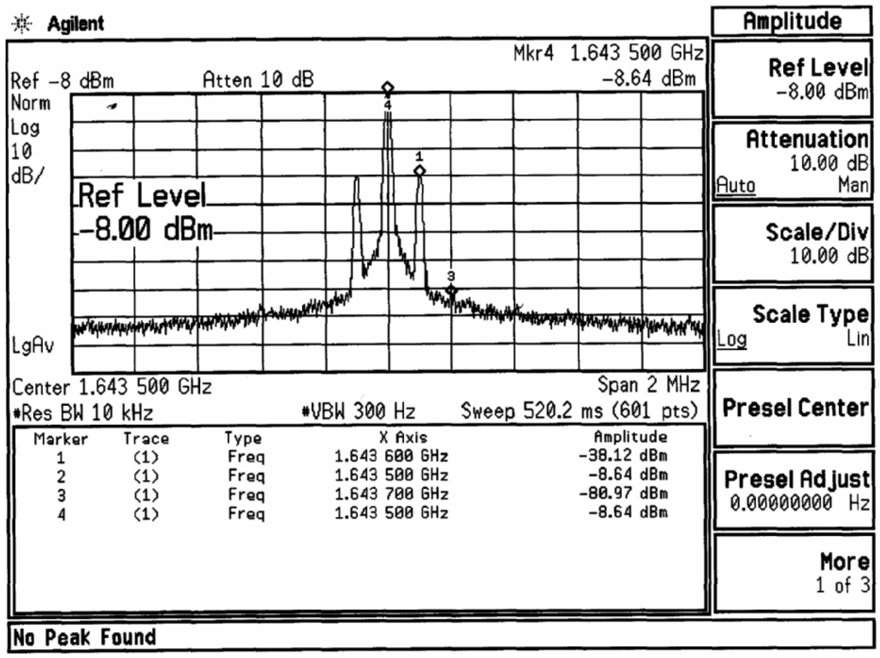

(a)

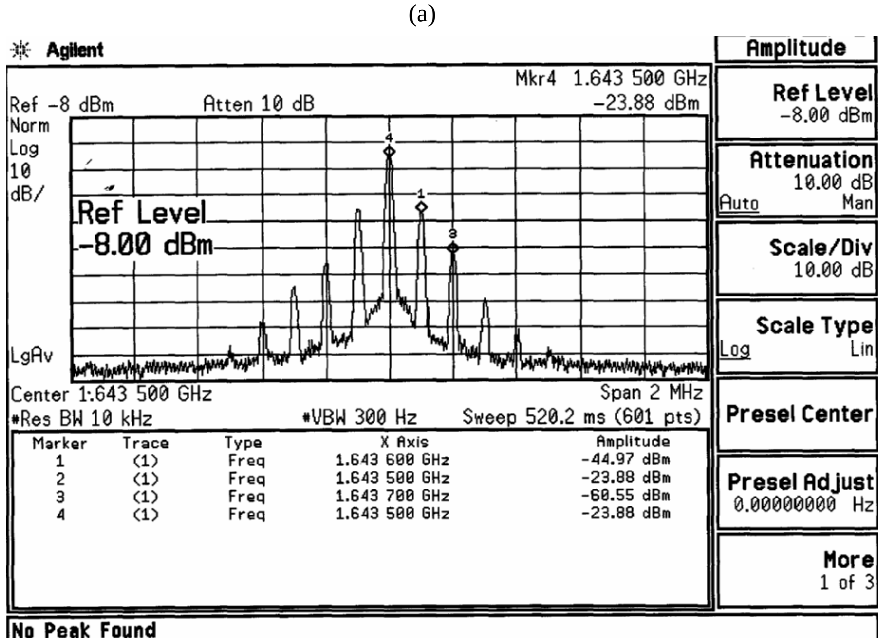

(b)

Figure 4: The amplitude modulation frequency is 100 KHz and modulation depth is 5%, the spectrum of front-to-back of multipaction, (a) the spectrum of before multipaction break down, (b) the spectrum during multipaction break down.

5. CONCLUSIONS

The new method of AM detection of multipaction is sensitivly. It will work equally well with second harmonic method and nulling power forward/reverse method. The new method can be used Ka band easily not limited to test system different from other method.

ACKNOWLEDGMENT

This work was supported by the National Key Laboratory Foundation of China (No. 9140C5303020704, 9140C5306010708).

REFERENCES

1. Cao, G.-M., Y. Nie, and J.-Q. Wang, "Multipactor on microwave components," *Journal of Astronautic Metrology and Measurement*, Vol. 25, No. 4, August 2005.
2. Udiljak, R., D. Anderson, P. Ingvarson, and U. Jordan, "New method for detection of multipaction," *IEEE Transactions on Plasma Science*, Vol. 31, No. 3, June 2003.
3. Golikov, V., S. Hienonen, and P. Vainilainen, "Passive intermodulation distortion measurements in mobile communication antennas," 0-7803-7005-8/01, IEEE, 2001.
4. Woo, R., "Final report on RF breakdown in coax transmission lines," NASA Report, No. 32-1500, October 1970.
5. Woode, A. and J. Petit, "Investigations into multipactor breakdown in satellite microwave payloads," *ESA Journal*, Vol. 14, No. 4, 1990.
6. Kravchuk, L. V. and G. V. Romanov, "The computer code for investigation of the multipactor discharge in RF cavities," 0-7803-5573-3/99, IEEE, 1999.

Peculiar Radar Cross Section Properties of Metamaterials

Wan-Zhao Cui, **Wei Ma**, **and Lede Qiu**
National Key Laboratory of Space Microwave Technology
Xi'an Institute of Space Radio Technology, Xi'an 710100, Shannxi Province, China

Abstract— In this paper, peculiar radar cross section properties of metamaterials are obtained, and the connections between the radar cross section, the polarizability and the permittivity are investigated, respectively. These results have shown that the polarizability and radar cross section of the sphere made of metamaterials if the permittivity ε_r is less than -2 are much larger than the case of conventional material. Moreover, the interested insights of metamaterials for potential applications in radar are provided.

The term "metamaterial" refers to any material that is artificially constructed for the purpose of achieving desired properties [1]. In electromagnetics, a metamaterial (MTM) can be created by constructing a "specific" structure with elements of size less than the wavelength of the incoming electromagnetic wave. Because the bulk properties of this material no longer depend on the materials used, but depend on the geometry of the structure, the resulting material can be engineered for any purpose, and can even achieve behaviors that are not found in nature.

In 1968, lossless propagation of an electromagnetic wave in the MTM with negative permittivity (ε) and negative permeability (μ) was first investigated by V. G. Veselago [2], and was experimentally verified in 2001 based on split-ring resonators and rods [3]. V. G. Veselago speculated on the possible existence of MTMs and anticipated their unique electromagnetic properties [2]. The unique properties of MTMs have allowed novel applications, concepts, and devices to be developed1. Science magazine even named MTMs as one of the top ten scientific breakthroughs of 2003 [4]. Planar metamaterials have been realized experimentally by several research groups [5].

In this paper, peculiar radar cross section (RCS) properties of metamaterials are obtained, and the connections between the radar cross section, the polarizability and the permittivity are discussed, respectively. These results have shown that the polarizability and radar cross section of the sphere made of metamaterials if the permittivity ε_r is less than -2 are much larger than the case of conventional material. These results provide some interested insights and ideas for potential applications in radar.

1. RADAR CROSS SECTION

The important concept of radar cross section carries the dimension of a surface, and is a measure how much an object scatters electromagnetic energy in the backscattering direction. This monostatic RCS is defined by [6]

$$\sigma_{RCS} = \lim_{r\to\infty} \frac{4\pi r^2 |E_s|^2}{|E_i|^2} \tag{1}$$

where E_s is the amplitude of the scattered field in the distance of r of the object in the backscattering direction when it is illuminated by a plane wave with electric field amplitude E_i. On the other end of the frequency spectrum, in electrostatics, the concept of electric polarizability is extremely essential. The static dipole moment P is induced by an object because of the existence of a static exciting field E_{st}, and the polarizability is,

$$P = \vec{\alpha} \cdot E_{st} \tag{2}$$

In general, the polarizability $\vec{\alpha}$ is a dyadic but for symmetric objects, like sphere or cube it is a multiple of the unit dyadic, equivalent to a scalar α. For a dielectric sphere, the polarizability is [7]

$$\alpha = 3V\varepsilon_0 \frac{\varepsilon - \varepsilon_0}{\varepsilon + 2\varepsilon_0} \tag{3}$$

where V is the volume and $\varepsilon = \varepsilon_r \varepsilon_0$ is the absolute permittivity of the sphere. The polarizability is often given in the dimensionless normalized form $\alpha_n = \alpha/(\varepsilon_0 V)$, and for the sphere it is

$$\alpha_n = \frac{\alpha}{\varepsilon_0 V} = 3\frac{\varepsilon_r - 1}{\varepsilon_r + 2} \tag{4}$$

In low frequencies, the scattering from a polarizable object can be calculated from the far field of a Hertzian dipole with the dynamic dipole moment amplitude [8], and the field amplitude in the backscattering direction is

$$|E_s| = \frac{\omega^2 \mu_0 p}{4\pi r} \tag{5}$$

Since the static dipole moment is connected with the incident field as $P = \alpha E_i$, and the connection between the low-frequency limit of the radar cross section and the static polarizability of the object is as following:

$$\alpha_n = \frac{\sqrt{4\pi\sigma_{RCS}}}{k_0^2 V} \tag{6}$$

where $k_0^2 = \omega^2 \mu_0 \varepsilon_0$ with the free-space parameters μ_0, ε_0.

2. DISCUSSION

The polarizability is an important concept in the modeling of materials in general. Effective medium theories make a use of this quantity very much. The connections between permittivity and α_n are shown in Fig. 1. If the sphere is made of MTM, whose effective materials parameter $\varepsilon_r = 0$, then

$$\alpha_n = -1.5. \tag{7}$$

The parameter $\alpha_n < 0$ means the obtained direction of polarization is opposite to the assumed direction. Similarly, we obtain

$$\alpha_n = \lim_{\varepsilon_r \to -2^-} 3\frac{\varepsilon_r - 1}{\varepsilon_r + 2} = +\infty \tag{8}$$

$$\alpha_n = \lim_{\varepsilon_r \to -2^+} 3\frac{\varepsilon_r - 1}{\varepsilon_r + 2} = -\infty, \tag{9}$$

and α_n may be very large at some cases, for example, if $\varepsilon_r = -2.1$

$$\alpha_n = 930 \tag{10}$$

much large the traditional materials, in the conducting limit the normalized polarizability of a sphere using conventional materials — **nonmetamaterials**

$$\alpha_n = \lim_{\varepsilon_r \to \infty} 3\frac{\varepsilon_r - 1}{\varepsilon_r + 2} = 3 \tag{11}$$

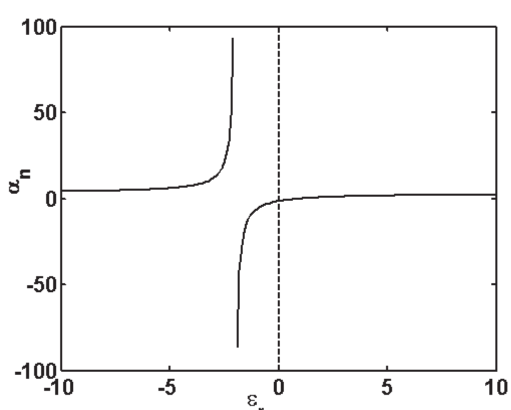

Figure 1: The connections between the permittivity ε_r and the polarizability α_n.

In the low-frequency limit, where Rayleigh scattering is dominant [9], this parameter has the dependency of frequency. Therefore, from the cross section in the low-frequency limit we can estimate the polarizability of the sphere. However, if $\alpha_n < 0$, Equation (6) will not hold, and the general equation for Equation (6) is

$$|\alpha_n| = \frac{\sqrt{4\pi\sigma_{RCS}}}{k_0^2 V} \tag{12}$$

As long as we are around the proper frequency so that Rayleigh scattering dominates, the obtained RCS of the sphere give with reasonable calculation times an accuracy of three significant digits in α_n, so it is important that the analysis is done in sufficiently low frequencies. The Rayleigh-scattering approximation for the parameter as a function of permittivity (at the frequency of 100 kHz) is illustrated in Fig. 2. The radius of the sphere is 1 m. Obviously, the radar cross section of the sphere made of metamaterials if the permittivity ε_r is less than -2 are much larger than the case of nonmetamaterials.

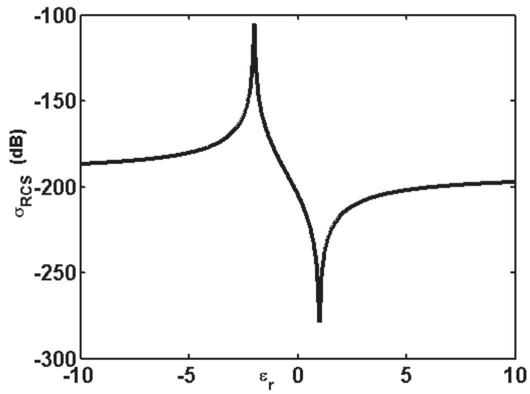

Figure 2: Low-frequency limiting approximation (Rayleigh) for the connection between the relative permittivity and radar cross section (in dB) of the spherical object.

3. CONCLUSIONS

In this paper, peculiar radar cross section properties of metamaterials are obtained, and the connections between the radar cross section, the polarizability and the permittivity are discussed, respectively. These results have shown that the polarizability and radar cross section of the sphere made of metamaterials if the permittivity ε_r is less than -2 are much larger than the case of nonmetamaterials, and provide some interested insights and ideas for potential applications in radar. Although the present method only dealt with a sphere, our conclusions with a cube showed quantitatively very similar results.

ACKNOWLEDGMENT

This work was supported by the National Key Laboratory Foundation of China (No. 9140C53040207 04).

REFERENCES

1. Caloz, C. and T. Itoh, *Electromagnetic Metamaterials: Transmission Line Theory and Microwave Applications*, Wiley, New York, 2005.
2. Veselago, V. G., "The electrodynamics of substances with simultaneously negative values of ε and μ," *Sov. Phys.-Usp.*, Vol. 10, No. 4, 509–514, 1968.
3. "Breakthrough of the year: The runners-up," *Science*, Vol. 302, No. 5653, 2039–2045, 2003.
4. Shelby, R. A., D. R. Smith, and S. Schultz, "Experimental verification of a negative index of refraction," *Science*, Vol. 292, No. 5514, 77–79, 2001.
5. Engheta, N. and R. W. Ziolkowski, *Metamaterials: Physics and Engineering Explorations*, IEEE Press, 2006.
6. Harrington, R. F., *Time-Harmonic Electromagnetic Fields*, McGraw-Hill, New York, 1961.
7. Sihvola, A., *Electromagnetic Mixing Formulas and Applications*, ser. *Electromagnetic Waves*, Vol. 47, IEE, London, UK, 1999.
8. Kong, J. A., *Electromagnetic Wave Theory*, EMW Publishing, Cambridge, MA, 2000.
9. Sihvola, A., T. K. Sarkar, and B. Kolundzija, "From radar cross section to electrostatics," *IEEE Antennas and Wireless Propagation Letters*, Vol. 3, 324–327, 2004.

Rectangular Waveguide Band Pass Filter with Capacitive Coupling Iris

Shengxian Li[1,2], **Junmei Fu**[2], **and Xuda Wu**[1]

[1]School of Electronics and Information Technology
Xi'an Jiaotong University, Xi'an 710049, China
[2]Xi'an Institute of Space Radio Technology, Xi'an 710100, China

Abstract— A novel rectangular waveguide band pass filter (BPF) with capacitive coupling iris is presented in this paper. The S parameters of capacitive and inductive iris are achieved by Mode Matching Technique (MMT), and different S21 performance is compared between them. As example one Ku band waveguide BPF with capacitive coupling iris is simulated, the simulated responses show that the isolation at low and high frequency stop-band is almost symmetric compared to BPF with inductive coupling iris.

1. INTRODUCTION

Rectangular waveguide filters play important role in microwave system, such as satellite communication system, radar system, etc. Inductive iris is often used as coupling element in rectangular waveguide band pass filter. For this kind of BPF, the response at out-band is usually asymmetric, often the rejection at low frequency stop-band is lager than that at high frequency stop-band [1].

Capacitive coupling iris is often used in the waveguide low pass filter [2], but that it used as coupling element in waveguide BPF is not reported. In this paper, rectangular waveguide BPF with capacitive coupling iris is presented, different S21 performance between capacitive and inductive coupling iris is discussed, so different stop-band performance between waveguide BPF with capacitive and inductive coupling iris is obtained.

As example, one Ku band waveguide BPF with capacitive coupling iris is simulated, the simulated responses show that the isolation at low and high frequency stop-band is almost symmetric compared to BPF with inductive coupling iris.

2. CAPACITIVE AND INDUCTIVE COUPLING IRIS

Capacitive and inductive coupling iris are shown in Fig. 1(a) and Fig. 1(b), These structures can be divided into waveguide junctions and one section small waveguide, the only discontinuity is the junction of rectangular to rectangular waveguide, which is shown in Fig. 2, and it can be simulated by mode matching technique (MMT), the procedure is described in the following.

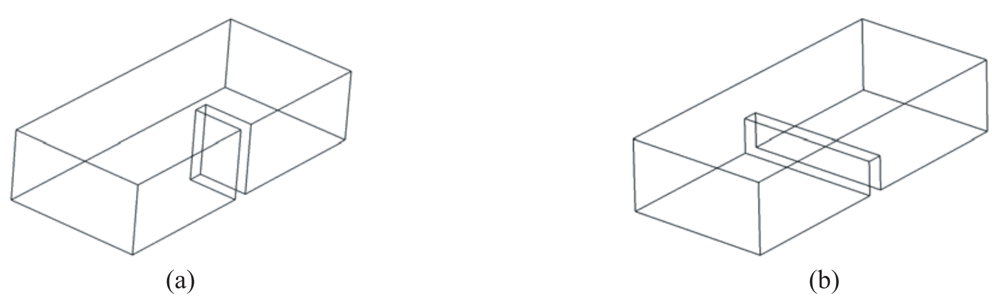

Figure 1: The structure of different rectangular coupling iris, (a) Inductive iris, (b) Capacitive iris.

The boundary conditions for waveguide junction in Fig. 2 are listed here:

$$\vec{E}_{t2}(x,y)\,|_{z=0} = \begin{cases} \vec{E}_{t1}(x,y)\,|_{z=0} & ((x,y)\in s_0) \\ 0 & ((x,y)\in (s_1-s_0)) \end{cases} \tag{1}$$

$$\vec{H}_{t2}(x,y)\,|_{z=0} = \vec{H}_{t1}(x,y)\,|_{z=0} \quad ((x,y)\in s_0) \tag{2}$$

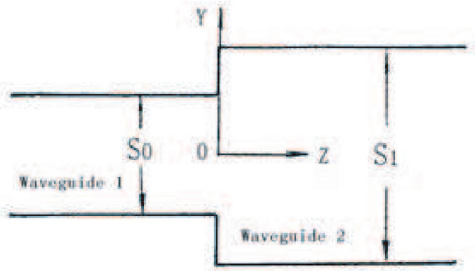

Figure 2: Waveguide junction.

The tangential E field can be expanded as follows:

$$\begin{aligned}\vec{E}_{ti}(x,y) &= \sum_{m,n} a^{+}_{i,mn}\vec{e}^{\,(h)}_{i,mn}(x,y) + \sum_{m,n} a^{-}_{i,mn}\vec{e}^{\,(h)}_{i,mn}(x,y)\\ &\quad + \sum_{m,n} b^{+}_{i,mn}\vec{e}^{\,(e)}_{i,mn}(x,y) + \sum_{m,n} b^{-}_{i,mn}\vec{e}^{\,(e)}_{i,mn}(x,y) \quad (i=1,2)\end{aligned} \tag{3}$$

$\vec{e}^{\,\mu}_{i,mn}(\mu = h, e)$ is the modal function of guide $i(i = 1, 2)$.

Assume

$$\begin{aligned}A_{i,mn} &= a^{+}_{i,mn} + a^{-}_{i,mn}\\ B_{i,mn} &= b^{+}_{i,mn} + b^{-}_{i,mn}\end{aligned} \tag{4}$$

and we get

$$\vec{E}_{ti} = \sum_{m,n} A_{i,mn}\vec{e}^{\,(h)}_{i,mn} + \sum_{m,n} B_{i,mn}\vec{e}^{\,(h)}_{i,mn} \tag{5}$$

Expression (5) is matched by $\vec{e}^{\,\mu}_{2,mn}(\mu = h, e)$, and after using the orthogonally of guide 2 modes, we get

$$\begin{bmatrix}[A_1]\\ [B_1]\end{bmatrix} = \begin{bmatrix}[H] & [K]\\ [Q] & [E]\end{bmatrix}\begin{bmatrix}[A_2]\\ [B_2]\end{bmatrix} \tag{6}$$

and we suppose

$$[[M]] = \begin{bmatrix}[H] & [K]\\ [Q] & [E]\end{bmatrix} \tag{7}$$

$[M]$ is called electrical filed coupling matrix:

$$\begin{aligned}H_{mn,pq} &= \frac{\sqrt{Z^{(h)}_{2,pq}}}{\sqrt{Z^{(h)}_{1,mn}}} N_{1,mn}N_{2,pq}\oint_{s0} \vec{e}^{\,(h)}_{1,mn}(x,y)\cdot\vec{e}^{\,(h)}_{2,pq}(x,y)dxdy\\ K_{mn,pq} &= \frac{\sqrt{Z^{(e)}_{2,pq}}}{\sqrt{Z^{(h)}_{1,mn}}} N_{1,mn}N_{2,pq}\oint_{s0} \vec{e}^{\,(h)}_{1,mn}(x,y)\cdot\vec{e}^{\,(e)}_{2,pq}(x,y)dxdy\\ Q_{mn,pq} &= \frac{\sqrt{Z^{(h)}_{2,pq}}}{\sqrt{Z^{(e)}_{1,mn}}} N_{1,mn}N_{2,pq}\oint_{s0} \vec{e}^{\,(e)}_{1,mn}(x,y)\cdot\vec{e}^{\,(h)}_{2,pq}(x,y)dxdy\\ E_{mn,pq} &= \frac{\sqrt{Z^{(e)}_{2,pq}}}{\sqrt{Z^{(e)}_{1,mn}}} N_{1,mn}N_{2,pq}\oint_{s0} \vec{e}^{\,(e)}_{1,mn}(x,y)\cdot\vec{e}^{\,(e)}_{2,pq}(x,y)dxdy\end{aligned} \tag{8}$$

Similarly we can use H-field mode matching to deduce the following matrix equation:

$$-\begin{bmatrix}[C_2]\\ [D_2]\end{bmatrix} = [M]^T\begin{bmatrix}[C_1]\\ [D_1]\end{bmatrix} \tag{9}$$

Here,

$$\begin{aligned} C_{i,mn} &= a_{i,mn}^{+} - a_{i,mn}^{-} \\ D_{i,mn} &= b_{i,mn}^{+} - b_{i,mn}^{-} \end{aligned} \tag{10}$$

Then, the generalized S-matrix of waveguide junction can be obtained from following

$$\begin{bmatrix} [a_1^-] \\ [b_1^-] \\ [a_2^-] \\ [b_2^-] \end{bmatrix} = [S] \begin{bmatrix} [a_1^+] \\ [b_1^+] \\ [a_2^+] \\ [b_2^+] \end{bmatrix} \tag{11}$$

and it can be divided into 4 sub-matrixes:

$$\begin{aligned} [S_{11}] &= \left\{M^T M + I\right\}^{-1} \left\{I - M^T M\right\} \\ [S_{12}] &= 2\left\{M^T M + I\right\} M^T \\ [S_{21}] &= M\left\{I + [S_{11}]\right\} \\ [S_{22}] &= M[S_{12}] - I \end{aligned} \tag{12}$$

Two waveguide junction and one section small waveguide are cascaded to obtain the whole S-parameter of capacitive and inductive iris structure. Of course the iris structure can also be simulated by commercial software such as HFSS, CST.

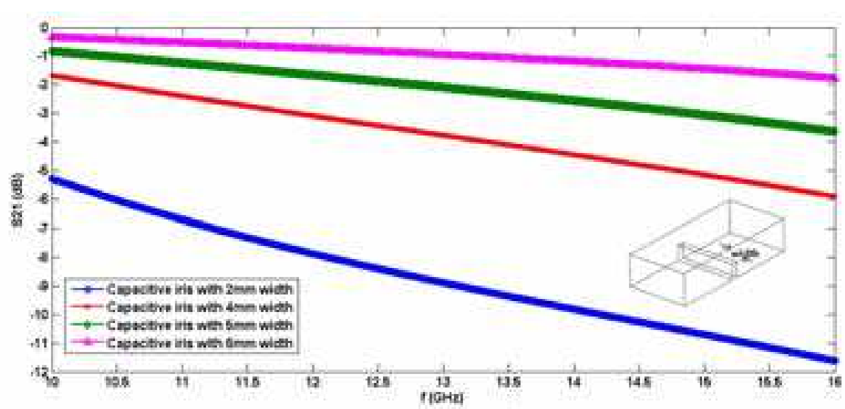

(a)

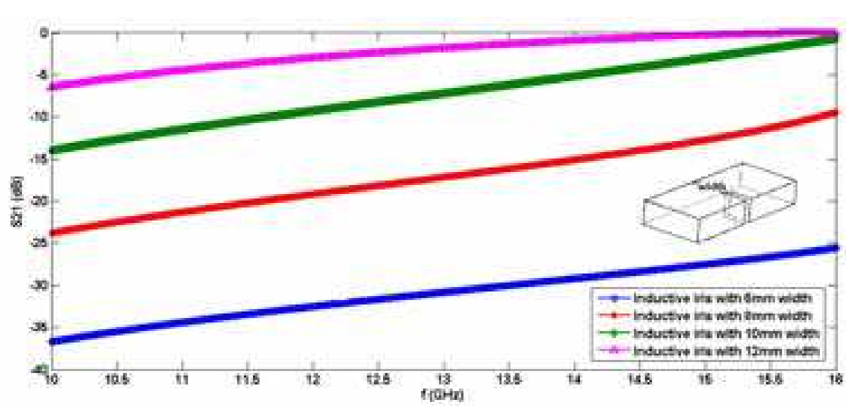

(b)

Figure 3: The S21 response of WR75 waveguide coupling iris, (a) For different width of capacitive iris, (b) For different width of inductive iris.

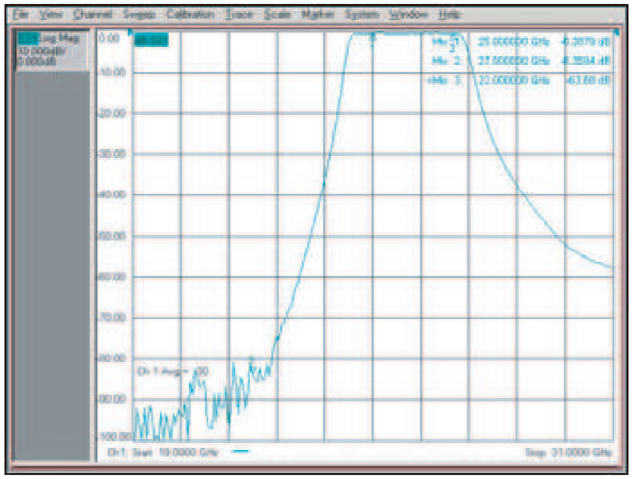

Figure 4: The S21 experiment response of WR34 BPF with inductive coupling iris.

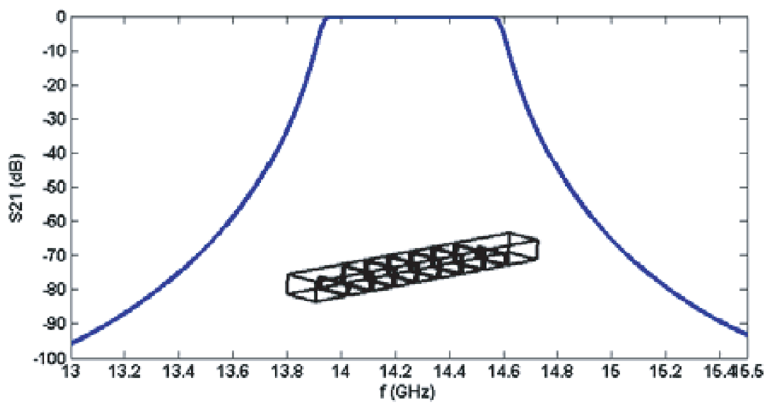

Figure 5: The simulated S21 response of WR75 BPF with capacitive coupling iris.

3. NUMBERICAL RESULT

The scattering matrix of WR75 waveguide capacitive and inductive coupling iris are simulated by MMT above, the amplitude responses of S21 are shown in Fig. 3(a) and (b) for different width of coupling iris, and the thick of all iris is 2 mm, the frequency is from 10 GHz to 16 GHz.

It is obvious that variation of S21 as frequency is different from Fig. 3. For capacitive coupling iris, the S21 amplitude decreases as increasing of frequency, but it is opposite for inductive iris.

Because of different S21 response and high-pass performance of rectangular waveguide, different

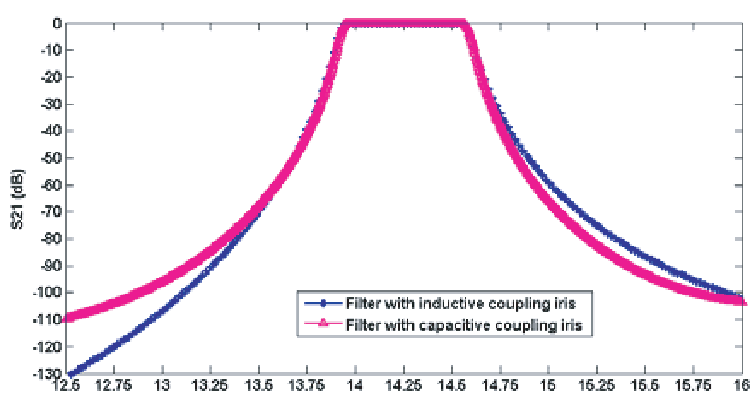

Figure 6: The simulated responses of BPFs with capacitive and inductive iris.

S21 performances are obtained for BPF with capacitive and inductive coupling iris. For inductive iris waveguide BPF, the out-band performance at low frequency is better than that at high frequency, it can be validated by paper [1] and experiments result which is shown in Fig. 4.

For capacitive iris waveguide BPF, the out-band rejection is almost symmetric, the simulated s21 response is shown in Fig. 5.

The comparison of S21 response between the two kinds of iris BPF is shown in Fig. 6, and the rejection of BPF with capacitive iris at low and high frequency stop-band is almost symmetric compared to BPF with inductive iris.

4. CONCLUSION

Rectangular waveguide BPF with capacitive coupling iris is presented in this paper. The S parameters of capacitive and inductive iris are achieved by MMT, and different S21 performance is compared between them. As example one Ku band waveguide BPF with capacitive coupling iris is simulated, the simulated responses show that the isolation at low and high frequency stop-band is almost symmetric compared to BPF with inductive coupling iris.

REFERENCES

1. Arndt, F., R. Beyer, J. M. Reiter, T. Sieverding, and T. Wolf, "Automated design of waveguide components using hybrid mode-matching/numerical EM building blocks in optimization-oriented CAD frameworks–state-of-the-art and recent advances," *IEEE Trans. Microwave Theory Tech.*, Vol. 45, 747–760, Jan. 1997.
2. Hauth, W., R. Keller, and U. Rosenberg, "CAD of waveguide low-pass filters for satellite applications[J]," *17th EuMc Proc.*, 151–156, Rome, 1987.

Study on W-band PLL Frequency Synthesizer for Space Communications

Haihong Ma[1] **and Xiaohong Tang**[2]

[1]Laboratory of Microwave Technology
Xi'an Institute of Space Radio Technology, Xi'an 710100, China
[2]School of Electronic Engineering
University of Electronic Science and Technology of China, Chengdu 610054, China

Abstract— As one of the key parts of millimeter-wave systems, the demands for millimeter wave frequency synthesizer become more and more urgent than ever, especially in W-band. In this paper, with the combination of the technique of PLL, DDS and multiplier, a W-band PLL frequency synthesizer with low phase noise has been presented, which is characterized by nice performances, and it has good foreground for its application in millimeter-wave space communications.

1. INTRODUCTION

With the rapid development of millimeter-wave technology, its application is mainly aimed at the fields of radar systems and space communication [1]. At 2005, the first 95 GHz millimeter-wave interferometer for velocity measurement in our country has been designed, which is used to measure the parameters of artillery inner ballistic trajectory [2].

Because of the unknown channel behavior and the development level of hardware at these frequencies, actual disquisition on W-band space communication systems are based only on feasibility studies [3]. Due to atmospheric absorption, frequency around 60 GHz cannot be utilized effectively, so W-band (75–100 GHz) is considered as a "technological frontier" for space communication [4, 5]. More interest in W-band arises. At 2006, NASA launched a new LEO satellite mission (CloudSat) to study clouds and climate, and a weather W-band radar at 94 GHz was on board, which was the first mission carrying a space-qualified W-band radar system [6]. WAVE (W-band Analysis and Verification) is a project proposed for the ASI to design and develop a W-band geostationary payload, which aimed at the experimental studies of the W-band channel and possible utilization in satellite data communications, its uplink is 81∼86 GHz, and downlink is 71∼76 GHz [7].

Millimeter-wave frequency synthesizer is one of the key parts of millimeter-wave systems. The demand for it with good performances is more and more urgent than ever, especially in W-band. Phase-locked technique has been widely used to design frequency synthesizer with low phase noise and high frequency stability. As one of the crucial performance indexes of frequency synthesizer, phase noise has always been the emphasis for electronic engineers to study. In this paper, a W-band PLL frequency synthesizer with low phase noise has been presented.

2. DESIGN OF LOW PHASE NOISE W-BAND PLL FREQUENCY SYNTHESIZER

In order to achieve hopping frequency synthesizer, DDS is a usually used frequency synthesis technique. However, in W-band, the frequency synthesizer can not be achieved by the sole use of DDS because of the high frequency. PLL is another effective frequency synthesis technique. So the technique of PLL and DDS should be combined. According to the analysis [8], the phase noise of the millimeter-wave PLL frequency synthesizer can be estimated using L_{LO} and L_{IF}, which can be easily measured with the spectrum analyzer. The relationship among the phase noises can be simply expressed as follows:

$$L_O \approx \max\{(L_{LO} + 20\lg M),\, L_{IF}\} + 6\,\text{dBc/Hz} \tag{1}$$

where, L_O represents the phase noise of the expected millimeter-wave frequency; L_{LO} represents the phase noise of microwave frequency synthesizer; L_{IF} represents the phase noise of phase-locked interim frequency; M is the harmonic value of MMW harmonic mixer.

Therefore, in order to obtain a low-phase-noise W-band PLL frequency synthesizer, an ultra-low phase-noise microwave frequency synthesizer and a low-phase-noise phase-locked interim frequency are absolutely necessary. Usually, by phase-locked technique, the low phase noise interim frequency can be obtained because of its low working frequency. So the key is to design local frequency synthesizer with low phase noise.

In this paper, with the combination of the technique of PLL, DDS and multiplier, an X-band frequency synthesizer with low phase noise is designed. Then, the microwave local frequency and the basic frequency of millimeter wave VCO are mixed through harmonic mixer to obtain millimeter-wave interim frequency. After the interim frequency is locked by PLL, the W-band frequency synthesizer is finally achieved. Fig. 1 gives the block diagram of W-band hopping frequency synthesizer.

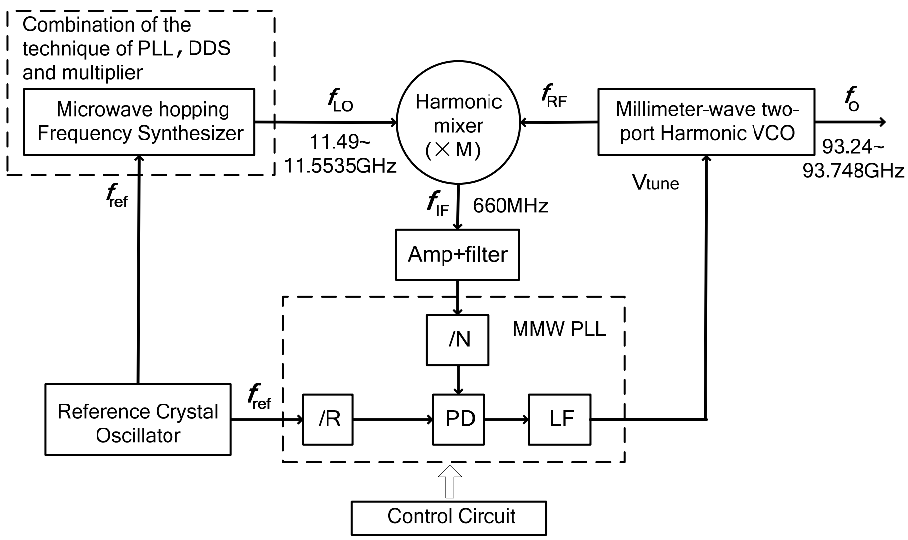

Figure 1: Block diagram of W-band hopping frequency synthesizer.

The W-band hopping frequency synthesizer is mainly composed of reference crystal oscillator, microwave hopping frequency synthesizer, millimeter-wave harmonic mixer, millimeter-wave PLL, and millimeter-wave two-port harmonic VCO. Where, the local section generates X-band local signal from external 100 MHz reference crystal oscillator. And this LO has a function to change frequency with using external command. The millimeter-wave two-port harmonic VCO is a special oscillator designed for millimeter-wave PLL, which is designed on the technique of harmonic extraction [9]. The fundamental-wave frequency would be locked at 46.62∼46.874 GHz, and its 2nd-harmonic frequency at 93.24∼93.748 GHz could be output from another port.

From Fig. 1, the output frequency of W-band frequency synthesizer should be described by the following formula:

$$f_O = 2f_{RF} = 2(Mf_{LO}\langle f_{DDS}\rangle + f_{IF}) \tag{2}$$

where, M is the harmonic value of MMW harmonic mixer.

It's obviously that the hopping frequency bandwidth of W-band PLL frequency synthesizer doubles than the microwave local source. At the same time, the single interim frequency is locked by the millimeter-wave phase-locked loop, the realization of corresponding power amplification and filtering is correspondingly simple.

3. EXPERIMENT RESULTS

In the designed W-band hopping frequency synthesizer, its output frequency range is 93.24∼93.748 GHz, the bandwidth is 508 MHz, and the stepping frequency is 4 MHz. With the Agilent E4440A spectrum analyzer and harmonic mixer, the characteristics are measured. Fig. 2(a) shows its sweep frequency range, and Fig. 2(b) gives its hopping rule.

From Fig. 2(a), the sweep frequency range is 93.24∼93.748 GHz, which agrees with the requirement of system. And the output power level is comparatively smooth. At the same time, because of the big attenuation of harmonic mixer, the output power showed in the spectrum analyzer is low.

With spectrum analyzer and harmonic mixer, the corresponding spectrums of 128 frequency point could be measured. Here, as an example, the spectrum of highest frequency of 93.748 GHz is presented as Fig. 3.

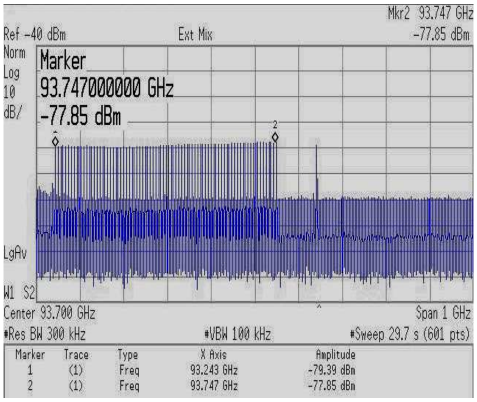

(a) The range of sweep frequency

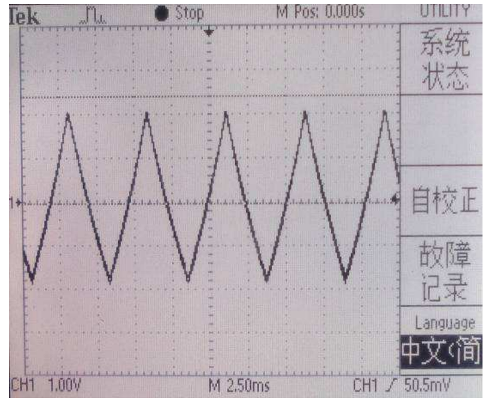

(b) The rule of hopping

Figure 2: The characteristic of W-band hopping frequency synthesizer.

From Fig. 3, we can see that the phase noise of W-band PLL frequency synthesizer is about $-82\,\mathrm{dBc/Hz@10\,KHz}$, $-83\,\mathrm{dBc/Hz@100\,KHz}$, which is better than some design about millimeter-wave frequency synthesizer.

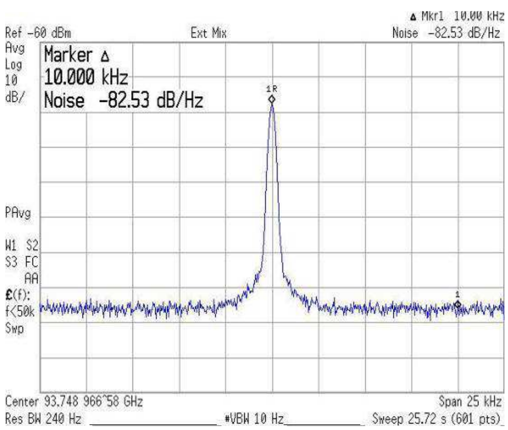

(a) span_25 KHz

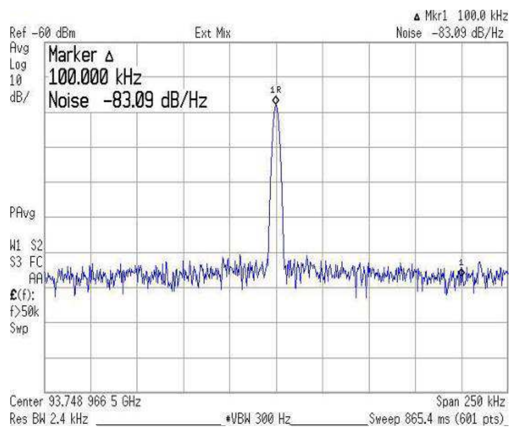

(b) span_250 KHz

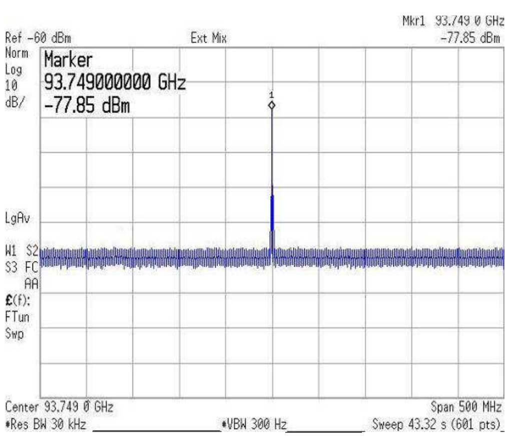

(c) span_500 MHz

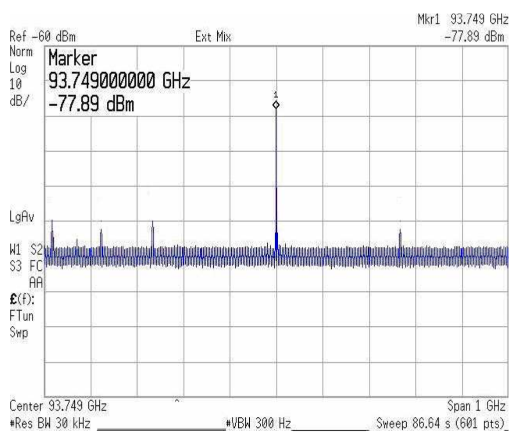

(d) span_1 GHz

Figure 3: The spectrum of 93.748 GHz.

In the method of PLL with mixer, the millimeter-wave frequency synthesizer is substantively achieved by the interim frequency being phase-locked. In this design of W-band PLL frequency synthesizer, the interim frequency of 660 MHz is locked. And Fig. 4 gives its spectrum.

Figure 4 shows that the phase noise of interim frequency is about $-103.5\,\mathrm{dBc/Hz@10\,KHz}$. It is obvious that phase noise of the phase-locked interim frequency is far better than the W-band PLL frequency synthesizer. So during the process of PLL, the phase noise of phase-locked interim frequency can not be equivalent to the PLL frequency synthesizer.

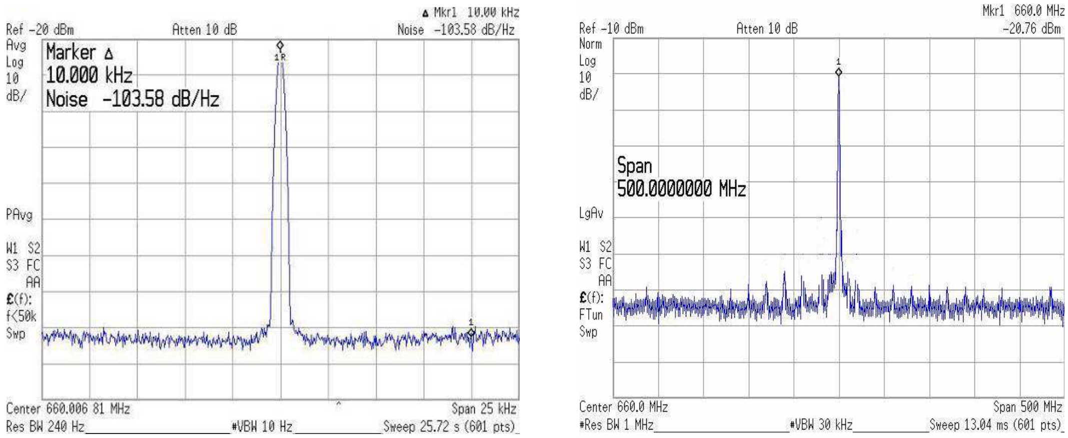

(a) span_25 KHz (b) span_500 MHz

Figure 4: Spectrum of the interim frequency (660 MHz).

4. CONCLUSION

In this paper, combined with the frequency synthesis technique of multiplication, PLL and DDS, a method to design W-band PLL hopping frequency synthesizer with low phase noise has been presented, by adopting a low-phase-noise hopping microwave LO. Such W-band frequency synthesizer is characterized by nice performances, which has good foreground for its application in millimeter-wave communications.

ACKNOWLEDGMENT

This work was supported by the National Key Laboratory Foundation of China (No. 9140C53030207 04).

REFERENCES

1. Tokoro, S., K. Kuroda, and A. Kawakubo, "Automotive electronically scanned millimeter-wave radar," *SICE Annual Conference*, 42–47, Fukui, August 4–6, 2003.
2. Ma, H., X. Tang, and Z. He, "The study and application of 3 mm PLL frequency synthesizer," *Journal of Microwave*, Vol. 22, No. 3, 58–61, April 2006.
3. Jebril, A., M. Lucente, E. Re, et al., "Perspectives of W-Band for space communications," *IEEEAC Paper # 1312*, Version 4, Updated December 11, 2006.
4. Perrotta, G., "Early experiments with W-band satellite links," *IEEEAC Paper # 1047*, Version 2, Updated November 14, 2005.
5. Pollard, B. D. and G. Sadowy, "Next generation millimeter-wave radar for safe planetary landing," *Aerospace, 2005 IEEE Conference*, 1213–1219, March 2005.
6. LaBelle, R., "Space qualification of W-band devices for the CloudSat cloud profiling radar," *Proceedings of the 36th European Microwave Conference*, 1469–1472, 2006.
7. Jebril, A., M. Lucente, M. Ruggieri, and T. Rossi, "WAVE — A new satellite mission in W-Band," *IEEEAC Paper # 1007*, Version 6, Updated December 8, 2004.
8. Ma, H., X. Tang, F. Xiao, and X. Zhang, "Phase noise analysis and estimate of millimeter wave PLL frequency synthesizer," *International Journal of Infrared and Millimeter Waves*, Vol. 26, No. 2, 271–278, February 2005.
9. Davis, R. G. and M. J. Lesson, "Phase-locked millimeter-wave two-port second-harmonic Gunn oscillators," *IEEE Transactions on Microwave Theory and Techniques*, Vol. 39, No. 10, 1746–1753, October 1991.

Theoretical Analysis of Composite Right/Left-handed Coupled Transmission Line Resonators

Tiancun Hu and Wei Ma
National Key Laboratory of Space Microwave Technology
Xi'an Institute of Space Radio Technology, Xi'an 710100, China

Abstract— A novel resonator based on composite right/left-handed coupled transmission line (CRLH-CTL) is proposed. This novel resonator is analyzed using the even and odd mode approach. It has been shown that there are two resonant frequencies which correspond to odd mode resonant frequency and even mode resonant frequency, respectively. The unloaded Q of the odd mode resonance is higher than the unloaded Q of the CRLH-TL resonator because of coupling between two single resonators. The simulation is accomplished with the Ansoft designer. The simulation results agree well with the theoretical analysis.

1. INTRODUCTION

Recently, a resonator based on composite right/left-handed transmission line (CRLH-TL) with the characteristics of $\beta = 0$ at non-zero frequency was presented in [1], the resonant frequency is independent of the physical length, the unloaded Q is independent of the series resistance. While, the unloaded Q is not very high. In order to increase the unloaded Q, a novel resonator based on composite right/left-handed coupled transmission line is presented.

This novel resonator is analyzed using the even and odd mode approach. It has been shown that there are two resonant frequencies which correspond to odd mode resonant frequency and even mode resonant frequency, respectively. The odd mode unloaded Q is higher than the even mode unloaded Q. The simulation of the composite right/left-handed coupled transmission line resonator is carried out and the results agree well with the theoretical analysis.

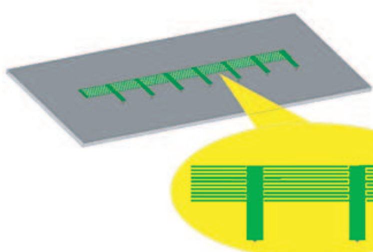

(a)

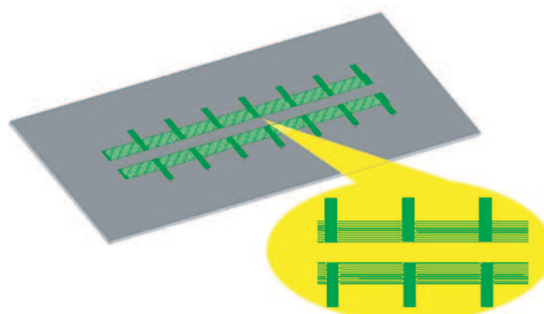

(b)

Figure 1: (a) CRLH-TL implemented with microstrip technology [1], (b) CRLH-CTL implemented with microstrip technology.

2. THEORY

The CRLH-TL introduced by Caloz [2] is constituted of interdigital capacitors and stub inductors with microstrip technology as shown in Fig. 1(a). The CRLH-CTL consists of two CRLH-TLs placed parallel to each other and in close proximity as show in Fig. 1(b). In such a configuration there is a continuous coupling between the electromagnetic fields of the two CRLH-TLs. CRLH-CTLs are utilized extensively as basic elements for directional couplers, filters, and a variety of other useful circuits.

The CRLH-TL resonator was presented by Atsushi Sanada [1]. The resonant frequency of the CRLH-TL resonator obtained by applying the Bloch-Floquet theory is given as

$$\omega = \frac{1}{\sqrt{L_L C_R}} \tag{1}$$

and its unloaded Q is given as

$$Q_0 = \frac{1}{G}\sqrt{\frac{C_R}{L_L}} \tag{2}$$

The equivalent circuit of the CRLH-CTL is shown in Fig. 2.

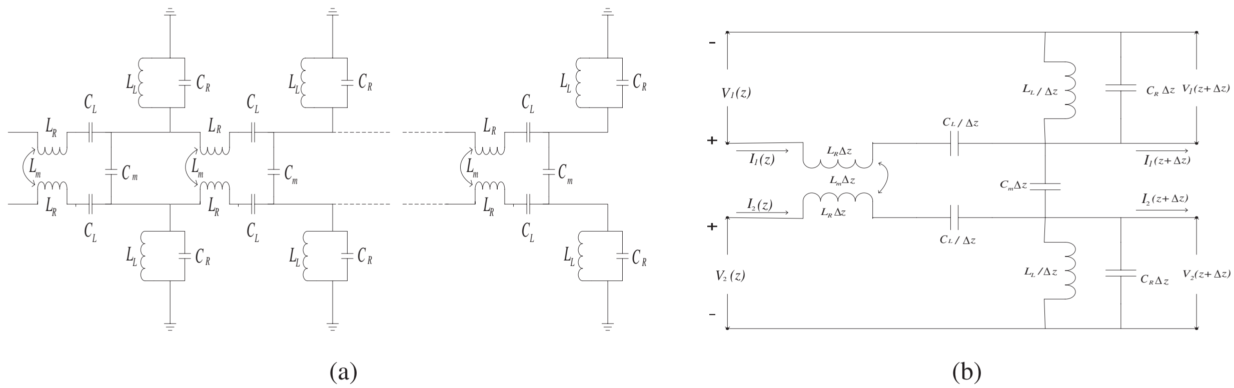

Figure 2: (a) Equivalent circuit of CRLH-CTL, (b) Equivalent circuit of unit cell of CRLH-CTL.

In Fig. 2(a), L_m and C_m are the mutual inductance and coupling capacitance between two CRLH-TLs, respectively. The transmission equation of the CRLH-CTL describes as follow:

$$\frac{dV_1(z)}{dz} = -\left(j\omega L_R + \frac{1}{j\omega C_L'}\right) I_1(z) - j\omega L_m I_2(z) \tag{3}$$

$$\frac{dI_1(z)}{dz} = -\left(\frac{1}{j\omega L_L} + j\omega C\right) V_1(z) + j\omega C_m V_2(z) \tag{4}$$

$$\frac{dV_2(z)}{dz} = -\left(j\omega L_R + \frac{1}{j\omega C_L}\right) I_2(z) - j\omega L_m I_1(z) \tag{5}$$

$$\frac{dI_2(z)}{dz} = -\left(\frac{1}{j\omega L_L} + j\omega C\right) V_2(z) + j\omega C_m V_1(z) \tag{6}$$

where $C = C_R + C_m$.

The even and odd mode method is the most convenient way of describing the behavior of CRLH-CTL. In this method wave propagation along a coupled pair of lines is expressed in terms of two modes corresponding to an even or an odd symmetry about a plane that can, therefore, be replaced by a magnetic or electric wall for the purpose of analysis [3]. The analysis of CRLH-CTL can be converted into the analysis of CRLH-TL excited by the odd mode voltage and even mode voltage, respectively. The characteristic of CRLH-CTL can be divided into odd mode characteristic and even mode characteristic.

(1) Excited by even mode voltage

If $V_1 = V_2 = V_e$, $I_1 = I_2 = I_e$, Eqs. (3)$\sim$(6) can be written as

$$\frac{dV_e(z)}{dz} = -\left(j\omega L_R + \frac{1}{j\omega C_L} + j\omega L_m\right) I_e(z) = -Z_{1e} I_e \tag{7}$$

$$\frac{dI_e(z)}{dz} = -\left(\frac{1}{j\omega L_L} + j\omega C - j\omega C_m\right) V_e(z) = -Y_{1e} V_e \tag{8}$$

where $Z_{1e} = j\omega L_R + j\omega L_m - j1/\omega C_L$, $Y_{1e} = j\omega C - j\omega C_m - j1/\omega L_L$.

The resonant frequency of even mode is

$$\omega_e = \frac{1}{\sqrt{L_L C_R}} \tag{9}$$

The unloaded Q of even mode is

$$Q_e = \frac{1}{G}\sqrt{\frac{C_R}{L_L}} \tag{10}$$

where G is the conductance between the conductor and the ground.

(2) Excited by odd mode voltage

If $V_1 = -V_2 = V_o$, $I_1 = -I_2 = I_o$, Eqs. (3)$\sim$(6) can be written as

$$\frac{dV_o(z)}{dz} = -\left(j\omega L_R + \frac{1}{j\omega C_L}\right) I_o(z) + j\omega L_m I_o(z) = -Z_{1o} I_o \tag{11}$$

$$\frac{dI_o(z)}{dz} = -\left(\frac{1}{j\omega L_L} + j\omega C\right) V_o(z) - j\omega C_m V_o(z) = -Y_{1o} V_o \tag{12}$$

where $Z_{1o} = j\omega L_R + 1/j\omega C_L - j\omega L_m$, $Y_{1o} = 1/j\omega L_L + j\omega C + j\omega C_m$

The resonant frequency of odd mode is obtained by replacing C_R with $C + C_m$ in Eq. (1) as

$$\omega_o = \frac{1}{\sqrt{L_L(C + C_m)}} \tag{13}$$

The unloaded Q of odd mode is

$$Q_o = \frac{1}{G}\sqrt{\frac{C + C_m}{L_L}} \tag{14}$$

Observing Eq. (9) and Eq. (13), we can find

$$\omega_o < \omega_e \tag{15}$$

Observing Eq. (10) and Eq. (14), we can find

$$Q_o > Q_e \tag{16}$$

3. SIMULATIONS AND DISCUSSION

In order to validate the theory shown here, the simulation is carried out with Ansoft designer. The CRLH-TL resonator implemented with microstrip technology is shown in Fig. 3(a). The CRLH-CTL resonator constituted of 1.5-cell open-ended CRLH-CTL is shown in Fig. 3(b). The input port and out port are the gap coupling port.

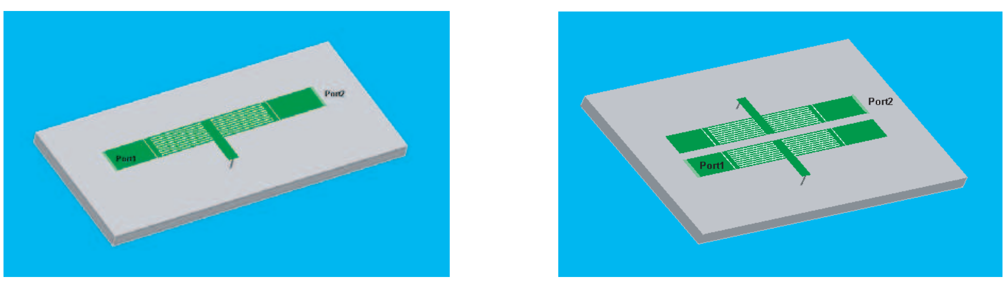

(a) (b)

Figure 3: (a) The layout of CRLH-TL resonator, (b) The layout of CRLH-CTL resonator.

The transmission characteristic of the CRLH-TL resonator is shown in Fig. 4(a). The resonant frequency from Fig. 4(a) appears at 1.922 GHz. A clearer frequency sweep from 1.8 GHz to 2 GHz with the step 0.0001 GHz is shown in Fig. 4(b). The transmission characteristic of CRLH-CTL resonator is shown in Fig. 4(c) with two resonant frequencies corresponding to odd mode resonant frequency and even mode resonant frequency. A clearer resonance curve from 1.8 GHz to 2 GHz is shown in Fig. 4(d).

The loaded Q determined by the "Half-power frequencies" method is given as [4]

$$Q_L = \frac{f_0}{f_2 - f_1} = \frac{f_0}{\Delta f} \tag{17}$$

f_0 is the resonant frequency, Δf is the half-power bandwidth of the resonance curve. The unload Q is determined by the following formula [5]

$$Q_0 = \frac{Q_L}{1 - |S_{21}(f_0)|} \tag{18}$$

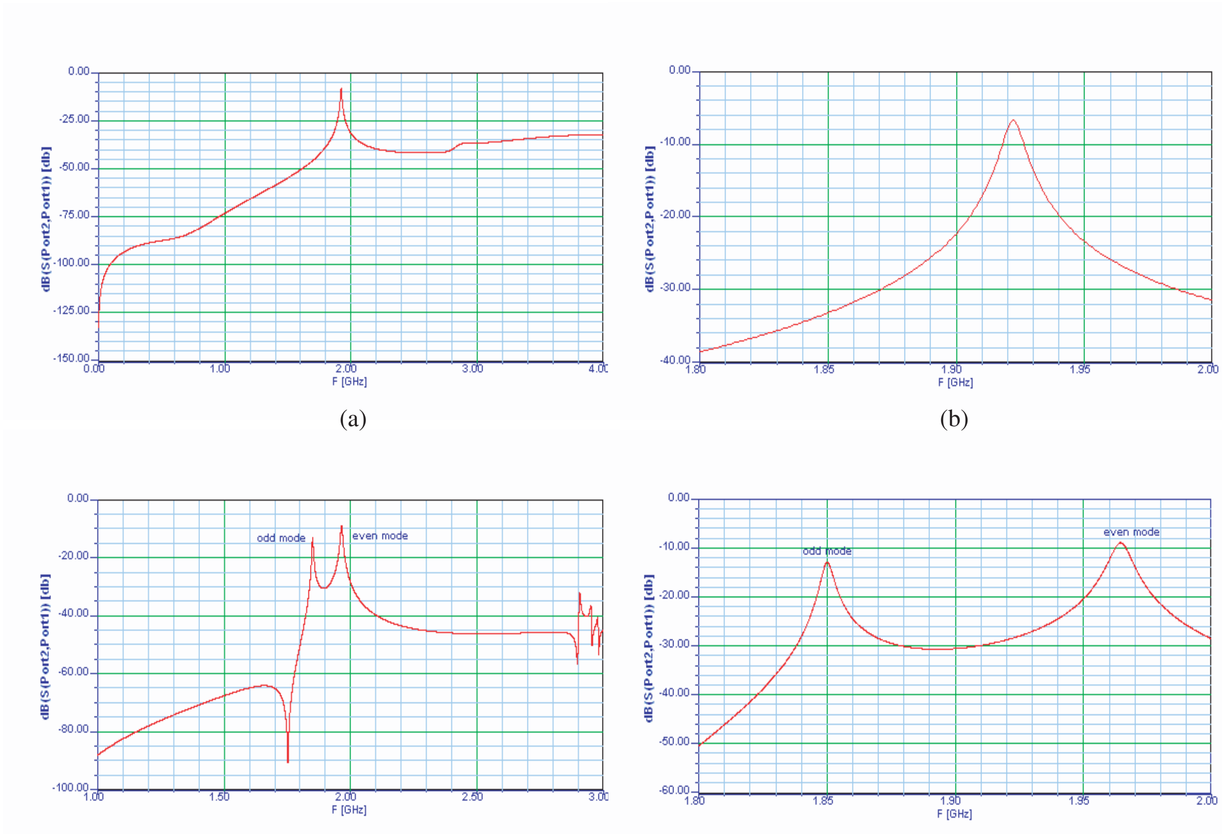

(a) (b)

(c) (d)

Figure 4: (a) The transmission characteristic of the CRLH-TL resonator from 0 to 4 GHz, (b) The transmission characteristic of the CRLH-TL resonator from 1.8 to 2.0 GHz, (c) The transmission characteristic of the CRLH-CTL resonator from 1 to 3 GHz, (d) The transmission characteristic of the CRLH-CTL resonator from 1.8 to 2.0 GHz.

The simulation and calculation results for CRLH-TL resonator and CRLH-CTL resonator are listed in Table 1. The odd unloaded Q of the CRLH-CTL resonator is higher than the unloaded Q of the CRLH-TL resonator. This maybe caused by the coupling between the two single CRLH-TL resonators, it increases the stored energy of the resonator.

Table 1: Comparison results for CRLH-TL resonator and CRLH-CTL resonator.

Resonator / Characteristic	CRLH-TL Resonator	CRLH-CTL Resonator	
		Odd mode	Even mode
Resonance Frequency (f_0)	1.922 GHz	1.850 GHz	1.964 GHz
$S_{21}(f_0)$	0.46	0.23	0.36
Half-power Bandwidth (Δf)	0.009 GHz	0.0045 GHz	0.0075 GHz
Loaded $Q(Q_L)$	213.6	411.1	261.9
Unloaded $Q(Q_0)$	395.5	533.9	409.2

4. CONCLUSIONS

A novel resonator based on CRLH-CTL is presented and its resonant frequency and unload Q is analyzed using odd and even mode approach and Bloch-Floquet theory. It has been shown that there are two resonant frequencies corresponding to odd mode resonant frequency and even mode resonant frequency, the unloaded Q of odd mode is higher than the unloaded Q of CRLH-

TL resonator. The validity of the theory has been proved through simulations. However, the CRLH-CTL resonator occupies larger area comparing to the CRLH-TL resonator.

ACKNOWLEDGMENT

This work was supported by the National Key Laboratory Foundation of China (No. 9140C53030207 04, 9140C5306010708).

REFERENCES

1. Sanada, A., C. Caloz, and T. Itoh, "Novel zeroth-order resonance in composite right/left-handed transmission line resonators," *Proc. of Asia-Pacific Microwave Conf.*, Vol. 3, 1588–1592, Seoul, Korea, 2003.
2. Caloz, C. and T. Itoh, "Novel microwave devices and structures based on the transmission line approach of meta-materials," *IEEE-MTT Int'l Symp.*, Vol. 1, 195–198, Philadelphia, PA, June 2003.
3. Gupta, K. C., R. Garg, I. Bahl, and P. Bhartia, *Microstrip Lines and Slotlines*, 2nd Edition, Artech House, Boston, 1996.
4. Rao, X. S., C. K. Ong, and Y. P. Feng, "Q-factor measurement of nonlinear superconducting resonators," *Electronics Letters*, Vol. 36, No. 3, 271–273, 2000.
5. Leong, K., J. Mazierska, and J. Krupka, "Measurements of unloaded Q-factor of transmission mode dielectric resonators," *Proceedings of IEEE MTT-S International Microwave Symposium*, 1639–1642, Colorado, USA, June 1997.

Automatic Digital Modulation Recognition Using Feature Subset Selection

Jie Li, **Jun Wang**, **Xiaoyan Fan**, **and Yi Zhang**

National Key Laboratory of Space Microwave Technology
Xi'an Institute of Space Radio Technology, Xi'an 710100, China

Abstract— Modulation type is one of the most important characteristics used in signal identification and monitoring. Modulation recognition systems should correctly classify the incoming signal's modulation scheme in the presence of noise. Automatic digital modulation recognition (ADMR) can be used for both military applications and civilian applications. Some examples are surveillance, electronic warfare, threat assessment, signal confirmation, interference identification and spectrum management.

In this paper, a new automatic digital modulation recognition method using ECOC-SVMs and GA is introduced. A new feature set combined statistical and spectral feature subset is used for modulation classification to make the SVMs classifier more robust to Gaussian noise. Moreover, GA is used to perform feature subset selection to reduce the input dimension and increase the performance of the ECOC-SVMs classifier. Compared to the conventional ANN method and the decision theoretic algorithm, the proposed method can recognize more digital modulation types. Furthermore, significant improvements can be seen particularly at a low SNR.

1. INTRODUCTION

Automatic recognition of digital modulation signals has seen increasing demand nowadays. The use of artificial neural networks for this purpose has been popular since the late 1990s.

ADMR is one kind of pattern recognition problems and there are different methods proposed for this subject. Decision theoretic approaches use probabilistic and hypothesis testing arguments to formulate the recognition problem but they have difficulties in forming the right hypothesis and setting the right threshold [1]. When training data are available, the artificial neural network approaches [1, 2] and other statistical recognition methods have been proposed. The ANN methods have gained popularity in the past decade but they couldn't avoid the problems of overfitting, local minimization, etc [4].

In this paper, a new ADMR method using SVMs and GA is introduced. 11 digital modulation types are considered: ASK2, ASK4, FSK2, FSK4, BPSK, QPSK, PSK8, MSK, QAM4, QAM8 and QAM16. Simulation results show that this method is more flexible, robust and effective than other existing approaches.

2. FEATURE EXTRACTION

Current ADMR systems often extract some distinct attributes called features before recognizing to reduce the size of raw signal data set. In this paper, we use a new combined feature set composed of a statistical feature subset and a spectral feature subset for the proposed ADMR.

2.1. Statistical Features

Supposing that we operate in a synchronous, coherent environment with single-tone signaling and that carrier, timing, and waveform recovery have been accomplished. After preprocessing, we obtain the baseband complex sequence that can be written as:

$$y(n) = w(n) + x(n), \tag{1}$$

where $x(n)$ is supposed to be a digitally modulated signal and $w(n)$ is an additive Gaussian noise sequence. $x(n)$ and $w(n)$ are independently and identically distributed (i.i.d.) and jointly uncorrelated stochastic sequences.

High order statistics (HOS) are used as a feature subset in our scheme because they characterize the shape of the distribution of the noisy baseband samples effectively [3]. Let $y(n)$ denote received complex baseband signal samples and its 2nd cumulants, 4th cumulants can be estimated from the samples by the process given below.

Remove the mean of $y(n)$.

$$y(n) \leftarrow y(n) - \hat{y}(n) \tag{2}$$

Compute sample estimates of C_{20}, C_{21} by the following formulae:

$$\begin{aligned}\hat{C}_{20} &= \frac{1}{N}\sum_{n=1}^{N} y^2(n) \\ \hat{C}_{21} &= \frac{1}{N}\sum_{n=1}^{N} |y(n)|^2\end{aligned} \tag{3}$$

where N is the length of samples and $\wedge$ denotes a sample average.

Sample estimates of the 4th cumulants are given by the following formulae.

$$\begin{aligned}\hat{C}_{40} &= \frac{1}{N}\sum_{n=1}^{N} y^4(n) - 3\hat{C}_{20}^2 \\ \hat{C}_{41} &= \frac{1}{N}\sum_{n=1}^{N} y^3(n)y*(n) - 3\hat{C}_{20}\hat{C}_{21} \\ \hat{C}_{42} &= \frac{1}{N}\sum_{n=1}^{N} |y(n)|^4 - |\hat{C}_{20}|^2 - 2\hat{C}_{21}^2\end{aligned} \tag{4}$$

Compute the normalized cumulants.

$$\vec{C}_{4k} = \hat{C}_{4k}/\hat{C}_{21}^2, \quad k = 0,\, 1,\, 2 \tag{5}$$

2.2. Spectral Features

Azzouz and Nandi [1] proposed a suitable spectral-based feature set for ADMR, which contains hidden information in instantaneous amplitude, instantaneous frequency, or instantaneous phase. In this study, it is used as a feature subset for modulation classification. The five features proposed are described as below:

- Standard deviation of the absolute value of the centered nonlinear components of the instantaneous phase: σ_{ap}.
- Maximum value of the power spectral density of the normalized centred instantaneous amplitude: $\gamma_{\max}$.
- Standard deviation of the direct value of the centered nonlinear components of the instantaneous phase: σ_{dp}.
- Standard deviation of the absolute value of the normalized centred instantaneous frequency: σ_{af}.
- Standard deviation of the absolute value of the normalized centred instantaneous amplitude: $\sigma_{a\sigma}$.

3. GA ECOC-SVM BASED DIGITAL MODULATION RECOGNITION

The proposed ADMR scheme is composed of four parts: signal data preprocessing, feature extraction, GA feature selection and SVMs classification. Firstly, we discuss the construction of multiclass SVMs classifier in detail. Then, the digital modulation recognition algorithm is introduced.

3.1. Multiclass Support Vector Machines Based on Error-correcting Output Codes

Support vector machines are originally designed for binary classification [4]. How to effectively extend it for multiclass classification is still an ongoing research issue [5]. The way we construct the multiclass classifier is by combining several binary SVMs, according to an error-correcting output codes (ECOC) scheme [5].

ECOC have been proposed to enhance generalization ability in pattern classification. Coding the classes using codewords suggests the idea of adding error recovering capabilities to decomposition methods, which makes classifiers are less sensitive to noise. This goal is achieved by means of the redundancy of the coding scheme, as shown by coding theory. By class coding scheme, we can implicitly decompose the k-polychotomy into a set of dichotomies $f_1, \ldots, f_B$, where B is the length of the codeword coding a class.

First, a collection of binary classifiers $\{f_1, \ldots, f_B\}$ are constructed and each classifier f_b is trained according to column b of decomposition matrix G [5], and $g_{ij} \in G$ is the target value of the jth decision function $D_j(x)$ for class i: where

$$g_{ij}(x) = \begin{cases} 1 \quad \text{if} \quad D_j(x) > 0 \quad \text{for class} \quad i, \\ -1 \quad \text{otherwise.} \end{cases} . \tag{6}$$

The jth column vector $g_j = (g_{1j}, \ldots, g_{nj})^T$ is the target vector for the jth decision function, where n is the appropriate class label. The ith row vector $(g_{i1}, \ldots, g_{iB})$ corresponds to a codeword for class i.

Then, we can find the class label of x by calculating its distance from each codeword. Introducing "don't care output" and denote its value by 0, we can define an error $\varepsilon_{ij}(x)$ by

$$\varepsilon_{ij}(x) = \begin{cases} 0 \quad \text{for} \quad g_{ij} = 0, \\ \max(1 - g_{ij} D_j(x), 0) \quad \text{otherwise} \end{cases} \tag{7}$$

where $g_{ij} D_j(x) \geq 1$ denotes that x is on the correct side of the jth decision function with more than or equal to the maximum margin and $g_{ij} D_j(x) < 1$ denotes that x is on the wrong side or even if it is on the correct side but the margin is smaller than the maximum margin.

Then the distance of x from class i is given by

$$d_i(x) = \sum_{j=1}^{B} \varepsilon_{ij}(x). \tag{8}$$

Thus x is classified into class:

$$\arg \min_{i=1, \ldots, n} d_i(x). \tag{9}$$

3.2. GA Based Feature Selection

Typical pattern recognition applications use feature selection to reduce input dimension and remove redundant input information, which implies a decrease in classification accuracy. In our ADMR application, GA is used to select the most suitable features for the particular recognizers in different SNR environment. Individuals represent subset of features by means of binary strings. Each string has a length L, which is the total number of input features we extract in preprocessing step for ADMR. In the genome string, a binary '1' denotes the presence of the appropriate feature at the corresponding index number and a binary '0' denotes an absence. The proposed ADMR algorithm can be shown in Figure 1.

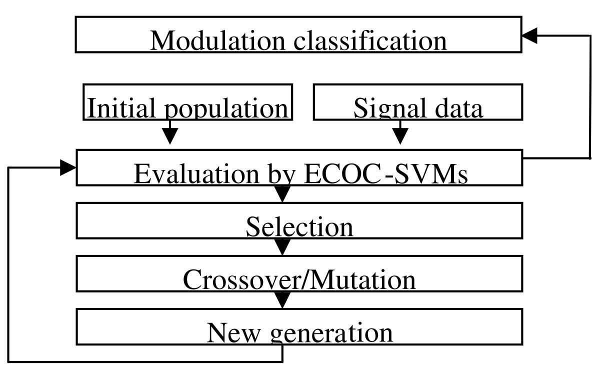

Figure 1: ECOC-SVMs classification with GA subset selection.

4. SIMULATION RESULTS

In this section, experiments are presented to illustrate the performance of the proposed recognition scheme. All the simulation signals are digitally generated in MATLAB environment. Random integers up to M-level ($M = 2, 4, 8, 16$) are generated by a uniform random number generator.

The simulation signals are also band-limited and additive white Gaussian noise is added according to different SNR.

We give an overall performance comparison on the decision-theoretic algorithm proposed in [3], the ANN method proposed in [1] and the proposed ECOC-SVMs method. Simulation results are shown in Table 1. As shown in the table, both the ANN method and the decision theoretic algorithm don't perform well at a low SNR, for instance, -5 dB. The ANN methods' shortcoming is that it doesn't work efficiently in a low SNR environment and it also needs a long training time. On the other hand, both the methods proposed in [1] and [3] can only recognize fewer modulation modes compared to the proposed ECOC-SVMs. The reason that the proposed GA ECOC-SVMs method is both robust and effective is not only the using of a better classifier structure but also the adoption of the optimized feature set.

Table 1: Overall performance comparison on the ANN method, the decision theoretic algorithm and the proposed ECOC-SVMs method.

SNR (dB)	Decision theoretic	ANN	GA ECOC-SVMs
	Overall perf. (%)	Overall perf. (%)	Overall perf. (%)
-5	48.85	63.62	91.99
0	56.34	83.02	98.48
5	81.12	92.26	98.91
10	96.75	97.40	99.13
15	98.56	98.32	99.78
20	99.32	99.50	99.99

5. CONCLUSIONS

In this paper, a novel automatic digital modulation recognition method using ECOC-SVMs and GA is introduced. Combined statistical and spectral feature subset is used for modulation classification to make the SVMs classifier more robust in Gaussian noise environment. Moreover, GA is used to perform feature selection to reduce the input dimension and increase performance of the ECOC-SVMs classifier. Compared to the conventional ANN method and the decision theoretic algorithm, the proposed method can recognize more digital modulation types. Furthermore, significant improvements can be seen particularly at a low SNR.

REFERENCES

1. Nandi, A. K. and E. E. Azzouz, "Modulation recognition using artificial networks," *IEEE Trans. Signal Processing*, Vol. 56, No. 2, 165–175, 1997.
2. Nandi, A. K. and E. E. Azzouz, "Algorithms for automatic modulation recognition of communication signals," *IEEE Trans. Communications*, Vol. 46, No. 4, 431–435, 1998.
3. Swami, A. and B. M. Sadler, "Hierarchical digital modulation classification using cumulants," *IEEE Trans. Communications*, Vol. 48, No. 3, 416–429, 2000.
4. Vapnik, V., "An overview of statistical learning theory," *IEEE Trans. Neural Networks*, Vol. 10, No. 5, 988–999, 1999.
5. Klautau, A., N. Jevtic, and A. Orlitsky, "On nearest-neighbor error-correcting output codes with application to all-pairs multiclass support vector machines," *Journal of Machine Learning Research*, Vol. 4, No. 12, 1–15, 2003.
6. Wong, M. L. D. and A. K. Nandi, "Automatic digital modulation recognition using artificial neural network and genetic algorithm," *Signal Processing*, Vol. 84, 351–365, 2004.

GL EM Mechanical and Acoustic Field Time Domain Modeling for Materials and Exploration with Dispersion

Ganquan Xie, **Jianhua Li**, **Lee Xie**, **and Feng Xie**
GL Geophysical Laboratory, USA

Abstract— In last few years, we proposed Global and Local field (GL) electromagnetic (EM), elastic and other field modeling in the frequency domain. In this paper, we propose GL modeling for EM, mechanical, and acoustic field in aperiodic space time domain and dispersion field in periodic space time domain. First, we derive magnetic, electric, elastic, and acoustic field differential integral equation in aperiodic and periodic space time domain. Based on these differential integral equations, we construct GL EM, mechanical, and acoustic field time domain modeling in aperiodic and periodic space domain. The EM field and mechanical field is different field in physical theory and application. However, they have some important relationship in the mathematical physical research and applications. In the macro scope and macro to micro mixed scope the coupled EM and mechanical field play important role. Our GL method can be used for EM, mechanic, acoustic, flow, quantum mechanics and their mixed coupled field modeling, in particular, for EM dispersion in photonic crystal, elastic dispersion in special rock, flow dispersion in pores media and other mixed periodic and aperiodic optical materials. The time domain GL method does not need to solve any large matrix, only 3×3 and 6×6 matrices needs to be solved. Moreover, the artificial boundary and absorption condition are unnecessary in the time domain GL method. Some applications in material science, dispersion of photonic crystal and exploration are described in this paper.

1. INTRODUCTION

The elastic, magnetic field and electric field differential integral equation were proposed by authors in 1985 [1] and 1995 [2, 3], respectively, in which the Green's kernel is integrative. The dual differential integral equations of these above equations were proposed in papers [4, 5]. In the paper [5], we proposed EM integral equation and its dual integral equation, also proposed magnetic and electric differential integral equation and their dual equations. Based on the EM integral equations and differential integral equations, we proposed the GL EM modeling in the frequency domain. The GL Metro Carlo EM inversion was proposed in [6]. The GL frequency domain elastic/plastic mechanical, flow, heat, and quantum modeling and applications are presented in the papers [7–9].

In this paper, we propose GL EM, mechanical, and acoustic modeling in space time domain and periodic lattice space domain. Our GL modeling methods are based on magnetic, electric, elastic, and acoustic differential integral equations in space time domain and periodic space time domain. The primary acoustic and elastic wave time domain differential integral equation have been proposed in author's papers for a novel inversion [10–12]. In this paper, we derive magnetic, electric, elastic, and acoustic field differential integral equation in the 2 time domain and aperiodic and periodic lattice space domain. Based on these differential integral equations, we construct EM mechanical and acoustic field GL modeling in aperiodic space time domain and lattice periodic space time domain. The Finite Element (FEM) and FD implicit time domain method need to solve large matrix equation which is great computational cost. The GL time domain modeling does not need to solve any large matrix, only needs to solve 3×3 or 6×6 matrix equations. Moreover, FEM and FD method need an artificial boundary and absorption boundary condition on it to truncate the infinite domain. The inaccurate reflection from the absorption condition on the artificial boundary will degrade the accuracy of the FEM and FD methods and crash the inversion. The GL space time domain modeling does need any artificial boundary and any absorption condition to truncate infinite domain. There is no error boundary reflection in the GL modeling methods [5, 6–9].

The GL method has more advantages to challenge FEM and FDTD method. The GL is not only very available for field propagation in the finite inhomogeneous domain which is embedded in infinite domain, but also suitable for field dispersion in the periodic lattice space domain [13].

Dispersion is a very important phenomenon in the electromagnetic, acoustic and elastic wave propagation in the dispersion media and flow in the soil and porous mediums. The full wave package is superposition of sub waves with various different phase velocity. Because the phase velocity depends on the wavelength or frequency, the wave will be dispersive propagation in the dispersion media and periodic lattice media.

Our GL electromagnetic modeling is useful for simulation of electromagnetic filed dispersion in the material, nanometer material, optical material, in particular, in the photonic crystals. Recent year, the photonic crystals (PhC) have great academic and industrial engineering applicable benefits to attract many scientists' and engineers' research interesting. The dispersion of the EM field in the photonic crystals can be controlled and engineering to manipulate the light and high frequency EM at its wavelength scale and propagation focus in certain specified direction. The photonic crystal is called as new generation of the semiconductor. The more common PhC devices are made by semiconductor slab with air-holes lattice using light defecting and technology and by dispersion engineering of photonic crystals [14].

The FDTD method and FEM are often used to simulate the EM field dispersion in photonic crystals and other optical materials. However, lattice of the photonic crystal needs to solve many EM eigenvalune problems. A real specimen of the crystal waveguide or device will contain very massive large N unit cells. The lattice cell space scale is usually of the order of one nm, so that the specimen with 1 μm has $N = 10^4$ unit cells. The FDTD and FEM are very difficulty to solve $N = 10^4$ large matrix EM eigenvalue and eigen state problem. In the other hand, FDTD and FEM need the absorption condition on the artificial boundary to truncate infinite domain for solving EM modeling problem. The most absorption condition (for example, PML) has error reflection in the corner on the artificial boundary. The error boundary reflection will degrade accuracy of the numerical EM field, in particular, the FDTD 3 and FEM scheme's error numerical dispersion will contaminate and confuse the physical dispersion of the EM field in photonic crystals.

The GL modeling overcome the difficulties of the FDTD and FEM method in the EM, elastic, and acoustic wave dispersion simulation. First, GL modeling does not need to solve any large matrix, it is fast to solve magnetic field dispersion propagation and eigenvalue problem in the lattice domain for obtaining the dispersion diagram and band structure of the photonic crystals. Second, GL does not need any artificial boundary and has no error boundary refection to degrade accuracy of the computational EM field and dispersion property. Third, the GL method consistently combines the analytical EM and numerical method that reduced the numerical dispersion to contaminate the physical dispersion. Therefore, the GL method is very useful for EM, elastic, and acoustic propagation in the space time domain, moreover, for their dispersion in dispersion material, optical materials and photonic crystals.

The EM field and mechanical field is different field in physical theory and application. However, they have some important relationship in the mathematical physical research and applications. The GL EM, mechanical, thermal, acoustic and flow coupled macro and micro modeling play important role in investigating nanometer mater material, optical nanometer mater material and photonic crystals. Also, our GL EM, mechanical, seismic, and acoustic space time domain modeling is very useful for geophysical and Earthquake exploration.

The GL EM, mechanical, and acoustic modeling and these filed differential integral equations in this paper are complete new and original research developments. We describe these contents in ten sections of this paper. The introduction is presented in Section 1. In Section 2, we propose a time domain magnetic field differential integral equation. The new 3D GL magnetic field time domain modeling is proposed in Section 3. In Section 4, we propose a time domain electric field differential integral equation. In Section 5, we propose a the new 3D GL electric field time domain modeling. An elastic mechanical field time domain differential integral equation is proposed in Section 6. In section 7, we propose a 3D GL elastic mechanical displacement field time domain modeling. Acoustic differential integral equations are proposed in Section 8, In Section 9, we propose a GL acoustic time domain modeling. A GL modeling for acoustic wave dispersion is proposed in Section 10. In Section 11, we propose GL modeling for EM dispersion in photonic crystals.

2. MAGNETIC FIELD DIFFEREIAL INTEGRAL EQUATIONS IN TIME DOMAIN

2.1. A Magnetic Field Differential Integral Equation in Time Domain

In this section, we propose the magnetic field differential integral equation in space time domain as follows

$$\begin{aligned} H(r,\,t) =& H_b(r,\,t) - \int\limits_{\Omega} (D(t) - D_b(t)) *_t \left(\nabla \times H^M(r',\,r,\,t)\right) *_t \left(\nabla \times H_b(r',\,t)\right) \mathrm{d}r' \\ & - \int\limits_{\ni\Omega} (\mu - \mu_b) H^M(r',\,r,\,t) *_t \frac{\partial}{\partial t} H_b(r',\,t) \mathrm{d}r', \end{aligned} \tag{1}$$

where

$$D(t) = \frac{1}{\varepsilon} e^{-\frac{\sigma}{\varepsilon} t}, \quad D_b(t) = \frac{1}{\varepsilon_b} e^{-\frac{\sigma_b}{\varepsilon_b} t}, \tag{2}$$

$H(r,\,t)$ is the magnetic field, $H^M(r',\,r,\,t)$ is the magnetic Green's tensor field function excited by the impulse magnetic moment, $H(r,\,t)$ and $H^M(r',\,r,\,t)$ are the magnetic field in the electric conductivity σ, dielectric ε, and magnetic permeability μ media, $H_b(r,\,t)$, is the magnetic wave field in the background σ_b, ε_b, and μ_b media, $\mu = \mu_b$, $*_t$ is convolution with respect to time t.

2.2. A Dual Magnetic Field Time Domain Differential Integral Equation

We propose the dual magnetic field time domain differential integral equation as follows

$$\begin{aligned} H(r,\,t) =& H_b(r,\,t) - \int\limits_{\Omega} (D(t) - D_b(t)) *_t \left(\nabla \times H_b^M(r',\,r,\,t)\right) *_t \left(\nabla \times H(r',\,t)\right) \mathrm{d}r' \\ & - \int\limits_{\Omega} (\mu - \mu_b) H_b^M(r',\,r,\,t) *_t \frac{\partial}{\partial t} H(r',\,t) \mathrm{d}r', \end{aligned} \tag{3}$$

where the $D_b(t)$ and $D(t)$ are denoted by (2).

2.3. The Second Magnetic Field Differential Equation

The magnetic field differential Equation (1) and its dual Equation (3) are equivalent to the second magnetic field differential Equations [2–4, 15] and MAXWELL equation in the time domain

$$\nabla \times \left(\frac{1}{\varepsilon} e^{-\frac{\sigma}{\varepsilon} t} *_t \nabla \times H(r,\,t)\right) + \mu \frac{\partial H(r,\,t)}{\partial t} = Q_M(r,\,t). \tag{4}$$

3. 3D GL MAGNETIC FIELD TIME DOMAIN MODELING

In this section, we propose 3D GL magnetic field modeling in space time domain as follows

3.1 The domain Ω is divided into set of the N sub domains $\{\Omega_k\}$, such that $\Omega = \bigcup\limits_{k=1}^{N} \Omega_k$, where the division can be mesh or meshless.

3.2 suppose that, when $k = 0$, $H_0(r,\,t) = H_b(r,\,t)$ is the global analytical magnetic field in space time domain and $H_0^M(r',\,r,\,t) = H_b^M(r',\,r,\,t)$ is the magnetic field space time domain Green's tensor excited bythe magnetic dipole source in the global background medium with constant EM parameter, or half space medium, or waveguide medium, or multiple layered medium. By induction, suppose that the time domain magnetic field $[H_{k-1}(r,\,t)]$, and magnetic Green's tensor $H_{k-1}^M(r',\,r,\,t)$ have been calculated in the $(k-1)^{\text{th}}$ step.

3.3 In Ω_k, we solve the EM the magnetic field differential integral equation system for Green tensor in space time domain which is based on the magnetic field differential integral Equations (1) and (3). By dual operation, the equation system is reduced into a 3×3 matrix equations. By solving the 3×3 equations, We obtain magnetic field Green tensor field $H_k^M(r',\,r,\,t)$.

3.4 We improved the Global magnetic field $H_k(r, t)$ by the local time domain magnetic field scattering filed in the sub domain Ω_k,

$$\begin{aligned} H_k(r, t) =& H_{k-1}(r, t) - \int\limits_{\Omega_k} (D(t) - D_b(t)) *_t \left(\nabla \times H_k^M(r', r, t)\right) *_t \left(\nabla \times H_{k-1}(r', t)\right) \mathrm{d}r' \\ & - \int\limits_{\Omega_k} (\mu - \mu_b) H_k^M(r', r, t) *_t \frac{\partial}{\partial t} H_{k-1}(r', t) \mathrm{d}r' \end{aligned} \tag{5}$$

$k = 1, 2, \ldots, N$, successively. The $H_N(r, t)$, is GL magnetic field solution of the magnetic field differential integral Equations (1) and (3).

4. ELECTRIC FIELD TIME DOMAIN DIFFEREIAL INTEGRAL EQUATION

4.1. An Electric Field Differential Integral Equation in Space Time Domain

In this section, we propose the electric field differential integral equation in space time domain as follows

$$\begin{aligned} E(r, t) =& E_b(r, t) - \int\limits_{\Omega} \left(\frac{1}{\mu} - \frac{1}{\mu_b}\right) \left(\nabla \times E^J(r', r, t)\right) *_t \left(\nabla \times E_b(r', t)\right) \mathrm{d}r' \\ & - \int\limits_{\Omega} (D(t) - D_b(t)) E^J(r', r, t) *_t E_b(r', t) \mathrm{d}r', \end{aligned} \tag{6}$$

where

$$D(t) = \left(\sigma + \varepsilon \frac{\partial}{\partial t}\right) \frac{\partial}{\partial t}, \quad D_b(t) = \left(\sigma_b + \varepsilon_b \frac{\partial}{\partial t}\right) \frac{\partial}{\partial t}, \tag{7}$$

$E(r, t)$ is the electric field, $E^J(r', r, t)$ is the electric Green's field function excited by the impulse current, $E(r, t)$ and $E^J(r', r, t)$ are electric field in the electric conductivity σ, dielectric ε, and magnetic permeability μ media, $E_b(r, t)$, is electric wave field in the background σ_b, ε_b, and μ_b media, $\mu = \mu_b$, $*_t$. is convolution with respect to time t.

4.2. Dual Electric Field Differential Integral Equation in Time Domain

We propose the dual electric field differential integral equation in space time domain as follows

$$\begin{aligned} E(r, t) =& E_b(r, t) - \int\limits_{\Omega} \left(\frac{1}{\mu} - \frac{1}{\mu_b}\right) \left(\nabla \times E_b^J(r', r, t)\right) *_t \left(\nabla \times E(r', t)\right) \mathrm{d}r' \\ & - \int\limits_{\Omega} (D(t) - D_b(t)) E_b^J(r', r, t) *_t E(r', t) \mathrm{d}r', \end{aligned} \tag{8}$$

where the $D_b(t)$ and $D(t)$ are denoted by (6).

4.3. The Second Order Electric Field Differential Equation

The electric field differential Equation (1) and its dual Equation (3) are equivalent to the electric field differential Equations [2–4, 15] and MAXWELL equation in the time domain

$$\nabla \times \left(\frac{1}{\mu} \nabla \times E(r, t)\right) + \frac{\partial}{\partial t} \left(\sigma + \frac{\partial}{\partial t} \varepsilon\right) E = Q_J(r, t). \tag{9}$$

5. 3D GL ELECTRIC FIELD TIME DOMAIN MODELING

In this section, we propose 3D GL electric field modeling in space time domain as follows

5.1 The domain Ω is divided into set of the N sub domains $\{\Omega_k\}$, such that $\Omega = \bigcup\limits_{k=1}^{N} \Omega_k$, where the division can be mesh or meshless.

5.2 suppose that, when $k = 0$, the initial Global electric field $E_0(r, t) = E_b(r, t)$ is the analytical electric field and $E_0^J(r', r, t) = E_b^J(r', r, t)$ is the electric field Green's tensor function in space ime domain magnetic excited by the electric dipole source in the global background medium with constant EM parameter, or half space medium, or waveguide medium, or multiple layered medium. By induction, suppose that the time domain electric field $E_{k-1}(r,\,t)$, and the electric Green's tensor $E^J_{k-1}(r',\,r,\,t)$ have been calculated in the $(k-1)^{\text{th}}$ step.

5.3 In Ω_k, we solve the EM Green tensor the electric differential integral equation system in space time domain, which is based on the electric field differential integral Equations (6) and (8). By dual operation, the equation system is reduced into a 3×3 matrix equations. By solving the 3×3 equations, we obtain electric field Green tensor field $E^J_k(r',\,r,\,t)$in space time domain.

5.4 We improved the Global electric field $E_k(r,\,t)$, by the local time domain electric field scattering filed in the Ω_k and time domain,

$$\begin{aligned} E_k(r,\,t) =& E_{k-1}(r,\,t) - \int\limits_{\Omega_k} \left(\frac{1}{\mu}-\frac{1}{\mu_b}\right)\left(\nabla\times E^J_k(r',\,r,\,t)\right) *_t \left(\nabla\times E_{k-1}(r',\,t)\right)\mathrm{d}r' \\ & - \int\limits_{\Omega} (D(t)-D_b(t))E^J_k(r',\,r,\,t) *_t E_{k-1}(r',\,t)\mathrm{d}r', \end{aligned} \tag{10}$$

$k=1,\,2,\,\ldots,\,N$, successively. The $E_N(r,\,t)$ is GL electric field solution of the electric field differential integral Equations (5) and (7) in space time domain.

6. ELASTIC MECHANICAL FIELD DIFFERENTIAL INTEGRAL EQUATION IN TIME DOMAIN

6.1. An Elastic Mechanical Displacement Field Differential Integral Equation in Time Domain

In this section, we propose the elastic mechanical displacement field differential integral equation in space time domain as follows

$$\begin{aligned} u(r) =& u_b(r) - \int\limits_{\Omega} \varepsilon^T\left(u^d(r',\,r,\,t)\right) *_t (D_b-D)\varepsilon\left(u_b(r',\,t)\right)\mathrm{d}r' \\ & - \int\limits_{\Omega} (\rho_b-\rho)u^d(r',\,r,\,t) *_t \frac{\partial^2}{\partial t^2}u_b(r',\,t)\mathrm{d}r', \end{aligned} \tag{11}$$

$$D_b = \begin{bmatrix} \Im_b & \\ & \mu_b I_3 \end{bmatrix}, \quad D = \begin{bmatrix} \Im & \\ & \mu I_3 \end{bmatrix}, \tag{12}$$

$$\Im_b = \begin{bmatrix} \lambda_b+2\mu_b & \lambda_b & \lambda_b \\ \lambda_b & \lambda_b+2\mu_b & \lambda_b \\ \lambda_b & \lambda_b & \lambda_b+2\mu_b \end{bmatrix}, \quad \Im = \begin{bmatrix} \lambda+2\mu & \lambda & \lambda \\ \lambda & \lambda+2\mu & \lambda \\ \lambda & \lambda & \lambda+2\mu \end{bmatrix}, \tag{13}$$

$$I_3 = \begin{bmatrix} 1 & & \\ & 1 & \\ & & 1 \end{bmatrix}, \quad \lambda = \frac{E\nu}{(1+\nu)(1-2\nu)}, \quad \mu = \frac{E}{2(1+\nu)}, \tag{14}$$

$u(r,\,t)$ is the displacement field with 3 components, $u^d(r',\,r,\,t)$ is the 3×3 displacement Green's field tensor function by the impulse displacement exited, $u(r,\,t)$ and $u^d(r',\,r,\,t)$ are elastic mechanical displacement field and Green's tensor in the Young modules $E(r)$, Poisson ratio $\nu(r)$, and material density $\rho(r)$ media, $u_b(r,\,t)$, and $u^d_b(r',\,r,\,t)$, are elastic mechanical displacement and Green's tensor wave field in the background E_b, ν_b, and ρ_b elastic media, $\varepsilon(u_b(r',\,t))$, 6×3 matrix, is the background media strain Green's tensor which is generated by the background media displacement Green's tensor $u^d_b(r',\,r,\,t)$, $\varepsilon^T(u(r',\,t))$ is 3×6 matrix and the transportation of the strain Green's tensor which is generated by the inhomogeneous media displacement Green's tensor $u^d(r',\,r,\,t)$, $*_t$ is convolution with respect to time t, $u^d_b(r',\,r,\,t)$, and $u^d(r',\,r,\,t)$ are 3×3 Green's tensor function in the space and time domain. $\lambda(r)$ and $\mu(r)$ Lame's parameter coefficients.

6.2. Dual Elastic Mechanical Displacement Field Time Domain Differential Integral Equation

we propose the dual elastic mechanical displacement field integral equation in space time domain as follows

$$\begin{aligned} u(r) = & u_b(r) - \int_{\Omega} \varepsilon^T \left(u_b^d(r', r, t) \right) *_t (D_b - D) \varepsilon \left(u(r', t) \right) \mathrm{d}r' \\ & - \int_{\Omega} (\rho_b - \rho) u_b^d(r', r, t) *_t \frac{\partial^2}{\partial t^2} u(r', t) \mathrm{d}r', \end{aligned} \tag{15}$$

where the D_b and D are denoted by (12)–(14).

6.3. The Second Order Elastic Wave Differential Equation

The elastic wave differential integral Equation (11) and its dual equation are equivalent to the second order elastic wave differential equation in time domain,

$$\nabla \cdot (D(r) \varepsilon(u(r, t))) - \rho \frac{\partial^2 u(r, t)}{\partial t^2} = f(r, t), \tag{16}$$

where elastic plastic matrix D is denoted by (12), ρ is density, $f(r, t)$ is the souse term, $u(r, t)$ is unknown displacement vector function.

7. 3D GL ELASTIC MECHANICAL DISPLACEMENT FIELD MODELING IN TIME DOMAIN

In this section, we propose the 3D GL elastic mechanical displacement field modeling in space time domain as follows

7.1 The domain Ω is divided into set of the N sub domains $\{\Omega_k\}$, s.t. $\Omega = \bigcup_{k=1}^{N} \Omega_k$, where the division can be mesh or meshless.

7.2 suppose that, when $k = 0$, the elastic displacement $u_0(r, t)$, $u_0(r, t) = u_b(r, t)$ and $u_0^d(r', r, t) = u_b^d(r', r, t)$ in (9) is the global analytical elastic field displacement and elastic mechanical displacement Green's tensor in space time domain and in the global background medium with constant elastic parameter, or half space medium, or waveguide medium, or multiple layered medium. By induction, suppose that the time domain elastic displacement wave field $u_{k-1}(r, t)$, and elastic displacement wave field Green's tensor $u_{k-1}^d(r', r, t)$ have been calculated in the $(k-1)^{\text{th}}$ step.

7.3 In Ω_k, we solve the elastic time domain Green tensor differential integral equation system which is based on the Equations (11) and (16). By dual operation, the equation system is reduced into a 3×3 matrix equations. By solving the 3×3 matrix equations, we obtain time domain elastic displacement wave field Green tensor field $u_k^d(r', r, t)$.

7.4 We improved the Global elastic mechanical displacement wave field $u_k(r, t)$, by the Local time domain elastic scattering filed in the Ω_k,

$$\begin{aligned} u_k(r) = & u_{k-1}(r) - \int_{\Omega_k} \varepsilon^T \left(u_k^d(r', r, t) \right) *_t (D_b - D) \varepsilon \left(u_{k-1}(r', t) \right) \mathrm{d}r' \\ & - \int_{\Omega_k} (\rho_b - \rho) u_k^d(r', r, t) *_t \frac{\partial^2}{\partial t^2} u_{k-1}(r', t) \mathrm{d}r', \end{aligned} \tag{17}$$

$k = 1, 2, \ldots, N$, successively. The $u_N(r, t)$ is GL elastic mechanical displacement field solution of the elastic mechanical differential integral Equations (11) and (15) and elastic wave Equation (16).

8. ACOUSTIC WAVE FIELD DIFFERENTIAL INTEGRAL EQUATION IN TIME DOMAIN

8.1. An Acoustic Wave Field Differential Integral Equation in Time Domain

In this section, we propose the acoustic wave field differential integral equation in space time domain as follows

$$u(r,\, t) = u_b(r,\, t) + \int\limits_{\Omega} \left(k(r) - k_b(r)\right) \nabla G_b(r',\, r,\, t) *_t \nabla u(r',\, t) \mathrm{d}r', \tag{18}$$

where $u(r,\, t)$ is the acoustic wave field, $u_b(r,\, t)$, is the background incident acoustic wave field, $k(r)$ is inhomogeneous coefficient, $\sqrt{k(r)}$ is the wave velocity, $\sqrt{k_b(r)}$ is the background wave velocity, the background coefficient $k_b(r)$ is homogeneous mediums or layered mediums or waveguide, $G_b(r',\, r,\, t)$, is background Green's function of the acoustic wave equation, $*_t$ is the time convolution.

8.2. A Dual Acoustic Field Differential Integral Equation in Time Domain

We propose the dual acoustic wave field differential integral equation in space time domain as follows

$$u(r,\, t) = u_b(r,\, t) + \int\limits_{\Omega} \left(k(r) - k_b(r)\right) \nabla G(r',\, r,\, t) *_t \nabla u_b(r',\, t) \mathrm{d}r', \tag{19}$$

the Equation (16) is the dual equation of the Equation (15).

8.3. The Second Order Acoustic Differential Equation

Acoustic wave field time domain differential integral Equation (18) and its dual Equation (19) are equivalent to the second acoustic differential equation in time domain [15, 16] as follows

$$\nabla \cdot (k(r) \nabla u(r,\, t)) - \frac{\partial^2 u(r,\, t)}{\partial t^2} = f(r,\, t), \tag{20}$$

where $k(r)$ is acoustic wave coefficient, $u(r,\, t)$ is unknown scale acoustic wave.

9. 3D GL ACOUSTIC WAVE FIELD TIME DOMAIN MODELING

In this section, we propose the new 3D acoustic wave field GL time domain modeling as follows

9.1 The domain Ω is divided into set of the N sub domains $\{\Omega_k\}$, such that $\Omega = \bigcup\limits_{k=1}^{N} \Omega_k$, where the division can be mesh or meshless.

9.2 suppose that, when $k = 0$, the initial Global electric field $u_0(r,\, t) = u_b(r,\, t)$ is the analytical time domain magnetic field and $G_0(r',\, r,\, t) = G_b(r',\, r,\, t)$ is the acoustic wave field Green's function excited by the acoustic dipole source in the global background medium with constant acoustic parameter, or half space medium, or waveguide medium, or multiple layered medium. By induction, suppose that the time domain acoustic wave field $u_{k-1}(r,\, t)$, and Green's tensor $G_{k-1}(r',\, t)$ have been calculated in the $(k-1)^{\mathrm{th}}$ step.

9.3 In Ω_k, we solve the time domain acoustic Green function differential integral equation system which is based on the acoustic wave field differential integral Equations (18) and (19). By dual operation, the equation is reduced into a 3×3 matrix equations. By solving the 3×3 equations, We obtain time domain acoustic field Green tensor field $G_k(r',\, r,\, t)$, in time domain.

9.4 We improved the Global electric field $u_k(r,\, t)$, by the local time domain acoustic wave field scattering filed in the Ω_k,

$$u_k(r,\, t) = u_{k-1}(r,\, t) + \int\limits_{\Omega_j} \left(k(r) - k_b(r)\right) \nabla G_k(r',\, r,\, t) *_t \nabla u_{k-1}(r',\, t) \mathrm{d}r' \tag{21}$$

$k = 1,\, 2,\, \ldots,\, N$, successively. The $u_N(r,\, t)$, is GL acoustic field solution of the acoustic field differential integral Equations (18) and (19) and acoustic wave differential Equation (21).

10. GL MODELING FOR EM DISPERSION IN PHOTONIC CRYSTALS

10.1. A GL Magnetic Modeling for EM Field Dispersion

In this section, we propose the 3D GL magnetic modeling for the EM field dispersion in the photonic crystals as follows

(10.1) The lattice unit cell domain Ω_{UC} is divided into set of the N sub domains $\{\Omega_{UCj}\}$, such that $\Omega_{UC} = \bigcup_{j=1}^{N} \Omega_{UCj}$, where the division can be mesh or meshless.

(10.2) suppose that, when $j = 0$, $H^B_{k,0}(r) = H^B_{k,b}(r)$ is the global analytical periodic magnetic field and $G^{M,B}_{-k,0}(r', r) = G^{M,B}_{-k,b}(r', r)$ is the analytic periodic magnetic field Green's tensor excited by the magnetic dipole source in the global background dielectric lattice medium in the unit cell, the $H^B_{k,b}(r)$ and $G^{M,B}_{-k,b}(r', r)$, are periodic function. By induction, suppose that the periodic magnetic field $H^B_{k,j-1}(r)$, and the magnetic Green's tensor $G^{M,B}_{-k,j-1}(r', r)$ have been calculated in the $(j-1)^{\text{th}}$ step.

(10.3) In each sub cell Ω_{UCk}, we solve the magnetic field Green tensor differential integral equation system based on the magnetic field differential integral equations. By dual operation, the equation system is reduced into a 3×3 matrix equations. By solving the 3×3 equations, We obtain magnetic field Green tensor field $G^{M,B}_{k,j}(r', r)$.

(10.4) We improved the Global magnetic field $H^B_{k,j}(r)$ by the local sub cell domain magnetic field scattering filed

$$\begin{aligned} H^B_{k,j}(r) =& H^B_{-k,j-1}(r) + \int\limits_{\Omega_{UCj}} \left[\left(\frac{1}{\sigma_b + i\omega\varepsilon_b(r')} - \frac{1}{\sigma + i\omega\varepsilon(r')}\right)\right. \\ & \left.(\nabla - ik) \times G^{M,B}_{-k,j}(r', r) \cdot (\nabla + ik) \times H^B_{k,j-1}(r')\right] \mathrm{d}r', \end{aligned} \tag{22}$$

(10.5) When $j = 1, 2, \ldots, N$, successively, (10.2)–(10.4) form the GL modeling finite iteration circle. The $H^B_{k,N}(r, t)$ is GL magnetic field solution of the magnetic field differential integral equation in the unit cell of the periodic lattice [16], also $H^B_{k,N}(r, t)$ is GL periodic solution of the following second magnetic field differential equation,

$$(\nabla + ik) \times \left(\frac{1}{\sigma + i\omega\varepsilon}(\nabla + ik) \times H^B_{k,N}\right) + i\omega\mu H^B_{k,N} = Q_M, \tag{23}$$

where $H^B_{k,N}(r, t)$ is magnetic field in N^{th} GL iteration, subscript k is crystal moment, the superscript B denotes the Lattice Bloch model. Finally, we obtain the magnetic field in time domain,

$$H(r, t) = \int\limits_{-\infty}^{\infty}\int\limits_{-\infty}^{\infty} H^B_{k,N}(r) e^{ikr - i\omega t} \mathrm{d}k\mathrm{d}\omega, \tag{24}$$

10.2. GL EM Modeling for EM Eigenfield and Eigenvalue Dispersion

The GL Magnetic lattice periodic field modeling (13.1)∼(13.5) can be used for solving magnetic Filed Bloch lattice periodic eigenvalue and eigenfunction problem.

(10.1') is same as (10.1), (10.2') is same as (10.2)

(10.3') In each sub cell Ω_{UCk}, we solve the magnetic field Green tensor differential integral equation system based on the magnetic field differential integral equations for the lattice eigenvalue and eigenfunction. By dual operation, the equation system is reduced into a 3×3 matrix equations. By solving the 3×3 equations, We obtain magnetic field Green tensor field $G^{M,B}_{k,j}(r', r)$,

(10.4') is same as (10.4)

(10.5') When $j = 1, 2, \ldots, N$, successively, (10.2')–(10.4') form the GL modeling finite iteration circle. The $H^B_{k,N}(r, t)$ is GL magnetic field eigenfunction solution of the magnetic field differential integral equation in lattice periodic domain, also is the GL solution of the following second magnetic field eigenvalue equation

$$(\nabla + ik) \times \left(\frac{1}{\sigma + i\omega\varepsilon} (\nabla + ik) \times H^B_{k,N}(r) \right) = -i\omega(k)\mu H^B_{k,N}(r), \tag{25}$$

$H^B_k(r)$ is periodic magnetic with periodic L in Bloch model. $\omega_N(k)$ is the eigenfrequency, We can obtain diagram of $\omega_N(k)$ for controlling EM dispersion in the photonic crystals and dispersion engineering of photonic crystals, k is crystal moment.

$$\omega^2_j(k) = W\left(H^B_{k,j}(r)\right), \tag{26}$$

The $W(.)$ is eigenstate energy. Finally, we obtain the magnetic field in time domain,

$$H(r, t) = \int_{-\infty}^{\infty} H^B_{k,N}(r) e^{ikr - i\omega(k)t} \mathrm{d}k. \tag{27}$$

11. SIMULATION

The size of the bulk photonic crystal material is $1000 \times 800 \times 800\,\mathrm{nm}^3$. The crystal bulk is periodic structure and lattice constant $L = 20\,\mathrm{nm}$. The size of lattice unit cell is $20 \times 20 \times 20\,\mathrm{nm}^3$. There are $50 \times 40 \times 40$ unit cells in the crystal bulk. The high and low dielectric parameter tri periodic repeatedly distributes in the bulk photonic crystal material, the electric conductivity σ and magnetic permeability μ are constants. The discrete crystal moment $k = (k_x, k_y, k_z)$ are in the irreducible Brillouin zone. The GL magnetic dispersion modeling (10.1')–(10.5') is used to solve the magnetic Bloch eigenvalue and eigenfuction problem for the above crystal moments k and make dispersion diagram. To chose a frequency ω_q such that EFC $\omega(k_x, k_y)$, $\omega(k_z, k_x)$ are local k-coordinate axis parallel contours such that $\nabla_{\beta||}\omega = 0$. Use the ω_q and point source to excite We use the GL magnetic dispersion modeling (10.1)$\sim$(10.5) to simulate magnetic field to propagate in the periodic photonic crystal, The magnetic dispersion propagation is excited by a point source at middle point of the left edge and with dispersion engineering ω_q and obtained collection magnetic field guide which are shown in figure.

12. APPLICATIONS

The 3D and 2D GL EM, mechanical, acoustic modeling in time domain have wide applications in sciences and engineering. First, it can be used to simulate EM field 13 propagation, moreover, dispersion propagation in the macro materials, nanometer materials, optical materials, and photonic crystal etc. the material sciences and engineering, Second, It is useful to simulate and reconstruct imaging in radar and antenna in the communication, Atmosphere, and space sciences and engineering, Third, it can used for EM stirring in the metal and steel continuous cast, geophysical, space, and Earthquake exploration. The EM field and elastic field and acoustic field have different means and properties in the physics and mathematics. In general, they are studying in separate research area. However, there are Some relationships between them. Maxwell, One of the EM founders, was moving to EM field research from his elastic research and his optical-elastic methods. Maxwell first did bring the Newton mechanical and continuous mechanical into electromagnetic MAXWELL Equation. Therefore, there are some intrinsic relationship between the EM, elastic and acoustic field. The coupled GL EM, elastic, flow, and heat field modeling is necessary for investigating macro and micro material properties.

Recent year, the photonic crystals (PhC) have great academic and industrial engineering applicable benefits to attract many scientists' and engineers' research interesting [14]. The dispersion of the EM field in the photonic crystals can be controlled and engineering to manipulate the light and high frequency EM at its wavelength scale and propagation focus in certain specified direction. In [14], the FDTD was used to simulate the EM dispersion propagation in the photonic crystal devices. However, FDTD scheme's numerical dispersion will contaminate the physical EM dispersion, its error boundary reflection from the artificial boundary will degrade the numerical EM's accuracy and destroy the EM real dispersion, FDTD's matrix equation is too big the nanometer photonic crystal material. In particular, FDTD will meet more difficulty to simulate the coupler of the cavity, photonic crystal wave guide, and othe aperiodic optical maerials. Our GL EM, mechanical, and acoustic separate modeling nd their coupled modeling are useful for simulation of

EM, elastic, acoustic filed dispersion in the material, nanometer material, optical material, and the photonic crystals, in particular, they are suitable to simulate EM dispersion propagation in the coupler periodic crystal and aperioic materials.

We are developing the GL EM. Mechanical, and acoustic time domainmodeling software for material, nanometer material, optical material, photonic crystals, EM stiring, and geophysical Exploration.

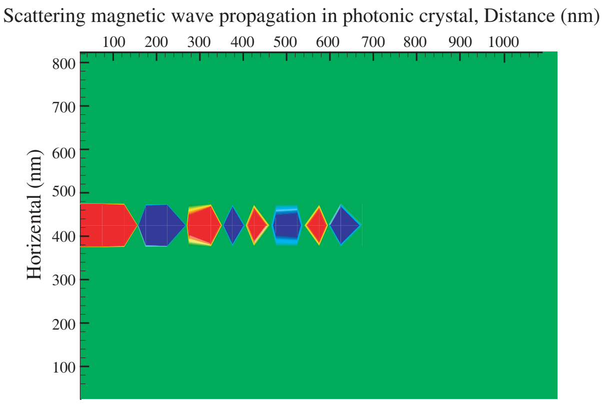

Figure 1: Scattering magnetic SH_z field in Section 1 (z=20 nm) of Photonic Crystal.

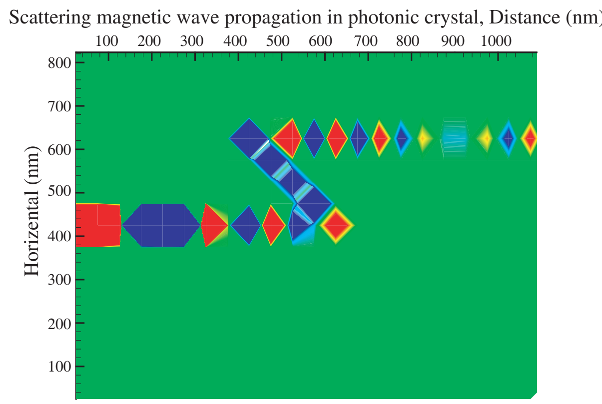

Figure 2: Scattering magnetic SH_z field in Section 2 (z=60 nm) of Photonic Crystal.

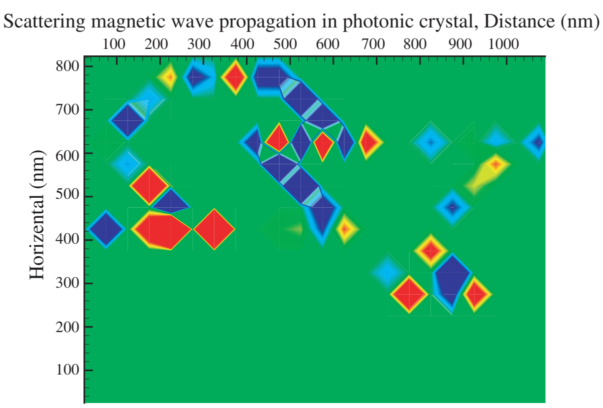

Figure 3: Scattering magnetic SH_z field in Section 3 (z=100 nm) of Photonic Crystal.

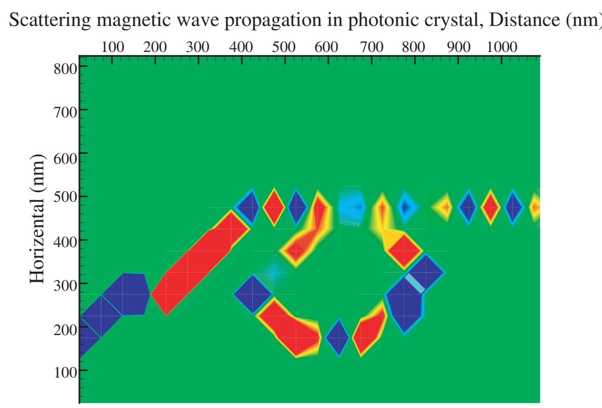

Figure 4: Scattering magnetic SH_z field in Section 4 (z=150 nm) of Photonic Crystal.

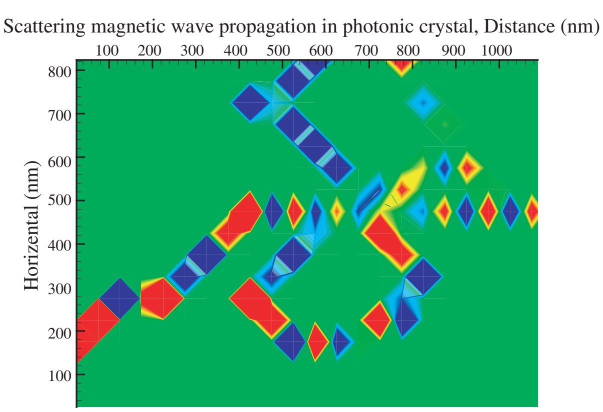

Figure 5: Scattering magnetic SH_z field in Section 5 (z=200 nm) of Photonic Crystal.

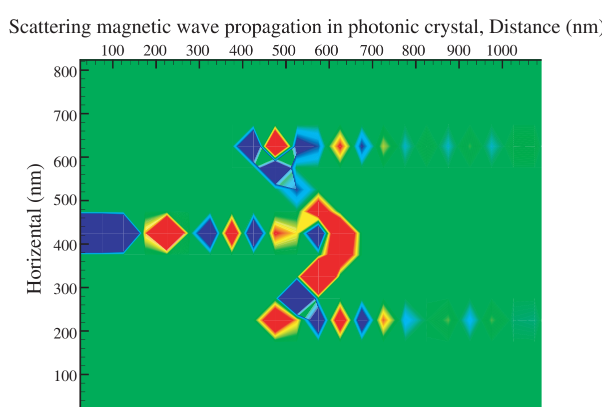

Figure 6: Scattering magnetic SH_z field in Section 6 (z=260 nm) of Photonic Crystal.

13. CONCLUSION

Many simulations show and validate that the GL EM, mechanical, and acoustic time domain modeling are fast and accurate and stable and have the advantages over FEM and FDTD method. These advantages are described in the context of the paper. The EM mechanical and acoustic field time domain GL modeling for materials and exploration with dispersion have wide applications in nanometer materials, optical materials, dispersion engineering of Photonic crystals, nondestructive testing, desctructive mechanics, and geophysical exploration. The GL EM, mechanical, and acoustic time domain modeling algorithms, new EM. Elastic and acoustic differential integral equation in mixed aperiodic and periodic space time domain 14 and software are developed and patented by authors in GL Geophysical laboratory and all rights are reserved by authors in GLGEO.

REFERENCES

1. Xie, G. and Y. M. Chen, "A modified pulse spectrum technique for solving inverse problem of two-dimensional elastic wave equation," *Appl. Numer. Math.*, Vol. 1, No. 3, 217–237, 1985.
2. Xie, G. and J. Li, "New parallel SGILD modeling and inversion," *Physics D*, Vol. 133, 477–487, 1999.
3. Xie, G., J. Li, E. Majer, D. Zuo, and M. Oristaglio, "3-D electromagnetic modeling and nonlinear inversion," *Geophysics*, Vol. 65, No. 3, 804–822, 2000.
4. Xie, G. and J. Li, "New parallel GILD-SOR modeling and inversion for E-O-A strategic simulation," *IMACS Series Book in Computational and Applied Math.*, Vol. 5, 123–138, 1999.
5. Xie, G., F. Xie, L. Xie, and J. Li, "New GL method and its advantages for resolving historical diffculties," *Progress In Electromagnetics Research*, PIER 63, 141–152, 2006.
6. Xie, G., J. Li, L. Xie, and F. Xie, "GL metro carlo EM inversion," *Journal of Electromagnetic Waves and Applications*, Vol. 20, No. 14, 1991–2000, 2006.
7. Li, J., G. Xie, L. Xie, and F. Xie, "A 3D GL EM modeling and inversion for forest exploration and felling," *PIERS Online*, Vol. 3, No. 4, 402–410, 2007.
8. Xie, G., J. Li, F. Xie, and L. Xie, "3D GL EM and quantum mechanical coupled modeling for the nanometer materials," *PIERS Online*, Vol. 3, No. 4, 418–422, 2007.
9. Xie, G., J. Li, L. Xie, F. Xie, and J. Li, "The 3D GL EM-flow-heat-stress coupled modeling," *PIERS Online*, Vol. 3, No. 4, 411–417, 2007.
10. Xie, G., "A new iterative method for solving the coefficient inverse problem of wave equation," *Comm. on Pure and Applied Math.*, Vol. 39, 307–322, 1986.
11. Xie, G. and J. Li, "Nonlinear integral equation of coefficient inversion of acoustic wave equation and TCCR iteration," *Science in China*, Vol. 32, No. 5, 513–523, 1989.
12. Xie, G. and J. Li, "New iterative method for solving scattering problem of 3-D wave equation," *Science in China*, Vol. 31, No. 10, 1195–1202, 1988.
13. Li, J., G. Xie, L. Xie, and F. Xie, "GL time domain modeling for EM acoustic and elastic wave field with dispersion in crystal and porous material," to appear in *PIERS 2008 in Hangzhou* and *PIERS Online*.
14. Shi, S. and D. W. Prather, "Lasing dynamics of a novel silicon photonic crystal cavity lasing dynamics of a novel silicon photonic crystal cavity," *PIERS Online*, Vol. 3, No. 5, 746–750, 2007.
15. Xie, G., C.-C. Lin, and J. Li, "GILD EM modeling in geophysics and nanometer materials using a magnetic field integral equation," *Three Dimensional Elctromagnetics III*, Vol. 3, 11–12, 2003.
16. Li, J., G. Xie, and L. Xie, "3D and 2D GL modeling for EM mechanical and heat field with dispersion in mixed aperiodic and periodic space time domain for material sciences and exploration," GL Geophysical Laboratory technological patent report, GL2007-1, 2007.

Three Component Time-domain Electromagnetic Surveying: Modeling and Data Analysis

Chow-Son Chen[1], **Wei-Hsuan Chiu**[1], **and Ching-Ren Lin**[2]

[1]Institute of Geophysics, National Central University, Taiwan
[2]Institute of Earth Sciences, Academia Sinica, Taiwan

Abstract— A comparative numerical modeling using single component (measuring the vertical component of the field, Hz) time-domain electromagnetic measurements (TEM) receiver and three component (measuring Hx, Hy and Hz) TEM receiver was undertaken. A forward modeling approach was used to compute the voltage response of half-space containing one or more conductive bodies excited by a bi-polar square waveform. Although this was a conductor scattering, it was particularly useful as a practical use for the unexploded ordnance (UXO) detection. Unlike the single component data, results from the three component data are unambiguous as to the location and orientation of conductors. Measuring adding of the horizontal components of the secondary magnetic field leads to not only provide the best indication of target location, but also can be used to determine size, orientation, and characteristics of the targets, especially for the horizontal extending target. A three-component TEM field experiment at a well-documented wells site, NCU campus, were consistent with the effects predicted by our theoretical modeling. As a result, the 3-component TEM survey is a must for the high resolution EM in the engineering purpose.

1. INTRODUCTION

In the traditional frequency-domain electromagnetic (FEM) methods of exploration the ground is energized by passing an alternating current (ac) through an ungrounded loop situated usually on the surface of the earth. The primary field of the loop will induce eddy currents in all conductors present in the earth. The secondary electromagnetic (EM) fields due to these induced currents, together with the primary EM field, are recorded with a suitable receiver at various points in space. In general, the secondary EM field at the receiver, which contains all the information regarding the underground conductors, may be several orders of magnitude smaller than the primary field. Under these conditions the separation of the measured total EM field into its primary and secondary parts is difficult. This fact led to the idea of using time-domain electromagnetic measurements (TEM), often referred to as transient EM techniques [4].

In TEM measurements a strong direct current (dc) is usually passed through an ungrounded loop. At time $t = 0$ this current is abruptly interrupted. The secondary fields due to the induced eddy currents in the ground can now be measured with a suitable receiver in the absence of the primary field. For poor conductors, the initial voltages are large but the field decays rapidly. For good conductors the initial voltages are smaller but the field decays slower. We thus have a simple criterion of recognizing and differentiating the effects of various conductors.

Near-surface TEM surveys have traditionally been simply one or more Hz loops (measuring the vertical component of the field) for the purpose of unexploded ordnance (UXO) detection. However, in this paper, we offer a numerical modeling of the TEM three-component (Hz, Hx and Hy) responses of vertical or horizontal conductors in the earth. Based on numerical modeling, we devise a three-component TEM field experiment at a well-documented wells site, NCU campus. We find three-component TEM anomalies which correlate with known wells, and which are consistent with the effects predicted by our theoretical modeling. We conclude that the 3-component TEM survey is a must for the high resolution EM in the engineering purpose.

2. THEORETICAL BACKGROUND AND MODELING

In order to understand the TEM responses with a rectangular transmitter loop excited by a bi-polar square waveform with exponential rise-time and ramp turnoff, a forward modeling approach was used. To compute the voltage response of half-space containing one or more conductive bodies is the bases of the case of metal detection. Of course, the theoretical responses derived from these targets are inductively coupled. Based upon frequency domain, integral equation thin sheet theory, a program LEROI compute the combined EM effects of multiple conductors in a layered host was employed [5].

Figure 1 shows the calculated profile plots from a plate (conductance 3000 S) in conductive host with the resistivity of 100 ohm-m. Figure 1(b) is the survey map showing the location of the plate and survey lines. Figure 1(c) shows the calculated TEM transient voltage (in μV) along line 6 ($y = 6$) of Hz, Hx, and Hy component, top down respectively. The conductive features are clearly anomalous with strong negative values relative to background for Hz profile; the calculated Hx anomalies are dipolar with a negative/cross-over/positive anomaly as the target is approached and crossed; the calculated Hy anomalies are similar to Hz but the polarity of the anomaly is reversed. In each case, the cross-over point is centered over the target. Figure 1(d) shows the calculated TEM transient voltage (in μV) along line 10 ($y = 10$). The dominant difference is of no Hy anomaly since y component is parallel to the plate, which is assumed to be of no thickness. Figure 1(e) shows the calculated TEM transient voltage (in μV) along line 14 ($y = 14$). The profile is quite similar to the profile 6, but Hy component in opposite polarity.

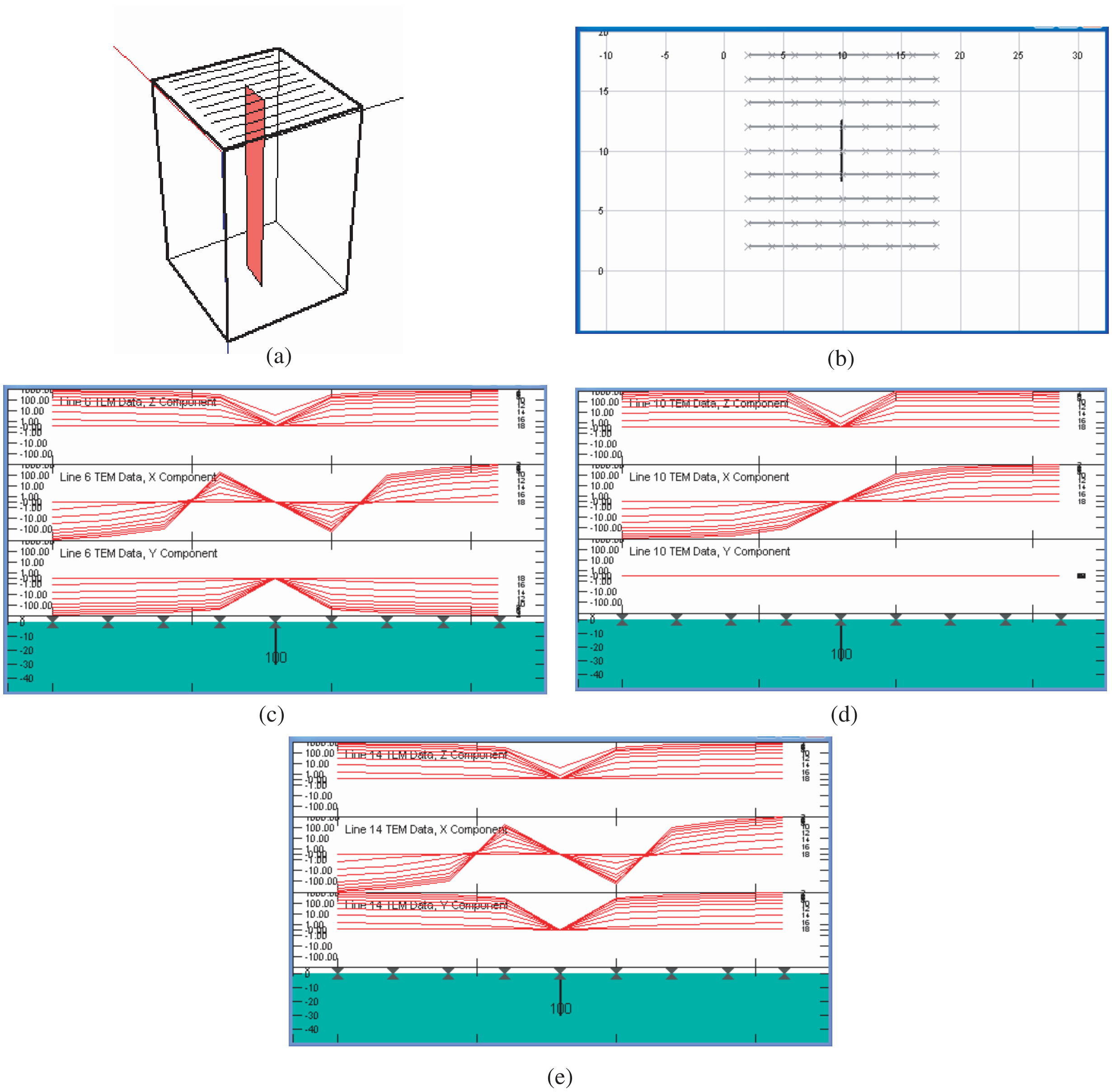

Figure 1: Computed three-component transient voltages for the TEM profiles of a vertical plate (conductance 3000 S) in a conductive host (100 ohm-m). (a) The perspective displays of the three-dimensional model. Transmitter loop position and survey lines are displayed on top surface at ground level. Target plate (in red color) suggests depth and three-dimensionality. (b) The survey map showing the location of the model plate (in black bar) and survey lines. (c) The calculated TEM transient voltage (in μV) along line 6 of Hz, Hx, Hy component, and the earth model, top down respectively. (d) Line 10. (e) Line 14.

As the target conductor becomes horizontal, the calculated profile plots and plane plots are created as in Figure 2. After examine and comparing among the plots, the horizontal component is better for horizontal target identification than the vertical component does, since only horizontal components can display the anomaly of conductive target (Figures 2(c), (d), and (e)).

3. THREE-COMPONENT TEM FIELD EXPERIMENTS

A comparative survey using three-component (measuring Hx, Hy and Hz) TEM receiver was undertaken at a test site; we concentrated on the six wells in the Groundwater Research Well Field on NCU campus, four of them are stainless steels casing and the other two are plastic wells (Figure 3(a)). The campus is located at the Taoyuan Tableland; their deposits consist of an upper sequence of a red-brown lateritic soil over rounded sandstone clasts (up to boulder size) in an uncemented matrix of sand, silt, and clay, and a lower sequence of interbedded, well-consolidated sand, silt, and clay. The lower clay layer composed of laterally continuous clay from 34 m to the

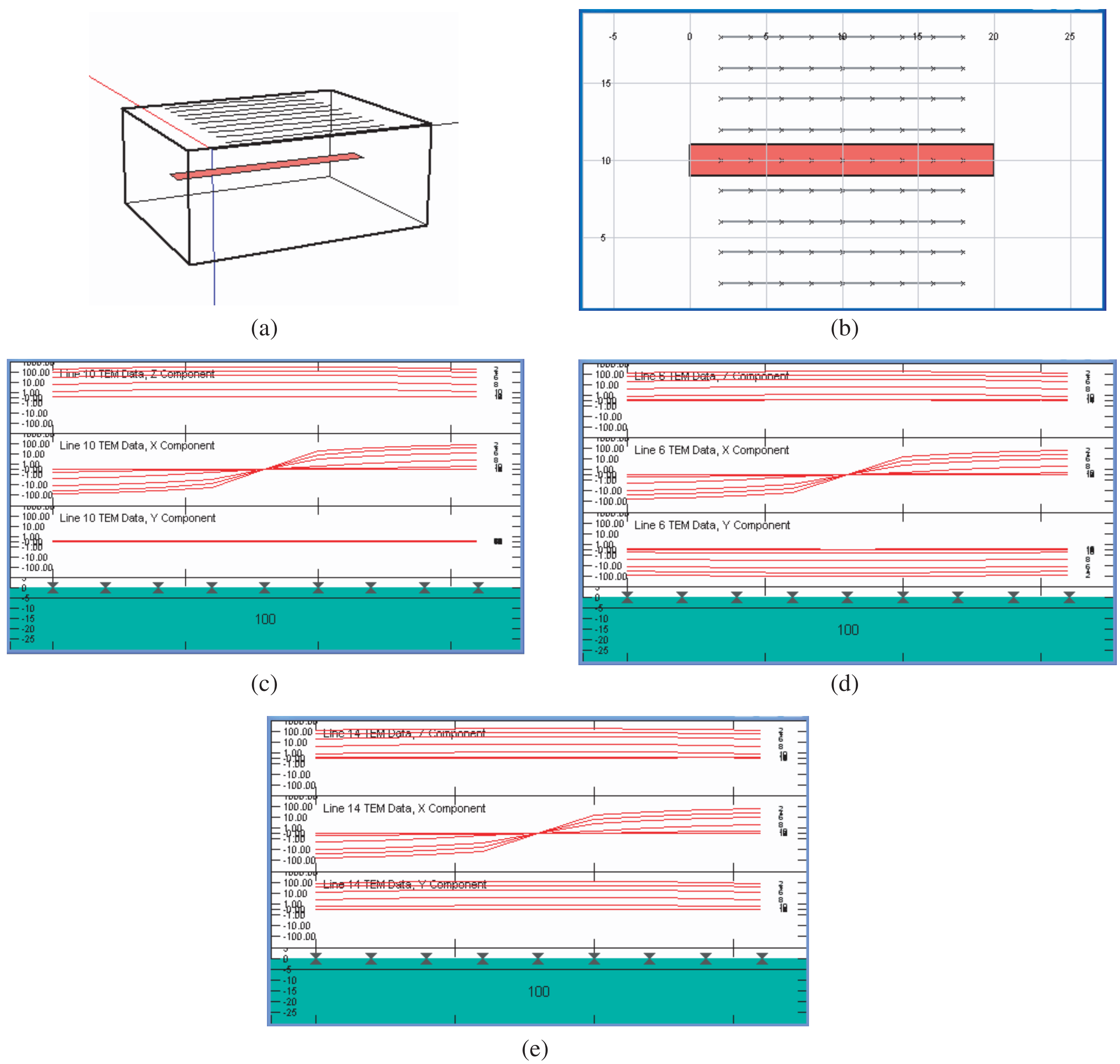

Figure 2: Computed three-component transient voltages (in μV) for the TEM profiles of a horizontal plate (conductance 3000 S) in a conductive host (100 ohm-m). (a) The perspective displays of the model. Transmitter loop position and survey lines are displayed on top surface at ground level. Target plate (in red color) suggests depth and three-dimensionality. (b) The survey map showing the location of the model plate (in red color) and survey lines. (c) The calculated TEM transient voltage (in μV) along line 6 of Hz, Hx, Hy component, and the earth model, top down respectively. (d) Line 10. (e) Line 14.

wells depth 35 m [3].

3.1. Field Experiments

For ours three-component TEM survey, a 50% duty cycle, time domain, square wave electric current (50 amps) was transmitted into the ungrounded transmitter square loop of wire measuring 20 m on each side. In this survey, these magnetic fields are detected with three-orthogonal ungrounded Roving Vector Receiver. The measurements are made at 18 to 20 times (or "windows"), from about 0.5 to 30 ms, after the transmitter is turned off in order to measure the decaying response of the background earth as well as secondary fields from strong conductors (such as metallic objects) after the background earth response has decayed to near-zero values. SIROTEM TEM [1] was used for this purpose. An area measuring 20 meters by 20 meters around the central six wells in the Groundwater Research Well Field was surveyed in detail to establish the extent of the subsurface metal, as well as to detect any other nearby anomalies.

3.2. Data Analysis and Interpretation

Other than the profile display as in the previous numerical modelling, we organized all the experimental profiles and plot the results as a plane view, so as to exam the anomaly in two dimensional distributions. Figure 3(b) shows the Hz survey results in plan view at 1.687 ms after the transmitter is turn-off. At time 1.687 ms, the subsurface metal casings in the wells site are clearly anomalous, it close correlated to the wells site. As time increased to 5.087 ms, all the six anomalous of the associated with well casings is clearly seen that extend below to the deeper depth (not shown here), although well 3 response weaker, and we strongly suspected the lacking of metal casing for this well during the drilling works.

Figure 3(c) shows the wells TEM responses of the horizontal component, calculated from the Hx and Hy data. Only metal casings, well 1, 2, and 4, are close correlated the TEM anomalies to the well sites from shallow to depth; the plastic casings, well 5 and 6, are response TEM signal weak. This demonstrates that the important and superior of the horizontal TEM component in vertical target detection; it adds the capability of the illuminations of the orientations and characters of the metal target. However, the horizontal signal is weaker than that of the vertical, this is the reason why we transmitted the higher current to 50 A in this experiment. This behavior is predicted by our theoretical modelings (Figure 1 and Figure 2).

In the experiment of extending the survey to surrounding areas, about 50 m to the west, a similar anomalies were encountered that were evident in the horizontal component data but not in the Hz data. Figure 4(a) shows the location, and Figure 4(b) is an east-west trending anomalous zone at early time crossing through the grid at $y = 16$ m, moving from west to east along the survey line.

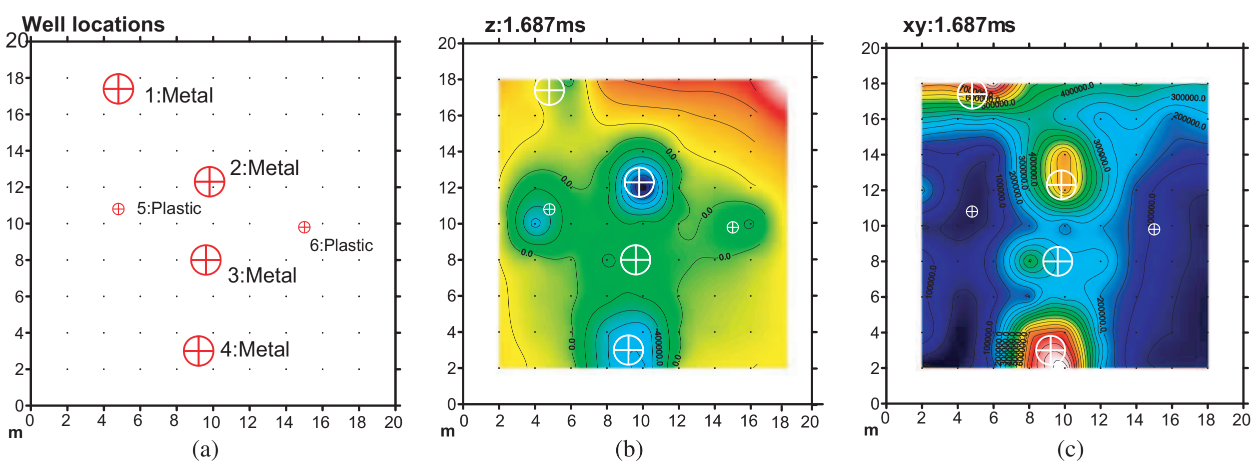

Figure 3: Measured three-component transient voltages (in μV) for the TEM map around the wells site on NCU campus. (a) The survey map showing the location of the TEM soundings (black dots) and the location of wells: the bigger cross for metal casing and the smaller one for plastic casing. (b) Vertical component TEM survey results in plan view around the well field at delay time 1.687 ms. Evidence is strong anomaly near well locations. (c) Horizontal component TEM survey results in plan view for the same area at delay time 1.687 ms. Compared with the vertical component, the horizontal component TEM anomalies are more response to the casing characteristics, metal and plastic.

This linear anomaly is the result of a buried power line that comes into the survey grid from the west, connecting to the electrical access cover ($x = 12$ m, $y = 16$ m), and continues out of the grid to the east toward another light pole. Because the horizontal power line is very shallow, about 1 m below the surface, the anomaly dismissed as time increased to 2.087 ms (not shown here). We note that the strong anomaly at the coordinate $(12, 16)$, which is last to the later time is the electrical access cover on the surface. We also note that there is a weak TEM response for the vertical component measurement (Figure 4(c)); if only vertical component measurement for this survey as traditional exploration approach, then a great risk would be encountered for this case.

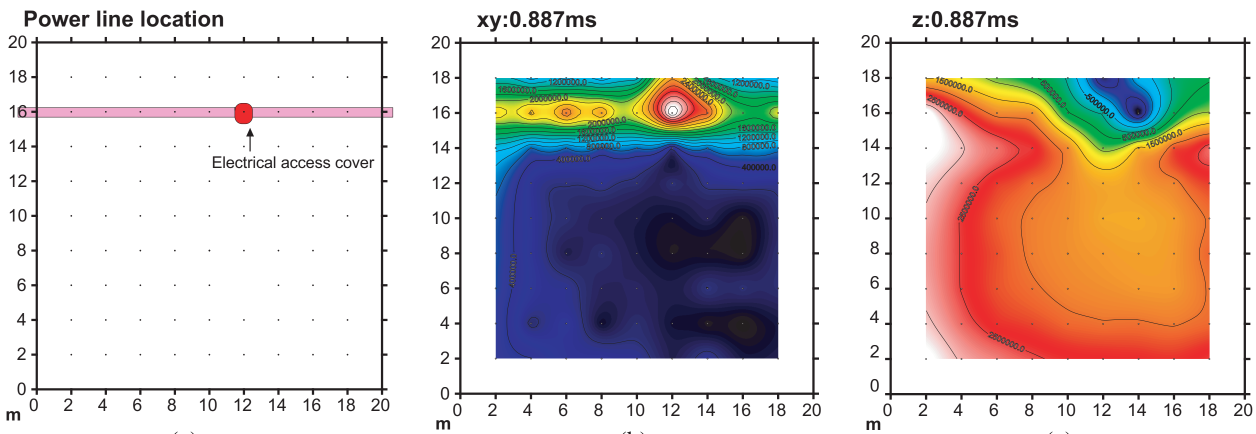

(a) (b) (c)

Figure 4: Measured three-component transient voltages (in μV) for the TEM map around a horizontal pipe. (a) A buried power line at depth about 1 m that comes into the survey grid from the west, connecting to the electrical access cover ($x = 13$ m, $y = 18$ m), and continues out of the grid to the east toward another light pole. (b) Horizontal component TEM survey results in plan view at time 0.887 ms. An east-west trending anomalous zone crosses through the respected grid. (c) Vertical component TEM survey results in plan view for the same area at time 0.887 ms: weak response for pipes, while strong response for surface metal cover.

4. CONCLUSIONS AND FUTURE WORK

In this paper, we have demonstrated numerically that three-component TEM measurements can potentially give access to conductor information in conductive earth. We analyze 3-axis TEM data from known well site and detect transient voltage anomalies which are consistent with our theoretical modeling and which can be correlated with well locations in the conductor host. From this and other surveys, it is apparent that there is much useful information in the horizontal components of near-surface TEM surveys. The Hz data, which displays only uni-polar, negative anomalies, are usually stronger data, and provide the best indication of target location. Hx and Hy data are by nature weaker for the horizontal transmitter, but can be used to determine size, orientation, and characteristics of the conductive targets, especially for the horizontal extending target (i.e., power line, sewer line, etc.). Carlson and Zonge [2] reached the similar conclusions. We are encouraged by the correspondence between the TEM anomaly and the conductor information, and believe that the use of multi-component data to locate conductors will be a must for a high resolution EM method for engineering purposes.

Undoubtedly some possible factors may cause this technique to fail: (1) High cultural background noise levels overwhelmed the anomaly. To increase the signal to noise ration, higher magnetic dipole moment of the transmitter is a good choice; these include high transmitter currents, large transmitter loop, or using multiple-turn transmitter loops. (2) Using wrong time windows would lose the target signals; for example, ours horizontal target (Figure 4) detection experiment would be failed if skip the time window around 0.887 ms.

Recently, we are doing deeper exploration by using magnetotellurics (MT) study for Taiwan's tectonic structure. Professors Xie and Li's AGILD MT and CSMT modeling and inversion, as in reference [6–9], are useful tools, and the new study results will be reported in the next paper.

REFERENCES

1. Buselli, G. and B. O'Neill, "SIROTEM — A new portable instrument for multichannel transient electromagnetic measurements," *Austral. Soc. Expl. Geophys.*, Vol. 8, 82–87, 1977.

2. Carlson, N. R. and K. L. Zonge, "Minerals exploration methods modified for environmental targets," *Exploration Geophysics, Australian Society of Exploration Geophysicists*, Vol. 34, 114–119, 2003.
3. Chen, C.-S. and C.-C. Chang, "Use of cumulative volume of constant-head injection test to estimate aquifer parameters with skin effects: field experiment and data analysis," *Water Resources Research*, Vol. 38, No. 5, 1056, 10.1029/2001WR000300, 2002.
4. Nabighian, M. N., *Electromagnetic Methods in Applied Geophysics: application*, Society of Exploration Geophysicsts, Vol. 2, 425, 1991.
5. Raich, A. P. and F. Sugeng, "Predicting the transient EM response of complex structures using the compact finite element method," *Exploration Geophysics*, Vol. 20, 51–55, 1989.
6. Xie, G., J. Li, E. Majer, D. Zuo, and M. Oristaglio, "3-D electromagnetic modeling and nonlinear inversion," *Geophysics*, Vol. 65, No. 3, 804–822, 2000.
7. Xie, G., J. Li, and F. Xie, "Advanced GILD EM modeling and inversion," *PIERS Online*, Vol. 1, No. 1, 105–109, 2005.
8. Xie, G., J. Li, and F. Xie, "2.5D AGILD electromagnetic modeling and inversion," *PIERS Online*, Vol. 2, No. 4, 390–394, 2006.
9. Li, J., G. Xie, L. Xie, and F. Xie, "New stochastic AGLID EM modeling and inversion," *PIERS Online*, Vol. 2, No. 5, 490–494, 2006.

Experimental Study on Noise Coupling among Multiple Power Areas through Edge Coupling and via Penetrations

Gang Feng and Jun Fan
Electromagnetic Compatibility Laboratory
Department of Electrical and Computer Engineering
Missouri University of Science and Technology
(University of Missouri-Rolla)
Rolla, MO 65409, USA

Abstract— High-frequency noise can be coupled among multiple power areas through edge coupling and via penetrations. Cavity models with both vertical and horizontal connections are used to model the coupling characteristics. Experimental study was conducted to validate this modeling approach. The measured and modeled results agree very well up to several GHz, demonstrating the effectiveness of the approach. Although there are some discrepancies especially at high frequencies possibly due to the neglect of the fringing effect in the cavity connection model, the modeling approach has been demonstrated to be effective and useful for engineering applications in practical designs.

1. INTRODUCTION

With the continuous evolution of semiconductor technologies, digital circuits work at higher frequencies with lower supply voltages. Reducing simultaneous switching noise (SSN) becomes an increasingly critical while challenging objective in high-speed PCB and package designs. Power distribution network (PDN) modeling may become a necessity to achieve the design objective [1–7]. Among various modeling approaches, cavity model method [8–10] has been widely adopted because of its simplicity and accuracy. By applying segmentation method [11, 12], cavity models can be used to analyze irregular-shaped power plane pair and can also be connected to blocks modeled using full-wave methods [4]. In practical high-speed PCB designs, there are often more than one pair of power and ground planes. In [7], a vertical connection method was developed so that cavity models could be used to analyze a three-layer PDN structure. This paper continues the work by further validating the vertical connection method with measurements. A test board with four planes was fabricated. Experimental results demonstrated the effectiveness of the method, as discussed in the following sections.

2. VERTICAL CONNECTION METHOD

The vertical connection method developed in [7] is described here for further discussions. Figures 1(a) and 1(b) show a three layer power-plane structure. The middle plane is only half the size of the top and bottom planes. The vertical connection method can be explained by using this structure as an example. Because skin effect dominates at high frequencies and current only flows at the outer surface of conductors, direct coupling through a plane is negligible since current can hardly flow directly from the top surface to the bottom one by vertically passing through the plane conductor. Therefore, when plane areas at different voltage levels overlap, noise can only be coupled among the vertically aligned regions through edges or via penetrations. By ignoring the fringing field, the structure shown in Figures 1(a) and 1(b) can be divided at the edge of the middle plane into three cavities: α, β, and η, where α and β form the left portion of the structure and are vertically aligned, and η is the right portion of the structure. Cavities α and β are coupled, only through Cavity η by the edge coupling mechanism in this example. They can also be coupled through via penetrations if there are vias passing through both cavities. To characterize the edge coupling and to eventually connect the three cavities together, auxiliary ports are defined at the interface wall between the cavities. As shown in Figures 1(c) and 1(d), a group of auxiliary ports, denoted as "c", are defined in the right wall of Cavity α. Another group with the same number of auxiliary ports as in "c", denoted as "d", are defined in the right wall of Cavity β. These two groups of ports are vertically aligned at the same locations when looking at the top, as shown in Figure 1(c). Correspondingly there are auxiliary ports defined in the left wall of Cavity η, denoted as "f". The number of the ports is the same as in "c" and "d", and the ports are at the same locations as well. The number of these auxiliary ports is determined by the highest frequency of interest. Usually at least 8 ports per wavelength are recommended. In Figure 1, two external ports, "p" and "q", are defined in Cavities α and β, respectively, in addition to the auxiliary ports.

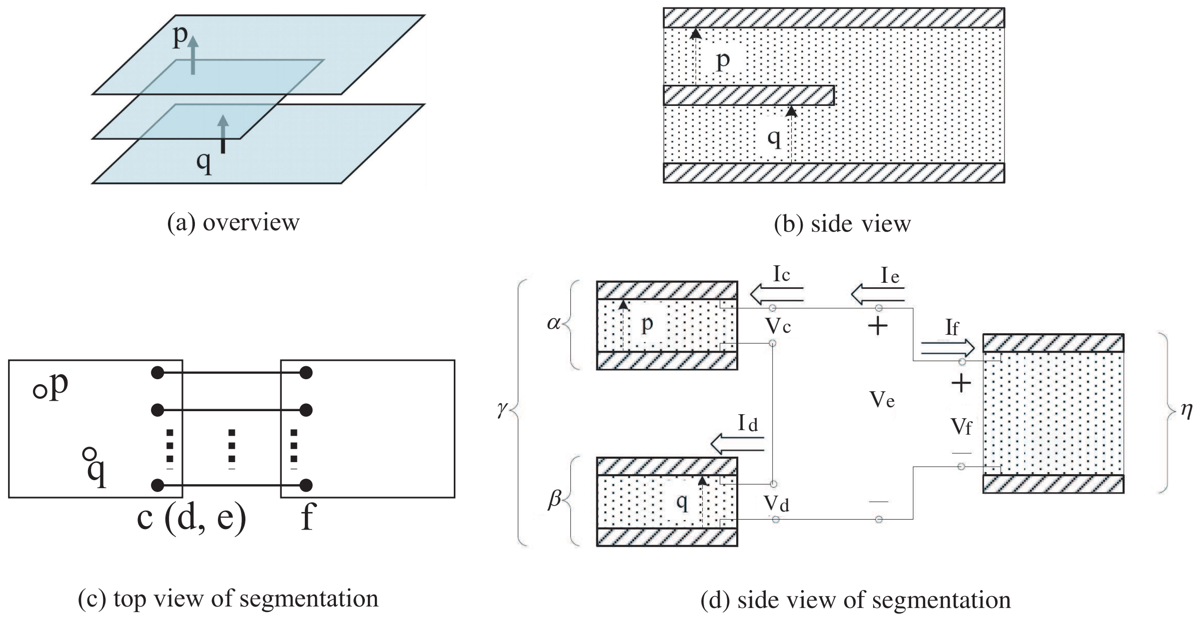

Figure 1: Vertical connection of cavities in a multiple plane structure.

In most of the cases, the spacing between the planes is much smaller than the size of the planes. The plane-pair structure can then be regarded as a 2D cavity, i.e., E and H fields do not vary along the z axis (assuming that the z axis is normal to the power planes). These field modes are called TM_z modes, and are dominant in these plane-pair cavities. Since the fringing field is neglected and the PMC boundary is assumed at the interface wall between the cavities, the tangential components of both E and H fields should be continuous at the boundary. By enforcing the field continuity conditions, the voltage and current relationships among the three cavities result as

$$\begin{cases} V_f = V_c + V_d \\ I_f = -I_c = -I_d \end{cases} \tag{1}$$

It is worth mentioning that the above continuity conditions are based on the 2D cavity (TM_z modes only) assumption. So, the accuracy of this vertical connection method will deteriorate if the z-directional dimensions of the cavities are not small any more, which is very unlikely in any practical PCB and package designs.

For each cavity, the port voltages and port currents are related by its impedance matrix, which has closed form expressions for rectangular and some special triangular cavities [9]. The voltage-current equations for the three cavities can be written in sub-matrix form as

$$\begin{bmatrix} V_p \\ V_c \end{bmatrix} = \begin{bmatrix} Z_{pp} & Z_{pc} \\ Z_{cp} & Z_{cc} \end{bmatrix} \cdot \begin{bmatrix} I_p \\ I_c \end{bmatrix}, \quad \begin{bmatrix} V_q \\ V_d \end{bmatrix} = \begin{bmatrix} Z_{qq} & Z_{qd} \\ Z_{dq} & Z_{dd} \end{bmatrix} \cdot \begin{bmatrix} I_q \\ I_d \end{bmatrix}, \quad [V_f] = [Z_\eta] \cdot [I_f] \tag{2}$$

By solving Equations (1) and (2), the impedance matrix between the external ports can be obtained as

$$\begin{bmatrix} V_p \\ V_q \end{bmatrix} = \left[Z_{p'p'} - Z_{p'e}(Z_{ee} + Z_\eta)^{-1} Z_{ep'} \right] \cdot \begin{bmatrix} I_p \\ I_q \end{bmatrix}$$

where $Z_{p'p'} = \begin{bmatrix} Z_{pp} & 0 \\ 0 & Z_{qq} \end{bmatrix}$, $Z_{ee} = Z_{cc} + Z_{dd}$, $Z_{p'e} = {Z_{ep'}}^T = \begin{bmatrix} Z_{pc} \\ Z_{qd} \end{bmatrix}$.

All the impedance matrices are symmetric due to reciprocity.

3. TEST BOARD GEOMETRY AND MEASURMENT RESULTS

To validate the vertical connection method described in Section 2, a test board was built and investigated. The board is a standard four-layer PCB with an FR4 substrate material. As shown in Figures 2(a) and 2(b), there are four power and ground planes with different shapes. The first and the fourth planes are solid ground planes (denoted as GND1 and GND2, respectively), and are connected by one via. The second plane is a sensitive analog shape (SAS) power plane and the third is a voltage regulator module (VRM) power plane, whose geometries are shown in Figures 2(d) and 2(e), respectively. In order to investigate the coupling between the VRM and the SAS planes, one observation port is added between the VRM and GND1 planes and another between the SAS and GND1 planes. The positions of the ports and the ground via are shown in Figure 2(c).

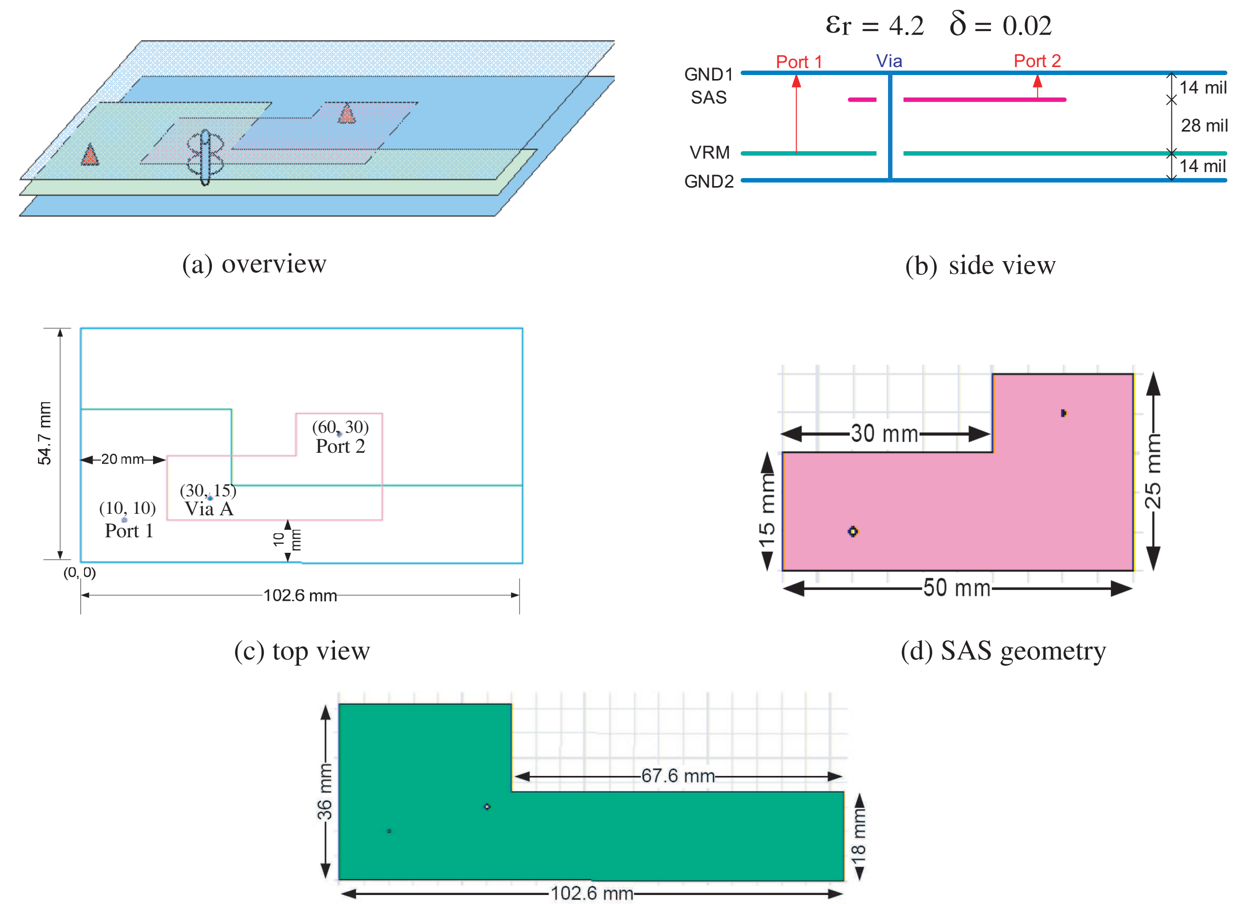

(a) overview

(b) side view

(c) top view

(d) SAS geometry

(e) VRM geometry

Figure 2: Test board geometry.

The test board geometry was modeled using the cavity models and the previously discussed vertical connection method. The entire procedure is similar to the simple case explained in Section 2. By projecting each plane to its adjacent planes, the entire structure was first divided into six irregular-shaped cavities. Sufficient auxiliary ports were defined at the boundaries between these cavities. An impedance matrix was then obtained for every cavity based on the cavity model method. Finally, by enforcing the field continuity conditions at the auxiliary ports, the impedance matrix among the observation ports was calculated.

The same geometry was measured using a vector network analyzer as well. The Z-parameters were calculated from the measured S-parameters. The measured and modeled results are compared in Figures 3 and 4. Overall speaking the agreement is very well up to a few GHz. When frequency increases, the difference between the measurement and modeling slightly increases as well, possibly because the fringing field is neglected in the modeling approach.

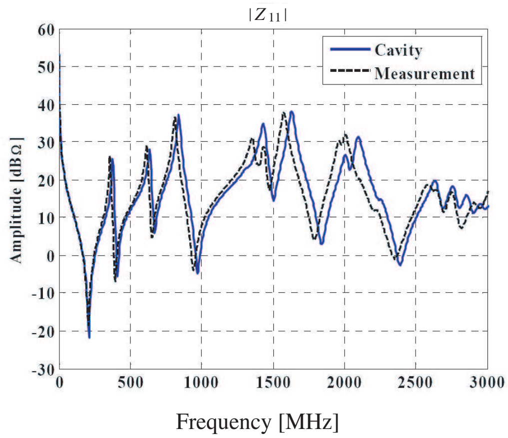

Figure 3: Comparison of the measured and modeled $|Z_{11}|$ for the test board shown in Figure 2.

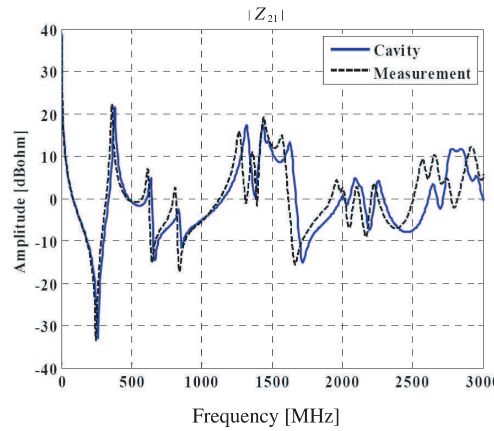

Figure 4: Comparison of the measured and modeled $|Z_{21}|$ for the test board shown in Figure 2.

4. CONCLUSIONS

The vertical connection method was validated experimentally, as reported in this paper. With this method, it becomes possible to use the cavity models to analyze the multiple plane-pair structures that are common in high-speed PCB and package designs. This method was developed based on the 2D cavity assumption with the TM_z modes only, which applies for most practical PCB and package designs.

REFERENCES

1. Lei, G. T., R. W. Techentin, P. R. Hayes, D. J. Schwab, and B. K. Gilbert, "Wave model solution to the ground/power plane noise problem," *IEEE Trans. Instrum. Meas.*, Vol. 44, 300–303, Apr. 1995.
2. Lei, G. T., R. W. Techentin, and B. K. Gilbert, "High-frequency characterization of power/ground-plane structures," *IEEE Trans. Microwave Theory Tech.*, Vol. 47, 562–569, May 1999.
3. Na, N., J. Choi, S. Chun, and M. Swaminathan, "Modeling and transient simulation of planes in electronic packages," *IEEE Trans. Adv. Packag.*, Vol. 23, 340–352, Aug. 2000.
4. Selli, G., J. L. Drewniak, R. E. Dubroff, J. Fan, J. L. Knighten, N. W. Smith, D. McCoy, and B. Archambeault, "Power integrity investigation of BGA footprints by means of the segmentation method," *IEEE Int. Symp. Electromagn. Compat.*, Chicago, Illinois, 2005.
5. Mao, J., C. Wang, G. Selli, B. Archambeault, and J. L. Drewniak, "Memory DIMM DC power distribution analysis and design," *IEEE Int. Symp. Electromagn. Compat.*, 2003.
6. Wang, Z. L., O. Wada, Y. Toyota, and R. Koga, "Modeling of gapped power bus structures for isolation using cavity modes and segmentation," *IEEE Trans. Electromagn. Compat.*, Vol. 47, 21–218, May 2005.
7. Feng, G., G. Selli, K. Chand, M. Lai, L. Xue, and J. L. Drewniak, "Analysis of noise coupling result from overlapping power areas within power delivery networks," *IEEE Int. Symp. Electromagn. Compat.*, Portland, Oregon, Aug. 2006.
8. Okoshi, T. and T. Miyodhi, "The planar circuit — an approach to microwave integrated circuitry," *IEEE Trans. Microwave Theory and Tech.*, Vol. 20, 245–252, Apr. 1972.
9. Okoshi, T., *Planar Circuits for Microwaves and Lightwaves*, Springer-Verlag, Berlin, Germany, 1985.
10. Lo, Y. T., D. Solomon, and W. F. Richards, "Theory and experiment on microstrip antennas," *IEEE Trans. Antennas Propagat.*, Vol. 27, 137–145, Mar. 1979.
11. Okoshi, T., "The segmentation method – an approach to the analysis of microwave planar circuits," *IEEE Trans. Microwave Theory and Tech.*, Vol. 24, 662–668, Oct. 1976.
12. Chadha, R. and K. C. Gupta, "Segmentation method using impedance matrices for analysis of planar microwave circuits," *IEEE Trans. Microwave Theory and Tech.*, Vol. 29, 71–74, Jan. 1981.

Polarization-dependent Memory of Light via Ultrashort Pulse Laser Irradiation

Y. Shimotsuma[1], **M. Sakakura**[1], **P. G. Kazansky**[2]
J. Qiu[3], **K. Miura**[4], **and K. Hirao**[4]

[1]Innovative Collaboration Center, Kyoto University, Japan
[2]Optoelectronics Research Centre, University of Southampton, United Kingdom
[3]Department of Materials Science and Engineering, Zhejiang University, China
[4]Department of Material Chemistry, Kyoto University, Japan

Abstract— The remarkable phenomena in ultrafast light-matter interactions manifested as an evolution of one-dimensional metal nanoparticles in liquid ablation are observed. The polycrystalline copper nanowires with a length of 1.0 μm and a diameter of 85 nm are successfully formed only under the linear-polarized laser irradiation. The growth mechanism of copper nanowires under the femtosecond laser irradiation was suggested to be a nucleation growth process. The formation mechanism of copper nanowires can be interpreted in terms of a created pattern via coupling between photon and surface plasmon waves; consequently a material could memorize the direction of the light polarization.

1. INTRODUCTION

The size and shape of nanoscale materials provide important control over many of the physics and chemical properties, including electric and thermal conductivity, luminescence, and catalytic activity [1]. In particular, there is intense interest in synthesis and morphology control of nano-sized metal and semiconductor particles, which exhibit surprises and novel phenomena based on the unique properties called the quantum size effect [2]. In the last decade, composite materials containing copper nanoparticles found various applications in different fields of science and technology [3–6]. However, various "bottom-up" approaches for making anisotropic-shaped colloidal nanoparticles have been found, with most of these solution methods being based on a thermal process. On the other hand, "top-down" approaches have been developed for producing metal and semiconductor nanowires, nanobelts, and nanoprisms [7–9]. We recently reported the periodic nanostructures composed of oxygen depleted regions of 20 nm size with periods as small as 140 nm inside silica glass, are aligned perpendicular to the laser polarization [10]. The phenomenon could be interpreted in terms of interference between the incident laser light field and the generated bulk electron plasma waves, resulting in the periodic modulation of electron plasma concentration and the structural changes in transparent material. More recently, we have applied this nonlinear interaction between the photons and the plasmons in the nanoscale to preparation of one-dimensional copper nanoparticles from micro-flakes by using femtosecond laser pulses radiation in an ethanol solution at room temperature [11]. A photo-initiated process via femtosecond pulse-induced nucleation in alcohol suspension of copper flakes, followed by thermal treatments for growth into copper nanowires, was investigated. Polycrystalline copper nanowires with a length of 1.0 μm and a diameter of 85 nm were successfully formed under linearly polarized laser irradiation, compared to nanospheres under circularly polarized laser beam. Single crystalline copper nanospheres with a diameter of 10 nm have been kept the metallic state after long time laser irradiation and subsequent thermal treatment due to covering of the amorphous carbon layer which was formed by the photo-dissociation of the surrounding solvent. The structure and morphology of copper nanoparticles depended on surrounding solvent, which allowed us to investigate their structure and morphology evolution in various solutions. The polarization-dependent growth mechanism of copper nanowires was also proposed.

2. ONE-DIMENSIONAL COPPER NANOPARTICLES GROWTH

We used copper flakes produced by the chemical reduction method, which are 5 μm in size and 100 nm thick. A small amount of the copper flakes 0.36 mg, was mixed with 4.5 mL of alcohol (methanol, ethanol, and propanol) filled in a rectangular quartz vessel of $1 \times 1 \times 5\,\mathrm{cm}^3$. The laser radiation in Gaussian mode produced by a regenerative amplified mode-locked Ti:sapphire laser (Cyber Laser Inc., 230 fs pulse width, 1 kHz repetition rate) operating at a wavelength of

780 nm was focused via a 20× (numerical aperture = 0.40) microscope objective into the alcohol-suspended copper flakes placed on a magnetic stirrer. The polarization of the laser light was set linear or circular by a half-wave or a quarter-wave plate placed on the incident beam before the focusing optics. To keep as many copper flakes as possible suspended in a solution, we continuously stirred the suspension. The beam was focused in the suspension with a beam waist diameter and laser energy fluence estimated at $\sim 4\,\mu$m and $2.4 \times 10^3\,\mathrm{J/cm^2}$, respectively. After laser irradiation, the suspensions were left at rest in a temperature-controlled bath having a constant temperature of 40 or 60°C.

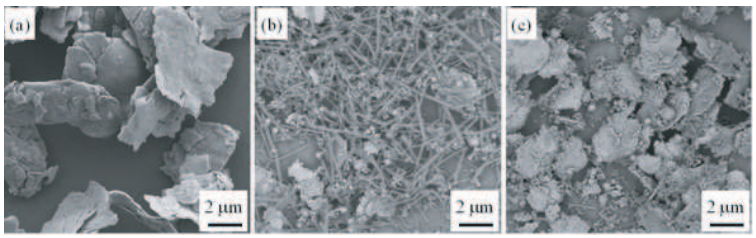

Figure 1: SEM images indicating the morphology changes of initial copper flakes (a) after linearly (b) and circularly (c) polarized femtosecond laser irradiation for 5 minutes, followed by and subsequent aging treatment at room temperature for 5 days.

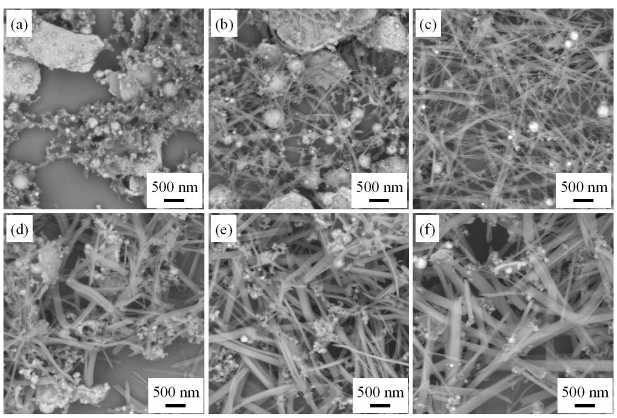

Figure 2: SEM images of the copper nanoparticles after linearly polarized femtosecond laser irradiation for 5 minutes and subsequent aging treatment at 40°C (a)∼(c) and 60°C (d)∼(f). Aging time is 12 hours (a), (d), 24 hours (b), (e), and 120 hours (c), (f), respectively.

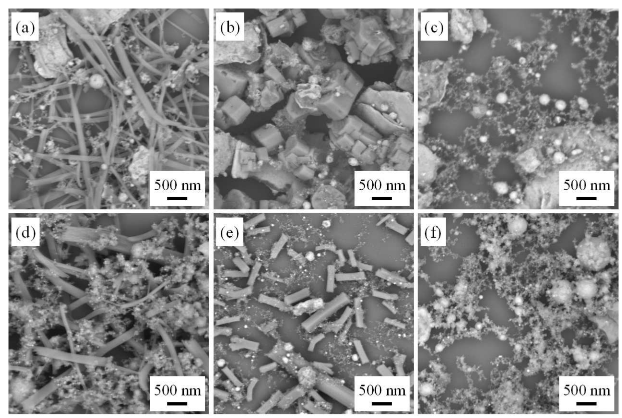

Figure 3: SEM images of copper nanoparticles after femtosecond laser irradiation for 3 minutes (a)∼(c) and 20 minutes (d)∼(f) and subsequent aging treatment for 5 days in ethanol (a), (d), methanol (b), (e), and propanol (c), (f), respectively.

Figure 1 indicates the typical SEM images of the morphology changes of initial copper flakes [Fig. 1(a)] after linearly and circularly polarized femtosecond laser irradiation for 5 minutes and subsequent aging treatment at room temperature for 5 days. In each polarization case, the copper nanospheres and unreacted starting copper-flakes are observed just after laser irradiation, while copper nanowires can be observed after linearly polarized laser irradiation and subsequent aging treatment [Fig. 1(b)]. On the other hand, in the case of circularly polarized laser irradiation, aggregates of copper nanospheres and unreacted starting materials can be observed, namely there is no apparent formation of copper nanowires [Fig. 1(c)]. These results evidently indicate that the formation of the copper nanowires was dependent on the incident light polarization, even though the ablated copper nanospheres just after the laser irradiation were still standing at room temperature for 5 days. We have also confirmed that the one-dimensional growth of copper nanoparticles occurs during the subsequent aging process. Fig. 2 shows SEM images of the copper nanostructures after 5 minutes of the linearly polarized laser irradiation and subsequent aging treatment at 40 and 60°C for several hours. These SEM observations reveal the diameter growth rate of copper nanowires increases in the aging temperature [Figs. 2(c), (f)]. In the early stage during aging process at 40°C, nanoscale web-like aggregates of nanoparticles can be observed [Fig. 2(a)]. This phenomenon is similar to the formation of unusual aggregated structures composed of both crystalline and amorphous silicon nanoparticles by the femtosecond laser ablation in the presence of a background gas [12]. These nanoscale web-like aggregates are expected to be evolved into copper nanowires [Figs. 2(a)∼(c)]. Indeed, the inner part of the copper nanowires was composed of polycrystalline metallic cooper [Figs. 4(d)∼(f)]. Detailed SEM observations indicated the diameter of copper nanowires was variable as a function of the aging time. After the subsequent aging treatment for 120 hours, the diameters of copper nanowires were eventually about 68 and 185 nm, and the lengths were about 7.5 and 3.5 μm at the aging temperature of 40 and 60°C, respectively. This indicates that an aspect ratio of the copper nanowires can be controlled by the change of the subsequent aging conditions.

3. SOLVENT EFFECT ON THE COPPER NANOPARTICLES FORMATION

The effect on the formation of copper nanoparticles by the surrounding solvent was also investigated. Although the nanoparticles prepared by 3 minutes of the laser irradiation in an ethanol were almost wire-like, the fraction of nanospheres increased in the laser irradiation time [Figs. 3(a), (d)]. In contrast, the nanoparticles prepared by the same conditions of the laser irradiation in a methanol were observed in the cubic nanostructures [Fig. 3(b)], while the nanorods were formed in the case of the long time laser irradiation (20 minutes) [Fig. 3(e)]. Besides, in the case of long time laser irradiation in ethanol and methanol, the nanospheres still exist after subsequent aging treatment for 5 days [Figs. 3(d), (e)]. However, the one-dimensional growth of the nanoparticles after laser irradiation and subsequent aging treatment occurred in both cases of ethanol and methanol; no morphology change was observed in the case of a propanol [Figs. 3(c), (f)]. Detailed TEM observations of copper nanowires and nanospheres indicate that the nanowires' surface are composed of polycrystalline Cu_2O [Figs. 4(a)∼(c)]. Furthermore, the cross-sectional observations clearly demonstrate that nanowires are partially oxidized from the surface to the depth of about 5 nm [Fig. 4(e)]. On the other hand, the inner part of the nanowires was composed of polycrystalline metallic cooper [Figs. 4(d)∼(f)]. Indeed, the electron diffraction patterns of the inner and surface parts indicate that the observed areas were composed of metallic copper [Fig. 4(f)] and Cu_2O [Fig. 4(c)], respectively. We have also confirmed that the nanospheres after long time laser irradiation in an ethanol are composed of single crystal of metallic copper. Fig. 5 shows TEM observations of copper nanospheres after femtosecond laser irradiation for 20 minutes in an ethanol. Red and blue arrows in Fig. 5(a) show the analysis points of the electron energy-loss spectroscopy (EELS). The EELS spectra near C-K and Cu-L edge evidently indicate that the copper nanospheres are covered by carbon layer [Figs. 5(b), (c)]. Results of the existence of the many single crystal of metallic copper in the case of long time laser irradiation indicate that these amorphous carbon layer produced by the dissociation of solvent prevents not only the aggregation and growth of

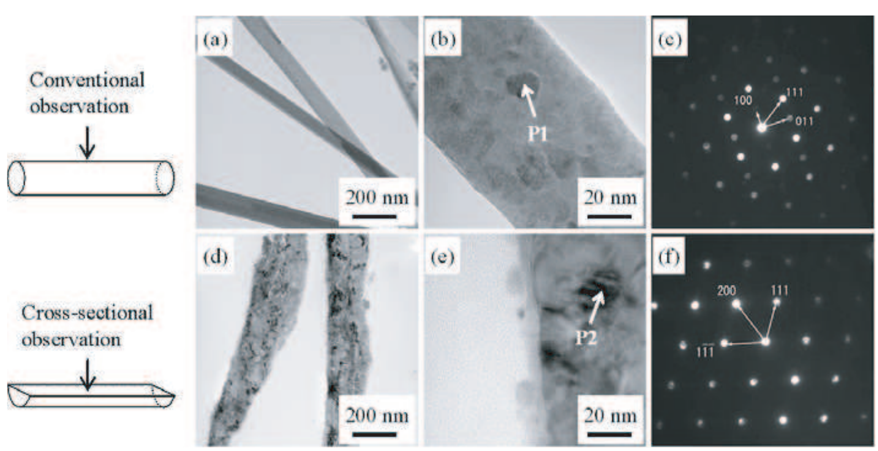

Figure 4: TEM observations of copper nanowires after femtosecond laser irradiation for 3 minutes. Schematic diagrams of the analysis methods are also shown on the left hand side. Two types of observations were carried out: conventional (a)∼(c) and cross-sectional (d)∼(f). The images are shown in two different scales: low magnification images (a), (d) and high magnification images (b), (e) for the same area. Arrows of P1 and P2 in Figures (b) and (e) show the analysis points of the electron diffraction pattern. The electron diffraction patterns of P1 and P2 are shown in (c) and (f), respectively.

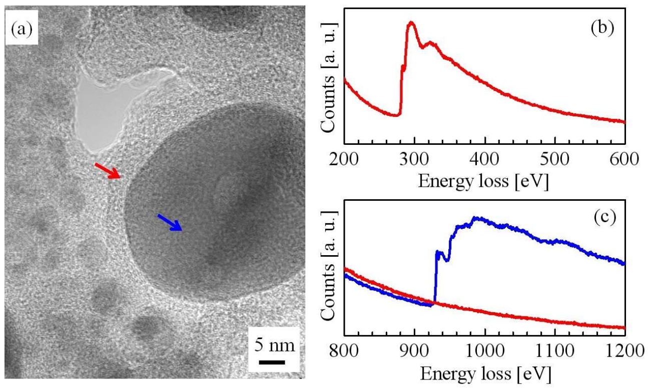

Figure 5: TEM observations of copper nanospheres after femtosecond laser irradiation for 20 minutes in an ethanol (a). Red and blue arrows in image show the analysis points of the electron energy-loss spectroscopy. The electron energy-loss spectra near C-K (b) and Cu-L edge (c) corresponding to the color of arrows are also shown.

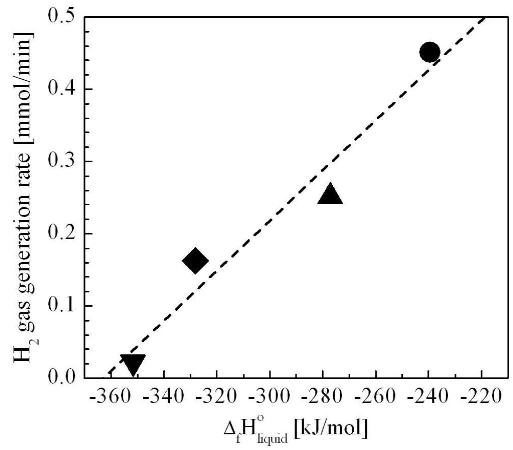

Figure 6: Hydrogen gas generation rate as a function of the standard enthalpy change of formation ($\Delta_f H^{\circ}_{liquid}$) of various alcohol solutions during femtosecond laser irradiation. Symbols of •, ▲, ♦, and ▼ are experimental data of methanol, ethanol, butanol, and pentanol, respectively. Dotted line indicates a linear fit through the data points.

nanospheres but also the oxidation. Indeed, hydrogen gas was generated by the photo-dissociation of solvent and act as a reducing gas (Fig. 6). The hydrogen gas generation rate is proportional to the standard enthalpy change of formation of solution. In particular, methanol has a profound inhibitory effect of oxidation. On the other hand, the covering effect by the photo-dissociated amorphous carbon appears prominently in the case of propanol.

4. MECHANISMS OF COPPER NANOWIRE FORMATION

The growth mechanism for one-dimensional copper nanoparticle was considered to be nucleation growth process. We have identified two distinctive stages in copper nanowire formation by femtosecond laser irradiation and subsequent aging treatment: (1) generation of copper nanospheres by the laser ablation on the initial flake surface, (2) growth of copper nanowires due to the aggregation of the ablated copper nanospheres. During the first stages of the laser ablation, the generation of copper nanospheres is affected by the laser polarization because the initial flakes remain stationary with respect to the direction of laser polarization during laser pulse width of 230 femtoseconds. In addition, the hydrogen gas generated by the photo-dissociation of solution prevents the oxidation of nanospheres during femtosecond laser irradiation. The copper nanospheres were ablated from the surface of initial flakes via interference between incident light field and the electric field of the surface plasmon waves (SPWs). The SPWs could couple with the incident light wave only if it propagates in the plane of light polarization [11]. This coupling occurs on the flake surface over a narrow region with a depth of the order of the skin depth ($d_p \ll \lambda$) due to the surface roughness on the initial flakes. Previous investigations suggested that either preimposed or self-generated deformations on the solid surface strongly affect laser energy absorption [13]. Evidence for small deformations comes from the wide spreading of the reflected radiation observed in experiments [14] Numerical simulations suggested that electron oscillations may grow for a step density profile much faster than the typical time scale of ion motion, leading to an oscillatory "rippling" of the critical surface ($n_e = n_c$) [15]. Such rippling is generated as a result of interference between the light field and the surface plasmon-polariton wave launched by initial random surface inhomogenities. During the second stages, the copper nanospheres which may be the aggregation of the laser ablated copper atoms and/or clusters could act as a nuclear of the growth of nanowire in alcohol solution. Although a part of the aggregates are oxidized to Cu_2O, most are kept the metallic state due to covering of the amorphous carbon layer which was formed by the photo-dissociation of the surrounding solvent. Such layer prevents the aggregation and growth of the nanospheres. The amount of the photo-dissociation of solvent is increased with the laser irradiation time and the length of carbon chain. By the competition between the oxidation to Cu_2O and the aggregation of metallic copper nanospheres, copper nanoparticles grow one-dimensionally into nanowires which have core-shell structure. In fact, it is well known that in the case of Cu_2O crystals, the O^{2-} ions in the (001) facet are more apt to hydrolyze, compared with those in the (111) facet, and the stacking along (001) directions therefore becomes energetically favorable [16]. A detailed mechanism of the copper nanowire formation is under investigation.

5. CONCLUSION

In conclusion we have demonstrated the morphology control of copper nanoparticles by femtosecond laser irradiation in an alcohol solution. The copper nanowires with a core-shell structure are formed depending on the surrounding solvent and laser irradiation time. An aspect ratio of the copper nanowires can be controlled by the change of the subsequent aging conditions. The formation mechanisms of copper nanowires are interpreted in terms of the competition between the oxidation to Cu_2O and the aggregation of metallic copper nanospheres. Another puzzling phenomenon is polarization-dependence of copper nanowires formation. Apart from the fundamental importance of the observed phenomenon as the first direct evidence of polarization-dependent memory of light, the observed copper nanowires could be useful for optical polarization control medium, electro-conductive nanomaterial, and probe for SPM.

ACKNOWLEDGMENT

The authors would like to thank Masayuki Nishi, Eric T. Y. Lee, and Atsuo Nakao from Kyoto University for helpful discussions. This research was partially supported by the New Energy and Industrial Technology Development Organization (NEDO), the Ministry of Education, Science, Sports and Culture, Grant-in-Aid for Exploratory Research, 2006, No. 18656192, and Scientific Research (A), 2005, No. 17206067.

REFERENCES

1. Lieber, C. M., "One-dimensional nanostructures-chemistry, physics & aplications," *Solid State Commun.*, Vol. 107, No. 11, 607–616, 1998.
2. Alivisatos, A. P., "Semiconductor clusters, nanocrystals, and quan-tum dots," *Science*, Vol. 271, No. 5251, 933–937, 1996.
3. Eastman, J. A., S. U. S. Choi, S. Li, W. Yu, and L. J. Thompson, "Anomalously increased effective thermal conductivities of ethylene glycol-based nanofluids containing copper nanoparticles," *Appl. Phys. Lett.*, Vol. 78, No. 6, 718–720, 2001.
4. Larsen, G. and S. Noriega, "Dendrimer-mediated formation of Cu-CuOx nanoparticles on silica and their physical and catalytic characterization," *Appl. Catal. A: Gen.*, Vol. 278, No. 1, 73–81, 2004.
5. Wang, H., Y. Huang, Z. Tan, and X. Hu, "Fabrication and characterization of copper nanoparticle thin-films and the electrocatalytic behavior," *Anal. Chim. Acta*, Vol. 526, No. 1, 13–17, 2004.
6. Patel, M. K., B. J. Nagare, D. M. Bayul, S. K. Haram, and D. C. Kothari, "Controlled synthesis of Cu nanoparticles in fused silica and BK7 glasses using ion beam induced defects," *Surf. Coat. Technol.*, Vol. 196, No. 1–3, 96–99, 2005.
7. Hu, J. T., T. W. Odom, and C. M. Lieber, "Chemistry and physics in one dimension: Synthesis and properties of nanowires and nanotubes," *Acc. Chem. Res.*, Vol. 32, No. 5, 435–445, 1999.
8. Pan, Z. W., Z. R. Dai, and Z. L. Wang, "Nanobelts of semiconducting oxides", *Science*, Vol. 291, No. 5510, 1947–1949, 2001.
9. Jin, R., Y. W. Cao, C. A. Mirkin, K. L. Kelly, G. C. Schatz, and J. G. Zheng, "Photoinduced conversion of silver nanospheres to nanoprisms," *Science*, Vol. 294, No. 5548, 1901–1903, 2001.
10. Shimotsuma, Y., P. G. Kazansky, J. Qiu, and K. Hirao, "Self-organized nanogratings in glass irradiated by ultrashort light pulses," *Phys. Rev. Lett.*, Vol. 91, No. 24, 247405(1–4), 2003.
11. Shimotsuma, Y., T. Yuasa, H. Homma, M. Sakakura, A. Nakao, K. Miura, K. Hirao, M. Kawasaki, J. Qiu, and P. G. Kazansky, "Photoconversion of copper flakes to nanowires with ultrashort pulse laser irradiation," *Chem. Mater.*, Vol. 19, No. 6, 1206–1208, 2007.
12. Tull, B. R., J. E. Carey, M. A. Sheehy, C. Friend, and E. Mazur, "Formation of silicon nanoparticles and web-like aggregates by femtosecond laser ablation in a background gas," *Appl. Phys. A*, Vol. 83, No. 3, 341–346, 2006.

13. Feurer, T., W. Theobald, R. Sauerbrey, I. Uschmann, D. Altenbernd, U. Teubner, P. Gibbon, E. Forster, G. Malka, and J. L. Miquel, "Onset of diffuse reflectivity and fast electron flux inhibition in 528-nm-laser-solid interactions at ultrahigh intensity," *Phys. Rev. E*, Vol. 56, No. 4, 4608–4614, 1997.
14. Zepf, M., G. D. Tsakiris, G. Pretzler, I. Watts, D. M. Chambers, P. A. Norreys, U. Andiel, A. E. Dangor, K. Eidmann, C. Gahn, A. Machacek, J. S. Wark, and K. Witte, "Role of the plasma scale length in the harmonic generation from solid targets," *Phys. Rev. E*, Vol. 58, No. 5, R5253–R5256, 1998.
15. Macchi, A., F. Cornolti, F. Pegoraro, T. V. Liseikina, H. Ruhl, and V. A. Vshivkov, "Surface oscillations in overdense plasmas irradiated by ultrashort laser pulses," *Phys. Rev. Lett.*, Vol. 87, No. 20, 205004(1–4), 2001.
16. Chen, Z.-Z., E.-W. Shi, Y.-Q. Zheng, W.-J. Li, B. Xiao, and J.-Y. Zhuang, "Growth of hex-pod-like Cu2O whisker under hydrothermal conditions," *J. Cryst. Growth*, Vol. 249, No. 1–2, 294–300, 2003.

Widening the Negative Effective Parameter Frequency Band of Resonant SNG Metamaterials

J. Zehentner and J. Machac
Czech Technical University in Prague, Technicka 2, 16627 Prague 6, Czech Republic

Abstract— This paper summarizes some ways of widening the frequency response of epsilon- and mu-negative metamaterials. The metamaterials are composed of resonant particles and their behavior is theoretically described in terms of coupled resonant circuits theory. The more particles participate in the tested system, the wider the frequency band of the system response. An additional, very important consideration in metamaterial applications is the demand for an isotropic medium. This requirement is therefore also taken into account in our experiments.

1. INTRODUCTION

Volumetric single negative (SNG) metamaterials, i.e., metamaterials with negative permittivity and positive permeability, or vice versa, generally consist of anisotropic resonant particles. There is only a narrow frequency band in which one of the effective parameters of the metamaterials is negative, due to the resonant behavior of the particles, and this seriously limits their technical application. Comparing to this the frequency band of LH planar transmission lines is much wider, even 100% as shown in [1]. These non-resonant structures, however, are not aimed for volumetric applications. This paper presents several ways of widening the frequency band of volumetric SNG metamaterials. This includes widening the medium response resulting from coupling the individual particles as a direct analogy of coupled resonators. The other effect taking place in systems of a large number of particles and leading to band widening is the dispersion of the geometrical and/or material parameters of the particles. In addition, the demand for an isotropic medium is a very important consideration in metamaterial applications.

In experiments to validate the concept of widening the operation band of an SNG metamaterial with negative permeability we used planar broadside coupled split ring resonators (BC-SRR) [2]. The particle consists of two split rings located on the two sides of the substrate, as shown in Fig. 1(a). The metamaterial exhibiting negative permittivity consists of a planar electric dipole loaded by the loop inductor, as shown in Figs. 1(b)–(d). The inductor has two turns utilizing both sides of the substrate in order to shift the medium response of the particle to lower frequencies [3, 4].

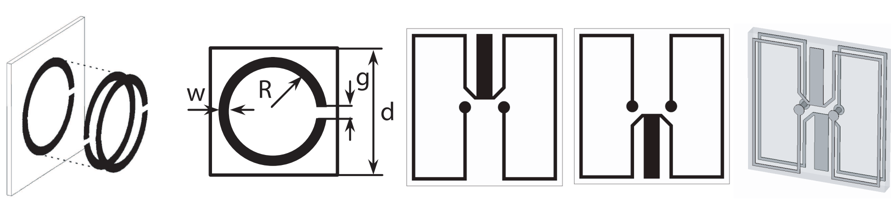

Figure 1: Planar particles used in SNG metamaterials. BC-SRR (a). Planar dipole, top (b) bottom (c) and 3D view (d).

2. A COUPLE OF RESONANT CIRCUITS

One way of extending the frequency response of a resonant circuit utilizes the concept of coupled circuits. The overall transmission of a couple of resonators depends on the coupling coefficient. The transmission admittance of the circuit in Fig. 2(a) is [5]

$$Y_{tr} = \frac{I_2}{U_1} = \frac{jX_v}{R_1R_2(1+jQ_1F_1)(1+jQ_2F_2)+X_v^2}, \tag{1}$$

where $\omega = 2\pi f$, $X_v = \omega M$, $M = k\sqrt{L_1L_2}$, $\omega_{01,2} = 1/\sqrt{(L_{1,2}+M)C_{1,2}}$, $F_{1,2} = \omega/\omega_{01,2} - \omega_{01,2}/\omega$, $Q_{1,2} = \omega_{01,2}L_{1,2}/R_{1,2}$, k is the coupling coefficient, and f stands for frequency. The frequency band of the response of the circuit from Fig. 2(a) can by widened in two ways. Fig. 3 shows the transmission admittance modulus as a function of frequency (1) in dependence on the coupling coefficient keeping all parameters constant, $R_1 = R_2 = 0.1\,\Omega$, $L_1 = L_2 = 1\,\text{nH}$, $C_1 = C_2 = 2.6\,\text{pF}$ chosen to get the response around 3.1 GHz, similar to the resonant frequency of the investigated particles. The change of the coupling coefficient can be achieved simply by changing the mutual position of particular inductors/particles in space. Fig. 4 documents the influence of capacitance C_1 on the coupled resonant circuits response for $k = 0.004$, and other parameters defined above. This is an analogy to the couple of particles with different parameters, and thus with different resonant frequencies.

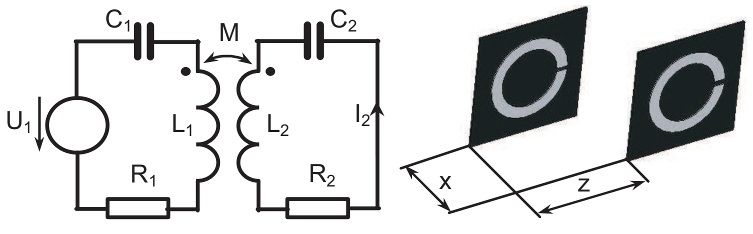

Figure 2: Coupled resonant circuits, equivalent circuit (a), two coupled BCSRRs (b).

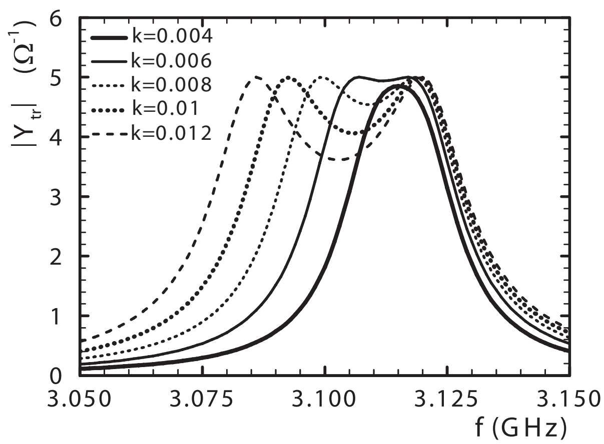

Figure 3: Transmission admittance (1) of the coupled circuits from Fig. 2(a) depending on the coupling coefficient.

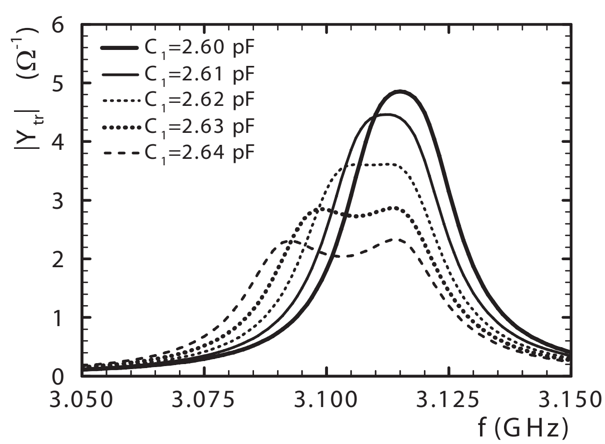

Figure 4: Transmission admittance (1) of the coupled circuit from Fig. 2(a) in dependence on the capacitance C_1.

The equivalent circuit of BC-SRRs is more complex than the simple LC resonant circuit shown in Fig. 2(a). For this reason, the frequency dependence of the transmission coefficient of a pair of BC-SRRs located in a waveguide behaves differently than does a pair of LC resonant circuits. The TEM waveguide with a rectangular cross-section $20 \times 10\,\text{mm}$ was used for the numerical simulation in the CST Microwave Studio. The mutual position of the particles is sketched in Fig. 2(b). The planar particles are parallel to the waveguide side walls and are located at the waveguide center symmetric to the longitudinal waveguide axis. The particles are of the same dimensions: side-width $d = 7\,\text{mm}$ of the squared substrate, 0.127 mm in thickness and permittivity 2.2, ring strip-width $w = 0.7\,\text{mm}$ and inner radius of the ring $R = 1.8\,\text{mm}$. The response of the TEM waveguide with a single BC-SRR for the two different values of the ring split-slot $g = 0.2\,\text{mm}$ and $g = 0.3\,\text{mm}$ calculated by the CST Microwave Studio is shown in Fig. 5(a). The particle is located in the middle of the waveguide parallel to the side walls. The resonant frequency is $f_{r1} = 3.024\,\text{GHz}$ for $g = 0.2\,\text{mm}$ and $f_{r2} = 3.056\,\text{GHz}$ for $g = 0.3\,\text{mm}$. In the case of two particles of the same gap-width located in the TEM waveguide, according to Fig. 2(b), we get different patterns than those shown by the model of the couple of identical LC circuits. The shape of the transmission characteristic of the TEM waveguide with the couple of these particles is not significantly changed by their position, and looks like the transmission characteristic of a single particle. The tighter the coupling, the more the response is detuned towards lower frequencies. This is due to the mutual inductance detuning the circuit. This is shown for the BC-SRRs with the gaps $g_1 = g_2 = 0.2\,\text{mm}$ in Table 1. The transmission characteristics in Fig. 5(b) document what happens when we combine these two effects. The two BC-SRRs are detuned by different gaps 0.2 and 0.3 mm, and their position is varied. For small distances z the mutual coupling of the particles is effective and their frequency response is wider than a single particle response, as shown in Fig. 5(a). At $z \geq 5\,\text{mm}$ the coupling is weak and the final characteristic is the superposition of the particular characteristics, as shown in Fig. 5(a). This, however, results in a sufficiently wider response than a single particle provides.

Table 1: Resonant frequency of the couple of identical BC-SRRs from Fig. 2(b) in dependence on their distance x calculated for $z = 0$.

distance x (mm)	resonant frequency (GHz)
1	2.599
3	2.942
5	3.018
7	3.024

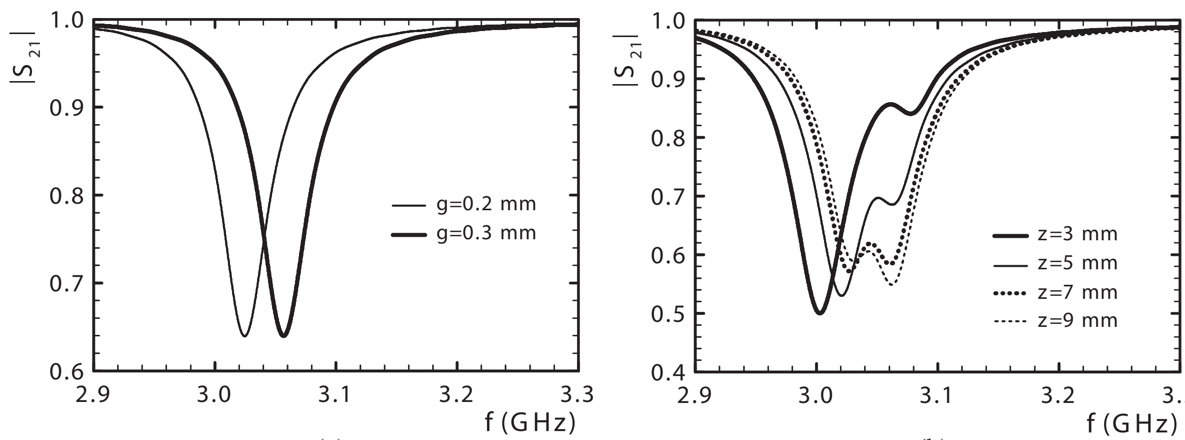

Figure 5: Calculated transmission of the TEM waveguide with a single BC-SRR of different gap widths (a), two BC-SRRs in dependence on their position defined in Fig. 2(b) for $x = 5\,\text{mm}$ (b).

3. SYSTEM OF PARTICLES

A more effective and lower-cost way of widening the frequency band of the SNG metamaterial response utilizes a system of a large number of particles properly distributed in the hosting material. There are also two mechanisms for widening the metamaterial frequency response that were introduced in the preceding paragraph. In a real system of particles these two effects are combined, and come into effect in the great number of particles periodically or randomly distributed.

The particles in such a system are coupled to each other with various coupling coefficients, and we can observe the same effect as exhibited by a couple of resonant circuits tuned to the same frequency for a certain coupling coefficient determined by the positions of the particles. The particles in the system differ slightly from each other due to the tolerances of the fabrication process in the geometrical dimensions of the conducting layout, and even due to the non-homogeneity of the substrate thickness and its permittivity. Consequently each particle has a different resonant frequency, and the frequency band of the system of particles is wider than that of a single particle. Generally, the more particles are present in the system, the wider the band and the higher the rank of isotropy.

4. EXPERIMENTS AND DISCUSSION

We have verified and evaluated the effects mentioned above for three different composites in the case of both epsilon-negative and mu-negative particles. As the reference, Fig. 6 shows the transmission of one epsilon-negative particle located at the center of the R32 waveguide [4]. The first tested system consisted of a periodic distribution of particles oriented in the same direction. The response of this medium remained anisotropic, as it was for a single particle. Transmission through this system of 147 epsilon negative particles located in an R32 waveguide, see the inset in Fig. 7, is shown in Fig. 7. The frequency band of this medium is considerably wider than that of a single particle, as shown in Fig. 6. At the same time, this system of particles has a more intensive response than that of a single particle.

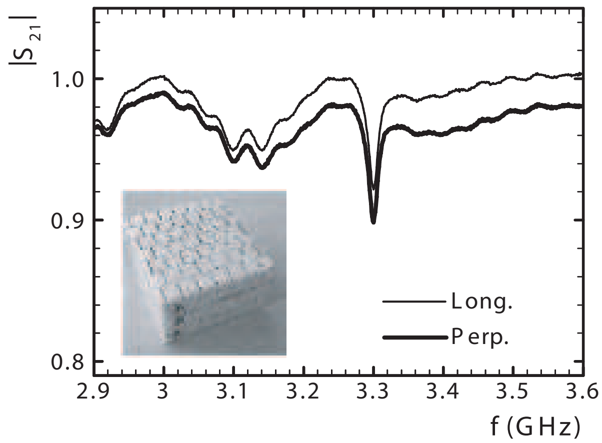

Figure 6: Measured transmission of an R32 waveguide with one epsilon-negative particle (Long. — oriented parallel to the waveguide longitudinal axis, Perp. — located perpendicular to the waveguide axis).

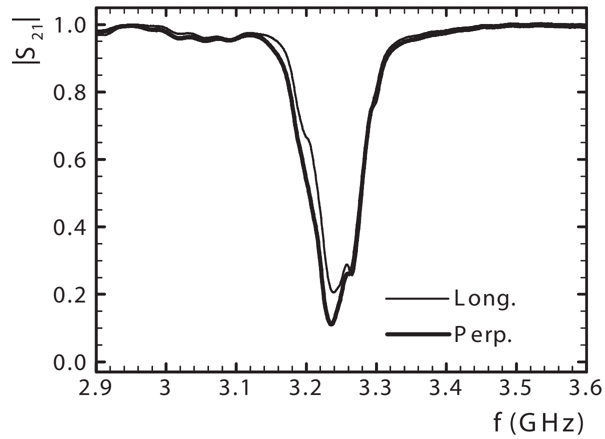

Figure 7: Measured transmission of an R32 waveguide with 147 epsilon-negative particles periodically distributed and aligned in one direction (Long. — located parallel to the waveguide longitudinal axis, Perp. — located perpendicular to the waveguide axis).

As mentioned above, a very important requirement in many metamaterial applications is the isotropy of their response. As stated, the system shown in Fig. 7 behaves anisotropically, i.e., the response depends on the electric field vector orientation. However, the isotropic response was obtained using quasi-randomly [3, 4] or fully randomly [1] distributed particles. Here, in Fig. 8, we present the behavior of a munegative metamaterial by means of the mean value and the dispersion of the transmission through the 64 systems, shown in the inset, and consisting of 243 BC-SRRs located in an R32 waveguide. These systems were obtained by sequential rotation of particular slices in the sandwich, as shown in Fig. 8. The particles in the slices are located at regular positions, but are randomly oriented. In this way we have obtained a quasi-2D isotropic mu-negative metamaterial. Note the considerably wider frequency band of the metamaterial response compared to the response

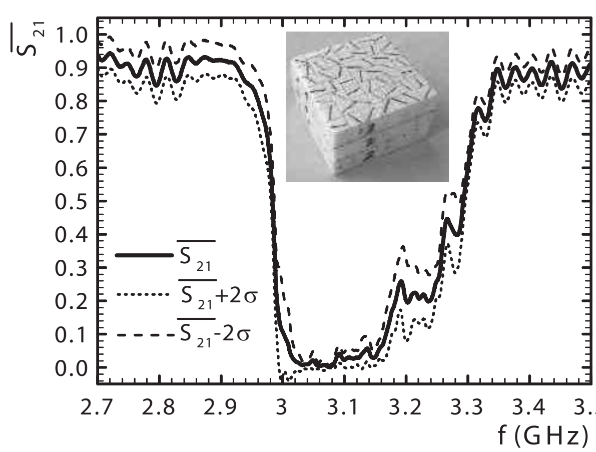

Figure 8: Arithmetic mean value of the transmission through 64 cubic samples in the R32 waveguide with 243 BC-SRRs and its disperse when the resonators are in the nodes of the squared net and are randomly oriented [2].

of a single BC-SRR, which is similar to that shown in Fig. 6 for a single planar dielectric dipole.

The system consisting of 264 BC-SRRs put into plastic shells in the form of a sphere filling the cube with side length 72 mm inserted into the raised R32 waveguide, see Fig. 9, exhibits the transmission plotted in Fig. 10. Now the resonators are fully randomly distributed and oriented, so on an average their mutual coupling is less intensive than in the preceding cases. The response of this system is therefore less intensive and its frequency band is narrower than in the two preceding cases, though still much wider than for a single particle.

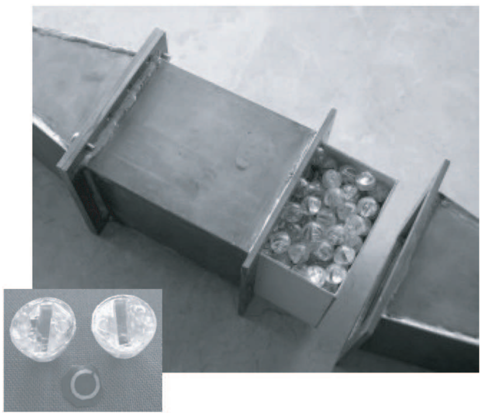

Figure 9: The isotropic mu-negative metamaterial inserted into the partly disassembled measuring setup.

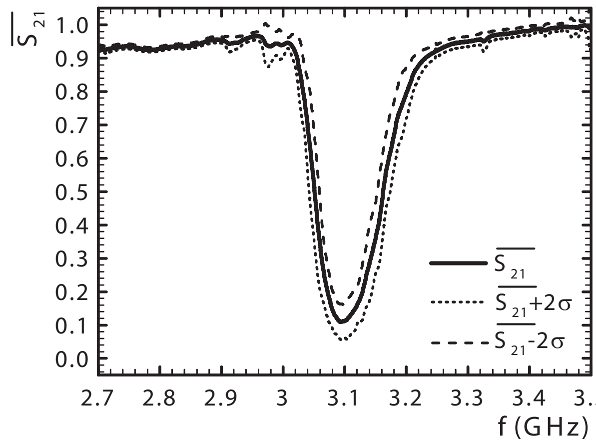

Figure 10: Arithmetic mean value of the transmission through 63 cubic samples in the squared R32 waveguide with 246 BC-SRRs and its disperse when the resonators in the shells are randomly distributed [2].

5. CONCLUSIONS

The paper presents widening of the operation frequency band of SNG metamaterials in terms of the frequency response to irradiation of the composite by the electromagnetic wave. This band is very narrow, due to the resonant characters of the 3D inclusions. According to a simple theory of coupled resonators, one way leads to a change of the coupling coefficient by changing the positions of the particles positions. Within the second way, we changed the resonant frequency of the particles while keeping their position constant. These two approaches were checked and demonstrated by the theory of coupled resonators and by numerical experiments, taking into account magnetic and electric dipoles. The two effects are superimposed in systems of metamaterials composed from a great number of inclusions.

It turned out that the width of the frequency response of the single particle is about 20 MHz, i.e, 0.64% of the resonant frequency. Using the system of 147 epsilon-negative particles periodically distributed and aligned in one direction we got the response-width 110 MHz, i.e., 3.55% relative band, defined at the level -3 dB of the S_{21} modulus. The 2D isotropic system consisting of 147 particles periodically distributed but randomly oriented offered a width of 200 MHz, i.e., 6.45%. The same system consisting of 243 particles offered a width of 330 MHz, i.e., 10.65%. With fully random distribution of particles we got a response-width of 150 MHz, i.e., 4.84% relative band, for a system consisting of 264 BC-SRRs boxed in plastic spherical shells. This is narrower than that for the 2D isotropic system, although we now had more particles. This is due to the less intensive mutual coupling between randomly distributed particles than the coupling between particles distributed periodically.

ACKNOWLEDGMENT

This work has been supported by the Grant Agency of the Czech Republic under project 102/06/1106 "Metamaterials, nanostructures and their applications".

REFERENCES

1. Caloz, C. and T. Itoh, "Novel microwave devices and structures based on the transmission line approach of meta-materials," *2003 International Microwave Symposium Digest*, Vol. 1, 195–198, Philadelphia, USA, June 2003.
2. Jelinek, L., J. Machac, and J. Zehentner, "A magnetic metamaterial composed of randomly oriented SRRs," *PIERS Proceedings*, 474–477, March 26-30, Beijing, China, 2007.
3. Machac, J., P. Protiva, and J. Zehentner, "Isotropic epsilon-negative particles," *2007 International Microwave Symposium Digest*, CD-Rom, TH4D-03, Honolulu, Hawaii, USA, June 2007.
4. Protiva, P., J. Machac, and J. Zehentner, "Particle for an isotropic metamaterial with negative permittivity," *EMTS 2007 — International Electromagnetic Theory Symposium URSI*, CD-ROM, Ottawa, ON, Canada, July 2007.
5. Cajka, J. and J. Kvasil, "Theory of linear circuits," 327, SNTL, Prague 1979, (in Czech).

Microwave Photonic Devices and Their Applications to Communications and Measurements

Tadao Nagatsuma[1,2] **and Yuichi Kado**[1]

[1]NTT Microsystem Integration Laboratories, NTT Corporation
3-1 Morinosato Wakamiya, Atsugi, Kanagawa 243-0198, Japan
[2]Graduate School of Engineering Science, Osaka University
3-1 Machikaneyama, Toyonaka, Osaka 565-8650, Japan

Abstract— Microwave photonics (MWP), which merges radio-wave and photonics technologies, has recently attracted increasing interest. This paper provides an overview of the status of MWP technology, focusing on a system concept and enabling devices, and describes some of the latest applications, such as high-speed wireless communications, non-invasive electric-field sensors, and spectroscopy.

1. INTRODUCTION

The recent explosive growth in communications has been brought about by wired (fiber-optic) and wireless (radio-wave) communications technologies. These two technologies have started to merge to create a new interdisciplinary area called **M**icrowave **P**hotonics (MWP) [1]. In addition, viewing the electro-magnetic spectrum with wavelengths progressively decreasing to the millimeter and submillimeter-wave bands on the radio-wave side and wavelengths progressively increasing to the infrared region on the light-wave side, we see that there is a large gap in utilization on the boundary between radio waves and light waves, i.e., the frequency band between 100 GHz and 10 THz. This untapped region represents a major resource for humankind in the 21st century (Fig. 1).

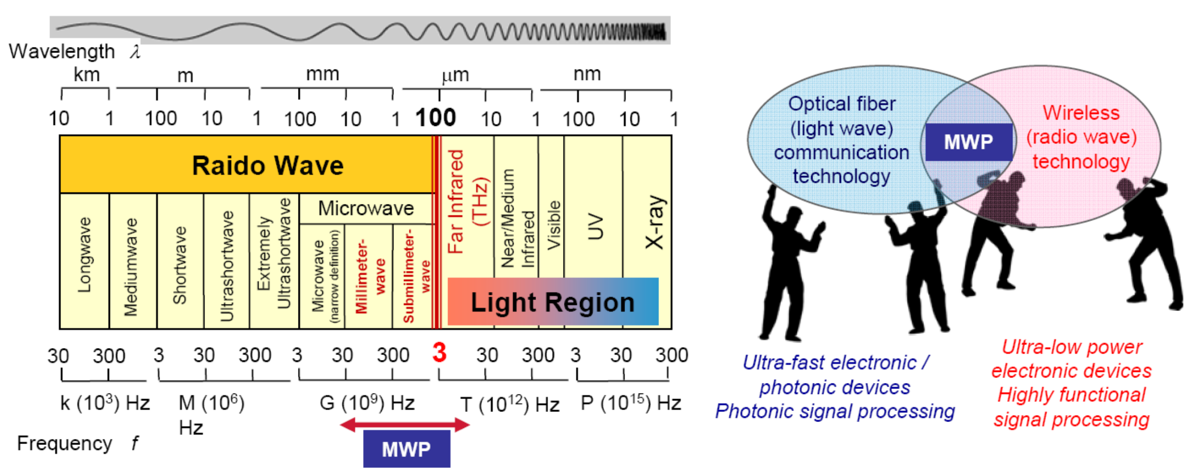

(a) (b)

Figure 1: Definition of MWP technology.

MWP technology aims at achieving advancement and improved functions in telecommunications systems that cannot be achieved by extension of individual technologies, mainly through the combination of radio-wave technology and photonic technology. At the same time, MWP technology is also expected to open up unused frequency bands through the fusion of different fields. The opening of new application fields other than communications is also expected.

This paper describes an overview of the status of MWP device technology and their latest applications.

2. MWP SYSTEM CONCEPT

Typical radio-wave application system is illustrated in Fig. 2. Wireless communication link consists of a transmitter (Tx) and a receiver (Rx) as shown in Fig. 2(a), and some kind of object is placed between the Tx and Rx in applications to measurement, testing, and sensing as shown in Fig. 2(b). Now, what happens when we introduce photonic technologies in Tx and Rx?

Figure 3 shows a block diagram of MWP-based transmitter, that is, a photonically assisted radio-wave transmitter. First, the optical (O) signal, whose intensity is modulated at microwave (MW) and/or millimetre-wave (MMW) frequencies, is generated by the optical MW/MMW signal source, and is delivered through optical fiber cables, and converted to the electrical (E) signal by a high-frequency O-E converter such as a photodiode. The converted signal is followed by a power amplifier and/or a frequency multiplier, and is finally radiated into free space by an antenna. The antenna unit can be separated and remotely controlled by optical fiber cables.

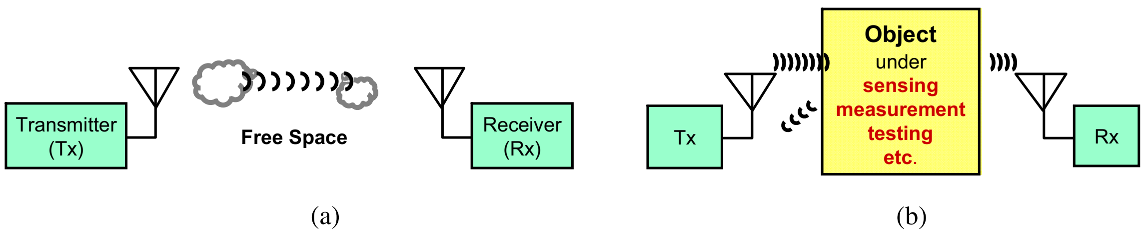

Figure 2: Radio-wave system for (a) communication, and (b) measurement.

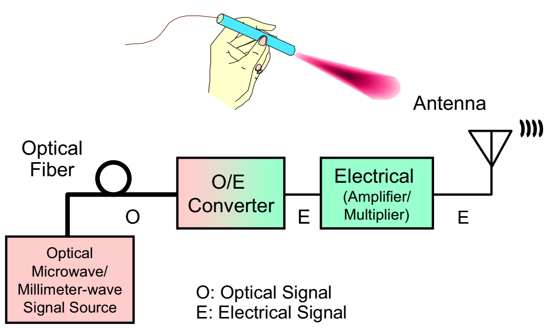

Figure 3: Photonically-assisted MW/MMW transmitter.

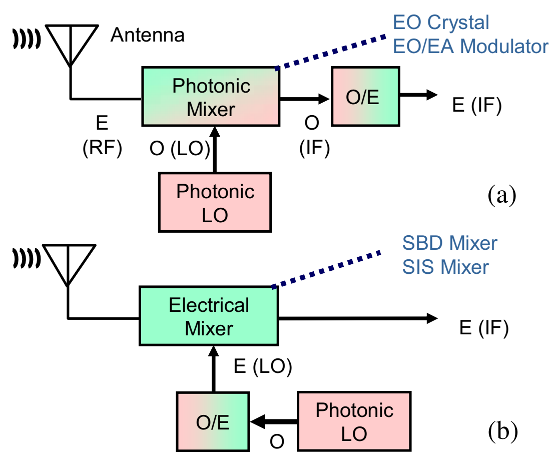

Figure 4: Photonically-assisted MW/MMW receiver.

Figure 4 shows two types of photonically-assisted radio-wave receivers; one employs a photonic mixer pumped by photonic local oscillator (LO) signals. Typical photonic mixer is a bulk electro-optic (EO) crystal, and optical modulator devices such as a $LiNbO_3$ waveguide EO modulator and a semiconductor electro-absorption (EA) modulator. Here, the optical intermediate frequency (IF) signal is converted to the electrical IF signal by a slow photodiode. The other type is based on a nonlinear electrical mixer such as a Schottky-diode mixer, and a superconducting (SIS) mixer. The LO signal is generated by a high-frequency photodiode followed by the optical MW/MMW signal source, as is used in the transmitter (Fig. 3).

3. ENABLING DEVICE TECHNOLOGIES

As for the optical MW/MMW source in Fig. 3, there are lots of options such as optical heterodyning using two frequency-tunable laser diodes, optical heterodyning using two modes filtered from a multi-frequency (wavelength) optical source or optical frequency comb generator (OFCG), the combination of a continuous-wave (CW) laser with an external modulator, and semiconductor mode-locked lasers (Fig. 5). Low-phase-noise and frequency-tunable optical MMW generators based on the optical heterodyning technique is shown in Fig. 6 [2].

Method	Frequency	Tunability	Stability/ noise
Heterodyning two LDs	Excellent >10 THz	Excellent >10 THz	Bad *frequency drift large linewidth*
CW LD + External modulator	Fair <100 GHz	Fair <100 GHz	Excellent *determined by electronics*
Mode-locked laser diode (passive/active)	Good Passive >1 THz Active 240 GHz	Bad <1 GHz	Excellent *only for active*
Optical comb (OFCG) + Filter	Excellent > 1THz	Excellent >1 THz	Excellent *determined by electronics*

Figure 5: Comparison of CW optical MW/MMW sources.

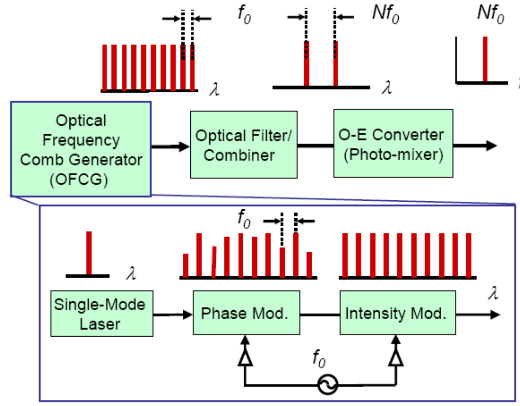

Figure 6: Example of optical heterodyning techniques.

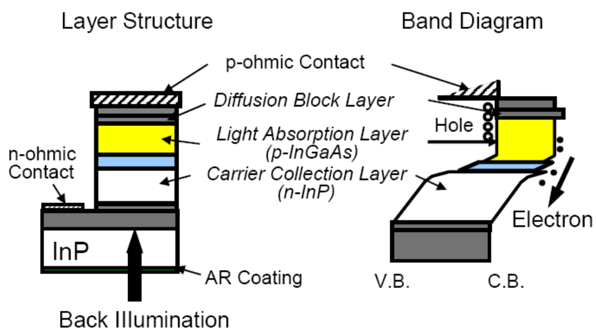

Figure 7: Structure of UTC-PD.

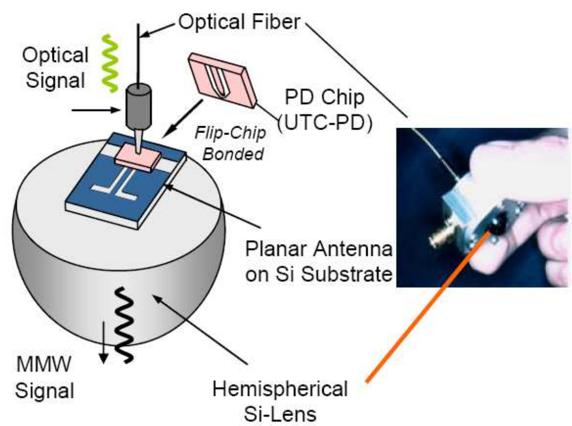

Figure 8: Example of photonic MMW emitter.

An O-E converter is a key device in the system. Since optical amplifiers with a high gain of over 30 dB and a large bandwidth of over 1 THz are now readily available, we need a high-power O-E converter to boost the signal generator performance. We used an ultrafast photodiode called a uni-traveling-carrier photodiode (UTC-PD), whose band diagram is shown in Fig. 7 [3]. Fig. 8 depicts an example of photonic MMW emitter, where the UTC-PD and the antenna are integrated [4].

As a good example of the photonic MMW receiver or detector, the electro-optic (EO) sensor made of a bulk EO crystal offers the largest bandwidth extending to the terahertz frequency region. The operation of the EO sensor is analogous to that of the down-converter in the electronic mixer operation as shown in Fig. 9(a). Fig. 9(b) shows the EO sensor attached to the optical fiber [5]. Highly sensitive EO materials used at an optical wavelength of 1.55 µm are CdTe and DAST. This EO sensor is also applicable to microwave regions, and is proven to be useful in the specific absorption rate (SAR) measurement at cellular phone frequency (1.5 GHz $\sim$ 2 GHz) [5].

4. SYSTEM APPLICATIONS

We have applied the photonic MMW transmitter to the 120-GHz-band wireless link system to realise a 10-Gbit/s transmission capacity [6]. Fig. 10 shows a block diagram of the wireless link. A high-gain Cassegrain antenna is used for a long distance (> 1 km) transmission. The wireless link can support the optical network standards of both 10 GbE (10.3 Gbit/s) and OC-192 (9.95 Gbit/s) with a bit error rate of 10^{-12}. We have also been successful in the wireless transmission of 6-channel uncompressed high-definition television (HDTV) signals using the link.

The ultralow-noise characteristics of the photonically generated MMW/THz-wave signal have been verified through their application to the LO for superconducting mixers in receivers used for radio astronomy. Radio-astronomical signals from the universe have been successfully observed using a 97.98-GHz photonic LO [7].

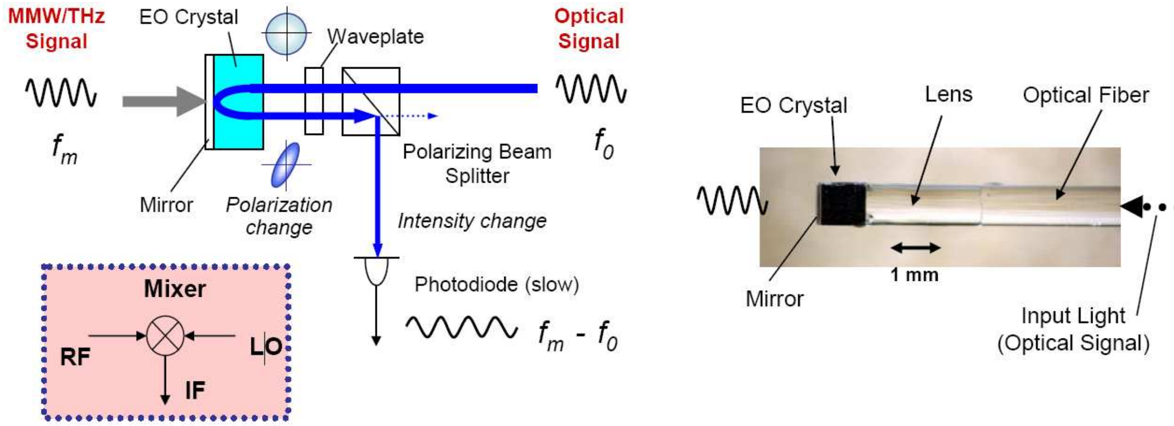

(a) (b)

Figure 9: Electro-optic sensor as photonic MMW down-converter, (a) block diagram, (b) example of EO sensor.

A great advantage of photonic LOs in spectroscopic measurement systems is their wide tunability. For this purpose, a wideband receiver has been tested with the same combination of superconducting mixers and a photonic LO at frequencies from 260 to 340 GHz [8]. MMWs/THz waves generated by the optical heterodyning using the OFCG and UTC-PD are successfully applied to the spectroscopy measurement [9, 10].

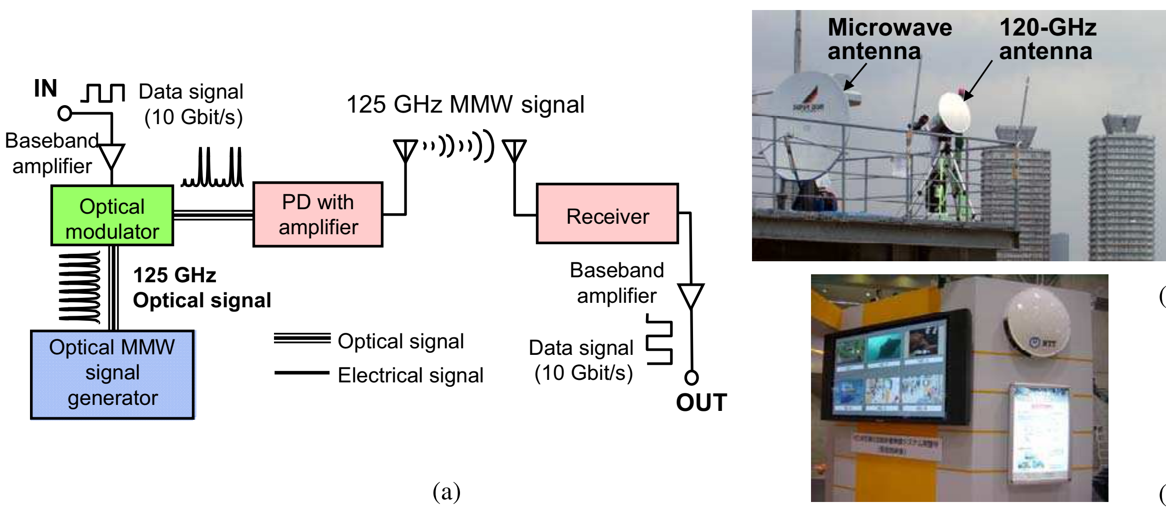

(a) (b) (c)

Figure 10: (a) Block diagram of 120-GHz-band wireless link. Photographs of (b) field trial and (c) application scene.

5. CONCLUSIONS

We described a brief overview of microwave and millimeter-wave photonics systems, and key devices incorporated in the system. The fusion of "wireless" and optical-fiber-based "wired" telecommunications technologies will continue to steadily advance in a form that will support the need for high speed and ubiquity in communications. Technology for the optical generation and detection of radio waves will become essential for various fields of measurement, as it facilitates the handling of ultra-high-frequency radio waves, which has been difficult with previous technologies.

ACKNOWLEDGMENT

The authors wish to thank Drs. A. Hirata, R. Yamaguchi, H. Takahashi, N. Kukutsu, H. Togo, N. Shimizu, H.-J. Song, T. Kimura, H. Ito, T. Furuta, T. Kosugi, K. Murata, K. Iwatsuki, H. Suzuki and M. Fujiwara for their contribution and support.

REFERENCES

1. Seeds, A., *IEEE Trans. Microwave Theory and Tech.*, Vol. 50, 877–887, 2002.
2. Hirata, A., et al., *IEICE Trans. Electron.*, Vol. E88-C, 1458–1464, 2005.
3. Ito, H., et al., *IEEE J. Lightwave Technology*, Vol. 23, 4016–4021, 2005.
4. Hirata, A., et al., *IEEE Trans. Microwave Theory Tech.*, Vol. 49, 2157–2162, 2001.
5. Togo, H., et al., *IEICE Trans. Electron.*, Vol. E90-C(2), 436–442, 2007.
6. Hirata, A., et al., *IEEE Trans. Microwave Theory Tech.*, Vol. 54, 1937–1944, 2006.
7. Takano, S., et al., *Publ. Astron. Soc. Japan*, Vol. 55, L53–L56, 2003.
8. Kohjiro, S., et al., *Tech. Digest of Intern. Workshop on Terahertz Technology*, 18B-6, 119–120, Osaka, 2005.
9. Song, H.-J., et al., *Tech. Digest of IEEE/LEOS Summer Topicals 2007*, TuC4.3, July 2007.
10. Shimizu, N., et al., *Tech. Digest of IRMMW/THz 2007*, 895–896, Sept. 2007.

Terahertz Emission from Two-dimensional Plasmons in High-electron-mobility Transistors Stimulated by Optical Signals

Y. M. Meziani[1], T. Suemitsu[1], T. Otsuji[1], and E. Sano[2]

[1]RIEC, Tohoku University, Sendai, Japan
[2]RCIQE, Hokkaido University, Japan

Abstract— We review on a recent advances of room temperature emission of terahertz radiation from a new developed devices. We interpret the results as a self oscillation of the plasma waves. The devices was stimulated by optical excitations.

1. INTRODUCTION

Developing solid states devices which can emit terahertz radiation at room temperature is very important for nowadays industrial applications. The oscillation of electron density in two-dimensional (2D) system of high-electron mobility transistors (HEMT's) have attracted much attention due to their potentiality promoting emission of terahertz radiation [1, 2]. For sub-microns size transistors, the resonant frequency falls in terahertz range and can be tuned by the electron density (i.e., the gate bias). Low temperature emission was experimentally reported first by impulsive excitation [3] and then by dc current excitation on 60 nm gate length HEMT device [4]. The emission at room temperature is under investigation and a signature of emission at room temperature was recently observed on GaN based transistors [5].

In the present work, we report on room temperature generation of terahertz radiations from two different architecture grating gate HEMT devices. Experimental results shows an enhancement of the emission by using double-decked HEMT. We interpret the emission as consequence of the self oscillation of the plasma waves promoted by optical excitation.

2. DEVICES STRUCTURE AND OPERATION PRINCIPLE

2.1. Metallic Grating Gate

The device structure is based on InGaP/InGaAs/GaAs material system and incorporates dual interdigitated grating gates (G1 & G2) that periodically localize the 2D plasmon in sub-micron regions with 100 nm interval (Fig. 1(a)). The 2D plasmon layer is formed with a quantum well in the InGaAs channel layer. The grating gate was formed with 65-nm thick Ti/Au by a standard liftoff process. Table 1 represents the characteristics of tree samples with different geometry. In case of sample 3, the GaAs substrat was thinned down to a thickness of 43 μm, and 100 nm thick ITO (indium titanium oxide) transparent metal was sputtered on the optically polished back surface to form the vertical cavity which make a resonant cavity of the emitted electromagnetic radiations.

Table 1: Samples dimensions.

	L_{G1} (nm)	L_{G2} (nm)	nb of fingers L_{G1}/L_{G2}	ungated (nm)	L/W (μm)
Sample 1	100	300	150/151	100	75/30
Sample 2	100	1800	37/38	100	75/30
Sample 3	70	350	60/61	80	30/75

2.2. Double Decked HEMT

The heterostructure of this device consists of double-decked high electron mobility transistor (HEMT) where the upper-deck HEMT works as a grating antenna to convert the non-radiative plasmonic wave in the lower-deck HEMT channel to radiative THz electromagnetic wave. Fig. 1(b) shows more details about the material structure of the device. The gate length is 100 nm for G1 and 350 nm for G2. The ungated region length is 100 nm. The total length and width is 30 μm and 75 μm respectively.

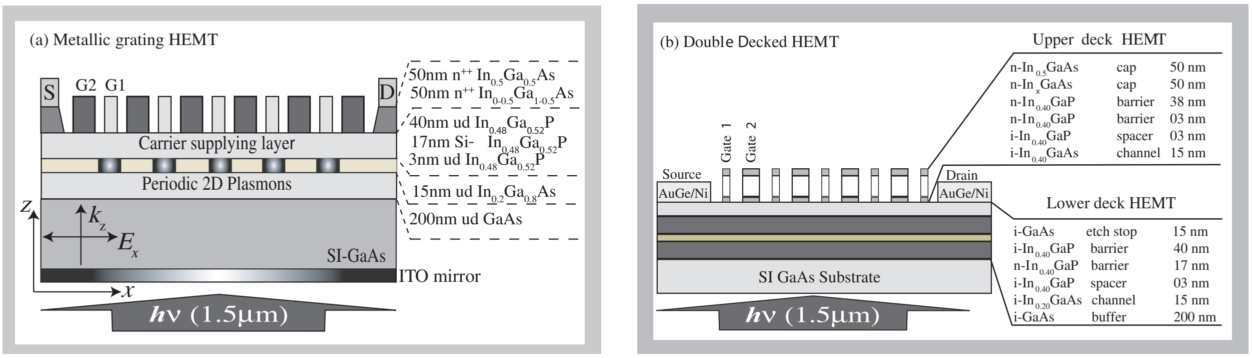

Figure 1: Device structure.

2.3. Operation Principle

When the plasmons cavities under G1 regions are highly charged ($n_s \approx 10^{12}\,\mathrm{cm}^{-2}$) and the regions under G2 are close to be depleted ($10^{10} \leq n_s \leq 10^{11}\,\mathrm{cm}^{-2}$), the photoelectrons are first generated under G2 regions due to the voltages applied on G2 and to more unoccupied electronic states (inset of Fig. 2(b)). If a specific drain-to-source bias is applied to promote a uniform slope along the source-to-drain direction on the energy band, photoelectrons under G2 are unidirectionally injected to one side of the adjacent plasmon cavity under G1. This may excite the plasmons under an asymmetric cavity boundary [2, 6]. It is noted that the laser irradiation may excite the plasmon not only in the regions under G1 but also in the regions under G2 if the cavity size and carrier density of the regions under G2 also satisfies the resonant conditions. The discrepancy between the gate biases of G1 and G2 can enhance the oscillations of the plasma waves via increasing the drift velocity of the photoelectrons injected in the plasmon cavities [7].

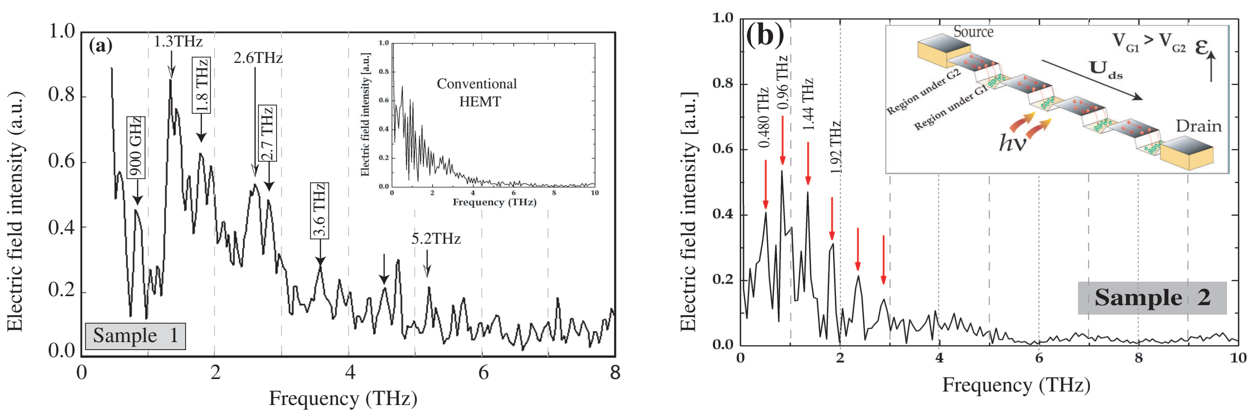

Figure 2: (a) Fourier spectrum for sample 1 with $L_{G2} = 300\,\mathrm{nm}$. The device was biased at $V_{DS} = 3\,\mathrm{V}$, $V_{G1} = 0\,\mathrm{V}$, and $V_{G2} = -1.4\,\mathrm{V}$. Inset shows the case of conventional HEMT without grating. (b) The same spectrum was obtained for sample 2 ($L_{G2} = 300\,\mathrm{nm}$, $V_{DS} = 3\,\mathrm{V}$, $V_{G1} = 0\,\mathrm{V}$, and $V_{G2} = -2.5\,\mathrm{V}$). Inset shows the self oscillation schematic principle.

3. RESULTS AND DISCUSSION

3.1. Reflecting Electrooptic Sampling

In order to study the emission of THz radiation from the device the temporal electromagnetic response to impulsive photoexcitation was measured at room temperature by using a dedicated reflective electro-optic sampling system (REOS). The device was subjected to a 1.5 μm fiber laser pulse with a FWHM of 70 fs from the back surface. More details about the experiment can be found in Ref. [8]. The final results are obtained after making Fourier transforms of the original temporal spectrum. Inset of Fig. 2(a) shows the Fourier transformed spectrum of a conventional HEMT without any grating. It shows monotonic decreasing as a function of the frequency. However for sample 1, biased at $V_{DS} = 3\,\mathrm{V}$, $V_{G1} = 0$ and $V_{G2} = -1.4\,\mathrm{V}$, shows a resonant-like peaks over a wide frequency range demonstrating emission of terahertz electromagnetic radiation. In particular, it's inferred that the spectral peaks at 900 GHz and its harmonic frequencies (1.8, 2.7, and 3.6 THz) are originated from the plasmon modes excited in the plasmon cavities under the G1 regions (Fig. 2-(a)). The other subset of residual peaks at 1.3 THz and its harmonic frequencies (2.6 and 5.2 THz) are originated from the plasmon modes weakly excited in the plasmon cavities under the G2 regions (Fig. 2(a)). This is because the electron density in the regions under G1 is higher by almost one order of magnitude than that in the regions under G2 while the cavity size of the regions under G1 is three times larger than those under G2 so that the plasmon-resonant frequencies among them becomes in close proximity. To avoid the resonance of the 2D plasmon under G2 regions, sample 2 with longer G2 (L_{G2} = 1800 nm) has been investigated. The correspondent Fourier spectrum is shown in Fig. 2(b). The fundamental frequency at 0.48 THz and its harmonics (0.96, 1.44, 1.92, and 2.88 THz) are clearly marked. The length of regions under G2 is 1800 nm therefore the resonant frequencies are much lower. Thereby the resonant of the regions under G2 are not observed for sample 2.

For both samples, the peaks are observed at specific bias conditions: V_{DS} = 3 V, V_{G1} = 0 V, $V_{G2} = -2.5$ V or -1.4 V. The drain-to-source bias was applied to increase the drift velocity of electrons in the channel which can enhance the oscillations of plasma waves. The potential discrepancy between V_{G1} and V_{G2} increase the drift velocity of the injected photoelectrons from the regions under G2 to the regions under G1 which can also enhance the plasmon resonance [7]. When the regions under G2 are depleted and the device is illuminated, photoelectrons are firstly generated in the cavities under G2 regions. Due to the slope of drain-to-source (V_{DS} = 3 V), the photoelectrons are injected to the G1 regions which enhance the plasmon instability leading to room temperature emission of THz radiation.

3.2. Bolometric Detection

The device is illuminated by a 1.5-μm CW laser from the backside. Electromagnetic wave emitted from the device is detected with a high sensitive Si-bolometer cooled down to 4.2 K through a filter permitting a frequency range between 0.5 to 3 THz. A lock-in technique is used for the measurement. The output of the bolometer is shown in left plot of Fig. 3 as a function of V_{DS} for double-decked HEMT. Drain-to-source bias increases to the knee voltage from which the transistor

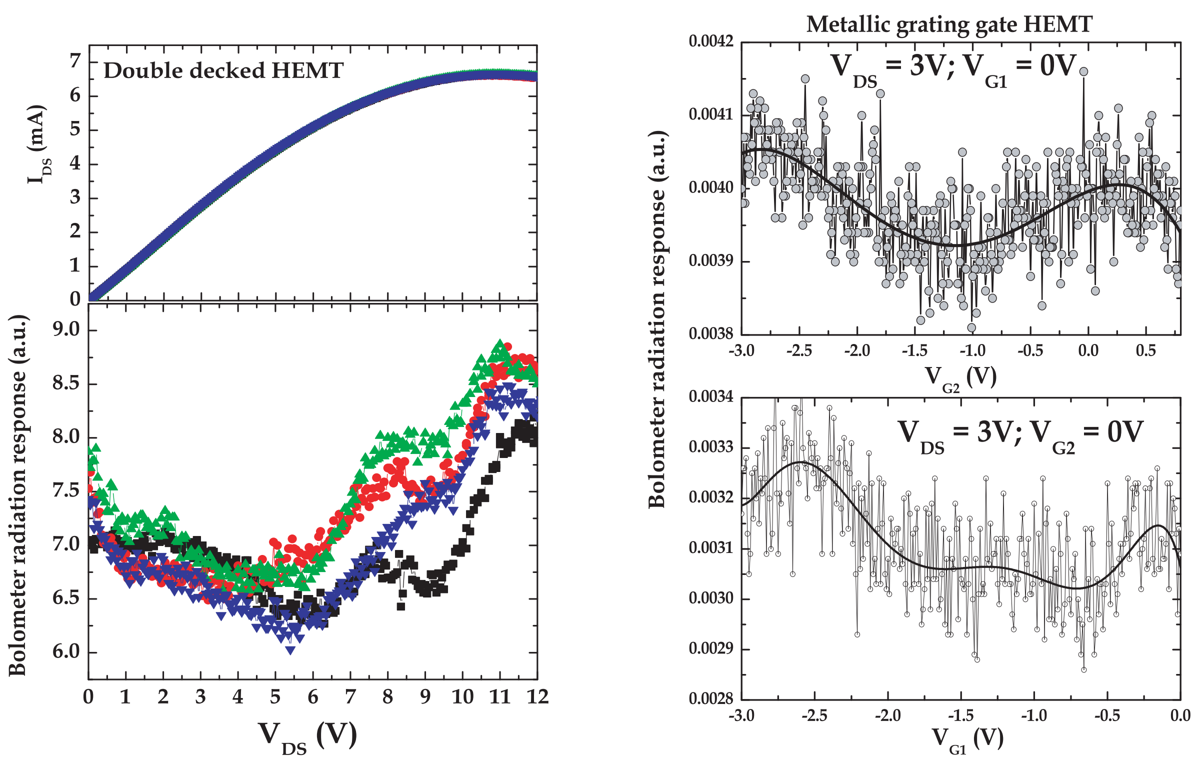

Figure 3: Left plot: Bolometer output (bottom) and drain current (I_{DS}) (top) of double-decked HEMT THz-wave emitter as a function of drain voltage (V_{DS}). Measurement took place four times. Right plot: Bolometer output for sample 3 (metallic grating gate HEMT) as a function of G2 and G1 bias. V_{DS} was fixed at 3 V.

is operated in the saturation region. The bolometer signal starts increasing at around 6 V and two clear peaks are observed at 8 and 11 V. These features were observed with good reproducibility as shown in left plot of Fig. 3. Note that the V_{DS} range is high because the double-decked HEMTs in this work suffer from large parasitic source and drain resistance. Nevertheless the double-decked device exhibits more drastic change in the bolometer signal with increasing V_{DS}. This result supports the idea of low-conductive gate stack to enhance the THz radiation efficiency [9], and therefore indicates that the proposed double-decked HEMT structure is a promising candidate to realize solid-state THz-wave emitters with high power and large efficiency. The right plot of Fig. 3 shows the bolometer response obtained on sample 3 (metallic grating gate). The signal is shown as a function of V_{G2} and V_{G1} where the drain-to-source bias was fixed at 3 V. Two peaks are observed: the first one around $V_{G2} \approx -2.6$ V related to the self oscillation of the plasma waves in the cavities under G2. The photoelectrons are generated under G2 regions and then injected to regions under G1 resulting in excitation of the plasma waves. The other peak around $V_{G2} \approx 0.25$ V. At this bias conditions both G1 and G2 voltages are similar, however the sheet electron density in the cavities under both regions are different due to the difference of the threshold voltage. The self oscillation of the plasma waves can also occur at this condition. According to well recognized responsivity ($10^5 - 10^6$ V/W) for the Si bolometer used, the emission power is roughly estimated to be 0.1 μW from a single device.

4. CONCLUSION

We reported on experimental investigations of room temperature emission of terahertz radiation from a developed devices. Double-decked HEMT shows a lower-noise signal as a function of V_{DS} than those obtained by metallic grating gates. The result was interpreted as a self oscillation of the plasma waves due to stimulation by optical excitations.

ACKNOWLEDGMENT

This work was financially supported in part by the SCOPE program from the MIC, Japan and by the Grant in Aid for Scientific Research (S) from the JSPS, Japan.

REFERENCES

1. Dyakonov, M. and M. Shur, "Shallow water analogy for a ballistic field effect transistor: New mechanism of plasma wave generation by dc current," *Phys. Rev. Lett.*, Vol. 71, 2465–2468, 1993.
2. Dyakonov, M. and M. S. Shur, "Detection, mixing, and frequency multiplication of terahertz radiation by two-dimentional electronic fluid," *IEEE Trans. Electron Devices*, Vol. 43, No. 3, 380–387, 1996.
3. Sekine, N., K. Yamanata, K. Hirakawa, M. Voseburger, P. Haring-Bolivar, and H. Kurz, "Observation of terahertz radiation from higher-order two-dimensional plasmon modes in GaAs/AlGaAs single quantum wells," *Appl. Phys. Lett.*, Vol. 74, No. 7, 1006–1008, 1999.
4. Knap, W., J. Lusakowski, T. Parenty, S. Bollaert, A. Cappy, V. V. Popov, and M. S. Shur, "Terahertz emission by plasma waves in 60 nm gate high electron mobility transistors," *Appl. Phys. Lett.*, Vol. 84, No. 13, 2331–2333, 2004.
5. Dyakonova, M., A. ElFatimy, J. Lusakowski, W. Knap, M. I. Dyakonov, M.-A. Poisson, E. Morvan, S. Bollaert, A. Shchepetov, Y. Roelens, C. Gaquiere, D. Theron, and A. Cappy, "Room-temperature terahertz emission from nanometer field-effect transistors," *Appl. Phys. Lett.*, Vol. 88, 141906(1–3), 2006.
6. Hanabe, M., T. Otsuji, T. Ishibashi, T. Uno, and V. Ryzhii, "Modulation effects of photocarriers on the terahertz plasma-wave resonance in high-electron-mobility transistors under interband photoexcitation," *Jpn. J. Appl. Phys.*, Vol. 44, No. 6A, 3842–3847, 2005.
7. Meziani, Y. M., M. Hanabe, T. Otsuji, and E. Sano, "Threshold behavior of photoinduced plasmon-resonant self-oscillation in a new interdigitated grating gates device," *Jpn. J. Appl. Phys.*, Vol. 46, No. 4B, 2409–2412, 2007.
8. Nagatsuma, T., "Measurement of high-speed devices and integrated circuits using electro- optic sampling technique," *IEICE Transactions on Electronics*, Vol. 76-C, No. 1, 55–63, 1993.
9. Otsuji, T., M. Hanabe, T. Nishimura, and E. Sano, "A grating-bicoupled plasma-wave photomixer with resonant-cavity enhanced structure," *Optics Express*, Vol. 14, No. 11, 4815–4825, 2006.